Power Transmission and Motion Control

PTMC 2006

Go to Contents Page

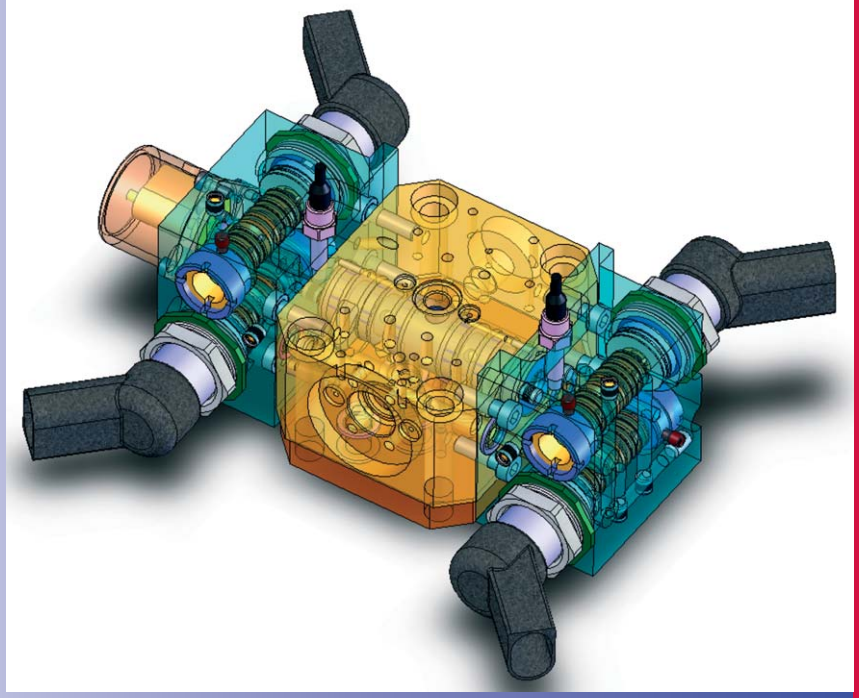

Dr D N Johnston
and Professor K A Edge
Editors

UNIVERSITY OF BATH

Centre for Power Transmission and Motion Control

Power Transmission and Motion Control

Power Transmission and Motion Control

(PTMC 2006)

Edited by

Dr D N Johnston
Workshop Organiser

Professor K A Edge
Acting Director

Centre for Power Transmission and Motion Control
University of Bath, UK

British Library Cataloguing in Publication Data

A catalogue record for this book is available from the British Library

Printed by:
Hadleys Ltd
13 Winstanley Way, Basildon, Essex SS14 3BP, United Kingdom
Tel: +44 (0) 1268 533121
Fax: +44 (0) 1268 286879
www.hadleyprint.com
e-mail: enquiries@hadleyprint.com

ISBN 08 6197 135 3

Printed in Great Britain

Front cover picture: Complete valve design
Back cover picture: An earthquake simulation table

Contents

Pneumatics

Applications

Systems and Control

Hydraulic Fluids, Sensors and Testing II

High Performance Valves

Return to Contents

Preface

The Power Transmission and Motion Control Symposium was held on 13-15 September 2006. It was co-sponsored by the IMechE and the Network of Fluid Power Centres in Europe (FPCE), and is the latest in a series which has been held annually at the University of Bath since 1988. The events have always attracted a global audience, and this time there were authors from 13 countries. Twenty-nine fully refereed papers were presented with a focus on motion control systems, with particular emphasis on hydraulic and pneumatic systems and components, including water hydraulics and 'smart' fluids and materials.

We would like to thank the authors for their contributions. Without the continued support and enthusiasm of authors, reviewers, delegates and staff, it would not have been possible to maintain such a long-running and successful series of events.

Special thanks are also due to Jane Phippen and Barbara Terry for their considerable assistance in compiling the material for this book and for organizing and ensuring the smooth running of the event. We are also grateful for the support from staff at Hadleys Ltd.

Professor K A Edge, *Acting Director*
Dr D N Johnston, *Workshop Organiser*
Centre for Power Transmission and Motion Control
Bath, September 2006

Centre for Power Transmission and Motion Control

FPCE
NETWORK OF FLUID POWER CENTRES IN EUROPE

Return to Contents

Energy Efficiency and the Environment

Calculation of the Energy Efficiency of a modern Hydraulic Injection Moulding Machine

J. Weingart, S Helduser
Institute of Fluid Power, Technische Universität Dresden, Germany

ABSTRACT

The paper deals with the energetic behaviour of hydraulic plants. A concept is introduced whereby one can calculate the energy efficiency of hydraulic systems right whilst the conception and dimensioning phase. The quality of the calculations is documented by the comparison with an experimental energy measured hydraulic system, in this case a injection moulding machine.

1 INTRODUCTION

Hydraulic drives have established their position in many stationary applications in the field of mechanical engineering and also in mobile machines. This fact results from their high power density, their compact design and the easy controllability of the hydraulic power. It is a clear advantage of hydraulic drives that their power density is one to two orders higher than that of electric drives: small natural inertia of the actuators, very small power/weight ratios and space requirements of the actuators and control elements. These properties make it possible to build compact and powerful drives.

The competition, which the hydraulic drive technology faces from electric drives, is often characterised by the fact that hydraulic drives have to compete with electromechanical solutions even in application fields that are typically hydraulic. As a result, they are forced to maintain their position whilst being subjected to an increasing pressure of demands made on them. The development of speed-variable electric drives and their invasion into applications that have undisputedly been reserved for hydraulic systems until now have established new and challenging demands on hydraulic systems.

A strong argument against the use of hydraulic drive solutions is the total efficiency that is not always optimised. When hydraulic drives are compared with electromechanical solutions, they demonstrate small power losses. Therefore, it is necessary to provide them with highly efficient motor-pump units (generative part), low-loss control and transformation components (conductive part) and motors and cylinders (actuator part)

Power Transmission and Motion Control 2006 Edited by Dr D N Johnston and Professor K A Edge

which display high efficiencies. To improve the competitiveness of hydraulic drive systems it is therefore of vital importance to deal with the question of the energetic optimum of the total system. In this regard it is very beneficial to be able to assess and optimise the overall hydraulic system already in the design and dimensioning phases. This includes the discovery of principal losses, which occur e.g. in valves controlled systems or in LS systems, and the discovery of losses that are decisively influenced by the structural design of the total system. Software that can be used to calculate the energy efficiency in hydraulic plants has proved to be very beneficial. A concept of this software is presented here. A hydraulic system, which has already been transferred into practice, has been chosen to illustrate the principal functioning and the practical feasibility of the software developed. An excellent example for the competitive situation between hydraulics and electromechanics is their application in injection moulding machines for plastic materials /1,2/.

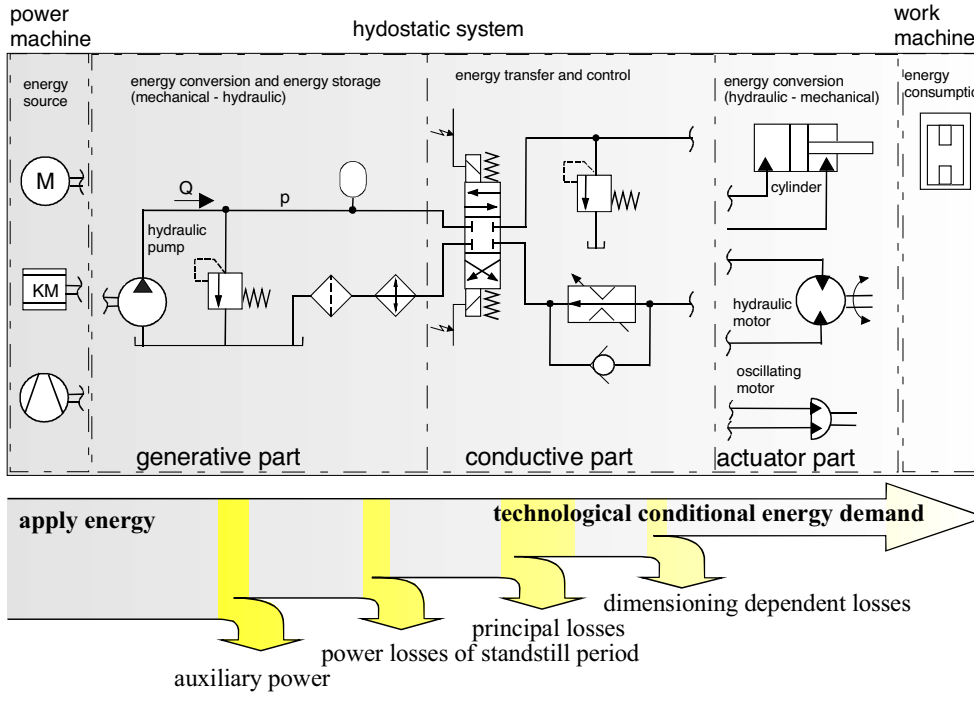

Fig. 1: Energy flow through a hydraulic system

2 SOFTWARE FOR ENERGY CALCULATION OF HYDRAULIC SYSTEMS

The calculation of the energy behaviour should be possible for any hydraulic system at variable work and load cycles. Hence commercial software for calculation of the dynamic behaviour of a hydraulic plant is considered. The selection of the simulation program was based on the aspect of importableness of an additional calculation plane for the energy analysis. All of the simulation results in this were carried out with the simulation software DSHplus from the company Fluidon GmbH.

2.1 Pilot surveys

The possible procedure to calculate the energy efficiency was based on a single hydraulic axis. The basic conceptual proceeding for the generation of the requiered software was then derived. For this purpose a valve controlled cylinder drive, as a typical drive structure in the hydraulics, was investigated. For the investigation of the energy efficiency it is necessary to understand the development of power over the axis.

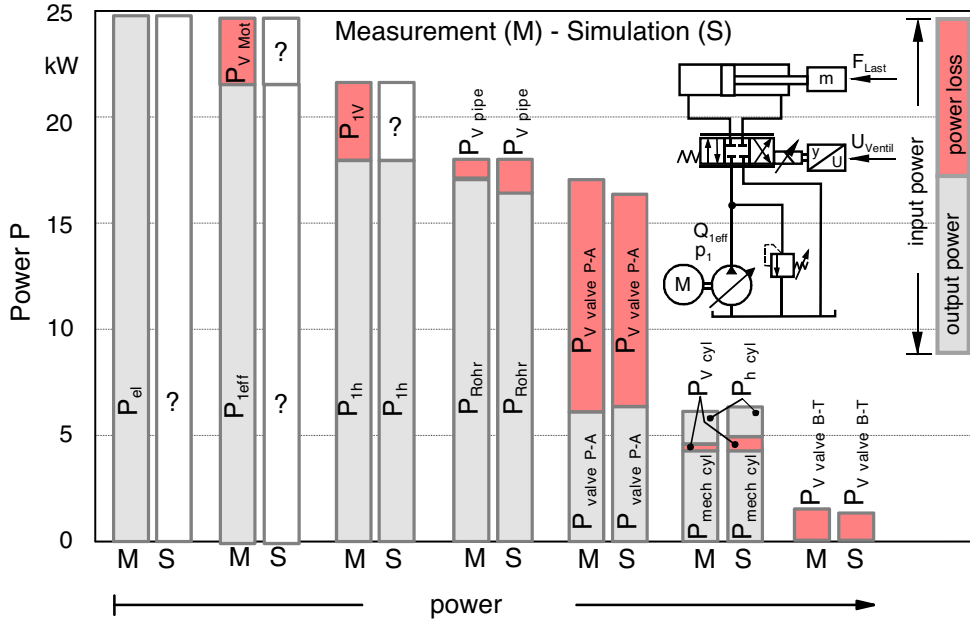

Fig. 2: Comparison of the results of measurement (M) and simulation (S)

Therefore it is advisable to find out the power loss P_V for each component of the axis. For the calculation of the development of power by means of the simulation software each element of the simulation model was extended from the level of the power balance. Thereto it is possible to take the resistance specification of several hydraulic components, that are incorporated in the simulation program.

Figure 2 shows the comparison of the results of measurement and simulation. The results characterise a static working point. Displayed is the power P as a couple of bars over each individual component of the cylinder axis. One for the measurement and one for the

simulation. One bar consists of three parts. The whole bar represents the input power Pzu, that is accepted by the components. Beyond the input power Pzu splits into the portion of the output power Pab (dark displayed) and into power loss Pv (bright displayed). The calculated and measured values for the conductive part (piping and valve) as well for the actorical part (cylinder) show an very good match. For the generative part of the hydraulic system it was not possible to calculate loss values. There is a lack of specification of loss characteristics for adjustable hydraulic displacement units.

2.2 Loss characteristics specification of hydraulic displacement units

The losses of hydraulic displacement units are allocated to hydraulic – mechanical losses and volumetric losses. In the catalogues of suppliers only few data of the whole operating map of the displacement unit are displayed (**Figure 3**).

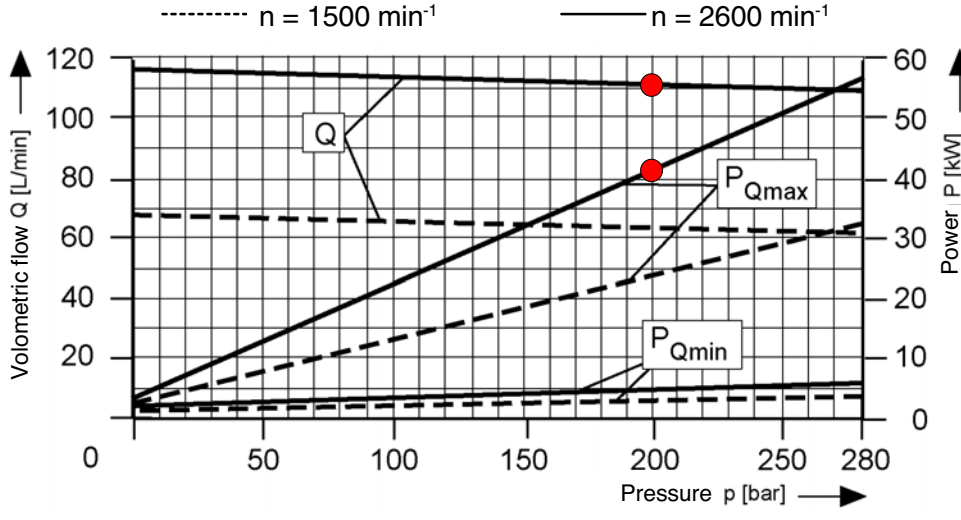

Fig. 3: Typical data of a supplier about the loss specification of a variable displacement pump

Thus a mathematical specification of the loss characteristics loss flow Q_V and loss torque M_V is necessary. That allows a calculation of the whole characteristic diagram of the displacement unit, based on the available catalogue values. The method of the Two Lines Model of Huthala /3/ describes the loss characteristics of constant units. The specification of the loss characteristics, depending on displacement angle α, is integrated in the software.

The principle of the Two Lines Model consists of the specification of the loss flow Q_V and of the loss torque M_V against the pressure p for minimum and maximum speed $n_{max,\ min}$ as well against speed n for minimum and maximum pressure $p_{max,\ min}$ (**Figure 4**). Thus the boundaries of the loss characteristic maps are described.

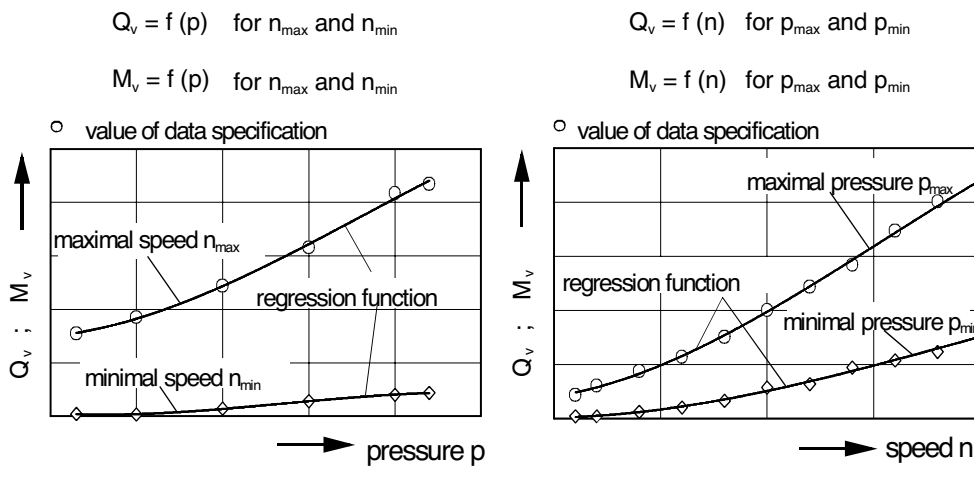

Fig. 4: Method of the Two Lines Model

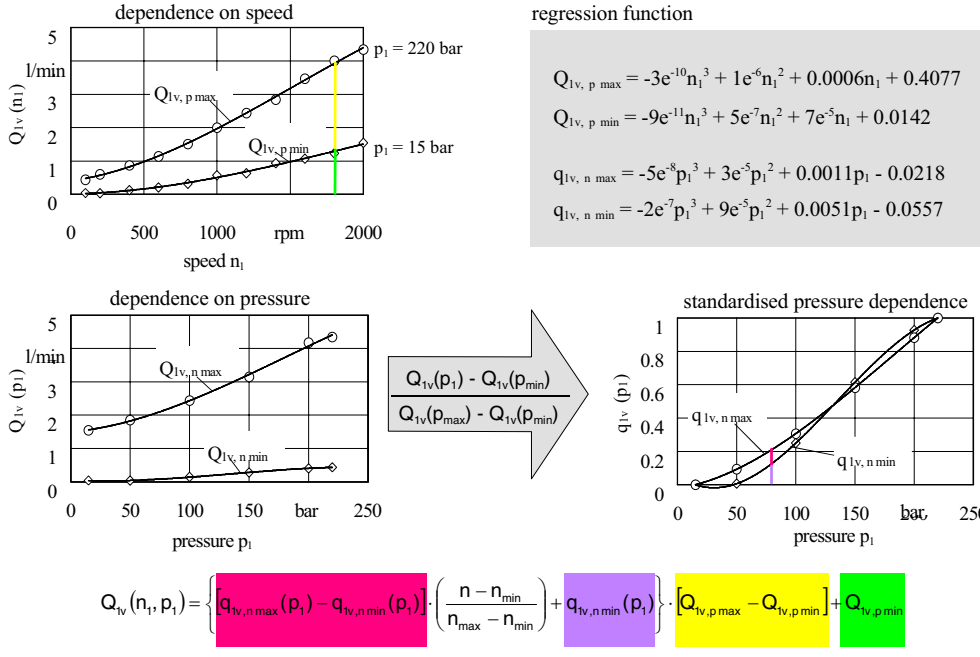

Fig. 5: Calculation of loss flow Q_V (n_1, p_1, $\alpha = \alpha_{max}$)

In **Figure 5** the methodology is displayed considering as example of the loss flow Q_V. From a few points, taken from the data of the supplier, a regression function is created. Therefore the loss flow is descibed with absolute values depending on the speed. The pressure-dependent loss flow is standardised between 0 and 1 from the minimum to the maximum pressure. This is done in each case for minimum and maximum speed. The

investigated regression functions hence can be abstracted to a mathematical term. The result is the loss flow Q_V (n_1, p_1) at maximum displacement angle α.

An equivalent proceeding is applied to specify the loss torque M_V. The thereby calculated loss characteristics were proved experimentally.

Figure 6 shows the loss flow Q_V, the loss torque M_V and the hence resulting loss power P_V exemplary for the analysed axial piston pump. This pump is used in the injection moulding machine, whose energy invetigation is shown below. The comparison of the measured and calculated loss characteristics shows a very good correlation. The flow loss diverge clearly from the catalogue values. The reason therefore is the dispersion of the pumps.

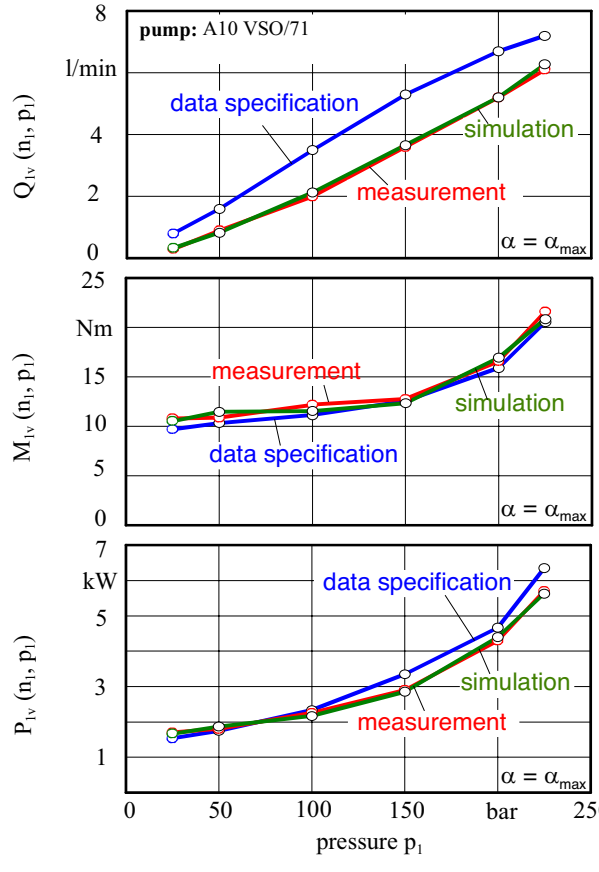

Fig. 6: Measured and calculated loss characteristics for an axial piston pump

So far the dependency of the loss parameters on the displacement angle α has not been considered. For that purpose the in Figure 5 displayed mathematical specification of the loss parameters is extended (**Figure 7**). It is assumed that the displacement angle dependent loss parameters vary much more with operating pressure than with variation of the speed. Because of this the speed-dependency for minimum and maximum operating pressure is

summarised. Afterwards the displacement angle dependent losses for minimum and maximum operating pressure will be standardised. Out of it one can create a factor, with that the mathematical specification can be extended for the loss flow Q_V (n_1, p_1, α_{max}). The result is the loss flow Q_V (n_1, p_1, α) depending on pressure, speed and displacement angle**.**

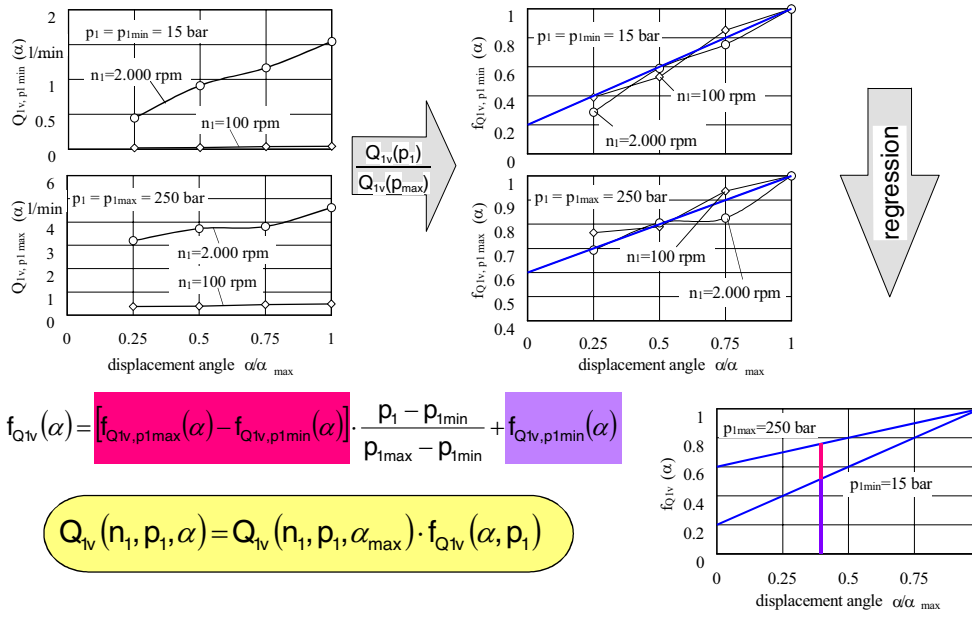

Fig. 7: Calculation of loss flow Q_V (n_1, p_1, α)

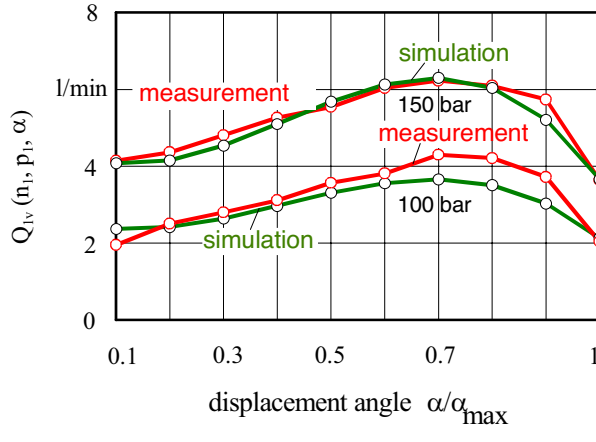

Fig. 8: Loss flow Q_V (n_1, p_1, α)

Figure 8 shows the measured and calculated loss flow Q_V depending on the displacement angle for two pressures.

The calculation of the loss parameter loss torque M_V has to be done in the same way.

2.3 Software tool

The above described specification of the loss parameters for adjustable hydraulic displacement units was converted into a discrete software tool. The discreteness has the advantage of independence from the simulation program. If need arises, it is possible to integrate the program into other simulation software or use it on its own. **Figure 9** displays several windows of the discrete software tool. One can import, save and retrieve data of several displacement units. The study has shown, that it makes sense to vary the degree of the polynomial of the regression function. This is feasible by one mouse click. In the result window the choice of the regression function can be monitored. The input values and the corresponding regression function are displayed.

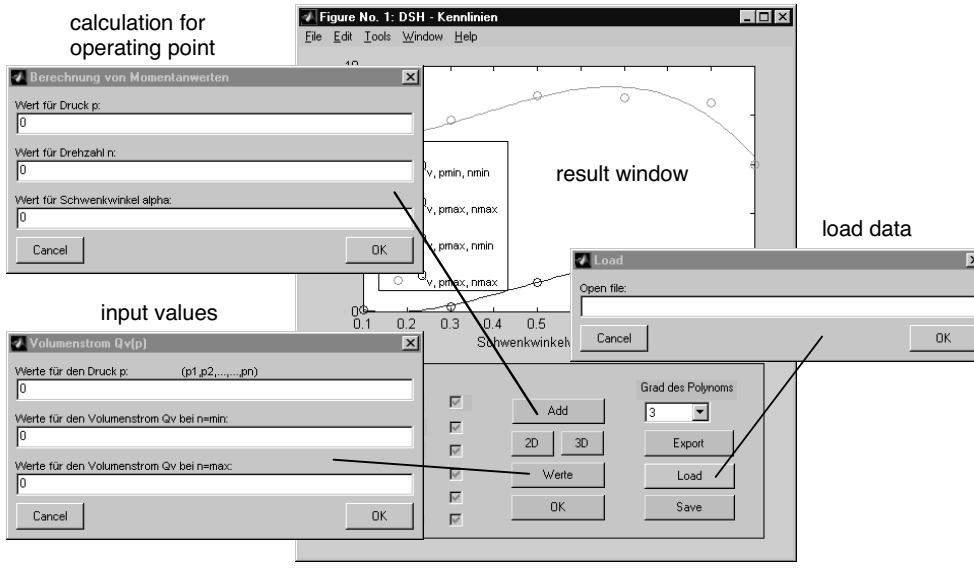

Fig. 9: User interface for software tool

For the accomplished workings the software tool for the specification of the loss parameters of adjustable hydraulic displacement units was integrated into the selected commercial simulation software. **Figure 10** shows the element "variable displacement pump" from DSHplus with integrated software tool.

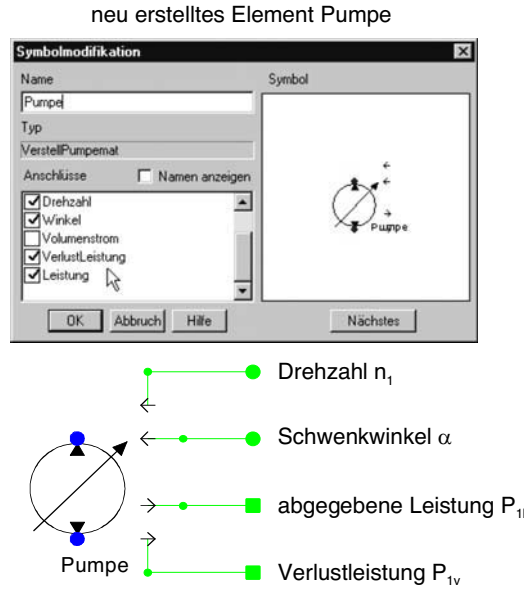

Fig. 10: Element variable displacement pump from the program library with software tool

3 ENERGETIC BEHAVIOUR OF THE MACHINE

The whole developed software for the energy analysis of hydraulic systems, consisting of the commercial simulation program extended by the level of power calculation with integrated software tool, was tested at a real hydraulic system.

The machine tested is a fully hydraulic machine with a clamping force of 600 kN. It is equipped with a single pump drive. The supply unit includes a standard asynchronous motor with a nominal power of P_N = 15 kW and a swashplate axial piston pump of the nominal seize 71 cm^3.

The principal structure consists of the four hydraulic axes – clamping unit, carriage cylinder, injection cylinder, screw drive motor and the supply unit. Ejector and possibly existing core pullers have not been part of the investigation.

A working cycle that is typical for this machine has been defined for further investigations. It is the combination of the motions of the individual axes as shown in **Figure 11**. It demonstrates the motions of the working cylinders for opening and closing the mould, the movement of the nozzle carriage unit and the injection and also the behaviour of the screw drive motor which is characterised by the plot of its rotational speed. Analogous to the circuit technique, the simulation model (**Figure 12**) of the injection moulding machine is divided into four hydraulic axes: the clamping unit, the carriage unit, the screw drive motor and the pump.

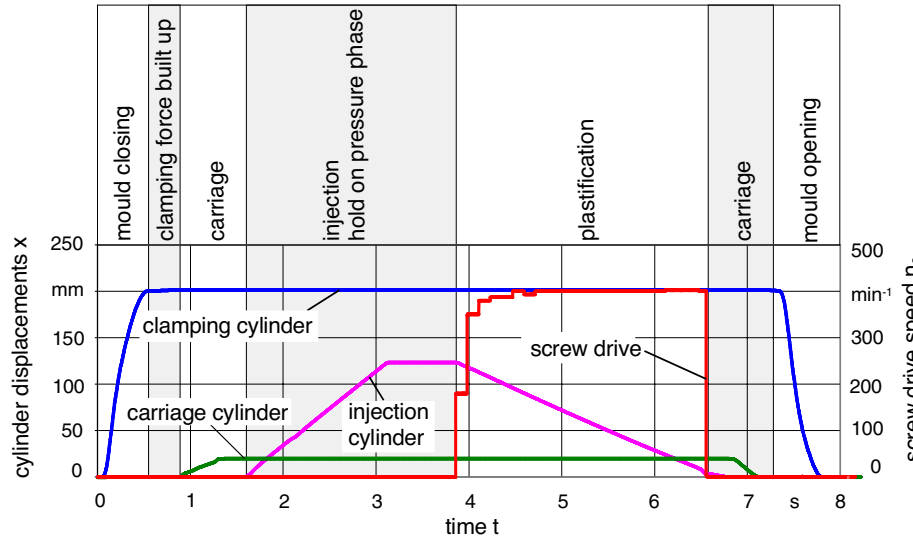

Fig. 11: Working cycle of the machine examined

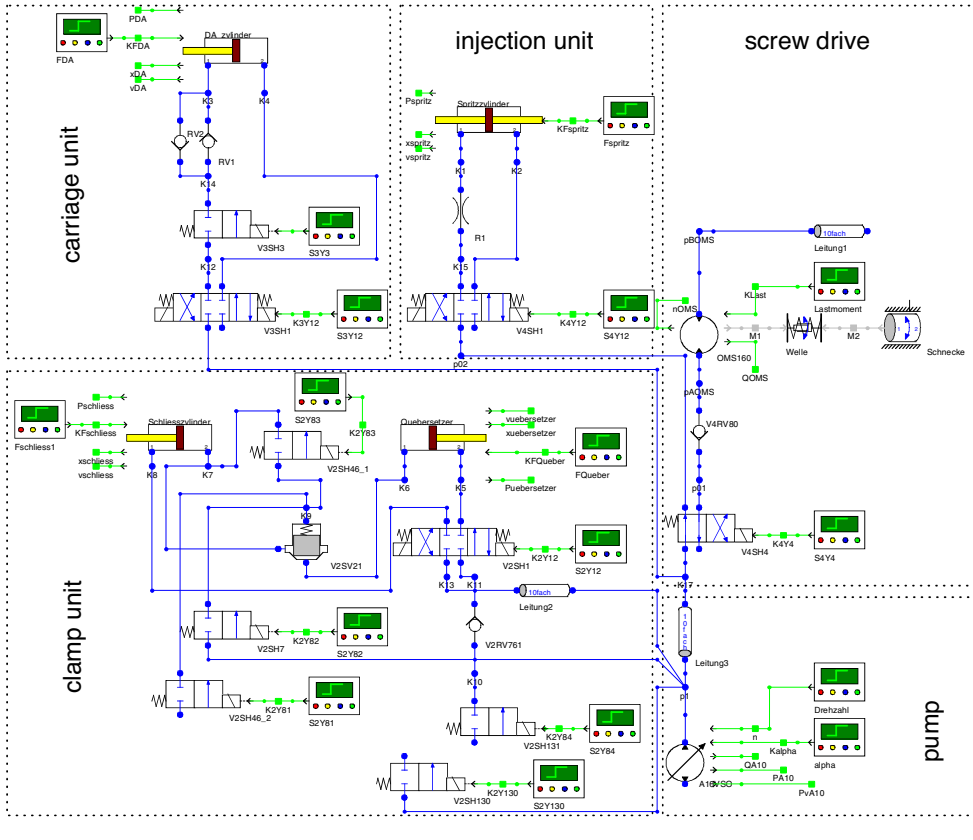

Fig. 12: Simulation Model for the injection moulding machine

Figure 13 shows the measured and calculated power and energy flow through the injection moulding machine. One can see a good correlation of measurement and calculation.

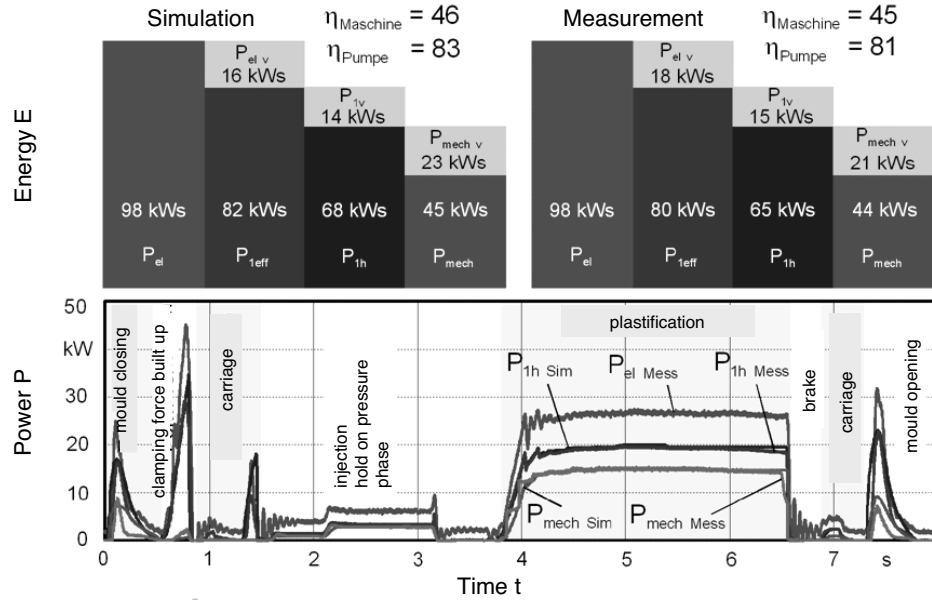

Fig. 13: Measured and calculated power flow in the machine

The result shows a very good total efficiency for the investigated fully hydraulic injection moulding machine. The biggest losses arise at the plastification. The applied plasticizing motor in this case was a low cost hydraulic motor. With a top quality component the total efficiency of the machine could be improved. In case of this fully hydraulic machine it would be in the range of fully electrical machines /4/.

4 CONCLUSIONS

The hydraulic drive technology is situated in permanent competition to other drive technologies. Electromechanichal systems, with the development of speed variable electric motors, thrust themselves into fields of applications, that previously were undisputedly reserved for hydraulics. Thereby the argument of better energy efficiency compared to hydraulic drive systems is used by the suppliers.

Because of this it is necessary to take the energy effriciency into consideration already in the conception and dimensioning phase of hydraulic systems. In this work a methodology to calculate the energy behaviour of a hydraulic plant is introduced. Commercial software for dynamic system simulation is extended by the level of power calculation.

An example of a fully hydraulic injection moulding machine and its components was used to demonstrate the capability of this calculation method. With the demonstration of the energy behaviour of the fully hydraulic injection moulding machine it was possible to show that with modern hydraulic drive concepts a very good total efficiency is achievable.

REFERENCES

/1/ Helduser, S.: Moderne hydraulische Antriebe und Steuerungen am Beispiel von Kunststoff-Spritzgießmaschinen
o+p 39 (1995) Nr.10

/2/ Feldmann, D.G.: Verbesserung der Wettbewerbssituation der Fluidtechnik
11. AFK, Aachen 1994

/3/ Huthala, K.: Comparsion of steady-state models of hydraulic pump
Proceedings of the 5th Scandinavian International Conference on Fluid Power (SICFP 98),
Linköping, 1997, Vol. 3, S. 139-156

/4/ Robers, Th.: Analyse des Betriebsverhaltens von vollelektrischen- gegenüber hydraulisch angetriebenen Spritzgießmaschinen
Dissertation 1994, RWTH Aachen

Improving efficiency in a linear cyclic motion

S HAIKIO, K HUHTALA and M VILENIUS
Institute of Hydraulic and Automation, Tampere University of Technology, Finland
J MÄKITALO
Finn-Power Oy, Kauhava, Finland

ABSTRACT

This paper deals with the energy consumption of the double-acting hydraulic cylinder. The main goal is to find out the method to maximize the efficiency of the hydraulic punching machine. There is presented a few alternatives to realize the system. The alternatives are analyzed by means of simulations with verified models.

The efficiency of the power unit has remarkable effect to the whole system. Variable pumps give flexibilities to save energy, but they are expensive and the control response is slow. The fixed pumps are cheaper, but there are some problems with energy efficiency on partial loads. The compressibility of the fluid also seems to be very remarkable to system characteristics.

According to the results the hydraulic supply power can be decreased 50% in the punching machine by means of the two pressure level system.

Power Transmission and Motion Control 2006 Edited by Dr D N Johnston and Professor K A Edge

NOMENCLATURE

$A_{1,2}$	Areas of punching cylinder [m^2]	p_r	Pressure level in the return chamber [Pa]
a	auxiliary variable [-]		
b	Viscous friction [Ns/m]	Δp	Change of pressure [MPa]
B_{eff}	Effective bulk modulus of system [MPa]	P_s	Power of punching period [W]
		R_m	Ultimate strength of sheet [N/mm^2]
F_{Cou}	Coulomb friction force [N]		
F_{load}	Load of punching piston [N]	t	Time of punching period [s]
F_s	Force of cutting [N]	V_0	Initial volume [m^3]
F_{s_sim}	Approximation cutting force [N]	ΔV	Change of volume [m^3]
h	Thickness of sheet [m]	W_s	Energy of one punching period [J]
l_p	Length of cutting line [m]		
m_{red}	Piston mass and reduced mass of fluid to piston [kg]	$\ddot{x}$	Acceleration of piston [m/s^2]
		$\dot{x}$	Velocity of piston [m/s]

1 INTRODUCTION

A double-acting hydraulic cylinder is used to realize the linear motion in many industrial applications. Hydraulic is almost irreplaceable in applications where high power level, stiffness and high accuracy is needed simultaneously. Examples of applications of the cyclic motion, where the motion starts from begin after each period, are forming, punching, pressing and cutting machines. In this paper the main aspect is to research the punching machine. The length of stroke varies from a three millimeters to forty millimeters in the studied applications. The maximum force is over 300 kN and the speed of cylinder is up to 1 m/s.

The curve of position of one cycle of the punching machine is shown in Figure 1. The cycle starts with the working stroke and after that follows the transfer time. During the transfer time the stroking cylinder is stopped and the working piece is shifted to the next position.

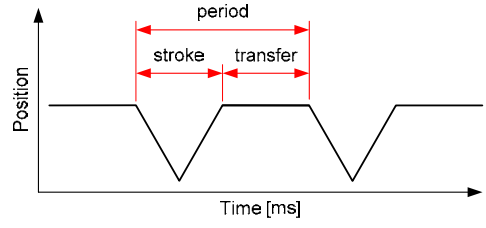

Figure 1. Typical duty cycle of the punching machine.

The maximum pressure and flow rate isn't needed simultaneously. The high pressure is needed only at part time of the stroke. During the fast out-stroke motion and return motion, the system is only partially loaded. The load varies during one cycle, but one has to pay attention to that the load varies between the stroke motions significantly. The system has to have power reservation to do the each cycle correctly. The typical flow rate and pressure level of one punching cycle of 1 and 7 mm plates are shown in Figure 2.

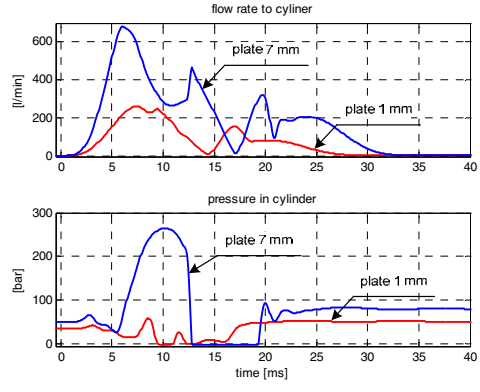

Figure 2. Typical flow rate and pressure level of punching of 1 and 7 mm plates.

At the beginning of the stroke the cutting tool is a few millimeters above the plate. When the piston is moving towards the plate, the load of the cylinder is only the inertia of the cylinder mass. When the tool meets the face of plate, the resistance is rising until the piece of plate is cut out. After this the load of the piston is disappeared very quickly. In Figure 3 there is presented the cutting process and in Figure 4 the typical force curve of cutting.

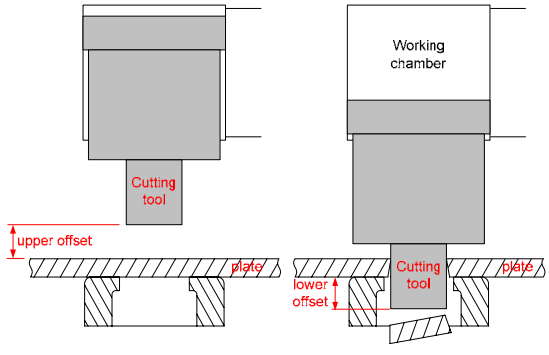

Figure 3. The cutting process

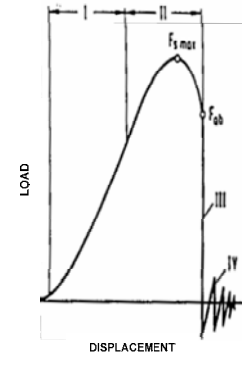

Figure 4. Typical cutting force curve [1]

The main goal of this study is to find out the solution to minimize the hydraulic power consumption of the punching machine. In the paper there is presented a few alternatives to realize the hydraulic circuit. In every case the double-acting cylinder is used with the servo valve.

2 BASIC CALCULATIONS

In the basic static calculations of the systems the mass of the fluid has reduced into the punching cylinder and the compressibility of the fluid has also taken into account. By means of the calculations the required power with different speed of stroke can be find out. The cutting force depends on thickness of sheet, material and length of cutting line. In the calculations the material of sheet and cutting line of tool is kept constant so the maximum 300 kN force is got with 8 mm sheet. The length of stroke depends on thickness of sheet. Calculated values are a good approximation of the system operating ranges. This information is necessary to compare the systems to others.

2.1 Compressibility of fluid

The compressibility of the fluid plays very important role in these systems, because the punching stroke is relatively short compared to the total stroke of the cylinder. The compressibility losses are more significant in short strokes.

The rising of the cutting forces is presented in Figure 4. The maximum cutting force can be calculated as follow:

$$F_s = l_p \cdot h \cdot R_m \tag{1}$$

where the l_p is the length of the cutting line, h is the thickness of the sheet and the R_m is the ultimate strength of the sheet.

In calculations and simulations there is used the following approximation of cutting force:

$$F_{s\_sim} = \left[-\frac{1}{2} \cdot \cos(2 \cdot \pi \cdot a) + \frac{1}{2} \right] \cdot lp \cdot h \cdot R_m, \tag{2}$$

where the a is a auxiliary variable that travel from zero to the thickness of sheet.

The theoretical need of energy in cutting is the area below the force curve (Figure 4). The cutting forces is lost rapidly, when the two thirds of the sheet has been cut. The area below the force curve can be calculated by integrating the force equation from zero to the point, where the piece of cutting is break down from sheet.

$$W_s = \int_0^{2/3 \cdot h} F_{s\_sim}\, dh \tag{3}$$

Theoretical needs of power can be calculated as follows:

$$P_s = \frac{W_s}{t}, \tag{4}$$

where t is the time of one punch.

The working chamber of the cylinder is connected to the control valve and the pressure level is depended on the load of the cylinder. Maximum pressure level during the punching period is calculated as follows

$$\Delta p = \frac{m_{red} \cdot \ddot{x} + b \cdot \dot{x} + \mu_{cou} + A_2 \cdot p_r + F_{load}}{A_1}, \quad (5)$$

where m_{red} is the piston mass plus the reduced mass of the fluid to the piston; b is the viscous friction, which is assumed to be 1500 Ns/m; F_{Cou} is the Coulomb friction force, which is experimentally defined to be 6000N, p_r is pressure level in return chamber and A_1 and A_2 are the areas of punching cylinder and F_{load} is the load of punching.

The compressed volume (depending on the pressure difference) can be calculated as follows:

$$\Delta V = \frac{V_0 \cdot \Delta p}{B_{eff}}, \quad (6)$$

Where V_0 is the initial volume of the cylinder and the hydraulic line between the cylinder and the servo valve, B_{eff} is the effective bulk modulus of the fluid plus pipes and hoses is assumed to be 1000 MPa.

3 DIFFERENT SOLUTIONS TO REALIZE THE CYCLE MOTION

There is presented alternatives to realize the cyclic motion in this chapter. The diameter of cylinder is calculated so that the maximum static force of the cylinder has to be at least 300 kN and the return force 60 kN. The maximum pressure level of the system is 300 bar. The used control valve is the servo valve. This requires also power to operate and it is taken into account in the calculations. The natural frequency is calculated in typical cutting point, which is 5 mm before the end of stroke.

3.1 2–edge control (Bypass control)

Roosen and Backé had named this system to bypass control. The system is presented in the conference paper, see reference [7]. In the paper there is compared the bypass control to 4-edge controlled system. According to the paper the energy saving is even 20 % compared to 4-edge control. The system consists of fixed displacement pump, pressure relief valve, control valve, cylinder and pressure accumulator (Figure 5). During the out-stroke motion the fluid is flowing to the cylinder without throttle losses. The throttle losses arise when the control valve is bypassing flow to the reservoir. The displacement at the piston rod side leads to an increase of the pressure in the accumulator. This energy is used to return the cylinder to the initial position. The natural frequency of the system is 1368 rad/s. The calculated operating range of the 2-edge controlled system is shown in Figure 6.

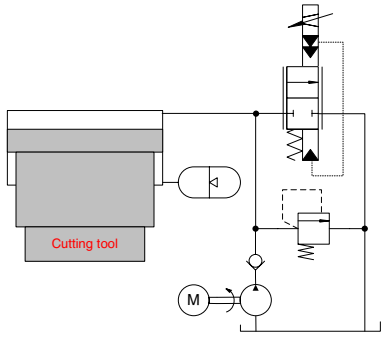

Figure 5. 2-edge controlled system.

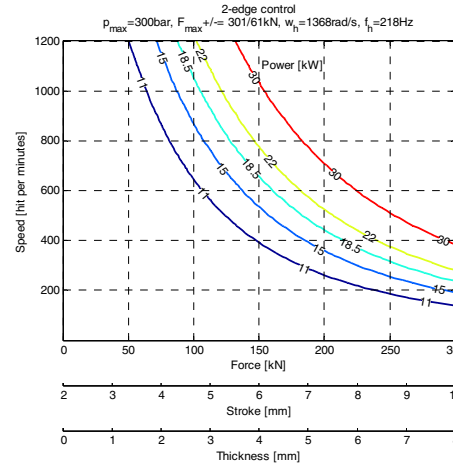

Figure 6. Calculated operating range of 2-edge controlled system.

Disadvantage of this system is the slow response time of velocity and pressure. The transient flow rate can be very high in this application and use of accumulator is impossible. The rising time of pressure depends on the initial volume of fluid and pressure depends on the resistance of the cylinder. For example, if the load generates 300 bar pressure to the working chamber of cylinder and there is 15 kW power available, the response time of pressure to maximum level is 29 ms.

This system is useful in the application, where the response time is sufficiently slow and the direct controlled valve is good enough. Using the pilot operated valve, it is impossible to generate the pressure to pilot line without extra pump.

3.2 3 –edge control

The system consists of pump, pressure relief valve, control valve and cylinder (Figure 7). In the punching event the instantaneous flow rate to the cylinder is quite large and accumulator in the supply line is necessary to compensate the flow variation. The pilot line to the servo valve can be taken from supply line. Natural frequency of the system is 1369 rad/s. The continuous operating range of the system is shown in Figure 8. The supply pressure is 300 bar.

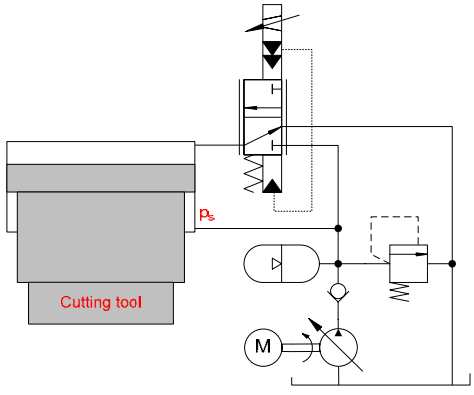

Figure 7. 3-edge controlled system.

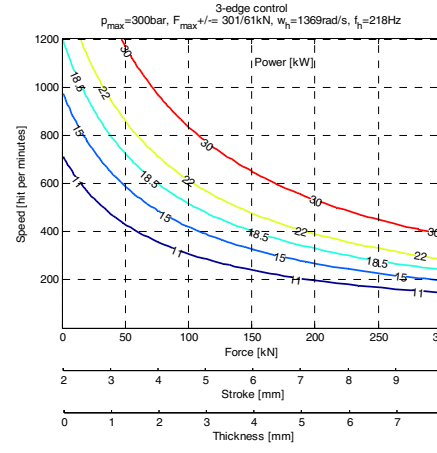

Figure 8. Operating range of 3-edge controlled system (pressure, 300 bar).

3.3 4 –edge control

Next the control valve is changed to 4-edge control valve (Figure 9). The natural frequency is now 1613 rad/s, which is a little higher than in the 3-edge controlled system. In Figure 10 there is presented the continuous operating range of the system, when the system pressure level is 300 bar.

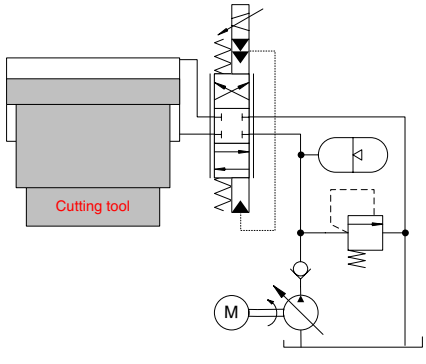

Figure 9. 4-edge controlled system.

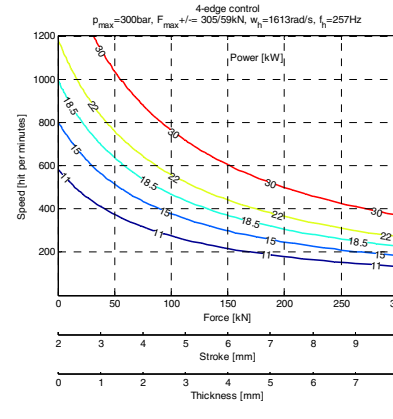

Figure 10. Operating range of 4-edge controlled system (pressure, 300 bar).

3.4 Multi area systems

The cylinder may have designed with several pressure chambers (Figure 11). The system is presented in the patent DE102004024354 A1 [5]. There is the extra volume in the top of the cylinder. This volume is switched to use by the selector valve, when the resistance of the cylinder is rising.

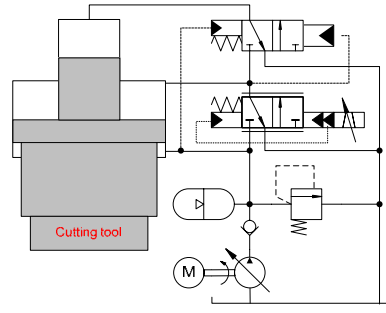

Figure 11. Cylinder with extra volume in the top of the piston.

In Figure 12 there is presented the other cylinder with several pressure chambers. The lowest chamber pumps the fluid from the reservoir to the supply line, when the load of the cylinder is low. When the pressure in the head of cylinder is rised by the load, the selector valve is switched to the other position. Now the fluid flows from the lower chamber to the reservoir. The return motion of the cylinder is done by the middle chamber. In this case the compressibility of fluid has a big role, because there are several pressurized chambers in the cylinder. The patent WO 2004/101263 A1 [4] is described more detailed of the system. In Figure 13 there is presented the continuous operating range of the system, when the system pressure level is 300 bar.

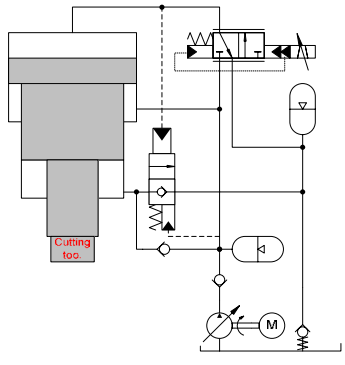

Figure 12. Three area system with pumping function.

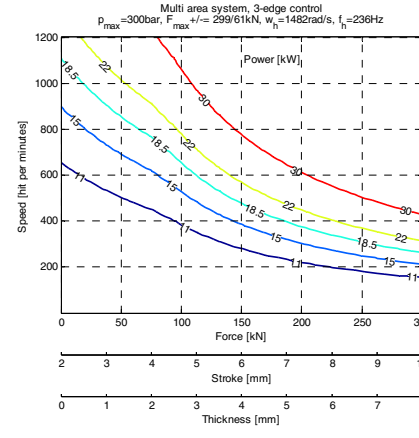

Figure 13. Operating range of three area system (pressure, 300 bar).

4 TWO PRESSURE LEVEL SYSTEMS

In punching machine the highest pressure level is only required a very short time, so it is natural to use two pressure level systems. The higher pressure can be realized by a high pressure pump or using a pressure booster.

In Figure 14 there is presented the two pressure level system, where the high pressure fluid is generated by using a booster pump. Normally the system is working with low pressure level, but when the cylinder meets resistance, the cylinder pressure increases to equal the pump supply pressure and the pressure booster begins to pump the high pressure fluid to the cylinder. The two pressure level system which is used for example in hydraulic press is shown in Figure 15. The low pressure line is used, when the cylinder resistance is low. The high pressure is generated only when the load of the cylinder is high. The problem of this system is that the pressure begins to rise not until the resistance of the cylinder is rising.

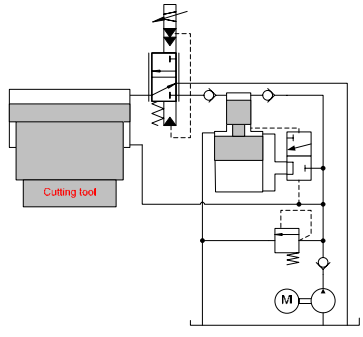

Figure 14. Booster generated high pressure level system.

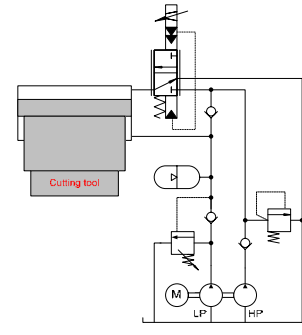

Figure 15. Parallel connected low and high pressure level system.

The disadvantage of the above mentioned systems is the low response time of pressure in the punching machine applications. In Figure 16 there is presented a genuine two pressure level system. There are two pressure circuits in the system and the high pressure level is selected by the pressure selector valve. Normally, when the resistance of cylinder is low, the low pressure circuit is used. When the load of the cylinder is rising, the pressure selector valve is switched to the other position and the high pressure circuit is used. The switching time of the pressure selector valve is 1 to 2 ms, so a little delay occur during the motion. The system is presented in the article [2].

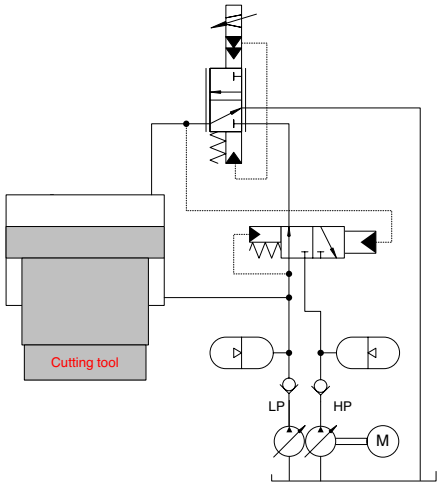

Figure 16. Two pressure level system.

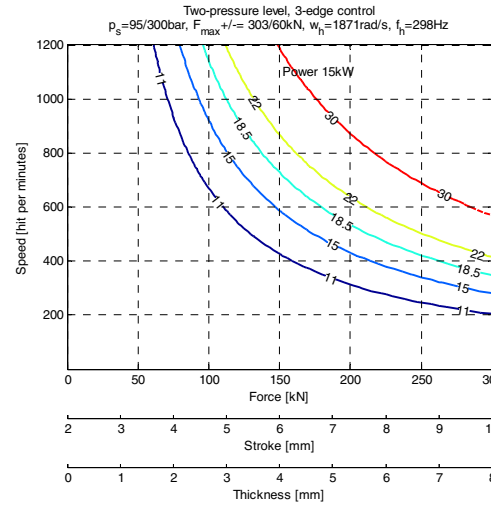

Figure 17. Operating range of two pressure level system.

4.1 Several pressure level cylinder

In Figure 18 there is presented the system where the several pressure levels in the cylinder are used. At first, when the load of the cylinder is low the low pressure level circuit is used and the lower chamber of the cylinder is connected to the low pressure circuit. When the load of the cylinder begins to rise, the selector valve connects the lower chamber of the cylinder to the reservoir. This decreases the resistance of the cylinder. If the load of the cylinder is still rising, the selector valve is connected into the high pressure circuit.

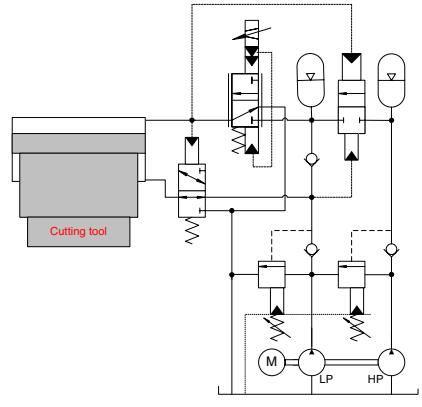

Figure 18. Several pressure level cylinder [3].

The hydraulic system can be also realized as a combination of the previous systems. The disadvantage of this system is the compressibility at the each volume and the switching delays in each selector valves.

4.2 Power unit calculation

The power unit can be realized either with a fixed or a variable displacements pump. By using the variable displacement pump it is possible to use the maximum power of the electric motor flexible. The disadvantage of this system is the price. The fixed displacement pump is cheaper, but there is problem to minimize the output losses of the power unit.

In Figure 19 there is presented the method to minimize the flow rate losses in the system. The output of the high pressure level pressure relief valve is connected to the low pressure level circuit.

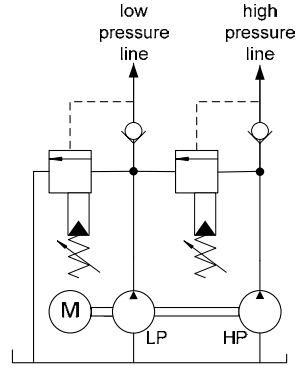

Figure 19. Power unit for two pressure level system.

In Figure 20 there is presented the calculated operating ranges of the different systems by using the variable displacement pump and the electric motor of power 18.5 kW. In Figure 21 there is presented the operating ranges with the fixed pumps. As it can be seen from figures the two pressure level system doesn't need so must power to cutting the sheet as the other systems.

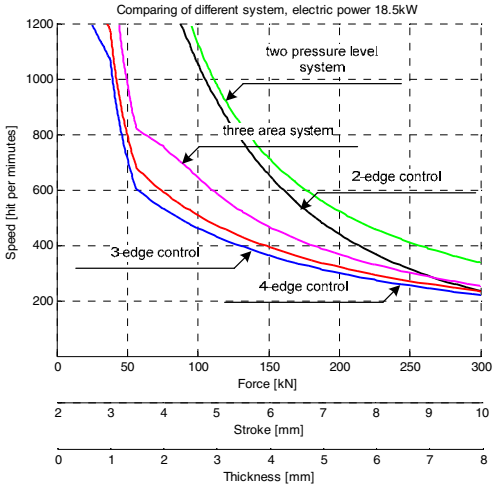

Figure 20.Operating range of the system with variable pump and 18,5 kW electric motor.

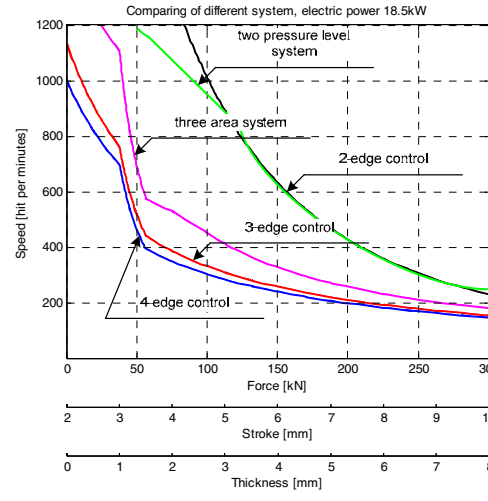

Figure 21. Operating range of the system with fixed pump and 18,5 kW electric motor.

The efficiencies of the studied systems have been compared in Figure 22. The efficiency of the system is calculated by comparing the need of power of each system to the theoretical needs of power (equation 4). As it can be seen from figure the efficiency with short length of stroke and low load of cylinder is poor. The compressibility of fluid plays in that case very important role.

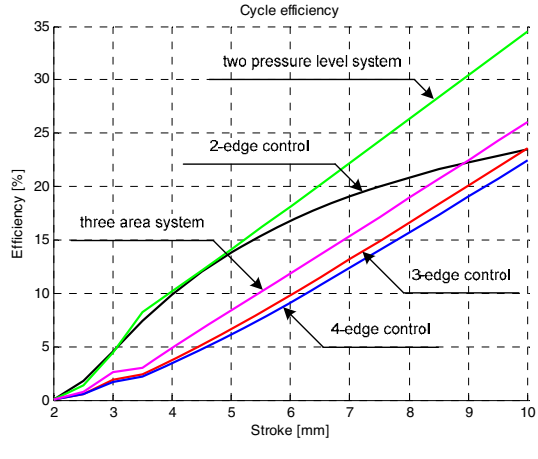

Figure 22. Comparison of efficiencies of the system

5 SIMULATION

Simulation of the different variations is done by AMESim simulation program. At the first the present machine is modeled and the model is verified. In the simulations the P-controller is used. The gain of the controller is changed depending on the length of stroke.

In Figure 23 there is presented the measured and the simulated results of the servo valve spool displacement and in Figure 24 the position curve of punching cylinder. It can be seen from Figure 24 that the simulated return motion (from 3 to 15 mm) is not as fast as measured one. There is lower gain in the simulation than in measurement because there is not allowed the overshoot during the motion.

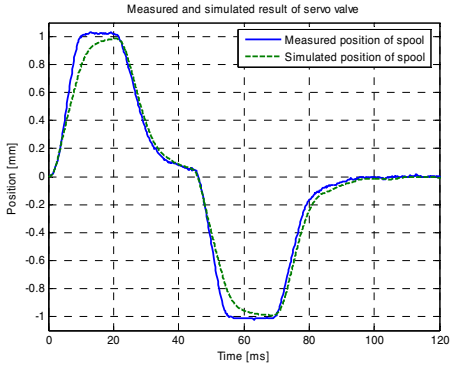

Figure 23. Servo valve spool lift (simulated and measured curves)

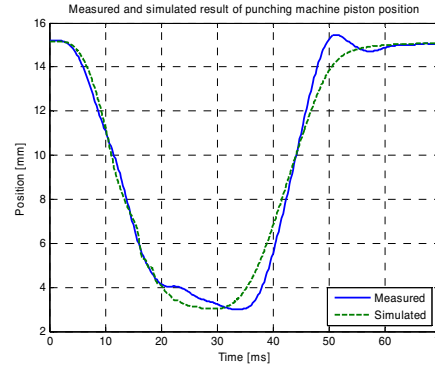

Figure 24. Punching cylinder lift (simulated and measured curves)

The simulation results of piston positions are shown in the next figures. In Figure 25 the thickness of sheet is 1 mm and 7 mm in Figure 26. As it can be seen from figures, the 4-edge controlled system is the fastest and 2-edge controlled system is the slowest. In Figure 25 there is oscillation after 50 second and in Figure 26 after 160 second in the 2-edge controlled system. In these points the sheet is cut and the load of cylinder is lost rapidly. The 2-edge by-pass controlled system isn't fast enough to slow down the speed of cylinder.

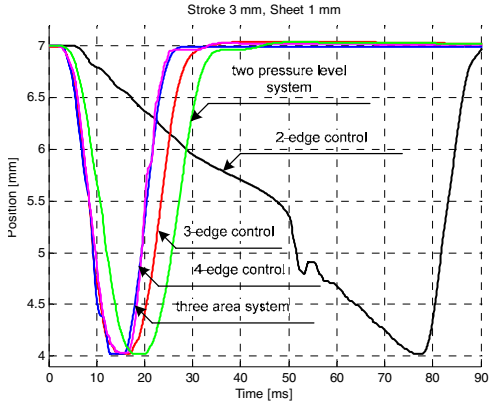

Figure 25. Simulated position curve of piston, thickness of sheet is 1 mm.

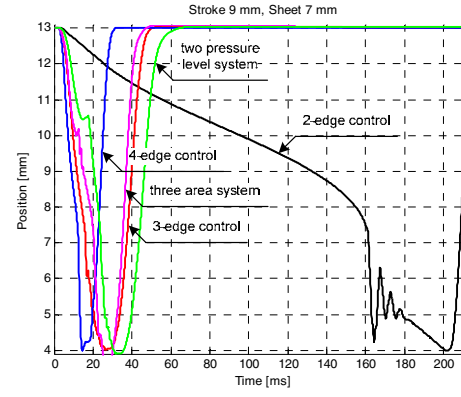

Figure 26. Simulated position curve of piston, thickness of sheet is 7 mm.

The simulated results of the required power of the studied systems are shown in Figure 27. The cutting speed is 200 hits per minutes in these curves. In the 3-edge, 4-edge and three areas system there is used the lower supply pressure level, when the thickness of sheet is less than 1.5 mm. The 2-edge controlled system has been simulated to 4 mm thickness of sheet, because after this there isn't enough time to do punching cycle correctly.

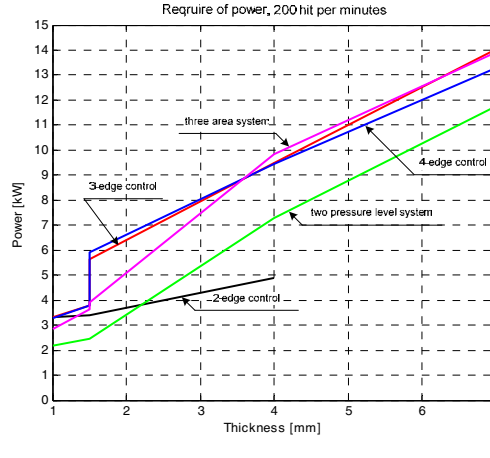

Figure 27. Simulated power consumption of the studied systems

6 CONCLUSION

The main target of this research has been study the energy efficiency system to punching machine. The two pressure level system seems to be the best from presented applications.

The power of the hydraulic pump can be reduced from 30 kW to 18.5 kW by means of two pressure level system. The disadvantage of two pressure level system is the slowness of the pressure selector valve. The punching could even stop, when the pressure level is changed to other.

7 REFERENCES

[1] Aaltonen, K., Andersson, P. and Kauppinen, V. 1997. Sheet metal working and tooling technology. WSOY. Porvoo. (in Finnish)

[2] Branz, Harald. 2000. Hydraulische Antriebe und Steuerungen für Werkzeugmaschine. O + P: Ölhydraulik und Pneumatik. Nr. 9 November 2000.

[3] Pat. US 5042362. Hydraulic control system for the drive control of a double-acting hydraulic cylinder. Germany. (Eckehart Schulze). Appl. 338223, 14.4.1989, (27.8.1991).

[4] Pat. WO 2004/101263 A1. Drive for a punch or forming machine. Bosch Rexroth AG, Germany. (Schmidt S.). Appl. PCT/DE2004/001031, 14.5.2004, (25.11.2004).

[5] Pat. DE 102004024354 A1. Antrieb für eine Stanz- oder Umformmaschine. Bosch Rexroth AG, Germany. (Schmidt S.). Appl. 102004024354.9, 14.5.2004, (5.1.2005).

[6] Richard T. Schneider. 2002. Don't overlook hydraulic pressure boosters. Hydraulics & Pneumatics, October 2002. Vol55 no.10.

[7] Roosen, K., Backe, W. 1997. Development and investigation of an energy saving hydraulic linear drive. Preprints of the Tenth Bath International Fluid Power Workshop, University of Bath, 10th-12th September 1997. England. p. 161-180.

CROSS UTILIZING DEGREE OF FREEDOMS OF BOOM IN ENERGY SAVING CONCEPT

Tapio Virvalo, Juho Seppälä
IHA/TUT, P.O.Box 589, 33101 Tampere, Finland

ABSTRACT

An important topic in R&D of mobile machines, for instance forest machines, is the improving of energy utilization. The efficiency or energy utilization is still very poor. Possibilities to utilize the gravitational force influencing one or two degree of freedom in some other degree of freedom are studied in a forward loader case. The basic idea studied is to use the outflow of the lift cylinder to drive the telescope cylinder. The outflow is used directly or via the accumulator. According to simulation quite remarkable reduce of energy consumption can be achieved.

1. INTRODUCTION

Modern forest mobile machines, like forward loaders and harvesters, are still manually controlled hydraulically driven, but strongly computerized machines. An example of typical forest machine is shown in Figure 1.

Figure 1. Forward loader (Ponsse)

There are some fully or semi-automatic functions, but most often a driver acts as a controller. There are several R&D trends in these kinds of mobile machines. Natural development during last decade has brought more integrated electronics also into mobile machines and their hydraulic components like valves, pumps, and actuators [1], [2], and [3]. All these mean tendency to increase automation in different tasks of these machines.

Power Transmission and Motion Control 2006 Edited by Dr D N Johnston and Professor K A Edge

However, it is seen that manual control will still be dominant many years. A trend is to increase automation step by step in order to improve the performance of machines and to help drivers as well as to make their work lighter and more efficient. The improvements of performance and effectiveness mean most cases faster movements and better dynamics of these machines.

An important topic in R&D of mobile machines is the improving of energy utilization. Total power levels, for instance, in forest machines are around 150-200kW. Booms of these kinds of machines are quite heavy and their reach range is large, Figure 2. Loads which might be around 500kg are both lifted up and lowered down several meters. The up- and downward velocities of loads might be around 2m/s.

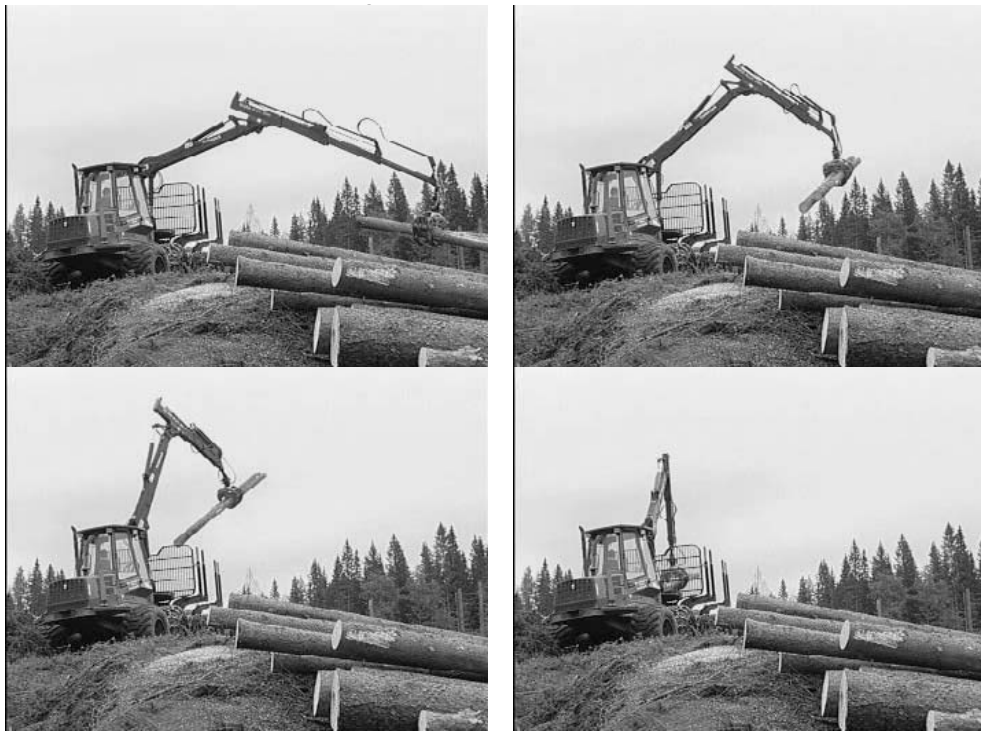

Figure 2. Example, a forward loader in work (Timberjack)

2. MOTIVATION OF STUDY

The efficiency or energy utilization of hydraulic booms is still very poor [4], [5], [6], and [7]. Applications where loads are under gravitational force are typical for so called secondary control systems. Secondary control systems are so far used in hydraulic motor applications [8], [9], [10], and [11]. Energy consumption reducing methods have also been used in heavy vehicles [12] and [13]. To apply the secondary control method variable

displacement motors are required. That is why this method can not be applied on cylinder drives used, for instance, in forward loaders.

Because forward loaders lift loads from ground to load space and vice versa under gravitational force, as can be seen in Figure 2, there might be some possibilities to store and restore energy in suitable parts of a work cycle. Studies have pointed out that modern forward loader booms and their mechanical structure and location of driving systems (hydraulic cylinders) are well designed [5] also from driving force point of view. This means that, for instance, the total flow rate is quite steady without remarkably flow rate peaks during normal work cycles. So there is quite a little to do with traditional ways in reducing of energy consumption. Of course, structures could be lighter but there is little to do at present cost-level because loads are heavy and the reach of these kinds of booms might be around ten meters. Most of real energy losses take place in hydraulic systems. For many reasons (cost, weight, required room, dynamics) only one pump is used and the boom is controlled by valves. Remarkable energy losses take place in valves and long hydraulic lines [14]. Using a multi-pump system improves energy utilization [15], but it is expensive and requires more room and weights more. Different kinds of methods have been studied to store energy of one cylinder driven Degree of Freedom (DoF) into hydraulic accumulator during lowering of load and then recover this energy in the same DoF during lifting of load [16], [17], [18], [19], [20], [21], and [22]. Some energy utilization improvements can be achieved with this method. An interesting and promising new method is so called hydro-transformer [23], [24], [25], [26], and [27]. This idea makes it possible to apply secondary control method on cylinder drives. However, hydro-transformers are still under development and some problems (noise, pressure oscillation, efficiency) wait for reasonable solutions. So far there are no published results of its influence on reducing of energy consumption in boom applications.

Because these kinds of booms are manually controlled there are quite a few sensors especially for control of movements of different DoFs. Manufacturers and users are very sceptical to add new and often quite expensive and tediously installed sensors. The study of possibilities to utilize direction control proportional valves as feedback transducers has already long time been in progress [28] and [29]. Some companies have also done the same kind of development work for a long time [30]. The basic idea is to compute the volume flow rate through the control notch of a valve by estimating the position of the spool and measuring the pressure drop across the control notch. The velocity and even the position of a hydraulic actuator can be estimated this way. Due to the simplicity and cost-effectiveness of this method it is a promising velocity and position sensor to mobile machine applications. In order to make this kind of solution real cost-effective, changes required into hydraulics of booms should be minimized. In practice this means that ordinary mobile valves should be used as far as possible. Specifications and performance of mobile valves are relatively poor. On the other hand quite low-level accuracy in velocity and position estimation is required due to manual control of booms.

In spite of applying energy consumption reducing concept the driver works as normally without noticing any changes in the behaviour of the boom. The control system has to know the velocity and orientation of the lift cylinder in order to switch the valves in smoothly way. If control valves could be used as velocity sensors, it might open some possibilities to reduce energy consumption without bringing significant additional costs.

3. BASIC IDEA OF STUDIED SYSTEM

The studied idea is depicted in Figure 3 [31]. For instance, based on the required velocity of the lift cylinder and measured pressure differences over the valves V1 and V2 the estimated volume flow rates through both valves of the lift cylinder are calculated. If the pressure of the lift cylinder is a certain amount higher than the accumulator line pressure, the volume flow from the lift cylinder is directed to the accumulator line through the valve V2 otherwise to the tank line through the valve V1. The volume flow from the lift cylinder can be also directly used in the telescope cylinder and in this way to reduce energy consumption. All this means that there has to be a certain smooth switching function between the valves V1 and V2 depending on actual conditions of pressures.

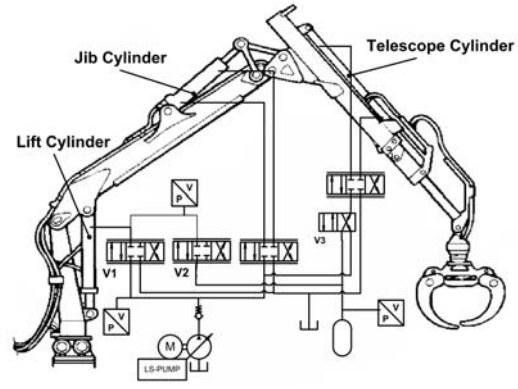

Figure 3. Hydraulic diagram of studied example boom

Based on the required velocity of each of DoF (given by a driver with his joy-sticks) and measured pressure differences over the control notches of the valves the estimated velocities of each DoF are computed. From estimated velocities the position of each DoF is computed in order to get the boom orientation. The accuracy of the position computing is improved by several suitably located reference points. Because the velocity of the lift cylinder has to remain unchanged in spite of switching between the valves V1 and V2, the right control signals of the valves have to be known. Regardless of which one of the valves is actively used the corresponding control signals of both valves are calculated according to actual velocity control signal and pressure differences.

In order to guarantee, that the telescope cylinder can be driven in all circumstances the valve V3 is added. If the pressure in the accumulator line is not high enough, the supply pressure of the telescope cylinder valve can be switched into the pump output pressure.

The same principle can be extended also between the jib and telescope cylinders on a suitable part of a working cycle.

4. EXPECTED CHALLENGES AND PROBLEMS

When direction control valves and pressure sensors together are used as velocity and position sensors in purpose to reduce energy consumption of hydraulic boom applications the following issues have to be considered:

* To avoid the oscillations of the valves (V1 and V2). According to presented idea the valves have to be switched from active to passive mode and vice versa during the movement of the load.
* To find out suitable pressure difference hysteresis for switching points of the valves. Because a certain pressure drop is needed in the control notches of the valves to maintain the required volume flow from the lift cylinder, the valves V1 and V2 have to be switched on and off. To reduce the risk of oscillation a certain hysteresis is needed between the switching points. When the actual pressure difference is lower than the pressure hysteresis, the hysteresis value of the pressure difference is used in the volume flow rate estimation.
* To find out suitable filtering of measured pressures in order to guarantee reasonable pressure signals for velocity estimation.
* To guarantee smooth transition stage from the tank line to the accumulator line and vice versa.
* To estimate piston velocities.
* Suitable control schema, closed loop velocity control based on estimated volume flow.
* To realize the switching of valves so that the driver does not notice anything.

In this stage of the study the following issues are studied mostly by simulations, but some verification with experimental tests are also done:

* The basic functioning of the concept.
* Suitable switching logic of valves.
* Control schema as well as hysteresis of the pressure differences in the transition stage.
* Closed loop velocity controls of DoFs based on estimated volume flows.
* Required static and dynamic characteristics of valves.
* Influence of the valve switching on the dynamics of the boom.
* Reduction of energy consumption.

5. FEASIBILITY OF VALVE AS VELOCITY SENSOR

The simplified hydraulics of a hydraulic boom is presented in Figure 3. These kinds of booms are used to load and un-load for example timbers. From dynamics point of view the lift cylinder is most important as can be estimated according to Figures 1, 2, and 3. It offers also the best chances to store and recover energy. The feasibility to utilize the valve V1 as a velocity sensor is studied as an example of velocity estimation method.

As an example the simulated pressure responses of the lift cylinder in a certain part of un-loading cycle are shown in Figure 4. It is assumed that movements in both directions (un-loading and backward movements) follow the same trajectory which is approximately true also in real applications.

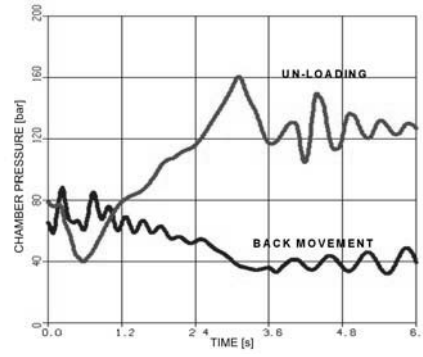

Figure 4. Simulated piston chamber pressure of lift cylinder in un-load and back movements during a part of work cycle

Due to different loads the chamber pressure of the lift cylinder is quite different during these two movements. The dynamic behaviour of pressures is reasonable smooth and due to suitable low-pass-filtering normal ripple of pressure measurement is very low. All these mean that there might be good possibilities to estimate the piston velocity based on pressure measurements.

The idea is to use as simple calculations in the velocity estimation as possible. As examples the volume flow error due to compressibility of media under pressure are shown in Figure 5 in the case of the lift cylinder un-loading and backward movements.

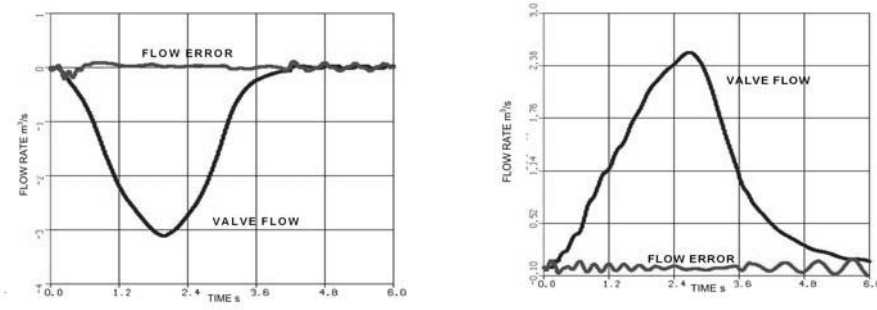

Figure 5. Simulated flow rate through valve and volume flow error during un-loading (left) and back movement (right)

At the ends of movements the error is remarkable due to the oscillation of the whole boom, but it is still reasonable low and it lasts relatively short time. Because these kinds of booms are manually controlled the estimation accuracy of velocity is not critical in these applications.

Dynamics of the valve and cylinder influence estimated velocity. If no dynamics is taken into the account the transient response of the estimated velocity differs significantly from the real velocity response as shown in Figure 6. In this case the natural frequency of the cylinder drive is 100rad/s and the bandwidth of the valve is 600rad/s. If the dynamics of the valve is used in the estimation the transient response is still the same kind as shown in

Figure 6. When the dynamics of the cylinder drive is described with a second order model and it is used as the dynamics of the valve in the velocity estimation the response of the estimated velocity is shown in Figure 6.

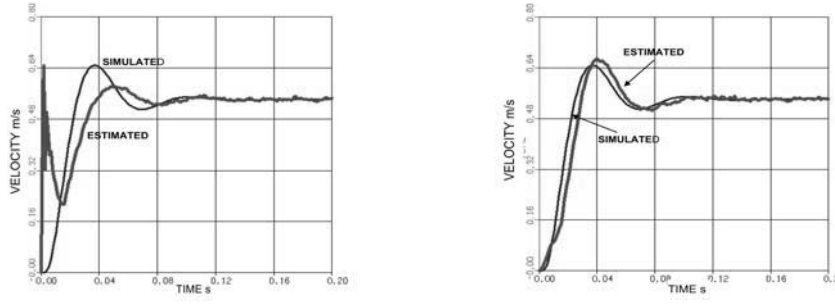

Figure 6. Simulated and estimated (also simulated) velocity responses, no dynamics included (left) and dynamics of cylinder included (right)

According to simulations it seems that it is a good practice to use the dynamics that is quite close to the cylinder drive dynamics in the velocity estimation.
In order to test idea further some experimental tests are carried out. A high quality servo valve is used first. The measured position of the valve spool is used in the velocity estimation during these measurements. Because the measured valve spool position is used directly in velocity estimation the dynamics of the estimation is too high. Using the dynamics of the cylinder as the dynamics of the valve in the velocity estimation the measured and estimated velocities match quite well. In practice this means that a reasonable estimation of the dynamics of cylinder drives has to be known. Fortunately, the dynamics of DoFs of booms does not vary a lot.

In order to get even better understanding about quality of the velocity estimation some additional tests are carried out. Figure 9 presents steady state response of a mobile valve when the relative control signal changes from -50% to +50%. Typical feature of mobile proportional direction valves can be seen clearly in Figure 7; remarkable dead band. It is

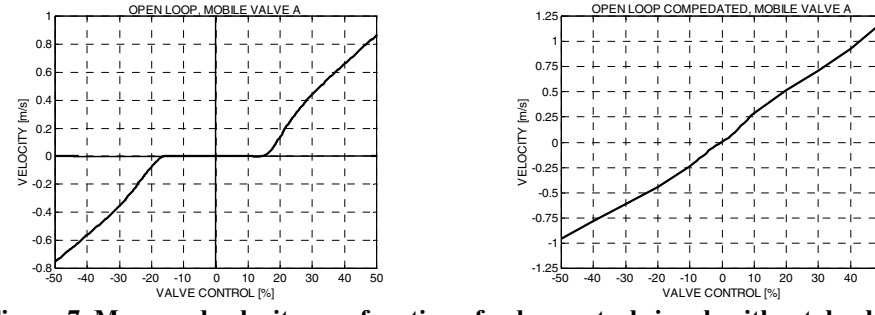

Figure 7. Measured velocity as a function of valve control signal, without dead-band compensation (left) and with dead-band compensation (right)

normal practice to compensate the dead band of mobile valves. The response of the measured velocity is also shown, when the dead band is compensated. The used mobile valve is a little bit special with significantly low hysteresis as can be seen in Figure 7.

As an example measured and estimated velocity and position responses of the cylinder are shown in Figure 8, when a mobile valve is used. The dynamics of the cylinder is included in the velocity estimation. The actual velocity is measured with the velocity sensor and the estimated velocity is computed based on the control signal of the valve and measures pressure difference over the valve.

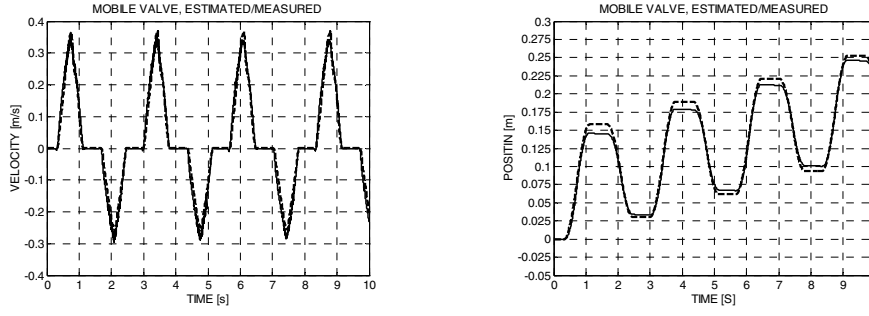

Figure 8. Measured (solid) and estimated (dash) velocity and position without dead band compensation

As an example step responses of the measured and estimated velocities are presented in Figure 9. The experimental set-up differs from the case shown in Figure 6. The dynamics of the valve is much higher than the dynamics of the cylinder in Figure 6. The situation is opposite in Figure 9. The dynamics of the mobile valve is included in the flow rate estimation in Figure 9. The measured and estimated velocity responses match reasonably well in the steady state and transition stage.

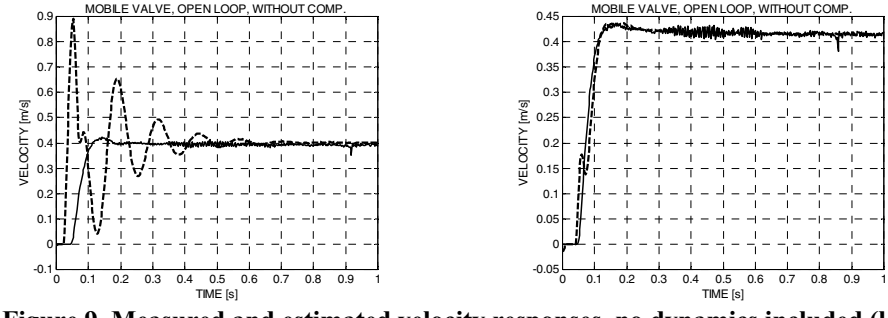

Figure 9. Measured and estimated velocity responses, no dynamics included (left) dynamics of valve included (right)

As a conclusion it can be said that rather high quality direction control mobile valves can be considered to offer quite good possibilities to be used also as a part of velocity sensors. The system dynamics has to be included into the velocity estimation in order to achieve reasonably good matching with a real velocity also in transient stages. When mobile valves are used the dead band compensation is also considered. Some studies show that quite simple hysteresis compensation might improve the performance of mobile valves [32]. When high accuracy is not needed, for instance in manual control, also mobile valves can be used in approximate velocity estimation.

6. STUDIED SYSTEM

The principles of the studied boom are shown in Figures 1 and 2. The basic studied hydraulics is depicted in Figure 3. The whole working range of the boom is shown in Figure 10 as well as the corner point of the movement path of the studied work cycle.

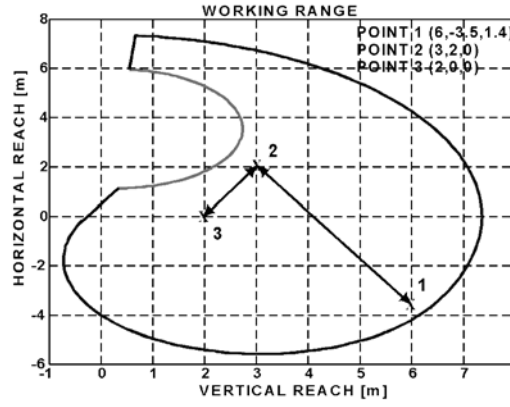

Figure 10. Work range of boom and corner points of movements of work cycle

The studied un-loading work cycle can be divided into four movements. First the load is gripped at the point 3 in the load space. Then it is raised to the point 2 over the bunk ends and lowered into the point 3 on the ground, where the load is released. Then the gripper (tip of the boom) is driven back to the point 3 via the point 2. In practice the boom has to be also rotated in these kinds of work cycles, but the rotational movement is not included into this study.

Two systems are compared: A) the traditional system with LS-pump and un-symmetric valves of the jib and telescope cylinders and B) the proposed system according to hydraulics shown in Figure 3. The proposed system has also a LS-pump and un-symmetric valves of the jib and telescope cylinders. In addition the valves V2 and V3, the accumulator, and two pressure sensors are included. In both cases the energy consumption of the whole un-loading work cycle is calculated.

7. RESULTS

The following principles are used in the modelling and simulations of the studied case.

* The rigid body model of the boom is used. The model is verified in steady state.
* The hydraulics is modelled in the normal way including typical non-linearities.
* The third order path generator is used to drive each DoFs.

For simplicity all four movements are calculated separately and the energy consumptions of each movement are summed in order to get the total energy consumption during one whole work cycle. Some relatively small errors are done in this kind of calculation, but they do not influence comparison result. The gripper weights 100kg and it is assumed that the load is 400kg. The whole cycle time is 14s. From the point 3 to the point 2 and back takes 3s in

both directions. From point 3 to the point 1 and back takes 4s in both directions. It is assumed that each movement profile is reasonably smooth. During the used work cycle the following movement of different cylinders take place, Table 1.

Table 1

	Mov. I (3 – 2)	Mov. II (2 – 1)	Mov. III (1 – 2)	Mov. IV (2 – 3)
Lift cylinder	Yes	Yes	Yes	Yes
Jib cylinder	Yes	Yes	Yes	Yes
Telesc. cylinder	No	Yes	Yes	No

The proposed system is based on an assumption that the required pressure to drive the telescope cylinder is lower than the pressure in the accumulator, Figure 3. This means, that the pressure in the lift cylinder during lowering the load should be fairly higher than the pressure of the telescope cylinder in forth and backward movements. This way a part of out-coming volume flow from the lift cylinder is used directly in the telescope cylinder and the rest of this volume flow is driven to the accumulator. In practice the lift cylinder is remarkably bigger than the telescope cylinder. For instance, in the studied case the piston diameter of the lift cylinder is 125mm and the telescope cylinder 50mm, respectively.

According to Table 1, in this example work cycle, the telescope cylinder moves in the same time with the lift cylinder during the movement II. The volume change of the lift cylinder should be at least so big that it covers the back-and-forth movement of the telescope cylinder. The system working principle means also that actually the telescope cylinder takes required oil volume from the accumulator line during movement II and from the accumulator during movement III. This gives the base to the size and pre-charge pressure of the accumulator.

The following computed hydraulic energy (pump output) is used in different parts of the working cycle of the traditional and proposed systems, Table 2.

Table 2

	Mov. 3 - 2	Mov. 2 - 1	Mov. 1 – 2	Mov. 2 -3	Whole cycle
Trad. [kNm]	33	78	88	4	203
Prop. [kNm]	33	44	78	4	159

The result shows that the energy consumption of the proposed system is significantly lower than the energy consumption of the traditional system.

8. DISCUSSION

According to the simulation results it seems that reasonable answers to the expected challenges and problems (chapter 4) have been achieved.

* In this stage of the study it can be stated that the proposed system functions properly. The energy reduction is around 20% in the studied case.
* It is possible to find suitable switching logic between valve V1 and V2.
* Some hysteresis between switching points is needed, but the range of hysteresis is not very critical.

* Experimental studies show that velocities of cylinders can be estimated accurately enough at least from energy consumption reducing point of view.
* Dynamics of mobile valves is high enough in the studied case.
* Influence of the valve switching in the proposed way is quite small on the dynamics of the boom.

Still there are questions waiting for more studies and answers. Quite many assumptions have to be done during this study. For instance the load is assumed to be 400kg. In practice loads vary in large range. It is possible that the pressure of the lift cylinder is not high enough to drive the telescope cylinder and fulfill the accumulator in all work cycles. That is why the valve V3 (Figure 3) is required. The switching between the valve V1, V2 and V3 and its influence on energy consumption has to be studied. The optimum size of the accumulator is also a little bit difficult question, especially, if the proposed idea is extended also between the jib cylinder and the telescope cylinder. The behavior of accumulators in these kinds of applications is not very clear [33]. Environment temperature and dynamic loading influence sometimes quite strongly to the performance of accumulators.

Nowadays the control valves of these kinds of booms are in the same compact package with common supply and tank lines. The allowed pressure in tank lines of these packages is quite low. This means that the proposed system can not be directly used with existing valve packages. This means some extra costs and maybe some problems in size and location of valves.

Simulation is used in this study. Of course, it causes some uncertainties for instance due to simplifying assumptions and numerous non-linearities. On the other hand the simulation model bases on well-known models of hydraulics and mechanical structure of the boom. Anyway, it can be considered that simulation results so far give promising basement for further studies.

9. CONCLUSIONS

According to this study mostly based on simulations the following conclusion can be made:

* Proposed method is working and it gives promising results for reducing energy consumption in forward loaders.
* Performance of traditional proportional mobile valves seems to be good enough.
* Dynamics of the DoF under control of the velocity estimation have to be estimated roughly.
* Robustness of proposed control method requires practical tests.

10. REFERENCES

1. https://www.ponsse.com/
2. www.deere.com/en_US/cfd/forestry/deere_forestry/
3. http://www.komatsuforest.fi/english/index.html
4. Virvalo, T. & Vilenius, M. 2000. The Influence of Pumps and Valves on the Efficiency of a Hydraulic Boom, Chapter 8. In: Garbacik, A. & Stecki, J.(eds.).

Developments in Fluid Power Control of Machinery and Manipulators. Cracow. Fluid Power Net Publication. pp. 183-207.
5. Xingui Liang, On Improving Energy Utilization in Hydraulic Booms, Acta Polytechnica Scandinavica, Mechanical Engineering Series No. 160, Tampere, Finland 2002.
6. Wei Sun: On Study of Energy Saving System for Hydraulic Manipulators. No. 519 Tampere University of Technology, Tampere, Finland 2004, 207 p.
7. X.G. Liang and T. Virvalo, What's wrong with energy utilization in hydraulic cranes, 5th International Conference on Fluid Power Transmission and Control, Hangzhou, China, 2001, pp.419-424.
8. R. Kordak, Hydrostatic Drives with Control of the Secondary Unit, The Hydraulic Trainer, Volume 6, Mannesmann Rexroth GmbH, 1996.
9. R. Werndin and J-O. Palmberg, Hydraulic Transformer in Low-Speed Operation – A Study of Control Strategies, 5th JHPS International Symposium on Fluid Power, Nara, Japan, 2002, vol.3 pp.849-854.
10. R. Werndin and J-O. Palmberg, Hydraulic Transformers – Comparison of Different Designs, 8th Scandinavian International Conference on Fluid Power, Tampere, Finland, May 2003, vol.1 pp.163-174.
11. X. Bing, Z. Bin, O. Xiaoping and Y. Huayong, The CPR System Adopting a New Hydraulic Transformer to Drive Loads and Its Design, 6th International Conference on Fluid Power Transmission and Control, Hangzhou, China, 2005, pp.100-104.
12. United States Patent 4098083: Hydraulic energy storage multi-speed transmission.
13. Stecki J. and Mathenson P.: Advances in Automotive Hydraulic Hybrid Drives. JFPS, November 7-10, 2005 Tsukuba, Japan.
14. Xingui Liang, Tapio Virvalo , Matti Linjama, The Influence of Control Valves on the Efficiency of a Hydraulic Crane, Proc. The Sixth Scandinavian International Conference on Fluid Power, page 392, Tampere, Finland, 1999.
15. R. Rahmfeld and M. Ivantysynova, Displacement Controlled Linear Actuator with Differential Cylinder – A Way to Save Primary Energy in Mobile Machines, 5th International Conference on Fluid Power Transmission and Control, Hangzhou, China, 2001, pp.296-301.
16. X.G. Liang and T. Virvalo, Development and Research of an Energy Saving Drive in a Hydraulic Crane, 7th Scandinavian International Conference on Fluid Power, Linköping, Sweden, May 2001, vol.2 pp.151-161.
17. X.G. Liang and T. Virvalo, Energy Reutilization and Balance Analysis in a Hydraulic Crane, 5th International Conference on Fluid Power Transmission and Control, Hangzhou, China, 2001, pp.306-310.
18. J. Nyman and K-E. Rydberg, Energy Saving Lifting Hydraulic Systems, 7th Scandinavian International Conference on Fluid Power, Linköping, Sweden, May 2001, vol.2 pp.163-177.
19. W. Sun and T. Virvalo, Accumulator-Pump-Motor as Energy Saving in Hydraulic Boom, 8th Scandinavian International Conference on Fluid Power, Tampere, Finland, May 2003, vol.1 pp.297-309.
20. W. Sun and T. Virvalo, Simulation Study on a Hydraulic-Accumulator-Balancing Energy-Saving System in Hydraulic Boom, 50th National Conference on Fluid Power, Las Vegas, Nevada USA, Mar 2005, pp.371-381.
21. J. Nyman, J. Bärnström and K-E. Rydberg, Use of Accumulators to Reduce the Need of Electric Power in Hydraulic Lifting Systems, 8th Scandinavian

International Conference on Fluid Power, Tampere, Finland, May 2003, vol.1 pp.311-326.
22. K-E. Rydberg , Energy Efficient Hydraulic Systems and Regenerative Capabilities, 9th Scandinavian International Conference on Fluid Power, Linköping, Sweden, Jun 2005, 5:2 Fluid Power Systems.
23. http://www.innas.com/IHT.html.
24. G. Vael, P. Achten and J. Potma, Cylinder Control with the Floating Cup Hydraulic Transformer, 8th Scandinavian International Conference on Fluid Power, Tampere, Finland, May 2003, vol.1 pp.175-190.
25. W. Ma and S. Ikeo, Robust Position Control of Hydraulic Cylinder Using Hydraulic Transformer, 4th International Fluid Power Conference, Dresden, Germany, Mar 2004, workshop pp.91-102.
26. Z. Bin, X. Bing, O. Xiaoping and Y. Huayong , Research on Performance of the Common Pressure Rail Adopting New Hydraulic Transformer to Drive Loads, 9th Scandinavian International Conference on Fluid Power, Linköping, Sweden, Jun 2005,
27. T. Ueno, K. Ito and S. Ikeo , A Robust Design of Velocity/Force Controller for Cylinder Using Hydraulic Transformer, 9th Scandinavian International Conference on Fluid Power, Linköping, Sweden, Jun 2005, 4:3 Hydraulic Transformers and Energy Recovery.
28. Kannisto S. and Virvalo T.: Valve Manufacturer Specification Based Hydraulic Velocity Servo. ASME, Mechanical Engineering Congress and Exposition, New Orleans, USA, CD-vol. 2: Fluid Power, 17.-22.11.2002, 6 p.
29. Kannisto S. : Hydraulic Direction Control Valve as a Measuring Orifice – Pressure Compensator Integrated Into Main Spool Control, Licentiate Thesis, Tampere University of Technology, 2002, 82 p.
30. Vickers/Eaton: http://hydraulics.eaton.com/products/valves_mobile_erc.htm
31. Virvalo, T. & Sun, W.: Improving energy utilization in hydraulic booms - what it is all about. ICFP'2005, April 5-8, Hangzhou, China, pp. 55-65.
32. Virvalo, T. : Compensation of dead band and hysteresis of proportional valve. 50th National Conference on Fluid Power, March 16-18, 2005, Las Vegas, Nevada USA, pp. 233-241.
33. K-E. Rydberg, Hydraulic Accumulators as Key Components in Energy Efficient Mobile Systems, 6th International Conference on Fluid Power Transmission and Control, Hangzhou, China, 2005, pp.124-129.

Energy Recovery of Hydraulic Elevator Using Accumulator

Huayong YANG, Bing XU, Wei SUN, Jianjie LIN
Institute of Mechatronics and Control Engineering, Zhejiang University
Hangzhou 310027, China. Email: yhy@zju.edu.cn

[ABSTRACT]
In the conventional valve controlled hydraulic elevator, by-pass throttle is commonly used to control the cabin speed. In this system design, when the cabin moves downwards, the entire potential energy of cabin is wasted and converted into fluid heat by throttling. This is why the energy consumption of a hydraulic elevator is much higher compared to that of the traction elevator. In this paper, some different methods of energy recovery using hydraulic accumulator have been introduced and discussed in detail. Experimental studies on energy-saving have been carried out to compare the energy consumption of different system designs of hydraulic elevator.

1 INTRODUCTION

The hydraulic elevator is one of the most popular types of elevator in Europe and North America. However, from the environmental protection point of view especially energy-saving, the hydraulic elevator is facing a serious challenge for its large power installation and energy consumption compared with those of the normal traction elevator. Hence, the reduction of the power installation and energy consumption of hydraulic elevators becomes the key focus of the industry.

In the conventional valve controlled hydraulic elevator, by-pass throttle is commonly used to control the cabin speed. In this system design, when the cabin moves downwards, the entire potential energy of cabin is wasted and converted into fluid heat by throttling. This is why the energy consumption of hydraulic elevators is much higher compared to that of the traction elevator. The

Power Transmission and Motion Control 2006 Edited by Dr D N Johnston and Professor K A Edge

system design of the conventional valve controlled hydraulic elevator is shown in Fig. 1. The energy consumption during the power transmission is shown in Fig. 2.

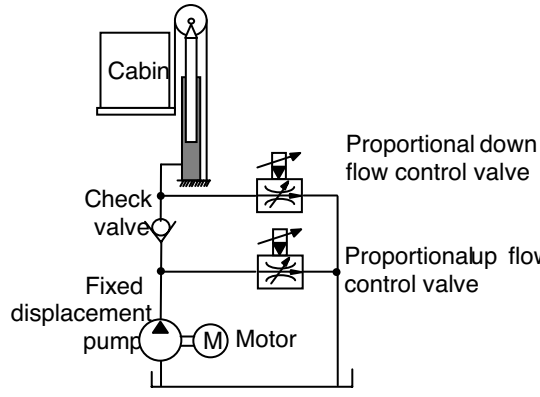

Fig. 1 System design of valve controlled hydraulic elevator

A number of techniques have been developed to reduce the power installation and energy consumption of hydraulic elevators, for instance, VVVF (Variable Voltage Variable Frequency) control, reducing the weight of cabin, and using energy-saving valves, together with the energy recovery, which is the best way to utilize the potential energy of the cabin. By storing potential energy in the accumulator during the cabin down-travel and reusing the energy during up-travel, not only can the energy demand be reduced, but also the power installation of the electric motor can be reduced considerably.

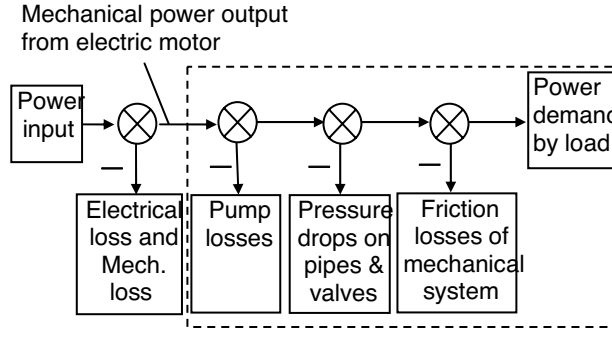

Fig. 2 Energy consumption during the power transmission

In a hydraulic elevator, there are 3 common methods that can be used to recover energy:

- Using a mechanical counter balance weight in the cabin hanging system (Fig. 3),

- Using the electric motor as an electrical generator during the cabin's down-travel (Fig. 4),
- Power regeneration using an accumulator (Fig. 5).

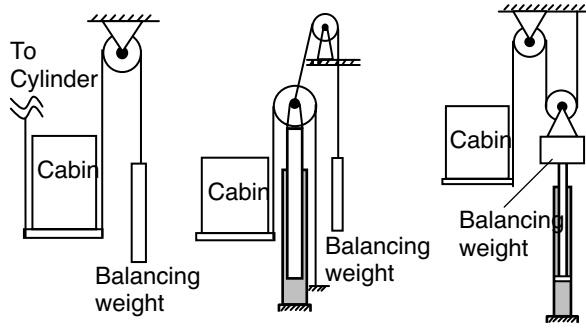

Fig. 3 Usage of mechanical counter balance weight

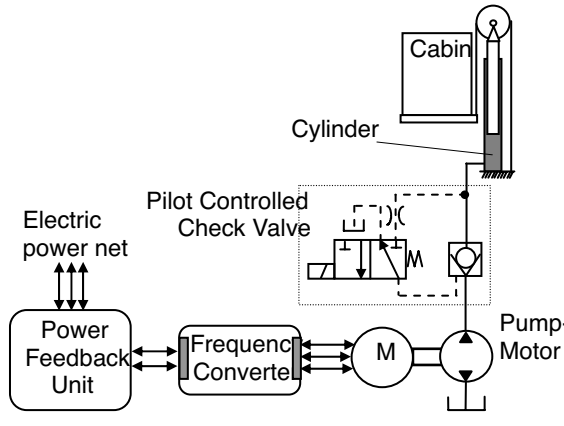

Fig. 4 Power regeneration using frequency converter and power feedback unit

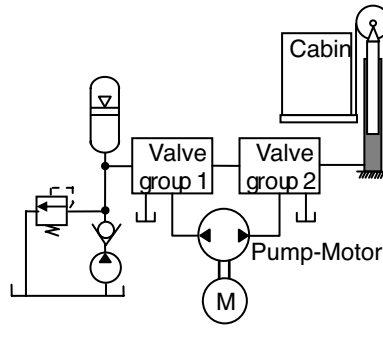

Fig. 5 Energy regeneration using accumulator

In this paper, different types of energy-saving hydraulic elevator using an accumulator are introduced. Some of them are the combination of the 3 methods mentioned above.

2 DIFFERENT TYPES OF ENERGY RECOVERY SYSTEMS USING HYDRAULIC ACCUMULATORS

2.1 Type 1: Valve Controlled Hydraulic Elevator Using Accumulator as Pressurized Oil Source

In 1992, J T Edwards described a system using a pressured oil source as the key component for conserving energy in hydraulic elevators [1]. L. Ran studied the use of an accumulator in hydraulic elevator and Fig. 6 [2] shows the elevator system using hydraulic accumulator as the pressurized oil source on the normal valve controlled hydraulic elevator. The pressure of the accumulator reduces the pressure difference of the pump; therefore, the energy consumption and power requirement of the electric motor can be reduced accordingly.

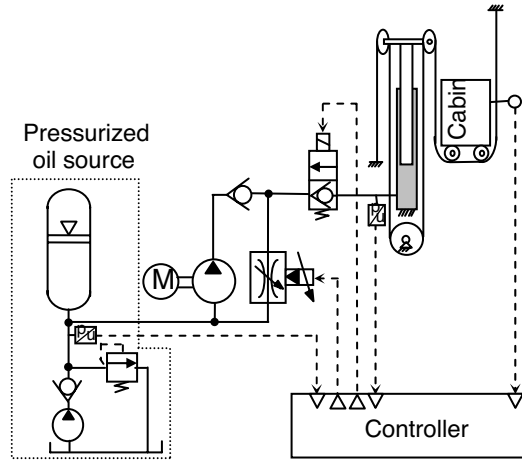

Fig. 6 Using pressurized oil source on the normal valve controlled hydraulic elevator

The most difficult point of Type 1 is the speed control valve because the pressure difference of the valve is not big enough to support any pilot control. To solve this problem, one extra pilot oil source is built especially for the speed control valve. [2]

2.2 Type 2: Frequency Converter Controlled Hydraulic Elevator Using Hydraulic Accumulator Counter Balance and Shaft-Speed Controlled Pump-motor Units

B. Xu developed another type of energy saving mechanism using both an hydraulic accumulator and a frequency converter as shown in Fig. 7.[3] The key components in Fig. 7 are the pump-motor units (PM1 and PM2), connected by a common shaft, together they act as a hydraulic transformer. PM1 is a high pressure small displacement pump. Thus, the high pressure accumulator (size is smaller when pressure is higher) acts as "balance weight" for the cabin. When the cabin is traveling upwards, the accumulator releases energy through motor PM1, which drives pump PM2 to raise the cylinder. When the cabin comes down, the potential energy is passed to the accumulator through the motor PM2 and pump PM1. In this energy-saving system, the converter controlled electric motor is the main speed control component, which either compensates the driving force when the output of motors (PM1 or PM2) is not big enough, or installs the energy when output of pumps (PM1 or PM2) is too much.

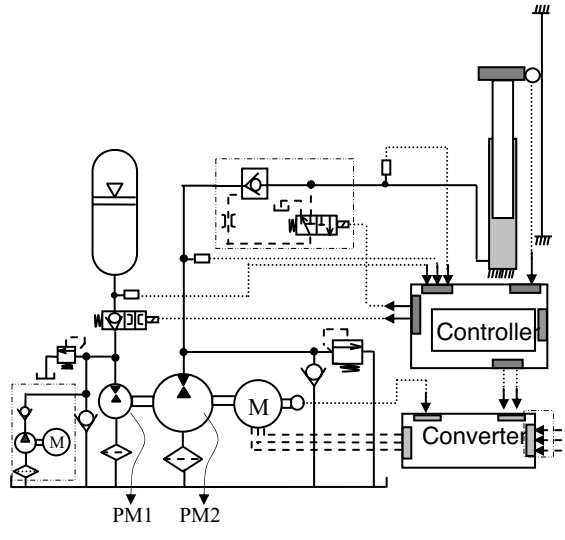

Fig. 7 Using accumulator as energy recovery component on a frequency converter controlled hydraulic elevator

The pump-motors (PM1 & PM2) and one converter driven electric motor-generator are energy exchanging components. The main shortcoming of the Type 2 circuit is that it is quite complicated and expensive.

2.3 Type 3: Frequency Converter Controlled Hydraulic Elevator Using Double-acting Cylinder and Hydraulic Accumulator Counter Balance in Closed-circuit

For the further developments of the hydraulic elevator, the following considerations should be taken into account:

- High efficiency, low energy consumption;
- Small volume of oil requirement;
- Simple structure;
- The power unit should be in small size, in order to avoid the use of a machine room;
- Controllability should be good.

One solution as shown in Fig. 8, developed by J Lin [4], exactly fulfills the above requirements. The proposed system has the following advantages:

- A double-acting cylinder is chosen instead of the plunger type cylinder to avoid the problem of compression rod stability.
- Hence, a higher pressure level can be chosen because the diameter of the piston is much smaller than the normal plunger; as the "hydraulic balance weight" of the cabin, the pressure of accumulator is also much higher than that in Type 1. Higher pressure means smaller flow rate and smaller components. Thus, the power unit of this solution can be very compact and it is easy to realize the no-machine-room installation.
- The structure is simple and symmetrical; it is easy to be manufactured;
- The controllability is very good because the control component is a vector-feedback converter controlled electric motor.

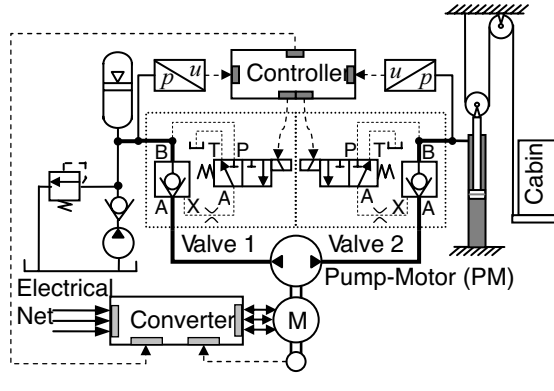

Fig. 8 Using accumulator and double-acting cylinder on a closed-circuit converter controlled hydraulic elevator

3 EXPERIMENTAL STUDY ON ACCUMULATOR

The accumulator is acting as the cabin's "hydraulic counter balance" (Fig. 8), which is changing all the time during the movement of the cabin. The gas state changing can be described by the following equation

$$p \cdot V^n = Const. \tag{1}$$

where

p =Nitrogen pressure in the bladder;

V =Volume of the Nitrogen in bladder;

n =Poly index of the Nitrogen in this accumulator;

This is a common equation to describe the behavior of the compression/expansion of air using a value for the poly index 1.0 and 1.4 in isothermal and adiabatic process respectively. According to the reference material [2, 5, 6, 7], the value of poly indexes of the nitrogen are quite different due to the different accumulators and different application environment. The experiment on this accumulator studied in this paper proved this phenomenon. (The studied accumulator is of the bladder type, the nominal volume is 63 L, and the measured values were taken indoors at a temperature 22 ~ 20ºC. The elevator is a 3 floor 3 stop hydraulic elevator with roping 4:2 suspensions.)

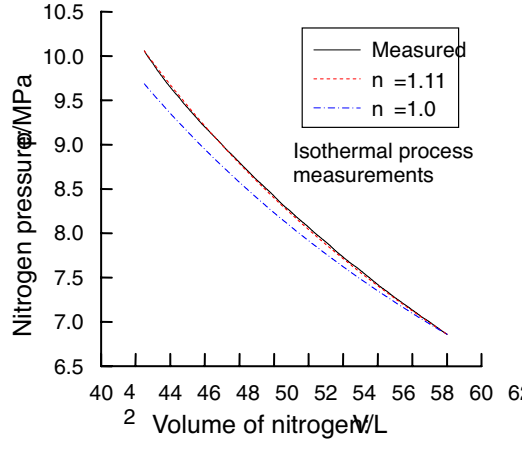

Fig. 9 Experimental measurement for the isothermal process in the applied accumulator [4]

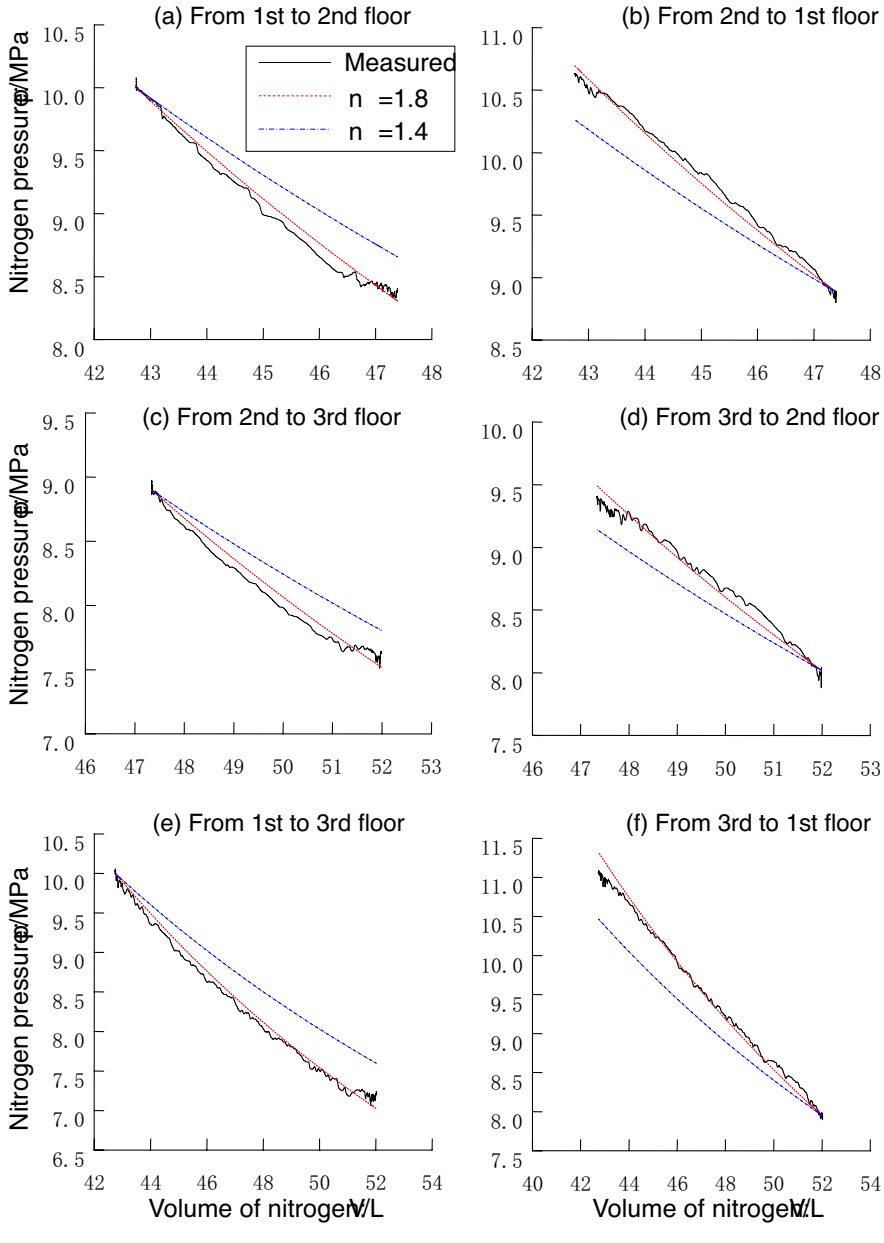

Fig. 10 Experimental measurement for polytrophic process in the applied accumulator [4]

According to the actual running of the elevator, the accumulator is working in the following processes:

- When the cabin stops at the ground floor for a long time, the nitrogen has enough time to finish the heat exchange process. In this case, the nitrogen follows an isothermal process

approximately as shown in Fig. 9, where the value of n_{ISO} is set at 1.11;

- When the cabin is moving, the change in the gas state relatively fast and approximates to an adiabatic polytrophic process, as shown in Fig. 10, where the value of n_{POLY} is set at 1.8 for both travel directions.

The elevator can be controlled with a good speed performance as shown in Fig. 11 when the research results of poly index and other factors, which include the pump-motor's leakage, mechanical friction and viscous friction, ambient temperature effects on the accumulator, oil compensation to accumulator, system temperature's effects on the control performance, cabin's speed control, vibration and noise study. The speed control study of different types of energy-saving hydraulic elevator will be discussed in detail in other publications. On the basis of the good speed control results, a series of experiments were carried out to investigate the power consumption characteristics of Type 3.

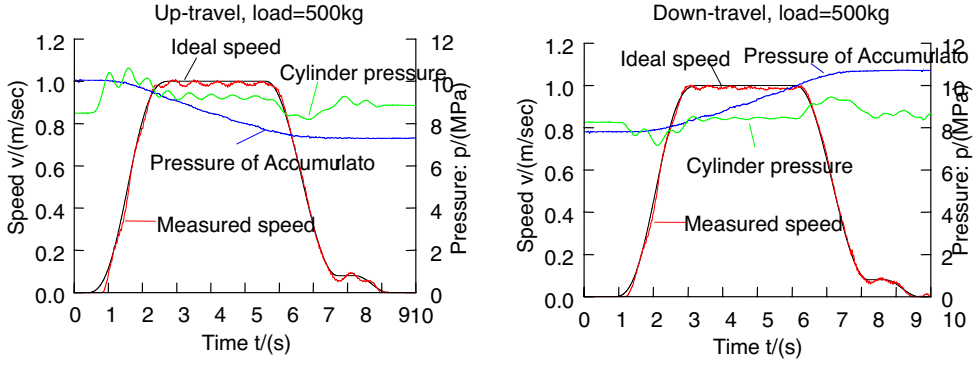

Fig. 11 Speed control performance of Type 3

4 EXPERIMENTAL STUDY ON ENERGY CONSUMPTION

4.1 Measurement condition

Oil temperature affects the power consumption by changing the pump volume efficiency and friction loss. In system the Type 3, when the temperature goes high, the pump volumetric loss will go up, but the friction loss (include mechanical friction and viscous resistance) becomes much smaller than that at low temperature. So the overall energy loss will come down, as the oil temperature becomes higher. Considering this temperature effect, the oil tank's temperature was kept at 26~30ºC and the oil temperature in the closed circuit was kept at 21~24ºC in order to obtain more accurate

measurements of the system power consumption.

The typical load in the cabin was chosen for empty load 0kg, half load 500kg, and full load 1000kg. The travel height was from the ground floor to the 2nd floor or from the 2nd floor to the ground floor.

4.2 Definitions for the measurements of power consumption

The energy loss or power consumption of each component or part of the system as shown in Fig. 2 cannot be measured directly. The only way is to measure flow rate and pressure, or current and voltage.

$$P_{\mathrm{a}} = p_{\mathrm{a}} \cdot q_{\mathrm{a}} \tag{2}$$

$$P_{\mathrm{va}} = p_{\mathrm{va}} \cdot q_{\mathrm{va}} \tag{3}$$

$$P_{\mathrm{vc}} = p_{\mathrm{vc}} \cdot q_{\mathrm{vc}} \tag{4}$$

$$P_{\mathrm{c}} = p_{\mathrm{c}} \cdot q_{\mathrm{c}} = 0.5 \cdot p_{\mathrm{c}} \cdot A_{\mathrm{c}} \cdot v_{\mathrm{j}} \tag{5}$$

$$P_{\mathrm{jz}} = (m_{\mathrm{j}} + m_{z}) \cdot (g \pm a_{\mathrm{j}}) \cdot v_{\mathrm{j}} \tag{6}$$

$$P_{\mathrm{im}} = \sqrt{3} \cdot U_{\mathrm{m}} \cdot I_{\mathrm{mt}} \tag{7}$$

where

P_{a} =Accumulator's power output (up-travel) or input (down-travel) ;

p_{a} =Pressure of the accumulator;

q_{a} =Flow rate of the accumulator;

p_{va} =Pressure of pump-motor (PM) (accumulator side);

q_{va} =Flow rate of PM (accumulator side);

P_{va}=PM's Power input (up-travel) to the accumulator or output (down-travel) from the accumulator

P_{vc}=PM's Power input (up-travel) to the cylinder or output (down-travel) from the cylinder

p_{vc} =Pressure of PM (cylinder side);

q_{vc} =Flow rate of PM (cylinder side);

P_{c} =Cylinder's power input (up-travel) or output (down-travel) ;

p_{c} =Pressure of the cylinder;

q_{c} =Flow rate of the cylinder;

A_{c}=Area of piston (rod side);

v_{j}=The speed of cabin;

P_{jz}=Power input (up-travel) or output (down-travel) of the cabin and load

m_{j}=Mass of cabin;

m_{z}=Mass of load;

a_{j}=Acceleration of the cabin;

P_{im}=Electric power input or output of the electric motor

U_m=Voltage of electric motor

I_{mt}=Active current input or output of the electric motor

In this experimental study, the energy loss of the converter is neglected because normally the efficiency of a converter is higher than 96%[4], which is much higher than other components in the hydraulic elevator system.

It would become too complicated if the current and voltage of the electric motor were detected directly. In the experimental study, the converter acted also as a measuring device. In order to carry out the vector control, the converter must measure the current and the voltage in real-time. The converter in this experiment could output these two signals in real-time by an analog port. These two signals were collected by the measuring computer, and the power input/output to the electric motor (it was also the power input to the system) could be calculated.

In order to obtain the information of power loss of each component, the following definitions and equations need to be clarified:

$$\Delta P_{sva} = \pm(P_a - P_{va}) \tag{8}$$

$$\Delta P_{svc} = \pm(P_{vc} - P_c) \tag{9}$$

$$\Delta P_{slft} = \pm(P_c - P_{jz}) \tag{10}$$

$$\Delta P_{smp} = P_{im} \pm (P_{va} - P_{vc}) \tag{11}$$

$$W_a = \int_0^t P_a \cdot dt \tag{12}$$

$$W_{im} = \int_0^t P_{im} \cdot dt \tag{13}$$

$$W_{jz} = \int_0^t P_{jz} \cdot dt \tag{14}$$

$$\eta_t = \frac{P_{jz}}{P_{im} + P_a} \quad \text{(up-travel)} \tag{15}$$

$$\eta_t = \frac{P_a}{P_{im} + P_{jz}} \quad \text{(down-travel)} \tag{16}$$

$$\eta_{te} = \frac{W_{jz}}{W_{im} + W_a} \quad \text{(up-travel)} \tag{17}$$

$$\eta_{te} = \frac{W_a}{W_{im} + W_{jz}} \quad \text{(down-travel)} \tag{18}$$

where

ΔP_{sva} =Power losses on valve 1, pipes and hoses at accumulator side;

ΔP_{svc}=Power losses on valve 2, pipes and hoses at cylinder side;

ΔP_{slft}=Power losses on cylinder, assembly pulley, roping, and cabin;

ΔP_{smp} =Power losses on the shaft of electric motor and pump-motor (PM);

W_a=Energy input to or output from the accumulator during a full operation (from start to stop);

W_{im}=Active energy exchange between the converter and electric motor during a full load operation;

W_{jz}=Energy input to or output from the cabin during a full load operation;

η_t=Overall efficiency of the hydraulic elevator system during a full operation;

η_{te}=The average efficiency of the elevator system during a full load operation.

4.3 Measurement result and analysis

In this experiment at study, the physical quantities related to power consumption (P_{va}, P_a, P_{vc}, P_c, P_{jz} and P_{im}) were measured. In order to show the power consumption of each component clearly, considering the similarity of (P_{va} & P_a) and (P_{vc} & P_c & P_{jz}), only three curves, P_a, P_{jz}, and P_{im}, were selected for display in the following figures, which are the experimental curves of power consumptions of each main component (or parts) during full up- and down-travel operation with the load 0 kg, 500 kg, and 1000 kg.

In Fig. 12 (a), P_a (power output from accumulator during operation) is on the increase following the increase rate of P_{jz} (power input to cabin during operation) before 2.5 second, indicating that the flow rate of the accumulator meets the demand of the speed increase of the cabin. Hence the product of flow rate and pressure (the output power) is increasing in spite of the accumulator pressure reducing during the same period. In the next period, 2.5 sec to 5.7 sec, P_a goes down following the drop in accumulator pressure while the flow rate is kept at a constant value as the cabin is running at constant speed. Meanwhile, the value of P_a is higher than P_{jz}, which means the energy being used to drive the cabin is mainly from the accumulator, so the value of power input to / output from the electric motor P_{im} can be kept small. The negative value of P_{im} before 1.8 second indicates the electric motor is acting as a load to the energy from the accumulator. As P_{im} goes positive after 1.8 second, the electric motor is used to compensate the power supply from the accumulator to meet the energy demand of the cabin or rather the load.

In the conventional valve control elevator, the electric motor is used to provide energy for the up travel, and some proportion of energy is also lost due to the throttle control, hence the power demand

of electric motor is rather high. During the down travel, the potential energy of cabin is used and the elevator is traveling down under its own weight, so the potential energy is converted into heat through the throttle control and additional cooling power may be required if necessary. In the system type 3 being discussed, the situation is rather different. During the elevator down travel, the potential energy of the cabin weight with no load is not big enough to counter balance the hydraulic energy installed in the accumulator and to drive the elevator down, so the energy supply from the electric motor P_{im} is required as shown in Fig. 12 (b). This means that during the cabin's down-travel, P_{jz}, (cabin's power output) plus P_{im} (electric motor's power output) minus the system power losses equals P_a (the power input to the accumulator), as written in equation (19):

$$P_a = P_{jz} + P_{im} - \Delta P \tag{19}$$

where

ΔP =The total power losses of the system

While in Fig. 12 (a) during the cabin's up-travel, the relation is:

$$P_{jz} = P_a + P_{im} - \Delta P \tag{20}$$

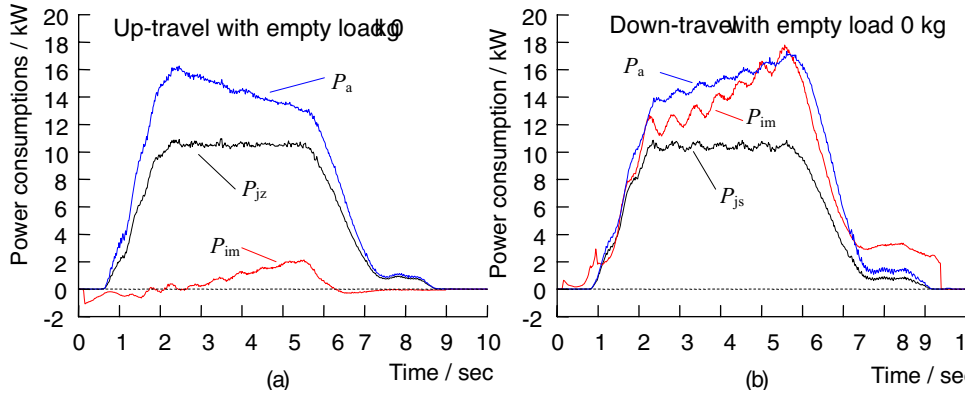

Fig. 12 Power consumption of main components during the operations with empty load

All the relations of the curves in Fig. 12, Fig. 13 and Fig. 14 can be described by equation (20) (for up-travel) and (19) (for down-travel). In Fig. 13, the levels of the power consumption (or power output) of the cabin and the accumulator are at proximately the same with half load (500kg). In this case, the output power of the electric motor is mainly used to overcome the power losses of the system.

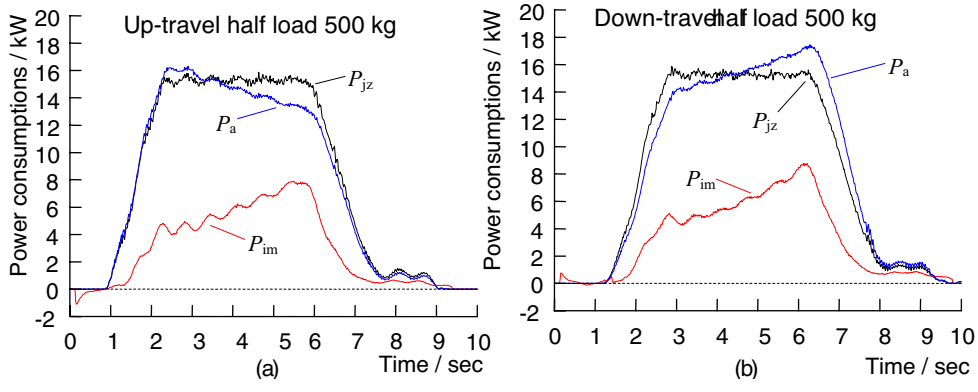

Fig. 13 Power consumption of main components during the operations with half load 500 kg

In Fig. 14 (a) (up-travel with full load), the electric motor's power output P_{im} is quite high in order to drive the heavy load together with the contribution from the accumulator. A similar situation occurred to P_{im} in Fig. 12 (b) during the elevator's down-travel when empty. On the other hand, in Fig. 14 (b) (down-travel with full load), the power output of the electric motor is very small since the heavy load has provided enough potential energy/power P_{jz} to meet the requirement of accumulator's energy P_a. A similar situation occurred while P_{im} in Fig. 12 (a) when the elevator up-travels with empty load.

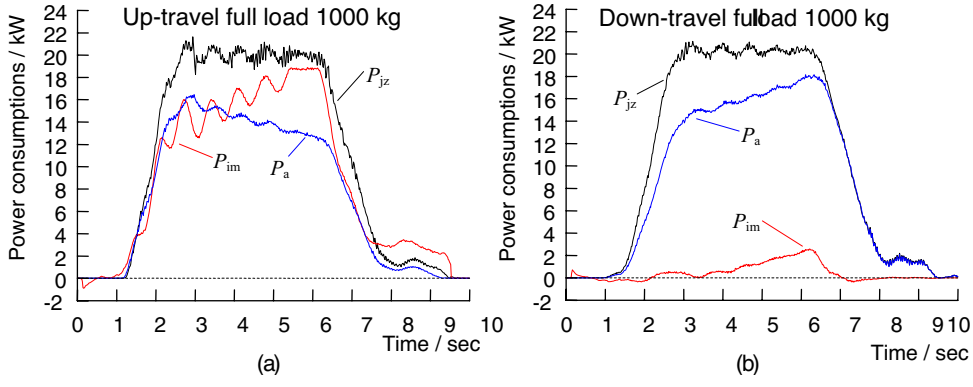

Fig. 14 Power consumption of main components during full load (1000 kg) operations

The similarity of the curves P_{im} shows that the accumulator is acting as the cabin's "varying counter balance". No matter it the cabin up- or down-travels, the power input to the elevator (the electric motor's power output) is compensating for difference of P_{jz} and P_a minus the system losses. This

can be written as:

$$\left|P_{\text{im}}\right| = \left|P_{\text{jz}} - P_{\text{a}}\right| - \Delta P \tag{21}$$

Based upon the results of power consumption, the power losses of each component (or part) can be calculated and plotted as shown in Fig. 15. For clarity, only the curves for up-travel are shown in Fig. 15, since the curves for light load down-travel and heavy load up-travel are similar, and the curves for heavy load down-travel and light load up-travel are similar.

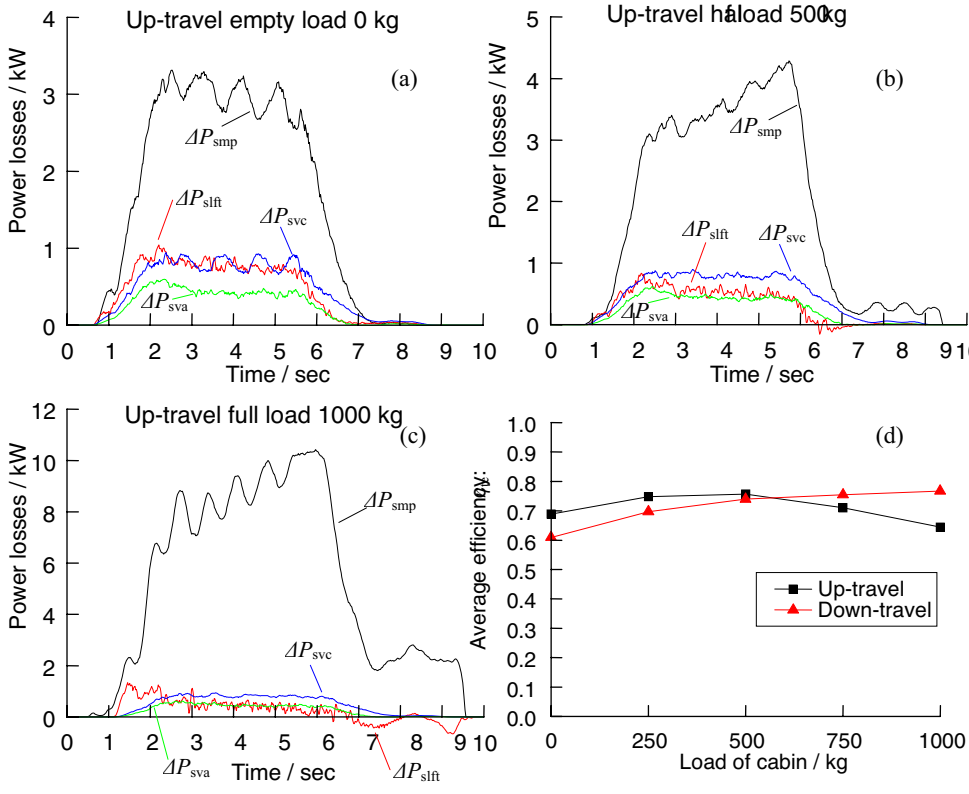

Fig. 15 Power losses of main components and Curves of "Efficiency to Load"

In Fig. 15, ΔP_{sva} (power losses on valve 1, pipes and hoses at accumulator side), ΔP_{svc} (power losses on valve 2, pipes and hoses at cylinder side), ΔP_{slft} (power losses on cylinder, assembly pulley, roping, and cabin), and ΔP_{smp} (power losses on the shaft of electric motor and pump-motor) are plotted to show the main power losses of the system. It can be seen the power loss on the shaft of the electric motor and pump-motor ΔP_{smp} is much higher than the other system power losses. This high power loss on the shaft is because of the low efficiency of the soil-submerged electric motor, which agitates

oil in the tank, and also the pressure losses and leakages of the hydraulic pump-motor (PM) unit.

In Fig. 15 (b) and (c), ΔP_{slft} (the power loss on cylinder, assembly pulley, roping, and cabin) goes negative at 6.4 second in Fig. 15 (b), and at 6.8 and 8.5 second in Fig. 15 (c). When ΔP_{slft} goes negative, it is not power losses anymore, but power contribution to the system. For the duration of the negative values of ΔP_{slft}, the elevator is decelerating and the inertial force of the moving parts (cylinder, roping, assembly pulley, and cabin) contributes to the driving power to the system. In order to evaluate the energy-saving performance of system Type 3 using equation (17) and (18), the average overall system efficiency variations with different load are calculated and shown in Fig. 15 (d), where the highest efficiency occurs when the elevator is half loaded.

Based on the results of power consumption and power losses, the overall system efficiency is plotted against time as shown in Fig. 16 with half load 500kg. There are peak periods at 6.5 to 8.0 second in Fig. 16 (a) and 6.5 to 7.5 second in Fig. 16 (b) on the curves. These two periods correspond with the elevator deceleration periods. The efficiency at these periods is higher than that at the rest of the time because of the inertial masses of the system moving parts, which introduce the energy during the elevator's accelerating and release the energy during the decelerating.

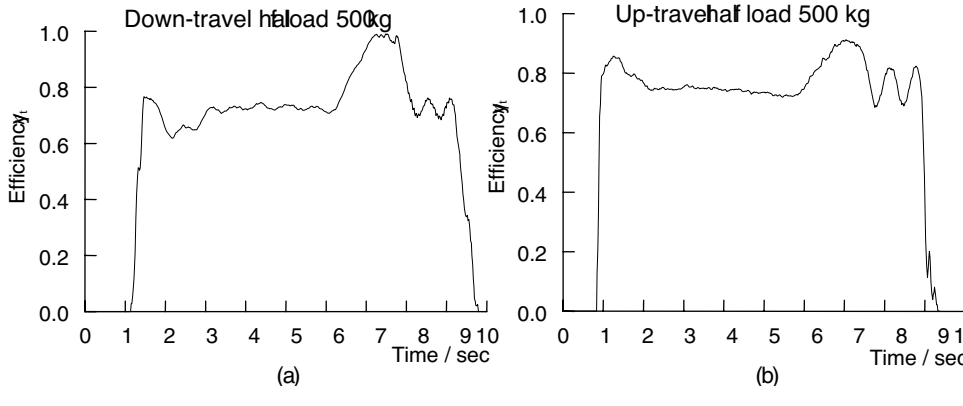

Fig. 16 Overall efficiency curves during the operations with half load 500 kg

5 EVALUATION

In this paper, comparisons are made between (I) normal valve controlled hydraulic elevators, (II) standard frequency converter controlled hydraulic elevators, (III) the system Type 2 (Fig. 7), and (IV)

the system Type 3 (Fig. 8). The basic parameters of the experiment elevators are given in Table 1, Table 2 and Table 3 give the detail comparisons on efficiency and power requirement.

To obtain the comparison of energy consumption between normal valve-controlled hydraulic elevators, standard frequency converter controlled hydraulic elevators, and system Type 3, the sum of energy consumption at empty, half, and full load conditions are calculated [4]. The result is shown in Table 4.

Table 1 Comparison of total average efficiency of different types of hydraulic elevator

Testing platform	In reference material [3]	In this paper
Height of each floor	4.04 m	2.85 m
Rated maximum load	800 kg	1000 kg
Rated Maximum speed	0.5 m/s	1.0 m/s

Table 2 Comparison of total average efficiency of different types of hydraulic elevator

Types of hydraulic elevator	Normal valve controlled	Standard frequency converter controlled	System Type 2	System Type 3
Total average efficiency	25%	44%	58%	71%

Table 3 Comparison of power requirement of different types of hydraulic elevator

Types of hydraulic elevator	Normal valve controlled	Standard frequency converter controlled	System Type 2	System Type 3
Power requirement (kW)	29~33	29~33	15~18.5	9.5~11

Table 4 Comparison of energy consumption of different types of hydraulic elevator

Types of hydraulic elevator	Normal valve controlled	Standard frequency converter controlled	System Type 3
Full load	334 kJ	153 kJ	93 kJ
Half load	270 kJ	124 kJ	60 kJ
Empty load	207 kJ	95 kJ	83 kJ
Sum of above	811 kJ	372 kJ	236 kJ
Rate of energy saving of Type 3	(811-236)/811 =70.8%	(372-236)/372 =36.3%	—

6 CONCLUSIONS

The following conclusions can be drawn based upon the comparisons mentioned above:

- Overall efficiency of a hydraulic elevator using an accumulator as the energy restoring component can reach 71%, much higher than the normal valve controlled hydraulic elevator (25%) and a standard frequency converter controlled hydraulic elevator (44%).

- The power requirement of a hydraulic elevator using an accumulator as the energy restoring component can be reduced to a level of a traction elevator (smaller than 11kW), which is much lower than that for a normal valve or standard frequency converter controlled hydraulic elevator (more than 29kW).

- Compared with a normal valve controlled hydraulic elevator, the rate of energy saving of a hydraulic elevator using an accumulator as the energy restoring component can be more than 70.8%. When compared with a standard frequency converter controlled hydraulic elevator, the rate of energy saving can be more than 36.3%.

7 REFERENCES

(1) Edwards J. T., *Conserving Energy in Oil Hydraulic Elevator System*, Elevator World, 1992, 40(7): 51~52
(2) Longlin Ran, *Study on a New Type of Speed Control System and Energy-Saving in Hydraulic Elevator*, Ph. D. Thesis, Zhejiang University, Hangzhou, 1998
(3) Bing Xu, *Study on Energy-Saving Control System of a VVVF Hydraulic Elevator Using Hydraulic Accumulator*, Ph.D. Thesis, Zhejiang University, Hangzhou, 2001
(4) Jianjie Lin, *Hydraulic Elevator of Energy-saving with the Closed Circuits*, Ph.D. Thesis, Zhejiang University, Hangzhou, 2005
(5) Shicai Feng, *Determination of theoretical and practical value of the poly index of bladder accumulator's*, Chinese Hydraulics and Pneumatics, 2002-5, page 3~5
(6) Ji Fan, Jin Wu, *Research on the energy performance of accumulator*, Chinese Hydraulic Industry, 1990-2, page 2~6
(7) Zhiming Wang, *Analysis of bladder accumulator*, Chinese Hydraulic Industry,

1991-2, page 35~38

(8) XU Bing, OUYANG Xiaoping, YANG Huayong. *Energy-Saving System Applying Pressure Accumulators for VVVF Controlled Hydraulic Elevators*. Fluid Power Systems and Technology Division. 2003 ASME International Mechanical Engineering Congress and Exposition. November 16-21, 2003. Washington, DC

(9) Xu Bing,Yang Jian, Yang Huayong, *Comparison of energy-saving on the speed control of VVVF hydraulic elevator with and without pressure accumulator*, Mechatronics, 2005(15), pp1159-1174

(10) Dongming Hu, Bin Xu, Jianjie Lin, Huayong Yang, *An energy-saving converter controlled closed circuit hydraulic elevator system*, Proceedings of 2005 Annual Assembly of the Chinese Association of Mechanical Engineering, pp303-304

(11) Jianjie Lin, Bing Xu, Huayong Yang, *Converter controlled hydraulic system with accumulator*, Chinese Journal of Mechanical Engineering, 7.2003

[1] Edwards J. T., *Conserving Energy in Oil Hydraulic Elevator System*, Elevator World, 1992, 40(7): 51~52
[2] Longlin Ran, *Study on a New Type of Speed Control System and Energy-Saving in Hydraulic Elevator*, Ph. D. Thesis, Zhejiang University, Hangzhou, 1998
[3] Bing Xu, *Study on Energy-Saving Control System of a VVVF Hydraulic Elevator Using Hydraulic Accumulator*, Ph.D. Thesis, Zhejiang University, Hangzhou, 2001
[4] Jianjie Lin, *Hydraulic Elevator of Energy-saving with the Closed Circuits*, Ph.D. Thesis, Zhejiang University, Hangzhou, 2005
[5] 封士彩，*气囊式蓄能器气体多变指数理论值和实际值的确定*，《液压与气动》，2002-5, page 3~5
[6] 范基，吴劲，*蓄能器的蓄能性能研究*，《液压工业》，1990-2, page 2~6
[7] 王志明，*气囊式动压蓄能器分析*，《液压工业》，1991-2, page 35~38

Return to Contents

Hydraulic Fluids, Sensors and Testing I

High-pressure properties of hydraulic fluids – measuring and differences

J-P Karjalainen, R Karjalainen, K Huhtala, M Vilenius
Tampere University of Technology, Institute of Hydraulics and Automation

ABSTRACT

Hydraulic fluid and its properties have a particularly significant role in accurate high-pressure systems design and performance, such as common rail diesel injection systems. However, for a designer there is quite inadequate and inaccurate information available on the properties of different types of hydraulic fluids – especially at high pressures.

In this paper the measuring principles for determining the most important fluid parameters – bulk modulus, density, sound velocity and viscosity – are introduced. The measurements were carried out with different types of commercial hydraulic fluids at pressures up to 1500 bar at different temperatures. The dynamic parameters (sound velocity, bulk modulus, density) were measured using a system based on defining the pressure wave propagation time in a rigid straight pipe. The viscosity was measured using a modified falling ball viscometer.

NOTATION

B_{eff}	Effective bulk modulus [Pa]
B_{sa}	Secant adiabatic bulk modulus [Pa]
B_{si}	Secant isothermal bulk modulus [Pa]
B_{ta}	Tangent adiabatic bulk modulus [Pa]
B_{ti}	Tangent isothermal bulk modulus [Pa]
c	Speed of sound in the fluid [m/s]
K	Calibration constant [-]
p	Pressure [Pa]
p_{atm}	Atmospheric pressure [Pa]
t	Falling time [s]
T	Temperature [ºC]
ν	Kinematic viscosity [m^2/s]
η	Dynamic viscosity [Pas]
ρ_n	Density at measured pressure and temperature [kg/m^3]
$\rho_{atm,T}$	Density at atmospheric pressure and at temperature T [kg/m^3]

Power Transmission and Motion Control 2006 Edited by Dr D N Johnston and Professor K A Edge

1. Measuring the dynamic parameters of hydraulic fluids

In systems demanding high accuracy the hydraulic fluid dynamics have an important role. The bulk modulus and density are the most important dynamic parameters, sound velocity can be calculated using these values. Fluid dynamics affect for example systems natural frequency, damping and pressure hammer phenomenon. Moreover, speed of sound in the fluid sets the upper limit to the control response speed. (6, 13, 14)

There have been more than one methods e.g. (7, 9, 12, 15) presented for measuring the dynamic parameters of a hydraulic fluid – some of which are even standardized. All the methods are more or less based on the idea of finding out the pressure wave propagation time in a straight pipe of known length. Most of the methods have a pump as a pressure source producing continuous pressure fluctuation into the line. This paper presents a different method where static pressure level is raised with an intensifier and a single pressure peak is produced into the line with a cylinder. An interesting discovery was that this method seemed to be giving different results for bulk modulus than at least one of a so called "continuous method" (11) which might be due to different heat transfer from the systems. This subject is discussed more in detail in chapter 3.

1.1 Basic principle

The basic principle is to measure the speed of sound in the fluid and then by using equations (1) (13) and (2) (4) iteratively calculate the density of the fluid and the effective bulk modulus of the system. Equation (2) assumes constant (isothermal) bulk modulus and more accurate value could be obtained by integration, if necessary. Fluid bulk modulus can be found out once the compliance of other components is removed from the effective value and the fluid is considered air free.

$$c = \sqrt{\frac{B_{eff}}{\rho_n}} \tag{1}$$

$$\rho_n = \rho_{atm,T} e^{\frac{p - p_{atm}}{B_{eff}}} \tag{2}$$

1.2 Measuring system

A schematic picture of the measuring system used is illustrated in figure 1. Instead of using a hydraulic pump producing continuous pressure fluctuation, static pressure level up to 1500 bar is produced with an intensifier. After the static pressure level is raised a single-acting cylinder is rapidly knocked to produce a single dynamic pressure peak into the fluid inside the measuring pipe. The propagation of this peak is measured with two piezo-electric pressure transducers located at known distance L from each other. From computationally calculated phase shift of the wave the speed of sound can be defined. Temperature is adjusted with an isolated and separate temperature control circulation run by a gear pump.

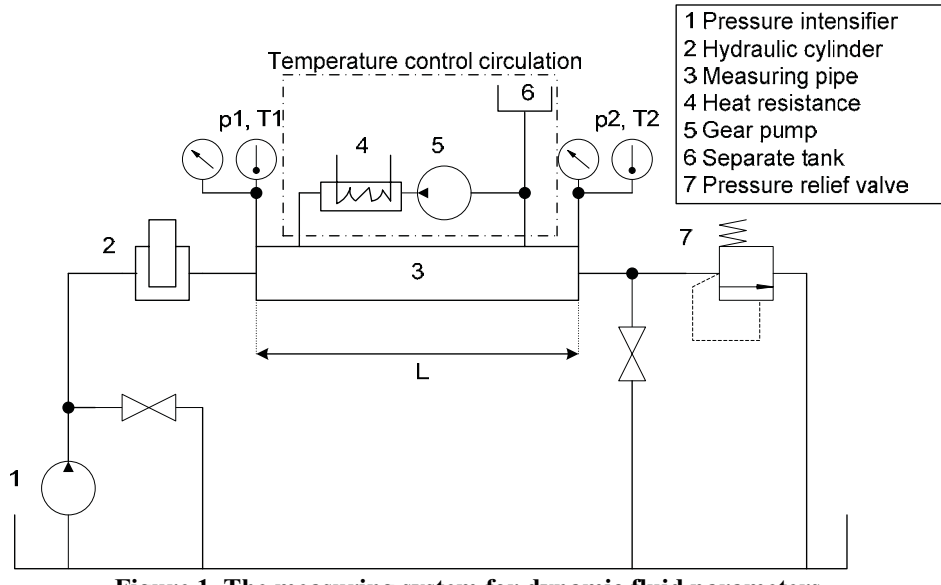

Figure 1 The measuring system for dynamic fluid parameters.

2. Measured dynamic parameters

Speed of sound in the fluid, bulk modulus and density were measured with five different types of commercial hydraulic fluids. Temperatures were 40ºC and 70ºC and pressure range was 100-1500 bar. The fluids and reported fluid characteristics are listed in table 1. The results of the measurements are presented and discussed in the following.

Table 1 The measured fluids.

Hydraulic fluid	Density, atm.pressure, 15 ºC temperature	Viscosity, 40 ºC temperature	Viscosity, 100 ºC temperature
ISO VG 46 Mineral oil	875 kg/m³	46 cSt	6,9 cSt
ISO VG 46 Pine oil	928 kg/m³	46 cSt	9,9 cSt
ISO VG 46 Synthetic HF-E fluid	928 kg/m³	46 cSt	9,1 cSt
ISO VG 46 High-VI mineral oil	880 kg/m³	46 cSt	8,4 cSt
SAE 10W-30 Diesel engine oil	880 kg/m³	73 cSt	11,3 cSt

2.1 Speed of sound in a fluid

The results of measured speed of sound in a fluid are presented in figures 2 and 3. The differences of absolute values between fluids are quite small. Moreover, all the fluids seem to behave according to the same trend. Speed of sound behaves quite linearly up to almost 1000 bar but after that it becomes more clearly of second order. Therefore a second order polynomial was fitted to all the measurements and as it may be noticed with good results. Even the measuring points at lower pressures, considered linear at first, actually seem to follow the parabola. Otherwise the speed of sound behaves as expected. It increases at rising pressure and decreases at rising temperature.

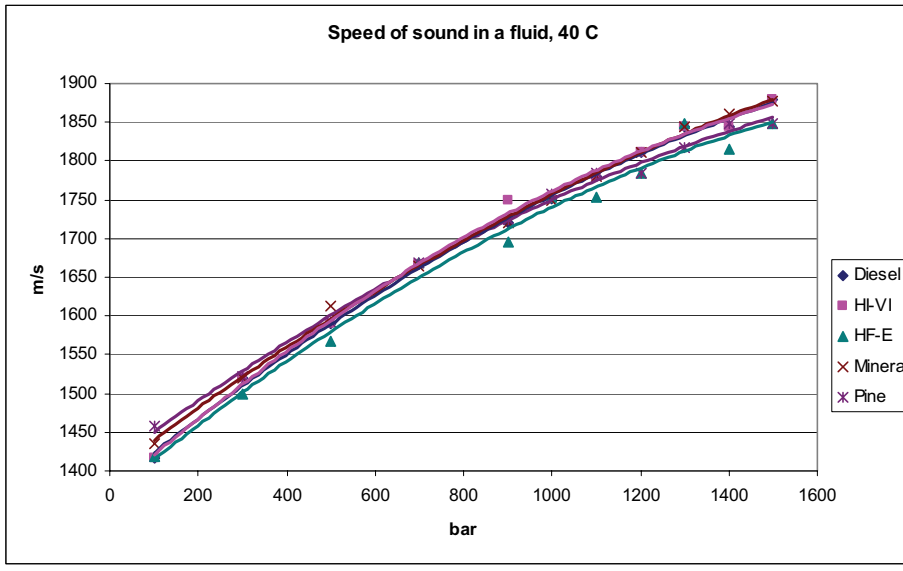

Figure 2 The measured speed of sound at 40 ºC and at pressures 100-1500 bar.

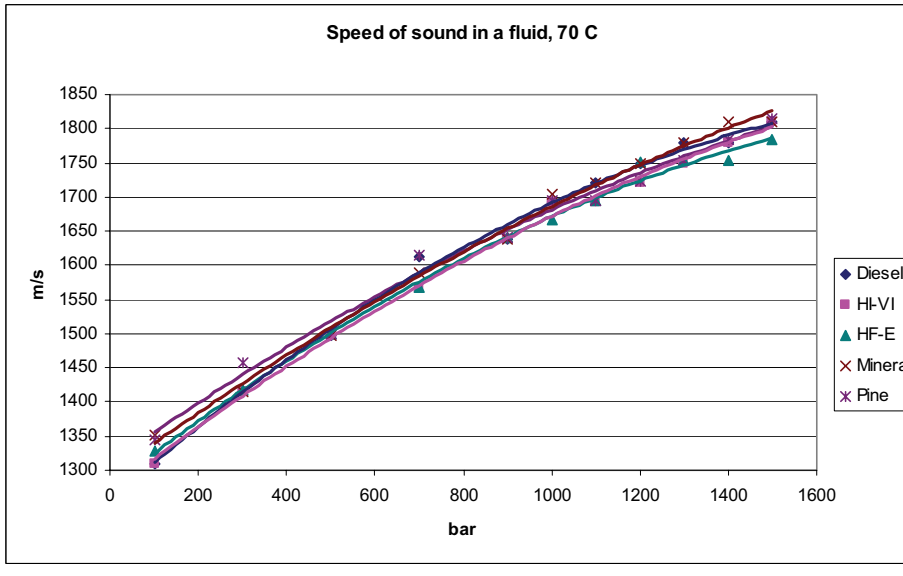

Figure 3 The measured speed of sound at 70 ºC and at pressures 100-1500 bar.

2.2 Fluid bulk modulus

Figures 4 and 5 illustrate the results of measured fluid bulk moduli. The small variation of speed of sound between different fluids might have made it intriguing to claim that there are no fluid related differences expected in control sense either. But having look at the results of bulk moduli it is clear this is not true. The difference between the absolute values of pine oil (having the highest values) and the three mineral oils is about 200 MPa which is quite big a difference especially at lower pressures – over 10%!

Although having differences between absolute values all the fluids are behaving according to the same trend. Again, after considering the bulk modulus linear a second order function was fitted to the measurements and as it can be noticed with good correlation. After this fitting it was also noticed that practically all the measuring points even at lower pressures follow the parabola. Otherwise the bulk modulus behaves according to theory, increases at increasing pressure and decreases at increasing temperature.

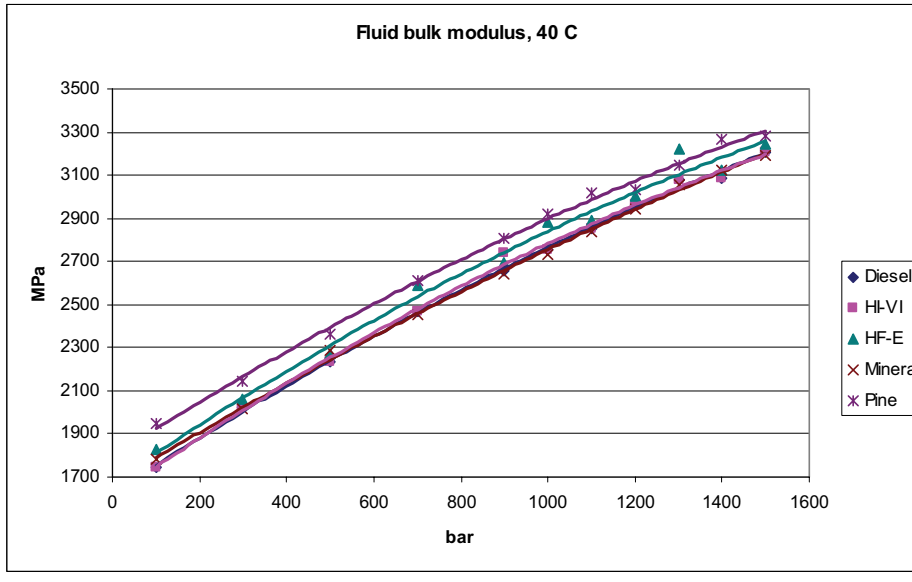

Figure 4 The measured bulk modulus at 40 ºC and at pressures 100-1500 bar.

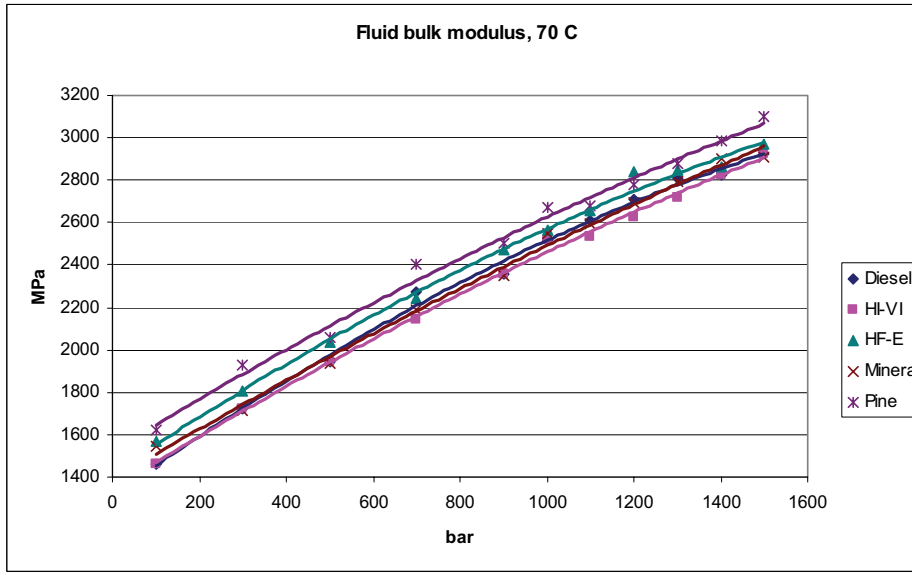

Figure 5 The measured bulk modulus at 70 ºC and at pressures 100-1500 bar.

2.3 Fluid density

The results of measured densities are presented in figures 6 and 7. Similar to speed of sound and bulk modulus a second order function was fitted to the measuring data with excellent correlation. Again, all the fluid densities follow the same trend. The differences between absolute values could in practice be read from table 1 due to a highly identical shape of the density parabolas. The density increases at increasing pressure and decreases at increasing temperature as it should.

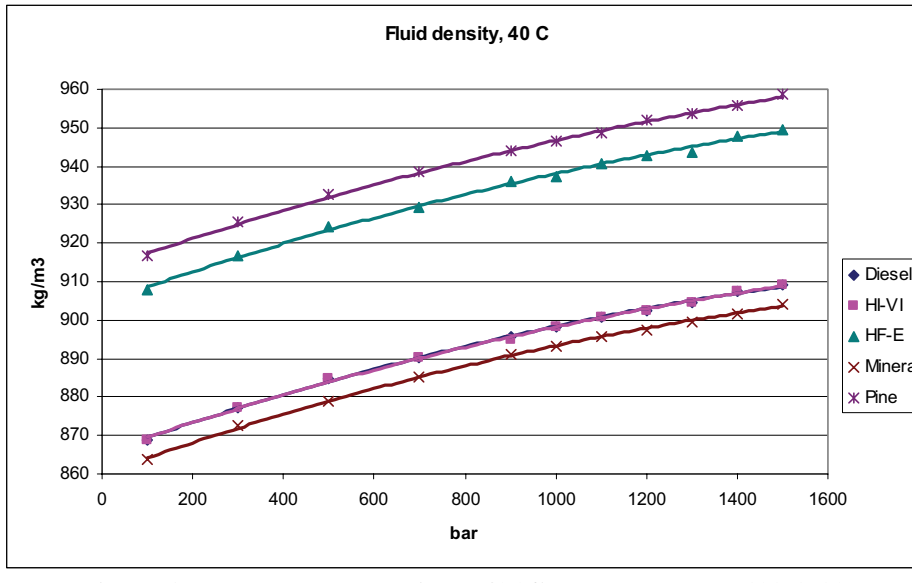

Figure 6 The measured density at 40 ºC and at pressures 100-1500 bar.

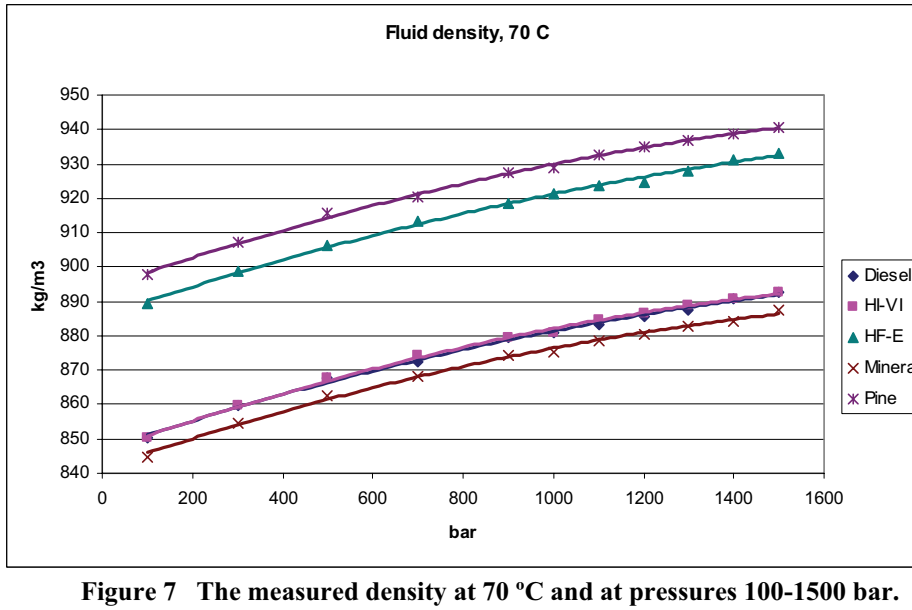

Figure 7 The measured density at 70 ºC and at pressures 100-1500 bar.

3. On the effect of measuring system on dynamic fluid parameters

Although the basic theory behind measuring dynamic fluid parameters is quite the same the actual system may be realized in more than one way, as already mentioned earlier. Probably the biggest difference comes from the pressure source to be used. One could use a hydraulic pump to produce both the pressure level and the continuous dynamic pressure wave fluctuation. On the other hand it is possible to raise the pressure level to some static level (e.g. with an intensifier) and then produce the rapid dynamic pressure peak separately (e.g. with a cylinder or a valve). However, it is worth mentioning that the higher the desired pressure level is raised the more difficult it becomes to find a suitable hydraulic pump, at least at reasonable price. All in all, the selection of the pressure source would seam to have an effect on the results of dynamic fluid parameters. This is discussed in the following.

The dynamic parameters of all the fluids introduced in table 1 were also measured using a radial piston pump system (figure 8) described more in detail in (11). Pressure was raised up to over 600 bar using a series of throttles and the pressure ripple from the pump produced continuous dynamic fluctuation into the measuring line. The fluid was ensured and monitored air-free and discovered pressure wave reflections were also sorted out with the adjustable damping chamber (1, 5, 8) (and also monitored). Otherwise the concept was the same, pressure wave propagation was measured from the phase shift between two piezo-resistive pressure transducers. The measured fluids and the structures and materials of both the systems were exactly the same. Therefore the results of the two systems should be highly comparable and possible uncertainties in for example structure compliances or water content of fluids were exactly the same for both the two systems.

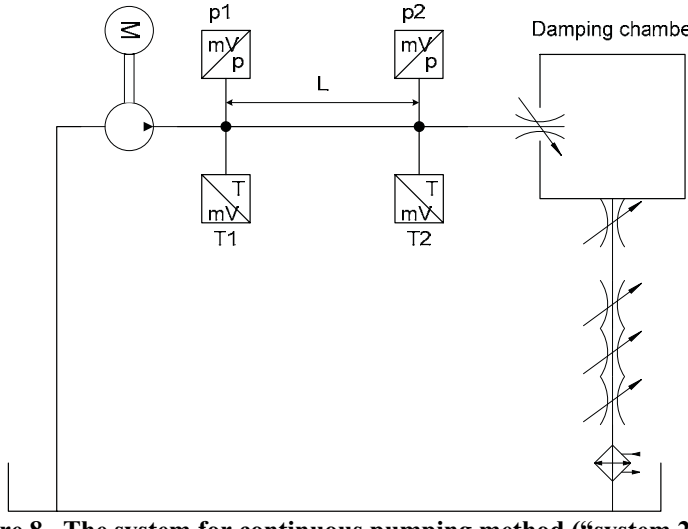

Figure 8 The system for continuous pumping method (“system 2”). (11)

The results of the “system 2” and the “system 1” (figure 1) are compared in figures 9 and 10. The fluid is ISO VG 46 mineral oil at 40 ºC, but exactly the same trend was discovered with all the other fluids and temperatures as well.

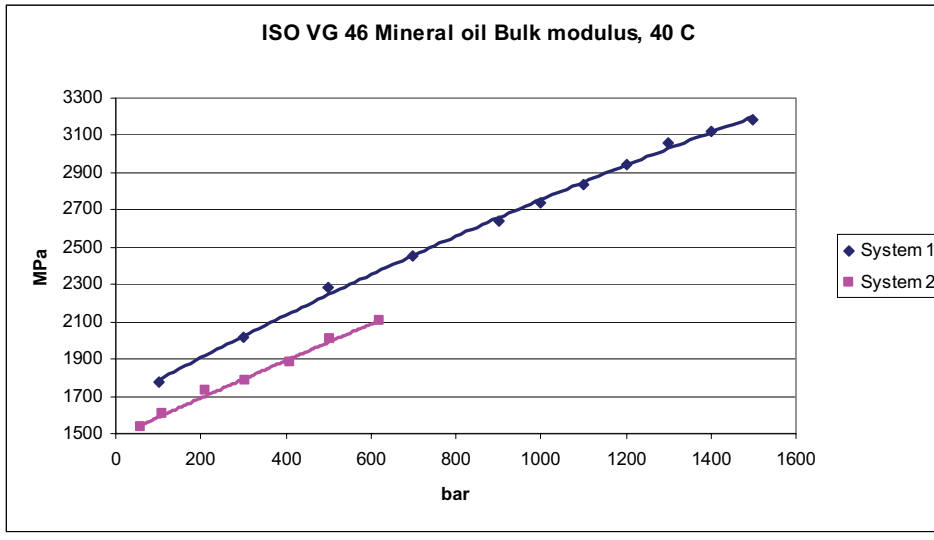

Figure 9 Comparing the measured bulk modulus at 40 ºC with two different systems.

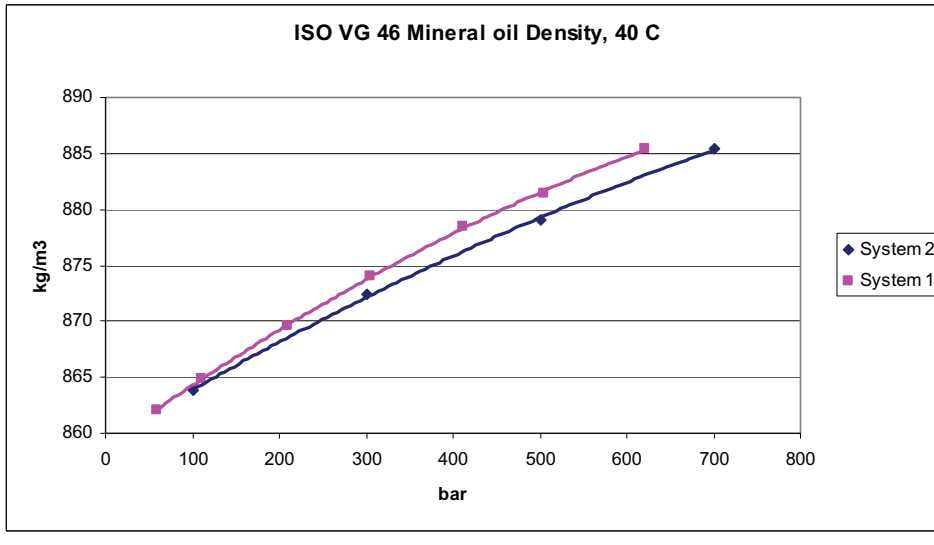

Figure 10 Comparing the measured density at 40 ºC with two different systems.

It can be noticed that the densities are in practice the same. But looking at the bulk moduli there is a clear 200 MPa difference between the absolute values while the trend of the results is exactly the same. What would these observations indicate? Independent simulations for dynamic fluid parameters explained in detail in (2, 11) were also carried out during the previous measurements (11). Then it was found out that the measured bulk moduli correlated best with calculated isothermal tangent values although the theory would have suggested otherwise – all these systems should measure the adiabatic tangent value. Performing the same simulations and comparing them to these new results gave different correlation. Now the calculated values did correlate best with calculated adiabatic tangent

values. This is also illustrated in figures 11 and 12. So it would be intriguing to at least suggest that the continuous pumping method would measure isothermal tangent bulk modulus and the single dynamic pressure peak system would measure the adiabatic tangent value.

The reason for different bulk moduli results between the two measuring systems is an interesting question. Some authors have suggested that the adiabatic compression process in hydraulic systems is not necessarily as easy to generalize (10). Usually an adiabatic process is considered fast for example compared to cylinder compression. But what is "fast enough"? An isothermal value should correlate with relatively slow compressions where the temperature remains constant and an adiabatic value describes a rapid change of state with constant enthalpy. The measured results would indicate that in continuous pumping there already happens heat energy transfer between the fluid and surroundings and that the actual situation in terms of fluid compression–decompression is closer to an isothermal process. Then by using a piston or a valve to produce a single rapid pressure peak into otherwise static situation would indicate the fluid compression–decompression to be closer to an adiabatic process with no heat energy transfer. This might have an important role in terms of system design and modeling because the absolute value difference between an isothermal and an adiabatic bulk modulus is quite remarkable. So the designer should have the knowledge on which of the values to use even if the actual measured parameters (or an accurate model) of the fluid itself would be otherwise known.

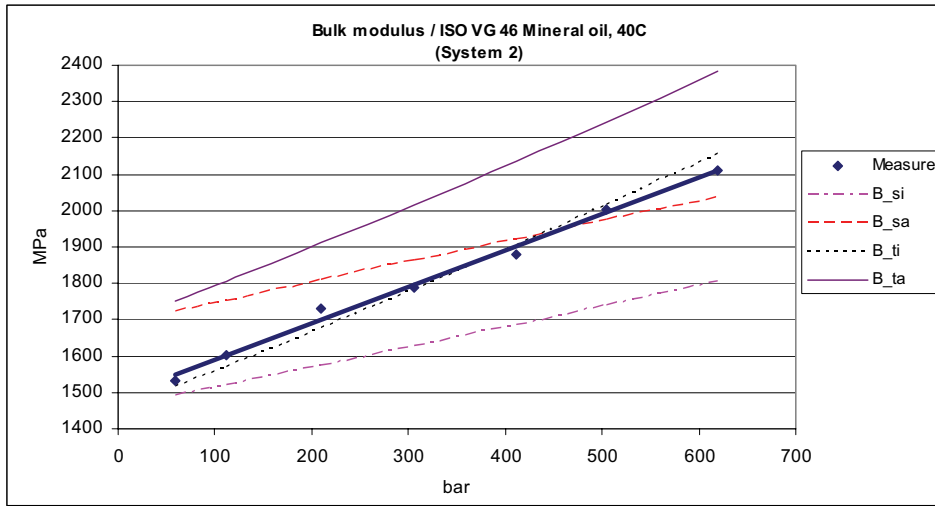

Figure 11 The measured and simulated results of bulk modulus at 40 ºC. (11)

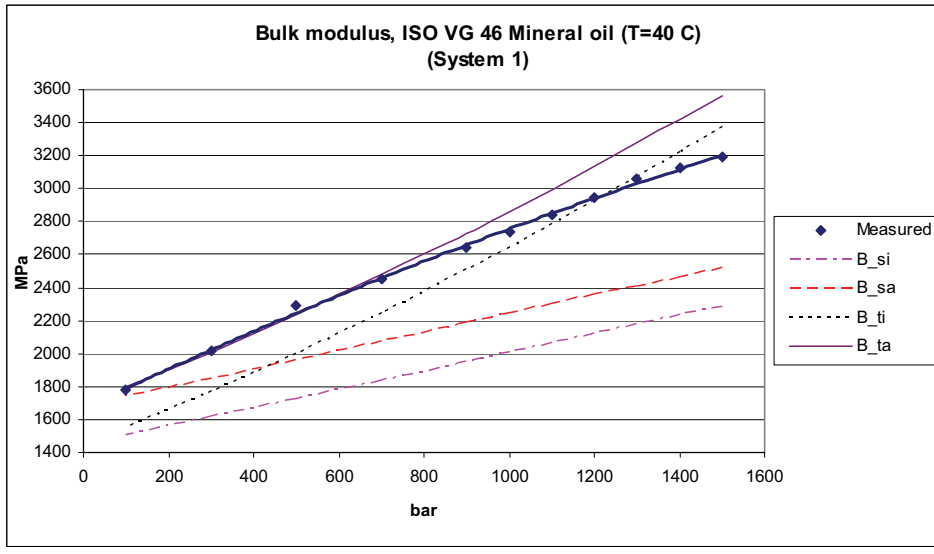

Figure 12 The measured and simulated results of bulk modulus at 40 ºC.

4. Measuring the viscosity of hydraulic fluids

In addition to fluid dynamics the viscosities of ISO VG 46 mineral oil and HF-E fluid (table 1) were measured using a specially developed measuring system. The concept is based on a conventional falling-ball viscometer only modified to be operable also at highly elevated pressures. Similar approaches are presented in chemical publications, e.g. in (3).

4.1 Basic principle

The basic principle of the measurements is familiar from the falling-ball viscometers used at air pressure. A steel ball inside a fluid-filled pipe falls between two fixed observing points and the falling time t is measured. After calibration and by knowing the properties of the steel ball and the density of the fluid the dynamic viscosity of the fluid can be calculated from the equation (3) (3). Then the kinematic viscosity can be calculated using the basic equation (4). The fluid density may be measured using the concept in chapter 1.

$$\eta = K(\rho_b - \rho_n)t \tag{3}$$

$$\nu = \frac{\eta}{\rho_n} \tag{4}$$

4.2 Measuring system

Schematic pictures of the hydraulic diagram as well as the viscometer itself are presented in figure 13. The viscometer rotates 180º round its axle. The observation of the ball is done electro-magnetically – optical or laser detection did not recognize the ball in all the fluids possibly due to darker color tones of the fluids. Once the ball reaches the observation point a sensor sends a signal to computational measuring program and starts a timer. The second

observation point shuts the timer. The timing system gave high repeatability. The diameter of the ball should not be selected too small or too large – at lower viscosities the falling time might become too quick and at higher viscosities too slow or even inconstant.

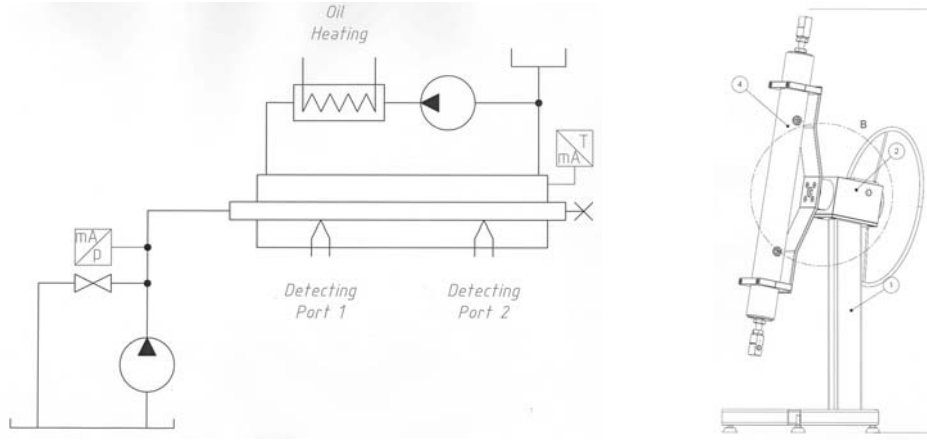

Figure 13 The measuring system for fluid viscosity.

Pressure level is raised with an intensifier up to 1500 bar and the system was designed to be fully de-aerated before measurements since air might distort the results (decrease actual viscosity). Temperature is maintained with an isolated control circuit run by a gear pump. Calibration should be performed at every measuring temperature individually because temperature expansion may change the clearances between the ball and the pipe due to different materials. Pressure should not have any effect due to heavy duty materials used. Calibration can be performed at air pressure using the fluid viscosity information in table 1 and Walther equation (5) (6) ($a \approx 0.8$, b and c are constants for the fluid concerned).

$$\boxed{\log^2(\nu + a) = b\log T + c} \qquad (5)$$

4.3 Measured viscosities

The viscosities of ISO VG 46 mineral oil and HF-E fluid in table 1 were measured at pressures of 100-1500 bar and at temperatures of 40 and 70 ºC. The results are presented in figure 14. Also the measured viscosities are following a parabola and as it can be seen from the results, the viscosity changes also heavily as a function of pressure especially at lower temperatures. The viscosity is more than doubled already at 500 bar. The viscosity of mineral oil seems to be changing more than the viscosity of HF-E at rising pressure. This might be explained by the different viscosity indexes of the fluids (mineral oil VI 100, HF-E VI 180). The lower the viscosity index the more the viscosity is changing, also as a function of pressure.

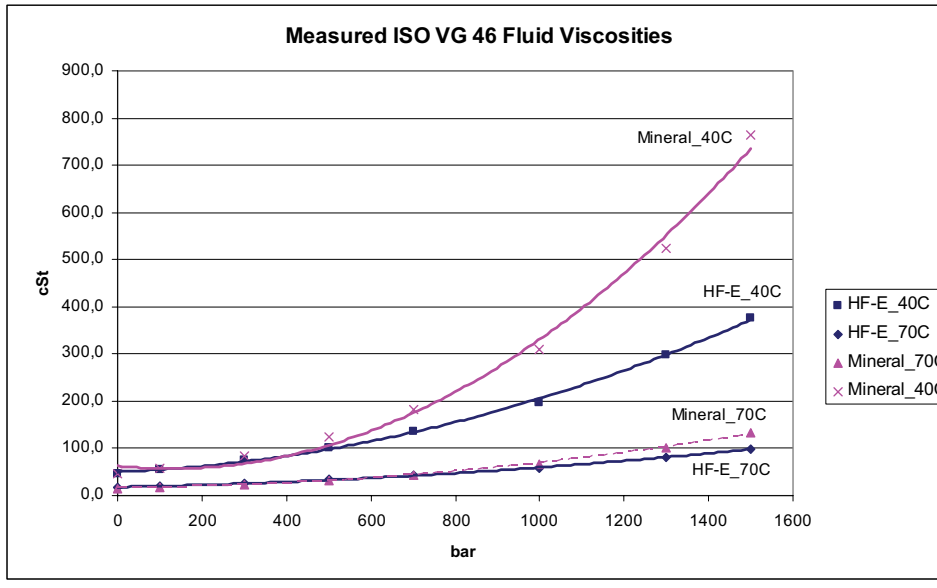

Figure 14 The measured viscosity of ISO VG 46 HF-E fluid at 40 ºC and 70 ºC.

An interesting phenomenon was discovered during the measurements. The fluid viscosity seemed to be showing some kind of capacitive behavior when pressure was suddenly dropped from higher level to lower. For example the mineral oil viscosity was measured at pressures of 0- 1500 bar (temperature 40 ºC) starting from the air pressure. After that the pressure was dropped from 1500 bar to air pressure again. After waiting 60 seconds the viscosity was measured and compared to the value measured earlier at the same conditions but prior to pressure raise. The measured viscosity was 54.7 cSt instead of earlier measured 46 cSt (difference over 18 %). The phenomenon is not permanent, after certain time the viscosity of the fluid returned to normal. Apparently, the phenomenon itself might be due to air bubbles coming out of solution when the fluid was rapidly depressurized or even from the cooling of the fluid after adiabatic expansion. Further research is needed but this might cause some unexpected fluid viscosity related dynamic behavior to systems where the pressure changes are large enough.

5. Conclusions

In this paper the high-pressure properties of hydraulic fluids are discussed and measuring systems for dynamic fluid parameters (speed of sound, bulk modulus and density) and viscosity are introduced. High-pressure dynamic properties of five different types of commercial hydraulic fluids were measured at pressures up to 1500 bar and at different temperatures. Two fluids were selected out of the same five representatives and the viscosities of those were measured also at different temperatures and at pressures up to 1500 bar.

Dynamic measurements did not reveal any differences between the fluid behaviors. However, there were quite significant differences in absolute values. Moreover, the results

indicated that the concept of adiabatic compression in hydraulic systems might be much more complex than usually suggested.

According to viscosity measurements the viscosity was also quite heavily pressure-dependent even at pressures well under 1000 bar. It was also discovered that the lower the viscosity index the more the fluid viscosity is pressure-dependent. The fluid viscosity was also discovered to show capacitive behavior when pressure was drastically dropped. For some period of time the fluid viscosity remained at a higher level than normal. Further research is needed, but this might cause some fluid viscosity related dynamic disturbance into systems with large pressure variations.

References

(1) Bergemann, M. 1993. Systematische Untersuchung des Geräuschverhaltens von Kolbenp. mit gerader und ungerader Kolbenz. DSc thesis. RTWH, Aachen. (pp. 27-32)
(2) Borghi, M., et al. 2003. A Numerical Approach to the Hydraulic Fluids Properties Prediction. Proc. 8th SICFP. Tampere University of Technology. (pp. 715-729)
(3) Daugé, P., et al. 2001. Development of an Isobaric Transfer Viscometer Operating up to 140 MPa. J. Chem. Eng. Data. vol. 46. American Chemical Society. (pp. 823-830)
(4) Garbacik, A., Stecki, J.S. 2000. Developments in Fluid Power Control of Machinery and Manipulators. Fluid Power Net publication. (pp. 227-257)
(5) Haarhaus, M. 1984. Geräuschentstehung und Geräuschminderung bei Axialkolbenpumpen in Schrägscheibenbauweise. DSc thesis. RWTH, Aachen. (pp. 33-37)
(6) Hodges, P. 1996. Hydraulic Fluids. London: Arnold. (167 p.)
(7) ISO 15086-2:2000. 2000. Hydraulic Fluid Power – Determination of the Fluid-borne Noise Characteristics of Components and Systems – Part 2 (27 p.)
(8) Jarchow, M. 1997. Massnahmen zur Minderung hochdruckseitiger Pulsationen hydrostatischer Schrägscheibeneinheiten. DSc thesis. RTWH, Aachen. (pp. 18-23, 29-31)
(9) Johnston, D., Edge, K. 1991. In-situ Measurement of the Wavespeed and Bulk Modulus in Hydraulic Lines. Proc.I.Mech.E., Part 1, 205. (pp 191-197)
(10) Kajaste, J., et al. 2005. Experimental Validation of Different Models for Effective Bulk Modulus of Hydraulic Fluid. Proc. 9th SICFP, Linköping Sweden. (16 p.)
(11) Karjalainen, J-P., et al. 2005. The Dynamics of Hydraulic Fluids – Significance, Differences and Measuring. Proc. PTMC 2005. University of Bath, UK. (pp. 437-450)
(12) Kojima, E., Yu, J. 2000. Methods for Measuring the Speed of Sound in the Fluid in Fluid Transmission Pipes. Society of Automotive Engineering, Inc. (10 p.)
(13) Merritt, H.E. 1967. Hydraulic Control Systems. USA: John Wiley & Sons Inc. (358 p.)
(14) Smith, jr. L.H., et al. 1960. Hydraulic Fluid Bulk Modulus – Its Effect on System Performance and Techniques for Physical Measurement. NFPA. (19 p.)
(15) Yu, J.,et al. 1994. The Variation of Oil Effective Bulk Modulus with Pressure in Hydraulic Systems. Jour.Dyn.Syst.,Meas.&Contr. vol.116. Trans.ASME. (pp.146-150)

A Multi-Sensor for Monitoring the Oil Condition of mobile working Machines in Operation

Prof. Dr.-Ing. Dr. h.c. Hans-Heinrich Harms1
Dr.-Ing. Dipl.-Wirtsch.-Ing. Jens Krallmann2

[1] Institute of Agricultural Machinery and Fluid Power, Technical University of Braunschweig, Germany
[2] Thomas Magnete, Herdorf, Germany

ABSTRACT

The main target for a development of a monitoring-system, which detects the oil condition reliably, is to extend the lifetime of the hydraulic oil, to avoid breakdowns and unplanned shutdowns, to minimize shutdowns because of maintenance and repairs, to accelerate the use of biodegradable hydraulic fluids and to compensate the higher costs by a longer lifetime. The oil sensor can measure different characteristics of oil reliably. In this case, the selection fell into two values, which can be measured with comparatively weighted averages. In a lot cases especially on agricultural tractors there is a very big problem with oil mixing by using various attachments. This mixing overlays the effect of oil ageing so that a valuation of the data could only be achieved by a human expert analysing the processes.

1. DEFINITION OF THE SYSTEM

When looking for an Online-Condition-Monitoring-System (OCM) it is important to define the system that is under investigation. As example, we will look at a combine harvester as shown in figure 1. However, there are various other machines of different models in different areas of applications that can be considered.

Power Transmission and Motion Control 2006 Edited by Dr D N Johnston and Professor K A Edge

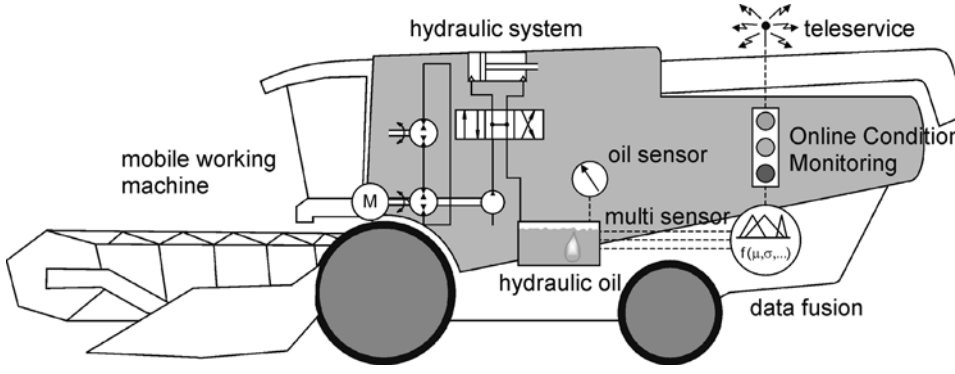

Figure 1 Definition of the system

Common characteristic of all mobile working machines is that beside transportation they mainly have to do an operating process. So you can easily call them a complete factory running on wheels. To do their job they normally have to carry fuel on the machine while operating. Mobile working machines mostly have a hydraulic system that is filled with hydraulic oil in most cases. Remote sensing is already available today for these oils and a sensor for measuring the temperature is standard here. But oils modify their qualities during operation; they age by different influences i.e. they modify their chemical structure. For a reliable statement about the oil state and the process of ageing, more than one measurement is necessary. Therefore, one requires multi remote sensing. A fusion is required because one would like only an individual status statement of these different data e.g. in the form of a traffic light that can be used as an Online-Condition-Monitoring display. Onto such an OCM system one can put a teleservice interface. With such a device one can also get information on the status on the oil state from a distance and/or receive it regularly.

To ensure trouble-free operation of machines, which use hydraulic technology, normally oil changes are required after a certain number of operating hours. The changing periods are adapted according to experience and a specific safety factor. Thus the oil is often in a good condition when the change takes place. In order to reduce this disadvantage, and for a complete condition monitoring of the oil, a sensor was developed which makes a statement on the oil condition possible. The most important parameter that indicates the ageing process of the oil is the Total Acid Number (TAN). But this value cannot be measured online. So it is to be replaced by another parameter that gives similar information.

The most important parameters that should be measured are the temperature, the viscosity, the TAN, the content of solid particles, the water content, the dielectric permittivity and the electric conductivity. Connections between the various parameters are extremely complex. Some values, such as the temperature, the viscosity, the dielectric permittivity etc. can be measured directly online with a miniaturized sensor (shown in figure 2). Although the TAN can only be measured offline, its value correlates with the viscosity and the dielectric permittivity and can be measured indirectly.

2. LAYOUT OF THE MULTI-SENSOR

These characteristic values are the resonance frequency (viscosity), the dielectric permittivity and the electric conductivity. Aided by the temperature and a sensor for measuring the water content, these elements are combined in a miniaturised sensor shown in figure 2.

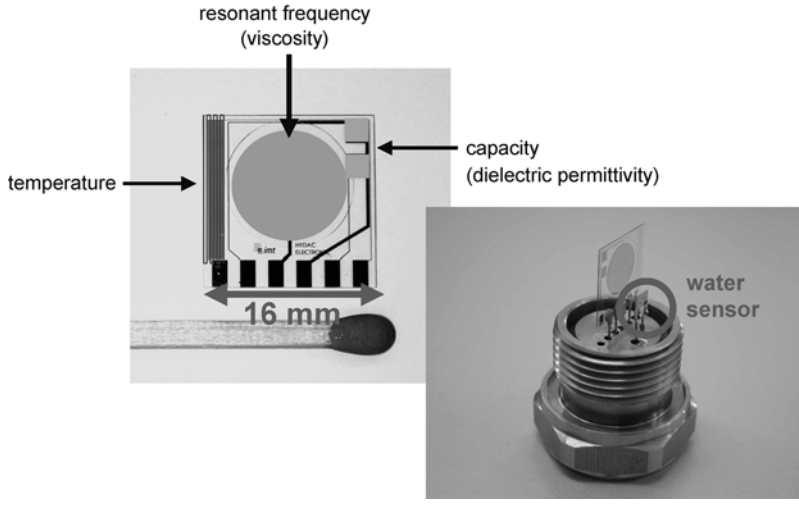

Figure 2 Multi-Sensor-system (source: HYDAC)

The required electrodes are integrated on a piezoelectric quartz crystal. A water sensor is also installed to record the relative humidity of the oil to give a full view on the oil condition. The multi-sensor was tested in different hydraulic systems. The results can be used as basic parameters for an OCM. Partners in this project are the Institute of Micro-technology at the Technical University of Braunschweig and HYDAC Electronic GmbH. The layout of the Multi-Sensor is shown in figure 3. The roundly shaped structure of the electrode, which is placed in the middle of the quartz, is used to determine the viscosity of the oil from the resonant frequency. The complete mounted sensor called HYDAC Lab is shown in figure 3.

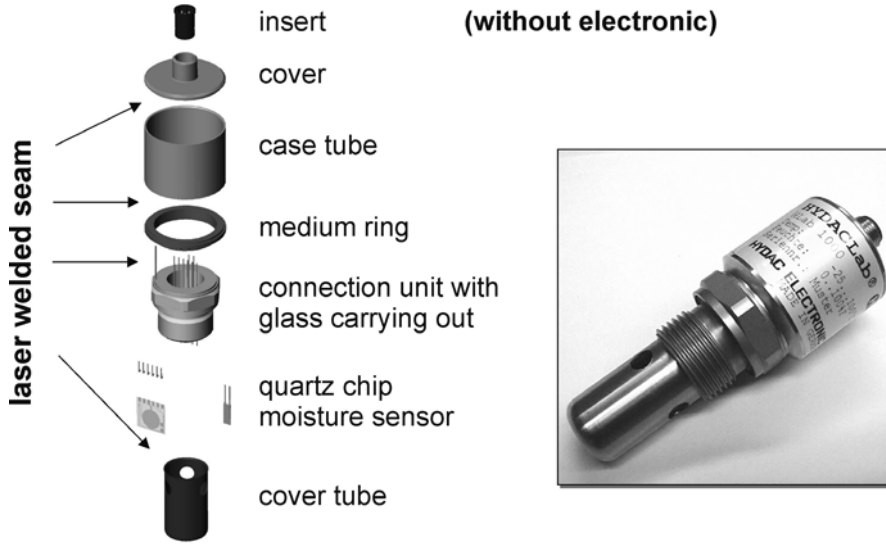

Figure 3 Design of the Multi Sensor (source: HYDAC)

Figure 4 illustrates the movement of the quartz and the fluid. The resonant frequency attained is caused by the geometry of the crystal. It drops when the sensor is in contact with other materials. In this case the resonant frequency depends on the viscosity and the density of the oil. As the density hardly changes during normal use, it depends mostly on the change in the viscosity. As the viscosity as well as the resonance frequency of the crystal, is very dependent on the oil temperature, it is necessary to detect this value on the quartz directly.

3. DATA FUSION AND CLASSIFICATION

How can these parameters be integrated in an entire OCM system? We only have discussed various sensor elements that supply different measured values to us up to now. We must now transfer this to an oil state. For this the absolute values for viscosity, an index would be necessary. Hydraulic oils used in mobile working machines are not the same in all cases. Different oils often have different formulations and additives. To find the special index for the used oil would not have reasonable maintenance expenditure. However in this case it is not necessary, because it is sufficient to measure the modifications of the parameters. In addition, this bypasses the problem that the sensor often shifts e.g. the frequency. Therefore, the structure is as follows (shown in figure 5): the sensors give their information via an electronic filter that ignores e.g. a short time after changing oil, sets automatically comparative values that includes an equalization of temperature. Other information includes the type of oil (e.g. a natural or synthetic ester or a mineral oil) and of machine. All these data are rated and indicate the oil quality. This may lead to a light signal.

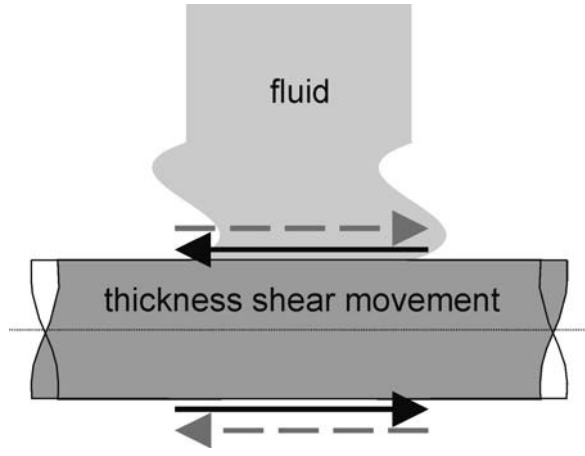

Figure 4 Measuring principle of the viscosity (source: HYDAC)

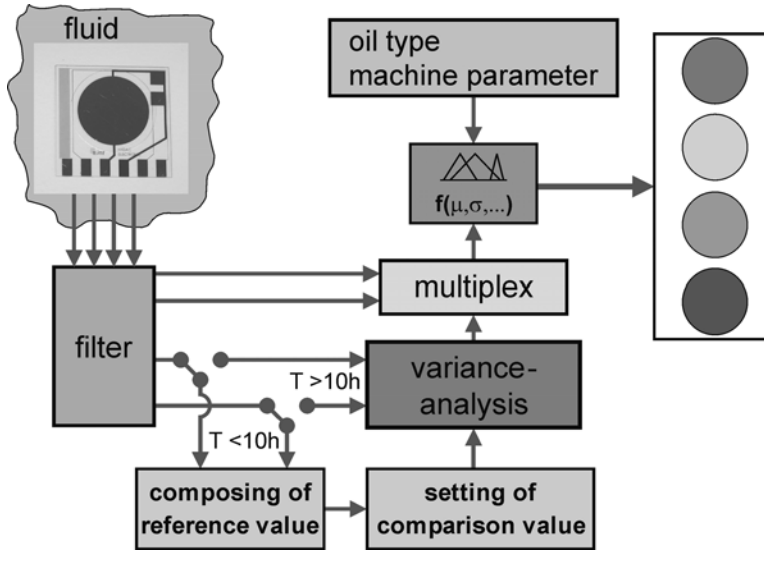

Figure 5 Structure of an OCM-System

A decisive point in this structure is the data fusion shown in figure 6. A data fusion may be based on different sources. It is comparable in many parts with the cognitive perception processes of the human being. Several pieces of information regarding the flow are combined to give an overall picture. For technical applications, there are two fundamentally different approaches for the fusion of data. As an example, a small cube may be thrown to a person. What does the catching person do: he or she fuses the data including all information visually and derives the flight path. Onto this method, in time she knows where the cube will arrive. There are now two possibilities. On the one hand a mathematical-physical

model calculates the curve by using the actual position, the speed, the acceleration and the direction of the motion of the cube and charges the further flight path. But this takes too much time to catch the cube. So the catching person takes another variant: classification. By means of experience, he can see a light and small object, moving very fast, thrown from below, has reached nearly the peak of its curve in a distance of about 1.5 m. The catcher includes different characteristic states and ordered them into classes. In such a way, he combines the combination of these individual classes are combined to estimate the flight path to catch the cube. As explained there are two possibilities how one can fuse data. If possible the mathematical-physical-method is preferred, as this method is more precise. However, sometimes it is too extensive or simply not possible to set up exact mathematical models either because the algorithms are missing or because no sensory data are available of sufficient accuracy.

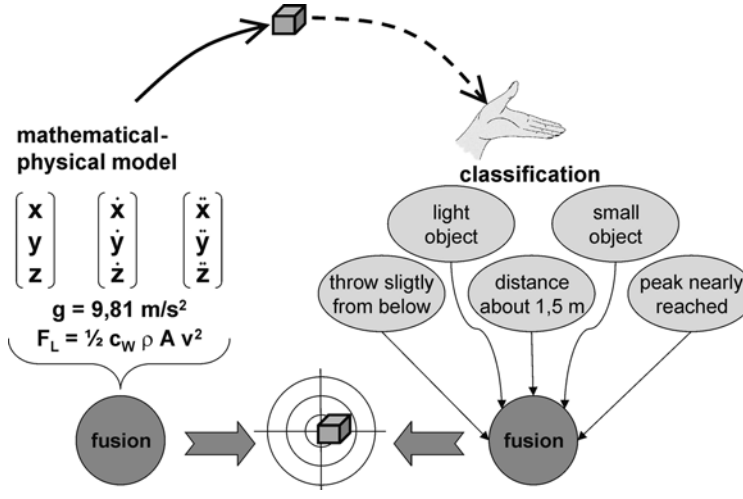

Figure 6 Data Fusion

Oil ageing is such a case. On account of the many different performance-influencing factors, up to now nobody has been able to set up a model in an easy and successful manner. As shown in figure 7 various parameters are measured.

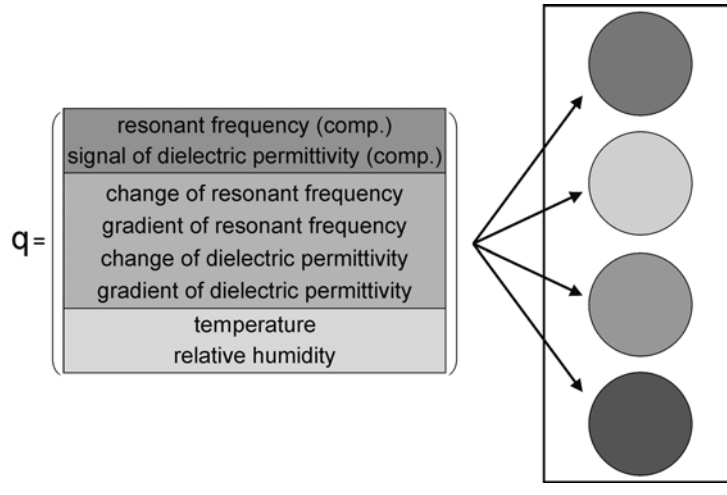

Figure 7 Classification

For the present case of application we now have a data record that consists of the following features: the resonance frequency and the dielectric permittivity, in each case temperature compensated. Using these parameters, the change compared to an initial value and the gradient of the change are calculated. Not only is the modification of the absolute value important, it can also be decisive in how fast the changes take place. Ageing processes of oil typically speed up at the end of their lifetime. Therefore the evolution can be estimated by observing this ageing process.

4. FUNCTION AND MEASUREMENTS

Figures 8 and 9 show readings taken from a test where the resonance frequency and the dielectric permittivity were measured. After about 450 hours of operation an accelerated ageing takes place showing a decrease in the resonance frequency and an increase in the dielectric permittivity. The comparatively quick progress of the ageing process is predominantly caused by oxygen and high temperatures. Towards the end of this test, about 10 % fresh oil was added twice. It can be seen that the measurements varied accordingly. However, the aging process cannot be halted by such an addition, because refilling with new oil doesn't have large influence on the process. Once the ageing process has commenced it can not be stopped.

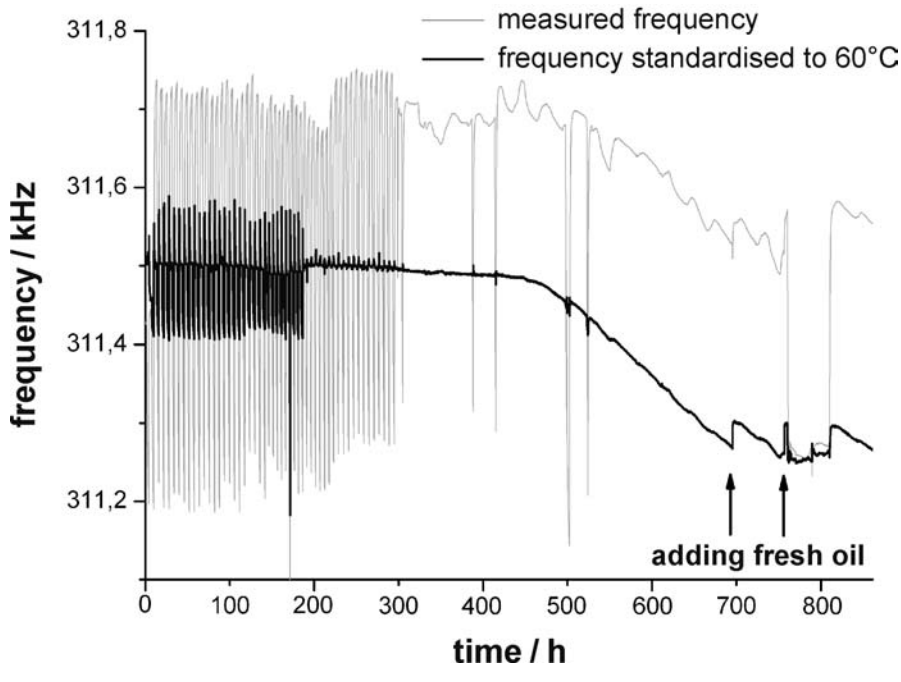

Figure 8 Readings of the frequency

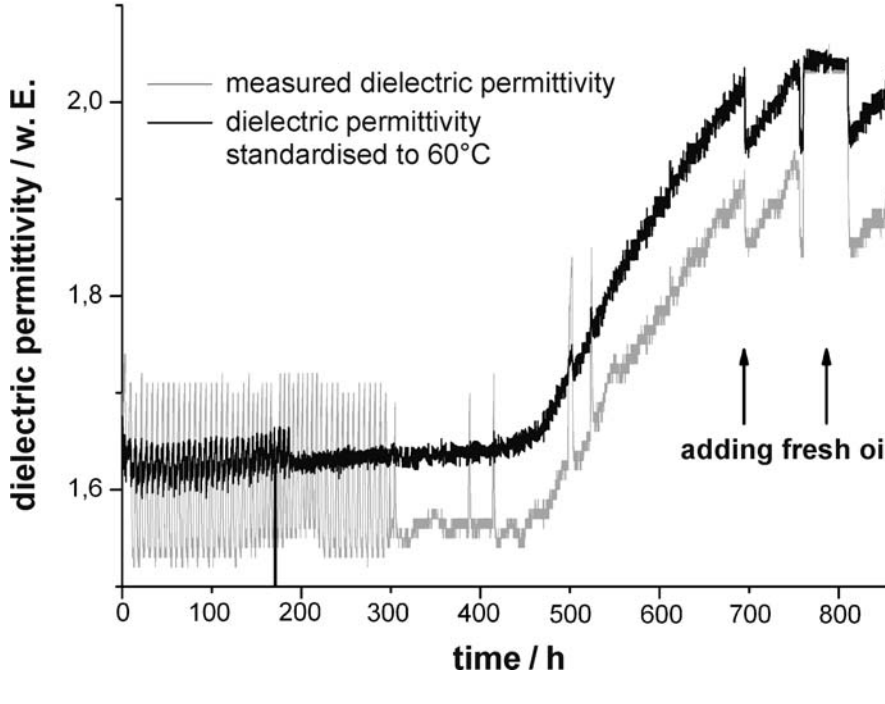

Figure 9 Readings of the dielectric permittivity

5. DESIGN OF A SYSTEM FOR ONLINE-CONDITION-MONITORING

To use these data for an OCM-System, the control unit operates with the change of the values only in order to avoid the effort of providing characteristic diagrams. Therefore reference values and the calculation of the temperature compensation are composed at the beginning of the measurements. The fusion of data is essential to generate a statement on the oil condition.

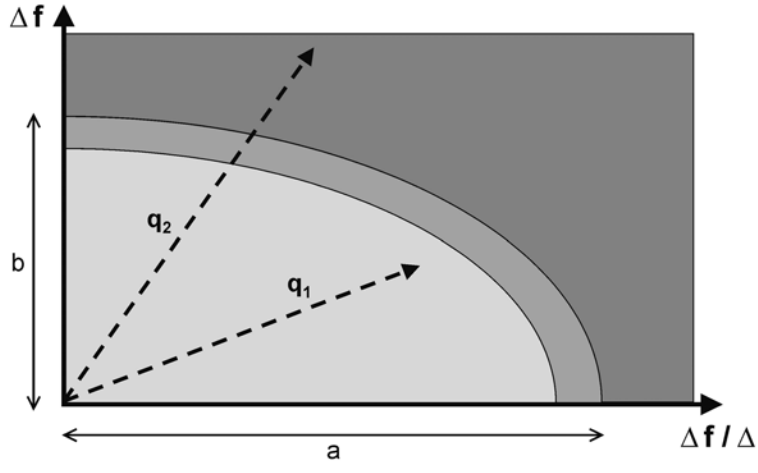

Figure 10 Parametric templates

This process can be done by several different methods, which operate at levels of varying complexity. In principle all methods that accomplish a classification of sets of data are appropriate. One way is to use statistical methods such as discriminant analysis. Other possibilities are the valuation of the parameters in a multi-dimensional feature space and the use of expert systems including Parametric Templates, Fuzzy-Logic, Neural Networks, Neuro-Fuzzy Combinations, Cluster Analysis, Dempster-Shafer-Theory, Bayes-Theorem … Data fusion, in particular the classification, is still not a fully established scientific discipline. Rather, it is a collection of different means and procedures of different disciplines including evaluation, artificial intelligence, pattern recognition, cognitive psychology and many more. Therefore, one of these methods is homogeneously not possible for representation and evaluation of the various procedures. 14 different methods were tested and the Parametric Templates and the Neural Network were examined more closely.

Figure 10 divides the state space into different sectors, which represents different states. Since we have our feature vectors, assignment to the different sectors is simple, as every state vector corresponds to a point in the n-dimensional space. In this diagram the absolute change of the frequency is displayed above the gradient. In this example the limit is represented by the absolute change of the frequency. The resonance frequency itself will not change more strongly. There is simultaneously a maximum value, which the gradient of change must not exceed. There is consequently a boundary here also. In reality, both values

always change. It is not possible for a value to remain at zero. Therefore, one must now find a relationship between these two values by finding a weighting factor of the various parameters. A possibility for this is the use of an elliptical relationship. Using the characteristic of the ellipse provides with the possibility to weight different individual parameters. In this example, the absolute change is weighted more strongly than the gradient. Each parameter has to be normalized in relation to his maximum deviation first. Then the weighting of each parameter is carried out via different semi-axes of the ellipse. Warning limits can be defined. Classification is very simple if the end of the vector is regarded an evaluated by an expert. But there might be a problem if the vector is in a field which is not assigned as a possible state.

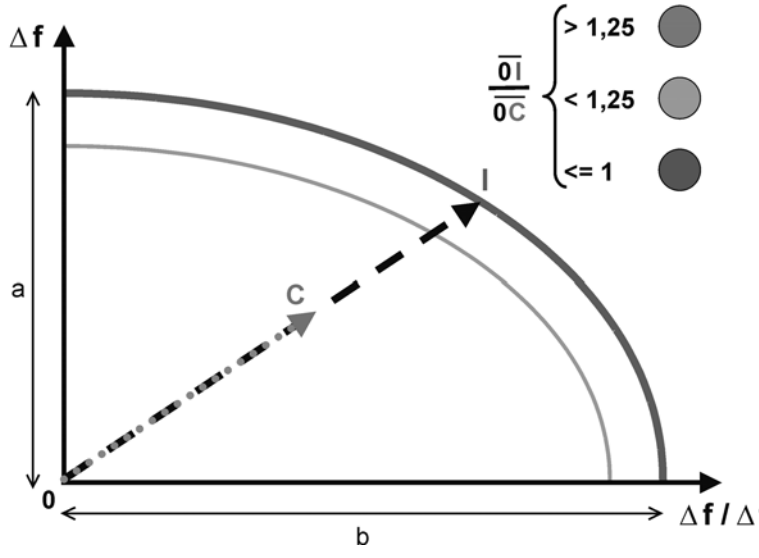

Figure 11 Parametric templates

The application of this procedure allows the display of the current oil state. The ratio of the distance to the intersection point and the current length of the vector (see figure 11) gives information about the ageing condition. But this quotient is only a clue. One cannot take this ratio as a percentage of the wear factor. The process should normally be continuous, but there is no proportional process in the normal proof.

Figure 12 shows this ratio in progress. The absolute value of the frequency is twice as strongly weighted as the gradient of the frequency in this example. The smaller the semi-axles of the ellipse the more important is this parameter. The ratio starts at an extremely high value that decreases. After reaching the warning level fresh oil is added partially after 695 h. Although the ratio increases for a short period, but the gradient of decreasing does not change, as was already seen in the readings. This indicates that the method is very close to reality and that partially added oil does not extend the oil operating life.

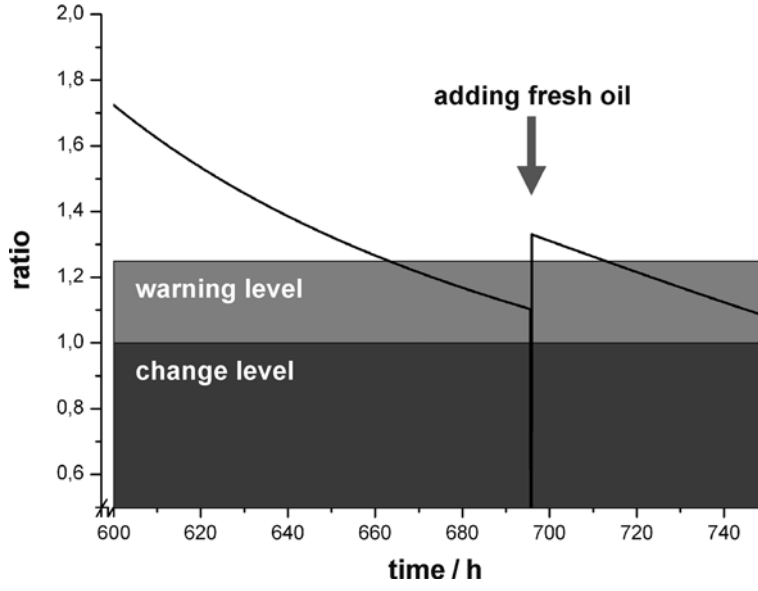

Figure 12 Ratio calculated by parametric templates

Figure 13 shows the principle of a neural network as another variant of valuation. A neural network is based on individual cells, the neurons that receive input signals. Every feature is provided with a weighting. Subsequent a simple mathematical operation is carried out and the input of the entry data record is converted into an output signal. It is possible to integrate threshold values, which hamper or support the ageing character in the calculation.

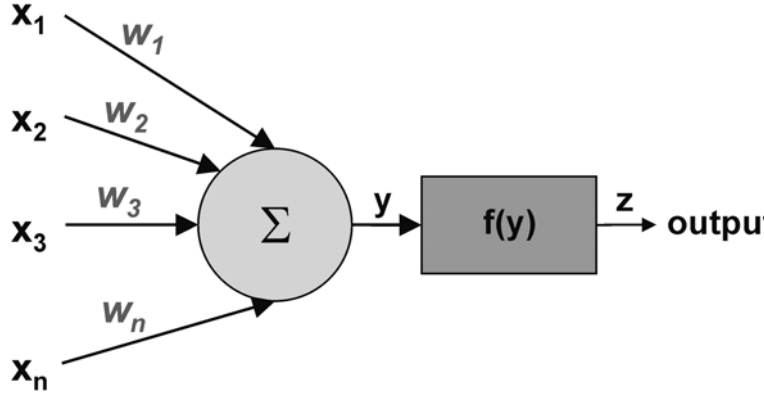

Figure 13 Neural network - single neuron

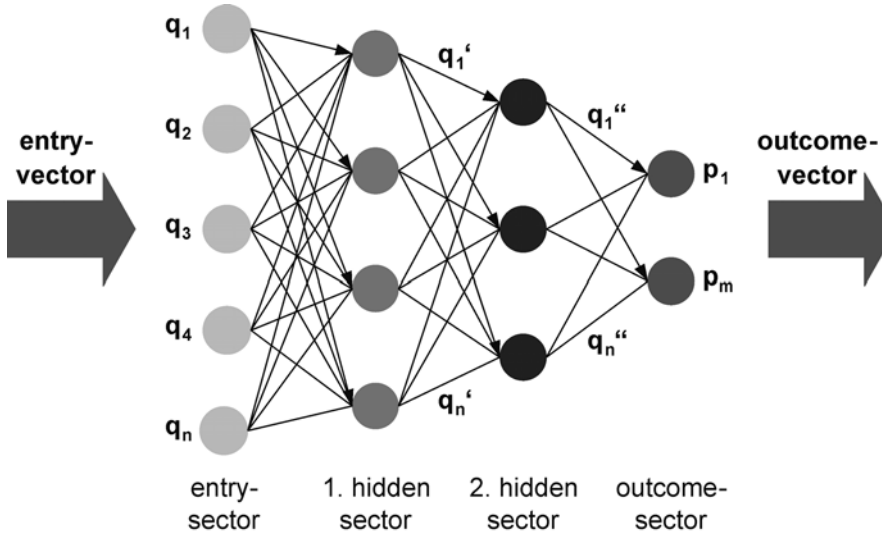

Figure 14 Neural network

Several neurons are then linked to an associated net as shown in figure 14. The net starts from an entry sector leading to several hidden sectors (in this example two). In these sectors logical operations take place and the data calculated and recorded. At the end there is an outcome vector that gives information regarding the condition of the oil. The main advantage of a neural network is the fact that the system is continuously self-learning. Data records given to the system modify the characteristic permanently to an optimal result. This is the learning process. The modifications, which are carried out in the learning process, refer to weighting the individual factors in this case. After training the network in this way, one can use it for classification of new unknown data. A problem using neural networks is that the logic cannot be understood after the assignment of the individual data records.

Using the neural network toolbox integrated in MATLAB Simulink a net was designed and applied to the measuring data. An interesting result shown in figure 15 was that it was not necessary for this method of assignment to know the absolute deviations and gradients. The use of the temperature compensated signals is completely sufficient here. This is understandable because neural networks use the relations only, e.g. the distances and the conditions of the individual data to prepare the rules. A neural network figures out the distances and gradients by itself. If these data are entered, one has redundant data records that do not improve the classification result. In worst cases this may lead to completely wrong and unexpected results. As an example, included in figure 15, is the result obtained following the adding of fresh oil after about 650 h. This resulted in the value of classification became worse, whereas in reality there was an improvement.

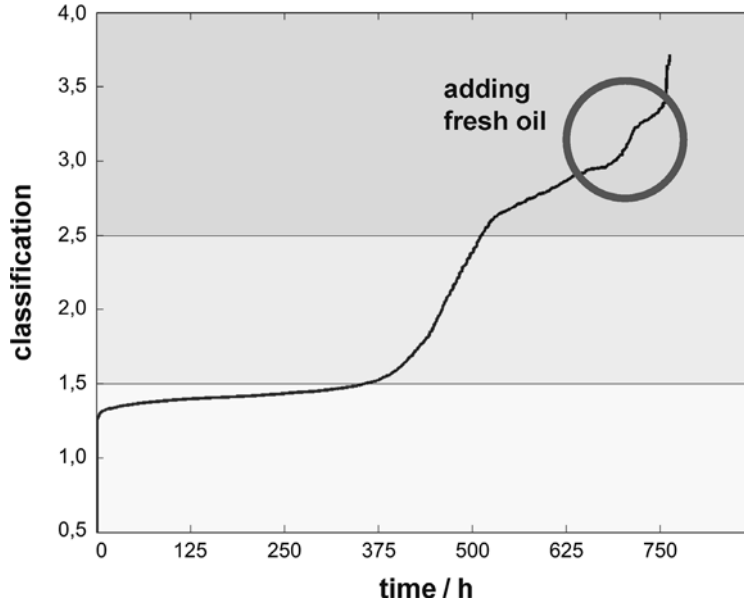

Figure 15 Classification by neural network

6. EVALUATION OF THE METHODS

Parametric Templates do have the advantage that this system is integrated in the common simulation tool MATLAB Simulink, so it is very simple to explain and easy to implement. Nearly no expert experience is necessary. But the method is very stiff, not flexible and there is no robust handling of unusual data possible. Therefore, this system is ideal for introducing a new sensor.

A neural network is a self-learning method, which can handle unusual data without conversion of the measured data. But the logic of the method is not understandable, very many data are necessary for the self-learning process and high expenditure is necessary for additional dimensions. So a neural network can be installed, when there is enough experience available and when there are enough sets of data records collected.

7. CONCLUSIONS

A multi-sensor monitoring the oil condition will have a big potential especially for mobile working machines. This can be achieved using a specific multi-sensor as described in the paper. However, one can also work with various sensors already available on the machine. The oil sensor can measure different characteristics of oil reliably. In this case, the selection fell into two values, which can be measured with comparatively weighted averages.

For the valuation and fusion of the data, different stages are possible. It always depends on the individual situation which parameters have to be selected. It should be determined generally whether a mathematical description is available. If a classification method is used, a suitable procedure must be selected on the basis of already available data and experience. This must be none of the procedures presented here; for other applications also, other procedures can be reasonable. In addition to raised reliability, economic advantages result in almost all applications. However, there are also restrictions on the sensor. An automated valuation of the data cannot be guaranteed for all applications.

Within the field trials undertaken on an agricultural tractor problem encountered with oil mixing by using various attachments. This mixing overlays the effect of oil ageing so that a valuation of the data could only be achieved by a human expert analysing the processes.

8. REFERENCES

[1] Rabe, J. Miniaturisierte Quarzresonatoren und Arrays fuer Analytik-Anwendungen in Fluessigkeiten, Berichte aus der Mikro- und Feinwerktechnik, Shaker Verlag Aachen 2003, ISBN 3-8322-2044-5

[2] Krallmann, J. Einsatz eines Multisensors fuer ein Condition Monitoring von mobilen Arbeitsmaschinen, Forschungsberichte des Instituts für Landmaschinen und Fluidtechnik, Shaker Verlag Aachen 2005, ISBN 3-8322-4740-8

[3] Meindorf, T. Sensoren fuer die Online-Zustandsueberwachung von Druckmedien und Strategien zur Signalauswertung, Reihe Fluidtechnik Band 39, Shaker Verlag Aachen 2005, ISBN 3-8322-4441-7

[4] NN Development of a System for Online Condition Monitoring (OCM) of Hydraulic Oils, Bioenergy and Residual Substances, Brochure of the Bundesministeriums für Bildung und Forschung, BMBF-FKZ 0330117, 2005

[5] Krallmann, J. and Mannebach, H. Ein Multisensor zur Ueberwachung von Hydraulikoelen, Proceedings Landtechnik 2004, Dresden, VDI-Verlag, Duesseldorf 2004, Page 107-113, ISBN 3-18-091855-1

A quasi-single-pass test method for fluid power filters

E Urata, K Suzuki and Y Kato
Faculty of Engineering, Kanagawa University, Japan

ABSTRACT

This paper discusses methods for measuring and evaluating the filtration performance of hydraulic filters and introduces a quasi-single-pass test method. One well-known method for evaluating filtration characteristics is the multi-pass method. Since the multi-pass test method was specified by the ISO 16889 standard, users believe that the "η#(beta)" measured by the standard expresses the filtration characteristic of a filter. However, there have been some suggestions that the beta is not consistent with field experience. Another criticism of the multi-pass test method is that it only deals with steady flow and so is not applicable to practical applications in which unsteady flow is unavoidable. This paper will show that even for steady-state filtration, evaluating filtration performance by the multi-pass test method is questionable. Instead of the multi-pass test method, we propose a test method that shows a single-pass test condition. Experiments carried out with the proposed method showed that flow rate and contamination levels at the upstream of a filter influence the filtration characteristic.

1 INTRODUCTION

In a multi-pass test, particles that pass through a test filter appear again at the entrance of the filter.[1, 2] In a single-pass test, particles that pass through a test filter do not appear again at the entrance of the filter. Single-pass tests were the normal test method used before the multi-pass test was introduced.

Figure 1 illustrates a typical single-pass test. A volume of fluid containing suspended particles passes through a filter test piece made from filter medium. The amount of the particles can be measured using a gravimetric method or a number counting method. The ratio of particles retained on the filter test piece to the total amount of particles in the fluid volume is called filtration efficiency. Figure 2 illustrates a simplified multi-pass test rig. Particles that pass through the filter circulate with the fluid. The amount of particles is measured using a number counting method. The ratio of particle numbers in unit volumes of fluid at the upstream and downstream of the filter is called the beta ratio.

Power Transmission and Motion Control 2006 Edited by Dr D N Johnston and Professor K A Edge

Comparing these test methods, the single-pass test is not suitable for testing an industrial filter element because the test requires a tremendous amount of sample fluid before the element is fully blocked. In contrast, the multi-pass test only requires a limited volume of fluid to test common industrial filter elements. Thus, the multi-pass test is easier to perform. However, there are some problems with this method that will be explained below.

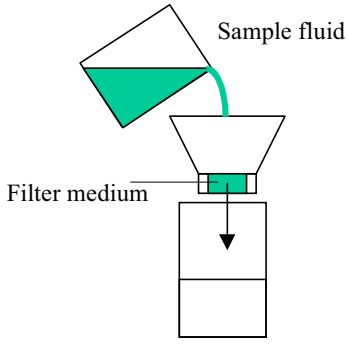

Fig. 1: Single-pass test

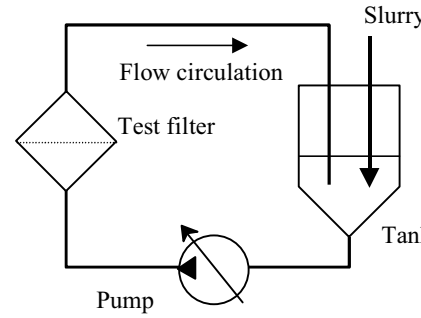

Fig. 2: Multi-pass test

A general rule for finding a physical characteristic of an object is that the measured results should not be influenced by the measuring system. When we study the input-output relation of a test object, the object should not influence the input to the test system. For a filter test, the object is the filter; the input is the contamination level of the upstream fluid. Therefore, in finding the filtration parameters inherent in a filter, the contamination level of the upstream fluid should be independent of the filter characteristic. However, in the multi-pass test, the test filter changes the contamination level of the upstream fluid throughout the test period. This breaks the general rule for finding the characteristics of a physical object. In this respect, the multi-pass test is seen as inconsistent.

The next point is data expression. The multi-pass test standards, old [3] and new, [4] express the filtration ability by “beta”, namely the quotient of upstream particle number density divided by downstream particle number density. If the upstream particle number density is proportional to the downstream particle number density, this quotient can give a characteristic parameter of the filter. However, we have neither proof nor experimental evidence for this. This paper will examine whether the downstream particle number density is proportional to the upstream particle number density. If the proportional relationship is verified, the data expression by “beta” will be accepted. Otherwise, the beta ratio will lose its scientific basis.

To obtain solutions to these problems, we shall perform tests in which the testing filter does not influence the upstream contamination level. Let us consider a test in which the fluid exiting from a test filter is made sufficiently clean compared to the fluid entering the test filter. We call this test method the *quasi-single-pass test*. With this procedure, we can realise the test condition of a single-pass test using a volume of fluid comparable with a multi-pass test. Figure 3 shows the idea of the quasi-single-pass test rig. In this test rig, although the fluid circulates as in the multi-pass test, most of the contaminants do not circulate.

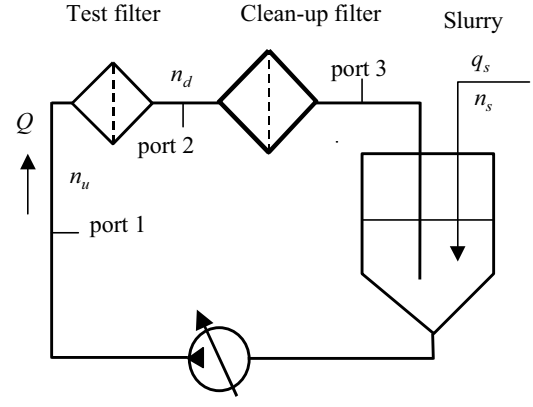

Fig. 3: Idea of quasi-single-pass test

The interest of filter users is the contamination level downstream of their filters while various parameters of hydraulic systems influence the contamination level. Therefore, it will be convenient if we have a functional relationship expressing the downstream contamination level with known parameters, for example, [5), (6)]

$$n_d \mid F(Q, \tau, n_u, M, t) \tag{1}$$

where n_d = number of particles per millilitre in the downstream fluid, n_u = number of particles per millilitre in the upstream fluid, Q = flow rate, τ = kinematic viscosity of fluid, M = amount of particles kept in the filter element, t = time.

The cancelled standard ISO 4572 assumed a constant value of beta and the following relation:

$$\eta \mid n_u / n_d . \tag{2}$$

Some decades after distribution of the standard, the time-dependence of the beta became recognised and its definition was changed by a ratio of time integrals of particle numbers defined by the following estimation: [4), (7)]

$$\bar{\eta}_{x(c)} \mid \sum_{i=1}^{Max} n_{ux}(t_i) \Big/ \sum_{i=1}^{Max} n_{dx}(t_i) \tag{3}$$

where t_i = i-th measuring time from test start, n_{ux} (t_i) and n_{dx} (t_i) = number of particles greater than size x per millilitre at time t_i in upstream and downstream fluid, respectively. This value does not depend on time; thus the apparent contradiction was removed. However, it does not help to find out the downstream contamination level.

To find a relationship such as Eq. (1), it is necessary to carry out experiments keeping the parameters n_u, Q and τ constant while M is a time-dependent variable. In this paper we will

introduce an experimental method that can supply suitable data necessary for developing mathematical models for the filtration process in fluid power filters.

Usual fluid power components, such as pumps, motors and valves, keep their performance characteristics for a long time, say more than five thousand hours. However, a fluid power filter changes its own performance continuously throughout its service life. The service history reflects the downstream contamination level and the pressure loss across the filter. Thus, a filter has hysteresis or a memory effect; the expression for the beta ratio (2) ignores this memory effect.

To reflect the memory effect, Bensch et al. proposed the repeated loading test.[8), (9)] They tried to test filters under simulation conditions more practical than the ISO 16889 test procedure. However, the results of a system simulation are influenced by all the system elements. Consequently, the particular characteristic of an element can hardly be extracted from the results. Therefore, we shall study the filter in its isolated state before going on to a simulation.

Thus, this study intends to estimate the filter's characteristics in its isolated state. We will show that the quasi-single-pass test is an effective test method. Section 2 explains the experimental method of the quasi-single-pass test; Section 3 describes the experimental results and then discusses them.

2 EXPERIMENTAL RIG AND TEST METHOD

2.1 Construction of a quasi-single-pass test rig

Figure 4 shows the circuit diagram that realises the idea shown in Fig. 3. The test rig uses tap water as working fluid.

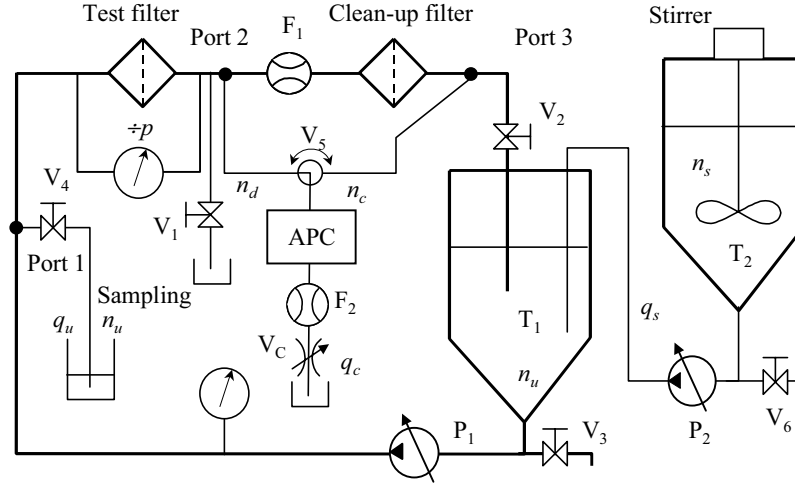

Fig. 4: Quasi-single-pass test rig

Basic construction
The main circuit begins from tank T_1, which is connected to pump P_1, the test filter, flowmeter F_1, the clean-up filter, and valve V_2 before returning to tank T_1. The main conduit is made of plastic pipe of internal diameter 20 mm. Tank T_1 is made of stainless steel. The bottom of the tank takes the form of a right circular cone to prevent contaminant being trapped. The capacity of the tank is 19 litres. Tank T_2 supplies contaminant to tank T_1 by pump P_2. The two tanks have identical dimensions and are made from the same material. The test dust is mixed with water in tank T_2 that has a stirrer to prevent sedimentation of the suspended test dust.

Measuring system
The circuit has three sampling ports: port 1 extracts sample fluid from upstream of the test filter; port 2 extracts sample fluid from downstream of the test filter; port 3 extracts sample fluid from downstream of the clean-up filter. Fluid from ports 2 and 3 are connected to an inline automatic particle counter by a switching valve V_5. The flow rate of the extracted fluid is set by valve V_C and monitored by flowmeter F_2. A stand-alone automatic particle-counter measures the contamination level of the fluid taken from port 1. The sampled fluid from port 1 is usually diluted by clean water for particle number counting.

A differential pressure sensor measures the pressure loss due to the test filter. Flowmeter F_1 monitors flow through the test filter. The flow through the test filter is adjusted varying pump speed; valve V_4 is opened for sampling.

List of component dimensions
Main pump, type: centrifugal pump.
Electric prime mover: 2.2 kW, three-phase 220 V inverter control.
Pump delivery: 0.04-0.15 m^3/min, total head: 44.5 m, material: stainless steel.
Slurry pump, type: tube pump. Flow rate: 0.12-4.2 L/min, velocity control range: 25-200 rpm, tube diameter: 1-12 mm.
Clean-up filter housing (2 pieces in series), diameter: 88.1 mm, length: 644.5 mm.
Test filter housing, diameter: 88.1 mm, length: 384.5 mm.
Clean-up filter cartridge, external diameter: 64 mm, internal diameter: 28 mm, length: 509 mm.
Pressure sensors: Bourdon gauges (monitor only). Strain gauge type differential pressure sensor, range: 500 kPa.
Flowmeter (F_1): rotameter, range: 5.8-58 L/min.
Test circuit, tube internal diameter: 20 mm.
Main tank: diameter 240 mm, length of straight tube: 400 mm, connected to right circular cone.
Slurry tank: same size as the main tank, vane-type stirrer installed.

2.2 Control of the test rig

Examination of uniformity of dust dispersion
Slurry is prepared by mixing a measured weight of ISO-12103-A2[(10)] test dust and water in a three-litre beaker. The beaker with the mixture is shaken using a rotary shaker for more than ten minutes. No dispersant is added when mixing the water with the test dust. To prevent sedimentation in the slurry tank, a vane-type stirrer is introduced. Samples taken

from the tank show it maintains stable particle number density during several hours of running.

Dispersion of particles in the test circuit was examined by the following procedure. First, the main pump was run with clean water. Then a certain volume of slurry was supplied to the main tank through the tube pump. With the main pump running, sampled fluid from port 1 was examined every 30 minutes for 4 hours and fluctuation of the contamination level was found to be less than 10 % for particles greater than 10 σm.

Temperature control
The initial design of the test rig included a heat-exchanger, although this was not required as it was possible to keep the temperature near room temperature by controlling the pump flow by adjusting the velocity of the electric motor. The temperature of the water during experiments was 20- 40 °C.

Clean-up of test circuit
Cleaning of the test circuit is carried out by repeated flushing and rinsing using tap water. The flow rate for flushing is at the maximum pump delivery and the flushing duration is about 5-10 minutes. After flushing, the clean-up filter cartridges are installed. The pump is then run and the contamination level of water in the circuit is monitored by the APC connected to port 2 or port 3. We estimated the cleanliness of the facility to be sufficient for a filter test when the number of particles greater than 2 σm was less than one in 1 mL of sampled fluid.

Clean-up of injection system
Cleaning of the injection circuit is carried out by washing and rinsing using tap water. Flushing of the tube and pump is carried out by returning the pump delivery flow to tank T_2.

2.3 Preparation of experiments

Preparation of main circuit
(1) Fill the circuit with tap water and circulate the water without installing the filter elements. Flow rate is about 40 L/min and the running time is about 10 minutes.
(2) Drain the water by opening valve V_3 (drain valve at the inlet of the pump).
(3) Repeat steps (1) to (2).
(4) Fill the tank with filtered water and circulate the water for about five minutes at a flow rate of about 30 L/min.
(5) Install the cartridge of the clean-up filter and circulate water for about ten minutes at a flow rate of about 30 L/min.
(6) Examine the cleanliness level of the fluid from port 2 or port 3 using inline APC. If the number of particles greater than 2 σm per mL is less than one, we regard the test rig to be sufficiently clean for a filter test.
(7) When the test rig is not sufficiently clean, continue to circulate the water for a few further 10 minutes.

Preparation of injection system

(1) Fill the tank with tap water and wash the tank wall using clean sponge.
(2) Drain off the water by opening valve V_6.
(3) Repeat steps (1) to (2) twice.
(4) Fill the tank with tap water and activate the stirrer for about 10 minutes. After that, fluid from the tank is examined. Usually, the number of particles greater than 10 σm is less than 5 per mL. If more particles are found, simply repeat the above clean-up process.
(5) The prepared slurry in the beaker is poured into the tank and the stirrer in the tank is activated.

Determination of test condition

Variables measured during operation of the test are the particle densities of fluid at the ports 1, 2 and 3, and the differential pressure across the filter. Other quantities are kept constant. The test condition is determined to keep a constant particle density at the inlet to the test filter. To do this, the slurry concentration and slurry flow rate are kept constant. The fluid volume in the test circuit is kept constant during testing because a change of the fluid volume induces a transient deviation of the fluid contamination level. The fluid volume is adjusted by bleeding from V_1.

Table 1: Experimental condition

Operating parameters	Numerical value
Fluid volume in test system V (L)	15
Test dust	ISO 12103-A2
Slurry volume V_i (L)	15
Test flow rate Q (L/min)	20,30,40
Slurry flow rate q (L/min)	0.18
Upstream contamination level C_1 (mg/L)	3,10,15
Slurry contamination level C_2 (mg/L)	$C_2=QC_1/q$

2.4 Carry out of the test

A test is carried out as follows:
(1) Start the main pump; set the flow rate. Measure the pressure drop across the filter housing.
(2) Stop the pump and install the filter element to be tested.
(3) Start the pump and set the flow rate by adjusting the electric motor. Measure the initial pressure difference.
(4) Start operation of the slurry pump at the start time of the test.
(5) The particle densities at ports 2 and 3 are measured every 10 minutes. Sampling from port 1 is done every 15 minutes. The differential pressure is measured every 5 minutes.
(6) The test is stopped when the test filter reaches the end of its service life. A rapid rise in the pressure difference or the particle density at port 2 indicates the end of the filter's life.

3 EXPERIMENTAL RESULTS AND DISCUSSION

Cartridges from the same batch are used for the following four experimental conditions:
Case 1; upstream level 3 mg/L with flow rate of 40 L/min
Case 2; upstream level 3 mg/L with flow rate of 30 L/min
Case 3; upstream level 15 mg/L with flow rate of 30 L/min
Case 4; upstream level 10 mg/L with flow rate of 40 L/min.

We will show first that the single-pass test condition was established in the experiment. Figure 5 shows particle number density at port 1 for Case 1. We can see that the particle density is kept fairly constant. Figure 6 shows the particle number density at port 3. The number of particles greater than 2 σm in the downstream of the clean-up filter approaches 1/10,000 of that in the upstream near the end of the test. The ratio is less than 1/10,000 during almost all the test period. For larger particles this ratio never exceeds 1/10,000. Similar results were obtained for the other three cases. These facts indicate that the clean-up filter achieves the single-pass test condition.

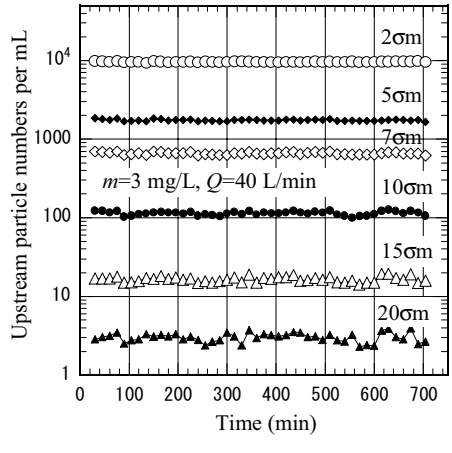

Fig. 5: Upstream (port 1) particle density

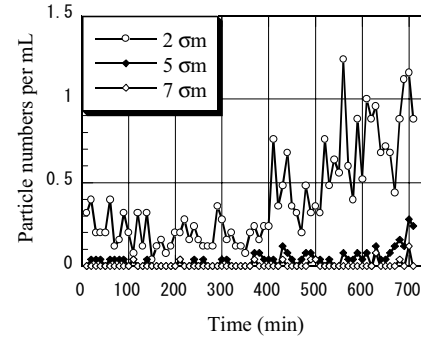

Fig. 6: Port 3 particle density

Next we will show the change of filtration performance with time. Figure 7 shows the change of particle density at port 2. It also shows the pressure loss of the filter element. These are a direct expression of the time-dependent filter characteristic. In this experiment, the pressure loss rises rapidly at about 600 minutes. Particles greater than 10 σm first appear at about 500 minutes. At the same time, smaller particles increase. We can recognise this more clearly by plotting the particle number on a linear scale, as shown in Fig. 8.

Next we compare the experimental results of the four cases. The abscissa in Figure 9 is the mass of dust added during the test. It is expressed by *Qmt* since the flow rate and the concentration of dust are constant. Let us call this quantity the "loading mass". The ordinate of the graph is the pressure loss per unit flow, which is called the "fluid resistance". The

four curves start from a common point and rise rapidly at different points. The point of the rapid rise depends on the experimental conditions, namely, the flow rate and the upstream contamination level. The curves indicate that a lower contamination level induces clogging with a smaller loading mass.

Figure 9 also indicates that a flow rate of 40 L/min results in earlier clogging than a flow rate of 30 L/min at the same contamination level of 3 mg/L. Thus, the loading mass for clogging is influenced by the test flow rate and the upstream contamination level.

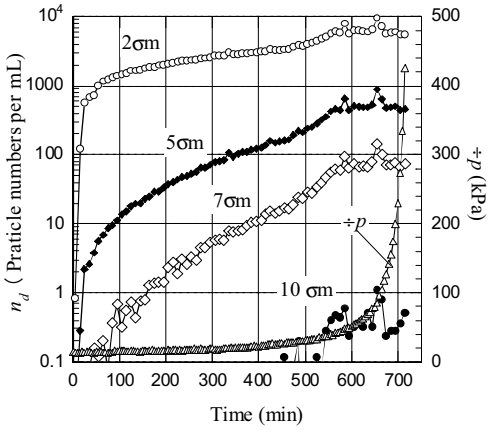

Fig. 7: Port 2 particle density

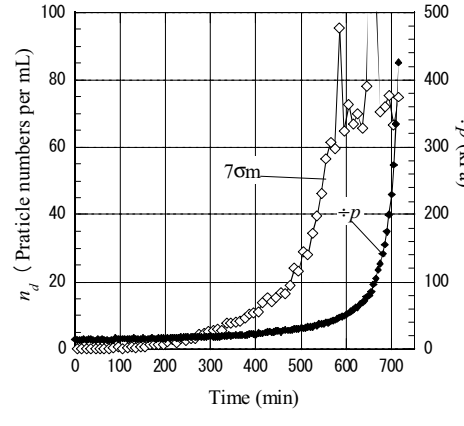

Fig. 8: Port 2 particle in linear scale

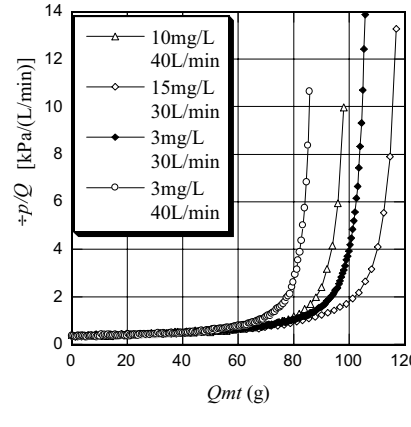

Fig. 9: Loading mass vs. pressure loss

Next we compare downstream particle densities. Figures 10 and 11 show particle numbers per mL per mg against the loading mass. Since the upstream particle density is proportional to the weight concentration, the curves will overlap if the downstream particle density is proportional to the upstream particle density. However, different curves were obtained for different upstream contamination levels. With the same flow rate of 30 L/min, the curves for 3 mg/L and 15 mg/L show distinct differences. Thus, the downstream particle density is not proportional to the upstream particle density. The downstream particle density rises by a smaller loading mass for a lower upstream particle density. In other words, the filtration characteristic degrades with smaller loading mass for a lower upstream contamination level. This feature is similar to the fluid resistance shown in Fig. 9. Comparing Figs. 9 and 11, we can see the rapid rise of pressure loss follows a distinct increase of downstream contamination level.

From these results we can conclude that clogging and degrading of a filter element occur with a smaller loading mass at a lower upstream contamination level. This suggests that an estimate of filter performance in proportion with upstream contamination levels is unsafe.

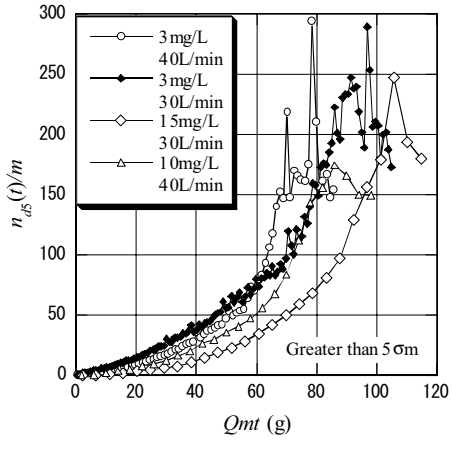

Fig. 10: 5 σm particles in downstream

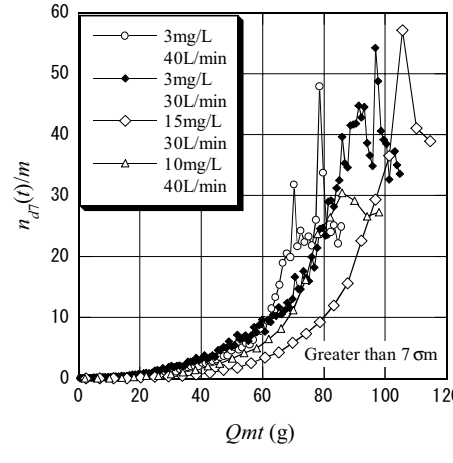

Fig. 11: 7 σm particles in downstream

We will now discuss the ratio of upstream and downstream contamination levels. We define the following quantity that approximates $\overline{\eta}_{x(c)}$ in ISO 16889:

$$\beta_x^*(t) = \frac{\int_0^t n_{ux}(t)dt}{\int_0^t n_{dx}(t)dt} . \tag{4}$$

Figure 12 shows the variation of $\eta_<^*(t)$ with time t. The figure compares Case 2 (m = 3 mg/L with Q = 30 L/min) and Case 3 (m = 15 mg/L with Q = 30 L/min). The tests were stopped when the pressure limit was exceeded. The contamination level of 3 mg/L results in a longer life than 15 mg/L. However, it is less than 5 times that of 15 mg/L.

Figure 13 shows the same data taking loading mass as the abscissa. This plot shows that $\eta_5^*(t)$ depends on the upstream level. The loading mass to be added to the filter becomes smaller for a lower upstream contamination level. This is an unfortunate characteristic since in a practical system the contamination level is lower and hence the life will be shorter than a proportional estimate from the test result. As seen from the plot, $\eta_<^*(t)$ changes with the loading mass. Thus, a single value of $\eta_<^*(t)$ at a particular point in time is not appropriate as a representative of filtration ability. Since $\overline{\eta}_{x(c)}$ in ISO16889 is a single value at the end of the multi-pass test period, its validity as a measure of filtration performance is questionable.

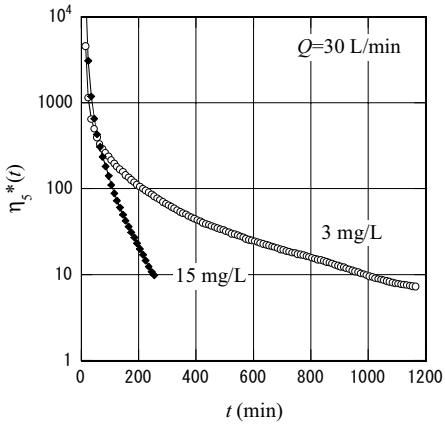

Fig.12: Time change of "beta*"

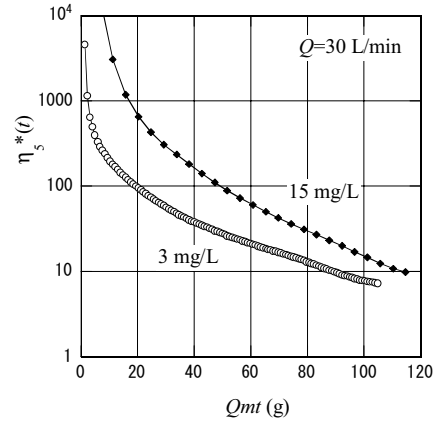

Fig.13: Loading mass vs. "beta*"

4 CONCLUSIONS

This paper showed a quasi-single-pass test that prevents a change of the upstream contamination level. The experiments showed that: the upstream level was kept fairly constant with the quasi-single-pass test; the upstream contamination level and flow rate both have an influence on filter performances. These results indicate that a multi-pass test method is not an effective means for finding filtration performance because the upstream contamination level changes during the multi-pass test. The experimental results also revealed that there is a non-linear relationship between the upstream and downstream particle number densities. This indicates that "beta" is not an appropriate parameter for expressing filter specification.

REFERENCES

(1) L. E. Bensch, E. C. Fitch and R. K. Tessmann, Contamination control for the fluid power industry, Pacific Scientific Co., (1978).
(2) J. S. Stecki (ed.), Total contamination control, Fluid Power Net Publication, (1998).
(3) ISO 4752, Hydraulic fluid power filters - Multi-pass method for evaluating filtration performance, (1986).

(4) ISO 16889:1999, Hydraulic fluid power filters - Multi-pass method for evaluating filtration performance of a filter element, (1999).
(5) E. Urata, Evaluation of filtration performance of a filter, PTMC2002, Professional Engineering Pub. Ltd. (U.K.), pp. 291-304, (Bath, 2002-9).
(6) E. Urata, Notes on Contamination Control, The Sixth JFPS Intl. Symp. on Fluid Power, Proc. CD-ROM, pp. 629-634 (Tsukuba, 2005-11).
(7) P. Dahmann, Untersuchungen zur Wirksamkeit von Filtern in hydraulischen Anlagen, Dissertation RWTH Aachen, (1992).
(8) L. E. Bensch and M. J. Day, A realistic Approach To Measuring Filter Performance, IFPE 2000, (2000).
(9) T. Namba and K. Izawa, Realistic Filter Performance Evaluation - Cyclic Stabilization Test, The Sixth JFPS Intl. Symp. on Fluid Power, Proc. CD-ROM. pp. 624-628. (Tsukuba, 2005-11).
(10) ISO12103-1**,** Road vehicles - Test dust for filter evaluation - Part 1: Arizona test dust (First Ed., 1997).

Return to Contents

Pumps, Fluid Dynamics and Noise

Return to Contents

On 3D viscid periodic wave propagation in hydraulic systems

By R. Scheidl and B. Manhartsgruber

Johannes Kepler University of Linz; Institute of Machine Design and Hydraulic Drives

ABSTRACT

It is well known that periodic waves in a straight pipe exhibit small dynamic boundary layers. A nice explanation of the characteristics of this boundary layer has been given by Gittler, Kluwick, and Brummayer using singular perturbation techniques and asymptotic expansions. They split the whole flow into a compressible bulk flow without any friction (omitting viscosity) which characterises the flow in nearly the whole cross section and a dynamic boundary layer which is strongly effected by viscosity. Their results tell that the effect of the boundary layer on the bulk flow in the centre is given by radial velocity components which work similarly to flexible walls which hinder the flow of an inviscid fluid in its interior if their tangent plane is not parallel to the main flow direction. On the other hand, the usual derivation of the transmission line equations does neglect any radial velocity component but uses the shear stresses at the boundary layer. Yet, the results of both approaches are nearly identical. This raises the question of the true physical background of the effect of the boundary layer.

In this paper it is shown that the findings of Gittler, Kluwick, and Brummayer regarding the nature of the dynamic boundary layers are also generally valid in the 3D case. The technique of matched asymptotic expansions is applied to analyse the boundary layer and match it to a wave equation with a small damping term for the pressure. Although this pressure wave equation is universally valid, the full boundary condition of a fluid sticking to the wall cannot be accounted for by this equation only. With an appropriate scaling at the system's boundaries an asymptotic expansion of the full equations, i.e. the continuity and the momentum equations of the viscid and compressible fluid, which fulfil the full boundary condition can be derived. This solution which is valid in a vicinity of the boundary describes the dynamic boundary layers of the full solution. The appropriate boundary for the pressure equation is obtained by matching it with the boundary layer results. The boundary condition relates the pressure to its gradient in the direction normal to the boundary which is proportional to the normal velocity. Physically, the viscid boundary layer is like a flexible wall with frequency dependent damping properties which by its

Power Transmission and Motion Control 2006 Edited by Dr D N Johnston and Professor K A Edge

breathing is dissipating energy and is the main damping mechanism for the wave propagation process.

1 NOMENCLATURE

c	Wave propagation speed	$\hat{p}$	Fourier Transform of $\widetilde{p}$
$\vec{\vec{D}}$	Deformation velocity tensor	$\hat{p}^{in}{}_k$, $\hat{p}^{ou}{}_k$	Term of order k of the inner (^{in}) and outer (^{ou}) asymptotic expansion of $\hat{p}$
D_{ij}	Components of $\vec{\vec{D}}$	P	Pressure scale for nondimensionalisation
E	Fluid compression modulus	$t,\ \dot{(\,)} = \frac{\partial}{\partial t}$	Physical time and time derivative
$E_{\xi}^{(k)}, E_{\xi^{bl}}^{(k)}$	Expansion operators for outer and inner co-ordinates	tr	The trace of a tensor
f	Nondimensional frequency	$\vec{v}$	Fluid velocity vector
$\vec{\vec{I}}$	Identity tensor	$v_i, i = 1..3$	Components of $\vec{v}$
j	Imaginary unit		
L	Length scale for nondimensionalisation	$\widetilde{\vec{v}}$	Nondimensional fluid velocity vector
p	Physical pressures	$\hat{v}_i, i = 1..3$	i-th component of the Fourier Transform of $\widetilde{\vec{v}}$
$\widetilde{p}$	Nondimensional pressure	$x_i, i = 1..3$	Co-ordinates
Δ, ∇	Laplacian and Nabla operator	$\vec{\vec{\sigma}}$	Cauchy stress tensor
ε	Nondimensional friction parameter	τ	Nondimensional time
μ	Dynamic viscosity of fluid	ω	Scaling frequency
$\nu = \frac{\mu}{\rho_0}$	Kinematic viscosity of fluid	$\xi_i, i = 1..3$	Nondimensional co-ordinates at the boundary
ρ, ρ_0	Fluid density and its reference value at zero pressure	$\xi_i^{bl}, i = 1..3$	Nondimenional co-ordinates for the boundary layer

2 INTRODUCTION

In conventional hydraulics, wave propagation effects play a significant role only in transmission lines. The dynamical behaviour of such lines has been an important subject of fluid power research and numerous mathematical models have been developed to study wave propagation processes ((1) gives an overview until 1986). In many practical purposes the effects of fluid friction on the dynamics of the system – which result in a frequency dependent damping - have to be modelled quite accurately. The most compact description of the transmission line dynamics taking fluid viscosity into account is given in the frequency domain ((2)). Time domain modelling is much more complex. There, the complex friction behaviour is modelled by some approximation of the inverse Laplace transformation of the wall shear stress (see for instance (3)), since exact formulas can't be found.

If frequencies go up into the ranges of several kilo-Hertz, the spatially one-dimensional transmission line models may loose their validity. Reasons are either that in parts of a transmission line other than axial flow velocities and pressure gradients become significant or that wave propagation phenomena are exhibited by some other fluid filled cavities. In such cases 3D wave propagation models must be established. For a general geometry of a cavity reasonable analytical mathematical models for such 3D viscid wave propagation could not be found by the authors. Several Finite Element programs (like, e.g., Abaqus (4)) offer the modelling and simulation of acoustic fields. But no general purpose programs exist that support the study of viscid wave propagation in fluids. The authors have supervised a master's thesis (5) which uses the Finite Element software hp-FEM (6), developed at the Institute of Computational Mathematics of Linz University by J. Schöberl, to analyse the 3D viscid wave propagation in hydraulic cavities. There, the linearised equations of motion and continuity of a compressible Newtonian fluid are solved numerically in the frequency domain. High accuracy can be achieved if a fine resolution of the dynamic wall boundary layers in the finite element mesh is done. Since the boundary layer becomes thinner with higher frequencies, different grids should be used for different frequencies in order to avoid unnecessary high computational effort. The generation of different grids is a drawback for a fast computation of the frequency response behaviour over a large frequency range.

Frequency domain modelling promises to yield the most compact description of the dynamic behaviour of the system. In (11) it was demonstrated how frequency domain models of a transmission line can be combined with time domain computation of nonlinear hydraulic systems by applying Fast Fourier transform and its inverse respectively. Although in this work periodic systems have been investigated there is a realistic perspective to generalise this technique for transient processes. The classical transmission line model was used as a benchmark.

In a thesis by Brummayer (7) a singular perturbation approach for the viscid wave propagation in lines, originally developed by Kluwick and Gittler (8) for gas filled tubes, for the computation of viscid wave propagation in hydraulic lines was applied. This work exhibits the physical nature of the friction phenomenon very clearly. The flow in the line consists of a friction dominated dynamic boundary layer which brings all velocity components to zero at the wall of the line and an inviscid flow in the remaining part of the

pipe. The inviscid part is effected by friction not by a shear stress but by radial velocity components that are created by the boundary layer and transmitted to the inner parts of the pipe. The results of this approach are nearly identical to other results, e.g. of (2).

These findings motivated the authors to study the potential of a singular perturbation approach for the efficient computation of 3D viscid wave propagation processes and to better understand the physics of the flow processes. This paper shows first results.

3 BASIC EQUATIONS OF 3D VISCID WAVE PROPAGATION

Starting from the full equations of motion and continuity in an Eulerian reference frame (Cartesian co-ordinates (x_1, x_2, x_3))

$$\begin{aligned} &\rho \dot{\vec{v}} + \rho (\vec{v}.\nabla)\vec{v} = \nabla \vec{\sigma} \\ &\dot{\rho} + \nabla(\rho \vec{v}) = 0 \end{aligned} \tag{1}$$

inserting there the material law of a weakly compressible Newtonian fluid without cavitation and bulk-viscosity, the definition of the deformation velocity tensor components

$$\begin{aligned} &\vec{\sigma} = -p\vec{I} - \tfrac{2}{3}\mu (tr\vec{D})\vec{I} + 2\mu \vec{D} \\ &\rho = \rho_0 \left(1 + \frac{p}{E}\right) \\ &D_{ij} = \frac{1}{2}\left(\frac{\partial v_i}{\partial x_j} + \frac{\partial v_j}{\partial x_i}\right) \end{aligned} \tag{2}$$

and omitting nonlinear terms and terms which are small in the order p/E compared to 1 results in the following two linear partial differential equations

$$\begin{aligned} &\dot{\vec{v}} = -\frac{1}{\rho_0}\nabla p + \frac{\mu}{\rho_0}\left(\Delta \vec{v} + \tfrac{1}{3}\nabla(\nabla \cdot \vec{v})\right) \\ &\frac{\dot{p}}{E} = -\nabla \cdot \vec{v} \end{aligned} \tag{3}$$

3.1 A viscid wave equation for the pressure

Applying the divergence to the first equation of (3) and inserting the second equation as an identity results in a wave equation (4) for the pressure only. At first glance, this result seems very advantageous, since the solution of a partial differential equation for only one scalar variable is easier than for two variables, one being a vector.

$$\ddot{p} - c^2 \Delta p = \tfrac{4}{3} \nu \, \Delta \dot{p} \,, \;\; c = \sqrt{\frac{E}{\rho_0}} \tag{4}$$

But, (4) only can be solved independently from (3) if the pressure or its gradient are given at the whole boundary. This is rarely the case in fluid power applications. The usual condition that the fluid sticks to a solid boundary cannot be accounted for by the pressure only. In the inviscid case, however, only the velocity component normal to the boundary vanishes which is equivalent to a vanishing pressure gradient in the normal boundary direction. Thus, (4) only can be solved in the general case in combination with (3), which without a further analysis is no improvement for many numerical methods.

However, (4) allows the qualitative statement that for a small viscosity ν the effect of the fluid friction on the pressure field is very small.

4 NONDIMENSIONAL EQUATIONS IN FREQUENCY DOMAIN

In the sequel nondimensional values related to the following scales are used.

$$p = \tilde{p}\, P; \;\; \vec{v} = \tilde{\vec{v}} c \frac{P}{E}; \;\; x_i = \tilde{x}_i L; \;\; t = \frac{\tau}{\omega}; \;\; \omega = \frac{c}{L}; \;\; \nabla = \frac{1}{L} \tilde{\nabla}; \quad \varepsilon = \frac{\nu}{cL} \tag{5}$$

P is a typical pressure amplitude of the wave, L a typical reference length, like the length of a transmission line. This scaling makes both, $\tilde{p}$ and $\tilde{\vec{v}}$ to be of order one.

With the Fourier Transform

$$\hat{p}(f) = \int_{-\infty}^{\infty} \frac{e^{-j f \tau}}{\sqrt{2\pi}} \tilde{p}(\tau) d\tau; \;\; \hat{v}(f) = \int_{-\infty}^{\infty} \frac{e^{-j f \tau}}{\sqrt{2\pi}} \tilde{\vec{v}}(\tau) d\tau \tag{6}$$

equations (3) and (4) take the following form in frequency domain

$$j f \, \hat{v} = -\tilde{\nabla} \hat{p} + \varepsilon \left(\tilde{\Delta} \hat{v} + \tfrac{1}{3} \tilde{\nabla} \left(\tilde{\nabla} \cdot \hat{v} \right) \right) \tag{7}$$

$$j f \, \hat{p} = -\tilde{\nabla} \cdot \hat{v}$$

$$- f^2 \hat{p} - \tilde{\Delta} \hat{p} = j f \tfrac{4}{3} \varepsilon \tilde{\Delta} \hat{p} \tag{8}$$

ε is a very small quantity in the order of $(10^{-5} \div 10^{-7})$ for typical values of ν, L, c. It is, in some sense, an inverse Reynold's number. The terms in all equations of (7) and (8) with a coefficient ε only can become significant where the velocity or the pressure field have strong local changes. Due to the scaling (5) the nondimensional wave length is of order 1

for $f = O(1)$. Local changes only occur at the boundaries due to the vanishing fluid velocity. Thus, (7) and (8) are singularly perturbed systems in the parameter ε (see, e.g., (9, 10) for singular perturbation theory[1]). The solution is dominated in a larger part of the domain by the reduced equations, which are obtained if the perturbation parameter ε is set to zero, which in our case is the inviscid case. The reduced equations have a reduced order regarding the highest spatial derivative. This does not allow all physical boundary conditions to be fulfilled, in particular the sticking condition. In small zones at the boundaries so called boundary layers occur which locally correct the solutions of the reduced system to fulfil the boundary conditions.

5 MATCHED ASYMPTOTIC EXPANSIONS OF THE 3D VISCID WAVE EQUATION

5.1 The outer expansion

An appropriate set of so called gauge functions (see (9)) of our problem is the sequence $\varepsilon^{k/2}, k = 0,1,2,3,\ldots$. The outer expansion is an asymptotic expansion of the solution outside the boundary layers (the outer range). It is represented here as a series in the gauge functions of the Fourier transform of the pressure and the velocity

$$\begin{aligned} \hat{p}^{ou} &= \hat{p}^{ou}{}_0 + \sqrt{\varepsilon}\,\hat{p}^{ou}{}_1 + \varepsilon\,\hat{p}^{ou}{}_2 + \ldots \\ \hat{v}_i^{ou} &= \hat{v}_i^{ou}{}_0 + \sqrt{\varepsilon}\,\hat{v}_i^{ou}{}_1 + \varepsilon\,\hat{v}_i^{ou}{}_2 + \ldots \end{aligned} \tag{9}$$

In the outer range the solutions of the reduced equations are a good approximation of the full solution. For general form of the hydraulic duct in which wave propagation takes place, numerical methods, e.g. the Finite Element method, can be used to obtain approximate solutions. This is not discussed further here. As pointed out in 3.1 this cannot be done for the pressure wave equation (3) or (8) respectively due to missing boundary conditions. To obtain appropriate boundary conditions the boundary layer equations must be solved and matched to the outer solution. This matching provides the boundary conditions for the outer solution.

5.2 The inner expansion

At the system's solid boundaries a co-ordinate system $\left(\xi_1^{bl}, \xi_2^{bl}, \xi_3^{bl}\right)$ is used to resolve the boundary layer. The first two axes are tangential the third is perpendicular to the tangent

---

[1] Perturbation methods aim to derive solutions of equations as formal power series in the perturbation parameter ε. For singular perturbation problems which exhibit boundary layers no uniformly valid power series expansion exists. Solution must be split into an external expansion off the boundary and an inner expansions at the boundary.

plane, as shown in Figure 1. We assume that the curvature radii of the boundary as well as the wave length $2\pi c/(f\omega)$ are much larger than the thickness of the boundary layer to avoid cumbersome calculations due to the curved co-ordinate system. The normal direction ξ_3 is stretched by $1/\sqrt{\varepsilon}$. This scaling makes the friction term in the momentum equation of equal order of magnitude as the acceleration and pressure gradient terms.

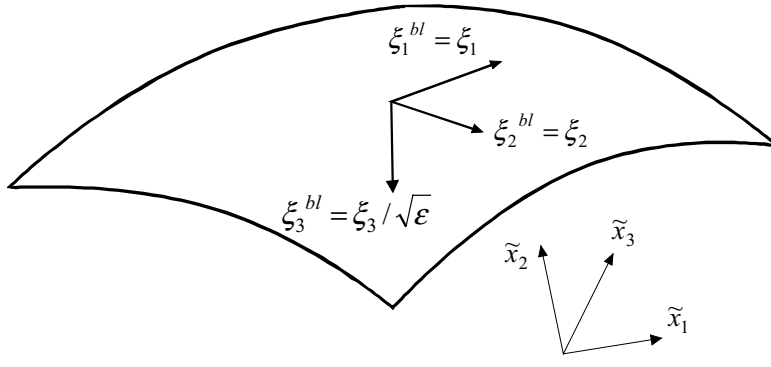

Figure 1: Boundary layer co-ordinate system and its scaling

Expressing (7) in boundary layer co-ordinates results in the following equations

$$
jf\begin{pmatrix}\hat{v}_1^{in}\\ \hat{v}_2^{in}\\ \hat{v}_3^{in}\end{pmatrix} = \begin{pmatrix}-\dfrac{\partial \hat{p}^{in}}{\partial \xi_1^{bl}}\\ -\dfrac{\partial \hat{p}^{in}}{\partial \xi_2^{bl}}\\ -\dfrac{\partial \hat{p}^{in}}{\sqrt{\varepsilon}\,\partial \xi_3^{bl}}\end{pmatrix} + \varepsilon\begin{pmatrix}\dfrac{\partial^2 \hat{v}_1^{in}}{\partial(\xi_1^{bl})^2}+\dfrac{\partial^2 \hat{v}_1^{in}}{\partial(\xi_2^{bl})^2}+\dfrac{1}{\varepsilon}\dfrac{\partial^2 \hat{v}_1^{in}}{\partial(\xi_3^{bl})^2}\\ \dfrac{\partial^2 \hat{v}_2^{in}}{\partial(\xi_1^{bl})^2}+\dfrac{\partial^2 \hat{v}_2^{in}}{\partial(\xi_2^{bl})^2}+\dfrac{1}{\varepsilon}\dfrac{\partial^2 \hat{v}_2^{in}}{\partial(\xi_3^{bl})^2}\\ \dfrac{\partial^2 \hat{v}_3^{in}}{\partial(\xi_1^{bl})^2}+\dfrac{\partial^2 \hat{v}_3^{in}}{\partial(\xi_2^{bl})^2}+\dfrac{1}{\varepsilon}\dfrac{\partial^2 \hat{v}_3^{in}}{\partial(\xi_3^{bl})^2}\end{pmatrix} + \\
\frac{\varepsilon}{3}\begin{pmatrix}-\dfrac{\partial}{\partial \xi_1^{bl}}\\ -\dfrac{\partial}{\partial \xi_2^{bl}}\\ -\dfrac{\partial}{\sqrt{\varepsilon}\,\partial \xi_3^{bl}}\end{pmatrix}\left(\frac{\partial \hat{v}_1^{in}}{\partial \xi_1^{bl}}+\frac{\partial \hat{v}_2^{in}}{\partial \xi_2^{bl}}+\frac{1}{\sqrt{\varepsilon}}\frac{\partial \hat{v}_3^{in}}{\partial \xi_3^{bl}}\right) \qquad (10)
$$

The solution is represented by an asymptotic expansion

$$
\begin{aligned}
\hat{p}^{in} &= \hat{p}^{in}{}_0 + \sqrt{\varepsilon}\,\hat{p}^{in}{}_1 + \varepsilon\,\hat{p}^{in}{}_2 + \ldots \\
\hat{v}_i^{in} &= \hat{v}_i^{in}{}_0 + \sqrt{\varepsilon}\,\hat{v}_i^{in}{}_1 + \varepsilon\,\hat{v}_i^{in}{}_2 + \ldots
\end{aligned} \qquad (11)
$$

Inserting (11) in (10) and collecting orders of $\sqrt{\varepsilon}$ results in the following set of equations

Order $O\left(\varepsilon^{0}\right)$ and $O\left(\varepsilon^{-1/2}\right)$

$$
\begin{aligned}
j f \hat{v}_1^{in}{}_0 &= -\frac{\partial \hat{p}^{in}{}_0}{\partial \xi_1^{bl}} + \frac{\partial^2 \hat{v}_1^{in}{}_0}{\partial \left(\xi_3^{bl}\right)^2} \\
j f \hat{v}_2^{in}{}_0 &= -\frac{\partial \hat{p}^{in}{}_0}{\partial \xi_2^{bl}} + \frac{\partial^2 \hat{v}_2^{in}{}_0}{\partial \left(\xi_3^{bl}\right)^2} \\
j f \hat{v}_3^{in}{}_0 &= -\frac{1}{\sqrt{\varepsilon}} \frac{\partial \hat{p}^{in}{}_0}{\partial \xi_3^{bl}} + \frac{4}{3} \frac{\partial^2 \hat{v}_1^{in}{}_0}{\partial \left(\xi_3^{bl}\right)^2} - \frac{\partial \hat{p}^{in}{}_1}{\partial \xi_3^{bl}} \\
j f \hat{p}^{in}{}_0 &= -\left(\frac{\partial \hat{v}_1^{in}{}_0}{\partial \xi_1^{bl}} + \frac{\partial \hat{v}_2^{in}{}_0}{\partial \xi_2^{bl}} + \frac{1}{\sqrt{\varepsilon}} \frac{\partial \hat{v}_3^{in}{}_0}{\partial \xi_3^{bl}} + \frac{\partial \hat{v}_3^{in}{}_1}{\partial \xi_3^{bl}} \right)
\end{aligned}
\tag{12}
$$

The two terms in the third and fourth equation with a coefficient $1/\sqrt{\varepsilon}$ must vanish in order to make the asymptotic expansion valid. Thus we have

$$
\frac{\partial \hat{p}^{in}{}_0}{\partial \xi_3^{bl}} = 0; \quad \frac{\partial \hat{v}_3^{in}{}_0}{\partial \xi_3^{bl}} = 0 \tag{13}
$$

Since $\hat{v}_3^{in}{}_0 = 0$ at the boundary ($\xi_3^{bl} = 0$) the second equation in (13) means that $\hat{v}_3^{in}{}_0 \equiv 0$.

In other words, the normal fluid velocity in the boundary layer is of order $O\left(\sqrt{\varepsilon}\right)$. This reveals that the lowest order of the asymptotic expansion of the boundary layer solution corresponds to the boundary condition of the inviscid wave equation, namely that the velocity and the pressure gradient in the normal direction vanish. Furthermore, re-evaluating the last equation of (12) with the last findings yields $\frac{\partial \hat{p}^{in}{}_1}{\partial \xi_3^{bl}} = 0$.

The third equation of (12) is now fulfilled trivially and does not provide any further information. We have to add the next order of this equation to involve a pressure term, which differs from the solution of the inviscid case.

$$
j f \hat{v}_3^{in}{}_1 = -\frac{\partial \hat{p}^{in}{}_2}{\partial \xi_3^{bl}} + \frac{4}{3} \frac{\partial^2 \hat{v}_1^{in}{}_1}{\partial \left(\xi_3^{bl}\right)^2} + \frac{1}{3} \frac{\partial^2 \hat{v}_1^{in}{}_0}{\partial \xi_1^{bl} \partial \xi_3^{bl}} + \frac{1}{3} \frac{\partial^2 \hat{v}_2^{in}{}_0}{\partial \xi_2^{bl} \partial \xi_3^{bl}} \tag{14}
$$

The boundary condition for the inner solution requires that all velocity components vanish at $\xi_3^{bl} = 0$. At the solid boundaries no pressure can be prescribed. Indeed, the pressure

variable $\hat{p}^{in}{}_0$ which is still present in our equations can only be determined by the matching of the inner to the outer expansion (see Section 5.3).

Equations 1,2,4 of (12) and equation (14) can be solved. The solutions are

$$\hat{v}_1{}^{in}{}_0 = \frac{j}{f}\frac{\partial \hat{p}^{in}{}_0}{\partial \xi_1{}^{bl}}\left(1 - e^{\sqrt{f/2}(-1-j)\xi_3{}^{bl}}\right),\ \hat{v}_2{}^{in}{}_0 = \frac{j}{f}\frac{\partial \hat{p}^{in}{}_0}{\partial \xi_2{}^{bl}}\left(1 - e^{\sqrt{f/2}(-1-j)\xi_3{}^{bl}}\right)$$
$$\hat{v}_3{}^{in}{}_1 = -\sqrt{f/2}\,(1+j)\,\hat{p}^{in}{}_0\left(1 - e^{\sqrt{f/2}(-1-j)\xi_3{}^{bl}}\right) \tag{15}$$
$$\hat{p}^{in}{}_2 = \sqrt{f^3/2}\,(-1+j)\,\hat{p}^{in}{}_0\,\xi_3{}^{bl}$$

(15) shows that the thickness of the boundary layers is of order $O\left(\sqrt{\varepsilon/f}\right)$ if measured in the outer scale. The tangential velocity components show up the typical distribution in the normal direction as indicated in Figure 2. They are 90° phase shifted to the pressure gradient, their amplitude is inversely proportional to the frequency. The normal velocity is of order $O\left(\sqrt{\varepsilon}\right)$, has a distribution in normal direction equivalent to the tangential components, but a quite different frequency dependency and a phase shift of 235° (see Figure 2). The pressure which is constant in the normal direction in the order ε^0 has a superimposed ε^1 order component $\hat{p}^{in}{}_2$ which causes a linear pressure change in the normal direction.

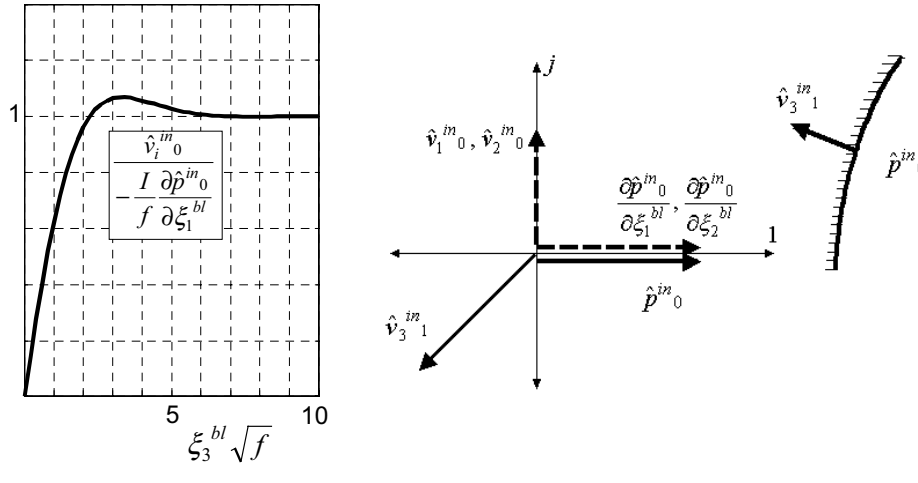

Figure 2: Distribution of the tangential velocities at the boundary layer according to the inner expansion up to order ε^0, phase shift of boundary layer velocities relative to pressure and pressure gradients respectively, and orientation of normal velocity relative to the pressure

5.3 Matching of the inner and outer expansions

Inner and outer expansions have to be adapted by a so called matching. Using expansion operators (see (9)) the matching condition for the pressure reads

$$E_{\xi^{bl}}^{(k)} E_{\xi}^{(k)} \hat{p} = E_{\xi^{bl}}^{(k)} E_{\xi}^{(k)} E_{\xi^{bl}}^{(k)} \hat{p}, \quad k = 0, 1, 2, \ldots \tag{16}$$

$E_{\xi}^{(k)} \hat{p} = E^{(k)} \hat{p}^{ou}$ is the outer and $E_{\xi^{bl}}^{(k)} \hat{p} = E^{(k)} \hat{p}^{in}$ is the inner expansion of the pressure Fourier transform in terms of our gauge functions $\sqrt{\varepsilon}^{k}$. For $k = 0$, (16) yields

$$\begin{aligned} &E_{\xi^{bl}}^{(0)} E_{\xi}^{(0)} \hat{p}(\xi_1,\xi_2,\xi_3) = E^{(0)} \hat{p}^{ou}{}_0\left(\xi_1,\xi_2,\sqrt{\varepsilon}\xi_3{}^{bl}\right) = \hat{p}^{ou}{}_0(\xi_1,\xi_2,0) = \\ &E_{\xi^{bl}}^{(0)} E_{\xi}^{(0)} E_{\xi^{bl}}^{(0)} \hat{p}\left(\xi_1,\xi_2,\xi_3{}^{bl}\right) = E_{\xi^{bl}}^{(0)} E_{\xi}^{(0)} p^{in}{}_0(\xi_1,\xi_2) = \hat{p}^{in}{}_0(\xi_1,\xi_2) \end{aligned} \tag{17}$$

In a similar manner, for $k = 1$ one gets if results from above are exploited

$$\frac{\partial \hat{p}^{ou}{}_0}{\partial \xi_3}(\xi_1,\xi_2,0) = 0 \tag{18}$$

For $k = 2$ the matching procedure (16) results in the following equations

$$\begin{aligned} &E_{\xi^{bl}}^{(2)} E_{\xi}^{(2)} \hat{p}(\xi_1,\xi_2,\xi_3) = \hat{p}^{ou}{}_0(\xi_1,\xi_2,0) + \varepsilon \tfrac{1}{2} \frac{\partial^2 \hat{p}^{ou}{}_0}{\partial\left(\xi_3{}^{bl}\right)^2}(\xi_1,\xi_2,0)\left(\xi_3{}^{bl}\right)^2 + \\ &\qquad \varepsilon \frac{\partial \hat{p}^{ou}{}_1}{\partial \xi_3{}^{bl}}(\xi_1,\xi_2,0)\xi_3{}^{bl} + \varepsilon\, \hat{p}^{ou}{}_2(\xi_1,\xi_2,0) \\ &E_{\xi^{bl}}^{(2)} E_{\xi}^{(2)} E_{\xi^{bl}}^{(2)} \hat{p}(\xi_1,\xi_2,\xi_3) = \\ &\qquad E_{\xi^{bl}}^{(2)} E_{\xi}^{(2)} \left(\hat{p}^{ou}{}_0(\xi_1,\xi_2,0) - \varepsilon \frac{\sqrt{2}}{2} f^{\frac{3}{2}} (1-j)\, \hat{p}^{in}{}_0(\xi_1,\xi_2)\xi_3{}^{bl} \right) = \\ &\qquad \hat{p}^{ou}{}_0(\xi_1,\xi_2,0) - \varepsilon \left(\frac{\sqrt{2}}{2} f^{\frac{3}{2}} (1-j)\, \hat{p}^{in}{}_0(\xi_1,\xi_2)\xi_3{}^{bl} \right) \end{aligned} \tag{19}$$

Comparing both results of (19) and inserting identity (17) yields the wanted boundary condition for the outer expansion of the pressure

$$\frac{\partial \hat{p}^{ou}{}_1}{\partial \xi_3}(\xi_1,\xi_2,0) = -\frac{\sqrt{2}}{2} f^{\frac{3}{2}} (1-j)\, \hat{p}^{ou}{}_0(\xi_1,\xi_2,0) \tag{20}$$

Additionally, we get

$$\frac{\partial^2 \hat{p}^{ou}{}_0}{\partial\left(\xi_3{}^{bl}\right)^2}(\xi_1,\xi_2,0)=0, \quad \hat{p}^{ou}{}_2(\xi_1,\xi_2,0)=0 \tag{21}$$

6 RESUME

(20) confirms the findings of (7, 8) qualitatively. The pressure gradient $\frac{\partial \hat{p}}{\partial \xi_3}$ corresponds to the negative velocity time derivative, in the frequency domain $-j\,f\,\hat{v}_3$. The pressure oscillations $\hat{p}$ cause a phase shifted velocity $\hat{v}_3$ oscillation (normal to the boundary), which is strictly dissipative because a rising pressure causes an outward velocity (in direction $-\xi_3$) (for explanation see also Figure 2). This is the mechanism how the viscid boundary layer has dissipative effect on the nearly inviscid flow field in the interior of the domain.

The pressure derivative is of order $\sqrt{\varepsilon} f^{\frac{3}{2}}$. The limit of the viscid case for vanishing viscosity and the a priori inviscid case are identical in terms of the pressure field (they are not in terms of the velocity field if the supremum norm is used for comparison and the sticking boundary condition for the velocity is valid!).

The result (20) enables the viscid case to be computed using acoustic models (like Finite Element acoustic elements), provided they offer the modelling of general, linear, frequency dependent boundary conditions equivalent to (20).

But even if the numerical computation is carried out for the viscid case (e.g., by computing (4)), (20) is of great help. As already pointed out above, for higher frequencies the boundary layer becomes very thin which requires a fine resolution of the computation grid or mesh respectively to obtain a result with a good accuracy. The mesh has to be adapted to every frequency computed, at least for higher frequencies, which increases the computational effort considerably.

This analysis has been carried out in frequency domain, simply to be able to have a well defined boundary layer. In the transient case, the physical boundary layer is a mixture of all the frequencies involved and currently no other ways are known to cope with this case in the time domain but with history integrals of approximations of these (like in (3)) or to carry out a mixed time and frequency domain computations (as performed for the periodic case in (11)).

ACKNOWLEDGEMENT

The authors gratefully acknowledge the sponsoring of this work by the 'Linz Center of Competence in Mechatronics' in the framework of the K*plus* program of the Austrian

government. This program is funded by the Austrian government, the province of Upper Austria and the Johannes Kepler University Linz.

REFERENCES

(1) Stecki, J., Davis, D., Fluid Transmission Lines – Distributed Parameter Models, Part1: A review on the State of the Art, Proc. Instn. Mech. Engnrs. Part A, 200 (1986), pp. 215-228.

(2) D'Souza, A., Oldenburger, R., Dynamic Response of Fluid Lines, Trans. ASME, Journal Basic Engng, 86 (1964), pp. 589-598.

(3) Zielke W., Frequency-Dependent Friction in Transient Pipe Flow, Trans. ASME, Journal Basic Engng., 90 (1968), pp. 109-115.

(4) Hibbitt, Karlsson & Sorensen Ic., Abaqus User's manual, Version 6.1, 2000.

(5) Furtmüller, J., Berechnung einer Rohrströmung mit der Methode der Finiten Elemente und Vergleich mit analytischen Lösungen, Master's thesis, Johannes Kepler University Linz, 2006.

(6) Schöberl, J., Start Project: 3D hp-Finite Elements: Fast Solvers and Adaptivity, sponsored by the Austrian Science Foundation (FWF), http://www.hpfem.jku.at/index.html?/joachim/ (March 2006).

(7) Brummayer, M., Wellenausbreitungsvorgänge in hydraulischen Wellenkonvertern unter Berücksichtigung von Reibungseffekten, doctoral thesis, Johannes Kepler University Linz, 2000.

(8) Gittler, Ph., Kluwick, A., Dispersive Wandreibungseffekte bei hochfrequenten Wellen in gasgefüllten Rohren, ZAMM 69 (1989), 578-579.

(9) Eckhaus, W., Asymptotic Analysis of Singular Perturbations, North- Holland, 1979.

(10) Kevorkian, J., Cole, J.D., Perturbation Methods in Applied Mathematics, Series: Applied Mathematical Sciences, Vol. 43, Springer, 1980.

(11) Manhartsgruber, B., Mikota, G., Scheidl, R., Modelling of a Switching Control Hydraulic System, Mathematical and Computer Modelling of Dynamical Systems, 11 (2005), pp. 329-344.

Overcoming self-excited oscillations and noise in hydraulic jet-pipe servo-valve using magnetic fluid

Songjing Li* Shuqian Jia Shuming Wang****
*Box 459 Harbin Institute of Technology, Harbin, China, 150001
**Box 9200-77 Long March Aerospace Control Engineering Corporation, Beijing, China, 100076

ABSTRACT

In order to overcome self-excited high frequency oscillations and noise appearing sometimes during the working of hydraulic jet-pipe servo-valve, application of magnetic fluid (MF) in hydraulic jet-pipe servo-valve is developed in this paper. Large damping can be introduced into the servo-valve if magnetic fluid is filled into the working gaps of hydraulic servo-valve torque motor. Construction of hydraulic jet-pipe servo-valve with magnetic fluid is introduced. The noise signals are tested and recorded when magnetic fluid is applied or not in the servo-valve. Experimental results are compared and analyzed using FFT and wavelet analysis. It is shown that noise of servo-valve is depressed when magnetic fluid is applied. Finally the damping force exerted on the torque motor armature by magnetic fluid is studied.

1. INTRODUCTION

Hydraulic jet-pipe servo-valve has larger resistance to oil contaminations, but lower responding speed and stability than hydraulic flapper nozzle servo-valve [1]. When hydraulic oil is jetted out from the jet-pipe, cavitations or even shear-layer oscillations are very likely to appear inside the flow field between jet-pipe and the two receiving ports where the jet flow goes in. Therefore, if the construction parameters of hydraulic jet-pipe servo-valve or torque motor were not selected correctly, self-excited high frequency pressure oscillations and noise will most probably exist during the working of hydraulic servo-valve [2]. It is difficult to remove the high frequency oscillations and noise even if the construction parameters, such as the magnetization of permanent magnet or the distance between jet-pipe and receiving ports, are modified. Hence the hydraulic control system in which the servo-valve is used will lose its stability.

In order to improve the performance of hydraulic servo-valve and overcome the self-excited high frequency oscillations and noise, magnetic fluid is filled into the working gaps of hydraulic servo-valve torque motor in this paper. As magnetic fluid shows an increased

Power Transmission and Motion Control 2006 Edited by Dr D N Johnston and Professor K A Edge

saturation magnetization when it is exposed to an external magnetic field, many applications of magnetic fluid have been developed, such as damper, sealing, quality improvement in speaker, efficiency improvement in electric motor and so on [3-6]. When magnetic fluid is filled in the working gaps between the torque motor armature and cores, larger damping forces can be applied to the torque motor due to the higher saturation magnetization of magnetic fluid. The focus of this paper is to test and analyze the noise of hydraulic jet-pipe servo-valve when magnetic fluid is used or not in the servo-valve.

2. INTRODUCTION OF TEST RIG

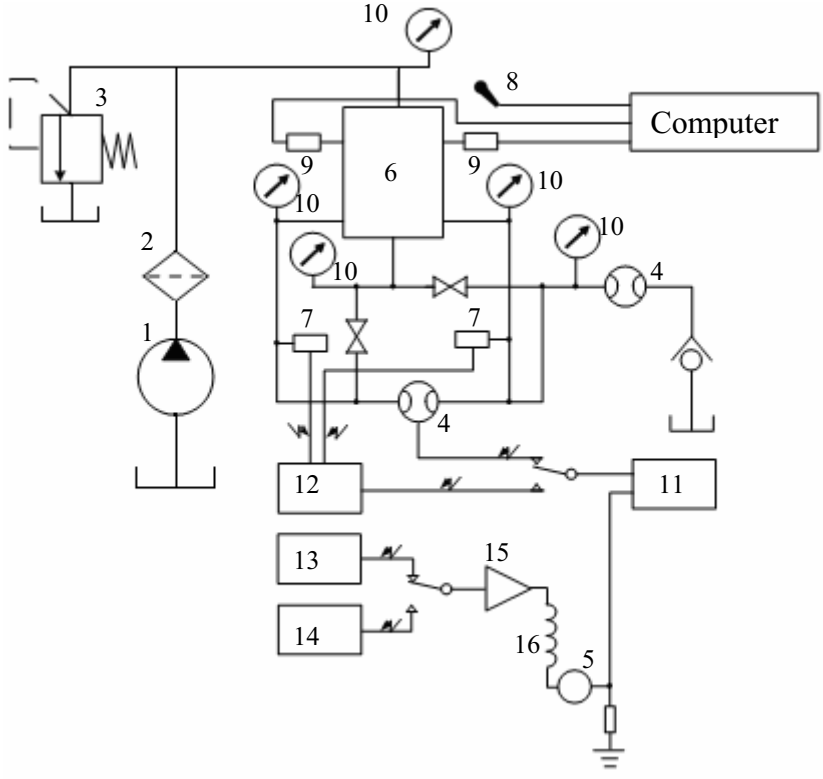

Figure 1 Schematic of hydraulic servo-valve test rig

The test rig for the static characteristics testing of hydraulic servo-valve is shown in figure 1. The test rig basically consists of hydraulic pump 1 and filter 2, relief valve 3, flow rate meter 4, electric current meter 5, tested valve 6, some pressure gauges 9 and transducers 7. Component 11, 12, 13, 14, 15 and 16 are X-Y plotter, signal transfer electric circuit, manual controller, automatic controller, amplifier and servo-valve coil respectively. In order to record the self-excited pressure oscillations of the servo-valve, two piezoelectric pressure transducers 10 for dynamic pressure testing are used. The microphone is used to record the noise signals. The electric control circuit includes the electric power supply and amplifier for the servo-valve, the pressure transducer and the flow meter. The electric

current meter 5 is used to show the input electric current to the servo-valve. The tested pressure oscillation data is transferred into the computer through the acquisition system linked with the transducers. The two transducers are connected respectively with the two ports which receive the flow coming out from the jet-pipe and running into the two chambers besides the spool. The noise recorded by the microphone is saved into computer by the Microsoft tape recorder software. In this paper, experiments are carried out when a certain value of control current is supplied to the coil of the servo-valve. If the current is the rated current of the valve and the supply pressure is the rated pressure, the flow rate supplied by the valve will be the rated flow rate.

3. TEST OF SELF-EXCITED NOISE

Noises near the servo-valve are tested using the microphone when the supply pressures of the test rig are 21MPa and 10MPa respectively. The microphone is placed about 0.02m away from the servo-valve. The sample frequency of the microphone and the recording process is 22.05 KHz. When the noise of hydraulic servo-valve is recorded, the background noise is recorded as well. That does not matter, as only the difference between the noises under different test conditions is of interest. The test method does not need to be as accurate as the international standard test of noise is. The rated electric current, supply pressure and flow rate of the servo-valve being tested are 10 mA, 21 MPa and 100 L/min respectively.

3.1 Noise wave signal

When the supply pressure is 10MPa, the self-excited noise of the servo-valve almost can not be heard. But when the supply pressure is raised to 21MPa, the self-excited noise appears. It shows the existence of the self-excited oscillations of the jet-pipe inside the servo-valve. The two power signals of the noise when the test supply pressures are 10MPa and 21MPa are shown in figure 2 (a) and (b) respectively. The waves are shown in the amplitude ratio which is the tested sound pressure level ratio to a reference sound pressure level given by the recording software. PU means Processing Unit.

Figure 2 (a) shows that the noise wave has only a low frequency component. It is the noise of the test background, basically the noise of hydraulic supply power. While figure 2 (b) shows that the wave contains not only a low frequency component, but also a high frequency component. The high frequency component is supposed to be the self-excited noise. It also shows that the self-excited oscillations and noise tend to appear when the supply pressure of servo-valve is raised up.

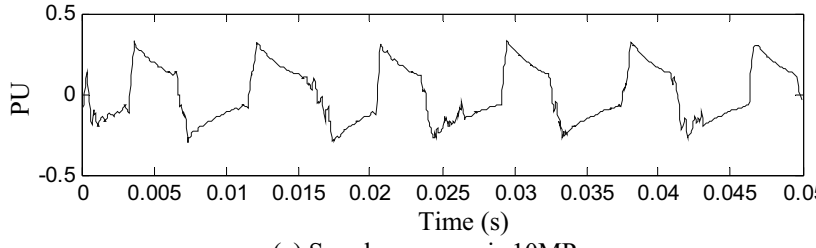

(a) Supply pressure is 10MPa

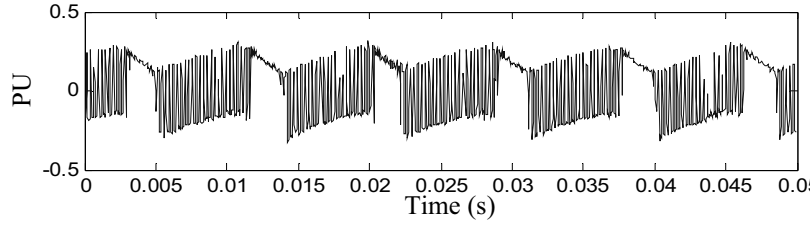

(b) Supply pressure is 21MPa

Figure 2 Tested noise wave signals

3.2 FFT analysis of the tested results

The tested noise signals of the servo-valve can be analyzed using FFT method. The FFT analyzed results of the two tested noise signals are shown in figure 3.

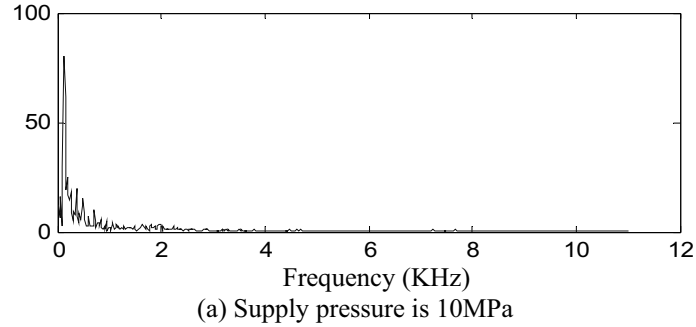

(a) Supply pressure is 10MPa

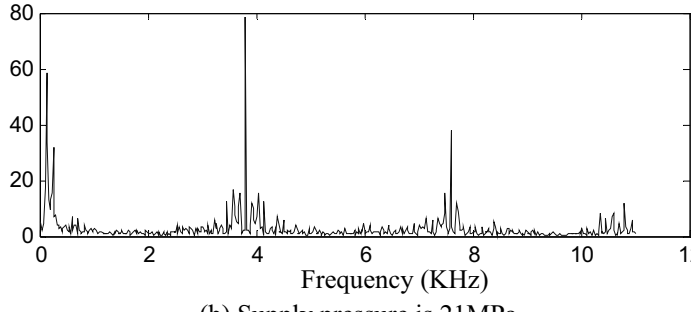

(b) Supply pressure is 21MPa

Figure 3 FFT analysis of noise signals

From the FFT analysis results in figure 3, it can be seen that the background frequency is about 120Hz and the frequency of the high frequency noise is about 3.8KHz. The background frequency is mainly the frequency of hydraulic power supply.

From [2], if the frequency of oscillations and noise inside hydraulic valves goes up to as high as several KHz, the oscillations and noise are most probably because of the shear-layer instability inside the flow field. So we can conclude that there is shear-layer instability inside the flow field of the tested jet-pipe servo-valve in this paper.

4. SERVO-VALVE WITH MAGNETIC FLUID

4.1 Introduction of construction

The construction of jet-pipe servo-valve with magnetic fluid is shown in figure 4 [7]. The servo-valve is provided by a Chinese servo-valve manufacturer. It contains torque motor, jet-pipe and valve parts. As the driving part of the servo-valve, the torque motor moves the jet-pipe to a rotation angle after a current is supplied to the motor. If there is no power supply to the torque motor, under the working of the permanent magnet, the jet-pipe will stay at the neutral position between the two ports receiving the flow. If magnetic fluid is filled into the gaps between the torque motor armature and cores, it will show a large saturation magnetization when exposed to the magnetic field of the motor. Thus extra damping can be exerted on the armature to suppress the oscillations of the jet-pipe and armature. Magnetic fluid will stay inside the gaps between armature and cores because of the permanent magnetic field even if the power of the motor is turned off.

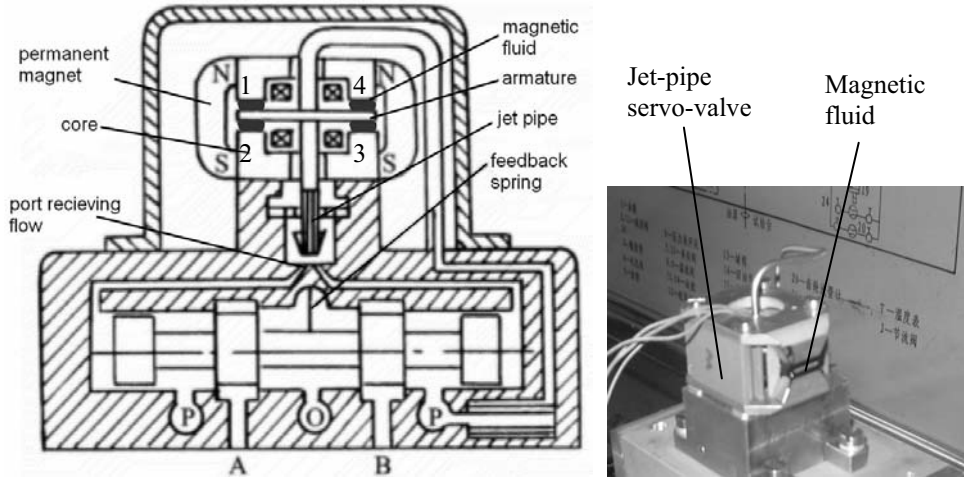

Figure 4 Construction of jet-pipe servo-valve with magnetic fluid

4.2 Properties of magnetic fluid

There are different types of magnetic fluids with different properties. The most important properties for magnetic fluids are their saturation magnetization, viscosity and magnetic permeability. For damping application, saturation magnetization of magnetic fluid is important. The higher the saturation magnetization is, the larger the damping effect. The properties of magnetic fluid used in the experimental study in this paper are shown in figure 5. The magnetic fluid is produced by Heilongjiang Institute of Chemical Engineering in China. And the properties in figure 5 are provided by the producer. The saturation magnetization is about 400 Gs and the relative magnetic permeability when magnetic fluid gets saturated is nearly 1.5.

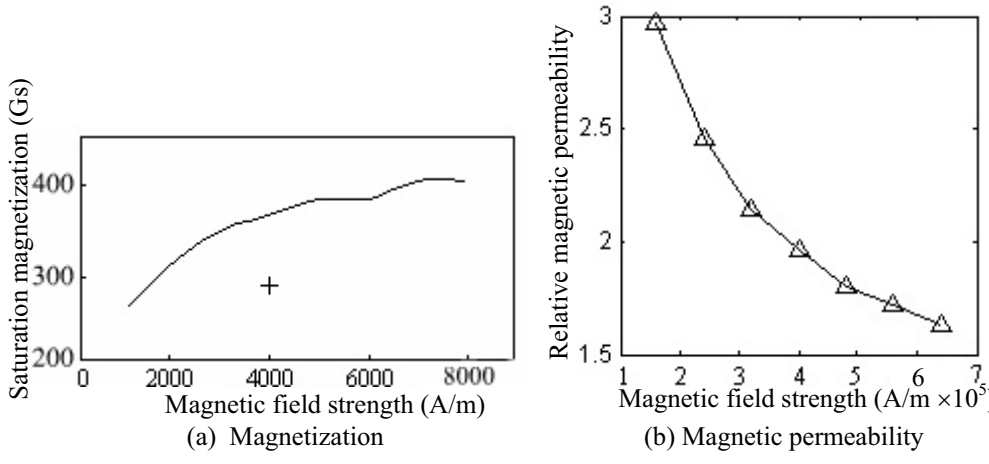

Figure 5 Properties of magnetic fluid

5. TEST RESULTS WHEN MAGNETIC FLUID IS APPLIED

An experiment was carried out when magnetic fluid was filled in the working gaps of the torque motor. The noise wave of the servo-valve is recorded and compared with that when magnetic fluid is not applied, as shown in figure 6. The tested noise signals are analyzed using FFT and wavelet toolbox in MATLAB. The FFT analyzed results are shown in figure 7. The wavelet analyzed results are compared and shown in figure 8.

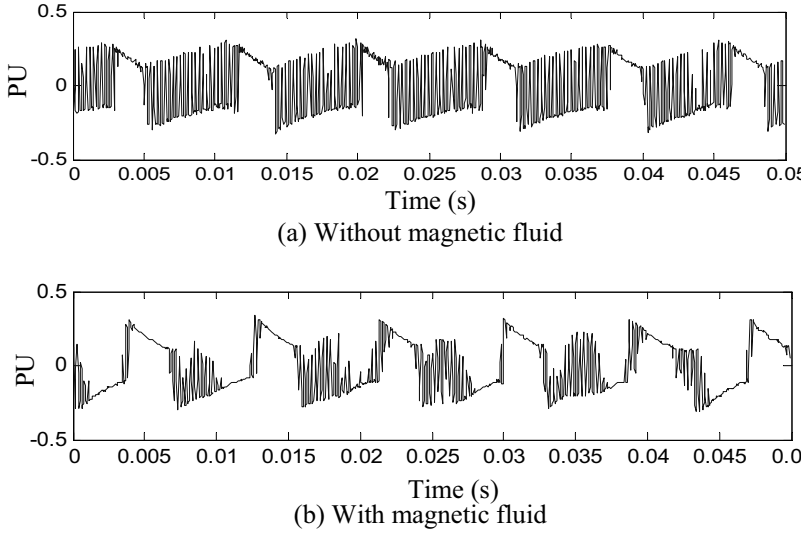

Figure 6 Tested noise wave signals

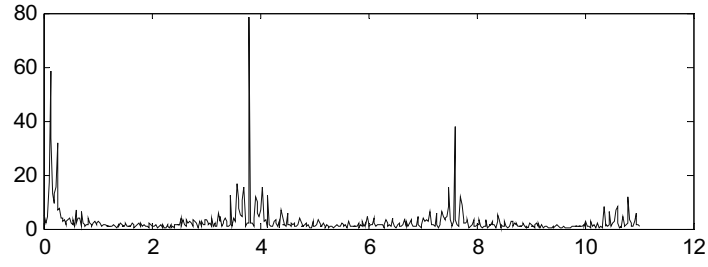

(a) Without magnetic fluid

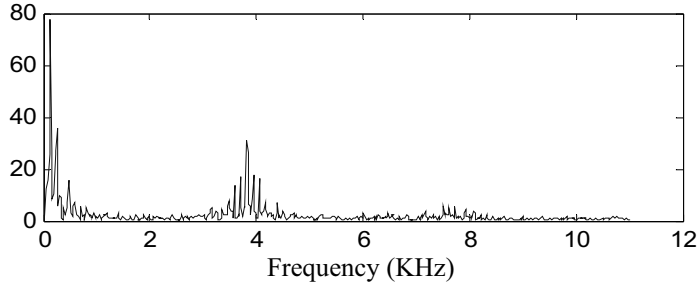

(b) With magnetic fluid

Figure 7 FFT analysis of noise signals

The FFT analysis results in figure 7 show that the amplitude of high frequency noise at about 3.8KHz is reduced significantly after magnetic fluid is applied in the servo-valve. But the noise was not gotten rid of entirely. There is still noise audible.

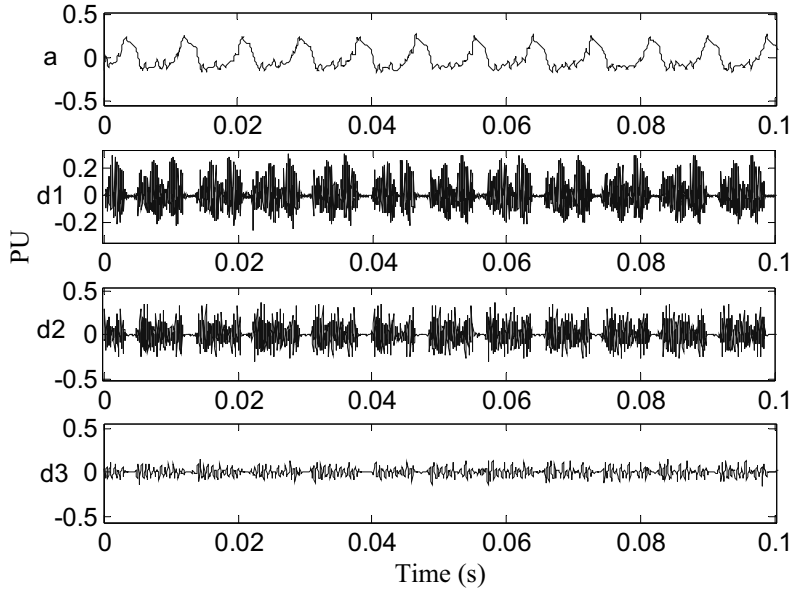

(a) Without magnetic fluid

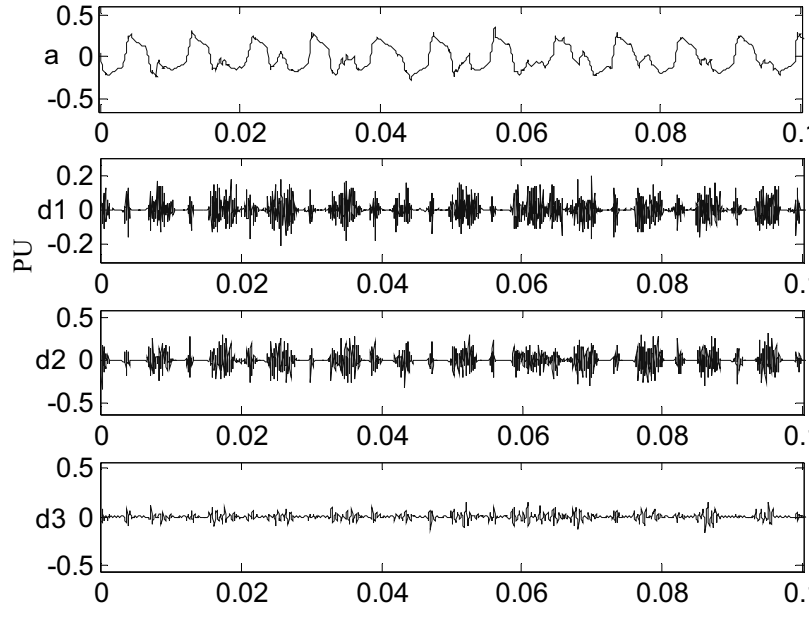

(b) With magnetic fluid

Figure 8 Wavelet analysis results

The tested noise signals of the servo-valve can also be resolved into several basic waves by wavelet analysis. In this paper, the wavelet toolbox in MATLAB is used for the analysis. If 4 levels wavelet analysis is used, the two tested noise signals shown in figure 6 can be resolved into four waves, as shown in figure 8 (a) and (b). In figure 8, the d1, d2 and d3 are the details of the tested sound wave signal upon the basic wave signal a. It will be more obvious to see the difference of the noise after the noise signals are resolved into several detail waves using wavelet analysis method.

Figure8 (a) and (b) show that the resolved waves are one low frequency, two high frequency and one semi frequency waves. The low frequency waves in (a) and (b) are almost the same in frequency and amplitude. The high frequency waves d1 and d2 in figure 8 (a) have larger amplitudes and longer durations. While the high frequency waves d1 and d2 in figure 8 (b) have smaller amplitude and shorter durations. It shows that when magnetic fluid is applied in the servo-valve, the self-excited oscillations and noise are suppressed to some extend.

6. CALCULATION OF DAMPING TORQUE

When magnetic fluid is exposed to magnetic field, because of the higher saturation magnetization, there will be stress working on the surface of the torque motor armature due to magnetic fluid, as shown in figure 9.

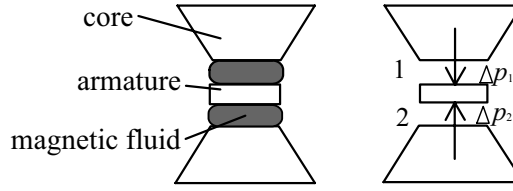

Figure 9 Schematic of stress due to magnetic fluid

The stress can be written as [8-9]:

$$\Delta P = \int_0^H M_s dH \ , \qquad (1)$$

where M_s , H are the saturation magnetization of magnetic fluid and magnetic field strength inside the working gaps of the torque motor respectively. When magnetic fluid gets saturated, its saturation magnetization M_s is taken as a constant. If magnetic flux leakage is neglected, the magnetic field strength inside magnetic fluid is taken to a constant too. The formula (1) can be written as: $\Delta P = M_s H$.

Magnetic field strength H is a function of coil current *I* and rotation angle of the armature θ . That is: $H = f(I, \theta)$.

Damping torque due to magnetic fluid can be calculated as:

$$T_{mf} = 2(\Delta P_1 - \Delta P_2) \times A \times a \ = 2M_s \times f(I, \theta) \times A \times a \, , \qquad (2)$$

where ΔP_1 , ΔP_2 , A , a are respectively the stress due to magnetic fluid in gap 1 and gap 2, area normal to the magnetic flux in the working gaps and radius of armature from pivot to center of pole face.

As torque motor in hydraulic servo-valve works at the neutral position during most of the working time, in order to simplify the mathematical model and analysis of the damping torque due to magnetic fluid, the model of damping torque can be linearized at the neutral position. That is: $T_{mf} = K_t \times I + K_a \theta$, where K_t and K_a are respectively the damping torque coefficient and magnetic spring constant due to magnetic fluid. From formula (2), K_t and K_a can be calculated by the multiplication of the saturation magnetization of magnetic fluid M_s , area normal to the magnetic flux in the working gaps A and radius of armature from pivot to center of pole face a .

7. DISCUSSION AND CONCLUSIONS

From the noise test and study above, we can conclude that magnetic fluid can exert large damping forces on the torque motor armature. So that it can be used to overcome the self-excited oscillations and noise in hydraulic jet-pipe servo-valve to some extent. The noise was not gotten rid of entirely by the application of magnetic fluid. For the application in this paper, magnetic fluid with higher saturation magnetization is preferred. The damping torque can be increased if magnetic fluid with larger saturation magnetization is applied, so that the noise and oscillations in hydraulic servo-valve may be removed totally. In addition, the mathematical model of damping torque due to magnetic fluid shown in this paper is a static model and can not be used for more accurate analysis.

ACKNOWLEDGEMENTS

This paper is financially supported by the National Nature Science Foundation of China. The authors would like to give thanks to Heilongjiang Chemical Engineering Institute in China for the property figures of MF provided in figure 5 in this paper.

REFERENCE

[1] Merrit, H. E., “Hydraulic Control Systems”, John Wiley and Sons, Inc., 1967

[2] Weber, S. T., Porteiro, J. L. F., Rahman, M. M., & et al, “Self-sustaining flow oscillations in counterbalance valves,” Proceedings of Bath Workshop on Power Transmission and Motion Control, Bath, UK, September 1998, pp. 207-217

[3] Zou, J., Li, X., Lu, Y., et al, 2002, “Numerical analysis on the action of centrifuge force in magnetic fluid rotating shaft seals,” Journal of Magnetism and Magnetic Materials, **252**, pp.321-323.

[4] Uhlmann, E., Spur, G., Bayat, N., and et al, 2002, “Application of magnetic fluids in tribotechnical systems.,” Journal of Magnetism and Magnetic Materials, **252**, pp. 336-340

[5] Kunio, S., Shigemitsu, S., Atsushi S., and et al, 2004, “Effect of a magnetic cluster on the magnetic pressure of a magnetic compound fluid,” Fluid Dynamics Research, **34**, pp.21–32

[6] Nethe, A., Scholz, H., Stahlmann, D., et al, 2002, “Ferrofluids in Electric Motors—A Numerical Process Model,” IEEE Transactions on magnetics, **38**, pp.1177-1180

[7] Lei T., “Hydraulic Engineering Handbook”, Mechanical Industry Publishing House, 1980, pp.1217

[8] Polevikov, V., Tobiska, L., 2005, “Instability of magnetic fluid in a narrow gap between plates,” Journal of Magnetism and Magnetic Materials, **289**, pp.379-381

[9] Kunio, S., Shigemitsu, S., Atsushi S., and et al, 2004, “Effect of a magnetic cluster on the magnetic pressure of a magnetic compound fluid,” Fluid Dynamics Research, **34**, pp.21–32

Containing the cup in the Floating Cup axial piston machine

T.L. van den Brink, Peter A.J. Achten
Innas BV, Breda, The Netherlands

ABSTRACT

In a floating cup axial piston machine, each piston has its own cuplike cylinder, floating on a barrel plate. A hold down spring prevents these cups from tilting off the barrel plate but allows them to slide over it, along a very small track. This paper will focus on the design of a hold down spring. Friction between the cup and its adjoining parts is studied and found to influence the optimal design of the hold down spring. However, on the machine efficiency the effect of this friction is negligible.

Keywords: axial piston machine, floating cup principle, construction, hold down spring, friction.

Nomenclature

D	cup bottom diameter [m]	p,q	moment arms [m]
F_c	centrifugal force on cup [N]	s	stroke of piston [m]
F_{spring}	contact force of spring on cup [N]	r	radial cup position [m]
M_{tilt}	tilting moment on cup [Nm]	s	stroke of piston [m]
R	piston pitch circle radius [m]	u	displacement of barrel cup
R_{spring}	effective spring contact radius [m]		contact force [m]
a	cup center of gravity position [m]		-circle radius [m]
m	cup mass [kg]		angular velocity [N]

1 Introduction

In 2002 Innas presented a new displacement principle for hydraulic pumps, motors and transformers [1]. Compared to conventional bent axis and slipper type machines the most striking changes were the balanced and symmetrical construction, the fixed pistons and, probably the biggest change, the absence of a barrel. In the new design the conventional barrel, with its limited 7 or 9 bores, is replaced by a more than double number of cuplike cylinders, floating hydrostatically balanced on a barrel plate (figure 1). A more recent improvement is the ringless piston sealing [2]. Since 2002 tests at Innas and in the industry have confirmed a very high hydro-mechanical and volumetric efficiency and a very small torque variation and loss [3,4,5,6]. It is expected that the increased number of cylinders will decrease flow pulsation and noise levels without increasing the production costs.

Power Transmission and Motion Control 2006 Edited by Dr D N Johnston and Professor K A Edge

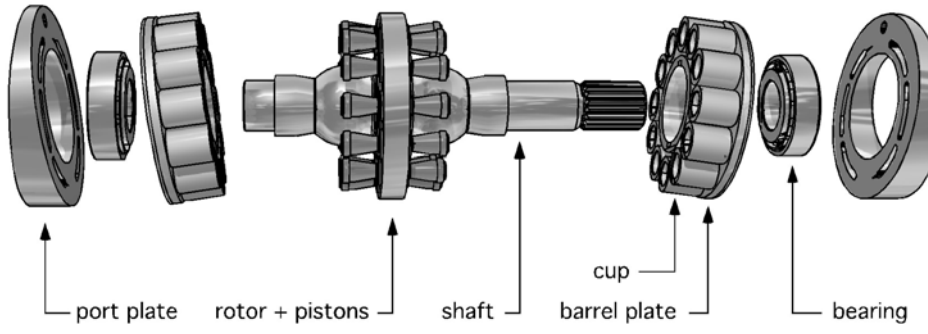

Figure 1: exploded view of the floating cup machine

already widespread in automotive production, can replace the usual milling and grinding of the conventional barrel. For other parts, like the port plates and the pistons, non-machining technologies are applicable too and they allow for a very competitive total cost price.

However, the separation of the cups from the barrel compels for some sort of containment of the cups. In the rotating machine, centrifugal forces act on the cup and without extra measures they will tilt off the barrel plate. In the first prototypes of the floating cup machine the cup was held down to the barrel with a holding plug and a positive hydrostatic balance force (figure 2). In this form-closed construction a minimal gap had to be allowed because of production tolerances. The seal land of the cup was balanced in such a way that, when pressurized, the cup was hydrostatically pressed to the barrel. When the cup was connected to the low-pressure kidney however, it tilted off the barrel at high speeds until it was caught by the plug. Connected to the high-pressure kidney again, the cup was pushed towards the barrel plate. But until it landed, there was extra leakage.

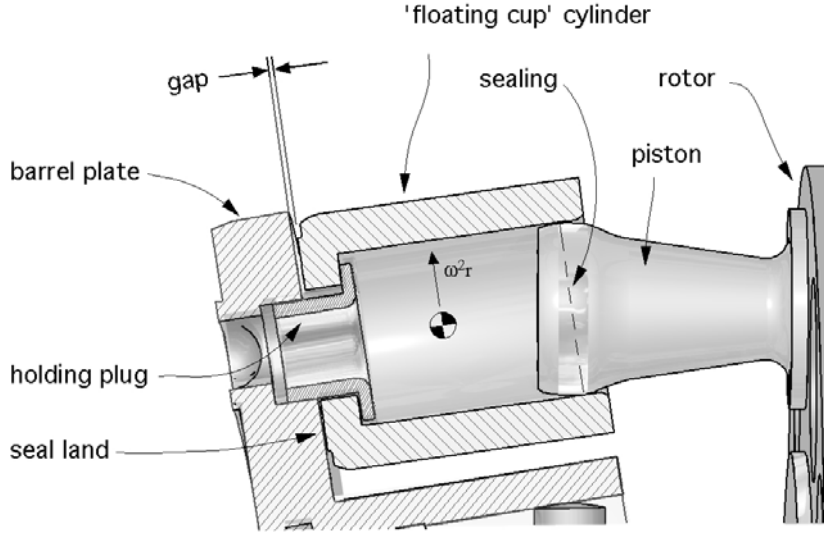

Figure 2: hold down by means of a plug, non-pressurized cup tilts from barrel plate

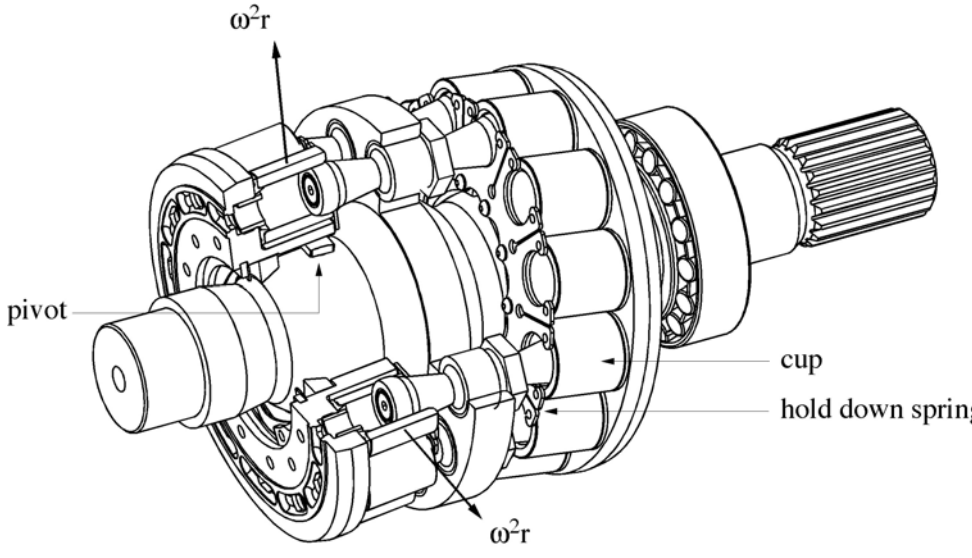

Figure 3: hold down by means of a hold down spring

It is known that optimizing the port plate grooves geometry can reduce noise and pulsation. This can only be done when the flow to and from the cylinders can be controlled by the grooves only and there is no uncontrolled secondary flow via a gap between the cup and the barrel plate.

In this paper an alternative construction is proposed: the hold down spring (figure 3). The spring presses the cup on the barrel plate whether it is pressurized or not and there is no need for a hydrostatic force anymore. This force-closed construction is less sensitive to production tolerances than the form-closed plug alternative and will therefore result in a cost reduction. The questions now arising are what minimal spring force is needed to prevent the cup from tilting and where on the top of the cup should this force be positioned?

When the situation is simplified by neglecting friction in the interfaces of the cup and its adjoining parts, the minimal spring force and optimal position of the spring force can be derived by analyzing the critical situation in which the centrifugal force exerts the largest tilting moment on the cup. This done in section 2.

However, friction in the aforesaid interfaces will increase the critical tilting moment. When friction is introduced in the calculation, the kinematics of the cups have to be taken into account as well and this makes the analysis rather complicated. Therefore the friction effects are not calculated analytically but numerically using a multi body model of the hold down construction. In paragraph 3 the kinematics are treated, to be followed by a study of the effect of friction forces in paragraph 4. The paper is concluded with a design of a hold down spring that will keep the cups on the barrel plate at a minimal hold down force.

2 Forces

Because of the spherical shape of the piston, the sealing line is always in a plane perpendicular to the axis of symmetry of the cup (figure 2). The seal land at the bottom of the cup is dimensioned in such a way that, when pressurized, the cup is hydrostatically in balance and no significant resulting hydrostatic forces on the cup remain. In figure 4 the centrifugal force on the cup and the reaction forces from the barrel, piston and hold down spring on cup are shown, assuming there is no friction. As the machine rotates, the piston head moves up and down in the cup. When the center of gravity of the cup coincides with the piston position (figure 4 left), the centrifugal force on the cup is conducted directly to the piston and no other reaction forces exist. When the piston moves away from this position an extra torque is created that tilts the cup from the barrel. This is prevented by pressing the cup to the barrel with a spring that acts on the top of the cup, which causes a contact force between barrel and cup (figure 4 right). The displacement u of the contact force to the spring force creates a moment that counteracts the tilting torque.

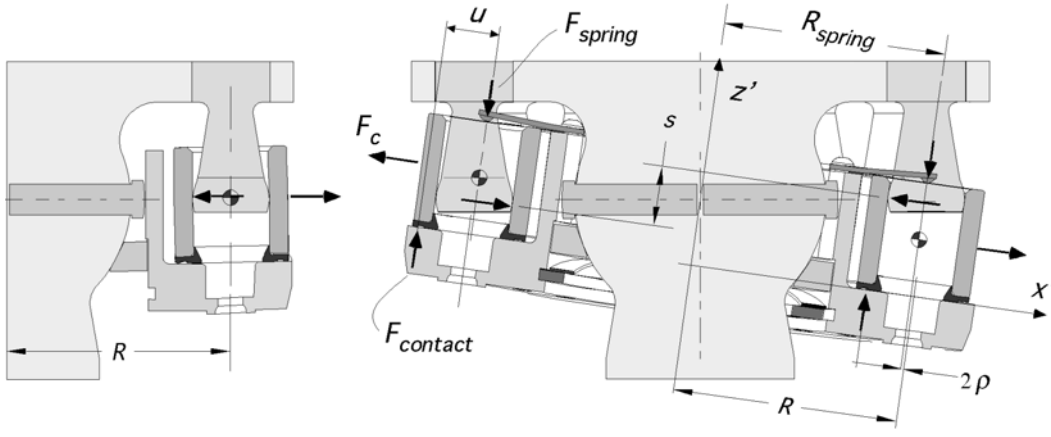

Figure 4: Forces on the cup, piston in middle position, TDC and BDC

Assuming the center of gravity of the cup coincides with the mean piston position and the spring force acts centrally on the top of the cup. In that case the maximum tilting torques are reached in TDC en BDC, because at that point the moment arm of the centrifugal force is maximal:

$$| M_{tilt} | = F_c \frac{s}{2} = {}^2 m\, r \frac{s}{2}$$

The equilibrium of the cup demands a displacement of the barrel-cup contact:

$$u = \frac{M_{tilt}}{F_{spring}}$$

The cup will not tilt as long as the position of the contact force lies within the outer circle of the cup bottom. To limit the displacement u to the cup bottom radius a minimal spring force is needed:

$$F_{spring} = \frac{M_{tilt}}{u} = \frac{^{2}m\ r\ s}{2\ u} = \frac{^{2}m\ r\ s}{4\ D},\ (u \quad \frac{D}{2})$$

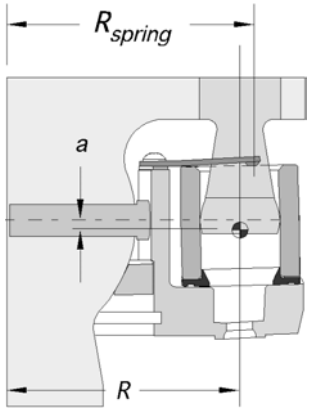

Figure 5: geometry

For a 2x12 piston 28cc floating cup machine this means a spring force of 55 N is needed for speeds up to 3500 rpm. The spring–cup contact is placed centrally on the top of the cups in TDC and BDC. However, when the cups are in TDC or BDC they are moved 2 radially inwards relative to the barrel (figure 4 right). The effective spring radius becomes:

$$R_{spring} = R \quad 2$$

In reality the center of gravity of the cup is not placed at the mean piston position but a little towards the cup bottom (figure 5).

This increases the tilting moment at BDC and decreases the tilting moment at TDC:

$$M_{tilt} \ = \ ^{2}m\ r\ a$$

Moving the spring–cup contact radially outwards can compensate this asymmetry:

$$F_{spring} \quad R_{spring} = \quad M_{tilt} \ = \ ^{2}m\ r\ a$$

$$R_{spring} = \frac{^{2}m\ r\ a}{F_{spring}}$$

Now the effective spring radius becomes:

$$R_{spring} = R \quad 2 \quad + \frac{^{2}m\ r\ a}{F_{spring}}$$

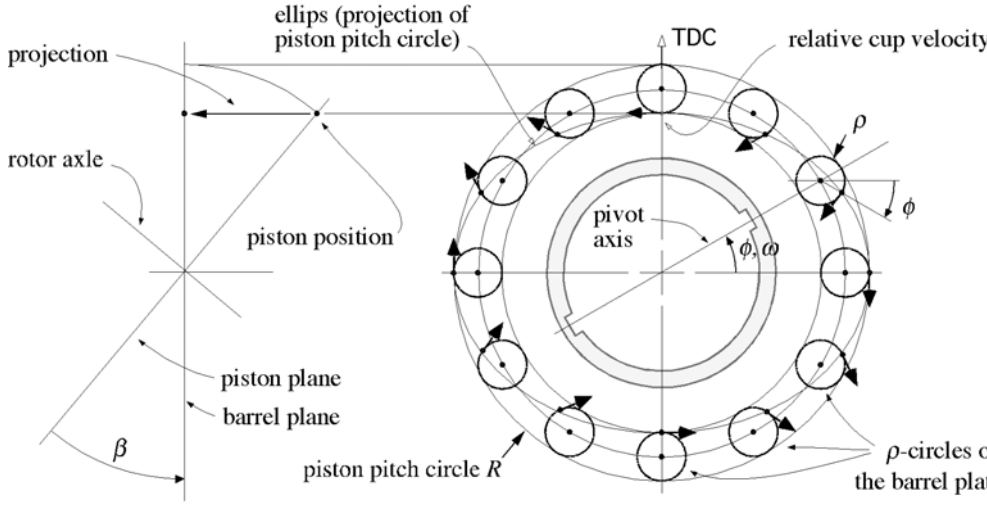

Figure 6: Relative movement of the cups on the barrel plate in case the barrel is driven by a constant velocity joint. In this example the number of pistons is 12 and the inclination between the rotor and the barrel is set at a value of β =40°.

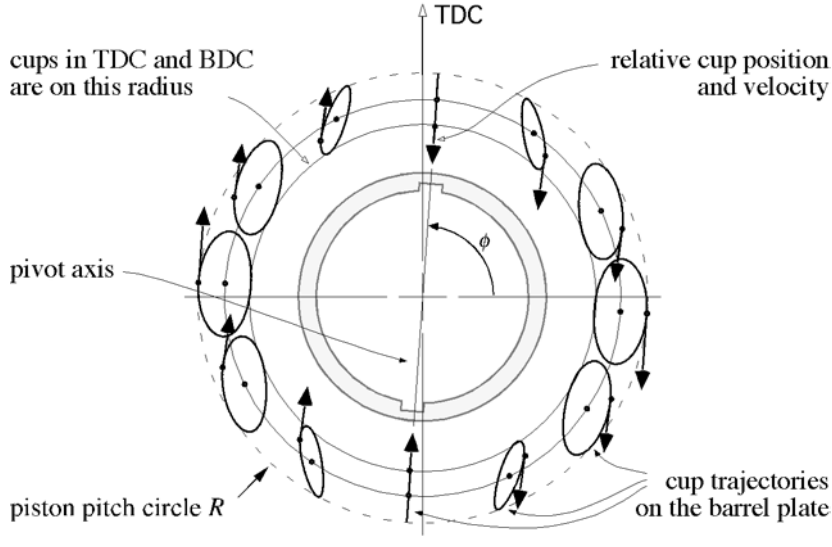

Figure 7: Relative movement of the cups on the barrel plate in case the barrel is driven by a pivot joint or some other kind of Cardan joint. In this example the number of pistons is 12 and the inclination between the rotor and the barrel is set at a value of β =40°.

3 Kinematics

In the floating cup machine the pistons are fixed onto the rotor (figure 1, 3). The barrel-cup assembly runs on the inclined face of the port plate. This inclination ensures that the pistons move relative to the cups and pump oil. The inclination of the barrel-cup assembly is only possible when the cups are free to slide over the barrel plate. In the rotating machine the pistons move up and down in the cups moving from bottom dead center (BDC) to top dead center (TDC) and vice versa. The cups slide over the barrel plate along a very small track. Friction forces are directed to the opposite of the velocities of these motions.

The relative motion of the cup to the barrel plate is not as obvious as the piston-cup motion and needs extra attention. Achten [7] has already described this relative motion extensively. His conclusions are presented here.

As the pistons rotate, the cups move along an ellipse, which is the projection of the piston pitch circle on the inclined barrel plane (figure 4). In case of a constant velocity joint between axle and barrel the cups move along a small circle on the barrel (‘ -circle’, Walzer [8]). In the floating cup machine, the barrel is coupled via two simple pivots, mounted in the axle, that slide in slots in the barrel (figure 3). Since this is not a constant velocity joint, there is a relative rotation between axle and barrel that deforms the circles to ovals (figure 5). This deformation is dependent on the angular position of the cup to the pivot axis. The latter is the axis through the pivots. The circles of the cups on the angular position of the pivot even degenerate to a line. The relative velocities of these cups are radial only, just as the friction forces between the barrel and these cups are. The relative velocity of the other cups becomes pure radial too, but not when the cup is at TDC or BDC. This difference becomes of significance in paragraph 4 when the friction forces are studied in detail.

In a floating cup machine the strength of the piston neck restricts the inclination to approximately 11º. At that inclination the -circles and ovals are so small that they can hardly be plotted. In the figures 3 and 4 the inclination is therefore increased to 40º.

4 Friction

So far the minimal spring force and the optimal effective spring radius have been determined for a frictionless hold down construction. When friction is introduced, the kinematics of the cups have to be taken in account which makes the analysis rather complicated. This is why the hold down construction has been modeled with a multi body package. In the multi body model the cup body is connected with joints to the barrel, the hold down spring and the piston.

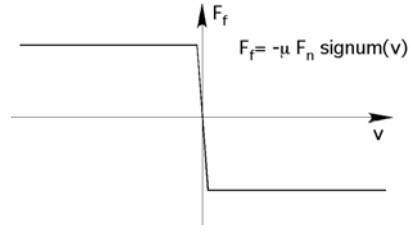

Figure 8: uniform friction model

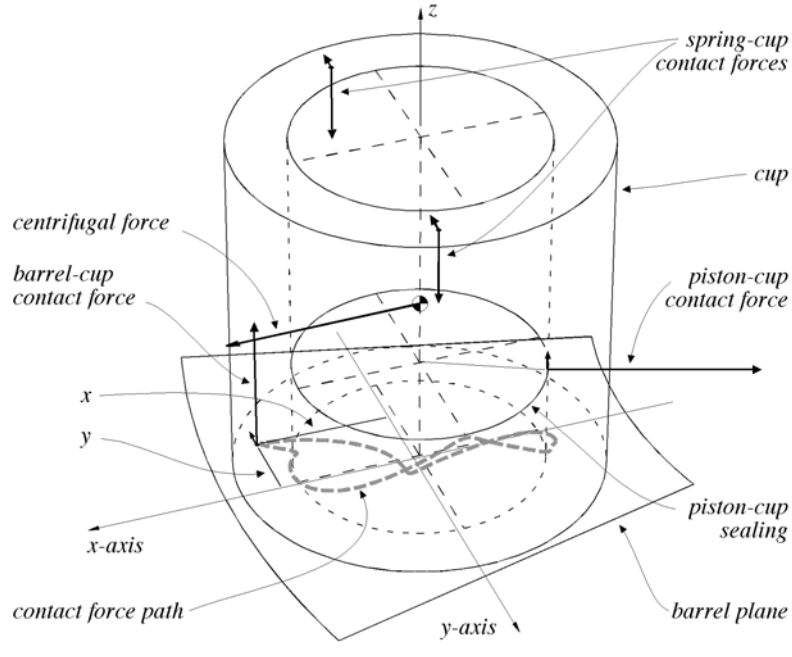

Figure 9: path of contact force, with friction

Although in reality the cup is free to tilt and even leave the barrel, in the model the joint between barrel and cup was modeled as a planar joint, only able to slide in the x- and y-direction over the barrel plane (figure 9). The translation in the z-direction and the rotations around the x- and y-axes were suppressed and reaction force F_z and moments M_x, M_y calculated. From these reactions the location of the contact force can be obtained:

$$x = \frac{M_y}{F_z}, \; y = \frac{M_x}{F_z}$$

When the machine rotates, the contact force moves along a path that is shown in figure 9. The cup will not tilt as long as the position of this contact force lies within the outer circle of the cup bottom.

Unpredictability is the nature of friction forces. The strategy chosen is to study friction in each of the interfaces of cup, piston, barrel and hold down spring separately and determine worst cases of combined friction effects. This is what you will find in the next paragraphs. Although in reality the sliding velocities are not constant, a simple uniform friction model was used, justified by the fact that worst cases are looked for only (figure 8).

In figure 14 contact force paths are shown for a construction with, and without friction. It is the critical situation for a 28 cc floating cup machine at 3500 rpm. Without friction the contact force stays exactly within the outer circle of the cup bottom ensuring the cup will not tilt. In the following paragraphs in each of the relevant interfaces friction is introduced separately at the same conditions to demonstrate its effect.

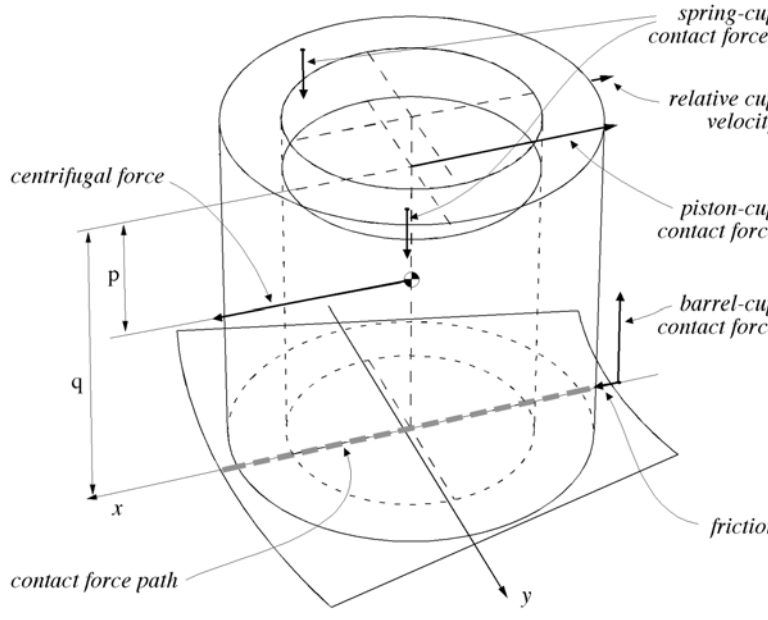

Figure 10: A cup at the angular position of the pivot. The friction forces between the barrel plate and the cup and the centrifugal force tilt the cup in the same direction. The piston is at BDC and than the moment arms of both forces are maximal.

4.1 Friction between cup and barrel

The friction force on the cup is directed opposite to the relative velocity of the cup to the barrel. The contact force and the friction coefficient in the cup-barrel interface determine its magnitude.

The largest total tilting moments on the cup are created when the centrifugal force and the friction forces tilt the cup in the same direction and the moment arms of both forces are maximal (figure 10). The moment arms become (sub-) maximal in BDC and TDC. Most cups move in tangential direction in BDC and TDC. Only the cups at the angular position of the pivots move in the radial direction (figure 5) and tilt the cup in the same direction as the centrifugal force. The largest tilting moment therefore works on these cups. Friction moves the contact force further outwards when the piston is in TDC, and inwards when the piston is in BDC. The moment arm of the friction force is longer in BDC because the cup center of gravity is placed somewhat below the mean piston position. In BDC the tilting moment becomes maximal. Compared to the frictionless situation, the diameter of the contact path is increased and its center is moved radially inwards. This is also true for the

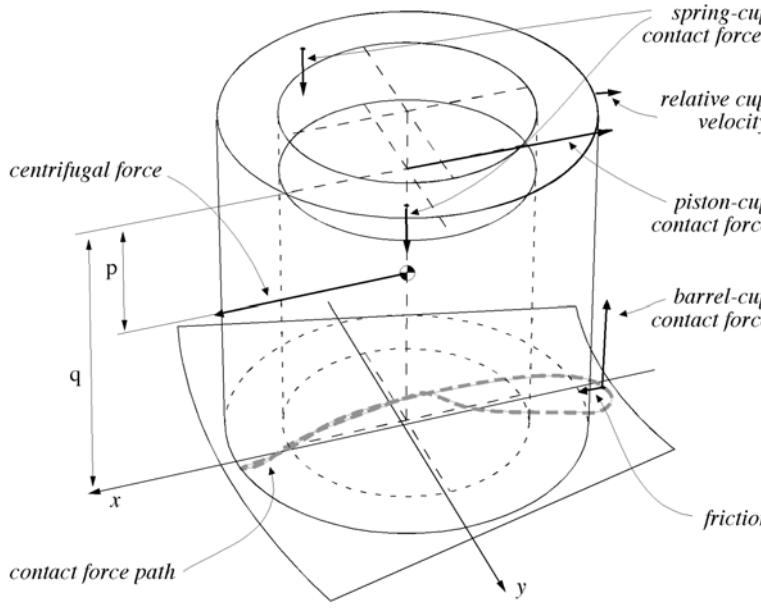

Figure 11: A cup at -30° to the pivot. The friction force between the barrel plate and the cup and the centrifugal force tilt the cup in the same direction. The piston is not yet in BDC and therefore the moment arms of both forces are not maximal yet.

cups that are not at the pivots angular position. However, for these cups the tilting moment is less critical because the maximal tilting moment of the friction force is not in the direction of the centrifugal moment. These cups do not move along a line but a small oval (figure 5) and their velocity at BDC is in the tangential direction. When they move in the radial direction the piston is not at its extreme position (figure 11).

To prevent the cup from tipping over, the spring force can be increased and the spring contact can be moved radially outwards. The contact paths of the cups at the angular position of the pivot are straight radial lines, the paths of the other cups show a tangential dimension which is caused by the friction in this direction.

4.2 Friction between cup and hold down spring

Friction at the top is very similar to the situation with friction at the bottom of the cup. The maximum moment arm of the friction force is now reached at TDC instead of BDC (figure 12). The center of the contact path is now no longer moved radially inwards but outwards.

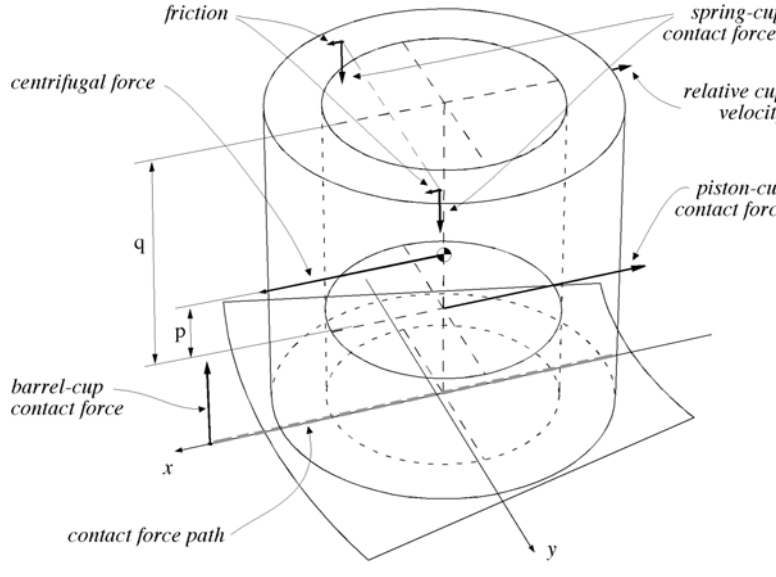

Figure 12: The cup at the angular position of pivot at TDC. The friction with the hold down spring and the centrifugal force tilt the cup in the same direction. The moment arms of both forces are maximal.

4.3 Friction between cup and piston

The centrifugal force presses the cup to the piston. When the piston moves up or down in the cup a friction force is created. This friction force is placed at the sealing circumference between both parts at an angle that is determined by the direction of the contact forces between both parts (figure 13). The critical situation is in TDC, when both the centrifugal force and the friction force are tilting the cup in the same direction and the piston moves up. At that moment the contact force between cup and barrel is minimal. Friction between cup and piston increases the diameter of the contact path and its center is moved radially outwards.

Because of the small clearance between cup and piston a clamping force can exist between both parts, which can make friction. This friction is assumed to be distributed evenly along the sealing circumference of the piston and cup. When the piston moves up the contact force between barrel and cup is decreased enlarging the diameter of the contact path. The center of this path remains the same when this load is applied. The effect of friction with the piston is indifferent to the angular position relative to the pivot. It applies to all cups equally.

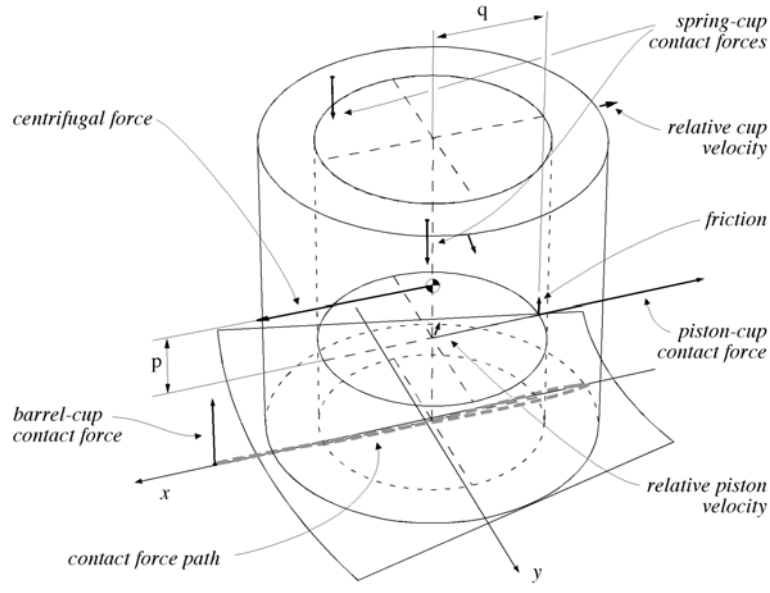

Figure 13: friction with piston, cup at 90º of pivot at TDC position

4.4 Combined friction

In the previous paragraphs the effect of friction in each of the relevant interfaces has been determined. It was shown that friction in each of the relevant interfaces enlarges the diameter of the contact force path and moves its center to a specific direction. Friction in the cup-barrel interface moves the path inwards while friction in the interface with the spring and the piston moves the path outwards (figure 14). This applies to all cups, not only to the cups at the pivots. It is now possible to define two worst-case situations in which the force path is moved outwards and inwards to the extreme (table 1). These worst cases are called 'outwards' and 'inwards'. A hold down spring design is now evaluated for both worst cases. The optimal design is defined as the spring force and the effective spring radius at which the contact force path becomes critical at both cases. In combined friction it is necessary to evaluate for cups at all angular positions relative to the pivot.

To determine the friction coefficients, dynamic friction forces were measured in a simple experiment outside the machine. In these measurements the dynamic friction coefficient never exeeded 0.15. Naturally friction is dependant on a lot of conditions and it is not easy to determine the exact governing friction coefficients. To get an indication of the sensibility to friction two sets of friction coefficients are defined, 'friction A' and 'B' in table 1. Figure 15 shows the worst-case situations 'inwards' (top) and 'outwards' (bottom) for the design for friction set A. For each set and the situation without friction an optimal design is calculated (table 2). Table 2 shows that the cup can be held down to the barrel with a limited hold down spring force and that friction causes a significant but limited increase of this force. It does influence the optimal geometry too.

Due to the limited normal forces and the small displacements, especially in the cup-barrel and cup-spring interfaces, the torque loss caused by friction is very small (table 3). Relative to the nominal torque of the machine these losses are negligible.

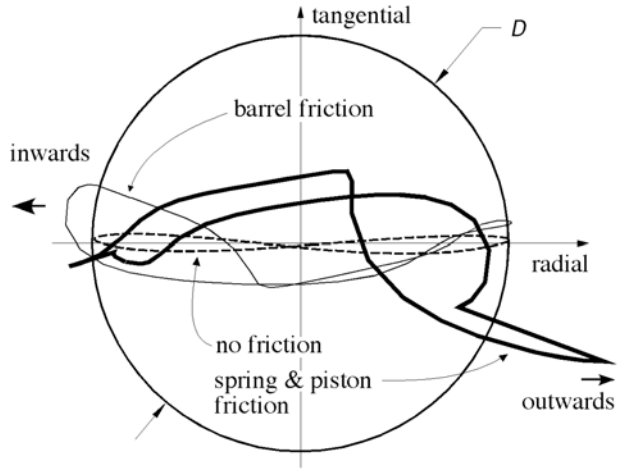

Figure 14: contact force paths with and without friction at the same spring force, effective radius and machine speed (3500 rpm) for a 28 cc floating cup machine

Table 1: worst-case friction coefficients and clamping force

	friction A		friction B	
	outwards	inwards	outwards	inwards
cup-barrel friction	0	0.1	0	0.15
cup-spring friction	0.2	0	0.3	0
piston-cup friction	0.05	0	0.075	0
clamping force [N]	20	0	30	0

Table 2: optimal hold down spring force and effective radius for a 28 cc floating cup machine with a maximal speed of 3500 rpm

	no friction	friction A	friction B
F_{spring} [N]	54	70	80
R_{spring} [mm]	38.99	37.9	37.5

Table 3: torque loss due to friction for a 28 cc floating cup machine at a speed of 3500 rpm.

	friction coefficient [-]	torque loss [Nm]
cup-barrel friction	0.1	0.07
cup-spring friction	0.2	0.14
piston-cup friction (clamping force 20 N)	0.05	0.45

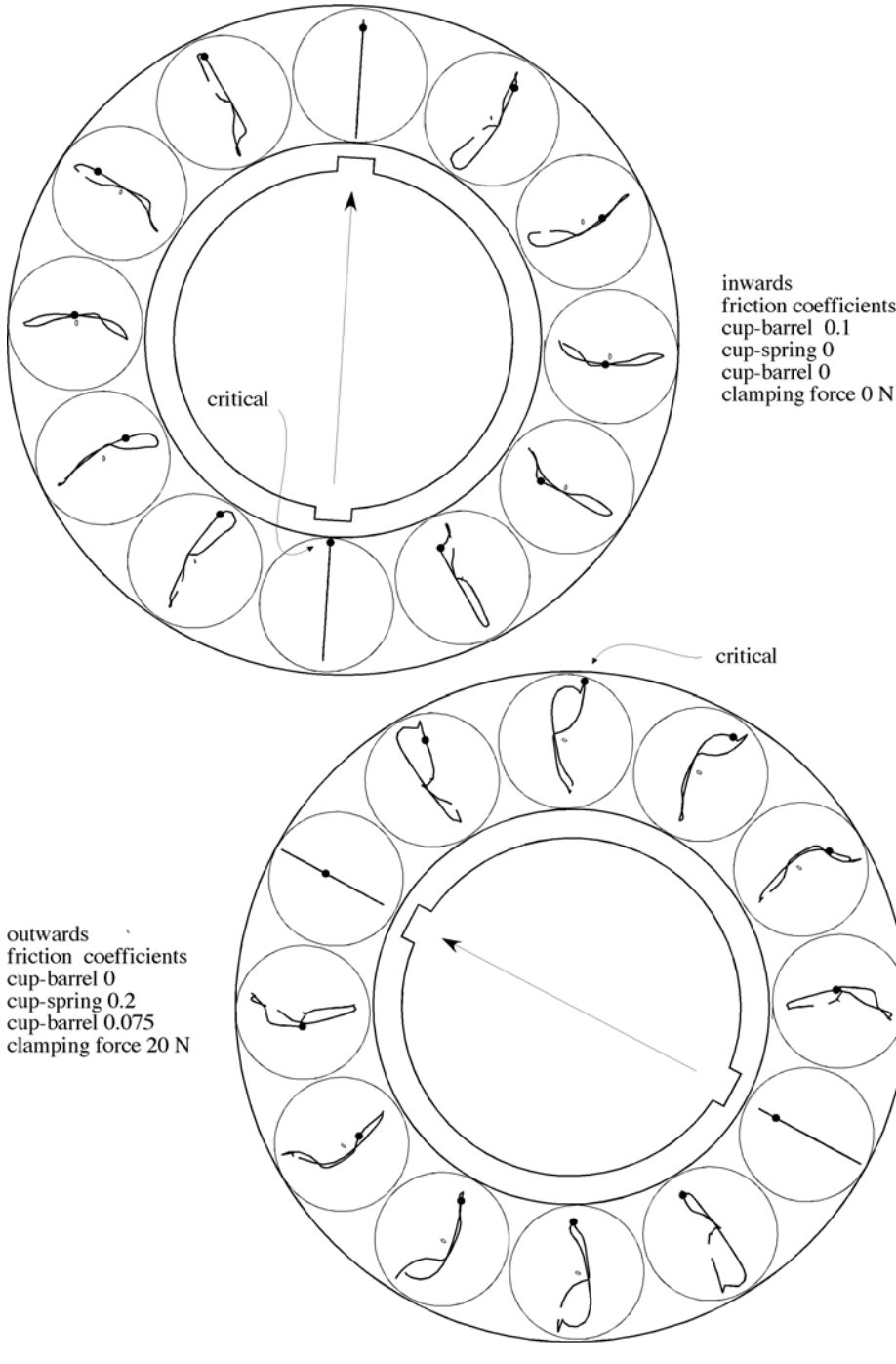

Figure 15: contact force paths for 28 cc floating cup machine at 3500 rpm with friction set A, the black dots show the actual position of the contact force between cup and barrel

5 Conclusion

The hold down spring is a viable alternative to hold down the cups to the barrel of the floating cup machine. It ensures that the cup is always pressed to the barrel plate. The gap between both parts remains closed and oil leakage is prevented. This facilitates the noise reduction by optimizing the port plate grooves. The new force-closed construction is less sensitive to production tolerances than the form-closed alternative with a hold down plug and therefore may result in a cost reduction.

The cup can be held down to the barrel with a limited hold down spring force. Friction in the interfaces of the cup with barrel, spring and piston causes a significant but limited increase of this force and does influence the optimal geometry. The effect of friction between piston and cup on machine efficiency however is very small. Due to the very small relative movement of the cup to the barrel and the hold down spring, the effect of friction between these parts on machine efficiency is negligible. Because friction may vary due to many conditions it is useful to optimize the design for a range of friction coefficients.

References

[1] **Achten, P.A.J.** 2002, *Dedicated design of the Hydraulic Transformer*, Proc. IFK.3, Vol. 2, IFAS Aachen, ISBN 3-8265-9901-2, p 233-248

[2] **Achten, P.A.J**. 2003, *Designing the impossible pump,* Proc. Hydraulikdagar 2003, Linköping University

[3] **Achten, P.A.J., Van den Brink, T.L., Paardenkooper, T., Platzer, T., Potma, H.W., Schellekens, M.P.A. and Vael, G.E.M.** 2003, *Design and testing of an axial piston pump based on the floating cup principle*, Proc. SICFP'03, Vol. 2, Tampere University of Technology, ISBN 952-15-0972-4 p. 805-820

[4] **Achten, P.A.J., M.P.A. Schellekens, H. Murrenhoff and M.Deeken**, 2004, *Efficiency and low speed behavior of the floating cup pump*, SAE 2004-01-2553

[5] **H. Murrenhoff and M.Deeken**, 2004,*Wirkungsgradmessungen an einer Kolbenpumpe - Abschlussbericht*, RWTHAachen

[6] **Achten, P.A.J.**,2005, "Volumetric losses of a multi piston floating cup pump", Proc. Of the 50th National Conference on Fluid Power, NCFP-paper I05-10.2

[7] **Achten, P.A.J., T.L. van den Brink.,J.W. Potma,H.W.** 2004, *Movement of the cups on the barrel plate of a floating cup, axial piston machine.* Int. Journal of Fluid Power, 5(2)

[8] **Walzer, W.** 1984, *Theoretische und experimentelle Untersuchung der Zylindertrommelmitnahme in Grosswinkel-Axialkolbenmaschinen.* PhD-thesis. Inst. für Fördertechnik der Universität Karlsruhe

Innas website: http://www.innas.com

A numerical model for the simulation of flow in hydraulic external gear machines

Paolo Casoli, Andrea Vacca, Gian Luigi Berta

Dipartimento di Ingegneria Industriale, Università degli Studi di Parma, Italy

ABSTRACT

The present paper describes a numerical model, developed by the authors, for the simulation of external gear pumps. The model has been implemented in AMESim® environment, developing new in-house C++ models.
The fluid dynamic model is based on a finite volume framework. The pump is described with a geometrical sub-model, which yields the actual values of the variable volumes (defined by teeth, housing, and side wear plates) and of the throat areas, as functions of shaft position. The model allows to predict the pressure evolution inside each tooth space, while considering cavitation and leakages in a simple manner. After pressure inside each tooth space is known, the forces suffered by the gears and the torque required to drive the pump are determined. The results have been verified through comparisons with some experimental data.

NOMENCLATURE

F	Resultant force	f	Force
L	Clearance length	h	Clearance thickness
Ns	Number of sub-surfaces	j	Unit vector
R	Base circle radius	$\dot{m}$	Mass flow rate
Re	Reynolds number	n	Angular velocity
S	Surface	p	Pressure
T	Torque	u	Peripheral velocity
V	Volume	x,y	Distance of the centre of pressure from gear centre
X, Y	Distances of line of action of force (components) from the gear centre	z	Number of teeth
b	Clearance width	Ω	Orifice cross sectional area
c_{eq}	Coefficient of discharge	γ	Angular direction of force

Power Transmission and Motion Control 2006 Edited by Dr D N Johnston and Professor K A Edge

ρ	Fluid density
μ	Fluid viscosity

Subscripts

d	delivery
s	suction
c	critical
eq	equivalent
f	force
i	index of volume
j,k	index
p	pressure
θ	gear angular position
n	number of teeth
m	maximum value admitted for the pump
max	maximum
tot	total
x,y	axis of reference
var	variable
1,2	driver gear (1) and driven gear (2)

Abbreviations

CV	control volume
TSV	tooth space volume

1. INTRODUCTION

Among positive displacement pumps the external spur gear are the most common pump in fluid power applications, owing to their simplicity and reliability, despite their unsuitability for variable displacement [1,2]. The development of simulation codes for the prediction of gear pumps behaviour at different operating conditions is of great interest for both researchers and manufacturers. Despite the fact that these pumps are based on a simple concept, they are as complex as to justify the development of simulation tools able to investigate possible improvements in terms of efficiency, noise, etc. keeping costs in due consideration.

Several aspects of gear pump design assume a crucial role in pump performance, namely tooth profile, geometry of recesses on bearing blocks as well as balancing the forces acting on each element. As a matter of fact, researchers have been involved for many years in the study of these machines: basic studies are due to Wilson [3] and Castellani [4]; in 1977 Fielding et. al. [5] presented a model that takes into account many effects on pressure ripple, inclusive of the forces acting on the gears; in the late ’80 Nervegna and Mancó proposed a simulation model for external gear pumps [6] and some experimental evaluations of pressure transients [7] in the machine. Several papers [8-11] are focused on the analysis of the inter-teeth pressure, of internal leakages, on the pressure distribution and resultant force on the gear side faces. Other researches analysed pump bearings performance and fluid borne noise [12, 13], while in [14] the effects of changing teeth geometry on pump flow ripple is described. The level of complexity induced the authors of these papers to develop specific numerical methods for the each problem, with the exception of [5], where geometrical description is however simplified.

The numerical model presented in this paper aims to simulate the flow throughout the pump, adopting a simple lumped parameter approach. The model takes advantage of a CAD tool, so as to describe the geometry of pump elements (teeth profile, bearing blocks, etc.) with a great accuracy. For the correct evaluation of the effects of gears rotation and meshing, several assumptions have been introduced in both the geometrical and the fluid dynamic procedures. The model, named HYGESim (HYdraulic GEar machines SIMulator), thanks to its implementation in the AMESim® environment, can be used not only for the pump design purposes, but also for investigating pump-circuit interactions. The paper

describes the main features of model implementation, focusing on the improvements introduced after the first release of the code, described in [15]. The fluid dynamic model has been improved in the description of the meshing zone. Moreover, the new version includes the analysis of both the instantaneous forces and the torques acting on the gears, starting from the results obtained from the fluid dynamic model and taking advantage of the potentials of the built-in CAD tool.
Although the results ensuing have been achieved assuming the pump working on its nominal geometry (directly evaluated from pump drawings), the calculation of forces suffered by gears represents first step toward the prediction of their radial displacement, which is well known to depend upon the actual operating conditions of the pump.

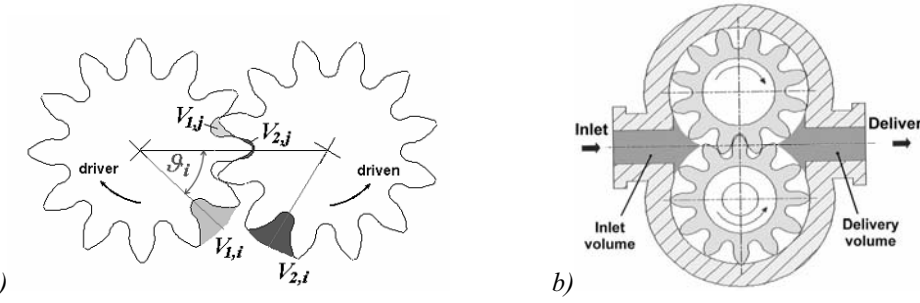

a) *b)*

Figure 1 – Control volumes assumed in the model: teeth space volumes (*a*); inlet and delivery volumes *(b)*

2. DESCRIPTION OF THE FLUID DYNAMIC MODEL

As a macroscopic description of flow characterizing the whole pump was in the authors scope, a lumped parameter approach has been chosen. Accordingly, the pump has been divided in control volumes (CVs), in which fluid properties are assumed uniform and dependent on time only. Through the evaluation of flow between adjacent CVs, from the mass conservation law and the fluid state equation the model is able to predict the pressure inside each CV as a function of time. Other significant parameters that characterize the pump operation, such as delivery flow rate (instantaneous and average), pressure ripples, etc., are evaluated as well.
The particular subdivision of the whole internal volume in CVs adopted by HYGESim is summarized in fig 1. As reported in fig. 1*a*, the model provides a control volume (CV) for each tooth space volume (TSV) of each gear. HYGESim can simulate machines with the same number of teeth on the driver and the driven gear; under this hypothesis, as highlighted in fig. 1*a*, during shaft rotation the generic TSV $V_{1,i}$ of the driver gear always meshes with the corresponding $V_{2,i}$ of the driven gear. Thus the model considers a number of pairs (equal to the number of teeth per gear) of corresponding TSVs. HYGESim considers further CVs, as reported in fig. 1*b*, for the inlet and delivery volumes of the pump. This framework is suitable for the description of the main features of pump operation; it differs from others previously conceived [6,7,8,11] in that only the flow in the meshing zone is accurately described. Therefore, a precise evaluation of the gaps connecting every TSV with neighbouring ones, and of the instantaneous volume of the CVs in the meshing zone has been implemented. Fig. 2*a* shows the results of calculation performed with a CAD procedure, starting from the pump drawings.

a)

b)

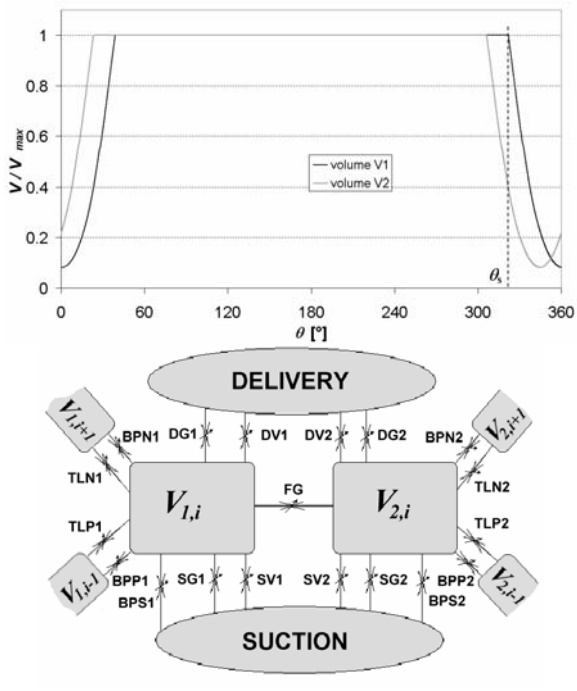

Figure 2 – *a)* Volume of corresponding teeth space volume as function of gear angular position ; *b)* Basic scheme of connections between the CVs of corresponding teeth space volumes

Connection	Description
FG	connection between the two corresponding teeth space volumes, open when they are meshing (fig. 3*a*)
DV1 (DV2)	connection between $V_{1,i}$ (or $V_{2,i}$) and the delivery volume through the gear whole depth (fig. 3*a*)
SV1 (SV2)	connection between $V_{1,i}$ (or $V_{2,i}$) and the suction volume through the gear whole depth (fig. 3*a*)
DG1 (DG2)	connection between $V_{1,i}$ (or $V_{2,i}$) and delivery port through the bearing blocks recesses (fig. 3*b*). Fig. 4 highlights other connections obtained through side grooves (commonly used for pump balancing) that can be considered together with DG1 (or DG2) orifices. DG1' and DG2' represent the backflow grooves, present in the pump taken as reference in this work
SG1 (SG2)	connection analogous to DG1 (DG2) with the suction port (fig. 3*b*)
BPP1 (BPP2) BPN1 (BPN2)	connections between adjacent teeth space volumes realized by the clearances among gear side faces and bearing blocks internal faces. BPP1 (BPP2) represents the leakage between a tooth space volume and the previous one on the same gear (fig. 5*a*). BPN1 (BPN2) is the analogous flow with the following tooth space volume
BPS1 (BPS2)	connection between a tooth space volume and shaft bearing (connected to the pump drain line), as reported in fig. 5*a*
TLP1 (TLP2) TLN1 (TLN2)	connections between adjacent teeth space volume realized by the clearances among teeth tip and pump casing. TLP1 (TLP2) indicates the leakage between a tooth space volume and the previous one on the same gear (fig. 5*b*). TLN1 (TLN2) is the analogous flow with the following tooth space volume

Table 1 . Description of connections represented by orifices in fig. 2*b*

Fig. 2*b* shows all the connections of a generic pair of TSVs, represented by variable orifices. The value of the throat area of each orifice is a function of the angular position of gears, and becomes null when the connection is not realized. Nomenclature used for orifices, in fig. 2*b*, is the same as that adopted in a previous work [15]. For the sake of brevity, only a brief description of connections is reported in tab. 1, for further details see [15]. Fig. 2*a* and fig. 6 exemplify some significant geometric results for the pump considered in this work.

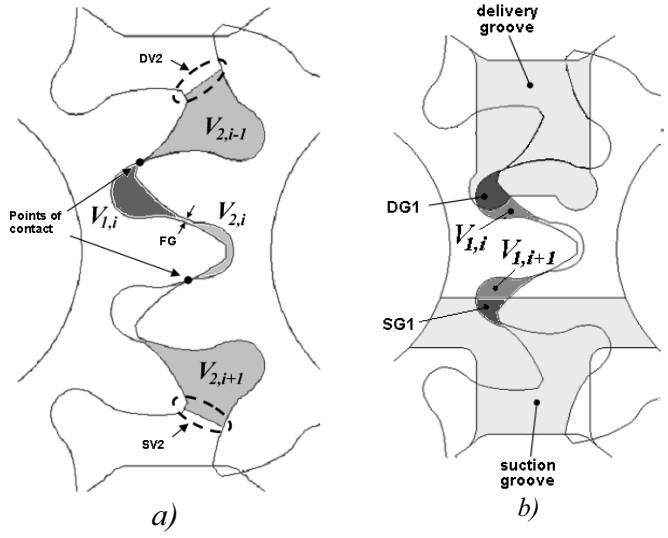

Figure 3 –
a) connection between V_2 and delivery (DV2), suction (SV2) and V_1 (FG).
b) connection between V_1 and suction (SG1) and delivery (DG1) through the recesses in the bearing blocks

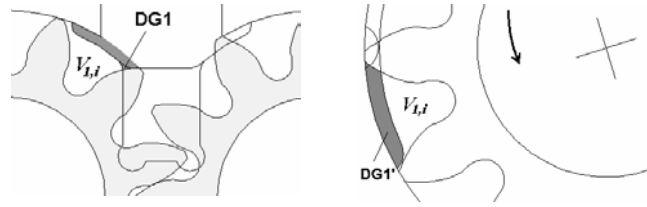

Figure 4 – Other connections represented by DG1. DG1' indicates the backflow grooves

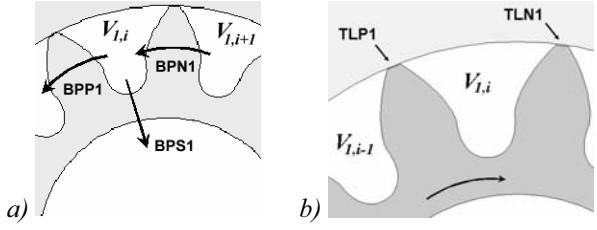

Figure 5 – Leakages:
a) through the clearances between gears lateral sides and bearing blocks internal surfaces
b) between adjacent TSVs at tooth tip

The flow rates between adjacent CVs are evaluated using the steady-state equation for orifices:

$$\dot{m}_{i,j} = \frac{\left(p_i - p_j\right)}{\left|\left(p_i - p_j\right)\right|} \rho\left(\overline{p_{i,j}}\right) c_{eq}\left(Re_{i,j}\right) \Omega_{i,j}\left(\theta\right) \sqrt{\frac{2\left(p_i - p_j\right)}{\rho\left(\overline{p_{i,j}}\right)}} \tag{1}$$

Indexes *i* and *j* in eq. (1) indicate any two CVs connected by an orifice whose throat area is $\Omega_{i,j}$. The coefficient of discharge is dependent on the Reynolds number, as suggested in [16, 17].

a)

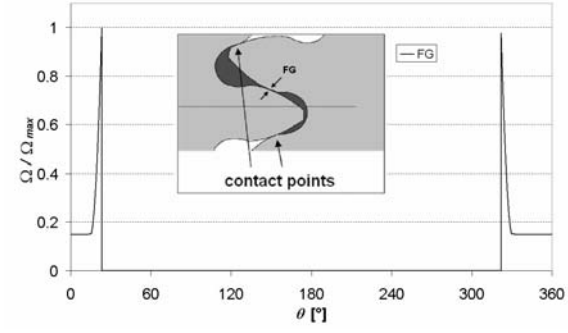

b)

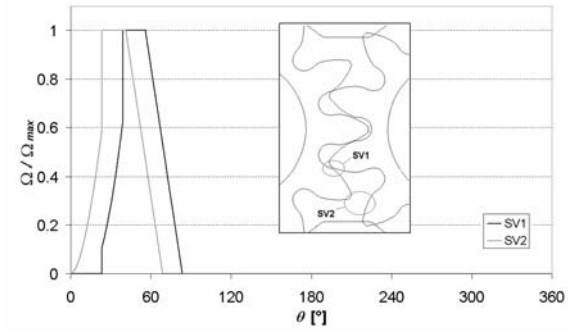

c)

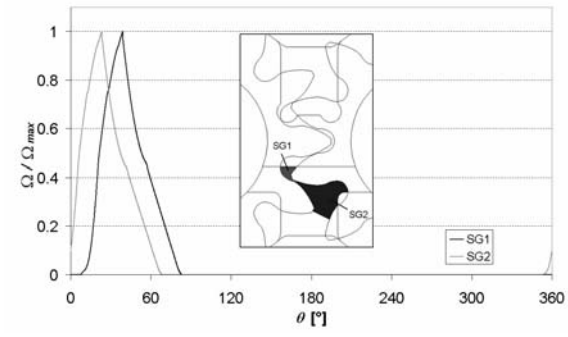

Figure 6 – Examples of calculations performed by the implemented CAD procedure for a couple of corresponding TSVs:

- *a)* Area of orifice FG
- *b)* Area of orifice SV1 and SV2
- *c)* Area of orifice SG1 and SG2

Leakage flows (connections BPP, BPN, BPS, TLP and TLN) are instead calculated with the modified Poiseuille equation [16]:

$$\dot{m}_{i,j} = \rho\left[-\frac{h^3}{12\mu}\frac{p_i - p_j}{L} + \frac{u}{2}\right]b \tag{2}$$

Eq. (2) accounts for relative motion of walls (in the case of leakage BPS the term u is null), while centrifugal forces are neglected. The three flows sketched in fig. 5*a* are evaluated separately, so that 2D effects are neglected in the clearances between gear side and bearing block, as discussed in [10]. This assumption has been adopted for its simplicity, thus permitting to introduce the effect of gear rotation on leakages in a lumped parameter model. Once all the flow rates are known, the model is able to predict the pressure course inside each CV of the pump, by means of the mass conservation law and the fluid state equation, that give:

$$\frac{\mathrm{d}p_i}{\mathrm{d}t} = \frac{1}{V_\mathrm{i}}\frac{\mathrm{d}p}{\mathrm{d}\rho}\bigg|_{p=p_i}\left[\sum\dot{m}_{in,i} - \sum\dot{m}_{out,i} - \rho\big|_{p=\bar{p}}\frac{\mathrm{d}V_i}{\mathrm{d}t} - \sum\left(\rho\big|_{p=\bar{p}}\frac{\mathrm{d}V_{var,i}}{\mathrm{d}t}\right)\right] \tag{3}$$

Eq. (3) differs from the typical Filling and Emptying equation for the last term in [] brackets. This term derives from the geometric assumptions done in the definition of CVs in the meshing range. In detail, the TSV $V_{1,i}$ is always defined by the minimum area surfaces that connect the two corresponding profiles of teeth of the two gears (fig. 7). In order to well simulate the course of the pressure inside the TSVs, it is of utmost importance that unrealistic volume discontinuities in the code are avoided. As a matter of fact, volume discontinuities due to rules used for the CVs definition would lead to pressure peaks according to eq. (3). Therefore the decrease of the volume from its maximum value (fig. 7*a*) has to begin before ϑ^* as highlighted in fig. 7*b* and 7*c*.

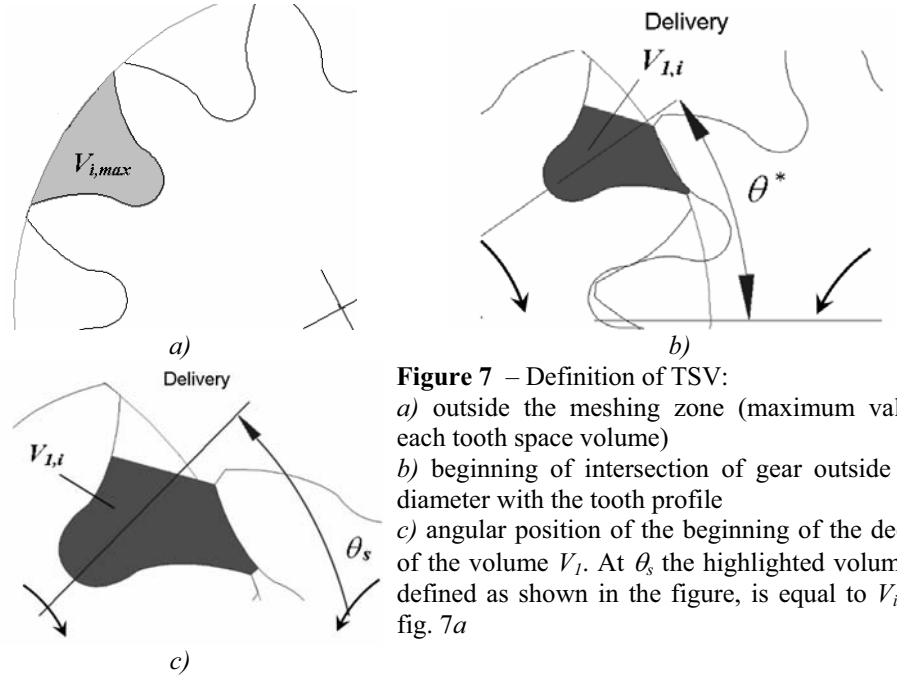

Figure 7 – Definition of TSV:
a) outside the meshing zone (maximum value of each tooth space volume)
b) beginning of intersection of gear outside circle diameter with the tooth profile
c) angular position of the beginning of the decrease of the volume V_1. At θ_s the highlighted volume $V_{1,i}$, defined as shown in the figure, is equal to $V_{i,max}$ of fig. 7*a*

It is important to notice how an initial discontinuity is introduced for area DV1 (fig. 8*a*). However, this discontinuity has no detrimental effect, because at the beginning of the meshing process the pressure in the tooth space volume closely approaches the delivery pressure.

As shown in fig. 2*a* and fig. 3, the volume $V_{1,i}$ first decreases until it becomes minimum for $\vartheta = 0^{\circ}$ then it starts to increase, reaching again its largest value at the opposite side, near the suction volume. Thus, analogous considerations can be made for the any $V_{2,i}$ and for SV1 (and orifices DV2 and SV2).

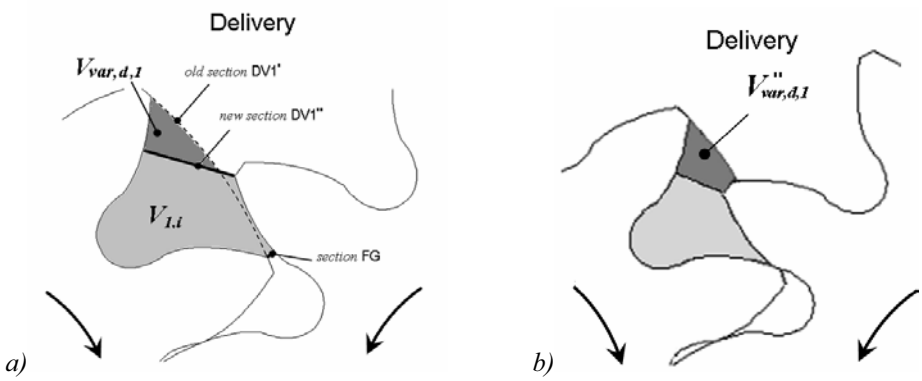

Figure 8 – *a*) Features for the definition of the tooth space CV in the meshing zone. Detail on the sudden change of orifice DV1. Volume $V_{var,d}$ is included in the delivery CV (fig. 2b); *b*) Increase of volume $V_{var,d}$ with shaft rotation

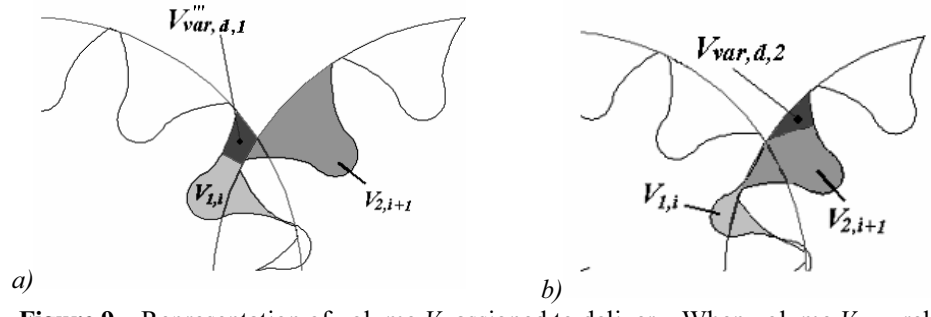

Figure 9 – Representation of volume V_d assigned to delivery. When volume $V_{var,d}$ related to $V_{1,i}$ disappears, another variable volume $V_{var,d}$ appears as a consequence of the definition of volume $V_{2,i+1}$

Fig. 8 shows how, as the shaft rotates, a variable volume ($V_{d,1}$) is generated which is assigned to the delivery space. This volume first increases, then, before the condition of minimum volume $V_{1,i}$ is reached, it decreases and finally disappears. As represented in figs. 9*a* and 9*b*, this happens when the volume $V_{2,i+1}$ (pertaining to the following pair of TSVs) enters into mesh, so that a new variable volume is created. Symmetrically, a variable suction volume, V_s, has to be defined in consequence of assumptions made in the definitions of tooth space CVs. The term under summation in eq. (3) accounts for these variable volumes, whose effect is described with the aid of fig. 10: the moving wall

(representative of the tooth that enters into mesh) causes a different reduction of the observed volume from the one represented in fig. 2*a*, because of the movement of the permeable surfaces (consequence of the discussed geometric assumptions) connecting suction and delivery CVs.

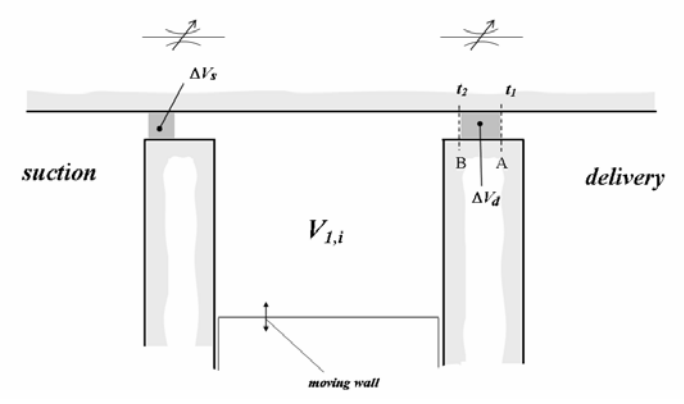

Figure 10 – Simplified scheme of tooth space CV with variable volumes

The numerical model has been implemented in AMESim® environment, developing built-in C++ models, by means of AMESet® facilities. A sketch of the model is displayed in fig. 11. Features and submodels in fig. 11 are quite similar to the model presented in [15]: the "Multi Ch" icons represent arrays of hydraulic chambers that evaluate eq. (3) for all the TSVs of both gears, including the internal leakages; orifice icons represent arrays of variable orifices. All geometrical data, as functions of the angular position of a reference tooth, are tabulated in ASCII files generated by the implemented CAD pre-processor. From the fluid dynamic point of view, the sketch in fig. 11 differs from the one presented in [15] for the better description of variable inlet and delivery volumes.

3. CALCULATION OF FORCES AND TORQUES

Another relevant improvement comes from the boxes in the bottom-right of fig. 11, that represent the calculation of forces and torques acting on the gears. The force that the fluid applies to each gear is calculated starting from the instantaneous pressure distribution according to the CVs defined (figs. 1 and 2). Only forces lying in a plane orthogonal to the gear axes are considered: the axial thrust evaluation is at the moment out of the author's scope.

Outside the meshing zone, every TSV has an impermeable surface of constant area S_{max} in contact with a gear, and the corresponding force is easily evaluated because only one CV is involved.

In the meshing zone, the same area S_{max} between two adjacent teeth of the same gear is subdivided in three parts S_1, S_2 and S_3 as represented in fig. 12*a* for driver gear, and fig. 12*b* for driven gear. Every sub-surface belongs to a different CV, so as to be subject to different values of pressure. For the sake of generality, as well as to better interface with the CAD pre-processor, the system of pressure forces acting on each gear is split in their x and y components (axes are defined in fig. 13). Therefore the surface corresponding to each tooth profile has been projected on a plane that is perpendicular to the direction of the force, as shown in fig. 12. For example, projections indicated with ${}^{I}x_{i,1}{}^{(+)}$, ${}^{I}x_{i,2}{}^{(-)}$, ${}^{I}x_{i,3}{}^{(+)}$ pertain to

forces $f_{y,i}$ acting on the driver gear, while ${}^{S^2}y_{i,1}{}^{(+)}$, ${}^{S^2}y_{i,2}{}^{(+)}$, ${}^{S^2}y_{i,3}{}^{(+)}$ concern forces $f_{x,i}$ acting on the driven gear. Superscript signs in parenthesis identify the way, according to conventions of fig. 13. The lengths ${}^{1}x_{i,1}{}^{(+)}$, ${}^{1}x_{i,2}{}^{(+)}$, ${}^{1}x_{i,3}{}^{(+)}$ and ${}^{2}y_{i,1}{}^{(-)}$, ${}^{1}y_{i,2}{}^{(+)}$, ${}^{1}y_{i,3}{}^{(+)}$ indicate the distance of the centre of pressure from the gear axis.

The model considers also the contribution of forces acting on tooth tips, assuming for each tooth a constant pressure equal to the arithmetical average of adjacent TSVs, which is the same as introducing a linear circumferential distribution. In the same gap (tooth tip-case) tangential forces are neglected.

In order to obtain the resulting pressure force acting on each gear, all the x and y components are added up:

$$F_{p,x}(\vartheta) = \sum_{i=1}^{z} \sum_{k=1}^{Ns} f_{x,i,k}(\vartheta) \qquad Ns = 1 \text{ or } 3 \tag{4a}$$

$$F_{p,y}(\vartheta) = \sum_{i=1}^{z} \sum_{k=1}^{Ns} f_{y,i,k}(\vartheta) \qquad Ns = 1 \text{ or } 3 \tag{4b}$$

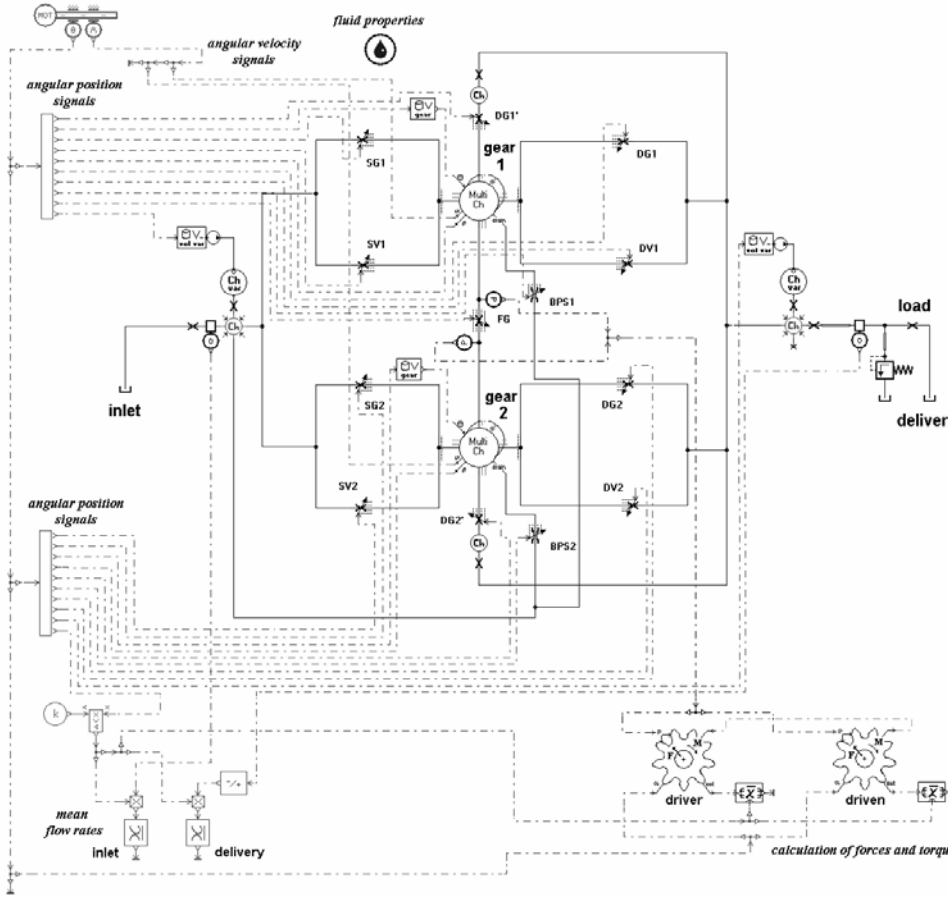

Figure 11 – AMESim sketch of HYGESim model

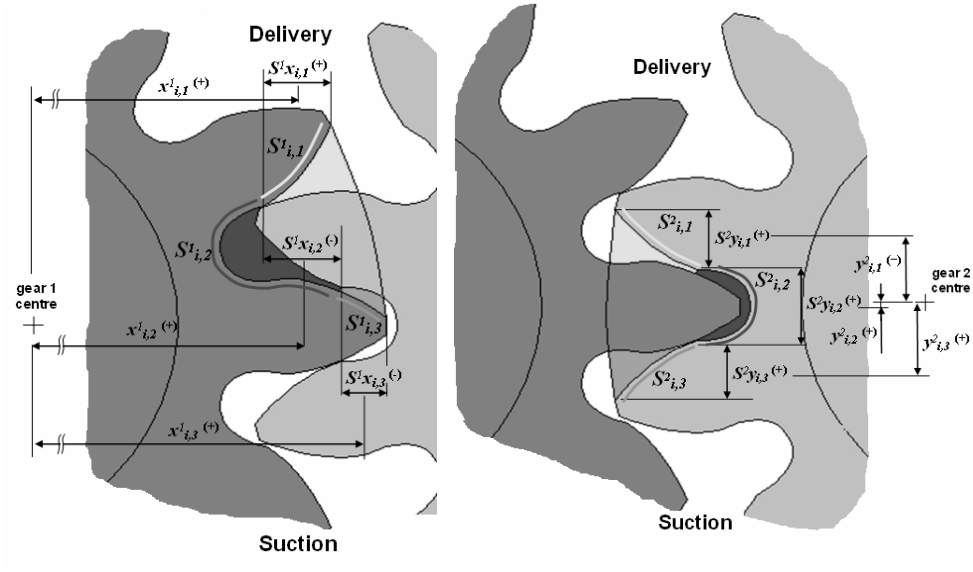

a) *b)*

Figure 12 – Subdivision of the surface between adjacent teeth on same gear for driver gear (*a*) and driven gear (*b*).
Part *a)* shows the projections of resulting surfaces for the calculation of forces along *y* direction; part *b)* shows the analogous projections for the evaluation of *x*-components. Signs on superscript, refer to the reference frame, for the distances from the gear centre, and to the way of corresponding force, according to notation specified in fig. 13

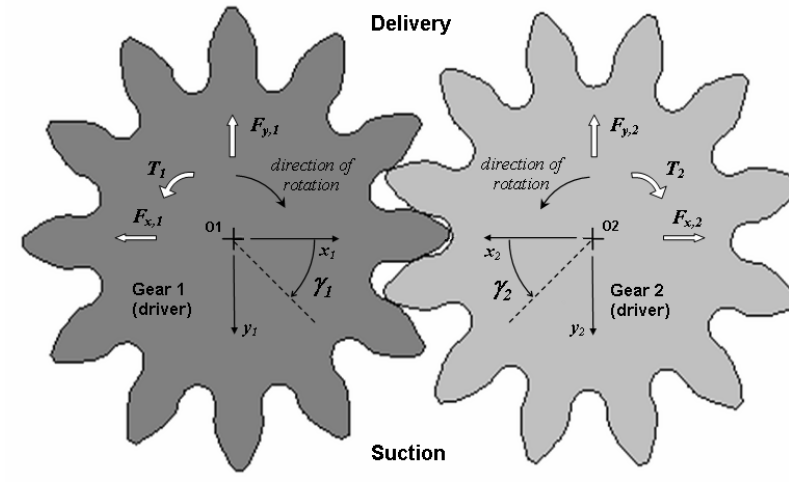

Figure 13 – Definition of the reference frame and of conventional sign of forces and torques

It is worthwhile to notice how the calculation of the resulting force on the driver gear requires the knowledge of the pressure in CVs of the driven gear and vice-versa.

The line of action of the resultant $\vec{F}_{p,y}$ is characterized by a distance $X(\vartheta)$ from the gear centre, while $\vec{F}_{p,x}$ acts at a distance $Y(\vartheta)$. $X(\vartheta)$ and $Y(\vartheta)$ are found applying the following equations [18]:

$$X(\vartheta) = \frac{\sum_{i}^{z}\sum_{k}^{Ns}\left(f_{y,i,k}(\theta)\cdot x_{i,k}(\theta)\right)}{F_{p,y}(\vartheta)} \qquad Ns = 1 \text{ or } 3 \tag{5a}$$

$$Y(\vartheta) = \frac{\sum_{i}^{z}\sum_{k}^{Ns}\left(f_{y,i,k}(\theta)\cdot y_{i,k}(\theta)\right)}{F_{p,x}(\vartheta)} \qquad Ns = 1 \text{ or } 3 \tag{5b}$$

Thus, for each gear the system of forces due to fluid pressure is equivalent to the resulting force $\vec{F}_{p,tot}$ applied at the gear centre and a torque T, given by:

$$\vec{F}_{p,tot}(\vartheta) = F_{p,x}(\vartheta)\vec{j_x} + F_{p,y}(\vartheta)\vec{j_y} \tag{6a}$$

$$T(\vartheta) = F_{p,x}(\vartheta)\cdot Y(\vartheta) + F_{p,y}(\vartheta)\cdot X(\vartheta) \tag{6b}$$

For the driven gear, the torque T is balanced by the contact force with the driver gear. A precise evaluation of the contact force should consider the characteristic of power transmission between gears. As well know, at least one pair of teeth are instantaneously in contact; this means that during the meshing cycle pairs of teeth share the load. The load distribution between two teeth is difficult to determine because of its dependence on many factors, i.e.: teeth deformations, tolerance, etc. [19]. Therefore simplified assumptions are deemed suitable for a lumped parameter model: independently of the angular position of gears the pitch centre is considered to be the fixed point of application of the contact force, which is forced to be constantly directed along the line of action.

Effects of the friction due to sliding teeth profiles are neglected. In fact in the case studied the friction forces are particularly low; moreover it is known that the sign of this contribution changes in proximity of the pitch point where sliding vanishes [19].

Therefore, once evaluated the force $\vec{f}_c$, the total force acting on each gear works out to be:

$$\vec{F}_{tot}(\vartheta) = \vec{F}_{p,tot}(\vartheta) + \vec{f}_c(\vartheta) \tag{7}$$

The total torque required at pump shaft, net of mechanical losses, is given by the sum of T_1 (eq. (6), driver gear) and the effect of $\vec{f}_c$:

$$T_{tot} = T_1 + f_c \cdot R_1 \tag{8}$$

4. RESULTS

The results of the fluid dynamic model have been compared with some available experimental data achieved from test campaigns carried out on a stock pump. In particular, the external spur gear pump used for model validation is a Casappa PLP20.11,2, characterized by a nominal displaced volume of 11.23 cm^3/r and 12 teeth per gear. Tests were performed at Casappa laboratories; further details concerning the test rig are reported in [20].
The test circuit has been modelled with the AMESim® sketch of fig. 14*a*, in which the HYGESim model is represented by a single icon. The model used between the pump and the load accounts for wave propagation and frequency dependent friction phenomena [17, 21, 22], and represents the short steel apparatus connected to the pump delivery flange that includes a pressure transducer and a relief valve (fig. 14*b*).

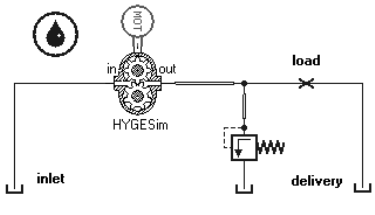

a)

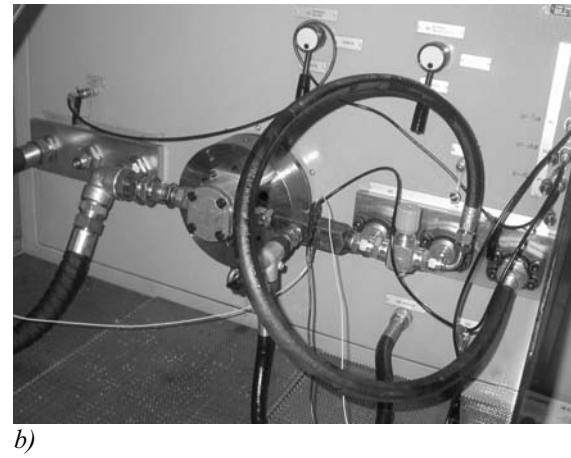

b)

Figure 14 - *a*) AMESim circuit used for simulation of tests. "HYGESim" icon represent the supercomponent obtained from the model of fig. 11
b) Picture taken during one of the performed tests

The setup of the discharge coefficients of orifices in the HYGESim model, for the evaluation of mass flow rates according to eq. (2), has been obtained by adjusting the values previously assumed from the data reported in [8,23] for similar conditions, on the basis of experimental results. Fig. 15 shows how a proper calibration of the model has permitted a good agreement between simulated results and experimental data for different pump operating conditions. Fig. 15 reports only the comparison of the pressure course at pump delivery, but for all the conditions examined it has been possible to verify how the measured flow rate well matches the simulated data. This result has been achieved thanks to the latest improvements on the fluid dynamic model, that allow a more precise evaluation of both pressures and flow rates. Hence, the model can be used for the prediction of the volumetric efficiency of pumps.
Both the experimental courses considered in fig. 15 differ from the simulated results for a low frequency trend, corresponding to the rotational frequency. Possible reasons of this discrepancy span from eccentricities of gears caused by dimensional tolerances and, secondly, to imperfections in the transmission and irregularities in the angular velocity of

the electric drive.

Fluid dynamic results provided by the simulations are very useful for understanding the working concept of the pump. For this purpose one of the most interesting features predicted by the model is the course of pressure inside a TSV during the shaft rotation, as shown in fig. 16. What is shown in fig. 16 is consistent with results discussed in [6]; the figure summarizes also the main geometrical features that affect the pressure inside volume $V_{1,i}$ on the driver gear. Furthermore, observing the trend of the delivery pressure, fig. 16 highlights the main causes of pressure ripple, given by the pressure peaks reached by each pair of corresponding teeth in the meshing zone. Therefore, the model is suitable for the prediction of maximum and minimum peaks of pressure reached inside the TSVs in the meshing zone (detail E in fig. 16). This information is useful for the evaluation of fluid borne noise, of forces acting on gears and, on the other hand, for the prediction of any possible onset of cavitation.

a)

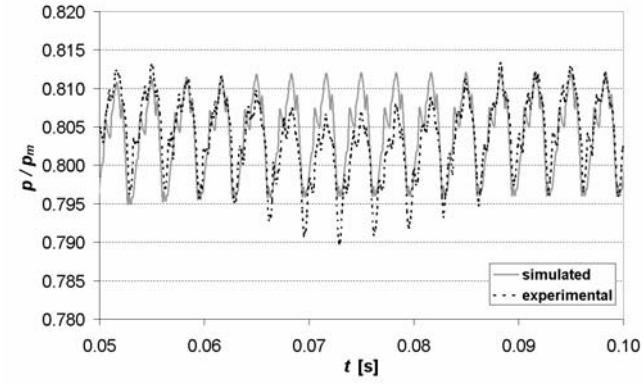

b)

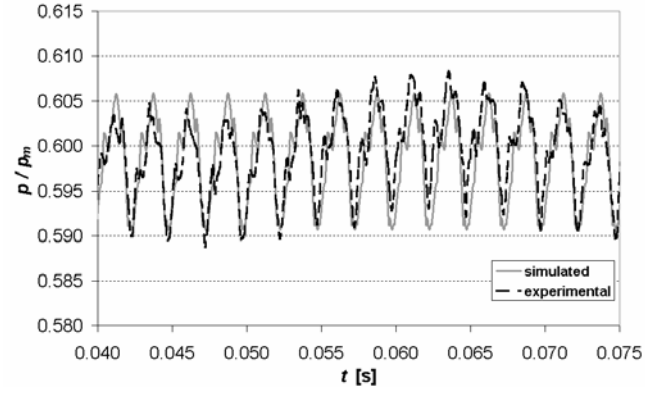

Figure 15
Measured and simulated delivery pressure
a) n = 1500 r/min
b) n = 2000 r/min

The 12 teeth of each gear are noticeable observing the 12 pressure peaks during a shaft revolution (0.04 s at 1500 r/min; 003 s at 2000 r/min), corresponding to 12 couples of teeth entering into mesh

It is well known that a widely used solution for the optimization of pump reliability and performance consists in a careful design of the grooves manufactured on the bearing blocks. It is very important to realize a good compromise between the maximum pressure reached in the meshing zone (responsible of pressure ripple, noise and structural stresses) and the amount of fluid that escapes from the delivery to the suction space through the

connections DG1 and SG2 (which affects volumetric efficiency). In deeper detail, fig. 17 schematises the solution adopted in the considered stock pump: for a little angular interval the inter-teeth volume is simultaneously connected to the delivery and to the suction CVs. With the purpose of showing the potential of the implemented CAD pre-processor – HYGESim combination as a design tool, some simulations have been carried out changing the design of the grooves on the delivery side. Fig. 18 compares the two cases: fig. 18*a* shows the design based upon the relationship described in [4], while in fig. 18*b* the radius of the recesses has been increased by 30%.

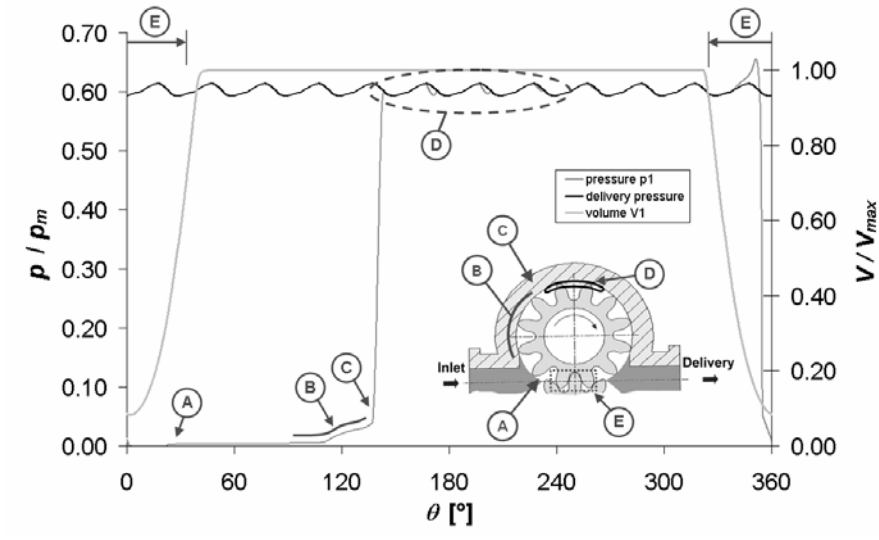

Figure 16 – Simulated pressure inside a TSV (n = 2000 r/min).

- **A.** The considered CV is outside the meshing zone;
- **B.** Effect of leakages;
- **C.** Effect of backflow groove (DG1') opening;
- **D.** Effect of backflow groove DG1' shape (relevant differences between delivery pressure and CV pressure)
- **E**. Meshing zone

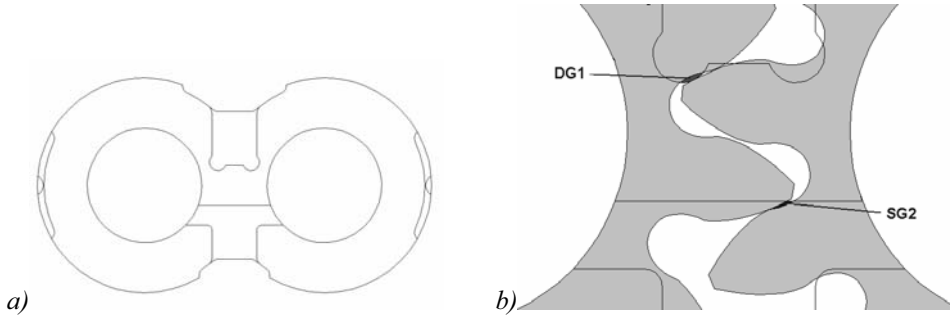

a) *b)*

Figure 17 – *a)* Standard design of grooves manufactured on the bearing blocks *b)* Detail of connections between inter-teeth volume and recesses

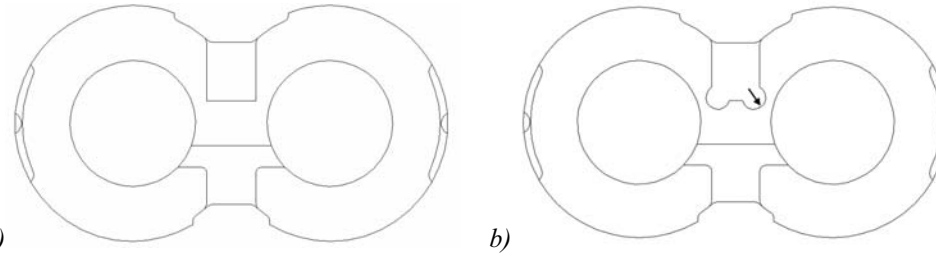

a) *b)*

Figure 18 – Alternatives considered for the design of the grooves manufactured on the bearing blocks

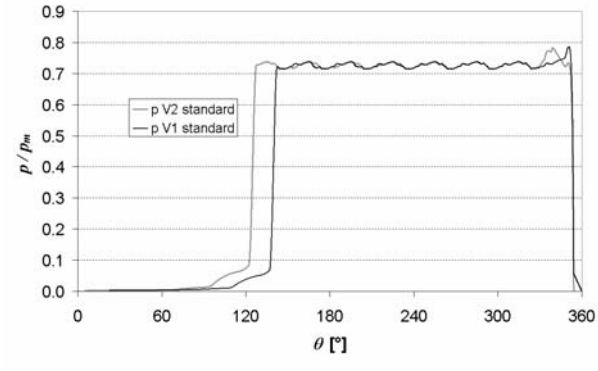

a)

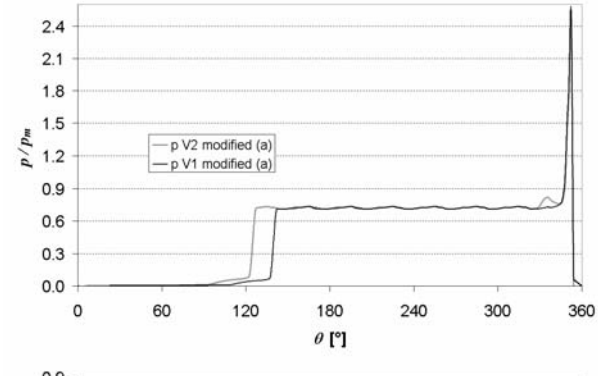

b)

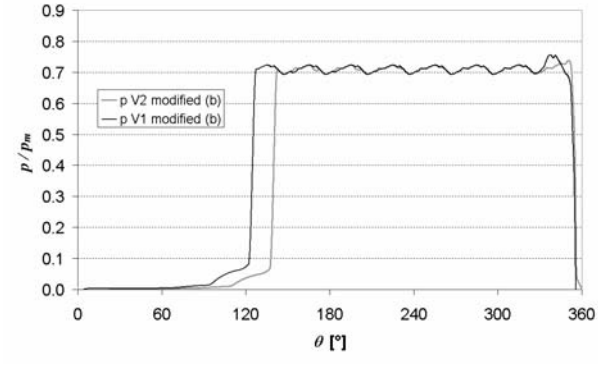

c)

Figure 19 – Pressure inside a couple of corresponding TSVs, changing the design of grooves (n = 1500 r/min):

a) standard design
b) modified design *a* (fig. 18*a*)
c) modified design *b* (fig. 18*b*)

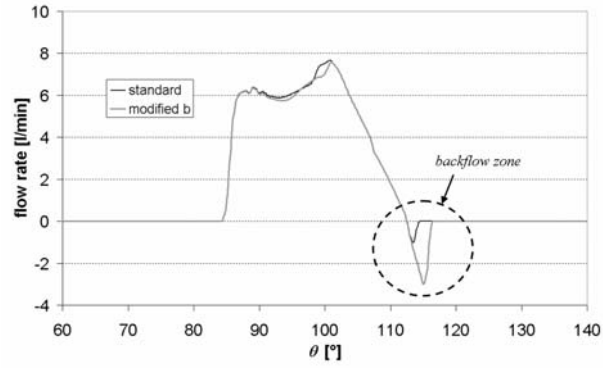

Figure 20 – Flow rates through orifice DG1 (n = 1500 r/min). To better display the backflow a different TSV, respect to fig. 19, has been considered

Results shown in fig. 19 are similar to the trend of fig. 16, with the addition of the course of the pressure inside a couple of corresponding TSVs on driven gear. Comparing the results obtained with the different designs of the bearing block, it is clear how the solution of fig. 18*a* is unacceptable, because of the intolerable pressure peak at the beginning of the meshing zone (fig. 19*a*). The standard case of fig. 17 represents the best solution; in fact adopting the design of fig. 18*b* the benefit of a slight reduction of the pressure peaks (evident through the comparison of figs. 19*a* and 19*c*) is overcome by a higher backflow from delivery to inlet (see fig. 20, where - for brevity - only results pertinent to orifice DG1 are represented).

a)

b)

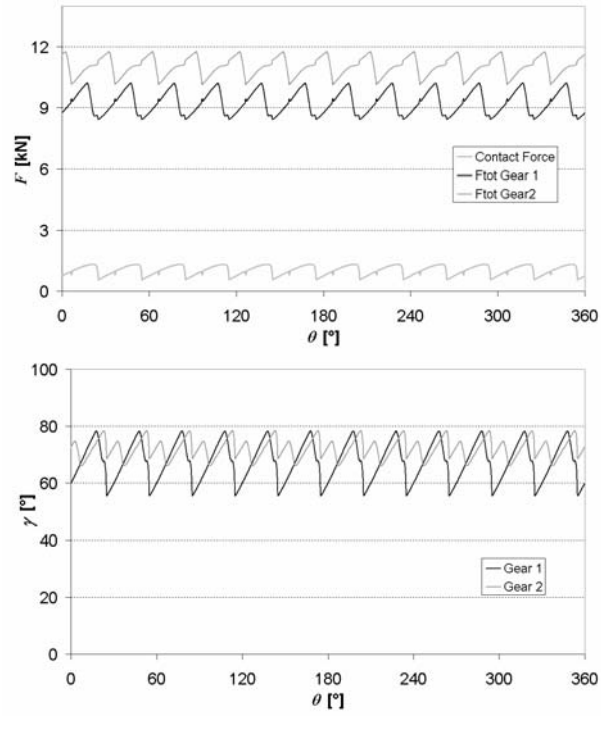

Figure 21 – Significant results provided by the module of calculation of forces and torques (n = 1500 r/min; $p_d / p_m \approx 0.8$):

a) force intensities (average values: $\overline{F}_1 = 9.25$ kN $\overline{F}_2 = 11.02$ KN; $\overline{F}_c = 1.03$ kN)

b) force angles (according to notation of fig. 12, average values: $\overline{\gamma}_1 = 67.6°$; $\overline{\gamma}_2 = 72.0°$)

c)

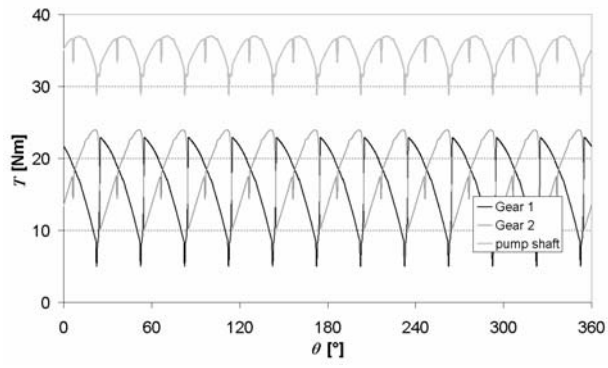

c) torques due to fluid pressure and total torque required at pump shaft ($\overline{T}_{tot}$ = 35.07 kN)

As concerns the model for the evaluation of forces and torques, a few significant results are displayed in fig. 21. In particular, diagrams of figs. 21*a* and 21*b* report the features (intensity and angular direction) of the force acting on each gear. Both forces are directed toward the suction side (fig. 21*b*); furthermore the effect of the contact force, involves a higher total force on the driven gear. Fig. 21*c* shows the predicted torques, for the working condition taken as reference. The curves T_1 and T_2 concern the torque caused by fluid pressure on each gear. For the driver gear, the torque T_2 is transmitted through the contact point and the resulting torque T_{tot}, required at pump shaft, is given considering also the contribution of T_1. The phase shift between T_1 and T_2 courses (about 15°) can be explained with fig. 19, observing the same angular shift on the diagram pertinent the maximum pressure value inside the two corresponding CVs $V_{1,i}$ and $V_{2,i}$ (the phase shift, approximately equal to 15° is principally due to the course of volumes, fig. 2*a*). On the other hand, the torque phase shift is just what could be expected from very simple considerations, in that it equals half the circumferential pitch. As an effect of the phase shift between T_1 and T_2, T_{tot} works out to be more uniform.

5. CONCLUSIONS

This paper presents the latest improvements introduced on a model for the simulation of external spur gear pumps developed by the authors. The simulation code, named HYGESim, aims at simulating the flow through the whole pump adopting a simple lumped parameter approach. The model, thanks to its implementation in the AMESim® environment, can be used not only for the analysis of pump design, but also to investigate the interactions with hydraulic systems.

In particular, the paper focuses the improvements performed on the fluid dynamic description of the meshing zone; moreover the new version of the code includes a model for the calculation of both the instantaneous forces and the torques acting on the gears, starting from the knowledge of pressure results of the fluid dynamic model. HYGESim takes advantage of the potentials of a developed CAD pre-processor tool, that is able to provide all the geometrical data required for the calculation as a function of the angular position of gears. Notwithstanding few simplifications have been introduced for the evaluation of leakages and assuming the ideal displacement of the gears, the results, in terms of pressure ripple, are satisfactory with respect to available experimental data. Moreover results presented in the paper show how, at this stage of development, the code permits a deep analysis of pump operation and allows good predictions of the effects of the most

significant geometrical design parameters, e.g. shape and dimensions of the grooves on the bearing blocks. In a future work, improvements will concern the modelling of leakage losses and the evaluation of the main geometrical parameters (like tooth space volumes, clearances, etc.), considering the effects of the forces on the position of the gears.

REFERENCES

[1] Ivantysyn J., Ivantysynova M., 2003, *Hydrostatic Pumps and Motors*, Tech Books Int., New Delhi, India

[2] Esposito A., 2000, *Fluid Power with Applications*, Prentice Hall Int. Inc.

[3] Wilson W. E., 1948, *Performance Criteria for Positive Displacement Pumps and fluid Motors*, Proc. of ASME semi-annual meeting, June 1948.

[4] Castellani G., 1967, *Pompe ad Ingranaggi a Denti Dritti*, Progetto delle Dentature, Giornata Mondiale della Fluidodinamica, FLUID'67, Oct. 13-14, MI, Italy.

[5] D.Fielding, K.Foster,C.J. Hooke, M.J. Martin, 1977, *Sources of pressure pulsation from a gear pump*, Seminar on "Quiet oil hydraulic systems", The Institution of Mechanical Engineers.

[6] Mancò S., Nervegna N., 1989, *Simulation of an External Gear Pump and Experimental Verification*, JHPS International Symposium on Fluid Power, Tokyo, Japan.

[7] Mancò S., Nervegna N., 1993, *Pressure Transient in an External Gear Hydraulic Pump,* Second JHPS International Symposium on Fluid Power, Tokyo, Japan.

[8] Eaton M., Edge K., 2001, *Modelling and Simulation of Pressures within the Meshing Teeth of Gear Pumps*, Int. Conf. on Recent Advantages in Aerospace Actuation Systems and Components, June 13-15, 2001, Toulouse, France.

[9] Bonacini C., Borghi M., 1990, *Calcolo delle Pressioni nei Vani fra i Denti di una Macchina Oleodinamico ad Ingranaggi Esterni*,Oleodinamica-Pneumatica, Nov.1990, Tecniche Nuove.

[10] Paltrinieri F., Borghi M., Milani M., 2004, *Studying the Flow Field Inside Lateral Clearances of External Gear Pumps*, 3rd FPNI-PhD Symposium on Fluid Power, Spain, June 2004.

[11] Zardin B., Paltrinieri F., Borghi M., Milani M., 2004, *About the Prediction of Pressure Variation in the Inter-Teeth Volumes of External Gear Pumps*, 3rd FPNI-PhD Symposium on Fluid Power, Spain, June 2004.

[12] Poy Ferrer M., Codina E., 2002, *Suction Capability of Gear Pumps*, 2nd Int. FPNI PhD Symposium, Italy, July 2002.

[13] Gutes M., Gamez Monter P.J., Castilla R., Codina E., 2000, *Journal Bearing Performance in Gear Pumps*, 1st Int. FPNI-PhD Symposium, Germany, Sept. 2000.

[14] Manring N. D., Kasaragadda S., 2003, *The Theoretical Flow Ripple of an External Gear Pump*, ASME Journal of Dynamic Systems, Measurement, and Control. Vol. 125.

[15] Casoli P., Vacca A., Franzoni G., 2005, *"A numerical model for the simulation of external gear pumps"* The sixth JFPS International Symposium on Fluid Power, Tsukuba, Japan, Novembre 07-11 2005.

[16] Blackburn J. F., Reethof G.., Shearer J. L.. 1966, *Fluid Power Control*. USA: MIT Press.

[17] IMAGINE S.A., 2004, AMESim® *and* AMESet® *version* 4.2 *User manual*, Roanne, France, September 2004.

[18] Dario Graffi, *Elementi di Meccanica Razionale* ,1982, Patron Editore, Bologna.

[19] Dennis P. Townsend, 1992, *Dudley's Gear Handbook* McGraw-Hill.

[20] Casoli P., Vacca A., Franzoni G., 2003, *A Numerical Model for Simulation of "Load Sensing" Spool Valves*, The 18th Int. Conf. on Hydraulics and Pneumatics, Prague, Czech Republic, September 2003.

[21] E.B. Wiley, V.L. Streeter,1993, Fluid transients in systems, Prentice Hall, Inc.

[22] W. Zielke, *Frequency dependent friction in transient pipe flow*, 1968, Journal of Basic Engineering, March 1968.

[23] Idel'cik E., 1986, *Memento del Pertes de Charge, Coefficients de Pertes de Charge Singulières et de Pertes de Charge par Frottement*, Edition Eyrolles.

Return to Contents

Pneumatics

Force control at low cost in pneumatic field

Xavier BRUN*, Mohamed SMAOUI*, Jean-Marie RETIF, Xue-Fan g LIN SHI**, Eric BI DEAUX*.**
***Laboratoire d'Automatique Industrielle, INSA Lyon, Bâtiment Saint Exupéry, 25 Avenue Jean Capelle , 69621 Villeurbanne Cedex, France, http://www-lai.i nsa-lyon.fr**
Email contact: xavier.brun@in sa-lyon.fr
****Centre Génie Electri que de Lyon, INSA Lyon, Bâtiment Léonard de Vinci, 21 Avenue Jean Capelle, 69621 Villeurbanne Cedex, France, http://cegely.cnrs.fr/**

ABSTRACT

At the present time in the pneumatic field, when a system requires a wide range of force control, servodistributors are currently used. On/off distributors are used when the system is simpler and only a small range of force values are required [1]. The work presented here consists of using on/off distributors in a system which requires a wide range of force values. This has been carried out in order to reduce the cost of complex systems [2-4], because present day distributors are five to ten times cheaper than servodistributors.
This paper presents a new control method applied to the electro-pneumatic field. This strategy originates from the hybrid control theory recently developed for the control of asynchronous or synchronous electrical motors, [5, 6]. This control strategy is an improvement of the proposed one in [4].
Based on both cylinder and distributor models, the hybrid control presented here chooses the best state for each on/off distributor to reach the desired force value. Hybrid control is based on a state space model for both the energy modulator and the continuous sub-process. For this model, a control vector, depending on the number of possible configurations for the energy modulator, is defined. Two formal approaches have been developed for choosing a control vector to track the reference state of interest in the state space. Experimental results are presented and discussed.

KEYWORDS hybrid control, on/off distributor, electro-pneumatic, experimental results, force control.

1. INTRODUCTION

At the present time in the pneumatic field, when a system requires a wide range of force control, servodistributors are currently used [7-11]. On/off distributors are used when the system is simpler and only a small range of force values are required [1]. The work presented here consists of using on/off distributors in a system that requires a wide range of force values. This has been carried out in order to reduce the cost of complex systems [2, 3], because present day distributors are five to ten times cheaper than servodistributors.
Using on/off distributors for reaching a desired force produces to a system with energy modulators (on/off distributors) and a continuous sub-process (cylinder). Such systems define a type of Hybrid Dynamic Process (HDP). Hybrid control [5,6, 12], which is an efficient approach for controlling this kind of system. It is based on a state space model for both the energy modulator and the continuous sub-process. For this model, a control vector, depending on the number of possible configurations for the energy modulator, is defined. A formal approach has been developed for choosing a control vector to track the reference state of interest in the state space. This control has been developed for the control of AC machines driven by inverters. Very good dynamic performance has been obtained (Retif 2004). In this paper, the hybrid control is applied for the force control of the pneumatic cylinder where the chosen state variables of interest are the pressure in each chamber noted p_P and p_N. In fact, the control of both pressures leads to the control of the pneumatic force. Usually in the electrical field, from where the hybrid control algorithm is issued, the time commutation of the transistors can be neglected, [5,6, 12] with regards to the sample time (respectively equal to few microseconds and few hundred microseconds). The main difficulty in our context is that the on/off distributors used are quite slow. In the electropneumatic field [13], the bandwidth of cheap on/off components is very small (between 5 and 20 Hertz) and cannot be neglected when the control frequency is of the same order. Some propositions were proposed in literature to increasing the dynamic performance of pneumatic servo-systems with digital valves. In this paper the aim is not to use PWM concept [14], for limited energy consumption, and not to increase the number of valves as in [15] for limited cost. This problem is not present when the power modulator is a servodistributor and therefore other control algorithms are used [8, 16-20], because hybrid control is not appropriate with this type of component.

Power Transmission and Motion Control 2006 Edited by Dr D N Johnston and Professor K A Edge

The study begins with the modelling of the continuous sub-process, then of the distributors, these are divided into two parts: static and dynamic models. The hybrid control algorithm is then developed. Finally, the first experimental results are presented and discussed and perspectives are announced for improving the performance of the system.

2. ELECTRO-PNEUMATIC SYSTEM MODELLING

In order to determine the best distributor state for reaching the desired output value, the hybrid control requires both cylinder and distributor control models. This model must use physical parameters which can be given by industrial manufacturers or which can be obtained easily from simple experimental tests. In fact the following approach must be easy to generalise to any other electropneumatic on/off distributor.

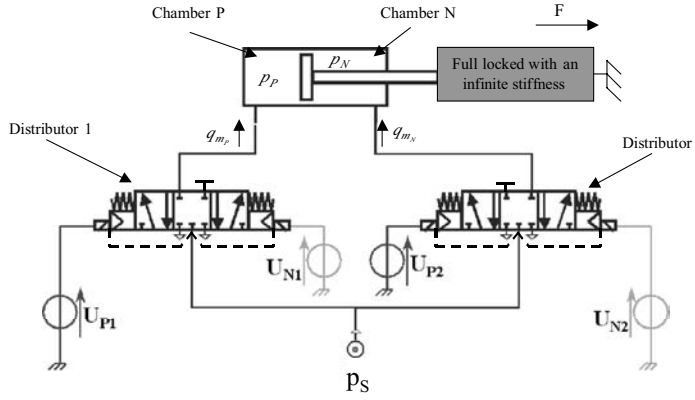

Figure.1: Schema of the electro-pneumatic system

The pneumatic system consists of a pneumatic cylinder and two electropneumatic on/off distributors. The notation 'P', respectively 'N' in Fig. 1 is attached to elements whose positive actuation induces an increase in the exerted force, or respectively, a decrease.
Table 1 shows the nine different combinations of control vectors (C1 to C9) which can be applied to the distributors. The '0' value corresponds to a null voltage and the '1' value corresponds to 5 volts. All the states where $U_{Px} = U_{Nx} = 1$, are prohibited to avoid short-circuits in the electrical distributors. :

	C1	C2	C3	C4	C5	C6	C7	C8	C9
U_{P1}	0	1	0	0	0	1	0	0	1
U_{N1}	0	0	1	0	0	0	1	1	0
U_{P2}	0	0	0	1	0	1	0	1	0
U_{N2}	0	0	0	0	1	0	1	0	1

Table 1: Applicablecontrols

2.1 Actuator

The system is composed of a single rod double acting linear pneumatic cylinder (32/20). The rod of the actuator is attached to a stop end. Considering that the stiffness is infinite, there are no variations in the volume of the cylinder chambers. In our case the piston position is set to obtain the same volume in both chambers of the actuator, noted V and equal about to 0.1 litre. The aim is to control the force exerted against the stop end. Considering that the dry friction forces can be neglected, the general principal of mechanics gives the expression of the force as a function of both pressures:

$$F = S_P p_P - S_N p_N - (S_P - S_N) p_E \tag{1}$$

So the force F can be controlled due to the control of the pressure in each chamber p_P and p_N.
With the following classical assumptions [21-22], the model used for the control law synthesis can be described by the system (2).

- air is a perfect gas and its kinetic energy is negligible in the chamber,

- pressure and the temperature are homogeneous in each chamber,
- the evolution in each cylinder chamber is supposed to be polytropic of index *n*,
- the temperature variation in each chamber is considered negligible with respect to the supply temperature,
- the mass flow rate leakage are neglected,
- supply and exhaust pressures are assumed to be constant.

$$\begin{cases} \dfrac{dp_P(t)}{dt} = \dfrac{nrT}{V} q_{m_P}\left(x_P(U_{P1}, U_{N1}, t), p_P(t)\right) \\ \dfrac{dp_N(t)}{dt} = \dfrac{nrT}{V} q_{m_N}\left(x_N(U_{P2}, U_{N2}, t), p_N(t)\right) \end{cases} \quad (2)$$

The main difficulty concerns the distributor mass flow rate modelling, q_m, described in the next part.

2.2 On/off distributor

The distributor used in this work is a 5 way / 3 position, centre position closed (from the Asco Joucomatic company) (Fig. 2a). Both components are supposed to be identical. There are two relays to move the spool to the left or to the right. These different positions allow the pressure to increase, decrease or stabilise in the chamber. According to classical hypothesis the establishment of flow is instantaneous, which means that the transient flows can be neglected, the modelling study of the distributor can be split into two parts : a static part giving the mass flow rate as a function of the distributor spool position x and of the output port pressure p $\left(q_m(x, p)\right)$ and a dynamic part characterising the spool dynamic $\left(x(U_P, U_N, t)\right)$. Figure 2b shows the system representation of the distributor model.

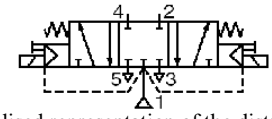

a/ Normalised representation of the distributor used

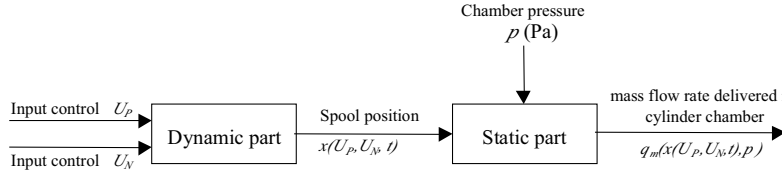

b/ Block diagram of the distributor model

Figure 2: Distributor

2.2.1 Dynamic part

The main drawback of on/off distributors compared to servodistributors is their high opening and closing time. In addition, for the components tested, the time is different for opening and closing, the closing time being about double the opening time. This difference is due to the force used to carry out the operation. The opening is carried out with the electro-magnetic force and the source pressure, while the closing is done by the mechanical force of the return spring. So, the component is asymmetrical.

This property has been compensated experimentally by applying a voltage, for a small time, on the opposite relay of the distributor in order to accelerate the spool to change position (go back to the centre or to the opposite side). The time of applying the voltage was specified for each distributor and tuned experimentally.

When connecting the distributor to a pneumatic chamber, it has been seen that the low dynamic is mainly due to the delay of 15 ms originating from high dry friction forces. Moving the spool then takes a few milliseconds. So, for a first control model, the displacement of the spool is supposed to be instantaneous and the dynamic part of the distributor model is just modelled as a delay (Fig. 3). The sampling period noted T_{st}, is then chosen as 20 milliseconds to guarantee that at each sampling time, the spool is either in an extreme position or in the central position. So the normalised position x of the spool, has only 3 different values : {-1 , 0 ,1}.

The consequence of the delay is that the variation of the pressure in a chamber for a control at time kT_{st} depends on the previous position of the distributor spool produced by the previous control at time $(k-1)T_{st}$. It means that

the effective application of the control is delayed (Fig. 3). This problem has to be taken into account in the control algorithm.

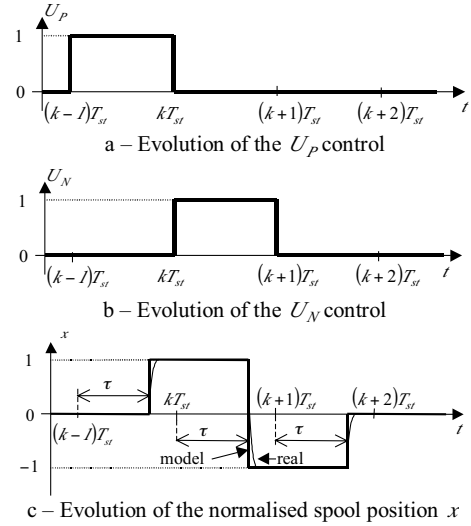

Figure 3: Example of the evolution of the normalised spool position of the distributor

According to the modelling hypothesis, the following dynamic model is then proposed with τ being the time delay of the spool to change position when the control is applied :

$$x\left(U_P(kT_{st}),U_N(kT_{st}),t\right)=\begin{cases}U_P\left((k-1)T_{st}\right)-U_N\left((k-1)T_{st}\right) & \text{if} \quad kT_{st}\le t<kT_{st}+\tau \\ U_P(kT_{st})-U_N(kT_{st}) & \text{if} \quad kT_{st}+\tau\le t<(k+1)T_{st}\end{cases} \tag{3}$$

With three possible states (Table 1) :

$$\begin{cases}U_P=0\\U_N=0\end{cases} \quad or \quad \begin{cases}U_P=1\\U_N=0\end{cases} \quad or \quad \begin{cases}U_P=0\\U_N=1\end{cases}$$

2.2.2 Static part

The static part of the on/off distributor model should consist of the expression of the mass flow rate through each useful restriction as a function of the chamber pressure p and of the normalised spool position x. As for the determination of the dynamic model, it has been considered that the movement of the spool is instantaneous, it is just necessary to know the mass flow rate characteristics of the on/off distributor for the full opening of the useful restrictions. According to Fig. 1 and 2, these restrictions are :

- restrictions 1 to 4 ($x_P=1$) and 4 to 5 ($x_P=-1$) for distributor 1,
- restrictions 1 to 2 ($x_N=-1$) and 2 to 3 ($x_N=1$) for distributor 2.

According to the ISO 6358 [23] standard, a test bench was realised (see Fig. 4a) to measure the mass flow rate characteristics to determine the flow parameters b and C used by the standard approximation (4). This model gives the mass flow rate evolution as a function of the upstream pressure and temperature and of the downstream pressure defined along the flow in the restriction.

Figure 4b shows an example of the experimental characteristics obtained compared to those obtained from the identified b and C parameters according to the ISO 6358 standard [23].

$$\text{if } \frac{p_{DOWN}}{p_{UP}} \le b \quad \text{(sonic flow)}, \quad q_m(p_{UP}, p_{DOWN}) = C\rho_0 p_{UP}\sqrt{\frac{T_0}{T_{UP}}}$$

$$\text{if } b < \frac{p_{DOWN}}{p_{UP}} \le 1 \quad \text{(subsonic flow)}, \quad q_m(p_{UP}, p_{DOWN}) = C\rho_0 p_{UP}\sqrt{\frac{T_0}{T_{UP}}}\sqrt{1-\left(\frac{\frac{p_{DOWN}}{p_{UP}}-b}{1-b}\right)^2} \tag{4}$$

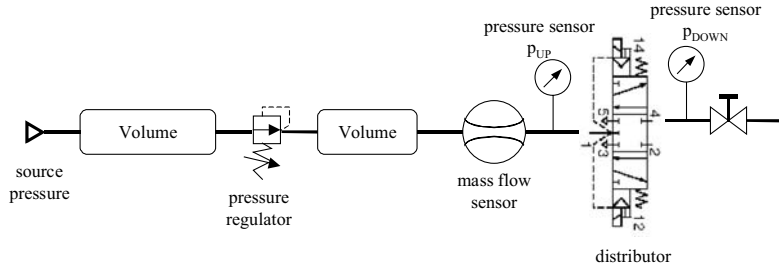

a/ Test bench for on/off distributor characterisation

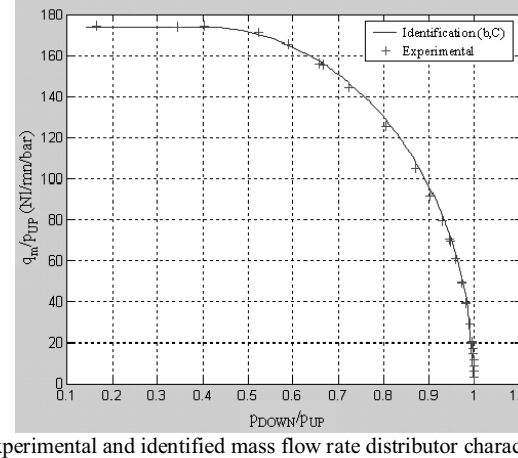

b/ Experimental and identified mass flow rate distributor characteristics

Figure 4: Distributor characterisation

As the four characteristics are very similar, the same couple of parameters (b,C) according to the ISO 6358 standard [23] has been determined for modelling every restriction :

- Critical pressure ratio $b = 0.4$,
- Sonic conductance $C = 174$ Nl/mn/bar

So the mass flow rates entering the 2 chambers can be expressed as a function of the spool position and of the chamber pressure by :

$$q_{m_P}(x_P, p_P) = \begin{cases} q_m(p_S, p_P) & \text{for } x_P = 1 \\ 0 & \text{for } x_P = 0 \\ -q_m(p_P, p_E) & \text{for } x_P = -1 \end{cases} \tag{5}$$

$$q_{m_N}(x_N, p_N) = \begin{cases} -q_m(p_N, p_E) & \text{for } x_N = 1 \\ 0 & \text{for } x_N = 0 \\ q_m(p_S, p_N) & \text{for } x_N = -1 \end{cases} \tag{6}$$

The q_m function in (5) and (6) is given by (4) in which the flow parameters b and C have the previous determined values and the upstream temperature is considered equal to the source temperature whatever the flow direction (according to hypotheses taken for the cylinder model section 2.1).
The equations (3) to (6) enable knowledge of each variable appearing in the system to be obtained (2) which together define the global control model of the system presented in Fig. 1.

3. HYBRID CONTROL

3.1 Hybrid Control Principle

Hybrid control uses a hybrid model where the continuous state variables of the continuous sub-process depend on the energy modulator's configuration:

$$\dot{\underline{X}}(t) = f\left(\underline{X}(t), \underline{U}(t)\right)$$

$\underline{X} \in \Re^n$ and $\underline{U}(t)$ is a m-dimensional vector that is finite

$$U \in \left\{U_1, U_2, ..., U_N\right\}, N \geq 2$$

For a short sampling period T_{st}, the model can be written as(Euler method):

$$\underline{X}(k+1) = \underline{X}(k) + f\left(\underline{X}(t), \underline{U}(t)\right) \cdot T_{st}$$

Assuming that full state is available for measurement, at time kT, the state $\underline{X}(k)$ is known. Via the dynamic model of the system (1), the state at time $(k+1)T_{st}$, noted $\underline{X}_j(k+1)$, $j \in N$, for each possible value of the control set can be calculated. N directions are defined as $\underline{dj} = \underline{X}_j(k+1) - \underline{X}(k)$.

For a given reference state $\underline{X}^{\#}$, Hybrid Control consists of calculating the N possible directions of the continuous state vector evolution d, choosing a control configuration in order to track this reference state in the state space.
For the bi-dimensional example in Fig. 5, the desired value (target point) can be placed in the plane X_1 and X_2. To track this reference, at each sample time, hybrid control proceeds as follows:

- it acquires the state of the system at time kT_{st} ($X_1(kT_{st})$ and $X_2(kT_{st})$ see Fig. 5)
- knowing the state of the system in the state space at time kT_{st}, this algorithm solves the system model equations, and calculates the different directions $\underline{dj}, 1 \leq j \leq N$ of the continuous state vector evolution corresponding to the application of j^{th} configuration of the energy modulator (d1 to d5 in Fig. 5)
- knowing the target point, this algorithm selects the optimal configuration. For this many techniques are possible. For example, the configuration chosen can be the one that minimises the Euclidean distance between the different reachable points and the target point.
- this algorithm chooses the shortest Euclidean distance (d4 in Fig. 5) and the corresponding control (U_4) is applied to the energy modulators for all the sampling period.

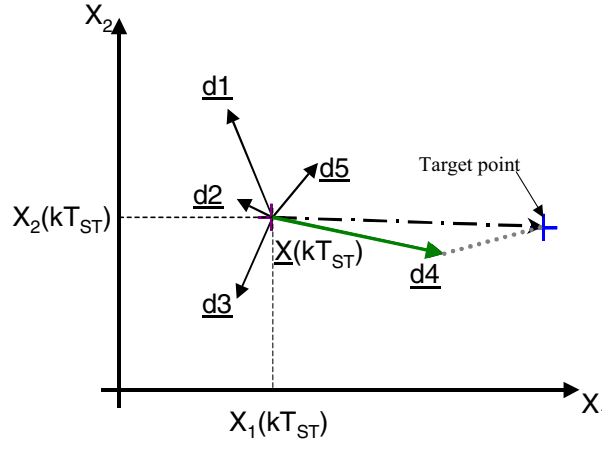

Figure 5: Principle of hybrid control

3.2 *Application to the pneumatic system*

3.2.1 Principle of the algorithm

For the system represented by Fig. 1, pressures in both chambers P and N constitute the state space $\underline{X}(t) = \left[p_p, p_n\right]^t$. The state space is of dimension 2, so it can be represented by a (p_N, p_P) plane. Two distributors enable three different states (pressure admission, closed and pressure exhaust) to be established leading to nine different control vectors C1 to C9 (see table 1).

The objective is, knowing the pressure at the sampling instant kT_{st}, to estimate the evolution of the pressures at the next sampling instant, $(k+1)T_{st}$, in both chambers P and N for the nine controls (C1 to C9) and then to choose the best control for reaching the desired force.

At each sample time, the pressure in each chamber is measured. The hybrid control algorithm calculates the nine directions d1 to d9 reachable at the next sample time in the state space by integrating the pressure differential system (2) using equations (3) to (6). See the block diagram in Fig. 6.

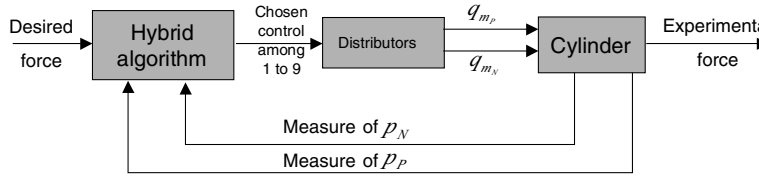

Figure 6: System structure

The target is fixed according to equation (1). For a given desired pneumatic force F, the target is defined by a one-dimensional equation:

$$p_P = \left(\frac{S_N}{S_P}\right) p_N + \left(\frac{F}{S_P} + \frac{S_P - S_N}{S_P} p_E\right) \tag{7}$$

So the target is a point of the straight line defined by equation (7) in the (p_N, p_P) plane. The algorithm calculates the nine possible directions (d1 to d9 in Fig. 7). Then it chooses the control configuration that corresponds to the lowest Euclidean distance in the physical domain (d6 for the desired force F1 and d4 for the desired force F2 in Fig. 7 because d6 leads out of the physical domain in this case).

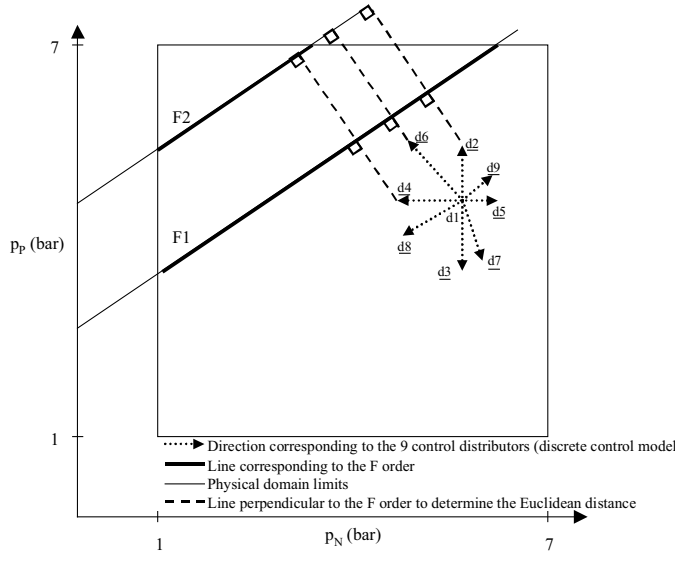

Figure 7 : Example of control choice

3.2.2 Principle of the modified hybrid algorithm

In this paper, a modified algorithm is proposed in order to achieve fast response without overshoot. Indeed, the hybrid control algorithm calculates the nine directions d1 to d9 reachable at the next sample time in the state space. The difference between the modified algorithm and the algorithm presented in the previous section is as follows:

- All the commands which cross the line are not taken in consideration by the algorithm : if a direction crosses the line, it is forbidden (d6 in Fig. 8).
- In the last step approaching the line the algorithm makes some adjustments to the time of the application of the command in order to reduce the steady state error. This adjustment is proportional to the distance between the line and the command (see Fig. 8).

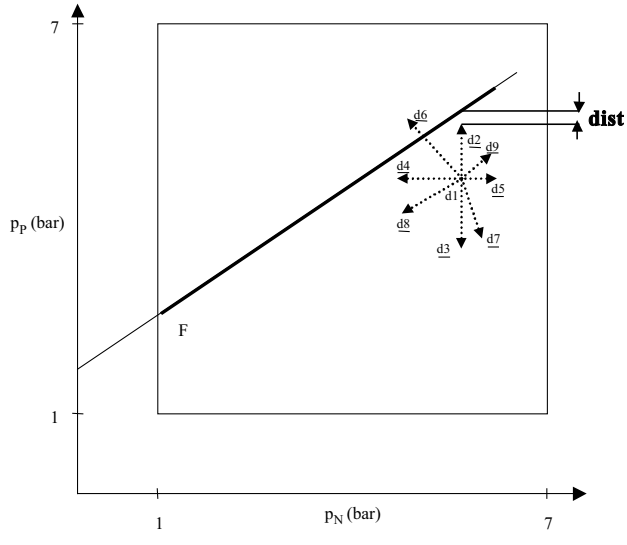

Figure 8 : Example of control choice

4. EXPERIMENTAL RESULTS

The proposed controller was implemented using a dSpace DS1104 controller board with a dedicated digital signal processor. Programs implemented in DS1104 were Matlab/Simulink ones with C code. Value 1 given by table 1 means that the relay of the distributor is supplied at 5V. Value 0 means 0V. The exhaust pressure value (1 bar) and the supply pressure (7 bar) limit the pressure. The desired force is 0N during 2.5 seconds and 260N during 2.5 seconds. At the beginning of the process, the pressure in the chamber P and N are equal to 1 bar.

This part will compare the two different algorithms. In the first plots (Fig. 9), the hybrid algorithm [4] is used. In the second plots (Fig. 10) the modified algorithm is used.

When the desired force becomes equal to 260 N, the control algorithms permit to increase the pressure in chamber P. An important overshoot of desired force can be seen in Fig. 9. A new control vector is selected by the hybrid control algorithm to decrease the force value and converges to the desired force. It is visible that the desired forces are quickly obtained but the steady state error is important (see time between 7 and 9 seconds in figure 9). Figure 10 clearly shows a reduction of the overshoot. This is due to the exclusion of a direction if it crosses the line. The adjustment of the time of the application of the command in the last step permit to reduce the steady state error.

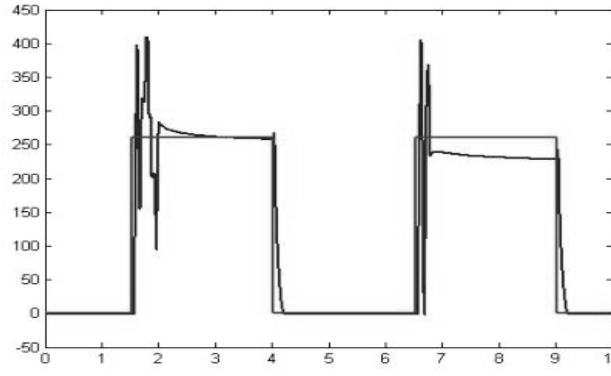

Figure 9 : Time evolution of the force (hybrid algorithm)

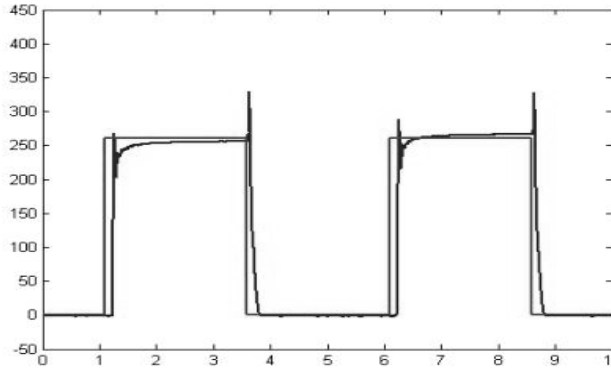

Figure 9 : Time evolution of the force (modified hybrid algorithm)

5. CONCLUSIONS

The contribution of this paper concerns the implementation of hybrid force controllers at low cost in pneumatic field. Firstly, the model synthesis and parameterisation of an on/off electropneumatic valve is presented. Secondly, the application of the hybrid method developed for electrical engine control [5, 6], of a system composed of a pneumatic cylinder and two on/off distributors designed for force control is studied. Two control algorithms are presented. Experimental results show that the principle of controlling the force by quantified components is realisable.

The main benefits of the modified hybrid algorithm are the reduction of the overshoot and the steady state error.

On/off control is a promising alternative for force control because of the low cost (compared to servodistributors) and the good performance obtained. Moreover there are no control parameters to tune. It is possible to improve the system in three different ways :

improvement of the control algorithm.

- add a closed loop by placing a force sensor at the end of the piston (to measure the force obtained) and to use a classical supplementary control loop as PID.
- to replace the distributors by ones which have a smaller sonic conductance C.

Future work will focus on improving the algorithm and applying a higher voltage to the distributor relay to reduce the spool delay.

Notation

b	critical pressure ratio
C	sonic conductance (Nl/mn/bar)
F	force (N)
S	piston cylinder area (m^2)
T	temperature (K)
T_{st}	sampling period (s)
U	boolean distributor input (null)
V	pneumatic cylinder chamber volume (m^3)
k	sampling period index
n	polytropic constant
p	pressure (Pa)
q_m	mass flow rate (kg/s)
r	perfect gas constant (J/kg/K)
t	time (s)
x	normalised position of the distributor spool (null)
τ	spool time delay to move after the control has been applied (s)
ρ	specific mass (kg/m^3)

Subscript and Superscript

UP	upstream
DOWN	downstream
P	relative to an increase of force
N	relative to a decrease of force
E	exhaust
S	supply
0	reference
1	distributor connected to chamber P
2	distributor connected to chamber N

References

[1] Ham, R.V, Verrelst, B., Daerden, F., Vanderborght, B., Lefeber, D. 2005. *Fast and accurate pressure control using on/off valves*, International Journal of Fluid Power, Vol 6, N°1.

[2] Van Varseveld, R.B., Bone, G.M. 1997. *Accurate position control of a pneumatic actuator using on/off solenoid valves*, Transactions on Mechatronics, IEEE/ASME, Volume 2, Issue 3, p 195-204.

[3] Legrand X., Retif J.-M., Smaoui M., Brun X., Thomasset D., Lin-Shi X. 2005. *Hybrid control with on/off electropneumatic standard valve for tracking positioning*, Bath Worksh. on Power Transmission & Motion Control, England.

[4] Sellier, A., Brun, X., Sesmat, S., Retif, J.M., Lin-Shi, X., Thomasset, D., Smaoui, M., *Hybrid Force control with on/off electro-pneumatic standard distributors,* Journal of Fluid Power, Vol 7, N°1, March 2006, p 51-59.

[5] Retif, J.M., Lin-Shi, X.F., Llor, A., Arnalte, S. 2004. *New control for a synchronous machine, the hybrid control,* EPE-11th International Power Electronics and Motion Control Conference.

[6] Retif, J.M., Lin-Shi, X.F., Llor, A. 2004. *A new hybrid direct-torque control for a winding rotor synchronous machine,* PESC'2004: 35th IEEE Power Electronics Specialists Conference.

[7] Ben-Dov, D., Salcudean, S.E. 1995. *A force controlled pneumatic actuator*, IEEE Transactions on Robotics and Automation, Vol 11, Issue 6, p 906-911.

[8] Edge, K.A, Figeredo, K.R.A. 1987. *An adaptively controlled electrohydraulic servo-mechanism: Part 1: Adaptive controller design - Part 2: Implementation.* In: Proc. Instn. Mech. Engrs. Part B, Vol 201, N°3, p 175-180 and p. 181-189.

[9] Richer, E., Hurmuzulu, Y. 2000. *A high performance pneumatic force actuator system : Part I – Nonlinear Mathematical Design, Part II – Nonlinear Controller Design,* Journal of Dynamic Systems Measurement and Control, Volume 122, Issue 3, p 416-425 and p 426-434.

[10] Yamada, H., Kudomi, S., Muto, T. 2003. *Development of a pneumatic force display (application to a master slave system)*, International Journal of Fluid Power, Vol 4, n°1.

[11] Yin, Y.B., Araki, K. 1998. *Modelling and analysis of an asymmetric valve controlled single-acting cylinder of a pneumatic force control system*, SICE'98. Proceedings of the 37th SICE Annual Conference, Chiba, Japan, p 1099-1104.

[12] Morel, F., Retif, J.M., Lin-Shi, X.F., Llor, A. 2004. Fixed switching frequency hybrid control for a permanent *synchronous machine,* IEEE International Conference on Industrial Technology (ICIT'04), Tunisia.

[13] Burrows, C.R. 1972. *Fluid Power Servomechanisms*. London : Van Nostrand Reinhold Company, 237 p.
[14] Parnichkun, M., Ngaecharoenkul, C. 2001, *Kinematics control of a pneumatic system by hybrid fuzzy PID*, Mechatronics, Vol 11, Issue 8, p1001-1023
[15] Belforte, G., Mauro, S., Mattiazzo, G. 2004. *A method for increasing the dynamic performance of pneumatic servosystems with digital valves*, Mechatronics, Vol 14 Issue 10, p 1105-1120
[16] Noritsugu, T., Wada, T., Yanosaka, M. 1988. *Adaptive control of electropneumatic servo system.* In: 2nd Int. Symp. On Fluid -Control, Measurement, Mechanics and flow visualisation. Sheffield, England, p. 285-289.
[17] Brun, X., Thomasset, D., Bideaux, E. 2002. *Influence of the process design on the control strategy: application in electropneumatic field*, Control Engineering Practice, Volume 10, Issue 7, p 727-735.
[18] Bouri, M., Thomasset, D., Scavarda, S. 1996. *Integral sliding mode controller of a rotational servodrive.* Third Japan Hydraulics and Pneumatics Society, Tokyo, p 145-150.
[19] Liu, P., Dransfield, P. 1993. *Intelligent control of air servodrives using neural networks.* Proc. of Second Japan Hydraulics and Pneumatics Society, Tokyo, p. 381-399.
[20] Brun, X., Thomasset, D., Scavarda, S. 2003. *Hybrid control for switching between position and force tracking,* The Fourth International Symposium on Fluid Power Transmission and Control, Wuhan, China.
[21] Shearer, J.L. 1956. *Study of pneumatic processes in the continuous control of motion with compressed air*. Parts I and II. Trans. Am. Soc. Mech. Eng., Vol. 78, p.233-249.
[22] Andersen, B.W. 1967. *The analysis and design of pneumatic systems*. New-York : John Wiley and Sons, 302p.
[23] International Standard ISO Norm 6358 1989. *Pneumatic Fluid Power- Components Using Compressible Fluids*, Determination of Flow-rate Characteristics.

Self-Organising Maps for Monitoring Pneumatic Systems

A. Zachrison and M. Sethson
Department of Mechanical Engineering, Linköping University, Sweden

ABSTRACT

This paper presents the application of a class of neural networks; self-organising maps, SOMs, in condition monitoring of pneumatic systems for the manufacturing industry, using data from both normal and faulty cases to train the SOM. Examples of faulty cases could here be changed mass and/or leaking valves, etc. It should then be possible to categorise new measurements by running them through the SOM. The focus of the paper is on interpretation of the categorisation process. The effect on the decision of using different sets of sensors is also discussed.

1 INTRODUCTION

Condition monitoring of systems and change detection in the systems are of great importance for an automated manufacturing system. Although condition monitoring is already widely used in machinery, the need for it is growing, especially as systems become increasingly autonomous and self-controlled. One of the toughest tasks concerning embedded condition monitoring is to extract the useful information and conclusions from the often large amount of measured data. The converse, drawing conclusions from a minimum of data is also of interest. In this case, interest is at least two-fold: to reduce costs (fewer sensors) and to create redundant monitoring and analysis systems. The use of self-organising maps, SOMs, for embedded condition monitoring may be of interest for the component manufacturer who does not have information about how the component is to be used by the customer, or in what applications and load cases.

Automating monitoring and analysis means not only being able to collect prodigious amounts of measured data, but also being able to interpret the data and transform it into useful information, e.g. conclusions about the state of the system. However, as will be argued in this paper, drawing the conclusions is one thing, being able to interpret the conclusions is another, not least concerning the credibility of the conclusions drawn. This has proven to be particularly true for simple mechanical systems like pneumatics in the manufacturing industry.

Self-organising (feature) maps, SOMs, [1,2] are one way to organise and find the knowledge in vast amounts of data. This property of the SOMs can also be used for monitoring applications

Power Transmission and Motion Control 2006 Edited by Dr D N Johnston and Professor K A Edge

in a number of different ways, ranging from parameter estimation [3–5], quantisation error and forbidden area of neurons [6] to categorisation [7]. In contrast to the normal use of classification algorithms, the objective here is not only to make the decision, but rather to make a gradual classification, while retaining the SOM's visualisation property.

In the forbidden area method, the SOM is trained with both fault-free and faulty data. The faulty data is then assembled in one or more regions in the neuron lattice, which become the forbidden areas. This may be compared to support vector machines, SVMs [8], as another classifying tool. The main problem with SVMs in embedded condition monitoring is that the run-time of the SVM is not finite, as it is for to the SOM. The SOM has a finite and deterministic run-time and memory foot-print. The quantisation error method works by looking at the distance between the winning neuron and the feature vector; if this distance becomes larger than a threshold, an alarm is triggered. Kassin et al. [6], argue that the quantisation error measure is the best measure when training the SOM only on normal (non-faulty) data. In this paper, the focus is on the forbidden area of neurons method (i.e. a purely classification based method). However, the quantification error method is still useful for some cases, as will be shown later.

2 TEST SETUP

The test setup consists of a rod-less pneumatic cylinder, controlled by four on/off-valves. See figure 1 for a schematic view of the system.

The piston is controlled in an open-loop fashion, partly due to the fact that open-loop control is quite common in pneumatics, especially in the manufacturing industry. On the other hand, in the industry it is most often a fixed position control and does not use any intermediate positions, as can be found in our sequence, shown in figure 2.

The system is run using six different test cases; these are three different mass loads and (non)leaking exhaust valves. The mass loads are 0, 10 and 20 kg respectively.

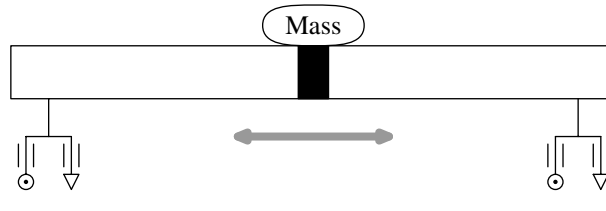

Figure 1: A schematic sketch of the test setup.

3 SELF-ORGANISING MAPS

Self-organising (feature) maps are a special kind of neural network first presented by Kohonen; see, for instance, [1,9]. The SOM was inspired by neurobiology, in particular by ideas derived from cortical maps in the brain. It has been shown in [10] that the SOM is able to explain the formation of computational maps in the primary visual cortex of the macaque monkey. As such, the SOM can still be viewed as a model of the brain.

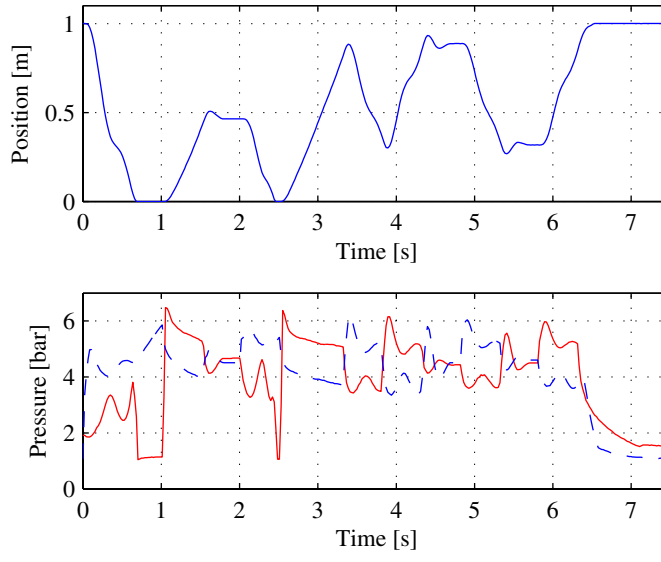

Figure 2: An example of the outcome of the used input sequence. In this example, the mass load is 10 kg and there are no leakages in the exhaust valves. The lower graph shows the two chamber pressures.

The SOM works by approximating the probability distribution of the input vectors by its neurons' weight vectors. As such, it accumulates knowledge during training and this knowledge is distributed in the same areas as the input vectors. This allows the SOM implementation to keep a record of well-known regions in the input domain, and distinguish these from unknown, novel inputs.

Kohonen et al. present an overview of the application of SOMs in engineering applications in [11]. One common use for the SOM is to categorise data. Other uses are the closely related fields of data mining and encoding/decoding. Of special interest for this work is the use of SOMs for condition monitoring. Two ways of using the SOM for condition monitoring are discussed in [6]. First, the quantisation error between the winning neuron and the feature vector could be used; second, the SOM can be trained to include a forbidden area. Other examples of condition monitoring include automated fault detection in helicopter gearboxes [12] and the use of the SOM as a categoriser in [7]. The latter is concerned with condition monitoring by using the SOM as a categoriser, and also to some extent how to handle new conditions not previously known to the SOM.

A comprehensive text on neural networks in general, also covering SOMs, is [13], where both the Willshaw–von der Malsburg and the Kohonen models are discussed. However, the Kohonen model is the one that has received most attention in the literature, and which will be used in this work. A couple of other thorough texts on SOMs are [1] and [14]. The first is one of the first attempts to produce a complete overview of the algorithms, variations and ideas behind the SOM and the closely related learning vector quantisation.

One interesting feature of the SOM, especially with Kohonen's version, is the ability to per-

form dimensional reduction. An m-dimensional input signal is mapped onto the (usually) 2-dimensional neuron lattice. This property is used, for example, to encode an m-dimensional signal, (e.g. an image), by just storing which neuron receives the hit for each signal value (in the case of a two-dimensional lattice, two coordinates need to be stored as opposites to the m values in the signal). These m values might usually also need many more bits to be encoded than the position coordinates in the lattice.

3.1 SOM algorithm

The use of the SOM can generally be divided into three phases, of which the last two are used while training the SOM. These three phases (as described by Haykin [13]) are: the competitive process, the cooperative process, and the adaptive process.

3.1.1 Competitive Process

The competitive process consists of

$$i(\vec{x}) = \arg\min_j \|\vec{x} - \vec{w}_j\|, \qquad j = 1, 2, \ldots l \tag{1}$$

where $\vec{x}$ is the training vector, $\vec{w}_j$ is the weight vector of neuron j, i is the winning neuron, and l is the number of neurons in the lattice.

3.1.2 Adaptive Process

The standard learning rule is

$$\vec{w}_j(n+1) = \vec{w}_j(n) + \eta(n) h_{j,i}(n)(\vec{x} - \vec{w}_j(n)) \tag{2}$$

where n is the stimuli iteration, $\eta(n)$ is the time-dependent learning-rate parameter and $h_{j,i}(n)$ is the neighbourhood function, normally chosen as a Gaussian function that shrinks as time passes. This will make the neurons learn fast in the beginning, when the lattice is untrained; at the same time, the neurons closer to the best matching neuron will learn more compared to the rest. The winning neuron, i, will always have $h_{j,i}(n) = h_{i,i}(n) \equiv 1$.

3.2 Structure of the used SOM

The investigated sets of features (sensor signals) for stimuli are

$$[x_p, \dot{x}_p, p_A, p_B] \tag{3}$$

$$[x_p, p_A, p_B] \tag{4}$$

$$[p_A, p_B] \tag{5}$$

i.e. different combinations of piston position, velocity and the two chamber pressures. The velocity, $\dot{x}_p$, in (3) is not directly measured but calculated.

The input vector, $\vec{x}$, (and thus also the feature vectors, $\vec{w}_j$) are composed of two parts: an independent part and a dependent part (similar divisions of the input vector ban be found in [3] and [4]). The independent part, $\vec{x}^{ind}$, is formed according to one of (3) – (5). The dependent part, $\vec{x}^{dep}$, consists of two additional features, viz. the mass load, m, and a leak indicator, $leak$. Still, only the original features are used for the competitive process (1). This

will enhance the later use of the SOM to evaluate and categorise new measurements. This gives the following notation for the input vector, $\vec{x}$, and the modified competitive process:

$$\vec{x} = \left[\vec{x}^{ind\,\mathsf{T}}, \vec{x}^{dep\,\mathsf{T}}\right]^{\mathsf{T}} \tag{6}$$

$$i(\vec{x}) = \arg\min_j \|\vec{x}^{ind} - \vec{w}_j^{ind}\|, \qquad j = 1, 2, \ldots, l \tag{7}$$

As an example, (4) becomes

$$\vec{x} = [x_p,\, p_A,\, p_B,\, m,\, leak]^{\mathsf{T}} \tag{8}$$

In order to restrain one of the input dimensions from becoming too dominant, the actual values are scaled such that the normal values are within the interval $[0, 1]$ (outliers and extremes can still be outside this interval). A perhaps better scaling would be to translate the features used to build the input vector into a common mean, for instance 0 (with no loss of generality), and thereafter scale the features to a common variance.

In the literature, it has sometimes been suggested that $\vec{x}$ should be normalised (to unit length) before use. As stated for example by Kohonen in [9], this is not necessary in principle, although there may be advantages such as improved numerical accuracy due to the input vectors then having the same dynamic range. In an application where the absolute values of different features are of interest, such as the one in [4], the normalisation might not be desirable. The proposed normalisation scheme in the previous paragraph should basically give the same advantages, while still making the features easy to interpret, the only difference being the use of constant scaling.

4 CONDITION MONITORING

4.1 Classification based condition monitoring

One way to use the SOM for condition monitoring is to look at the winning neuron. This can be done either directly, by relating the position to a fault mode (forbidden area), or by constructing a path of the winning neurons from consecutive samples and looking at deviations from the expected path. Both these variations may be described as classification processes.

When looking at the winning neuron, the additional features added in (8) as compared to (4) are used to categorise the new input vector. Thus the *leak* feature in the winning neurons weight vector is a measure of how likely it is that the exhaust valves are leaking.

Most often when the SOM is used as a classifier, the SOM is trained on the scaled, unclassified input vectors, thus creating some kind of order among them. After the initial training, each of the neurons is compared to the input vectors and classified according to a majority vote (the input vectors classifications are known). The SOM is then able to classify new input vectors, although improved classification performance is normally achieved by using "learning vector quantisation", LVQ, to further train the SOM, see for example [9] and [14]. During this process, the decision borders are adjusted to become more optimal, by moving the neurons' weight vector closer to or further away from the input vector, depending on whether they belong to the same class or not. The important decision is *which* class wins, not which neuron

within that particular class wins, i.e. only the decisions at the borders count. An example of condition monitoring using LVQs can be found in [15].

In contrast to the normal use, as stated in the previous section, the objective in this work is not only to make the decision, but rather to make a gradual classification, while still retaining the SOM's visualisation property. To achieve this, the classifications of the input vectors are appended to the training vectors and the classification parameter undergoes the same adaptation in the weight vectors as the rest of the features (although they are not part of the competition as shown in (7)). As a result, even though the leak classification of the training vectors is represented by 0/1, the neurons' classification will be somewhere in the interval $[0, 1]$. The values in between will to some extent show that this neuron was similar to training vectors from both classes, and also from which class most of the training vectors matching the neuron belong to. The neuron is thus on the border.

In figure 3 a simple illustrative example is shown of the difference between the standard LVQ-classification and the gradual SOM-classification proposed here (also used in e.g. [3, 4]). The classification from a standard LVQ is shown using triangles (which results in either faulty or non-faulty), and from the scheme proposed here using boxes. The standard classification tells the user which class is most similar to the input, while the proposed scheme also indicates how distinct the classification is. The drawback of the proposed scheme is that the classification is ambiguous, see for example neurons 5 and 6 in figure 3; do these two neurons represent faulty conditions or not? At the same time, this is exactly the property used to get the gradual classification used to indicate that something is happening in the monitored system. These intermediate classifications require the user to interpret the results.

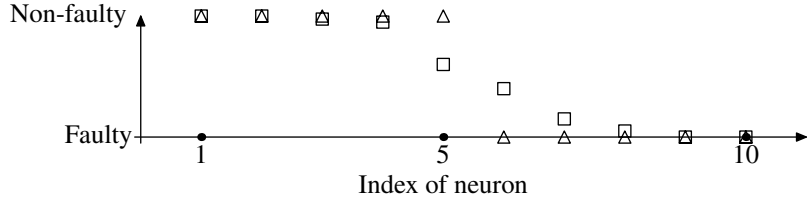

Figure 3: A fictitious example comparison of LVQ vs. the proposed SOM classification. 10 neurons are situated along the x-axis, each as classified by the LVQ is denoted by a triangle. The corresponding SOM classification according to the scheme in this work is denoted by boxes.

Feed-forward neural networks could also (although not necessarily) offer the gradual classification property, as they are normally better suited for approximation of functions. However, in contrast to these, the SOM-based method offers some advantages, in particular the possibility to visualise the clustering of the neurons. This shows what knowledge is accumulated in the SOM lattice, as well as the distribution of knowledge between different fault modes or working states. Areas with a high population of neurons indicate that a large number of quite similar training vectors have been used. To get a useful gradual classification from the feed-forward networks, training data with partial faults should be used.

4.2 Quantisation error

For a SOM trained only using data from the normal state of operations, it is argued for example in [6] that the quantisation error, q.e., is the best measure for condition monitoring. The

quantisation error (9) is the distance between the input vector and the winning neuron in the feature space.

$$\text{q.e.} = \|\vec{x} - \vec{w}_i\| \tag{9}$$

This measure is calculated using only the known features, i.e. without the added information in, for example, (8), m and $leak$ (just like in the modified competitive process (7)).

The basic idea here is that in a highly excited area of the lattice, the weight vectors of the neurons will be similar and thus an input vector matching one of those neurons should only be a small distance away, $\|\vec{x} - \vec{w}_i\|$, in the feature space. In the rarely visited areas of the lattice, the neurons are further apart, which in turn results in matches even though the input vectors are further away from the winning neuron in the feature space.

Although this measure was originally intended for the case stated above (a SOM trained using only normal state data), it is nonetheless of interest when the SOM is trained using not only normal state data, but also data from fault modes. In this case, the q.e. will be small also in the case of the fault mode known to the SOM. New conditions (fault modes unknown) will, however, result in a large q.e.: the SOM thus carries the valuable knowledge that the system has reached a new situation/state.

5 RESULTS

5.1 SOM and test data

The SOM is trained using a set of training vectors that consists of 100 data sequences (95%) from the normal state (10 kg and no leak) and 5 sequences (5% of the total training set) from test runs with 10 kg mass load and leaking exhaust valves. Each sequence consists of 340 samples, thus resulting in a total training set of 35,700 training points. Only the features in (3) to (5) are used to find the winning neuron, i.e. the additional features m and $leak$ are not used in the matching process. The same is true when calculating the q.e.

The training of the SOM is performed by choosing a random training point for each training round. Then the algorithm in section 3.1 is used and the neurons are modified according to (2). The number of training rounds used for the different SOMs are shown in table 1. Worth noting is that the SOMs based on the small and medium sized feature vectors are trained considerably less than what the rule of thumb in [13] says (i.e. ~ 500 training rounds/neuron).

Table 1: Training of the SOM.

Feature vector set	Training rounds
Large, (3)	600,000
Medium, (4)	200,000
Small, (5)	200,000

The test (validation) data used is two new measurements of the normal case (10 kg mass load and no leak), one set with 10 kg and leaking exhaust valves, and finally one set with 20 kg and no leak. These four sets are combined into one large sequence used for test purposes in the rest of this section. In the figures showing the combined data set, vertical dashed lines indicate when one set transforms into the next set. The first half of the graphs, see for example

figure 4, (the first two sequences) is valid for the normal state of the system, see figure 2 for an example of what these look like. In the third quarter, the normal mass load is used, but the exhaust valves are leaking. In the last quarter, the mass load is almost doubled.

5.2 Leak indicator

After matching each data point in the test set against the neurons in the SOM, the leak indicator in the weight vector of the winning neuron can be studied, and the graphs in figure 4 can be constructed. As can be seen here, it is fairly easy to determine whether the exhaust valves are leaking or not.

Initial tests, comparing the classification scheme proposed in 4.1 to LVQ 1, do not indicate any improvement from using the LVQ 1 algorithm.

5.3 Quantisation error

The quantisation error for the combined sequence is shown in figure 5. As can be seen, in the part of the sequence with the normal state, the q.e. is, as expected, quite small. The same is true for the third quarter, as the SOM is also trained on this fault mode. Although there are some spikes and short periods with a high q.e. during the third part, the differences between the first three parts are small, indicating that the SOM has modelled the system/sequence quite well. The spikes are examples of condition that the SOM lacks knowledge about; this is caused by only 5% of the training data being from the leak condition. The last quarter represents a fault mode unknown to the SOM, which results in a large increase in the q.e. It is therefore apparent that the SOM has no previous corresponding knowledge of this system state.

5.4 A tour of the lattice

Similar conclusions (especially like the one from figure 4(b)) can be drawn by looking at the path created by the winning neuron throughout one cycle. In figure 6, the paths created by four different measurement are shown. When comparing the leaking valves case 6(c) to the normal state cases 6(a) and 6(b), the difference is obvious. The left side of the SOM lattice represents the leaking exhaust valves fault mode. Occasionally, the trajectory from the leaking case goes into the normal state region (c.f. the missed detections in figure 4). These occurrences describe system states where there is no difference between the faulty state and the normal state, e.g. starting and end points and some turning points.

5.5 Visualisation of the feature space

In figure 7, the feature space for the SOM trained using the three features in (4) is shown. To construct the graph, two thresholds for the *leak*-feature are chosen. The neuron is assumed to represent the normal state of the system if $leak \leq 0.2$ and the leakage state if $leak \geq 0.7$. The two states are represented by dots and asterisks respectively. The undecided neurons in between are shown by rings.

As expected, the large number of neurons represents the non-faulty normal state. In fact, only 1.37% of the neurons represent the leaking state and the leaking + undecided neurons make up 5.37% of the total SOM lattice. These figures are naturally strongly dependent on the decision levels for the *leak* feature, which was arbitrarily chosen here. Judging from figure 4, especially figure 4(b), both levels could be lowered without increasing the false alarm rate.

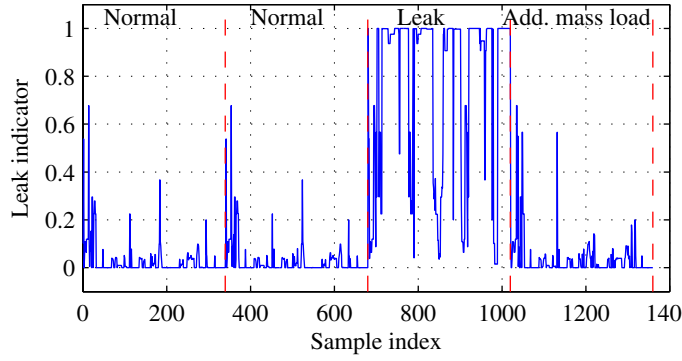

(a) The SOM build on the large feature vector (3).

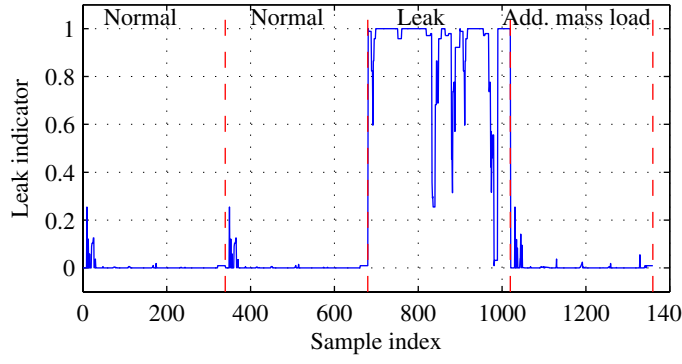

(b) The SOM build on the medium sized feature vector (4).

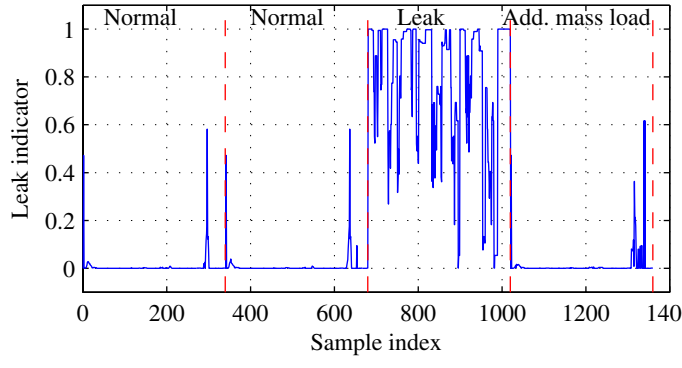

(c) The SOM build on the small feature vector (5).

Figure 4: The leak indicator from the SOM. A 0 denotes the normal state and 1 indicates leakages in both exhaust valves. The first two parts correspond to the normal state of the system. The third part has leaking exhaust valves and the final part has an increased mass load ($m = 20\,\mathrm{kg}$).

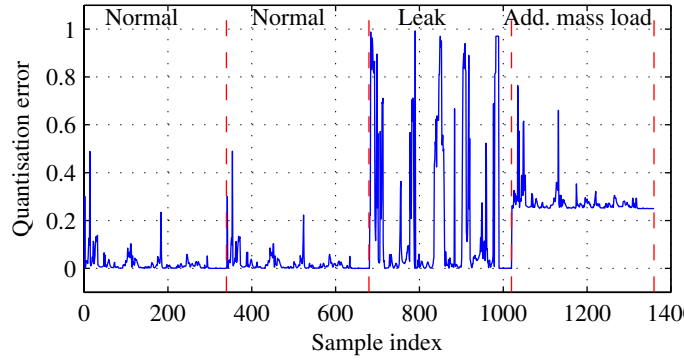

(a) The SOM build on the large feature vector (3).

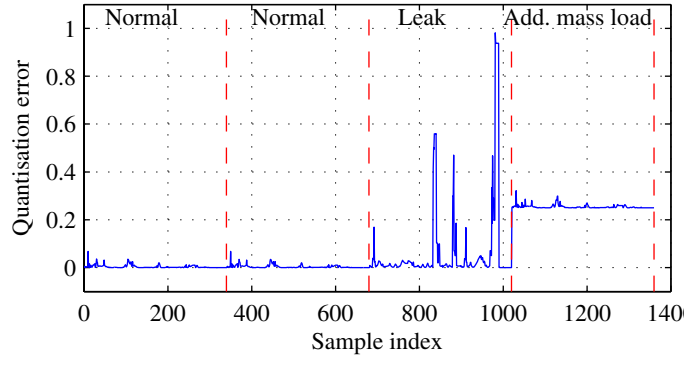

(b) The SOM build on the medium sized feature vector (4).

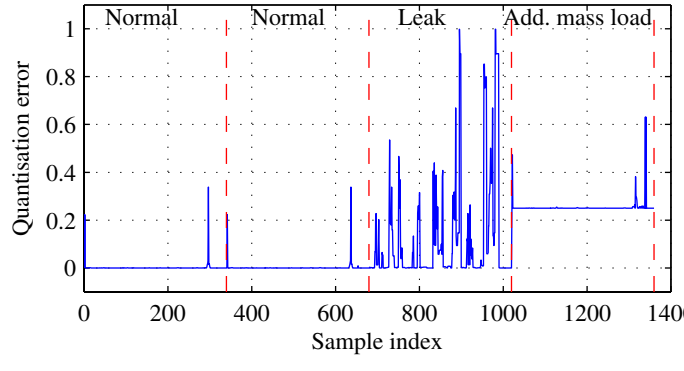

(c) The SOM build on the small feature vector (5).

Figure 5: The quantisation error for a sequence combined from four measurements (divided by vertical dotted lines). The first two parts correspond to the normal state of the system. The third part has leaking exhaust valves and the final part has an increased mass load ($m = 20$ kg).

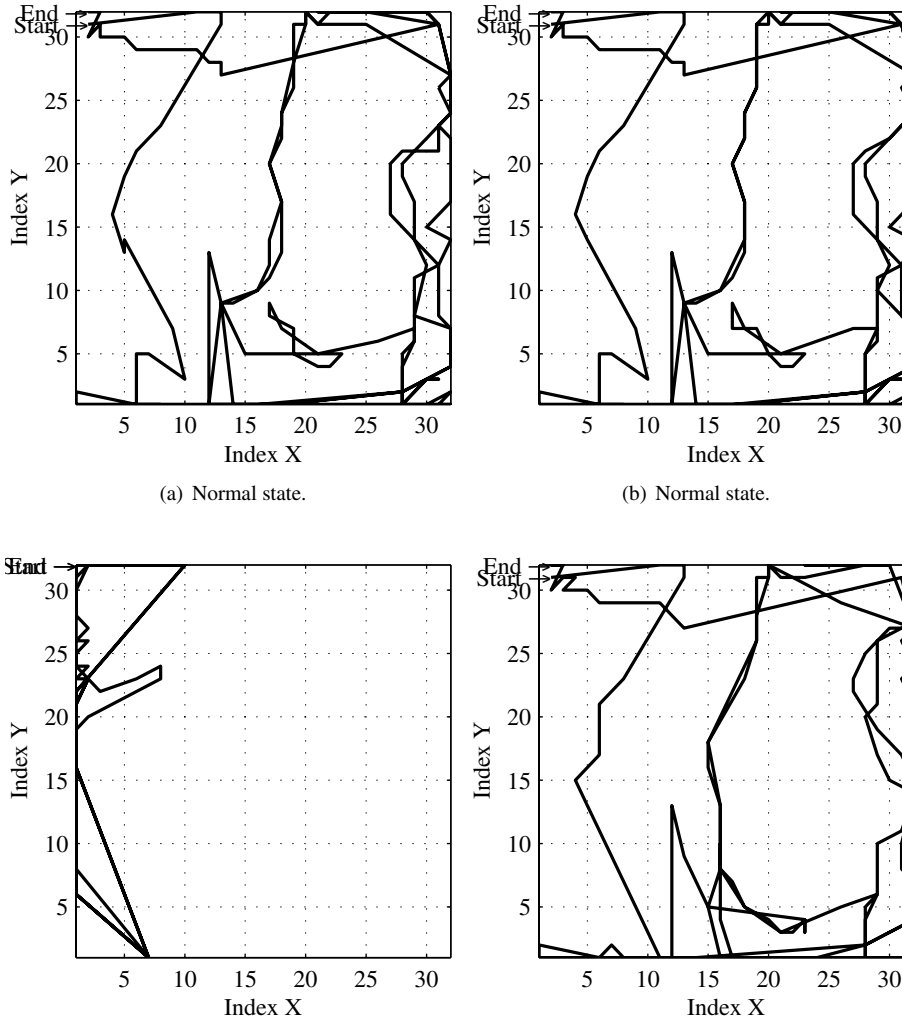

(a) Normal state.

(b) Normal state.

(c) Leaking exhaust valves.

(d) Additional mass load.

Figure 6: The trajectory created by the winning neuron in the SOM lattice.

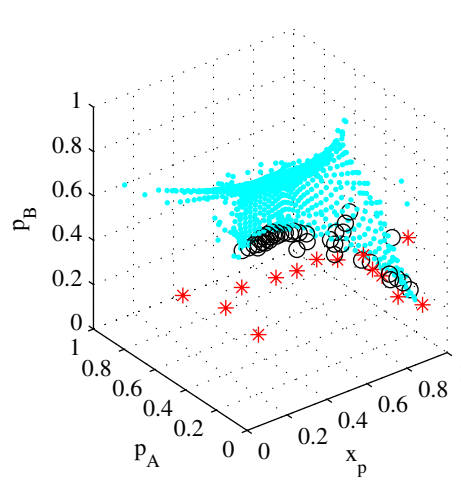

(a) 3D-view of the feature space.

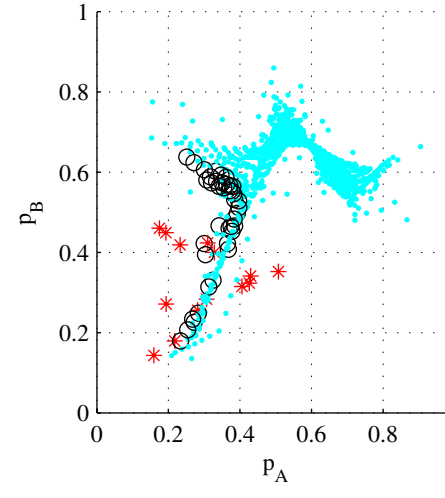

(b) A view of the two pressure features.

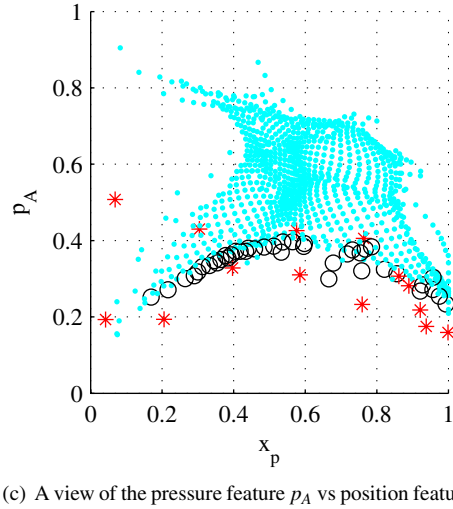

(c) A view of the pressure feature p_A vs position feature x_p.

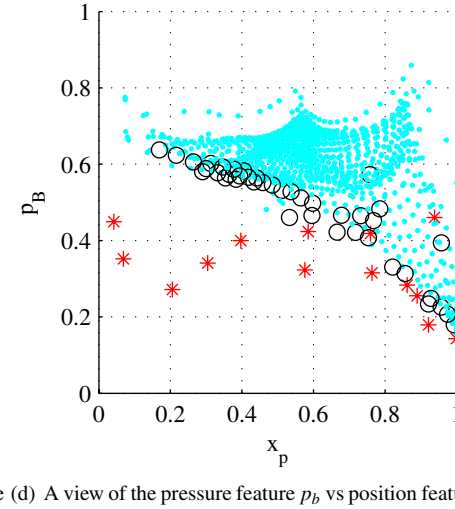

(d) A view of the pressure feature p_b vs position feature x_p.

Figure 7: Visualisation of the SOM features. Note that this is in the feature space, i.e. all parameters (p_A, p_B, and x_p) are normalised to the interval $[0,1]$. The dots represent the neurons whose feature vectors are classified as representing non-leaking conditions, i.e. the feature $leak \leq 0.2$. The asterisks are classified as leaking conditions, $leak \geq 0.7$. The rings are in between, i.e. $0.2 < leak < 0.7$.

6 DISCUSSION

The results from figures 4(b) and 5(b) are easily interpreted. However, the characterisation is not distinct for either the known or the unknown fault.

Probably the most common way to use SOMs for condition monitoring is to extract features (e.g. rise times, settling times, oscillatory frequencies, positions, and pressures at certain times etc.) from a sequence of measurements and feed these to the SOM. An advantage of this procedure is that the SOM lattice can normally be made smaller. In this work, the raw measurements are instead fed directly to the SOM to continuously produce a diagnosis/statement. As a consequence, the statements become somewhat noisier as compared to using certain derived features/statistics. On the other hand, this system is more flexible. However, a more-fine grained output is possible (using e.g. the classification scheme proposed in section 4.1).

When incorporating the classification in the dependent part of the feature vector, $\vec{w}^{dep}$, non-pure classifications will be returned for some input vectors. These input vectors represent states in between the normal state and the leaking exhaust valves state, i.e. a smaller leakage. When using the more traditional variations of the SOM and LVQ algorithms for classification, in order to be able to classify an input as a deteriorating valve (here a smaller leakage, possibly increasing), the lattice has to be trained using not only normal and faulty data, but also using "half"-faulty data. Simulation techniques may be of interest in such a study. Previous work in this project has related to this, [16]. This allows the stepwise identification of the degree of a fault, as in [15]. Using the proposed scheme, it is not possible to directly draw a conclusion of e.g. 25% leakage; on the other hand, the identification of intermediate faults comes naturally.

An interesting observation is that under the conditions used (the sequence, the sensors etc.), the best results are achieved using a feature vector consisting of x_p, p_A, and p_B. In other words, for the condition monitoring case studied here, a quasi-static model produces the best results.

7 CONCLUSION

Self-organised maps used as a technique for condition monitoring of pneumatic systems have been investigated using a pneumatic cylinder as the experimental test bench. One on the main differences between this work and several others using SOMs for condition monitoring, is that specific features are often identified and fed to the SOM, while the measurements here are directly and continuously fed to the SOM. Advantages and disadvantages of this are discussed.

The properties of the SOM that allow identification of known faults and detection of unknown faults/disturbances are also discussed and exemplified. The SOM trained to detect leaking valves also proved to be capable of detecting a changed mass load.

REFERENCES

[1] T Kohonen. *Self-Organization and Associative Memory*. Springer-Verlag, Berlin, 1984.
[2] T Kohonen. The self-organizing map. *Neurocomputing*, 21(1-3):1–6, 1998.

[3] F Schütte, S Beineke, H Grotstollen, N Fröhleke, U Witkowski, U Rückert, and S Rüping. Structure- and parameter identification for a two-mass system with backlash and friction using a self-organizing map. In *Proceedings of 7th European Conference on Power Electronics and Applications*, volume 3, pages 358–63, Trondheim, Norway, September 1997. Eur. Power Electron. & Drives Assoc., EPE Assoc., Brussels, Belgium.

[4] A Zachrison and M Sethson. Self-organising maps for illustration of friction in a pneumatic cylinder. In *The Ninth Scandinavian International Conference on Fluid Power, SICFP'05*, Linköping, Sweden, June 2005. Linköpings universitet.

[5] A Zachrison. *Selection Schemes and Neural Networks in Adaptive Real-Time Control – Predictive Simulation Adaptive Control*. Linköping Studies in Science and Technology. Thesis No. 1187, Linköpings universitet, Linköping, Sweden, September 2005. ISBN: 91-85457-11-6.

[6] M Kasslin, J Kangas, and O Simula. Process state monitoring using self-organizing maps. In I Aleksander and J Taylor, editors, *Artificial Neural Networks 2: Proceedings of the 1992 International Conference (ICANN-92)*, volume 2, pages 1531–4, Brighton, UK, September 1992. Elsevier, Amsterdam, Netherlands.

[7] V E Lumme. Distributed knowledge in automated remote monitoring. In O P Shrivastav, B Al-Najjar, and R B K N Rao, editors, *Proceedings of COMADEM-2003*, pages 209–18, Växjö, Sweden, August 2003.

[8] L Wang, editor. *Support Vector Machines: Theory and Applications*, volume 177 of *Studies in Fuzziness and Soft Computing*. Springer-Verlag Berlin Heidelberg New York, 2005.

[9] T Kohonen. The self-organizing map. *Proceedings of the IEEE*, 78(9):1464–80, September 1990.

[10] E Erwin, K Obermayer, and K Schulten. Models of orientation and ocular dominance columns in the visual cortex: A critical comparison. *Neural Computation*, 7:425–68, 1995.

[11] T Kohonen, E Oja, O Simula, A Visa, and J Kangas. Engineering applications of the self-organizing map. *Proceedings of the IEEE*, 84(10):1359–84, October 1996.

[12] L B Jack, M L D Wong, and A K Nandi. Modified Kohonen self organising map for automated fault detection in helicopter gearboxes. In O P Shrivastav, B Al-Najjar, and R B K N Rao, editors, *Proceedings of COMADEM-2003*, pages 591–600, Växjö, Sweden, August 2003.

[13] S Haykin. *Neural Networks: A Comprehensive Foundation (2nd. ed.)*. Prentice Hall, Upper Saddle River, NJ, 1999.

[14] T Kohonen. *Self-Organizing Maps*, volume 30 of *Springer Series in Information Sciences*. Springer-Verlag Berlin Heidelberg New York, 3rd edition, 2001.

[15] H Marzi. Real-time fault detection and isolation in industrial machines using learning vector quantization. *Proceedings of the Institution of Mechanical Engineers, Part B: Journal of Engineering Manufacture*, 218(8):949–959, 2004.

[16] A Zachrison and M Sethson. Simulation and selection schemes in machine self-awareness, a position control case study. In C R Burrows, K A Edge, and D N Johnston, editors, *Power Transmission and Motion Control 2004*, Power Transmission and Motion Control, pages 187–200. University of Bath, Professional Engineering Publishing, September 2004.

Return to Contents

Pneumatic servovalve models using artificial neural networks

J. Falcão Carneiro [a,b] **F. Gomes de Almeida** [a,b]
[a]Departamento de Engenharia Mecânica e Gestão Industrial da
Faculdade de Engenharia da Universidade do Porto
Rua Dr. Roberto Frias 4200-465 Porto Portugal.
[b]Instituto de Engenharia Mecânica, IDMEC, Pólo FEUP, Portugal

ABSTRACT

This paper presents a study where static models of the flow stage of a 3/2 pneumatic servovalve are obtained using artificial neural networks. For simulation purposes, a direct model is proposed in which the mass flow is determined for a given working pressure and control input. For control purposes, an inverse model is proposed in which the command input is determined given the working pressure and the desired mass flow. This approach enables the use of mass flow as the synthesised control action, thus rendering the overall pneumatic system affine. Therefore, control techniques requiring this condition on the system model can be directly used.

Under normal working conditions, both servovalve models provide an excellent agreement with experimental results taken from an industrial pneumatic servovalve. The direct model has a maximum error of 1.25% of the nominal mass flow (NMF). When the output of the inverse model is applied to the servovalve to achieve a desired mass flow, the error obtained has a maximum value of 1.3% NMF. Furthermore, the pressure gain curves of the direct and inverse models have a maximum error of, respectively, 2.44% and 1.72% of the supply pressure.

1. INTRODUCTION

Servopneumatic control complexity is mostly due to air compressibility, piston friction and non-linear behaviour of servovalves. Classical control theory is unable to cope with these features when high performance positioning tasks are required. In this paper we propose models for 3/2 pneumatic servovalves, one of the highly nonlinear elements of a servopneumatic system, for simulation and control purposes.

Power Transmission and Motion Control 2006 Edited by Dr D N Johnston and Professor K A Edge

The most common servovalve model found in literature neglects the servovalve dynamics and considers the orifices area to change linearly with the command input [1],[2],[3]. Neglecting the servovalve dynamics is a widely accepted assumption since it is typically much faster than the actuator dynamics. However, the assumption that the orifices area varies linearly with the command input can lead to important modelling errors near the spool central position [4].

Besides simplicity reasons, there is a more important motivation to consider the orifice area to vary linearly with the command input: this assumption makes the system affine in the control action, thus rendering it in a suitable form to apply advanced nonlinear control techniques like sliding mode control or nonlinear state feedback.

As far as the authors' knowledge goes, the main work developed to obtain a servovalve model that is simultaneously affine and does not assume a linear area variation is the one presented in [4],[5] and [6]. In these studies, a fictitious area $A^*(u)$ is used in order to put the system in an affine form. The controller can then be synthesized in order to generate $A^*(u)$ and the control action u can be obtained by inverting the function $A^*(u)$.

The approach followed in the present study uses artificial neural networks to model the servovalve. Neural networks have been successfully used in system identification and control tasks during the last decade [7],[8], but their use on pneumatic servovalves, as far as the authors' knowledge goes, hasn't been reported. In this work two models of 3/2 pneumatic servovalves are developed. The first one, intended for simulation purposes, is a direct model: given the working pressure and the command input, it returns the mass flow passing through the valve. The second one, intended for control purposes, is an inverse model: given the working pressure and the desired mass flow, it returns the command input that achieves the desired mass flow. The inverse model allows the system to be put in affine form and therefore advanced nonlinear control techniques requiring this condition can be used.

This paper is organised as follows. Section 2 presents an overview analysis of a servopneumatic system, followed by a short literature review on servovalve models. This section ends by presenting the modelling approach followed in this paper. Section 3 describes the experimental setup and procedure used to collect data from an industrial pneumatic servovalve. Section 4 presents the direct and inverse models obtained from that data. Section 5 will draw the main conclusions.

2. MODELLING PNEUMATIC SERVOVALVES

2.1 Introduction

Consider the pneumatic servosystem represented in Fig. 1, composed by a pneumatic cylinder moving a load M and two 3/2 servovalves that modulate the amount of air entering the cylinder. M is the actuator plus moving parts mass, F_{ext} represents all external and friction forces acting on the piston, $x, \dot{x}, \ddot{x}$ are the position, velocity and acceleration of the load. $P_{\text{A,B}}$, $T_{\text{A,B}}$ and $A_{\text{A,B}}$ are the pressure, temperature and piston areas of chambers A and B, respectively.

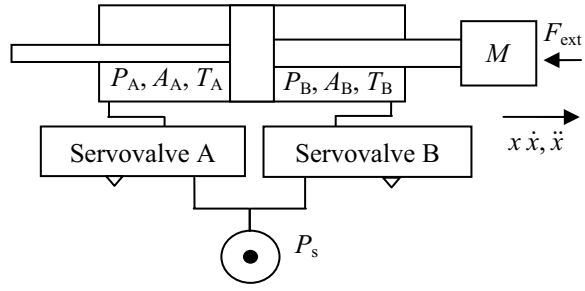

Fig. 1 Pneumatic servosystem

The analysis of the mathematical model of this system reveals three main blocks (see Fig.2): the servovalves, the actuator chambers and the motion model. In Fig. 2 $u_{A,B}$ and $\dot{m}_{A,B}$ are the command input and mass flow into chambers A and B, respectively.

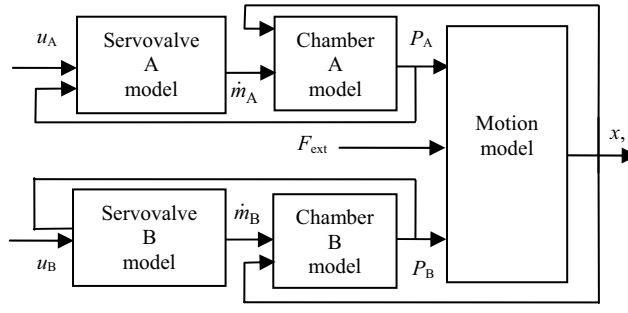

Fig. 2 Block models of a pneumatic system controlled with two 3/2 servovalves

The temperature dynamics in each chamber is typically neglected and a polytropic evolution of temperature is usually considered [1],[2],[3],[4],[5],[9],[10]. Under these assumptions, the pressure dynamics of each chamber may be generically given by

$$\dot{P}_{A,B} = f_1(P_{A,B}, x, \dot{x}, T_{amb}) + f_2(P_{A,B}, x, T_{amb})\dot{m}_{A,B} \tag{1}$$

where the functions f_1 and f_2 are dependent on the particular polytropic process adopted and T_{amb} is the ambient temperature. The motion dynamics can be obtained by applying Newton's second law:

$$M\ddot{x} = P_A A_A - P_B A_B - F_{ext} \tag{2}$$

Although the motion and thermodynamic models presented are quite generic, they suit the goals of the present work. The reader is referred to [9],[11] for further details.

2.2 Servovalve models

Consider the 3/2 servovalve represented in Fig. 3. Port A is connected to the cylinder, port S to the pressure source and port M to atmosphere. x_v is the spool position.

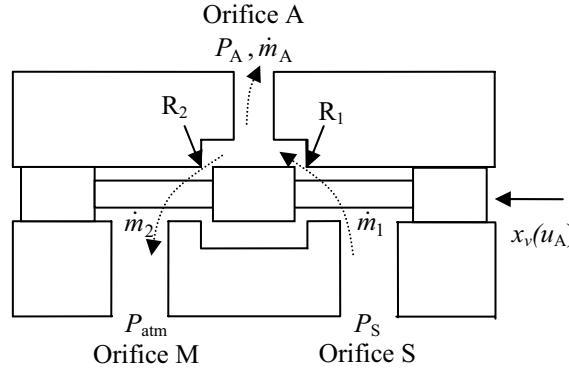

Fig. 3 Schematic representation of a 3/2 servovalve

The mass flow crossing orifice A in Fig. 3 can be determined by subtracting the mass flow crossing restriction R_2 ($\dot{m}_2$) from the mass flow crossing restriction R_1 ($\dot{m}_1$):

$$\dot{m}_A = \dot{m}_1 - \dot{m}_2 \tag{3}$$

The mass flow crossing each restriction R_i is based on the flow laws of an ideal throat (see Fig. 4) and is given by [11]:

$$\dot{m}_i(u, P_{ui}, P_{di}, T_{ui}) = \frac{C_{di} A_i(u) P_{ui} \sqrt{2}}{(RT_{ui})^{1/2}} Y\left(\frac{P_{di}}{P_{ui}}\right) \tag{4}$$

where

$$Y\left(\frac{P_{di}}{P_{ui}}\right) = \begin{cases} \left(\frac{\gamma}{(\gamma-1)}\left(\frac{P_{di}}{P_{ui}}\right)^{2/\gamma} - \left(\frac{P_{di}}{P_{ui}}\right)^{\frac{\gamma+1}{\gamma}}\right)^{1/2} & \text{if } \frac{P_{di}}{P_{ui}} > r \\ \left(\frac{2}{\gamma+1}\right)^{1/(\gamma-1)} \sqrt{\frac{\gamma}{\gamma+1}} & \text{if } \frac{P_{di}}{P_{ui}} \le r \end{cases} \tag{5}$$

In equations (4) and (5), u is the command input applied to the spool, P_{ui}, P_{di}, T_{ui} and $A_i(u)$ are defined for each restriction i (i=1,2) in the ideal throat of Fig. 4, C_{di} is the discharge coefficient of restriction i, R is the air perfect gas constant and r is the critical pressure ratio given by $r = (2/(\gamma+1))^{\gamma/(\gamma-1)} = 0.528$ for air.

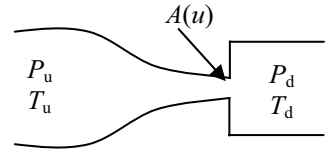

Fig. 4 Ideal Throat

Equations (4) and (5) for each restriction can now be substituted in (3). Noticing that $P_{d1}=P_{u2}=P_A$, $P_{u1}=P_S$, $P_{d2}=P_{atm}$, assuming that the variations of the cylinder chambers temperature with respect to ambient temperature are negligible [1],[2],[4],[5],[9] and accepting that the pressure source is at ambient temperature ($T_{u2}=T_{u1}=T_{amb}$), the mass flow through port A can be written as:

$$\dot{m}_A = \sqrt{\frac{2}{T_{amb}R}}\left(C_{d1}A_1(u_A)P_S Y\left(\frac{P_A}{P_S}\right) - C_{d2}A_2(u_A)P_A Y\left(\frac{P_{atm}}{P_A}\right) \right) \tag{6}$$

Equation (6) clearly highlights the nonlinear relation between the command input u_A and the mass flow at orifice A. Furthermore, it is not possible to make the command input to appear linearly in this equation and therefore the relation between the controlled variable (either force or motion) and the command input cannot be put in an affine form. However, advanced nonlinear control techniques like sliding mode control or nonlinear state feedback control usually require an affine form of the model.

This problem came across in [9], where a complex nonlinear dynamic model of a pneumatic servovalve is presented. Although the servovalve used in that study was a 5/2 valve, the overall concept can be applied to 3/2 servovalves. When using this model for force control in [10], the control synthesis was done in order to generate $A_1(x_v)$ and $A_2(-x_v)$. As it was assumed that $A_1A_2=0$ (see Fig. 5), and since the particular controller structure provided a physical understanding of when should $A_1(x_v)$ and $A_2(-x_v)$ be different from zero, it was possible to synthesise a control law in order either to generate $A_1(x_v)$ or to generate $A_2(-x_v)$. The control action was then found by inverting the function A_1 or A_2 using fractional power series.

The most typical solution found in literature is, however, to neglect servovalve dynamics and consider that the area of each restriction varies linearly with the command input. Fig. 6 represents this linear relation: restriction R_1 area is assumed to vary in direct proportion with the command input for $u>u_c$ and to have a constant (leakage) value A_L for $u<u_c$. The same line of thought applies to R_2, leading to equation (7). Furthermore, the area function is assumed to be symmetric around the misalignment u_c of the valve central position.

$$A_1(u) = \begin{cases} k(u-u_c) + A_L & \text{if } u > u_c \\ A_L & \text{if } u < u_c \end{cases} \qquad A_2(u) = \begin{cases} A_L & \text{if } u > u_c \\ -k(u-u_c) + A_L & \text{if } u < u_c \end{cases} \tag{7}$$

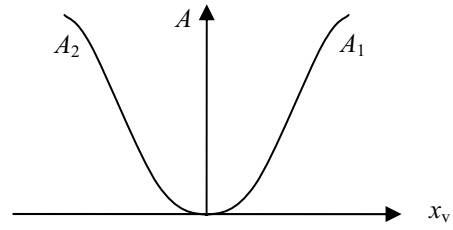

Fig. 5 Area versus control action: $A_1(x_v)A_2(-x_v)=0$;

Replacing equation (7) on (6) and noticing that at normal working conditions $P_{u1}=P_S$, $P_{d2}=P_{atm}$ and $P_{u2}=P_{d1}=P_A$ the mass flow at orifice A can be written as:

$$\dot{m}_A = D_1(P_S, P_A)u_A + D_2(P_S, P_A, A_L, u_c) \tag{8}$$

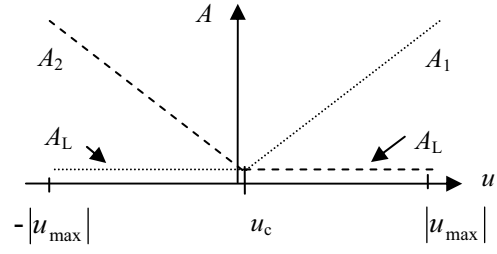

Fig. 6 Area versus control action: linear relation

In [2] the servovalve model was based in the approach given by (8) with $u_c=0$. Also in [1] and [3] the valve area is considered to vary in direct proportion to the control input, with $A_L=0$ and $u_c=0$.

Although having the advantage of being simple, this approach fails to provide an accurate model for small spool displacements near the central position. In fact, near the central position the leakage between spool and sleeve causes a nonlinear relation between input command and valve area [4],[9]. Since the servovalve model accuracy in this zone is very important for the static positioning error, it is desirable to obtain models that do not assume a linear area function.

An approach where the linear assumption is not used can be found in the works of Richard [4],[5]. Based on (6) the model of the mass flow leaving the servovalve and entering chamber A can be expressed as:

$$\dot{m}_A(u, P_A) = A_1(u)D_3(P_s, P_A) - A_2(u)D_3(P_A, P_{atm}) \tag{9}$$

Richard uses a nonlinear state feedback technique that requires an affine form of the control variable. In order to achieve it, Richard introduces a fictitious input $A^*(u)$ obtained by decomposing the area of each restriction into constant leakage areas A_{L1} and A_{L2} and a variable area $A^*(u)$ (Fig. 7):

$$A_1(u) = \begin{cases} A^*(u) + A_{L1} & \text{if } u > u_c \\ A_{L1} & \text{if } u < u_c \end{cases} \qquad A_2(u) = \begin{cases} A_{L2} & \text{if } u > u_c \\ -A^*(u) + A_{L2} & \text{if } u < u_c \end{cases} \tag{10}$$

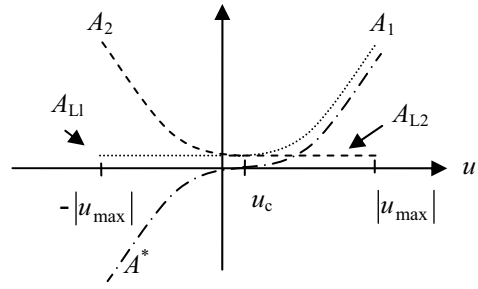

Fig. 7 Fictitious area definition

Substituting A_1 and A_2 given by (10) on (9) and assuming that $A_{L1}=A_{L2}=A_L$ leads to:

$$\dot{m}_A(u, P_A) = \dot{m}_{LA}(P_A) + \varphi(P_A, sign(A^*(u)))A^*(u) \tag{11}$$

where $\dot{m}_{LA}$ and φ can be deduced from experimental data. Since in expression (11) the mass flow is in affine form, the controller can be synthesized in order to generate $A^*(u)$. The real control variable u is found by inverting the function $A^*(u)$. One of the studies presented in [6] is also based in model (11). However, while in [4] the experimental data was collected restriction by restriction, in this study the experimental data was directly collected in port A of the valve. This approach is more generic than the previous ones since it does not impose a linear variation of the area and does not depend on a particular controller structure. However, it imposes a leakage area independent of the command input, and imposes several restrictions on the properties of $A^*(u)$, namely that it has to be invertible.

2.3 Proposed approach: direct and inverse models

Equation (6) shows that it is possible to establish a relation between the flow mass in outlet A, the pressure of chamber A and the command input applied to the spool. Equation (6) can be written for a given supply pressure as:

$$\dot{m}_A = f_A(u_A, P_A) \tag{12}$$

The knowledge of f_A therefore establishes a direct model of the servovalve: given the working pressure P_A and the command input u_A, the mass flow crossing orifice A can be determined. This was one of the approaches followed in [6], where f_A was approximated using polynomials. On the other hand, for a given pressure P_A, the function f_A^{-1} defined in (13) must exist since the relation between u and $\dot{m}_A$ is one-to-one.

$$u_A = f_A^{-1}(\dot{m}_A, P_A) \tag{13}$$

The knowledge of f_A^{-1} allows the use of equation (13) to determine an inverse model of the servovalve: the controller of the system provides a desired mass flow and given the working pressure P_A, the inverse model delivers u_A so that $\dot{m}_A$ is achieved. In this work neural networks are used to approximate f_A and f_A^{-1}. The next section describes the procedure used to obtain the experimental data for network training.

3. EXPERIMENTAL SETUP

3.1 Flow and pressure gain measurements

The servovalve tested in this work is a FESTO MPYE-5-1/8-HF-010-B with a nominal mass flow (NMF) of 700 slpm[1]. Although this is a 5/2 valve, two orifices were blocked in order to reproduce a 3/2 behaviour. The command input varies between 0 V – restriction R_2 fully opened – and 10V – restriction R_2 fully closed (see Fig. 3).

Each restriction was characterized individually according to its normal functioning at working conditions: for restriction R_1 the upstream pressure was held constant while varying the downstream pressure and for restriction R_2, the upstream pressure was varied while keeping the downstream pressure constant at atmospheric pressure. In both situations the mass flow was measured for different pressures and command inputs. The pressure steps were 0.5 bar, from $P=P_{atm}$ to $P=P_S$. The command input steps were 5% of the full scale value (FS) for $u \subset [0,4[\,\text{V}$ and $u \subset]6,10]\,\text{V}$ and 1%FS for $u \subset [4,6]\,\text{V}$. Pressure drops in flow meters are lower than 0.1 bar and were therefore neglected. Whenever necessary, leakage flows were compensated. Finally, an important feature of a servovalve is its pressure gain with zero mass flow. In fact, around equilibrium positions, the servovalve is required to operate near the central position of the spool. In this situation, a small change in the spool position leads to a high change in pressure. Therefore, it is vital to correctly capture this feature in order to achieve good modelling results.

3.2 Fitting ISO 6358 curves to experimental data

The experimental values obtained for each restriction were post processed by fitting, in a least squares sense, the ISO 6358 equation [12]:

$$\dot{m} = CP_u\rho_0\sqrt{\frac{293.15}{T_u}}\begin{cases}1 & \text{if } P_d/P_u \le b\\ \sqrt{1-\left(\dfrac{P_d/P_u - b}{1-b}\right)^2} & \text{if } P_d/P_u > b\end{cases} \tag{14}$$

In this equation C is the sonic conductance and b is the effective critical pressure ratio. The use of (14) to fit experimental results has several advantages. First, the P_A values in R_1 and R_2 measurements must be the same in order to apply (3). Experimental differences can therefore be corrected using equation (14). Second, the supply pressure suffered small deviations during measurements whose effects can be removed using (14). Third, since the maximum mass flow provided by the pressure source was 700 slpm, mass flows over that

[1] Although the unit for mass flow is kg/s in all equations, the more intuitive unit standard litres per minute at 0ºC and 1.01325×10^5Pa (slpm) is used whenever referring to experimental results/flow capacities.

value had to be estimated. Equation (14) is a robust way to perform such estimation. The *C* and *b* values obtained using this approach are presented in Fig. 8. A comparison between real data and the one given by (14) for both restrictions is presented in Fig. 9.

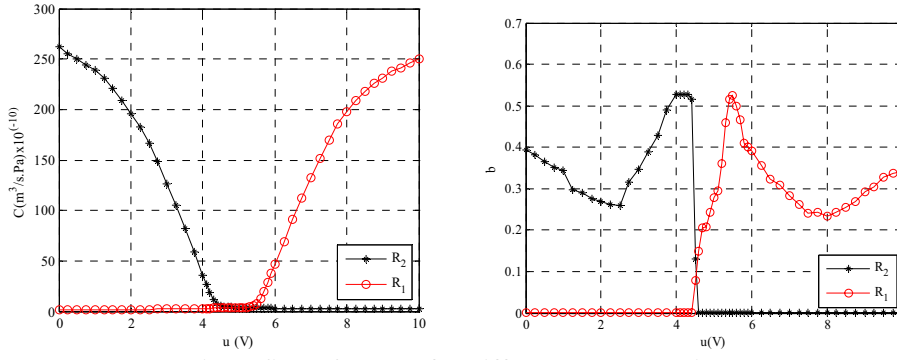

Fig. 8 *C* and *b* values for different command inputs

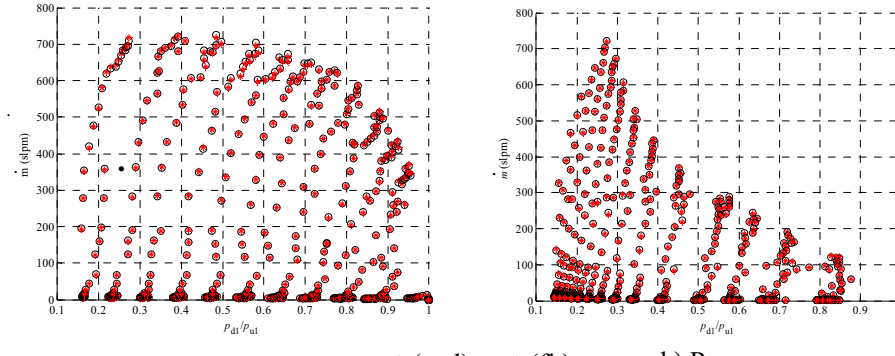

a) R_1 o $\dot{m}$ (real) * $\dot{m}$ (fit) b) R_2

Fig. 9 Fitting ISO 6358 on experimental data

3.3 Data set for neural network training and validation

The dataset obtained using the procedure presented above was used for neural network training and validation purposes. Fig. 10 presents the global static characteristics of the servovalve, represented by the surface $\dot{m}_A = f_A(u_A, P_A)$. The mass flow surface is represented in light grey and the pressure gain curve in black. This is the reference surface that both direct and inverse models must reproduce.

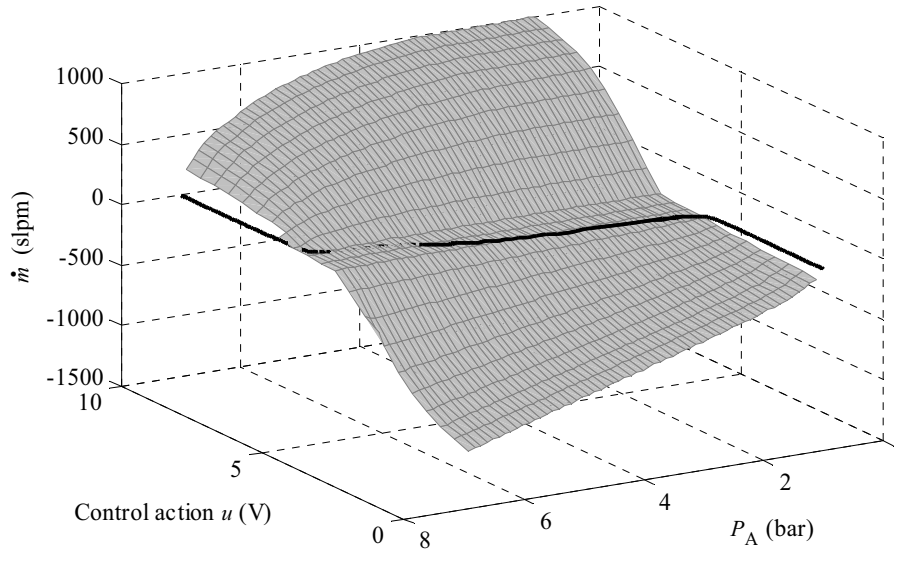

Fig. 10 Global static characteristics of the FESTO servovalve

4 NEURAL NETWORK SERVOVALVE MODELS

4.1 Short introduction on artificial neural networks

Artificial neural networks (ANN) appeared in the last two decades as a powerful tool for both function approximation and classification tasks. A neural network is an interconnected set of simple processing elements called neurons that implement a function over a weighted sum of its inputs. Each input to the neuron can be either an external input or an input from a previous neuron. The most common combination of neurons is the multilayer perceptron (MLP) network, built by grouping up the neurons in layers. The inputs of each neuron in each layer are either the output of the neurons in the previous layers or an external input. The procedure for selecting the parameters (weights) of the network that best approximates the desired input/output relation is known as network training. The training algorithm used in this work is the Levenberg-Marquardt (LM) due to its good robustness and convergence proprieties. The reader is referred to [8] for further details on ANN.

4.2 Direct Model

The direct model represented by equation (12) was determined using a multilayer feedforward neural network having three layers L_1, L_2 and L_3. L_1 has 10 *tansig* neurons, L_2 has 6 *tansig* neurons and L_3 one linear neuron. All neurons are fully connected. The network for the direct model will be referred to as DANN.

The weights of each layer were trained using the LM algorithm and a regularized mean square error (MSE) as the error criteria. The training was stopped when the validation error started to increase. In order to avoid local minima, 100 different training sessions were performed starting from different random initial weights. The results of DANN training are

presented in Fig. 11. The small MSE (1.61 slpm^2) and maximum error of the training (8.78 slpm – only 1.25% of the NMF) reveal an excellent fit.

A common practice when using ANN is to test the ability of the trained networks with non-training data. This test was done in a simulation using 5000 randomly generated data points of u and P_A. These random data points were applied to DANN and to a routine that interpolates the training data. The error between interpolated and DANN mass flow was then calculated. The maximum absolute error in this experiment is 24.6 slpm, with mean μ = 0.026 slpm and standard deviation σ =1.3 slpm.

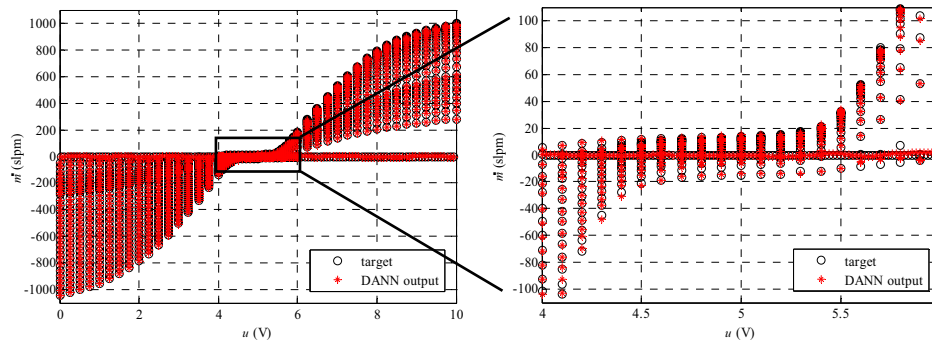

Fig. 11 Training results for DANN

The pressure gain delivered by DANN was tested in a simulation represented in Fig. 12a). The pressure gain obtained was then compared with the real one (see Fig. 12b)). There is an excellent fit with a maximum error of 2.44% of the supply pressure.

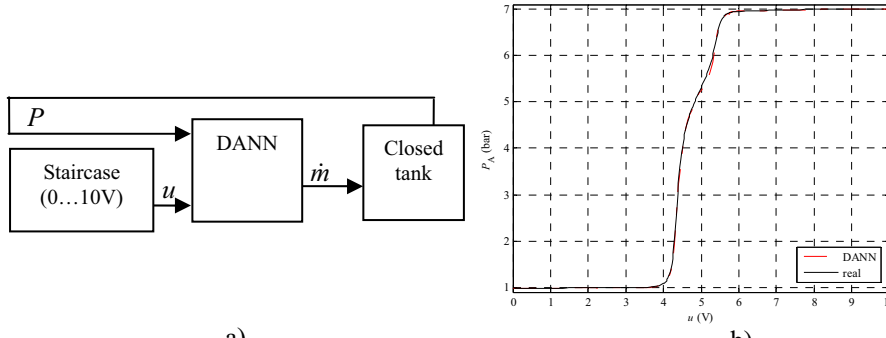

a) b)

Fig. 12 DANN pressure gain test/results

4.3 Inverse Model

The inverse model of equation (13) was determined using a multilayer feedforward ANN having three layers. The first layer has 10 *tansig* neurons, the second 6 *tansig* neurons and the third 1 linear neuron. Neurons are fully connected. The network for this model will be

referred to as IANN. The training procedure is identical to the one used with DANN. The results of IANN training are presented in Fig. 13. The training MSE is 1×10^{-3} (V^2).

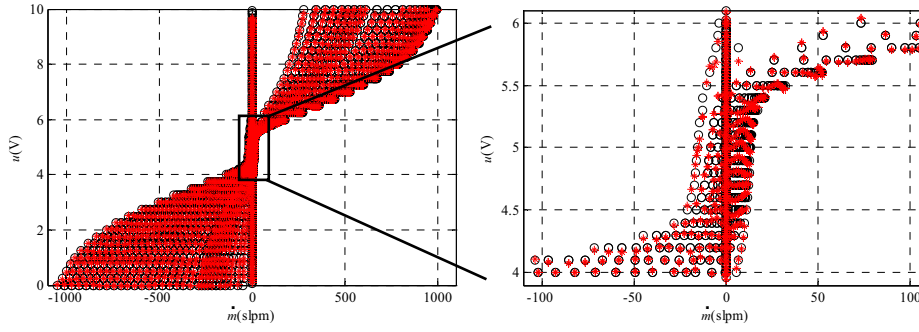

Fig. 13 Training results for IANN

Although the training error of the IANN network must be low, a more important issue is how this error on command input is reflected into mass flow prediction error. Three experiments were made in order to assess the error when predicting mass flow.

In the first experiment, P and $\dot{m}$ values of the training dataset were used to calculate the output of IANN. The mass flow caused by this output ($\dot{m}_{\mathrm{IANN}}$) is then determined by interpolating again in the training dataset – see Fig. 16. The error ($\dot{m}$ - $\dot{m}_{\mathrm{IANN}}$) of this experiment has a mean of $\mu = 0.055$ slpm, standard deviation of $\sigma = 2.21$ slpm and maximum value of 9.12 slpm – only 1.3% of the NMF.

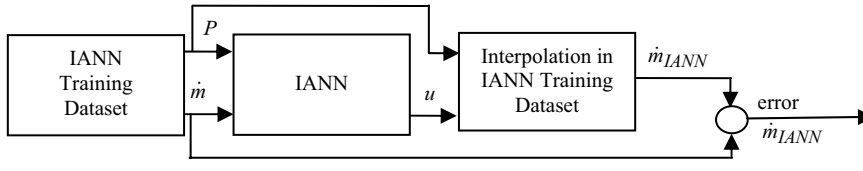

Fig. 14 Determining the IANN training mass flow error

The second experiment is essentially equal to the previous one but in instead of using training data, 5000 random pressure and command input combinations were used. In this experiment the maximum error is 29.55 slpm, with a mean $\mu = -0.0043$ slpm and standard deviation $\sigma = 2.68$ slpm. In the third experiment, instead of interpolating in IANN's training dataset, the mass flow crossing the servovalve was measured. Using P_{A} and $\dot{m}$ points near the central region of Fig. 10, IANN was simulated and the command input u_{IANN} was determined. Then, P_{A} and u_{IANN} were applied to the servovalve and the corresponding mass flow $\dot{m}_{\mathrm{SV}}$ was measured. The error ($\dot{m}_{\mathrm{SV}}$ - $\dot{m}$) in this experiment is presented in Fig. 15. It has a maximum value of 5.76 slpm, mean of $\mu = -0.05$ slpm and standard deviation of $\sigma = 2.2$ slpm. Finally, the pressure gain curve of the IANN network was determined by simulating IANN with experimental pressure and mass flow data. Fig. 16a) depicts the

simulation and Fig. 16b) a comparison between the experimental pressure gain curve (*u vs P*) and the one obtained with IANN (u_{IANN} *vs P*).

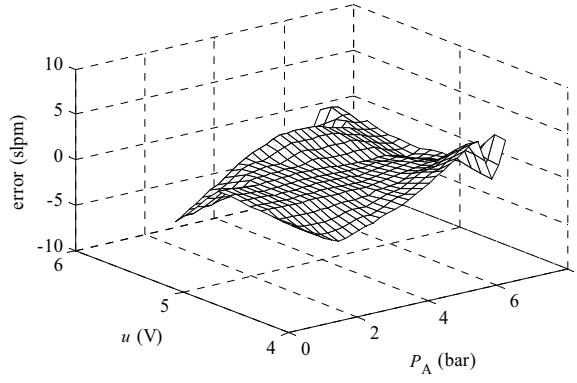

Fig. 15 Mass flow results for IANN: direct comparison with experimental data

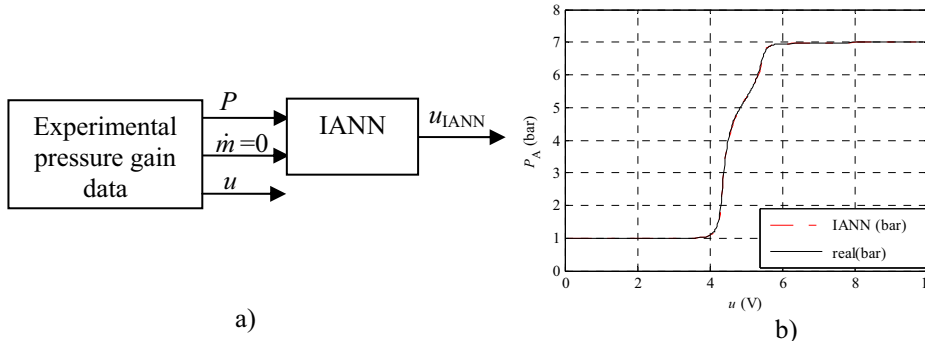

Fig. 16 IANN pressure gain test/results

There is an excellent fit with a maximum error between the two pressure gain curves of 1.72% of the supply pressure. A final remark to say that with a Pentium III, 1 GHz computer, both DANN and IANN take less than 100μs to run.

5. CONCLUSION

A new approach to 3/2 pneumatic servovalves modelling using artificial neural networks was presented. After highlighting the need to make the overall servopneumatic system affine, several solutions appearing in literature to this end were reviewed. Next, models using artificial neural networks were presented. Two models were proposed: a direct and an inverse model. The former is intended to be used in simulation, the latter in control tasks.

These models were experimentally tested using an industrial pneumatic servovalve. Results show that an excellent reproduction of the servovalve behaviour is obtained.

REFERENCES

1. **Pandian, S., Y. Hayakawa, Y. Kanazawa, Y. Kamoyama, and S. Kawamura**, Practical Design of a Sliding Mode Controller for Pneumatic Actuators. ASME J. Dyn. Syst., Meas., Control, 1997, 119, pp. 666-674.
2. **Drakunov, S., G.D. Hanchin, W.C. Su, and U. Ozguner**, Nonlinear control of a rodless pneumatic servoactuator, or sliding modes versus Coulomb friction. Automatica, 1997, 33(7), pp. 1401-1408.
3. **Pandian, S., F. Takemura, Y. Hayakawa, and S. Kawamura**, Pressure Observer-Controller Design for Pneumatic Actuators. IEEE/ASME Transactions on Mechatronics, 2002, 7(4), pp. 490-499.
4. **Richard, E.,** De la Commande Lineaire et non Lineaire en Position des Systems Electropneumatiques. PhD thesis, 1990, INSA-Lyon.
5. **Richard, E. and S. Scavarda**, Comparison Between Linear and Nonlinear Control of an Electropneumatic Servodrive. ASME J. Dyn. Sys., Meas., Control, 1996, 118, pp. 245-252.
6. **Thomasset, D., S. Scavarda, S. Sesmat, and M. Belgharbi**, Analytical model of the flow stage of a pneumatic servo-distributor for simulation and nonlinear control. The Sixth Scandinavian International Conference on Fluid Power, SICFP. Tampere, Finland, 1999, pp. 848-860.
7. **Narendra, K.**, Neural Networks for Control: Theory and Practice. Proceedings of the IEEE, 1996, 84(10), pp. 1385-1406.
8. **Noorgard, M., O. Ravn, N.K. Poulsen, and L.K. Hansen**, Neural Networks for Modelling and Control of Dynamic Systems: a practitioner's hanbook. 2003, Springer Verlag.
9. **Richer, E. and Y. Hurmuzlu**, A High Performance Pneumatic Force Actuator System: Part I - Nonlinear Mathematical Model. ASME J. Dyn. Syst., Meas., Control, 2000, 122(3), pp. 416-425.
10. **Richer, E. and Y. Hurmuzlu**, A High Performance Pneumatic Force Actuator System: Part II - Nonlinear Controller Design. Transactions of the ASME J. Dyn. Syst., Meas., Control, 2000, 122(3), pp. 426-434.
11. **McCloy, D. and H.R.Martin**, Control of Fluid Power: Analysis and Design. Engineering Science. 1980, Ellis Horwood.
12. **ISO 6358 Standard**, *Pneumatic fluid power -- Components using compressible fluids -- Determination of flow-rate characteristics*. 1989, International Organization for Standardization. p. 14.

Return to Contents

Applications

Comparison of EM A and H A performance for dynamic load simulators

Wissam K AR AM , Jean-Charles M ARE
Laboratoire de Génie Mécanique INSA/UPS
Départem ent de Génie Mécanique INSA
135 Avenue de Rangueil, 31077 Toulouse Cedex 4, France
Karam.wissam@insa-toulouse.fr Jean-charles.mare@insa-toulouse.fr

ABSTRACT

The performance of electro-mechanical actuators is evaluated in comparison with hydraulic actuators for dynamic loading applications. The first part is dedicated to the analysis of mechanical architectures with respect to integration and mechanical reduction. In the second part, a design methodology is proposed to optimise the selection of the motor-screw combination. The third part concerns the modelling of the actuator with special consideration to the nut-screw transmission. In the last part, the natural open loop dynamics of both kinds of actuators are compared to identify key design criteria.

1. INTRODUCTION

In the certification and qualification process, components are tested according to the in-service conditions. To fulfil this objective, test bench designers have to face with the selection of high performance dynamic loading systems. Such test equipments must be able to generate static and dynamic forces whatever the velocity of the moving load. A typical example corresponds to the testing of a single aisle commercial aircraft aileron actuator.

Until now, the electrohydraulic technology was the only available solution for such demanding tests (especially considering endurance). The recent improvement in the performance of electric motors, power electronics and mechanical transmissions offers more and more attractive solutions. Being now able to develop alternating forces for millions cycles, they are easy to control and operate, with lower energy consumption. They do not require any hydraulic power generation. They are less sensitive to pollution and offer a friendlier environment. Despite they are now widely used in position control applications, they are not yet considered for dynamic loading purposes due to the lack of knowledge in their design and operation as force controlled actuators.

Power Transmission and Motion Control 2006 Edited by Dr D N Johnston and Professor K A Edge

The main objective of the reported work is to clarify the potentialities and to point out the key design criteria that fix the performance level of force controlled EMAs (electro-mechanical actuators). The present application deals with the ground testing of aircraft actuators in the range of 50 kN stall force, 30 mm/s null load speed, 25 kN @ 26 mm/s nominal, 50 mm stroke. It roughly corresponds to single aisle aileron actuators of the Airbus A320 family.

The loading actuator must be able to generate:
- a permanent 50 kN stall force,
- 2000 cycles from stop-end to stop-end of the tested actuator without shock, at 12 kN,
- 6.5 million cycles of 18 kN statics + 2 kN/mm for a centred load having a 4 mm/s sine velocity profile, strokes from +/- 0.5 mm to +/- 5 mm,
- 1.7 million cycles of 9 kN statics + 0.5 kN/mm for a centred load having a 11 mm/s sine velocity profile, strokes from +/- 2 mm to +/- 8 mm.

The 100 mm stroke EMA on study has been designed and supplied by *SKF*. A *Haenchen* test bench HA (double rod of 50 mm diameter, 80 mm piston diameter, 100 mm full stroke) supplied at 150 bars and controlled by a flow servovalve is used as a reference for comparison.

2. MECHANICAL ARCHITECTURE

Dynamic load actuators have to operate in severe conditions. Firstly, they must develop alternative forces with possible zero crossing. Any present backlash will generate shocks that will decrease the service life and the control performance. Secondly, undesired phase lag will alter the characteristics of the generated load, e.g. inertial effect produced instead of pure spring effect. Consequently, equivalent inertia of moving parts, friction and compliances must be carefully managed during the design to ensure the consistency between open-loop performance and closed loop specified one. When managed properly, the actuator becomes easier to control.

The architecture design of HA is quite simple as it mainly involves a linear jack and a servovalve. Only a few additional components, not contributing to the dynamic performance, are used for safety purposes. Opposite to that, the selection of appropriated EMA architecture is of prime importance. The preliminary design fixes compliance, backlash, inertia, friction and compactness that have a very high influence on the final performance.

Industrial direct drive linear motors are unfortunately still limited to a few hundreds Newtons or a few millimetres per second (potential suppliers: Danaher, Copley, Oswald…). For this reason, high force load generators involve rotating electric motors that drive a rotation/translation motion transformer. In addition a mechanical reducer may be required for adaptation of the motor characteristic to the load one.

2.1 Electric motor

Putting aside brush motors that do not suit the lifespan requirements, synchronous motors offer the more relevant solution for 4 quadrants, alternating speed and high stall torque

applications. Some of them can be supplied as frameless or hollow shaft that allows an interesting compact design (Exlar for example).

2.2 Rotation/Translation transformer

With their poor efficiency, acme screws are generally irreversible and require excessive size when long life under dynamic loading is required. Replacing sliding by rolling, ball or roller-screws can fulfil high performance requirements and have become widely available as standard mechanical components (suppliers: SKF-Transroll, Thomson-Danaher, Rollvis, Nook, THK, Spiracon…), [1][2][3][4].

As displayed by Figure 1, four arrangements can be selected for this transformer. Designs ① and ③ are not applicable for ball screws (ball recirculation not possible at the screw level). For roller-screws, their stroke is limited due to the nut manufacturing constraints. On the other hand, design ① leads to very compact actuators when combined with hollow shaft motors. Design ② allows long strokes but requires a cover to protect threads against pollution and to preserve lubricant. In addition, journal bearing is difficult to integrate. In design ④, the nut is linked to the load through a rigid tube that protects in the same time the screw threads from any kind of pollution. Due to the easiness of its linear guiding, this architecture allows very long strokes (limited by buckling and transverse vibrations). It must be pointed out that in most of the designs, the load itself performs the antirotation function. This has two important drawbacks that do not concern HAs. Firstly, ball joints can't be used to connect the actuator to the load and to the test bench frame. Secondly, the load must be designed to hold the nut/screw friction torque transmitted by the loading actuator.

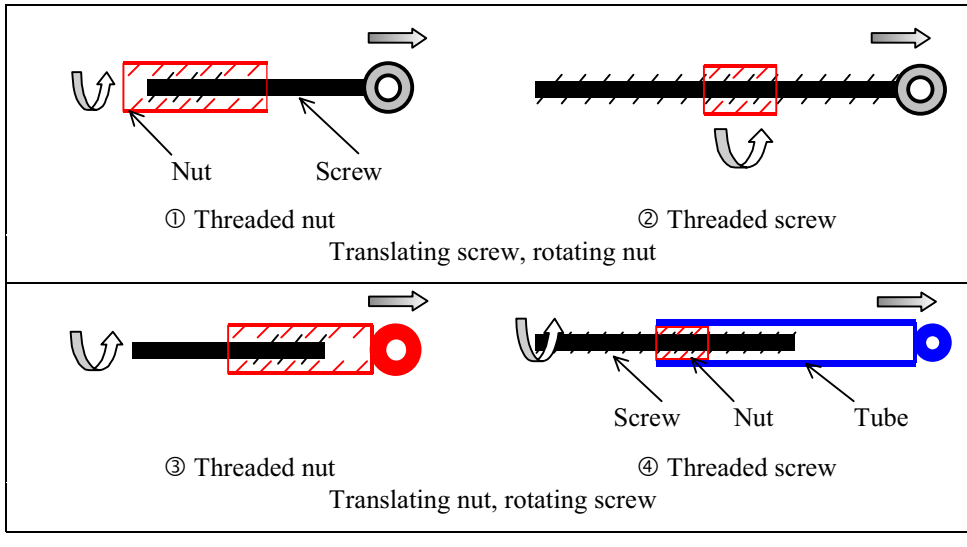

Figure 1: Screw design arrangements

2.3 Reducer

Depending on geometrical architectures, rotation to rotation reducer may be of different types:

- spur or helical gears allow a tandem design in which the motor axis is parallel to the screw one,
- bevel or worm gears lead to cross design as the motor axis is perpendicular to the screw one,
- direct drive or epicyclical gears are well adapted to in-line or compact design in which the motor and the screw axes are identical.

In low demanding applications, reducers are used to match the actuators motor impedance (T_0, ω_0) with the load impedance (F, V). Thus, an application, requiring high load and low speed, can be motorized by a low torque, high speed motor. When a high dynamic performance is requested with possible zero speed and zero force crossing, any present backlashes are lethal. On the other hand, reduction ratios induce very high equivalent inertias. For these reasons, direct drive is preferred as it allows rigid, backlash-free and reversible transmission.

2.4 Integration

Generic examples of direct drive roller-screw actuators are displayed on Figure 2. In addition to the motor and the roller-screw, the design has to integrate the motor angle sensor that is required by the motor power drive, the axial thrust bearing devices and possibly the jack extension sensor. In-line designs ④ and ⑤ leads to long actuators while concentric designs ①, ②and ③ take benefit from the hollow shaft motor to increase compactness. All designs have also to be compared with respect to inertia and stiffness.

3. POWER SIZING

The power sizing of an EMA consists in the selection of standard components to be integrated, mainly the motor and the screw. The motor operating domain is usually defined by the supplier at maximum continuous power, reference torque T_0 [Nm] and reference velocity ω_0 [rd/s], that corresponds to max voltage and max current. Consequently, a rectangular domain defines the motor power capability.

At first order, electrical to mechanical power transformation is fixed by three parameters; the motor pair (T_0 and ω_0) and the screw lead p [m]. Beside this continuous operation domain, the EMA may function in a transient operation domain and deliver higher forces. Unfortunately, this domain is not clearly defined by the power electronics and motor suppliers and the maximum transient force cannot be used securely during the power sizing process. Opposite to that, the hydraulic working area is absolutely bounded by the servovalve hydraulic characteristic that links the jack extension velocity V [m/s] and the delivered force F [N]:

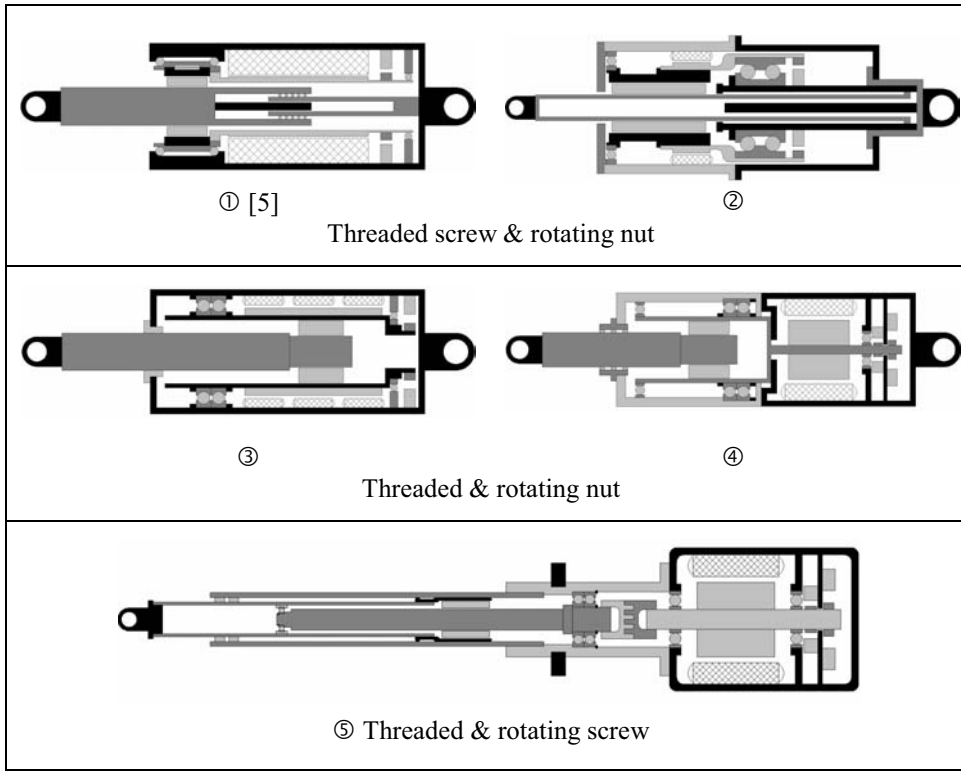

Figure 2: Example of roller-screw direct-drive EMAs

$$\frac{V}{S} = Q_n \sqrt{(P_s - \frac{F}{S}\mathrm{sgn}(V))/P_n} \tag{1}$$

where the nominal flow Q_n, [m^3/s], the jack area S [m^2] and the supply pressure P_s [Pa] are the three design parameters of the HA.

The nut-screw nominal diameter d [m] is directly related to mechanical resistance considerations (buckling, transverse vibrations and thread dynamic capacity). For high force and low stroke actuators, where buckling and transverse vibration are not critical, the dynamic capacity is the main design driver. At second order, the pair (p, d) alters both power transmission and mechanical resistance due to its influence on the mechanical efficiency and the screw dynamic capacity. Each individual criterion can be considered easily as it is quite well documented by the roller-screw suppliers in terms of analysis. Oppositely, the synthesis of an optimal selection of (p, d, T_0, ω_0) is a complex process that requires an appropriated methodology, as proposed below.

3.1 Machining

The pair (p, d) must be selected from a set of standard values relative to the SI or English units. To avoid any interference between the machining tool and the screw itself, the lead angle must be smaller than 10 °.

3.2 Life expectancy

The actuator should be able to achieve the needed amount of cycles with a reliability of 90%. Life expectancy is directly related to the dynamic capacity of the roller screw that depends upon the pair (p, d). Screws with superior diameter have higher contact and working areas that lead to higher dynamic load. On the other hand, an increase of the pitch makes the thread more resistant to shear forces allowing also higher loads.

The nominal life expectancy L_{10m} [m] of a single nut is calculated according to the common formula for rolling elements [2], given the dynamic load rating C [N] and the equivalent mean axial load F_m [N]:

$$L_{10m} = p\left(\frac{C}{F_m}\right)^3 10^6 \tag{2}$$

For complex operating cycles, the equivalent mean load is calculated from the minimum and maximum forces F_{mi}, F_{Mi} [N], the amplitude of displacement A_i [m] and their respected number of cycles N_i [2].

$$F_m = \sqrt[3]{\frac{\sum_i (F_{mi}/3 + 2F_{Mi}/3)^3 N_i A_i}{\sum_i N_i A_i}} \tag{3}$$

The sizing of the roller-screw must therefore fulfil the travel requirements:

$$L_{10\,m} \geq \sum_i 4 N_i A_i \tag{4}$$

By this mean, two roller-screws having identical dynamic capacities can achieve the needed amount of cycles with different reliabilities, depending upon the screw lead of each one. Split of double nuts allow preloading and permit a backlash free transmission. In this case, the lifespan calculus is similarly applied to each part of the nut.

3.3 Efficiency

Efficient roller-screw reduces the initial (motor size) and operating (energy consumption) costs. Beside these economic considerations, discontinuous efficiency or irreversible transmission causes serious problems for the design of high performance controllers. A special attention must therefore be paid to the evaluation of the nut-screw efficiencies. In practice, three values are used, depending on the mode of operation:

- direct efficiency (η_d) for "against load" when the power flows from motor to load,
- reverse efficiency (η_i) for "aiding load" and reversible transmission, when power flows from load to motor,
- pseudo efficiency (η_p) for "aiding load" and irreversible transmission, when both motor and load input power to the transmission (reversibility is ensured when $\eta_d > 0.5$).

The detailed calculus of roller-screws efficiency is complex. For this reason, roller-screws are assimilated to sliding screws having the same nominal diameter and screw lead, but with a modified friction factor μ [2]. Thus, their efficiencies can be expressed by:

$$\eta_d = \frac{1}{1+\mu/\beta} \qquad \eta_i = 1-\mu/\beta \qquad \eta_p = \frac{1}{-1+\mu/\beta} = -\frac{1}{\eta_i} \tag{5}$$

where $\beta = p/\pi d$ is the lead angle tangent.

The friction coefficient is typically given by the roller-screws suppliers as 0.01 in dynamic conditions (typically 0.003 to 0.01 for ball screws and 0.04 to 0.11 for acme screws). No information is provided concerning the breakaway friction coefficient that may reach twice the dynamic value. The corresponding direct and indirect efficiencies of roller-screws are plotted on Figure 3. To limit the difference between the "aiding" and "against" load operations, it is preferred that $\eta_i > 0.9\ \eta_d$. This constraint ensures a fully reversible roller-screw system with satisfactory efficiencies ($\eta_d > 0.76$ and $\eta_i > 0.69$).

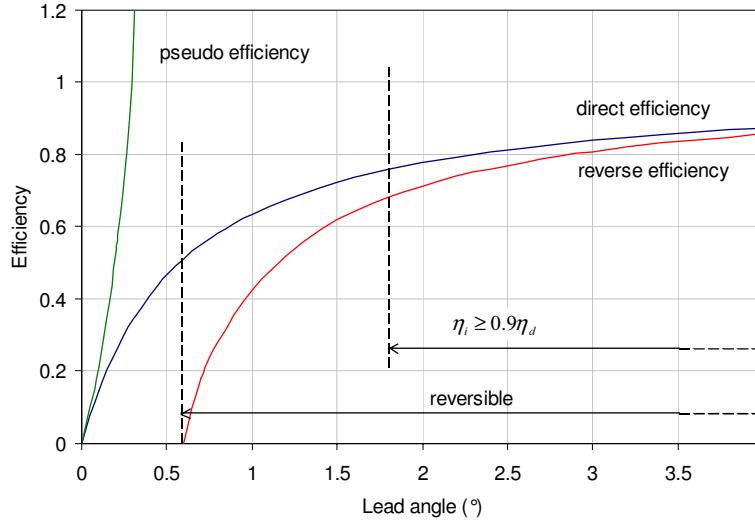

Figure 3: Efficiencies of roller-screws when assimilated to acme screws with μ=0.01

The above constraints are summarised on Figure 4 on which the grey area corresponds to the satisfying domain for the selection of the roller-screw. Each catalogue reference is represented by a triangle mark associated with the pair (d, p). To select one pair among these satisfactory values, additional criteria have to be taken into consideration, especially dealing with the motor/screw combination.

3.4 Torque and equivalent inertia

For against loads, the required driving torque is an increasing function of the screw lead p:

$$T_0 = Fp / 2\pi\eta_d(p) \tag{6}$$

From this point of view, choosing the lowest acceptable screw lead minimizes the motor reference torque.

On the other hand, the actuator's equivalent moving mass m_e [kg], equation (7), has to be minimized:

- huge values can cause lethal shocks when the actuator faces an obstacle like stop ends. For instance, a 55 kN stall force EMA with a 6.53 mm lead and 0.022 kgm^2 rotor inertia [4] produces an equivalent moving mass m_e = 21540 kg according to equation (7).
- from the control point of view, a high inertia increases the response time and lowers the natural frequency of the actuator.

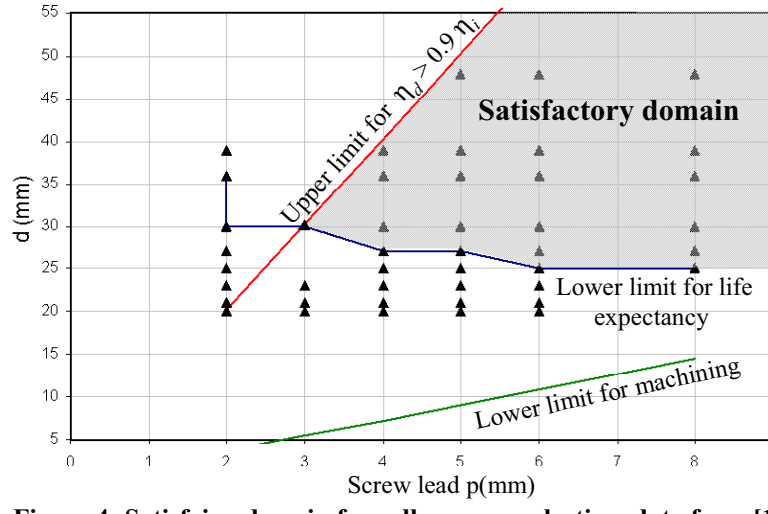

Figure 4: Satisfying domain for roller-screw selection, data from [1]

$$m_e = \frac{J_m(p)}{r^2} + m_r \qquad r = p/2\pi \tag{7}$$

with J_m [kgm²] inertia of the actuator's rotating parts
m_r [kg] actuator's rod mass

The rotating inertia J_m is highly dependant on the motor reference torque. As an example, for 1.7 to 55 kN, 10 inch stroke EMAs, the rotating inertia has been identified as a second order function of the reference torque [4]:

$$J_m = 185.10^{-6} + 65.10^{-6} T_0(p) + 4.10^{-6} T_0^2(p) = J_m(p) \tag{8}$$

From equations (6 to 8), it so appears that the equivalent mass m_e is a decreasing function of the screw lead introducing an opposite constraint. Considering that both of the constraints have equal importance, the optimal lead minimises the cost function $T_0 m_e$ as displayed on Figure 5.

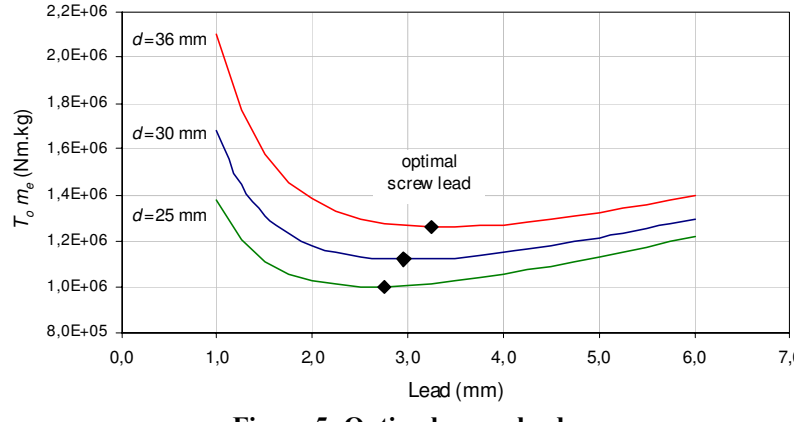

Figure 5: Optimal screw lead

Figure 4 indicates that the pair (d = 25 mm, p = 3 mm) does not fulfil the life expectancy. Thus, the cost function is minimised for the acceptable pair (d = 30 mm, p = 3 mm) that optimises globally the motor/screw sizing.

4. EMA MODELLING

The model structure of the EMA is displayed by the Bond-Graph of Figure 6. It is organised in such a way that it reproduces the functional combination of power electronics, electrical motor and nut-screw transmission. Functional power bonds are highlighted. The nut is driven by the motor while the screw translates, according to designs ③ and ④ of Figure 2. Causalities are assigned without conflict and fix the submodels interfaces. The force sensor is modelled as a spring with structural damping. Other compliances (bearings, anchorage to structure or to load, rod,…) may be considered if they contribute significantly to the low frequency behaviour. The model is implemented within the AMESim [6] simulation software from standard libraries, excepted the nut-screw which model has been specifically developed.

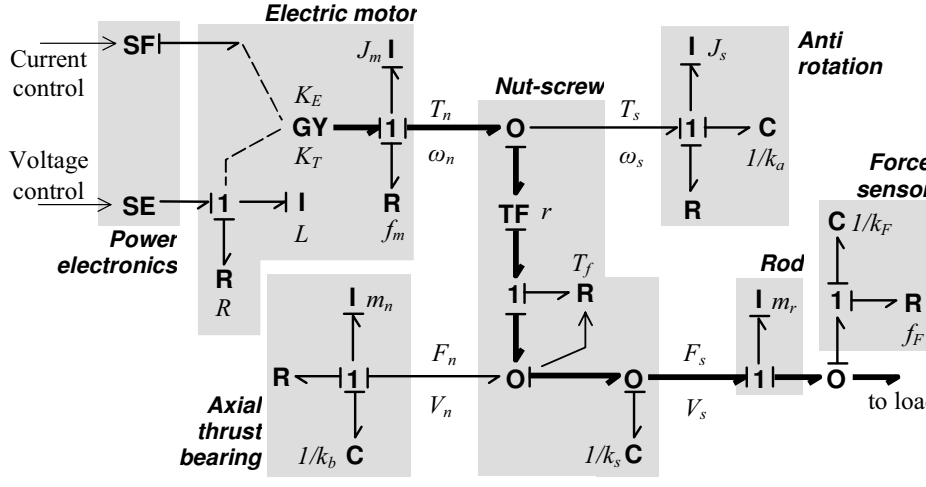

Figure 6: Bond-Graph model of the EMA

4.1 Roller-screw model

Realistic modelling of the nut-screw is of particular importance to get accurate EMA simulations. It can be seen on Figure 6 that a four bonds model has been developed, including translation and rotation for both nut and screw. This choice allows modelling the axial and anti-rotation compliances that may affect significantly the dynamic response of the EMA (see later). Moreover, most of the high performance EMA designs do not include the anti rotation function. Therefore, this function is to be performed by the driven load that must be able to hold the friction torque transmitted by the nut to the screw. It is so of particular importance to output this effect to the load submodel.

The roller-screw model is split in two parts: firstly a rigid and backlash free nut with friction losses and secondly the transmission compliance k_s that is rejected on the translation side. The latest can include the backlash effect for not pre-loaded nuts (typically 20 µm). As mentioned earlier, the roller-screw is considered as an equivalent rectangular thread screw. Consequently, a simple model of losses combines the direct, indirect and pseudo efficiencies presented in equations (5). It is then proposed to introduce the variable $\varepsilon = \mathrm{sgn}(FV)$ that defines the operating quadrant (+1 for against load, -1 for aiding load) and the index δ that introduces the reversibility (+1 if reversible, -1 otherwise):

$$T = F\frac{p}{2\pi}\left[\frac{1+\varepsilon}{2\eta_d} + \frac{1-\varepsilon}{2}\delta\eta_i^{\delta}\right] \tag{9}$$

In order to keep close to reality, the value of δ can be linked to the direct efficiency (+1 if $\eta_d > 0.5$, -1 otherwise). Furthermore, the discontinuous sign function involved by ε can be substituted by an hyperbolic tangent to ensure continuity around the null power transmission, using $\varepsilon = \tanh(FV/\mathcal{P}_0)$ where $\mathcal{P}_0$ [W] is a threshold power.

A more internal description of the screw [11] introduces explicitly the friction coefficient μ in the model that becomes:

$$T = \left[\frac{\tan\alpha + \mu\,\mathrm{sgn}(\mathcal{P})}{1 - \mu\,\mathrm{sgn}(\mathcal{P})\tan\alpha}\right]\frac{d}{2}F \tag{10}$$

This time, it is possible to reproduce the influence of the sliding velocity V_s [m/s] on friction. It allows including the Coulomb, Stribeck and viscous effects [7][8]:

$$\mu = \mu_C + (\mu_S - \mu_C)\exp\left[-\left(V_s/V_r\right)^2\right] + f_\mu|V_s| \tag{11}$$

$$V_s = \frac{d\cos\beta}{2}\omega_{sn} \tag{12}$$

with
- μ_C [-] Coulomb friction coefficient
- μ_s [-] Stribeck friction coefficient
- f_μ [s/m] viscous coefficient
- V_r [m/s] reference velocity for stribeck effect
- V_s [m/s] sliding velocity
- ω_{sn} [rd/s] relative velocity between the screw and the nut

Key simulation results are presented on Figure 7. As indicated by the upper plot, the nut-screw is run in all quadrants by forcing a sine wave nut velocity and a sine wave external axial load on screw. The corresponding efficiency is given in the lower plot. It lays between direct indirect values excepted when altered by the Stribeck effect around the null velocity.
As the μ function combines with the sign of power in equation (10), this model is not able to generate any friction loss at null speed. However, the breakaway effect at "near zero" sliding speed can be reproduced by an appropriated setting of V_r and $\mathcal{P}_0$. If necessary, more complex friction models like Dahl, Lu-Gre or Reset integrator can be used to generate pure static friction. It must be kept in mind that they increase the model order and require additional unknown friction parameters.

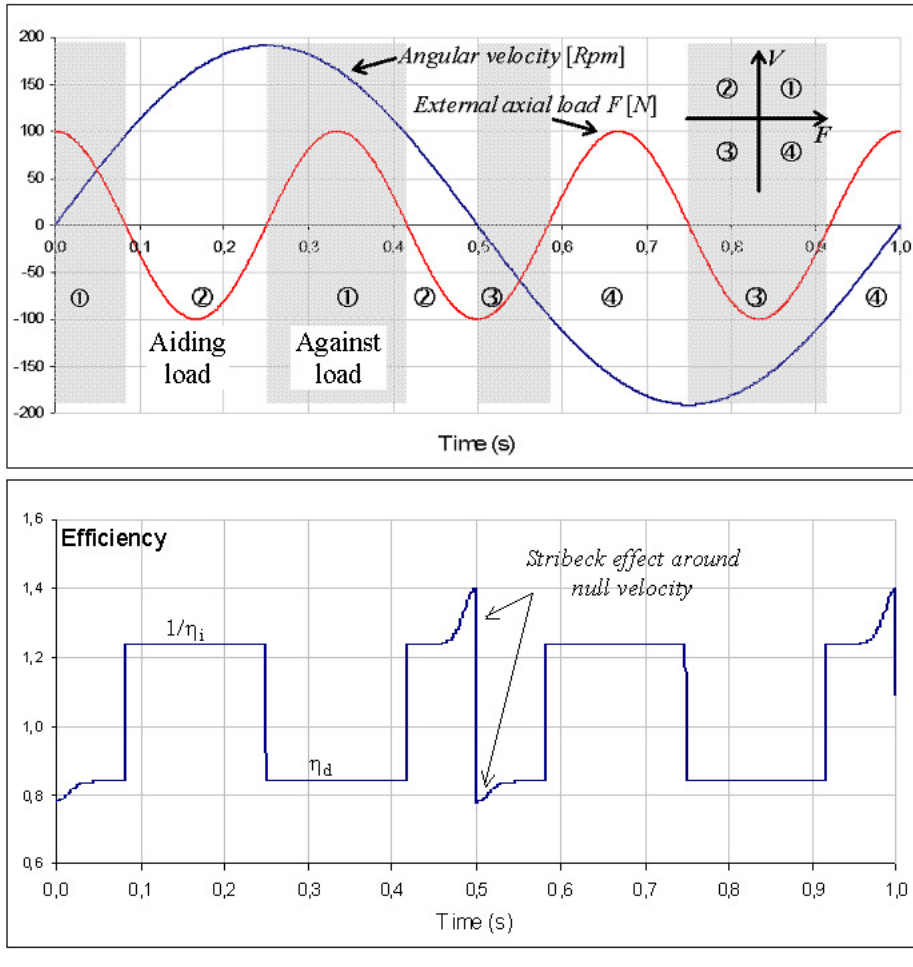

Figure 7: Simulation results of nut-screw friction losses

4.2 Motor model

Medium and high power EMAs are equipped with brushless synchronous motors that can be assimilated to DC motors for simulation purposes [9]:

$$U = L\frac{dI}{dt} + RI + K_e\omega_m \tag{13}$$

$$C_e = K_T I \tag{14}$$

with

L [H]	equivalent DC motor inductance
R [Ω]	equivalent DC motor resistance
K_e [Vs/rd]	equivalent DC motor electromotive constant
K_T [Nm/A]	equivalent DC motor torque constant
U [V]	equivalent DC voltage supplied to motor
I [A]	equivalent DC current supplied to motor

The DC motor equivalent resistance and inductance are equal to one-third of the values that are measured between phases on the brush-less motor. The EMA motor can be either controlled by voltage of by current, as displayed on the left side of Figure 6.

4.3 Power electronics

Nowadays, industrial power electronics offer multiple control strategies: torque, acceleration, speed or position control, involving filtering, feed-forward and PID controllers. They can be easily set in a user-friendly environment. Unfortunately, the motor control itself is never documented in detail. In this situation, the control designer is unable to evaluate the closed-loop limits induced by the measurement, the filtering and the sampling effects that apply to motor variables.

5. EMA DYNAMICS

The ability of an actuator to operate as a dynamic loading system is easily evaluated in a first step when it is supposed to generate the force on a blocked load. Correspondingly, the following results fix useful key-points that further helps the control design when a more complex load moves in response to the applied force [10].

The natural dynamics of the EMA depends on its mechanical compliances. Unfortunately, it is difficult to get accurate and detailed values from the EMA suppliers. At the component level, the nut-screw compliance is most of the time available in catalogues, in the best case as typical and guarantied values. On the other hand, thrust bearings compliances are difficult to obtain. This becomes more critical when frame and rod compliances have to be quantified. In the present application, the overall EMA stiffness, supplied by *SKF*, is 1.5 10^8 N/m with a total inertia of rotating parts J_m = 0.0139 kgm^2. No detailed data being available, the screw-nut compliance has been evaluated thanks to roller-screw catalogues to k_s = 3 10^8 N/m, leading to an axial thrust bearing compliance of k_b = 3 10^8 N/m.

In comparison, the HA compliance calculated with an 8000 bar Bulk modulus and 20 % dead volumes is twice lower (0.88 10^8 N/m), with a rod mass of 10 kg. On its side, the stiffness of the force sensor *HBM U10* is ten times higher (k_F = 16.7 10^8 N/m). In the following developments, other compliances are supposed to have a negligible influence (rod, anti-rotation and body to structure anchorage).

Table 1 summarizes open loop dynamics of HA, current controlled EMA and voltage controlled EMA. In the HA case, the flow-pressure gain A [m^3/s/Pa] includes the jack internal leakage and the power valve non-linear hydraulic flow-pressure gain. The former is generally used to passively damp the high frequency modes located outside the servovalve bandwidth. The first order frequency is fixed by the hydraulic capacitance C_h [m^3/Pa]. This one also can be artificially increased by use of dead volumes to improve the rejection of load velocity disturbances [10]. In practice, the corresponding cut-off frequency is well below 10 Hz (1 litre dead volume and 0.01 l/mn/bar would give 0.36 Hz). So, the dominant open loop critical frequency (phase lag –180°) is fixed by the servovalve natural frequency: normal - below 100 Hz, high performance - about 200 Hz or very high performance - greater than 300 Hz. The rod mass m_r [kg] and the hydraulic capacitance fix the rod dynamics that is located much higher, even if the force sensor compliance is not considered (hydraulic mode is at 530 Hz).

The dynamics of the current controlled EMA is of second order. Its natural frequency is mainly fixed by the overall EMA stiffness (k_s and k_b in series) that combines with the rotor inertia. It must be emphasized that even a very high EMA stiffness (1.5 10^8 N/m) and a small motor inertia lead to a very low natural frequency (7.6 Hz) due to the contribution of the transmission ratio r. Rod and nut modes are located well above 1 kHz, about 2100 and 3200 Hz typically. In practice the closed-loop performance is bounded by the motor current loop that involves phase lags due to sampling and filtering.

The dynamics of the voltage controlled EMA starts with a first order which origin is similar to the hydraulic one. As for the current controlled EMA, the second order is fixed by the rotor inertia that combines with various compliances. The voltage control introduces an "electrical" stiffness k_e of 1.06 10^{10} N/m, 70 times the EMA global mechanical stiffness. This time, the equivalent stiffness results from the association in parallel of k_e, k_F series k_s and k_b. As k_F is very high compared with k_s, it is important to notice here that k_s and k_b practically combine in parallel instead of in series. Once again, rod and nut modes a located well above 1 kHz (about 2100 and 3200 Hz typically). Finally, the open loop performance critical frequency is fixed by the electromechanical mode.

Hydraulic actuator	Static gain due to hydraulic leakage $K_{QI}S/A$
	First order hydraulic time constant C_h/A Cut-off frequency $f = A/2\pi C_h$,
	Servovalve second order dynamics, **50** to **350** Hz given reference
	Second order of rod dynamics $f = \frac{1}{2\pi}\sqrt{\frac{k_h k_S}{(k_h + k_s)m_r}}$ (**2362 Hz**)
EMA, current control	Static gain[1] K_T/r (**2408 N/A**)
	Mechanical second order $f = \frac{1}{2\pi} r\sqrt{k_1/J_m}$ (**7.6 Hz**) k_1: equivalent stiffness of k_s, k_b and k_F in series
	High frequency modes (rod and nut) well above **1 kHz**
EMA, voltage control	Static gain[1] K_T/rR (**33.6 kN/V**)
	First order time constant $K_E K_T/k_1 r^2 R$ Cut-off frequency (**0.3 Hz**)
	Electromechanical second order, $f = \frac{1}{2\pi} r\sqrt{k_2/J_m}$ (**68 Hz**) k_2: equivalent stiffness of k_e, k_b and (k_F series k_s) in parallel k_e: electric stiffness $K_E K_T/Lr^2$
	High frequency modes (rod and nut) well above **1 kHz**

Note 1: loss-less roller-screw

Table 1: Comparison of blocked load, EMA and HA dynamics

6. SUMMARY

The aim of the present communication was to provide key considerations on the design and selection of EMAs for dynamic loading applications in comparison with HAs. Listing possible mechanical architecture, it has firstly been pointed out that direct drive satellite roller-screw jacks offer an interesting load capacity that is consistent with endurance testing. A methodology has been proposed for the motor / screw combination to include as early as possible control considerations into the mechanical design. Then, a simulation model has been developed paying a special attention to the nut-screw. The proposed model reproduces both direct and indirect efficiencies and is able to generate irreversibility. Model parameters are given at the friction coefficient level and allow to reproduce both Coulomb, Stribeck and viscous effects. The four bonds model is of particular importance as it outputs the friction torque that is usually hold externally by the load itself and it may be connected with an axial thrust bearing compliant model. Finally, the comparison of the open loop EMA and HA dynamics shows the importance of the EMA mechanical compliances. For the design of dynamic loading EMAs, it is still necessary to more involve the suppliers in order to get accurate information on the definition of the transient force capability, on the electronic power drive dynamics and on the separate values of axial thrust bearing and nut-screw compliances. The EMA actuator test-bench is now under construction at INSA Toulouse and will provide in mid 2006 an efficient validation mean while advanced controllers are being synthesised.

REFERENCES

[1] Rollvis satellite roller-screws technical data, pp 1-61, *Rollvis SA*, Geneva, Swiss
[2] SKF roller screws technical data 4351EN, pp 1-80, *SKF linear motion*, Montigny le Bretonneux, France
[3] Nook satellite roller-screws technical data NRS^{TM}, pp 176-194, *Nook industries,* Cleveland, USA
[4] Exlar inverted roller screws technical data, pp 1-38, *Exlar*, Chanhassen, USA
[5] **Grand. S, Valembois J-M**, Electromechanical Actuators Design for Thrust Vector Control, *Proceedings of the International Conference on Recent Advances in Aerospace Actuation Systems and Components*, pp 21-28, November 24-26, Toulouse, France, 2004
[6] AMESim, *Advanced Modelling Environment for Simulation*, Imagine SA, Roanne, France
[7] **Olson H., Astrom K.J., Canudas de Wit C., Friction Models and Friction Compensation**, November 28, 1997, www.control.lth.se/~kja/friction.pdf
[8] **Papadopoulos E.G., Chasparis G.C.,** Analysis and Model Based Control of Servomechanisms with Friction, *ASME Journal of Dynamic Systems, Measurement and Control*, Volume 126, Issue 4, pp 911-915, December 2004
[9] **Aghili F., Buehler M., Hollerbach J. M.**, Optimal Commutation Laws for Torque Control of Synchronous Motors, *Proceedings of the American Control Conference,* pp 1968-1973, Albuquerque, New Mexico, June 1997
[10] **Maré J-C., Moulaire P.,** Force control of Electrohydraulic Actuators Driving Various Mechanical Load Impedances, *Proceedings of the 2 Internationales Fluidtechnisches Kolloquium,* pp 149-162, Dresden, Germany, 16-17 March 2000
[11] **J.E. Shigley,** Mechanical engineering design, 7th edition-2004, pp 400-405

Return to Contents

Modeling and control of marine engineering systems .

T.Heeringa

Project manager Boskalis Westminster Dredging.

P.O. Box 45,

3350 AA Papendrecht.

The Netherlands

Abstract

The traditional modeling approach in engineering is mathematical, but thanks to the advances in computer technology it is now possible for the practical engineer to model systems in a more "user friendly" way.
This paper will demonstrates the power and simplicity of Bond Graphs in modeling systems.
Bond Graph modeling was originally developed in the late 1950s by the late Prof. Henry M. Paynter of M.I.T.
Prof. Paynter acted well before his time as the main advantage of his creation, other than the modeling insight that it provides and the ability of effectively dealing with mechatronics, came into fruition only with the recent advent of modern computer technology and the tools derived as a result of it, including symbolic manipulation, MATLAB and SIMULINK and the simulation package 20-sim which allows direct input of the Bond Graph.
To avoid destructive torsional vibrations is of major importance in marine power train design. During transient loads extreme conditions have been observed and efficient methods and tools to analyze such cases are of primary interest to the industry. The system to investigate is a dredge pump drive train in a hopper dredger.
The Bond Graph model will include a lumped mass model of the diesel with a simple model of the speed governor, the clutch and the hydraulic controlled gearbox.
After the modeling the control of non linear systems with non linear controllers will be discussed.

1. Introduction.

One typical characteristic of marine engineering is that it is concerned with systems, and as a consequence with the interactions between the systems.

Power Transmission and Motion Control 2006 Edited by Dr D N Johnston and Professor K A Edge

The main sources of torsional vibration in marine power train systems are gas and oscillating mass forces in engine cylinders and hydrodynamic loads on propellers and pump impellers.
The excitation sources in a diesel engine are cyclic by nature, meaning that they vary periodically during the working cycle of the engine. The excitation sources of propellers and centrifugal pumps are periodic as long as they are not cavitating. During cavitations of the pump or propeller the excitation source is a mix of cyclic and random.
Dissipated vibration energy can cause excessive noise and severe damage to a vessels components or construction.
Nowadays the time scale of a project is restricted and therefore considerable benefit can be obtained by using computer simulations techniques to assess the performance of a conceptual design.
Bond Graphs have the advantage of being interdisciplinary and are used for structured modeling of energy and power transfer processes, including mechanical, electrical, hydraulic, and thermal processes and their combinations. Like block diagrams, the Bond Graph is a graphical representation form. But unlike block diagrams, Bond Graphs are derived directly from the physical system model, rather then through the equations of the system, and allows a more direct interface in tune with the engineer's thinking. See also the very clear explanation in (19) and (21) or visit the site www.bondgraphs.com .
To perform the modeling and the simulation, the simulation package **20-sim** from Controllab Products BV., Enschede, The Netherlands (see www.20sim.com) is used.
20-sim is an integrated modeling and simulation environment and models can be entered as block-diagrams, as Bond Graphs or as equations.
The often used Holzer method, see (2), for torsion vibration analysis is not very suitable for this hydraulic-mechanical system.

2. System description

Figure 1 depicts the system to investigate it 's torsional vibration behavior. It is the propulsion system and the dredge pump drive configuration on board of a hopper dredger. The main engine with on it 's flywheel side a flexible coupling with a clutch and then the propulsion gearbox with the propeller shaft and the controllable pitch (CPP) propeller. This pitch adjusting system with the load control of the main engine is a hydraulic control system but is not part of the modeling in this paper.
On the other side of the main engine (see fig. 1) there is a PTO shaft and mounted on that shaft is a flexible coupling with a clutch, an intermediate shaft, again a flexible coupling and then the dredge pump gearbox with the hydraulic "shunt" for speed control of the dredge pump, again an intermediate shaft and then the dredge pump.
The flexible couplings are necessary to protect gear wheels from failures due to torque fluctuations from the diesel engine and to allow some movements between diesel and gearbox because of the limited stiffness of the ship.

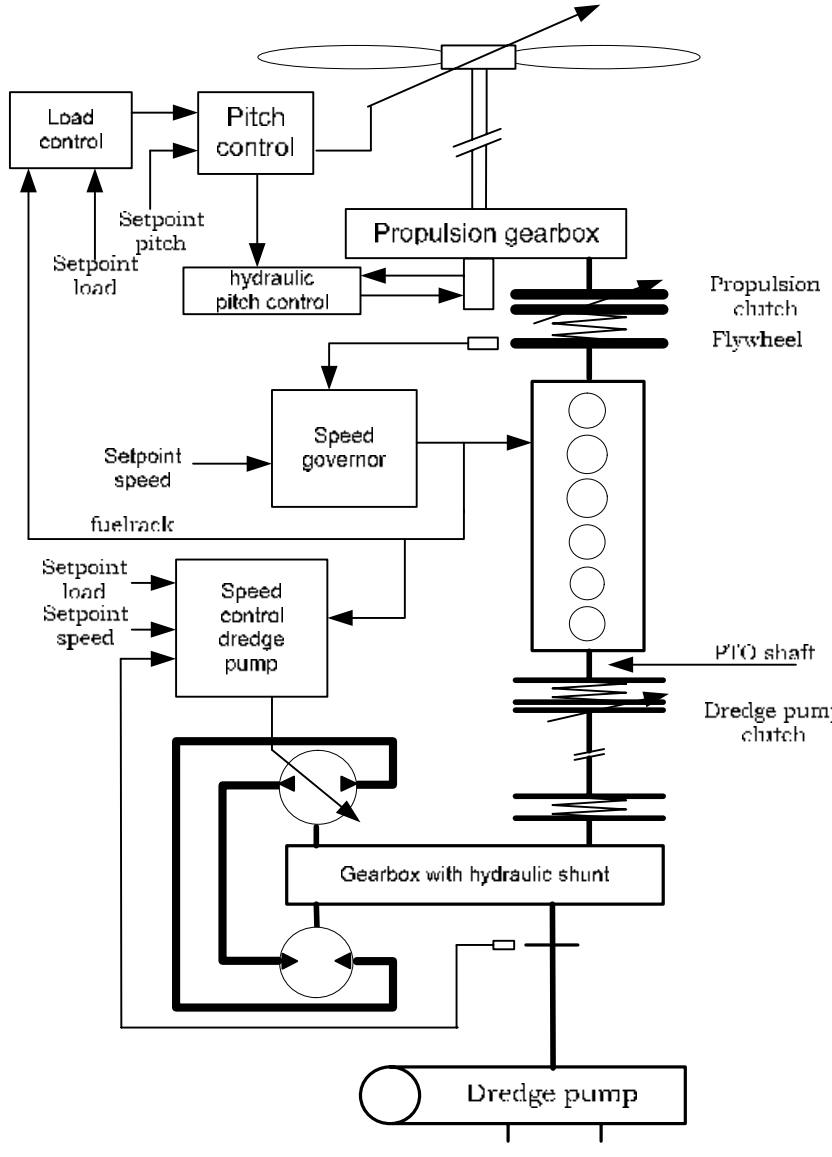

Fig. 1. Propulsion system and dredge pump drive with the control systems.

This figure depicts that the system is rather "dynamic", and therefore a proper investigation about the dynamics of the system under transient conditions is necessary.

3. The modeling of the gearbox.

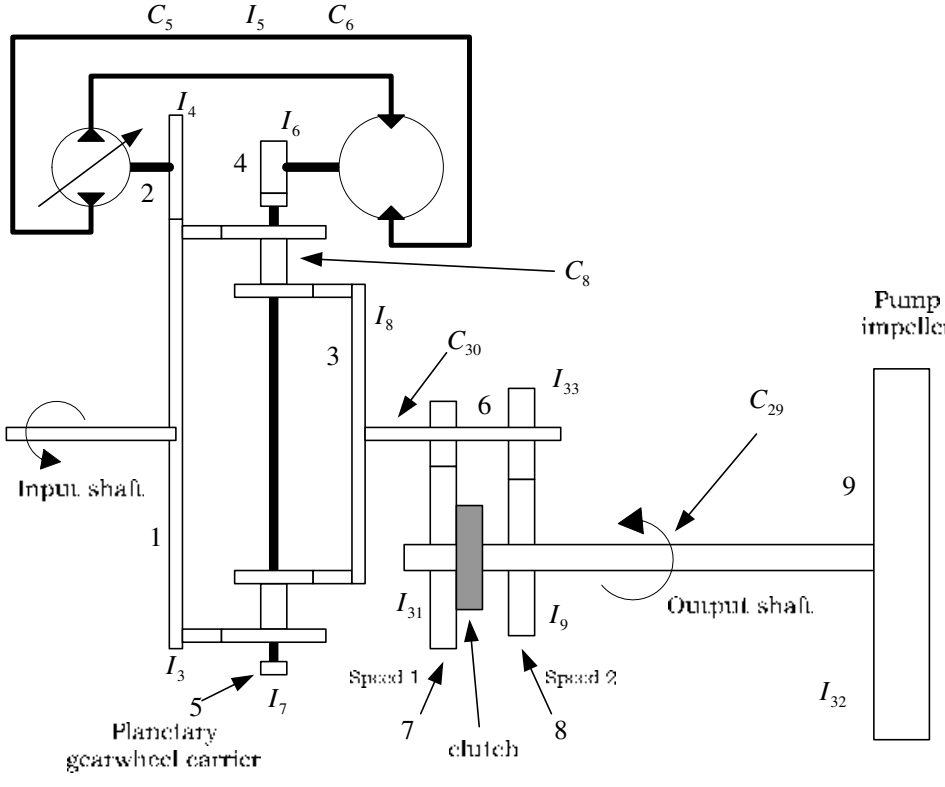

Fig. 2 Physical system of the gearbox with the "hydraulic shunt".

The italic letters refer to the Bond Graph symbols, see next page for a Bond Graph of the gearbox with the hydraulics. Fig 2 is a simple drawing of the working of the gearbox. The input gearwheel is driving besides the hydraulic pump also the planet wheels of the planet wheel carrier 5. When the planet wheel carrier is at stand still the gearwheel 3 is rotating in the opposite direction with the same speed as gearwheel 1. When the swash plate of the hydraulic pump is moving out of zero position then the hydraulic motor start turning and then the planet wheel carrier starts also turning. In this way it is possible to control the speed of gearwheel 3. The rotation of gearwheel 3 is transferred to 7 (speed 1) and to 8 (speed 2) and by the teeth clutch (which is connecting 7 or 8 to the output shaft) transferred to the output shaft.

3.1 Bond graph of the gearbox with "hydraulic shunt".

Fig. 2 consists only of masses and springs, in the real system there is damping and friction in the system. So far we have assumed that some parts of the system can be combined to form a single effective inertia. The input power to the gearbox is split up inside the gearbox in a "mechanical power part" and a "hydraulic power part", the Bond graph has also a "mechanical part" and a "hydraulic part".

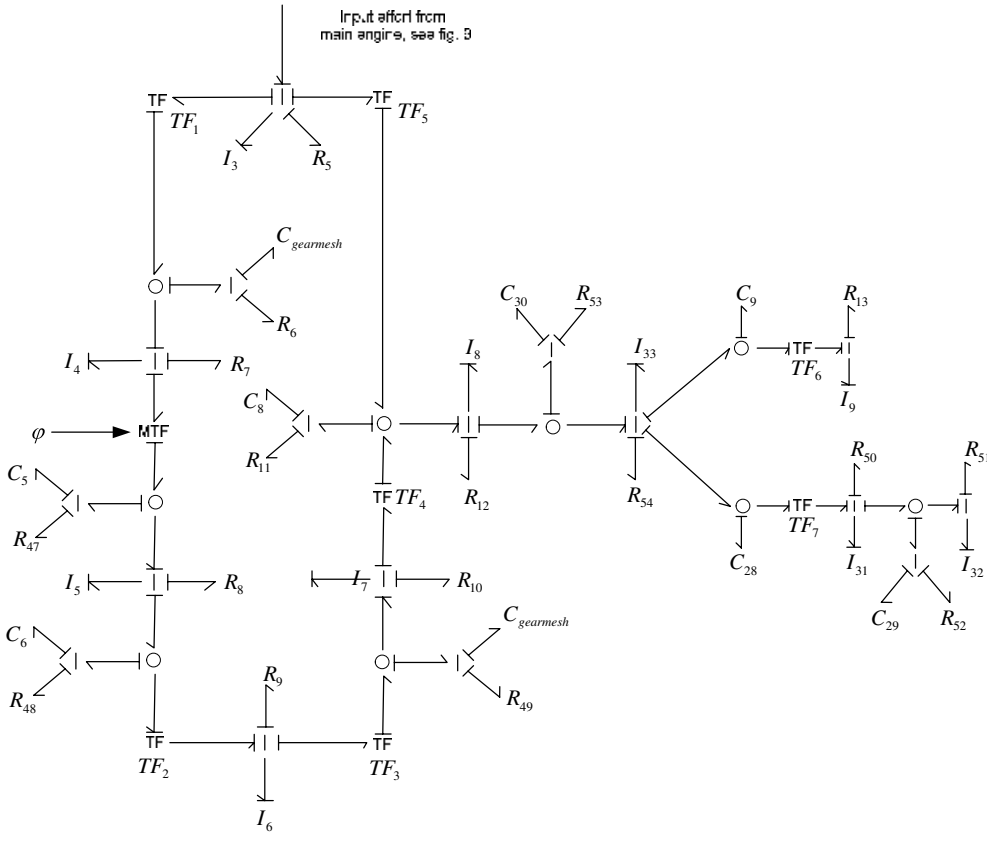

Fig. 3. The Bond Graph of the gearbox.

The mechanical power is transferred from gearwheel 1 (with inertia I_3), by the stiffness of the torsion shaft between the planetary gearwheels (C_8), to gearwheel 3 (with inertia (I_8).

The hydraulic power is transferred also by gearwheel 1 and the stiffness between the gearwheels 1 and 2 (inertia I_4) by the MTF in an hydraulic flow and pressure.
As the displacement of the hydraulic pump is adjustable, the pump can be seen as a MTF (modulated transformer) : the input flow (revolutions per second) : $[rad/\sec]$ is transformed to the output flow $[m^3.s^{-1}]$ and the output pressure $[N.m^2]$ is transformed to input torque $[Nm]$. The pump capacity (output) can be controlled by moving the swash plate position or angle from $\varphi = 0$ to $\varphi = \pm 19$ degrees.

Pump flow at full displacement: see (8). $Q = 1.28e-4 \quad [m^3.s^{-1}]$

Under normal circumstances the pump is regarded as a constant flow source. In general, a hydraulic pump is not a constant flow source, since positive displacement pumps inherently show flow fluctuations. See for an explanation the excellent book of Taco J. Viersma, (6).
As the pump capacity is a function of the sinus of the swash plate angle and the swash plate angle is max. 19 degrees:

$$Q = 1.28e-4 \times \frac{\sin\varphi}{\sin 19} \quad : \quad Const.1 = \frac{1.28e-4}{3.2556e-1} \times \sin\varphi$$

At a swash plate angle of 10 degrees Const. 1 in fig. 9. = 6.83e-6.
The essential action of hydrostatic machines is a transformer between mechanical and hydrostatic power. So an hydraulic motor can be represented by a transformer, the input flow variable [$m^3.sec^{-1}$] is transformed to the output flow variable [$rad.sec^{-1}$] and the effort hydraulic pressure is transformed to the effort torque.

From the motor data sheet of Hägglunds we derive: $TF5 = 500$

The hydraulic oil in the pipes between the hydraulic pump and hydraulic motor is modeled as two stiff nesses (C_5 and C_6) and one inertia (I_5), this is a simplification but for the purpose of the simulation sufficient. The hydraulic power is transformed back to mechanical power by TF 2 to gearwheel 4 (I_6) and from gearwheel 4 by TF 3 (gear ratio between 4 and 5 (I_7) and gear mesh stiffness to 5. And from 5 by TF4 (gear ratio between 5 and 3) and stiffness C_8 to gearwheel 3 (I_8)
The damping forces are presumed to be proportional to the relative velocities and are also used for stabilizing the simulation process, the purpose of the simulation was to find the resonance frequencies in the system. Also for that reason the friction 's are not that accurately modeled. Normally you start with a model which is as simple as possible (one looks for simple but relevant analogies, not for complex identities), to get a quick overview of the possible resonance frequencies in the system.
For the calculation of the parameter values we refer to (23)

4. A Bond Graph model of a diesel.

The diesel engine to model is a Wärtsilä 6L32 6 cylinder 4-stroke engine with a rated power of 2750 kW at 750 rpm. (see also the Wärtsilä 6L32 data sheets). As mentioned in the introduction a diesel engine is for torsional vibration analysis a cyclic vibration source. The cyclic vibrations can easily determined from the speed of the diesel engine and are called the vibration orders of the diesel. The first order is the speed of the crankshaft [revolutions/second]. When we have a 4 stroke engine we have also a halve order, a one cylinder 4 stroke engine is excited once per every two revolutions.

From the Fourier analysis we know that a periodic non sinusoidal form signal is build up of even and odd harmonics, so in the rotation of the crankshaft we find 0.5, 1st, 1.5, 2nd, 2.5, 3rd, 3.5, 4th, 4.5, 5th and higher orders.

Fig. 4 depicts a piston crank mechanism with the Bond Graph representation. By modeling a diesel engine in this way requires a lot of computation time and it appears that for torsional vibration analysis the Bond Graph representation from fig 4 can be simplified to the Bond Graph of fig. 5.

Classical analysis of vibrations involves transforming the physical system into a simplified equivalent dynamic system.
For systems subjected to torsion, this means splitting up the system in lumps with rigid body behavior. The lumps have a specified polar moment of inertia J and are connected by mass-less springs with the torsional stiffness k. Damping is attached to the lumps as internal torsional damping d. The number of inertia lumps included in a model defines the degrees of freedom and the number of states for simulation. Fig. 7 shows the dynamic representation of crank shaft with flywheel, pistons, viscous damper of the Wärtsilä 6L20 diesel and the Vulkan flexible coupling on the PTO shaft.

Figure 5 shows the Bond Graph of one cylinder with neighboring shaft elements used in the engine model, this simplification has proven to be sufficient for torsional vibration analysis.
In this vibration analysis the combustion process is simply modeled by a pressure variation in the form of a cosine form (see reference 3) of the force as depicted in figure 6. The mass-spring system is in this way excited with a signal which contains the harmonics to which the real system is subjected. Also this simplification has proven to be sufficient for torsional vibration analysis.

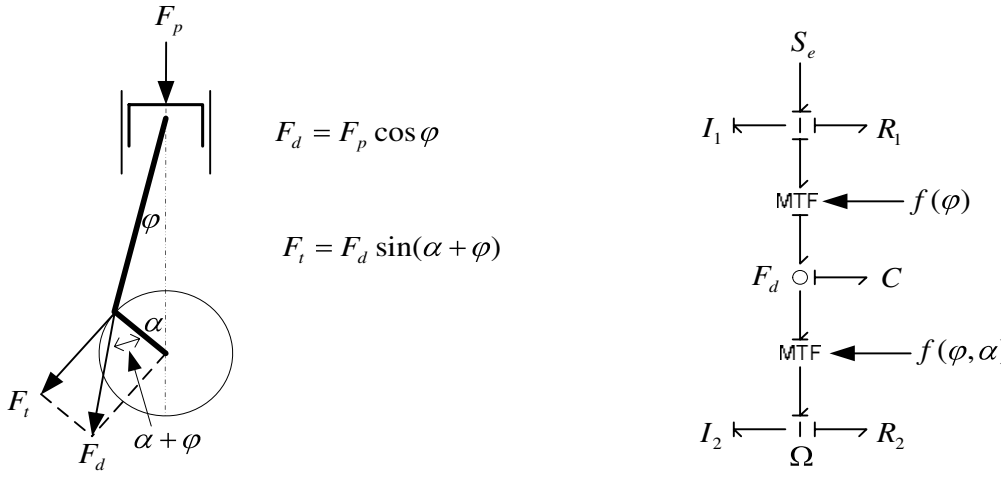

Fig. 4 Piston crank mechanism and the Bond Graph

S_e = force on piston from combustion

I_1 = mass of the piston I_2 = inertia crank + flywheel

C = stiffness rod + oil film

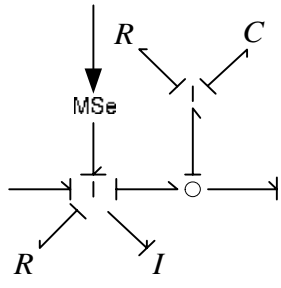

Fig. 5 Bond graph inertia piston and stiffness crank.

I = reduced inertia piston + crank.

C = stiffness crank shaft.

MSe = combustion force.

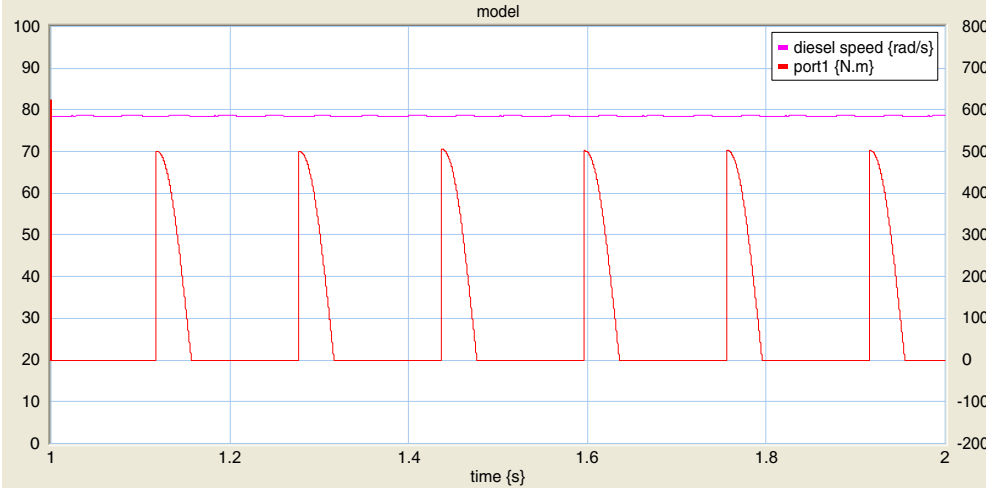

Fig. 6. Simulation of the combustion pulses.

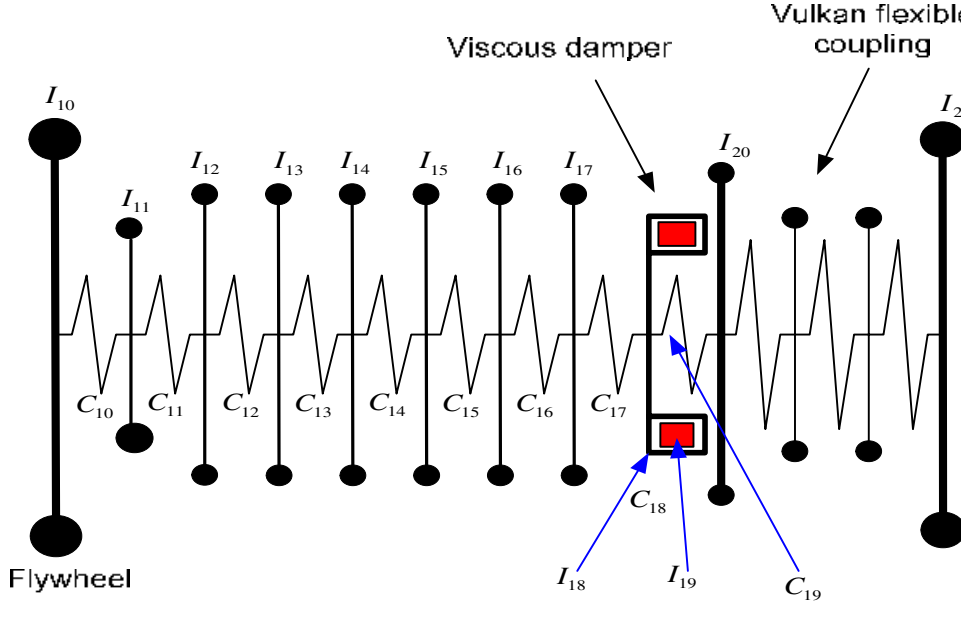

Fig. 7. Mass spring system of the crankshaft and pistons of a Wartsila 6L20 diesel.

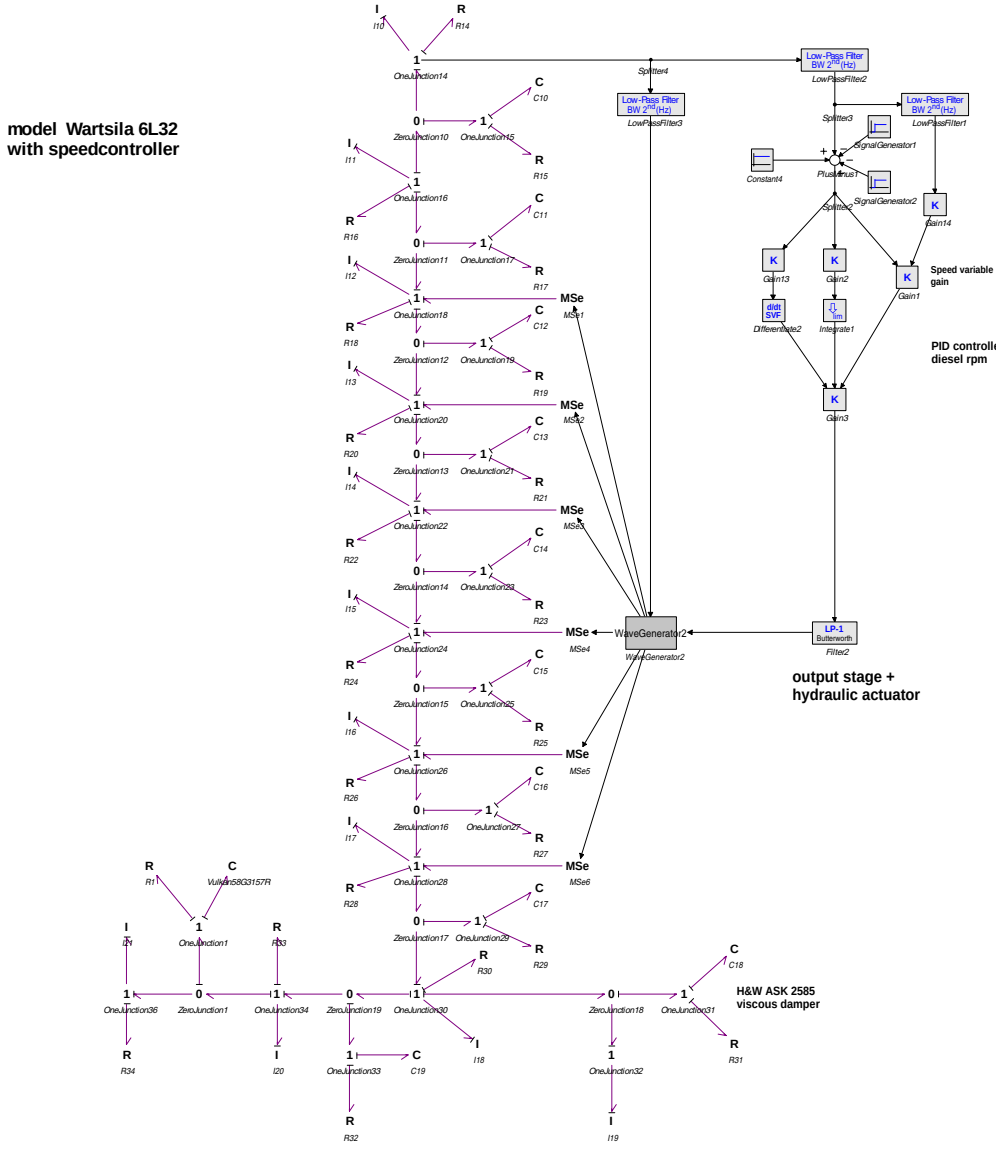

Fig. 8. Bond Graph of the 6 cylinder diesel.

Fig 8. depicts the Bond Graph of the 6 cylinder diesel with speed governor.

This figure depicts the crankshaft with the 6 combustion forces acting on it (6 times the Bond Graph from figure 5). The combustion forces are generated by a function generator ("wave

generator 2"). The speed controller of the diesel is the right hand side block diagram, simulating the electronic (digital) speed controller with the electro-hydraulic actuator to control the linkage of the fuel pumps. The electro-hydraulic actuator is modeled as a first order with a time constant of 80 msec. According the manufactures data the full movement of the output shaft, from a step of the input current, is 80 msec. The output of the actuator is connected to one of the inputs of the "wave generator" simulating the amount of fuel injected per cylinder (= amplitude of the combustion pulses).

The other input of the "wave generator" is connected to a low pass filter to get a smooth speed signal from the flywheel to generate the combustion pulses (= frequency of the combustion pulses). The electro-hydraulic actuator is a complicated mechatronic device but for this purpose is modeling as a first order block sufficient.
The speed controller of the diesel is a special PID controller, we refer to the Regulateurs Europa VIKING 25 data sheets.

The next page depicts the complete Bond Graph model of the diesel, the clutch and the variblock gearbox. The clutch model is taken from the model library in 20sim because to model a clutch is not an easy job and this simulation model was developed for torsional vibration analysis not for investigation of the clutch in mechanism. There are some good papers the describing the modeling of friction.(ref. 25) Measurements revealed that the behavior of this clutch is close to the real system.
The results of a simulation run with the simulation of the clutch in of the gearbox came pretty close to the real measurements so this model was detailed enough for the analysis of the dynamics at and after clutch of the gearbox.

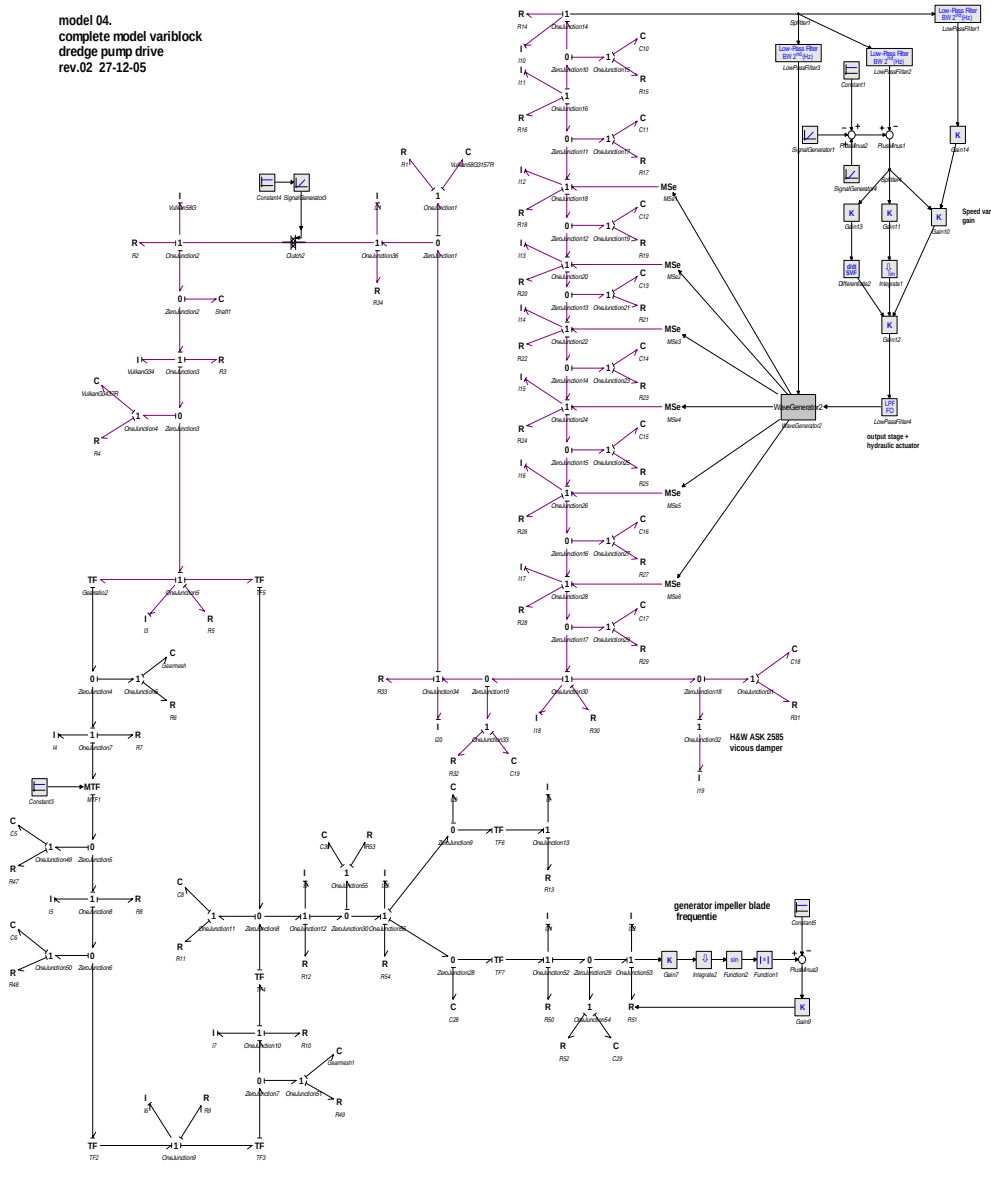

Fig. 9. Bond Graph model of the diesel motor with dredge pump drive.

Fig 9. depicts the Bond Graph of the 6 cylinder diesel with the speed governor and the hydraulic controllable gearbox for the dredge pump. With this model the dynamics at and after clutch in of the gearbox where investigated.

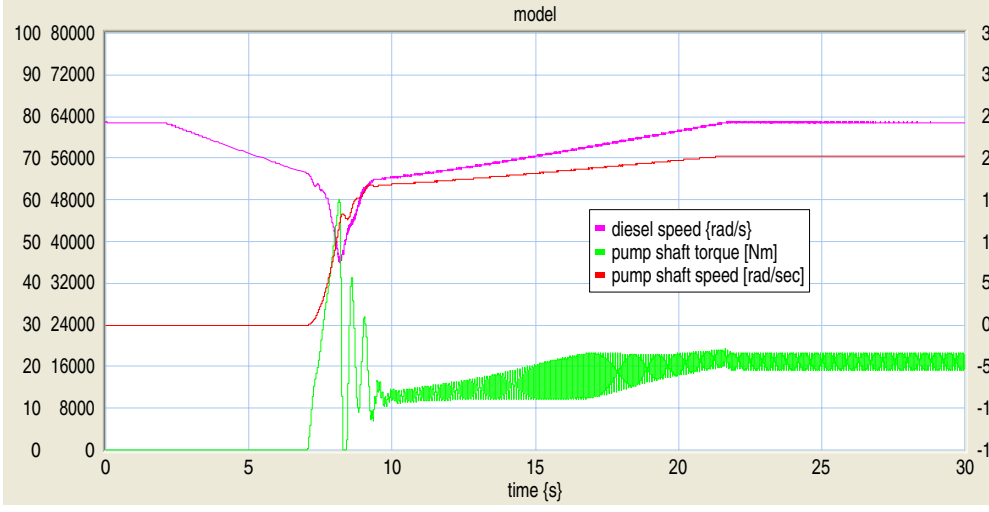

Fig. 10. Simulation output of the Bond Graph model.

The above simulation output depicts the simulation of the clutch-in of the gearbox. The upper graph is the diesel speed, the middle is the gearbox output shaft speed and the lower graph is the torque in the output shaft of the gearbox. At clutch-in command the diesel is lowered in speed to 600 rpm, then the gearbox is clutched in and after clutch-in the diesel is speed up to 750 rpm. The simulation revealed that after clutch in the torque in the shaft goes below zero which can cause “gear hammer”. At an inspection of the gearbox the surface of the teeth of the clutch give evidence for gear hammer. Simulation revealed that if the clutch-in time is shorter the oscillating torque goes far below zero. The clutch in mechanism is done by compressed air through an orifice which is factory set so the clutch-in time is not controlled but depends a little on the external system pressure of the compressed air system.
The simulation also reveals that during speed up of the dredge pump that a resonance frequency is passed the same can be seen from the real measurements in fig.12 .
The next simulation output (fig. 11) depicts the oscillations in the pump shaft at clutch in at high gear with different slipping time of the clutch.

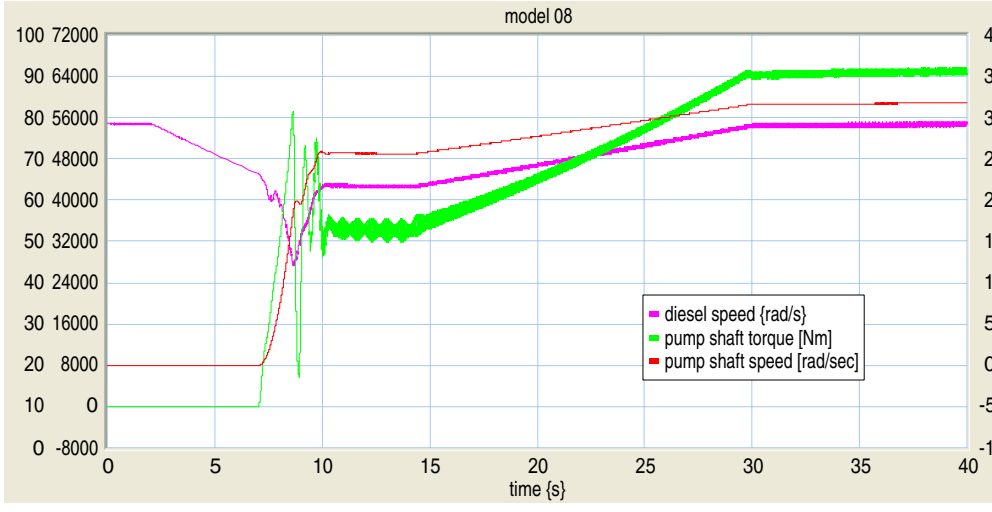

Fig. 11 clutch in time 1.6 second (high gear)

Fig.11 depicts that after a slipping time of 1.6 seconds of the clutch the torque oscillation stay above the zero line so there is no gear hammer.

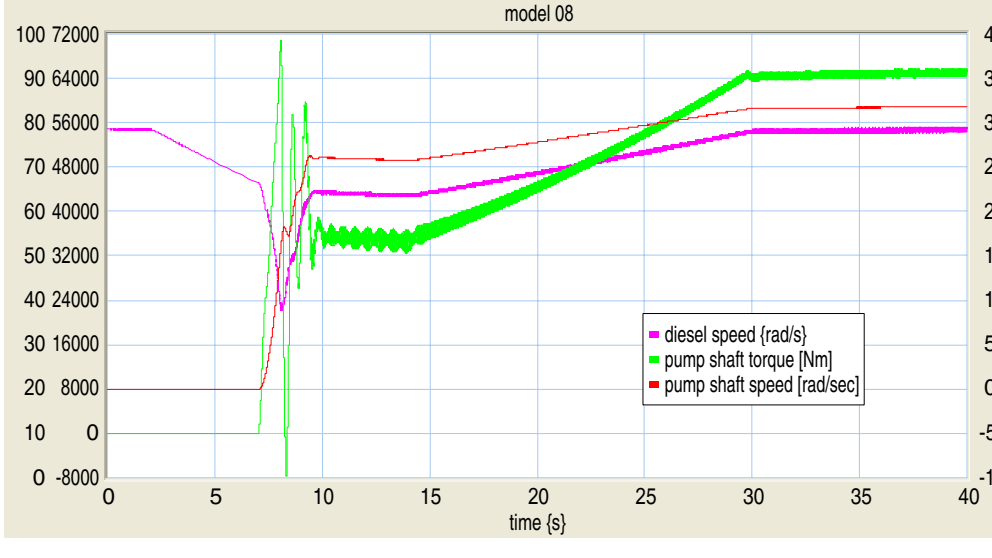

Fig 12. clutch in time 1 second.

Fig 12 depicts that after a slipping time of the clutch of 1 second the torque oscillation goes below the zero line so gear hammer will occur.

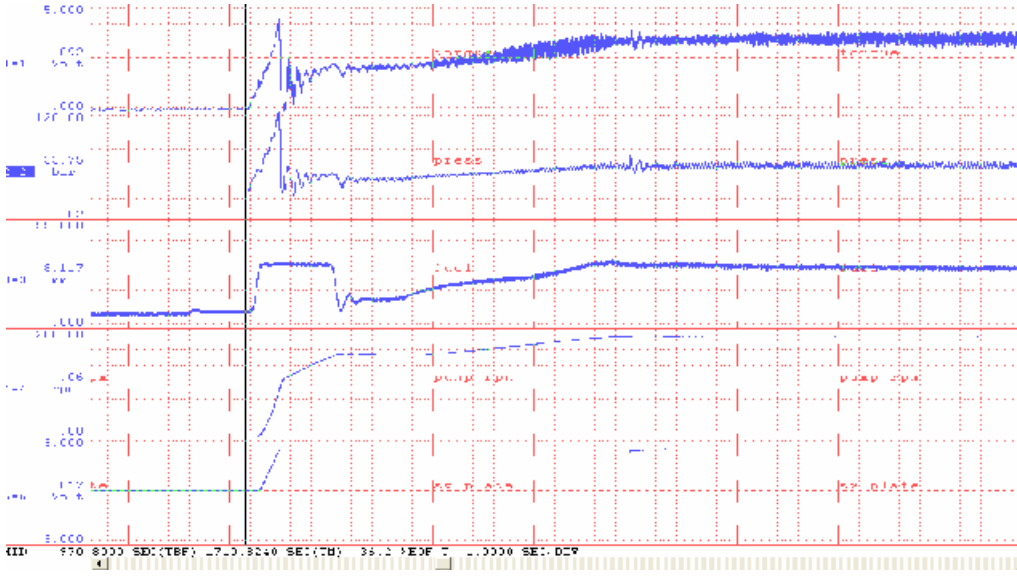

Fig . 13 measurement of clutch in at low gear.

Channel 1: pump shaft torque
Channel 2: system pressure
Channel 3: fuel rack diesel
Channel 4: pump rpm
Channel 5: swash plate from zero position to minimum pump speed.
Time scale: 1 sec/div.

The clutch-in procedure of the gearbox is as follows: the diesel is lowered in revolutions to 600 rpm. Then the clutch in command is generated, as soon as the electronics detect that the output shaft is moving the swash plate of the hydraulic pump is controlled to minimum rpm. position as depicted in the recording above 8 bar.) then the diesel is speeded up to the nominal speed of 750 rpm. After the diesel rpm. is 750 then the operator can enable the speed control of the pump shaft.

5. Speed control output shaft gearbox.

The speed of the output shaft of the gearbox is performed by the " hydraulic shunt'' the swash plate of the hydraulic pump is controlled by a speed controller and if necessary by a fuel rack controller of the main engine.

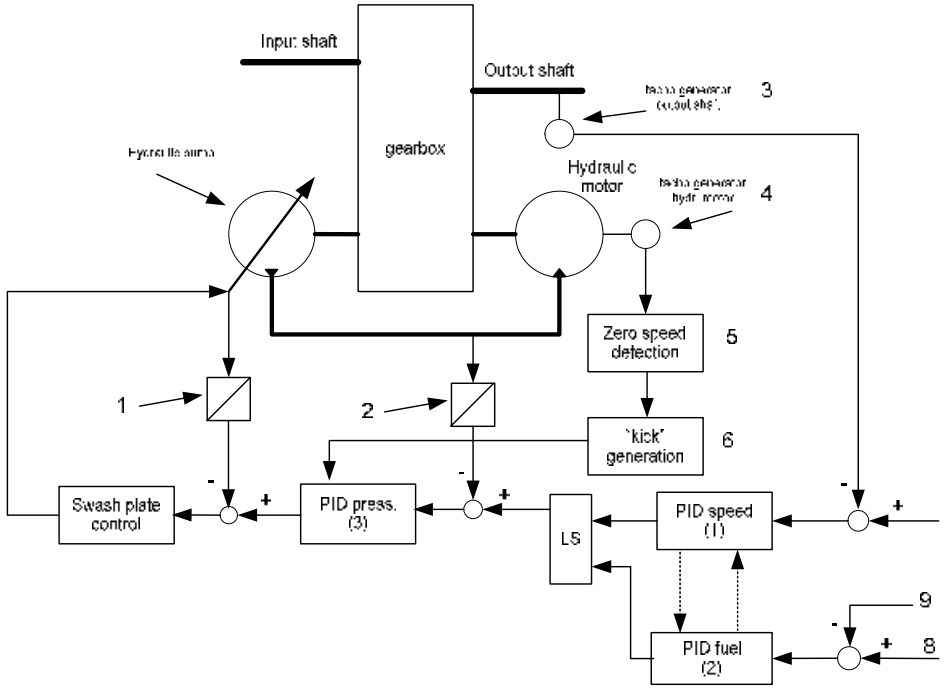

Fig 14. Simplified control block diagram.

Description of the blocks of fig. 14.

Block	Description
1.	transducer swash plate position.
2.	transducer hydraulic system pressure.
3.	tacho generator output shaft revolutions.
4	tacho generator hydraulic motor revolutions.
5	zero speed detection block hydraulic motors.
6	block to generate a hydraulic "kick" at zero speed detection of the hydraulic motors.
7	set point dredge pump speed
8	set point fuel rack or diesel load.
9	fuel rack diesel engine

As depicted in the block diagram the speed controller and the fuel rack controller are working in parallel, the dashed lines between the PID controllers are the tracking signals to ensure a "bump less" take over between the two PID controllers.

Also after clutch-in and before switch on the output of the speed controller and the pressure controller are set at the proper value. At switch on of the speed controller the pump shaft has a speed of 190 rpm in low gear and 300 rpm at high gear.
The output of the speed controller is set at the measured hydraulic pressure, and the output of the pressure controller is set at the measured swash plate position.
PID (1) is the dredge pump speed controller with 2 set 's of control parameters, during dredging the speed range is from 190 – 240 rpm. And during shore discharge the speed range is from 300 – 370 rpm.
PID (2) is the fuel rack or load controller of the diesel. During shore discharge the load on the dredge pump can be very fluctuating (depending on the density of the mixture in the pump). The load controller keeps the load on the diesel more or less constant by adjusting the speed of the dredge pump. See measurements in fig. 23.
PID (3) is the hydraulic system pressure controller, its proportional gain is adapted from the swash plate angle signal. As explained before, the flow of the pump is a function of the sinus of the swash plate angle and there fore the gain adaptation of the proportional part of the PID controller is introduced.

The PID controllers 1, 2 and 3 are more or less "fuzzy" controllers, the block diagram is depicted in fig. 15. This "modified" PID controller was developed from searching in literature and experiences with controlling non linear systems. With the function blocks fun3, fun4 and fun5 we can add a nonlinear gain, derived from the error signal, to the proportional, integral and derivative action. Also the up and down integration time, determined from the sign of the error signal, can be adjusted separately. With function block 2 the proportional gain can be adjusted by an external signal. For the load controller this works very well, for the proportional part we have a low gain at a small error signal and a high gain when the error signal is big. For the integral part we have a fast integration time at an overload and a slow integration time when the load is below the set point.
The tuning of this controller requires some experience and feeling.
As standard PID blocks does not have the above functionality the PID algorithm was programmed in the PLC from a functional description.

Recently Siemens came up with their function block FB41 which is a PID controller with the possibility of online access to the parameters , see fig. 16.

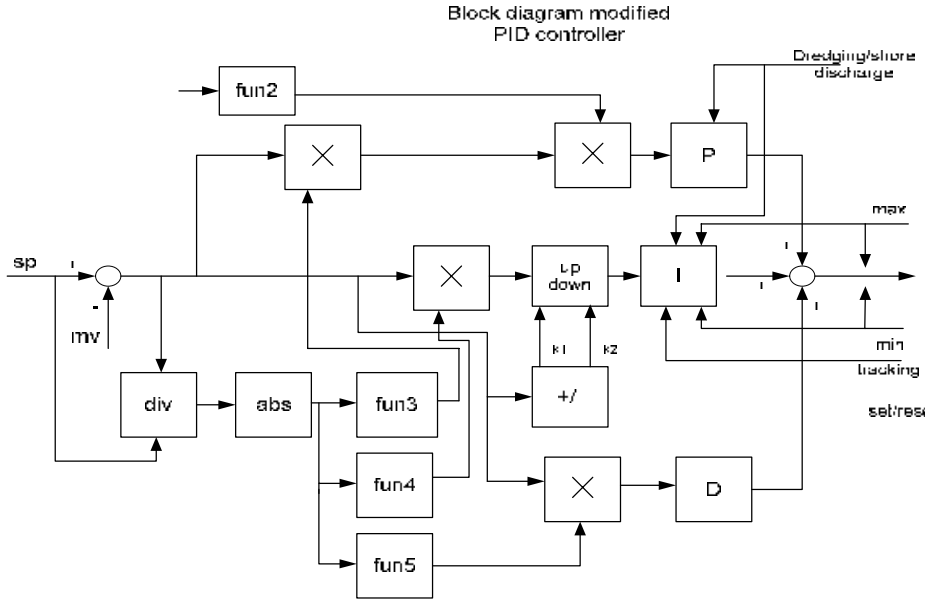

Fig. 15. Modified PID controller

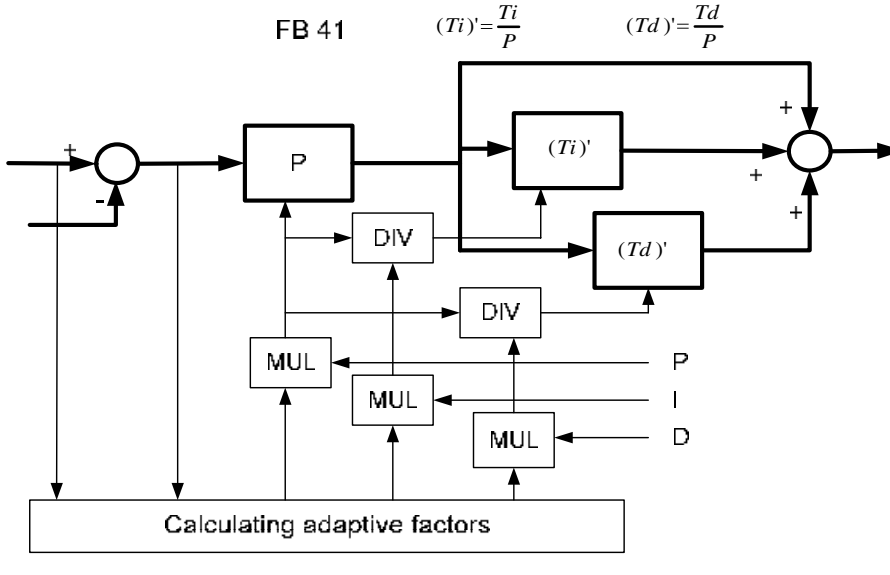

Fig. 16 Modified PID control with function block FB 41 of Siemens

We refer to the Siemens documentation “Continuous Control with SFB41/FB41 “Cont_C”.
As mentioned before this control configuration is based on previous experiences. Due to a lack of information, in particular the hydraulic servo mechanism to control the swash plate position, this control configuration is not yet modeled to verify if this control configuration is the most optimum.
To prevent wind-up of the integral part of the PID-controller which is not in charge, special actions are taken, so called tracking, to ensure a “bumbles” take-over between the PID controllers.
Also special actions are taken to ensure a “bumbles” switch-on of the speed controller, because the dredge pump shaft is running either 190 or 300 rpm at switch-on of the speed controller.

6. Stick-slip of the hydraulic motors.

At commissioning of the load controller of the diesel motor , to prevent overloading and overheating of the diesel, it appears that at slow crossing the zero speed of the hydraulic motors (see the recording below, fig. 17) they face “stick-slip” a phenomena well known from hydraulic cylinders at reversing of the movement or starting of the movement.
The manufacturer did some modification to the piston rings of the hydraulic motor but despite of that the stick-slip is still there. This phenomenon was disturbing the load control of the diesel so a solution has to be found.
It was decided to place a tacho generator on the shaft of one of the two hydraulic motors in order to detect precisely the stand still of the motors . After a few trials the right tacho was found to detect reliable the stand still of the motor. A mechanism was developed to generate an hydraulic “kick” to the motor after detection that the motor is not turning for one second.

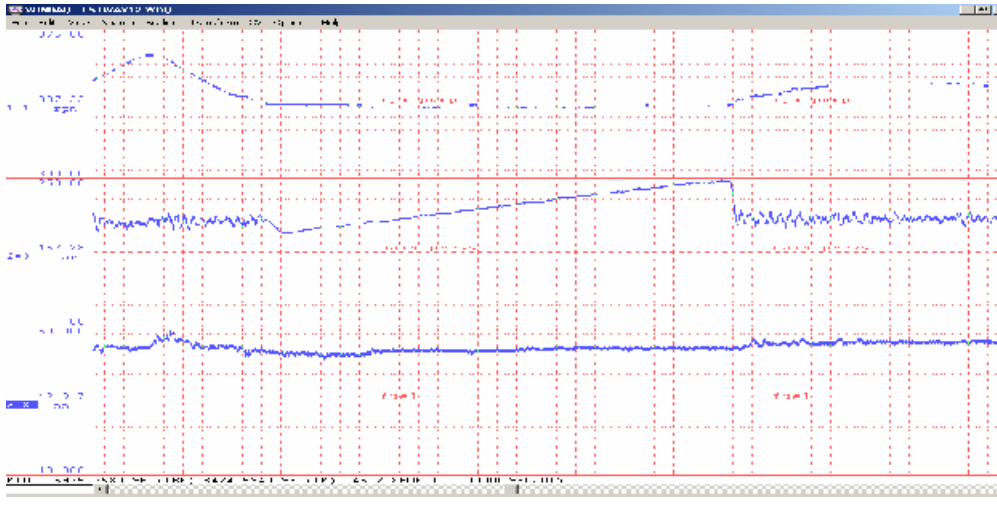

Fig. 17. “Stick slip”.

Fig. 17:
Channel 1: dredge pump rpm, channel 2 : system pressure and channel 3: fuel rack diesel.
Time scale : 1 sec/div.

At the start of the "stick-slip" the pressure is 157 bar, the pressure rises to 254 bar before the motor starts turning again.
To solve this problem a tacho generator was placed at the shaft of one of the hydraulic motors in order to detect the stand still of the hydraulic motors. After a few trials the right tacho was found to detect in a reliable way the stand still of the motor. A mechanism was developed to generate a "kick" after detection that the motor is not turning for 1 second see the recording in fig 18. Because of the flexible hydraulic hoses the hydraulic system is rather "dynamic" the amplitude of the "kicks" is kept small and if the motor is not turning after 5 "kicks" a "kick" with a higher amplitude is generated.

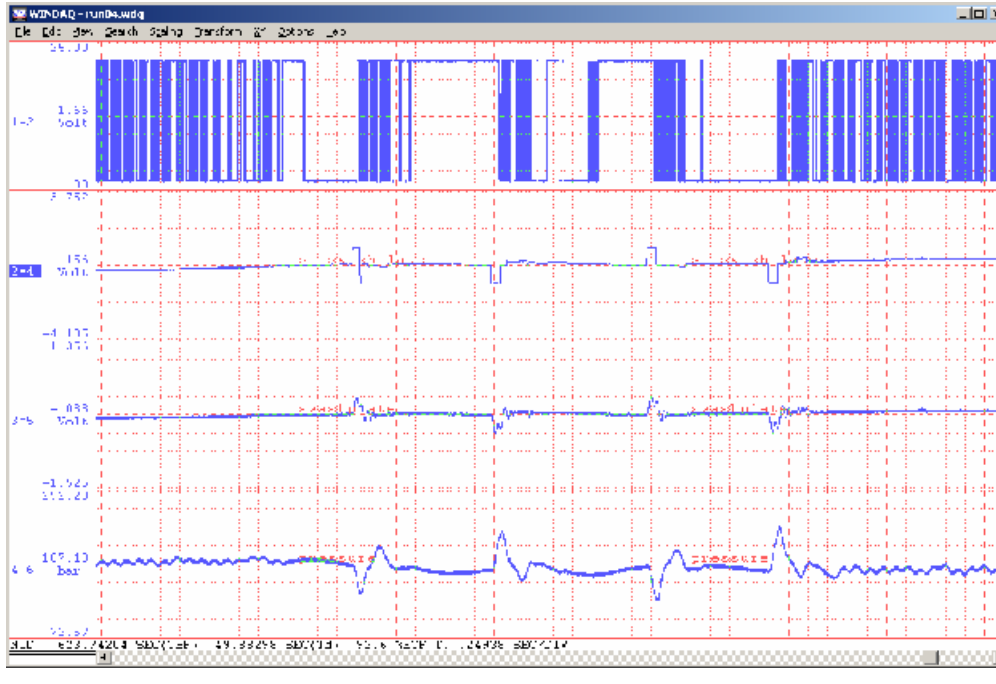

Fig. 18. System generates a "kick" of 0.1 sec. to make the system move again.

Channel 1: signal from the pulse tacho generator on the hydraulic motor.
Channel 2: set point swash plate position
Channel 3: swash plate position
Channel 4: system pressure
Time scale: 0.25 sec/div.

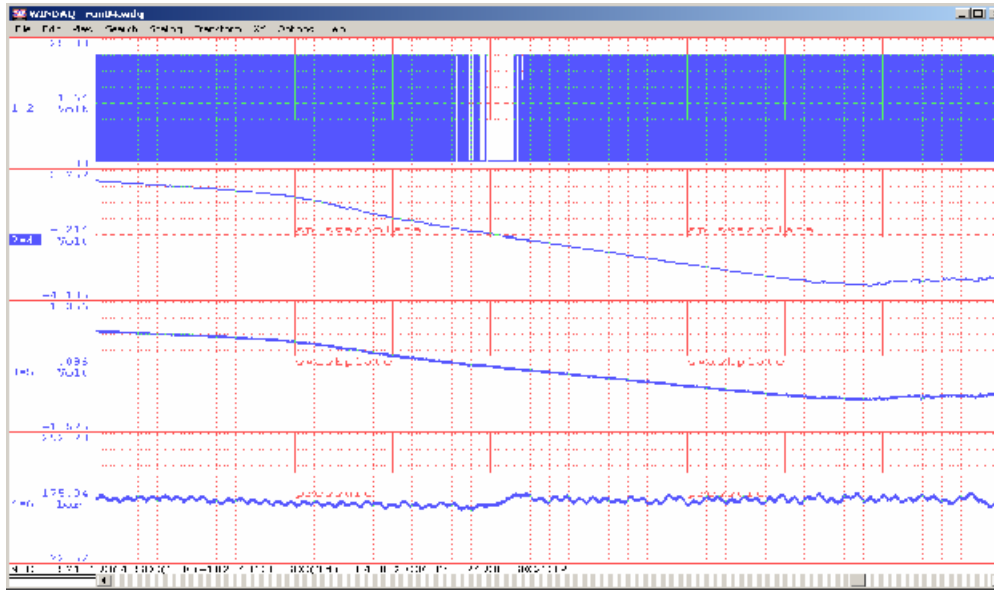

Fig. 19. No stick slip.

Channel 1: signal from the pulse tacho generator on the hydraulic motor.
Channel 2: set point swash plate position
Channel 3: swash plate position
Channel 4: system pressure
Time scale: 0.25 sec/div.

Fig. 19 depicts the speed reversing of the hydraulic motor without stick-slip. Note the “jump” in hydraulic system pressure because of the reversing of the efficiencies in the hydraulic circuit. The hydraulic motor becomes hydraulic pump and the hydraulic pump becomes hydraulic motor.

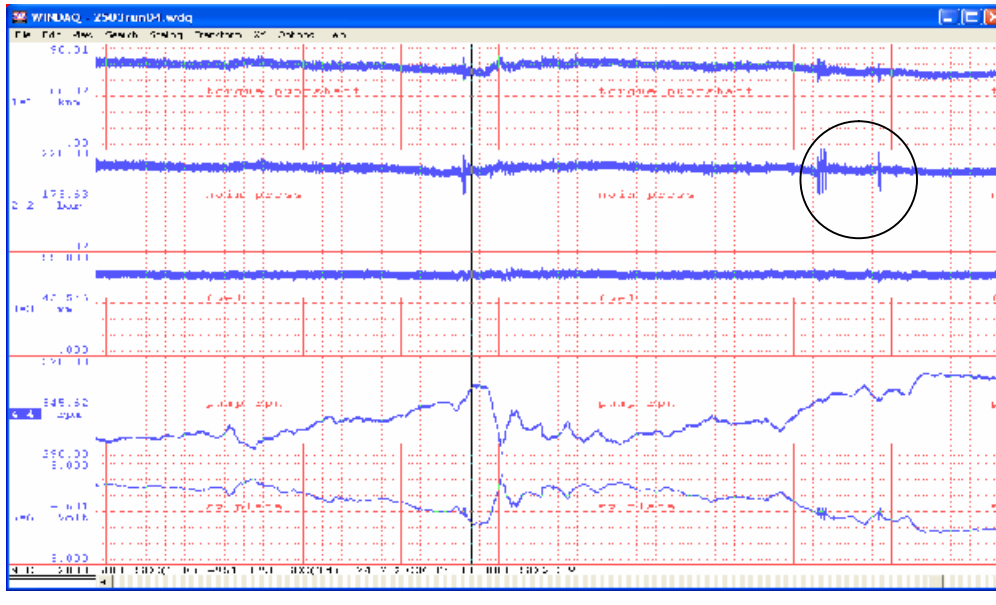

Fig. 20. Recording of the load control of the diesel.

Channel 1: torque in the pump shaft.
Channel 2: main pressure.
Channel 3: fuel rack diesel.
Channel 4: dredge pump rpm.
Channel 5: swash plate position hydraulic pump.
Time scale: 30 sec/div.

The load of the diesel is controlled by the adjusting of the speed of the dredge pump by the load controller. The load of the diesel (fuel rack) is kept on a constant value as indicated in the recording.
The vibrations in the pressure and torque measurements (indicated by the circle) are caused by the control mechanism which detects a stick slip and takes action.

7. **Conclusions.**

This paper depicts the power of Bond Graphs in modeling marine engineering systems. The first problem for a control engineer or systems engineer in front of a process to control is to obtain a precise and easily manipulated model with predictions corresponding to the real observations.
This paper depicts that the Bond Graph method is domain independent, mechanical and hydraulic systems are easily connected.
The use of 20sim as a simulation package make live a lot easier for the practical engineer because of the ability of direct input of the Bond Graph.
The modeling itself has broadened the insight and understanding of the system.
This is general: modeling a physical system gives more insight in the system

The most time consuming part of modeling is to get the right parameters of the system or the systems components. It depends largely on knowing the right man on the right place to get the information needed to set up a model that represent the physical system.

Measurements revealed that the simplifications in the modeling where allowed for this reason finding the resonance frequencies of the system, as mentioned before one looks for relevant analogies, not for complex identities.

The control of the system is not yet modeled to verify the control configuration with the non linear controllers but the practice depicts that the chosen configuration is not bad at all.

REFERENCES

[1] Modeling for transient torsional vibration analysis in marine power train systems. Kristine Bruun, Eilif Pedersen and Harald Valland. The Norwegian University of Science and Technology Department of Marine Technology.

[2] J.P. den Hartog. Mechanical Vibrations Dover, 1985. ISBN 0-486-64785-4

[3] S.T.Nannenberg. Bondgraaftechniek (in Dutch) Delta Press, 1987 ISBN 90-6674-1256

[4] Dean C. Karnopp, Donand L. Marlolis, Ronald C. Rosenberg. System Dynamics John Wiley. 2000 ISBN 0-471-33301-8

[5] Jean U. Thoma. Simulation by Bondgraphs. Springer, 1990 ISBN 3-540-51640-9 (very good for the practical engineer)

[6] Taco J. Viersma, Analysis, Synthesis and Design of Hydraulic Servo systems and Pipelines. 1980 Elsevier, ISBN 0-444-41869-5

[7] F.Fûresz, G. Hakay, I. Kroell Dulay, L. Lukacs. Fundamentals of Hydraulic Power Transmission. Elsevier, 1988 ISBN 0-444-98973-0

[8] B.S.Massey. Mechanics of fluids. ELBS edition, 1989 ISBN 0-12-436250- 3

[9] Denison Hydraulics. Hydrostatic transmission Application manual. Publ. SP1-AM330-A

[10] Hägllunds Drives. Product manual Compact. EN396-4

[11] Powerful Engineering. Book available from Hägglunds. No author data available.

[12] Peter Dransfield. Hydraulic Control Systems- Design and Analysis of Their Dynamics. Springer-Verlag , 1981 ISBN 0-387-10890-4

[13] Hallvard Engja. Modelling for transient performance simulation of diesel engines using Bond Graphs. ISME 1983, page 321 - 328.

[14] Hallvard Engja. The Bond graph technique as a powerful modeling tool. International symposium on Advances in Marine Technology, page 471 - 441.

[15] Vulkan Technical data sheet: RATO-ETD

[16] Jari Mäkinen, Robert Piche and Asko Ellman. Fluid Transmission Line Modeling Using a Variation Method. Journal of Dynamic Systems, Measurement, and Control, March 2000, Vol 112/page 153 - 162.

[17] J.W.Polder, Model of a Mechanical Transmission. Department of Mechanical Engineering Eindhoven, University of Technology Eindhoven 1969 , The Netherlands.

[18] Wright, R.Burton and G. Schoenau, Lumped Parameter Model of a Variable Displacement Pump.
The Journal of Fluid Control ( ) pp 37 – 57.

[19] Hallvard Engja, Application of Bond graphs for mathematical modelling and simulation of marine engineering systems.
Trans IMarE, Vol 110, part 4 pp 229-239.

[20] P.J.Gawthrop, Bondgraphs: A representation for mechatronic systems. Mechatronics Vol 1, No. 2 pp 127-156, 1991

[21] Peter Gawthrop,Lorcan Smith: Metamodelling: Bond graphs and dynamic systems. Prentice Hall ISBN 0-13-489824-9 1996.

[22] P.C.Breedveld and G.Dauphin-Tanguy: Bond Graphs for Engineers. North-Holland 1992.

[23] T.Heeringa: Engineering around a hydraulic controlled gearbox.
PTMC 2004 papers , pages 11 – 36.

[24] J.Thoma B.Ould Bouamama: Modelling and Simulation in Thermal and Chemical Engineering. Springer. ISBN 3-540-66388-6

[25] D.A. Haessig, B. Friedland. On the Modeling and Simulation of Friction. Transactions of the ASME Vol. 113, September 1991 pages 354 – 362.

Return to Contents

Design and implementation of a water hydraulic 6-DOF motion platform for real-time simulators

Tuija Palonen, Markus Rokala, Harri Sairiala, Janne Uusi-Heikkilä, Mika Hyvönen, Kari T. Koskinen
Institute of Hydraulics and Automation, Tampere University of Technology

ABSTRACT

This paper indicates the design and implementation of 6-DOF water hydraulic Stewart platform. It deals with adapting the motion platform to water hydraulics and control of the platform, specifying parts to be studied in more detail.

Four different washout filters for creating motion are studied in simulation model and validated with a test bench with one valve-cylinder pair. Mechanical construction of the platform has been started. Real-time simulators with motion platform demand fast and accurate response for valves and a good controller, since phase delays and fluctuations in the platform motion can cause motion sickness.

NOMENCLATURE

K = gain
Q = resonance frequency / transmission bands 3 dB bandwidth
t = time [s]
T_L = long time constant for otolith model [s]
T_s = short time constant for otolith model [s]
T_{ad} = adaptation time constant for otolith model [s]
T_a = long time constant for semicircular canal model [s]
T_e = short time constant for semicircular canal model [s]
T_U = adaptation time constant for semicircular canal model [s]
k = mid-frequency gain
s = Laplace transform variable
a = acceleration [m/s^2]
ω = angular velocity [rad/s]
LAN = Local Area Network
UDP = User Datagram Protocol
DOF = Degree Of Freedom

Power Transmission and Motion Control 2006 Edited by Dr D N Johnston and Professor K A Edge

1. GENERAL DESCRIPTION OF SIMULATOR

Research and implementation of a water hydraulic motion platform has been started. This study integrates the research of water hydraulics and virtual technologies. In the motion platform will be used in a real-time simulator construction that allows simulation of different vehicles with minimal changes. Figure 1 presents the layout of the simulator. There are four standard PCs, one for simulation of the vehicle (PC 1), one for control and position measurement of the platform (PC 2), one for generating graphics (PC 4) and an optional PC for the main loop (PC 3). The system is distributed through a Local Area Network (LAN), using UDP-protocol for communications.

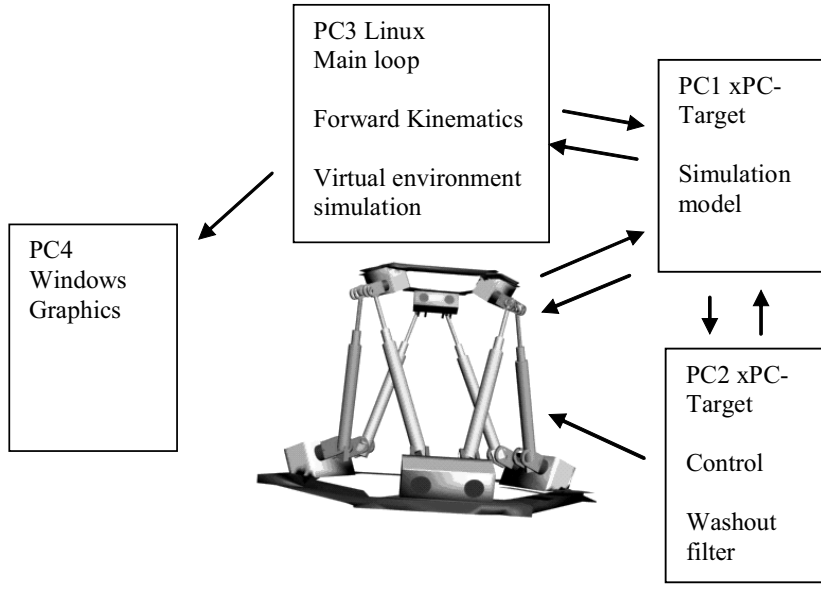

Figure 1 Structure of the simulator

1.1 Graphics generation

Three-dimensional graphics will be generated in a Windows-environment, using OpenGLPerformer® for real-time rendering. Because of platform motion, traditional 3D-stereovision with two projectors is difficult to implement. Instead of a projection screen, a head-mounted display will be used. To add more reality to the driving experience, 3-DOF (rotations) motion detection is used with a head mounted display. The image shall be created from the driver's point of view while using motion tracking and the head mounted display.

1.2 Main loop

In simple simulators, where the simulated vehicle does not have complex moving parts such as booms, PC 3 may not be needed. Other benefits are gained when using third PC: more efficient solving of the forward kinematics of the simulated vehicle and more realistic collisions calculation between the simulated vehicle and virtual surroundings.

1.3 Simulation computers

The simulation model is made with MathWorks Matlab® Simulink® and it based on the Simulink model of the Stewart platform. The model was modified so that the sub models of the water hydraulic valves and the cylinders are connected to the model. With the modified model, basic sizing is done and also the washout filters are tuned.

In the simulator, the simulation model works in real-time with MathWorks xPC Target (toolbox in Simulink® product family) software. The simulation model is distributed in the two standard PCs. PC 1 calculates the dynamics of the mobile machine on the platform and transfers the necessary information to the other simulation PC 2 and to the PC 4. Also, the interaction between the mobile machine and the terrain is modelled on PC 1. PC 2 calculates the reference values of the position of the cylinders and the desired openings for the valves. Washout filters are also on PC 2. PC 2 is fitted with two analogue input cards for acquiring the sensor signals and analogue output card for controlling valves.

2. IMPLEMENTATION OF MOTION PLATFORM WATER HYDRAULICS

The platform will have six SSH Stainless 40/25 cylinders with 400 millimetres stroke. Every cylinder has an integrated positioning sensor installed in a water resistant housing. Cylinders will be connected to valves with hoses, also between the pump and valves will be hose-connections. Figure 2 presents circuit diagram for the motion platform with intended pump and three accumulators.

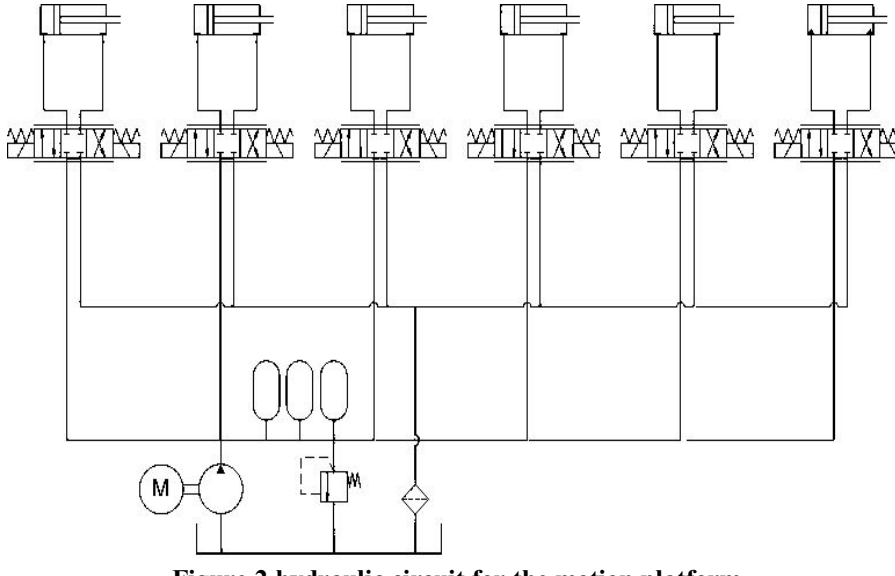

Figure 2 hydraulic circuit for the motion platform

2.1 Valves

Valves chosen for the platform were modified Sitek L22 4/3 proportional direction valves. Maximum supply pressure to these valves is 50 bar and they operate with tap water. Spool position is measured with an LVDT-sensor and it is controlled by a PI-controller. Original internal leak channels were replaced with external leak channels, which stabilize valve operation. The control voltage range for valve is –10 … 10 volts. Figure 3 presents dynamic step responses of the valve. Step response rise time between 10 … 90 % are from 20 to 200 milliseconds.

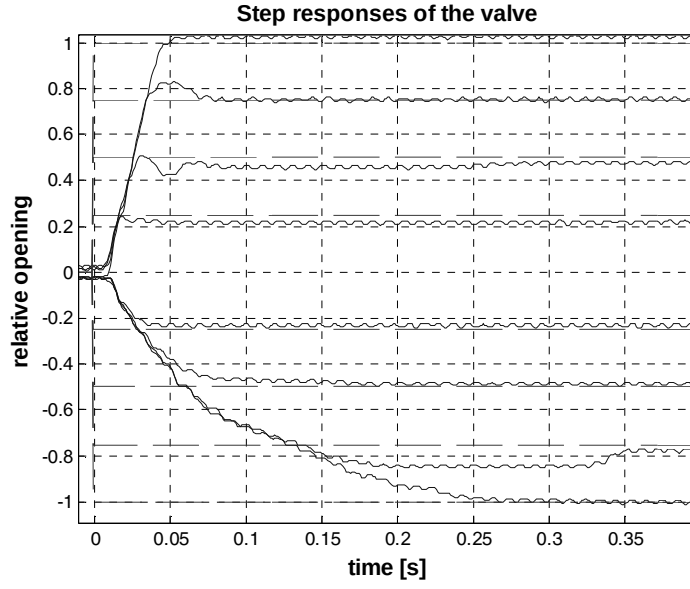

Figure 3 Step responses of the valve

3. THEORY OF WASHOUT FILTERS

The purpose for the motion algorithm (washout filter) is to create movement corresponding to the driving control. Correspondence of platform motion with motion of the view and driving control is important for avoiding simulator sickness. Washout filters simulate high frequency accelerations by tilting the platform and then returning the platform to base. Tilt simulates low frequency platform motion by using gravitational component, which is sensed as a continuous acceleration by driver. All-tough this research is focused only on the classical and human-based washout filter, several different ones exist, etc. predicative washout filter (5).

3.1 Classical Model

The first studied washout filter was the classical algorithm. Tilt system was added to the model later, so low frequency acceleration can be simulated by inclining the platform (3). As presented in Figure 4, high-pass filters take acceleration and velocities as inputs. Scaling of input is done by the filter gain, K. A second high-pass filter returns the acceleration to zero, and therefore the platform is returned to the base. The classical model has many

parameters, and selecting the right cut-off frequency, order of high-pass filters and parameter values is difficult. Wrong choice will be exposed in empirical test with human driver at the latest. First order high-pass filter is presented with transfer function:

$$\omega(s) = \frac{Ks}{s + \frac{2\pi}{t}} \tag{1}$$

Second order high pass filters are presented with the following transfer function:

$$a(s) = \frac{Ks^2}{s^2 + \left(\frac{2\pi}{Q}\right)s + \left(\frac{2\pi}{t}\right)^2} \tag{2}$$

Both filter types are also used for a human-based model (2).

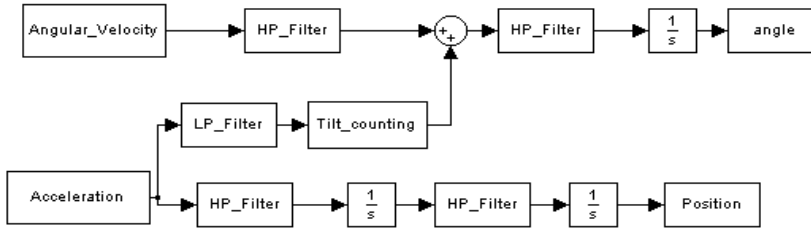

Figure 4 Block model of classical washout filter (1)

3.2 Human-based model

The human-based model does not use high-pass filters for first filtering. Instead of the high-pass filters, models of the human vestibular organs that consists otolith organs and semicircular canals are used. Filters for accelerations are replaced with otolith model, presented with following transfer function:

$$a(s) = \frac{k(Ts+1)}{(T_L s+1)(T_s s+1)} \tag{3}$$

Likewise, filters for angular velocities are replaced by semicircular canal model, presented with transfer function:

$$\omega(s) = \frac{T_a T_U s^2}{(T_a s+1)(T_e s+1)(T_U s+1)} \tag{4}$$

In Figure 5 is presented a block model of a human-based washout filter, where the previous model is used. Young and Oman (2) have presented these models, which use transfer functions and dead zone blocks. The dead zone cuts accelerations and angular velocities below the human sensing limit. The human-based model has smaller phase delay than classical because of dead zones. Because of ready made otolith and semicircular canal models, tuning human-based washout filter is less taxing than the classical one. Angular velocities are taken as input for the semicircular canal model and after that they are high-pass filtered for returning the platform to base orientation. After filtering, angular velocity is integrated to the angle reference value. Linear accelerations are input to the otolith model and like angular velocities, are high-pass filtered after that for returning platform to base. Accelerations are integrated twice for position reference (2, 4).

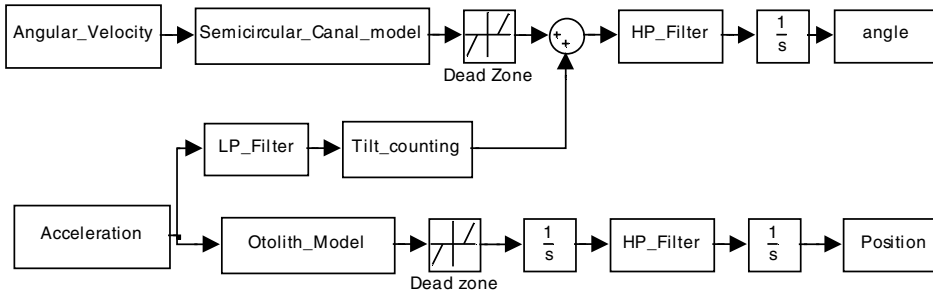

Figure 5 Block model for human based washout filter (2)

Table 1 Dead zones in human sensing system (2)

	Surge	Heave	Sway
dead zone m/s^2	0.17	0.28	0.17
	Roll	Pitch	Yaw
dead zone deg/s	3.0	3.60	2.6

4. SIMULATION OF WASHOUT FILTERS

4.1 Simulation arrangement

The simulation model of the Stewart platform was constructed for validating parameters of washout filters. Parallel kinematics and mechanical model of the platform are derived from the SimMechanics toolbox of Mathworks Simulink® program. The water hydraulic system was modelled in the IHA, using proportional valve models and accurate models of the cylinders. Exact data for valve simulation model were not available when the simulation model was constructed. In Figure 6 is presented the basic construction of the simulation model for the motion platform. Inputs are simulated translational accelerations and angular velocities that are filtered and integrated to position and angular motion platform. Parallel

kinematics solves actuator reference positions form platforms position and angle. The hydraulic model takes positions of the actuators as inputs and with the mechanical model simulates platform motion. The coordinate system used was: Z upwards, Y forward and X to the left.

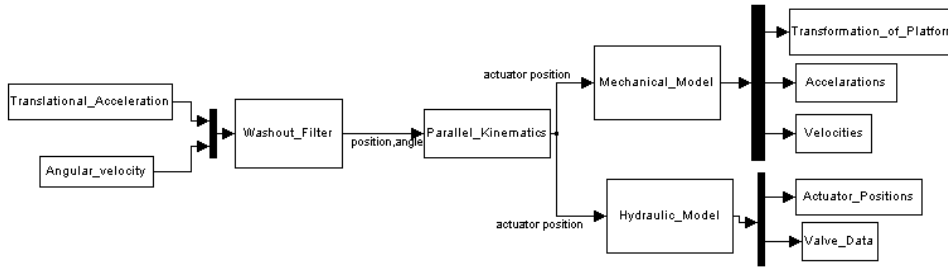

Figure 6 Structure of the simulation model.

A worst case scenario must be considered when setting up the parameters of the washout filters (5). Since platform motion will be used with different types of mobile machines, selecting of test functions was carefully planned. While larger mobile machines have low natural frequency, small ones have high natural frequency. Because of this, it was assumed that test functions should reflect acceleration frequency and amplitude of a small mobile machine. Fast ramp reflects well sudden change in machines lateral acceleration or angular velocity. For improving accuracy of washout filters, frequency of small mobile machine was scaled to the head of driver of the vehicle (1).

4.2 Simulation results

A classical filter with first order high-pass reacts fast to the changing of high-pass filter parameters. Fast chances of direction in acceleration were neutralized with a large time constant, which adds phase delay. Choosing of time constant was a compromise between phase delay and the oscillating variable. The acceleration in the simulations of the Stewart platform had tendency towards negative phase shift, which was used as corrective element to large time-constant. Changes in simulated angular velocities of the platform were abrupt, because large time was not used in filtering, since there was no tendency to negative phase-shift in the angular velocities of the platform.

Increase in the value of the parameter Q while using second order high-pass filters, adds sine like fluctuations to filtered variable. If value of parameter was kept below one, fluctuation was acceptable. Low value of Q lowered total gain of the filter, so actual filter gain K was chosen higher than with first order filters. Filtered variables vibrated more with second order filters. Using second order filters with classical model is questionable, because vibrations focused to the head of the driver have high amplitude and frequency (Figure 7).

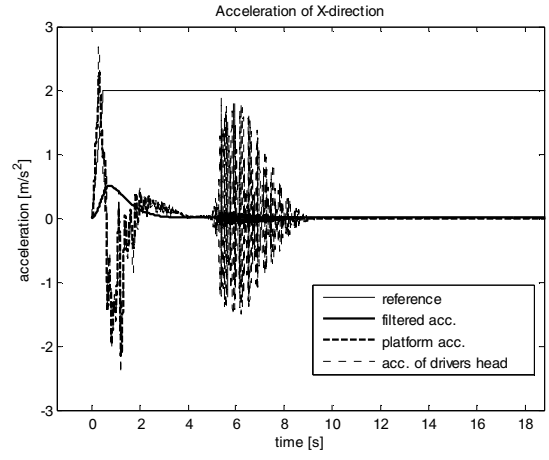

Figure 7 Acceleration of X-direction implemented by classical model with second order filters

While using human based washout filters, no notable differences between first and second order filters were found. When comparing different simulation results with each other, it can be seen that using second order filters in human based model resulted in the lower fluctuations.

Since Z-axis acceleration was selected for testing with the test bench, it was first studied thoroughly. Classical model gave higher amplitude and gentler slope in direction change to acceleration, because of larger time constant (Figure 8). However, in simulations, the platform acceleration followed better filtered acceleration of the human-based model than with classical model (Figure 9). As seen in the figure 10, classical model returns the platform to the base orientation and position substantially better than the human-based model.

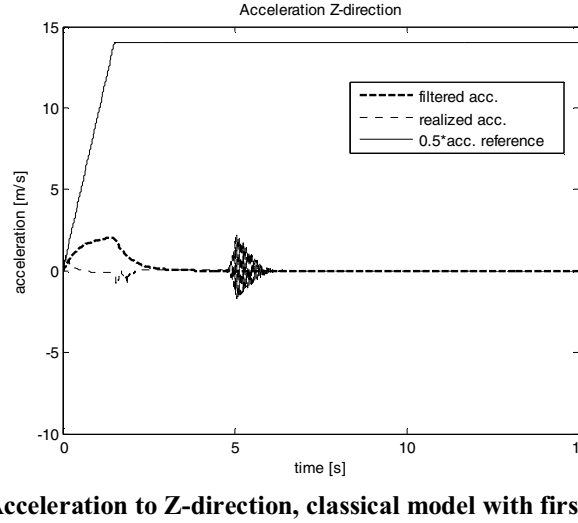

Figure 8 Acceleration to Z-direction, classical model with first order filters.

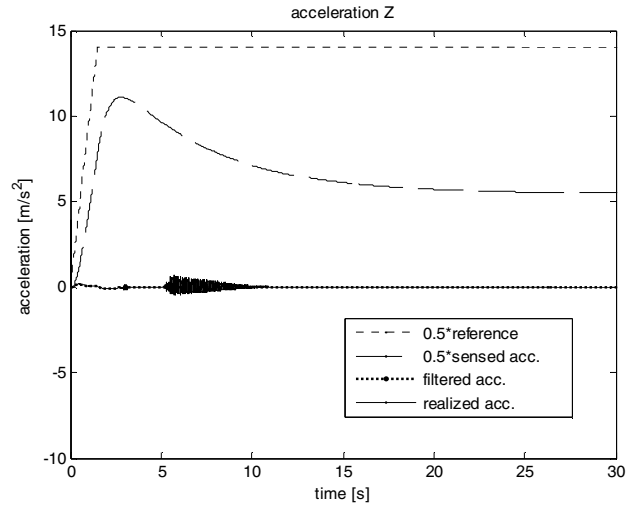

Figure 9 Acceleration to Z-direction, human-based model with second order filters.

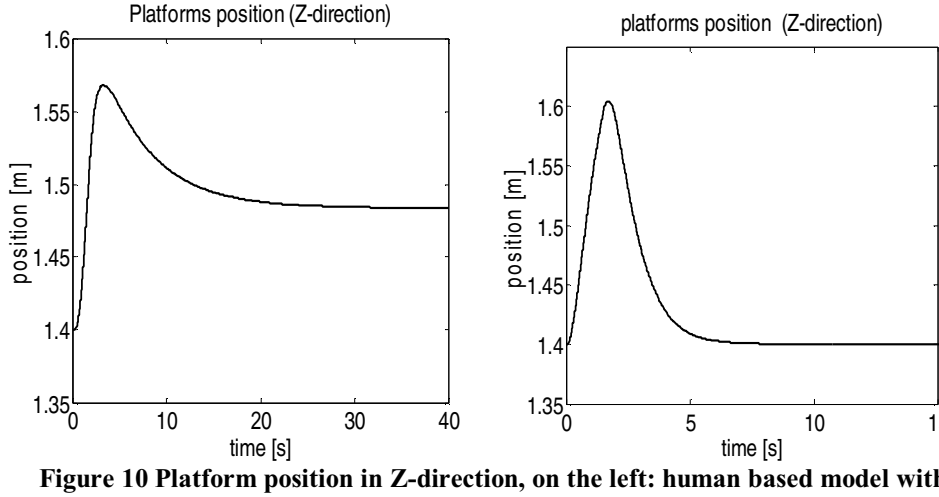

Figure 10 Platform position in Z-direction, on the left: human based model with second order filters. On the right: classical model with first order filters.

Angular velocities are more stable variables than accelerations, which can be seen with lower fluctuations of the filtered variable. The platform follows reference value with very low fluctuation, with all washout filters. Classical filters gave higher amplitude, leading to greater overshoot when the direction of angular velocity is changing. The human-based model causes step-like change in filtered angular velocity, which runs to platform orientation. By inspecting the platform orientation, benefits of first order classical model are seen, because the platform returns to the base orientation (1).

5. TEST RESULTS FOR ONE VALVE-CYLINDER PAIR

5.1 Test arrangement

Since it was not possible to install the cylinder in same position to the test bench and in the platform, it was given greater load mass than originally planned. In the platform, the cylinder will be installed at 60 degrees from the horizontal level. The test bench only allowed 40 degrees, because of this, load mass was added from 90 kilograms to 140 kilograms to create the same force on cylinder as in the initial position of the simulator. Two different position controllers were used, namely proportional with velocity feed forward (Figure 11) and a PI-controller. Supply pressure was kept at 30 bar. Figure 12 presents the test bench hydraulic circuit.

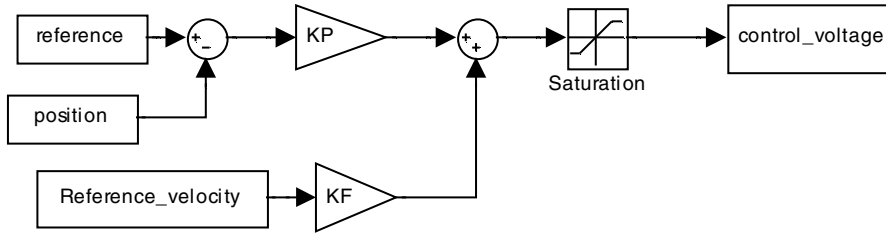

Figure 11 Proportional with velocity feed forward controller

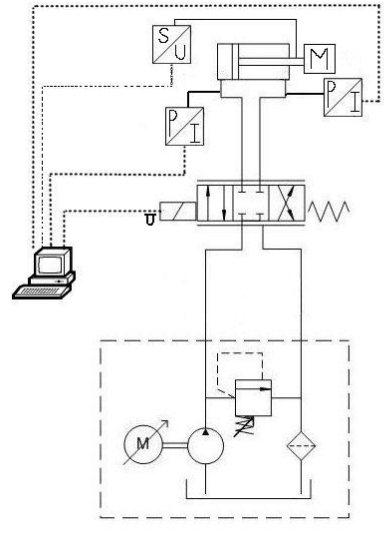

Figure 12 Hydraulic circuit of the test arrangement

5.2 Measurement results

The first thing to be noticed was stick slip motion in the slow cylinder velocities, caused by control parameters and friction. Tuning was compromise between this motion and following reference position. Although the feed-forward controller had a higher average position error than the PI-controller, values in measured position error, its peak value, median and standard deviation were lower than with the PI-controller. Figures 13 and 14 present measured position with both controllers compared to reference position generated by classical washout filter with first order filters.

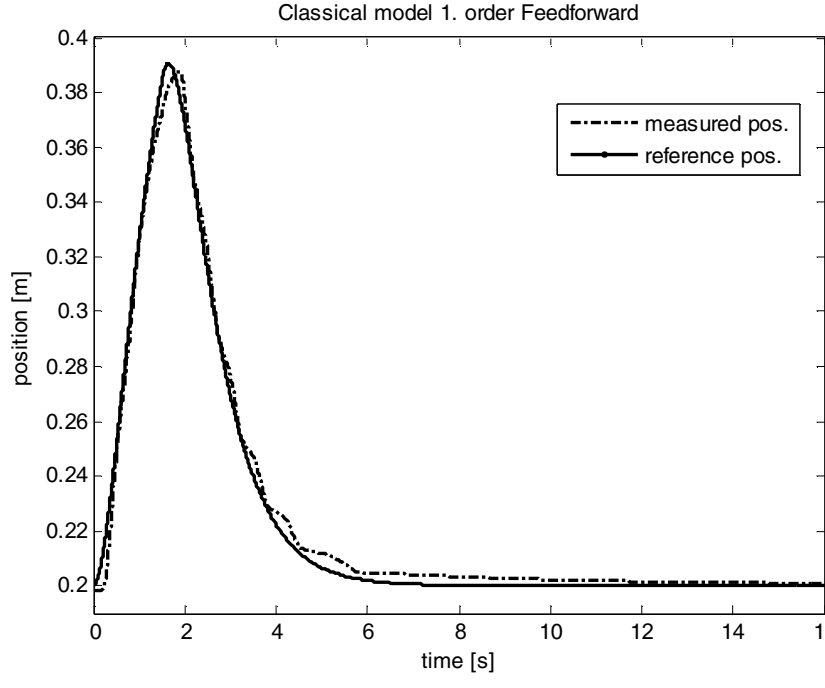

Figure 13 Feed-forward controller with classical model with first order filters.

In Figure 13 it can be seen that the measured position has some undershoot in the peak position, overshoot at the end position, where velocity of the cylinder is very low. Fluctuations have low amplitude, even as they have higher frequency than with PI-controller. High amplitude in fluctuation, as seen in figure 14 at time of five seconds, will be sensed by the driver of the vehicle.

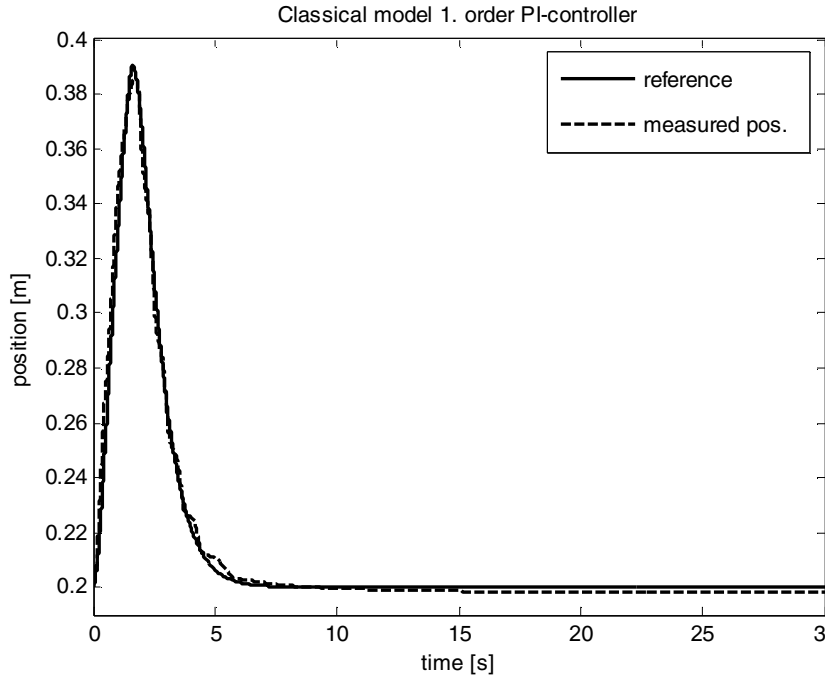

Figure 14 PI-controller with classical model with first order filters

While using human a based model with second order filters, advantages of feed-forward controllers are not so clear. Measured positions are compared in Figure 15 with reference position created by human based washout filter with second order filters. It can be seen that PI-controller still has higher peak values, but average position error, median of position error and frequency of fluctuations in are lower than with the feed-forward controller.

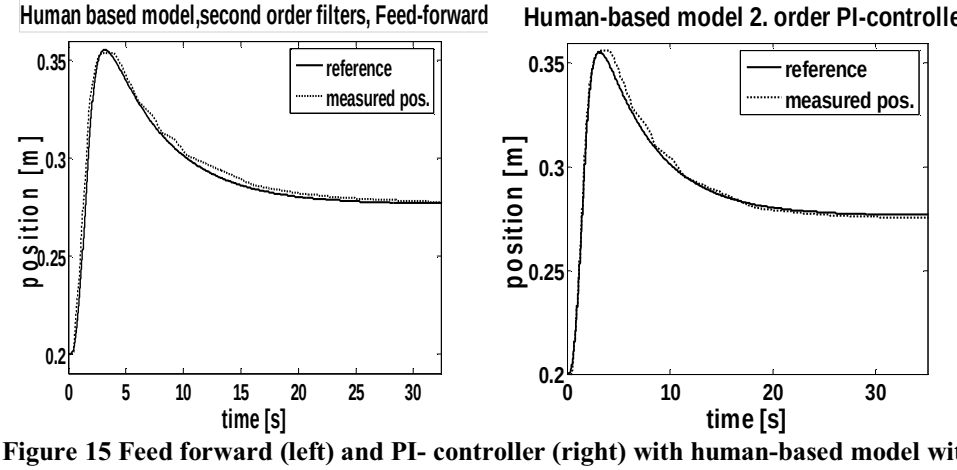

Figure 15 Feed forward (left) and PI- controller (right) with human-based model with second order filters

6. CONCLUSIONS AND DISCUSSIONS

Both types of washout filters have their own advantages and drawbacks. When comparing returning of platform, returning to base position and orientation, classical model with first order high-pass filters is most promising of the studied filters. Because of the high fluctuations in simulation results, real acceleration should be measured before choosing the filter.

If fluctuations in acceleration still exist in empirical tests, human–based model with second order filter must be chosen after re-tuning parameters. Re-tuning parameters means lowering the gain of the low-pass filter of the tilt system, weakening sensation of continuous acceleration of platform. This means much lower positioning error when returning the platform to the base position and orientation.

Both controllers still need adapting because of fluctuations in measured position. Depending on the washout filter, either a feed-forward or a PI-controller is used. A feed-forward gives better response with a classical algorithm, while PI is better suited to a human-based model.

Earlier observations and test bench measurements indicate that the selected valve will work in the platform.

A search for the better position controller is still continuing, while mechanical construction of motion platform is undertaken. The valve model shall be verified by making simulation model of the test bench and comparing measured result to simulation results of the test bench. After mechanical construction is connected with hydraulic system, test drives will begin, first without load and after that with load mass presenting simulated vehicle. A projection screen will be installed near platform and graphics generation from motion cue of platform will be tested. On this point, first empirical tests with a human driver can be undertaken. Washout filters will be fine tuned and final choice for the best filter will be done based on empirical tests.

References

[1] Palonen, T. 2006. Implementation of motion cueing algorithm and control of hydraulics for water hydraulic motion platform. Master of Science Thesis. Institute of Hydraulics and Automation, Tampere University of Technology. 65 p.

[2] Park, M., Lee, M., Yoo, K., Son, K., Yoo, W. & Han, M. 2001. Development of the PNU Vehicle Driving Simulator and Its Performance Evaluation. Proceedings of the 2001 IEEE International Conference of Robotics and Automation. Soul, Korea, May 21-26, IEEE, p. 2325-2330.

[3] Reymond, G., Heidet, A., Canry, M. & Kemeny, A. 2000. Validation of Renault's dynamic simulator for Adaptive Cruise Control experiments.

[4] Telban, R., Cardullo, M. & Houck, J. 1999. Developments in Human Centered Cueing Algorithms for Control of Flight Simulator Motion Systems. American Institute of Aeronautics and Astronautics. 11 p.

[5] Wang, S. & Fu, L. 2004. Predictive Washout Filter Design for VR-based Motion Simulator. Proceedings of the 2004 IEEE International Conference on System, Man and Cybernetics. Hague, Netherlands, October 10-13, IEEE, p. 6291-6295.

Return to Contents

Developing Intelligent Hydraulic Excavator

Karhu, O., Vilenius, J., Uusisalo, J., and Huhtala, K.
Tampere University of Technology, Institute of Hydraulics and Automation

ABSTRACT

In this work the objective is to make a hydraulic excavator attachment more comfortable, accurate, and safer to operate. A commercial hydraulic excavator with four cylinders and mechanically activated on/off-valves was chosen as a platform. The valves were replaced with electronically activated proportional mobile valves and a microcontroller unit was designed and built to control the valves. In this research the intelligent properties related to the control valve are added to the microcontroller unit of the excavator. Among these properties are dead zone compensation, spool offset adjustment, ramped control signals, diverse control curves, and safety features for fault situations.

1. INTRODUCTION

Distributed intelligence opens up many advantages in mobile machines. For most machines, there are various attachments that may have several actuators. Installing attachments like this becomes easier when the control system of the mobile machine does not have to take all the differences between attachments into account. Furthermore, when there is a microcontroller unit in the attachment, the control signals can be transmitted via digital bus instead of several analogue signals. The control data on the bus can consist of high level commands as the low level control signals are produced locally in the attachment.

The mobile machine and the excavator attachment that are used in this work are commercial products that have been modified at the Institute of Hydraulics and Automation at Tampere University of Technology.

1.1 Mobile machine

The hydraulic mobile machine used is an Avant 320+ that originally had mechanically operated valves (1). The valves have been replaced with electronically controlled proportional valves. An electronic control system with CAN bus and wireless teleoperation has been developed in previous research (2). Figure 1 shows the modified machine and a view from the driver's seat. Visible parts of the electronic control system in the photograph are the electronic joystick, the steering wheel, the accelerator pedal, and the display module. The input devices, sensors, and valves are connected to two MVMIO24 I/O modules that communicate with an MVDM586 display module via CAN using CANopen

Power Transmission and Motion Control 2006 Edited by Dr D N Johnston and Professor K A Edge

protocol. The display module is also the main controller of the system. The modules are commercial products from Axiomatic Technologies (3), (4). Battery voltage and CAN bus are wired to a four-pole connector behind the bucket. Since the excavator attachment communicates via CAN, there is no need for other electrical connectors.

Figure 1 Hydraulic mobile machine with electronic control system

1.2 Back hoe excavator

The excavator that is used in this research is made by Avant Tecno, as well. The platform is an Avant Backhoe 205 that has originally four mechanically operated valves. The valves have been replaced with a Sauer Danfoss PVG 32 sandwich type proportional mobile valve (5). The valve has six spools but two of them are not used. A photograph of the excavator installed on the mobile machine is shown in figure 2.

Figure 2 Modified back hoe excavator installed on the mobile machine

The main goal is to make the excavator more comfortable, accurate, and safer to operate. In previous research a control unit for the excavator has been designed and built (6). It is described in detail in chapter 2. Until now, the control unit of the excavator has been used

as a simple CAN interface. The control data that have been transmitted via CAN have consisted of PWM duty cycle values calculated by the main controller (6). In this work all the scaling, saturating and shaping of the input signal is implemented in the excavator control unit. Only the position data of input devices are transmitted in the control messages. The parameters of the functions will also be adjusted through the CAN interface. In future, employing angular and pressure sensors will be researched to perform positioning and load sensing related functions.

Mobile proportional valves are robust and inexpensive. They are, however, quite problematic in accurate control applications (7). The active zone of the flow curve is often narrow, the dead zone can be wide, and the maximum operating frequency is in the region of 5 Hz. The characteristics of a mobile valve may also change with operating conditions. This makes accurate closed loop applications challenging. The appropriate speed of the movements is also difficult to achieve. Therefore the control unit of a mobile attachment should be easily reconfigured for the diverse tasks of mobile machines.

2. CONTROL UNIT

The control unit of the excavator is enclosed in a small steel case that is resistant to dust and water. All the electronic components are chosen so that the demands of mobile applications are satisfied. The case is mounted on the valve block as shown in figure 3. There is also a photograph of the control unit showing the circuit boards inside. Battery voltage and CAN bus are wired from a four-pole connector to the control unit. There are four cables to valves that each carry battery voltage, ground, and control signals.

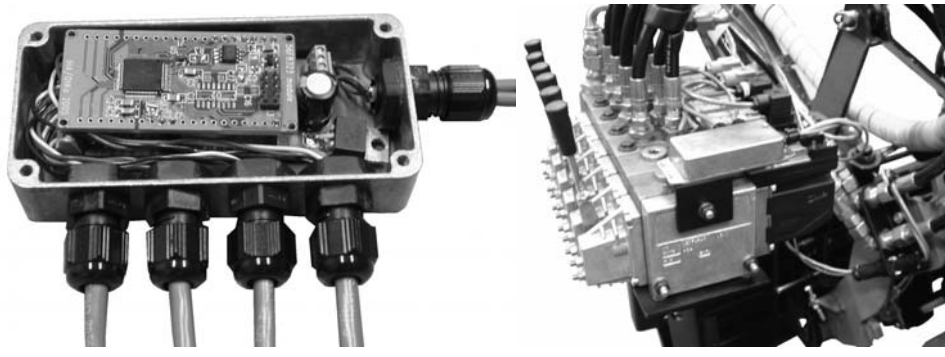

Figure 3 The control unit opened and installed on the valve block

2.1 Electronics

The control unit consists of two circuit boards. On top there is a microcontroller board that contains a Freescale 56F8323 hybrid microcontroller (8). The required external components including a ceramic resonator and LC filters are on the same board. There is also a CAN driver circuit and an option for a driver circuit for RS-232 communications. The microcontroller board is a flexible multipurpose controller that has 8 analogue inputs with 12-bit resolution, 6 PWM outputs with 3 optional current sense and fault inputs, and several digital interfaces. The 56F8323 has 32 KB of flash memory for the program and it performs

up to 60 millions of instructions per second. There are also efficient functions for digital signal processing. The block diagram of the microcontroller is shown in figure 4.

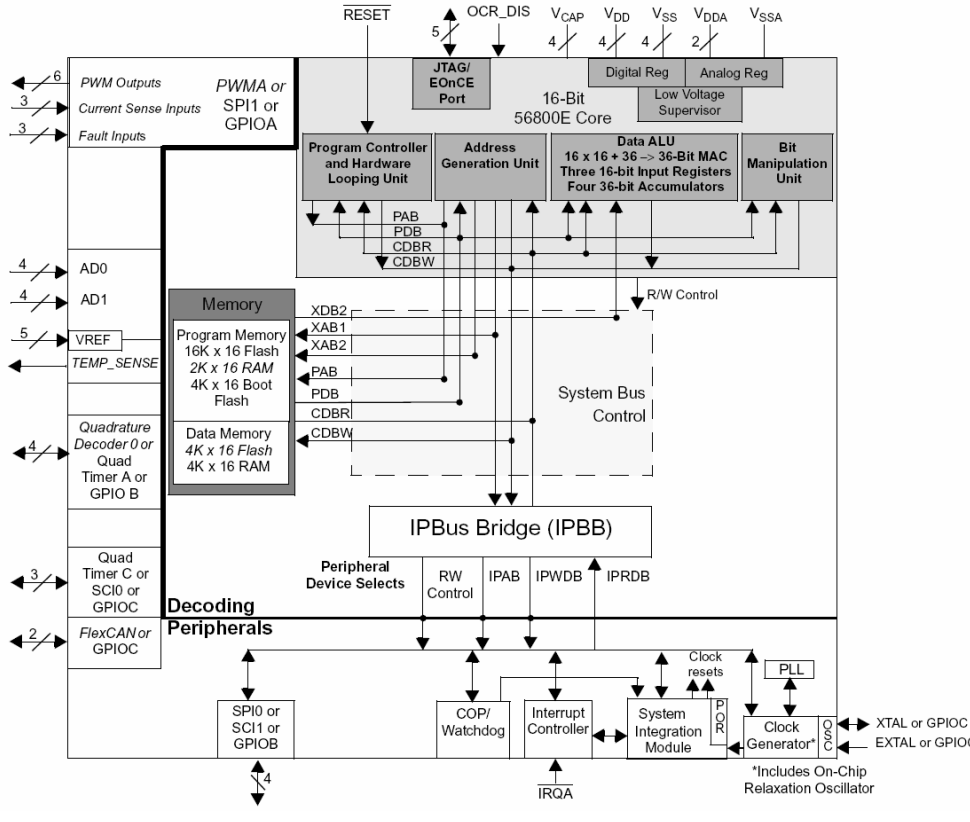

Figure 4 The block diagram of the 56F8323 hybrid microcontroller (8)

Under the microcontroller board there is a motherboard that contains a 5 V voltage regulator and a high frequency IPS024G MOSFET switch (9). The IPS024G switches the valve control outputs between ground and battery voltage according to the logic level PWM signals produced by the microcontroller board. There are also screw terminals for cables on the motherboard.

2.2 Software

The software was developed using a Metrowerks CodeWarrior C compiler and debugger. In figure 5 there is a flowchart of the software in the excavator control unit. At reset the peripherals are initialised: PWM frequency is set to 2 kHz, which is enough for most voltage controlled valves with internal filter. The CAN data rate is set to 125 kb/s which is the data rate of the CAN bus of the mobile machine. The CAN transceiver is configured to cause an interrupt when a message is received. A timer interrupt is set to occur every 1 ms. The parameters that have been stored to the flash memory of the microcontroller are read and the PWM channels are set to centre values according to corresponding parameters. The

main loop of the program is empty because all the functions are implemented in the timer and FlexCAN receive interrupt handlers.

The control unit is programmed to be sufficiently compatible with CANopen standard. The FlexCAN receive interrupt occurs every time a message is captured from the CAN bus into a message buffer. The interrupt handler locks the buffer, which prevents its contents from changing during the processing of the message. The message ID is checked for node number and message type. If a PDO (Process Data Object) message for the excavator unit is detected, the input signal variables are updated according to the message contents. If an SDO (Service Data Object) message for the excavator module is detected, its command byte is checked next. If the command is 'download', the object index and subindex are converted into an address of the flash memory and the parameter data is stored. To confirm that the parameter is updated, the data is read from the memory and transmitted in a confirmation SDO message. If the command is 'upload', the parameter value is read from the memory and transmitted in an answer SDO message. The parameter titles and corresponding indexes are shown in table 1. The functions related to these parameters are discussed in chapter 3.

Table 1 CANopen SDO map of the excavator control unit

Index		Subindex			
		0	1	2	3
0x2000	Lo word				
	Hi word	safety timer			
0x2001	Lo word				
	Hi word	centre 1	centre 2	centre 3	centre 4
0x2002	Lo word	dead zone p 1	dead zone p 2	dead zone p 3	dead zone p 4
	Hi word	dead zone n 1	dead zone n 2	dead zone n 3	dead zone n 4
0x2003	Lo word	saturation p 1	saturation p 2	saturation p 3	saturation p 4
	Hi word	saturation n 1	saturation n 2	saturation n 3	saturation n 4
0x2004	Lo word	rate of change p 1	rate of change p 2	rate of change p 3	rate of change p 4
	Hi word	rate of change n 1	rate of change n 2	rate of change n 3	rate of change n 4
0x2005	Lo word				
	Hi word	curve shape 1	curve shape 2	curve shape 3	curve shape 4
0x2080	Lo word	neutral zone p 1	neutral zone p 2	neutral zone p 3	neutral zone p 4
	Hi word	neutral zone n 1	neutral zone n 2	neutral zone n 3	neutral zone n 4

Index		Subindex			
		4	5	6	7
0x2080	Lo word				
	Hi word	direction 1	direction 2	direction 3	direction 4

Most of the signal processing is done in the timer interrupt handle. Every 1 ms the safety counter is incremented and the valve control values are calculated. The functions used in the calculation are discussed in chapter 3. Finally, the PWM duty cycles are updated.

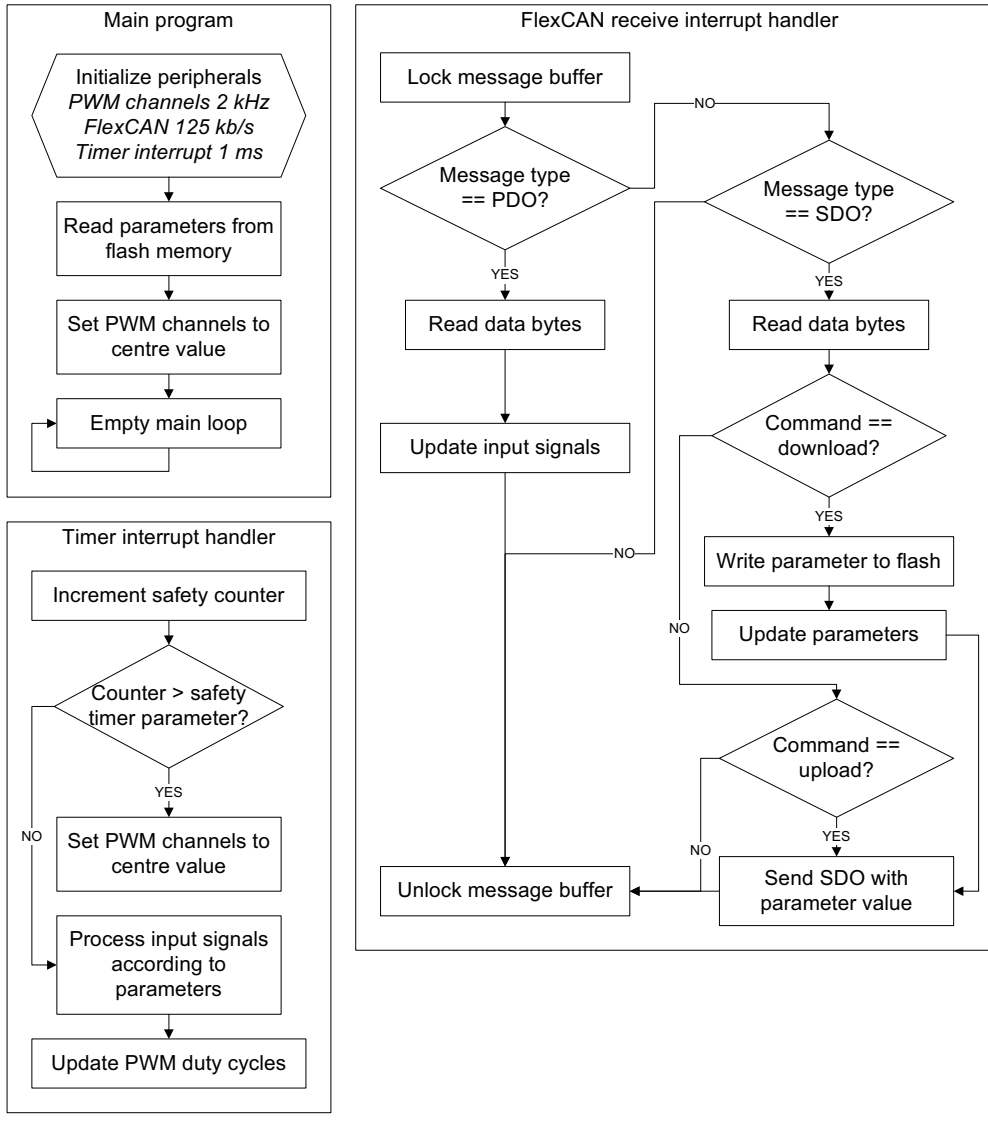

Figure 5 Flowchart of the software in the control unit

3. FUNCTIONS

The functions of the control unit are divided into spool related and input signal related. In this case, the spool related functions are considered the ones that define the limits of the active zone and centre position. The input signal related functions process the input signal that comes from a joystick, for example. All of these functions, apart from the safety timer, are individually configurable for each spool and input device.

3.1 Spool related

The spool related functions are the centre position, dead zone compensation, and saturation. The effect of these functions is shown in figure 6.

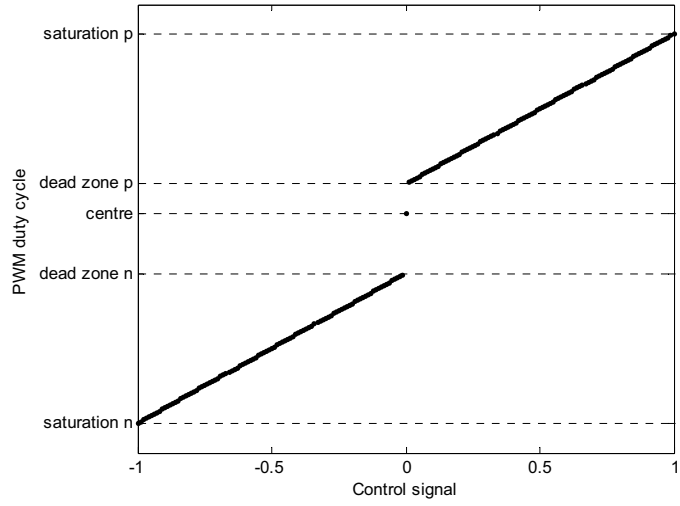

Figure 6 The effect of valve related parameters on PWM duty cycle

3.1.1 Centre position

When the input signal is zero, the valve should usually be closed. The centre position parameter defines the PWM duty cycle that closes the valve. This value is the one that is used at reset and when the receiving of the control values is interrupted for some reason.

3.1.2 Dead zone compensation

To increase the useful range of the input signal, the dead zone around the centre position of the spool can be removed. The dead zone parameters define the PWM duty cycles that move the spool to the edges of the dead zone.

3.1.3 Saturation

Most hydraulic cylinders in mobile applications are asymmetrical. Therefore the maximum control signal results in higher velocity in inward movement than outward movement. This is not a problem in all the applications but limiting the maximum opening can nevertheless be useful. This is the case, for example, when the spool would pass more volume flow at the extreme position than is available from the pump.

3.2 Input signal related

The input signal related functions include setting the neutral zone of the input device, reversing the signal, limiting the rate of change, shaping the control curve, and centring the spools when there are no control data received for a set time.

3.2.1 Neutral zone and direction

If the input device is a joystick, which is often the case, the centre value of the input signal is not precise. This would cause the spool to travel between the dead zone edges at random

when the joystick is in centre position. To solve this problem, there is a parameter for setting the neutral zone of the input signal. When the input signal is on the neutral zone, the valves are controlled with the centre value.

For some hydraulic actuators and input devices the direction of input device intuitively corresponds to the direction of the actuator. In this case, a good example is the lateral movement of the boom that is controlled by steering wheel. It is very difficult to control the boom if it moves right when the steering wheel is turned left. To avoid these problems, there is a direction parameter that causes the input signal to reverse if it is set nonzero.

3.2.2 Limited rate of change

Especially inexperienced operators may handle the input devices too aggressively causing the actuators to accelerate uncomfortably fast. There is a parameter that sets the maximum change of input signal in 1 ms. Every 1 ms the input signal is compared to current control value. If the difference is greater than the limited change, the control value is changed by the limited value. This results in smooth behaviour of the excavator. The rate of change should not, however, be limited to very small because it would cause long delays.

3.2.3 Control curve processing

For most operators it is most difficult to move the excavator slowly. Slow movements are needed to move the bucket to a desired position. To make this easier, the control curve can be shaped to change less in the vicinity of zero. A straightforward way to do this is to raise the absolute value of the control curve to a power while keeping its sign. The curve shape parameter defines the exponent of the curve. Figure 7 represents the effect of different exponents.

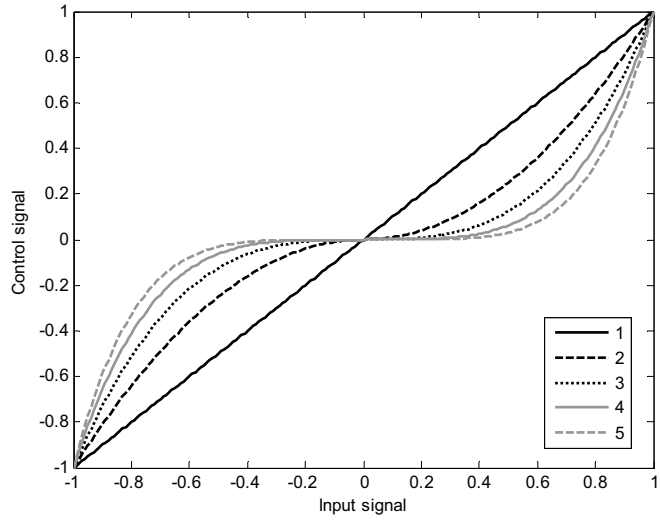

Figure 7 The control signal with different exponents

3.2.4 Safety timer

If the main controller of the mobile machine stops sending input signal data, the excavator should stop moving even if the last received input data was nonzero. The input signal can also be lost if the CAN cable, connector, or transceiver is damaged. The safety timer centres the spools when no PDO messages have been received during the time set by the parameter. The safety timer should be set to a time longer than the interval of the transmitted input signal messages but not much more than human reaction time.

4. TEST ARRANGEMENT

The excavator was connected to the mobile machine and parameter values were set. A laptop with a Kvaser USBcan II interface and CANKing analyzer software was used to set the parameters.

The control system of the mobile machine sends the position of input devices every 40 ms when the excavator mode is active. The safety timer was set to 100 ms which allows one message to be lost before the valves are centred. This is quick enough considering the dynamics of the excavator and human reaction time. The function was tested by sending PDOs to the excavator control unit every 40 ms from the analyzer laptop. As the PDO transmission was interrupted, all the cylinders stopped moving.

Optimal values for the spool related parameters were found by experimental tests. Because the control unit outputs the centre value when no input signal is present, the centre parameters were used to find the values where the dead zone ends. The value was changed slowly until the corresponding cylinder started to move. Then the value was changed back until the cylinder was at rest again. Because there was some hysteresis, the dead zone edge was set between these values. The centre position was set halfway between the negative and positive edges of the dead zone. The saturation values were set where the movement approximately reached its maximum velocity. For the lateral movement the inward saturation value was set so that the maximum velocity was equal to outward movement.

The input signal related parameters were set by experimental tests as well. The neutral zone was set at ±6% around the centre value, which proved to be suitable. Some input signals, including the one for the lateral movement, were set to be reversed. Different exponents for the control signal were tested and squaring the signal proved to be the most comfortable option. The rate of change was limited to a very small value which was increased until the delay was no more disturbing. This resulted in smooth movements.

5. FUTURE WORK

The control unit now includes functions that are useful when hydraulic attachments are controlled manually. Most of them are applicable to more intelligent functions utilising closed loop control. Future research will include choosing and installing angular sensors to the excavator. At first the sensors will enable bucket positioning and motion recording. Later on the excavator will be able to repeat work cycles and even dig autonomously as the commands from the main controller consist of depth and digging area, for example.

Pressure sensors could be utilised to distribute hydraulic power more evenly between cylinders. All these applications will probably require only minor changes to the electronics of the excavator control unit. Most of the work will be algorithm development.

6. CONCLUSIONS

The excavator control unit with its current software realizes an intelligent valve interface that makes the manual control of the excavator more convenient, accurate, and safer. The parameters of the control unit are easy to set and they shape the behaviour of the attachment considerably. This makes the mobile proportional valve more applicable to demanding closed loop control applications. The excavator control unit will offer a platform for several sophisticated applications in future.

REFERENCE LIST

(1) Avant 300 series, 500 series, Avant Tecno Oy, Ylöjärvi, Finland.

(2) A. Raneda, J. Vilenius, and K. Huhtala, ”Development of a teleoperated hydraulic mobile machine,” in Proc. 8th Scandinavian Int. Conf. Fluid Power, Tampere, Finland, 2003, pp. 449-459.

(3) Multipurpose I/O module MVMIO24, User Manual, Axiomatic Technologies Oy, 2002.

(4) HMI Display Module MVDM586, Technical Datasheet, Axiomatic Technologies Oy, 2003.

(5) PVG 32 Proportional Valves, Technical Information, Sauer-Danfoss, 2004.

(6) O. Karhu, J. Vilenius, J. Uusisalo, J. Moya, and K. Huhtala, ”Intelligent Excavator for Hydraulic Mobile Machine,” in Proc. 22nd Int. Symposium on Automation and Robotics in Construction, Ferrara, Italy, 2005, 5 p.

(7) J. Uusisalo, J. Vilenius, T. Krogerus, O. Karhu, and K. Huhtala, ”Automated Bucket Stabilizer for Hydraulic Mobile Machine” in Proc. 22nd Int. Symposium on Automation and Robotics in Construction, Ferrara, Italy, 2005, 7 p.

(8) 56F8323/56F8123 Data Sheet, Freescale Semiconductor Inc., Austin, TX, 2004.

(9) IPS024G Data Sheet, International Rectifier, El Segundo, CA, 2002.

Return to Contents

Systems and Control

Return to Contents

A new acceleration feedback design method for electrohydraulic motion control systems

A.R. Plummer
Manager – Control and Analysis, Instron Ltd, UK

Abstract
For at least four decades, the use of acceleration feedback has been known to be an effective tool for improving the transient response of electrohydraulic servosystems with inertia-dominant loads. However, in practice, the choice of acceleration feedback gain is still typically a matter of trial and error. Analyses which are available do not account for the valve dynamics in a sufficiently realistic (yet simple) way to be of use in many practical situations. In this paper a design method is proposed, and applied to a validated simulation of a seismic table. It is suggested that, in this case, differential pressure feedback (although nominally equivalent to acceleration feedback) is superior, as the sensitivity to mass variation is reduced.

1 INTRODUCTION

It is well known that electrohydraulic servosystems with large inertial loads are inherently lightly damped. This is due to the lack of damping (e.g. leakage or friction) associated with the 'bouncing' of the inertial load on the compressible oil volumes in the hydraulic cylinder. Within the testing industry, the following methods have been used to tackle this problem:

1. the use of a cross-port bleed to increase the leakage across the piston, which increases the damping;
2. adding a first order lag to the forward path of the controller so that 180° phase in the open-loop transfer function does not coincide with the resonant peak [1];
3. adding a notch filter to the forward path of the controller to attenuate the loop gain at the resonant frequency (if this frequency is known);
4. using cylinder differential pressure feedback;
5. using acceleration feedback.

The last option is the principal subject of this paper. The cost of an extra transducer (an accelerometer) is not usually a problem in testing machines, as these are usually high value systems, and experience has shown that acceleration feedback is a particularly

Power Transmission and Motion Control 2006 Edited by Dr D N Johnston and Professor K A Edge

effective way of tackling the resonance. However in practice the acceleration feedback gain is tuned manually, using trial and error. This paper proposes a practical analytical tuning method.

Simplistic analyses of acceleration feedback (e.g. [2]) which neglect valve dynamics do not, in general, give a good basis for controller design. More detailed analyses have been available for many years. Bell and de Pennington [3] use a first-order valve model. However as shown in Section 2, such a model can often be inappropriate.

The current work has been motivated by the need improve the control of earthquake simulation tables, sometimes known as seismic testing tables. These are used to impose multi-axis vibration on structures (perhaps scaled-down building models) to test their behaviour under earthquake conditions. Earthquake tables can accommodate payloads of at least several tonnes. The recently commissioned Japanese E-defense facility can handle payloads up to 1200 tonnes – large enough for the testing of substantial full scale buildings [4]. Figure 1 shows an example of table with a 5mx5m surface and a payload capacity of 20 tonnes.

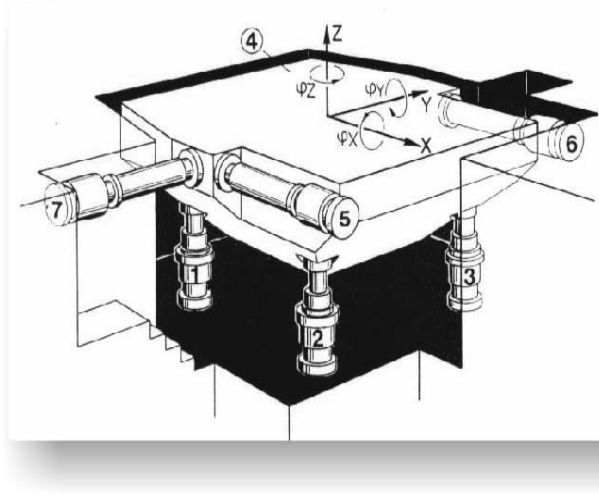

Fig 1. An earthquake simulation table

2 MODELLING FOR CONTROLLER DESIGN

A simple candidate model for an electrohydraulic actuator with an inertial load is:

$$y = \frac{e^{-s\tau}}{s\left(\frac{1}{\omega_n{}^2}s^2 + \frac{2\zeta}{\omega_n}s + 1\right)}u \qquad (1)$$

where y is the piston position, and u is the valve control signal. The control signal is scaled to give unity steady-state gain between control signal and piston velocity. The second order lag represents the well-known phenomenon of the mass oscillating on the compressible cylinder oil volumes; this is typically lightly damped, see e.g. [5]. Higher

order dynamics, in particular the valve dynamics, and also delays in a digital controller, are lumped together in a single dead time parameter τ. Taking account of valve dynamics is critical to deriving a high performance controller for all systems with actuator resonant frequencies greater than (typically) 10 to 20Hz. A second order valve dynamic model (e.g. [6]), or a second order model with dead time (e.g. [7,8]), will be more accurate, but will increase the complexity of the controller design.

This paper is concerned with the design of proportional position controllers with acceleration feedback, based on the model of equation (1). The first-order valve model of Bell and de Pennington [3] is often inadequate. In reality the valve phase lag is usually much greater than can be represented by such a model. An example is shown in Figure 2, which is the frequency response of spool position to valve control signal for a 3-stage 200 l/min valve. Valve phase lag reaches 180° at the –3dB magnitude point, rather than the 45° which would be given by a first order model. A second order plus dead time model is a reasonable fit to the frequency response:

$$y = \frac{e^{-0.002s}}{1.76x10^{-6}s^2 + 1.86x10^{-3}s + 1}u \tag{2}$$

However, if the actuator resonant frequency occurs in the region where the valve response is flat, a simple delay model e^{-sT}, with T = 0.004s, should be adequate for controller design.

As an example of the accuracy of the complete model in equation (1), Figure 3 shows a measured frequency response using the same valve to control a 340kN cylinder attached to an 11 tonne mass. A small cross-port bleed is used to increase the inherent damping in the system. The best fit model has the following parameters:

$$\omega_n = 145\,\text{rad/s} \qquad \zeta = 0.18 \qquad \tau = 0.0055s$$

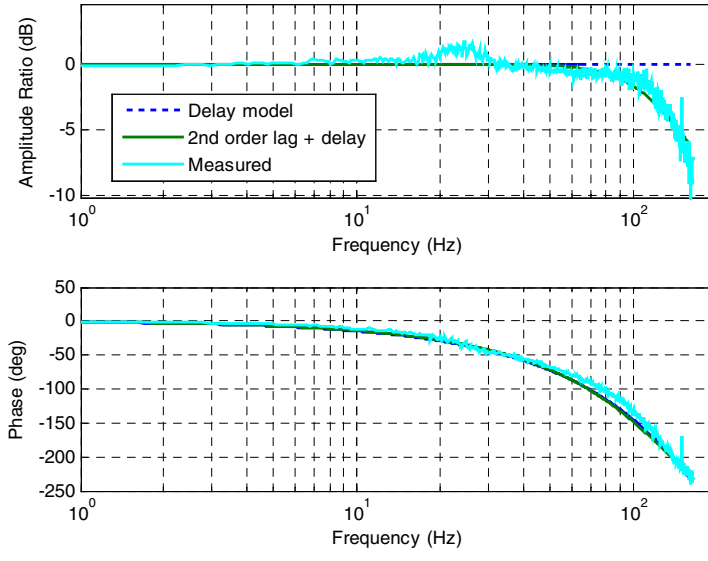

Fig 2. Valve frequency response (spool position over control signal)

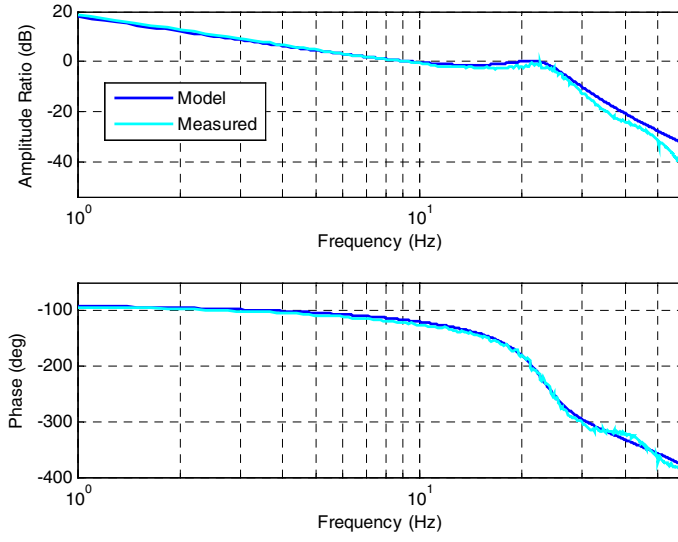

Fig 3. Plant frequency response (actuator position over control signal)

3 CONTROLLER DESIGN ALGORITHM

The closed-loop system is shown in Figure 4. It has the following transfer function:

$$y = \frac{k_p}{s\left(\frac{1}{\omega_n{}^2}s^2 + \frac{2\zeta}{\omega_n}s + 1\right)e^{s\tau} + \left(k_a s^2 + k_p\right)}u \tag{3}$$

The parameters in this equation can be normalized with respect to the plant natural frequency. Let:

$$s_n = \frac{s}{\omega_n} \tag{4}$$

$$T = \omega_n \tau \tag{5}$$

$$K_a = \omega_n k_a \tag{6}$$

$$K_p = \frac{k_p}{\omega_n} \tag{7}$$

Hence:

$$y = \frac{K_p}{s_n\left(s_n{}^2 + 2\zeta s_n + 1\right)e^{s_n T} + \left(K_a s_n{}^2 + K_p\right)}u \tag{8}$$

In the frequency domain, equation (8) becomes:

$$y = \frac{K_p}{\left(-2\zeta\omega^2 + j\omega(1-\omega^2)\right)\left(\cos\omega T + j\sin\omega T\right) + \left(K_p - K_a\omega^2\right)}u \tag{9}$$

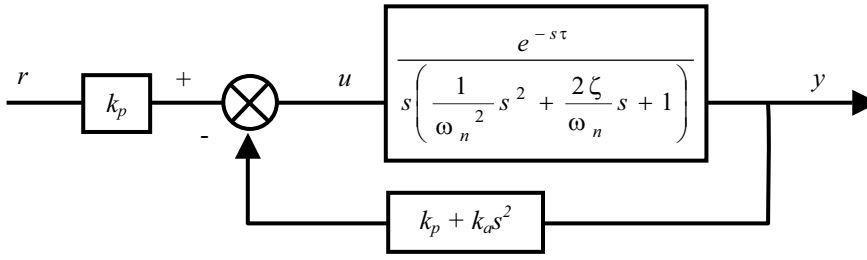

Fig 4. Closed-loop system

where ω is frequency as a multiple of the natural frequency ω_n. The characteristic polynomial is of infinite degree as it contains the time shift term, and so it is not amenable to many conventional design methods. The approach adopted here is to consider a polar plot of the plant characteristic polynomial in the frequency domain, and to calculate the additional term in the closed-loop characteristic polynomial such that this closed-loop polynomial has desirable properties. From equation (9), the plant characteristic function is:

$$P(j\omega) = \left(-2\zeta\omega^2 + j\omega(1-\omega^2)\right)\left(\cos\omega T + j\sin\omega T\right) \tag{10}$$

The modifier term in the closed-loop system is:

$$M(j\omega) = K_p - K_a\omega^2 \tag{11}$$

and thus the closed loop characteristic polynomial is:

$$C(j\omega) = P(j\omega) + M(j\omega) \tag{12}$$

An example polar plot of these three functions is shown in Figure 5. The example plant parameters are:

$$\zeta = 0.18 \qquad T = 0.80s$$

which are the values found for the actuator in Section 2, with the dead time normalised according to equation (5).

The following should be noted.

- The steady state value *C(0)* is always K_p, which, referring to equation (9) always gives unity steady state gain. The higher the value of K_p the better the disturbance rejection will be, at least at low frequency.
- *M(jω)* is always real, and so only the real values of *C(jω)* can be altered by the modifier.
- If the magnitude of *C(jω)* is less than *C(0)* at any frequency, this implies a closed-loop amplitude ratio of more than unity, such as might occur at a resonance.

Taking these factors into account, a desirable *C(jω)* would transcribe a circle centred on the origin, with the largest possible radius, until the highest possible frequency, and then increase in magnitude thereafter; this would give a flat closed-loop response with high bandwidth. This ideal can be translated into a practical controller design procedure by using *M(jω) (i.e.* K_p and K_a*)* to fix *C(jω)* onto this notional circle at phase angles of 0° and 90°. Specifically, as the imaginary values of *P(jω)* cannot be altered, choose the circle

radius to be the maximum of $\Im[P(j\omega)]$ (between phase angles of 0 and 180°). Let ω_I be the frequency at which this occurs. Then let:

$$K_p = \Im[P(j\omega_I)] \tag{13}$$

and

$$M(j\omega_I) = -\Re[P(j\omega_I)] \tag{14}$$

so

$$K_a = \frac{K_p + \Re[P(j\omega_I)]}{\omega_I{}^2} \tag{15}$$

These choices have been made in Figure 5. The figure shows how these choices map the plant to the closed-loop characteristic function.

Thus from equation (10), ω_I is the frequency at which the following is a maximum:

$$\Im[P(j\omega)] = -2\zeta\omega^2 \sin\omega T + \omega(1-\omega^2)\cos\omega T \qquad 0 < \angle P(j\omega) < 180° \tag{16}$$

Differentiating with respect to ω, the maximum occurs where:

$$0 = \omega(T\omega^2 - 4\zeta - T)\sin\omega T - (\left[2\zeta T + 3\right]\omega^2 - 1)\cos\omega T \qquad 0 < \angle P(j\omega) < 180° \tag{17}$$

This equation can be solved numerically for any given plant parameters ζ and T. In the case where $T = 0$:

$$\omega_I = \frac{1}{\sqrt{3}}$$

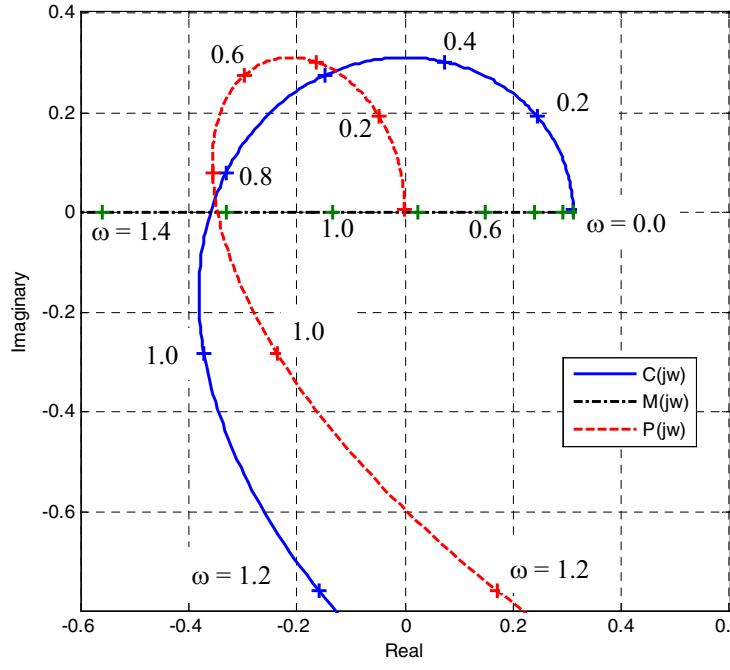

Fig 5. Characteristic functions

4. EXAMPLES AND COMPARISONS

The polar plots of the characteristic functions for some different dead time and damping ratio values are shown in Figure 6. The damping values chosen are typical for hydraulic servosystems. The proportional and acceleration gains in each case are calculated according to the equations in the preceeding section. Figure 7 shows the equivalent closed-loop magnitude frequency responses.

For comparison, Figure 8 shows the closed-loop responses with the same proportional gains, but with no acceleration feedback. As might be expected, the responses are very oscillatory, and some are unstable.

Figure 9 shows the responses obtained by neglecting the dead time T, i.e. the proportional and acceleration gains calculated for the T=0 scenarios are used unaltered for T=0.5 and T=1.0 for each of the three damping ratios. The closed-loop response deteriorates as the dead time increases.

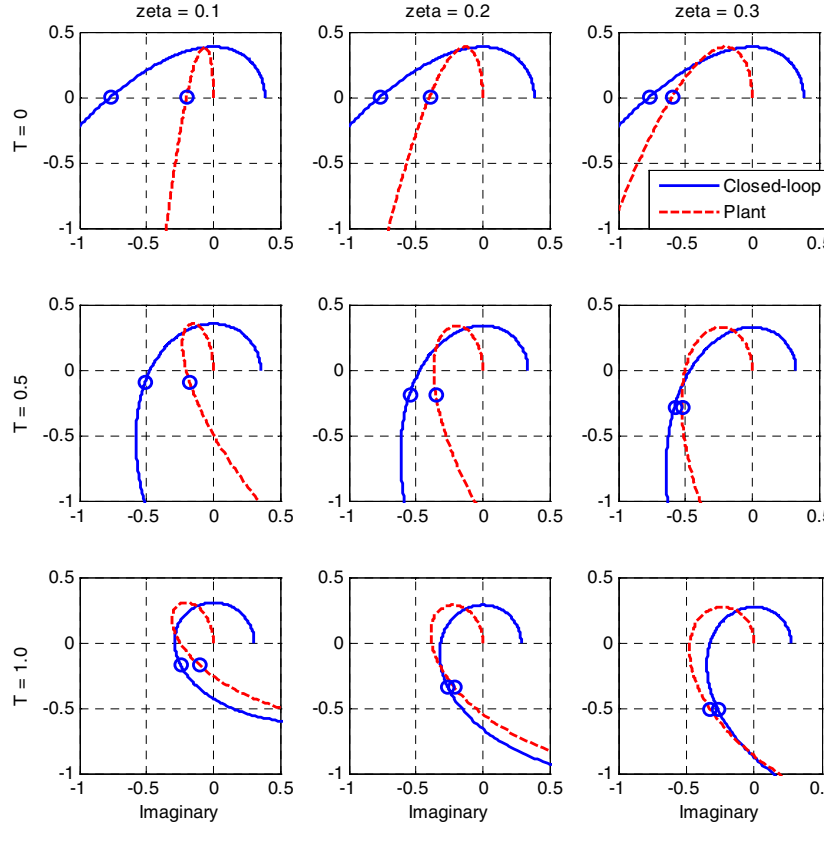

Fig 6. Characteristic functions for some example dead time and damping values, using proposed controller design method (circles indicate ω = 1.0 points)

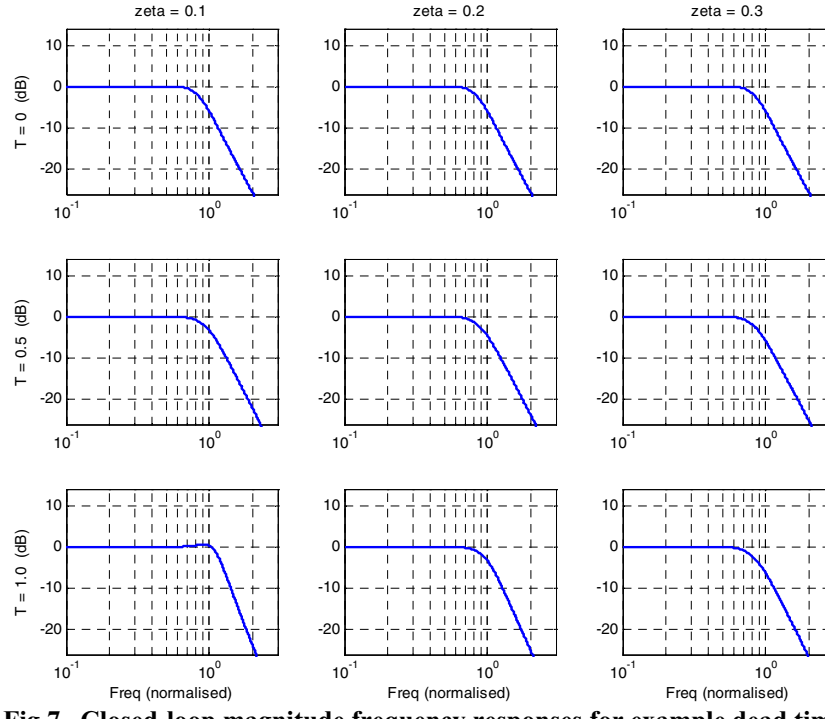

Fig 7. Closed-loop magnitude frequency responses for example dead time and damping values, using proposed controller design method

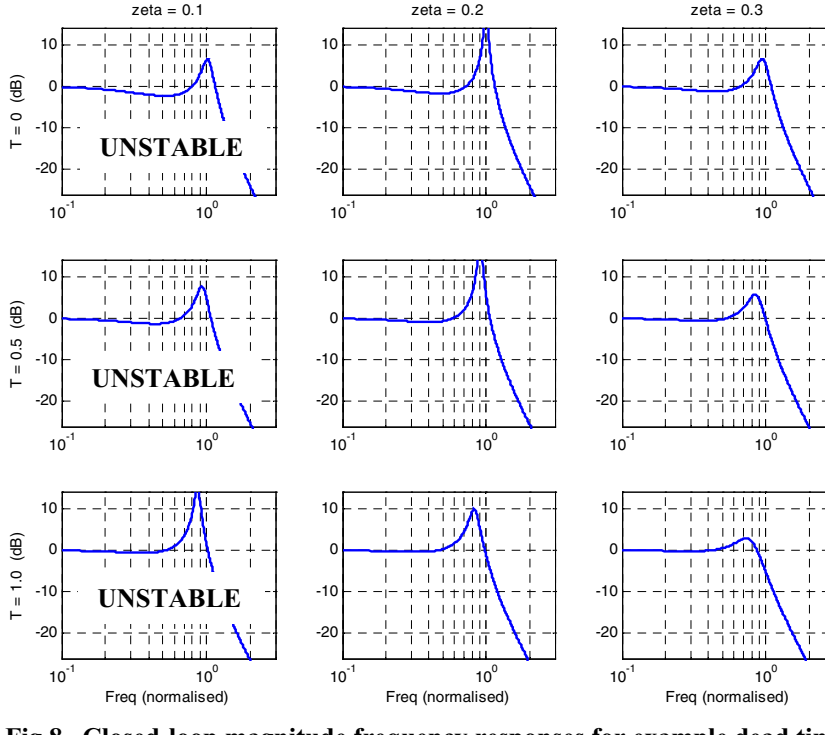

Fig 8. Closed-loop magnitude frequency responses for example dead time and damping values, with no acceleration feedback

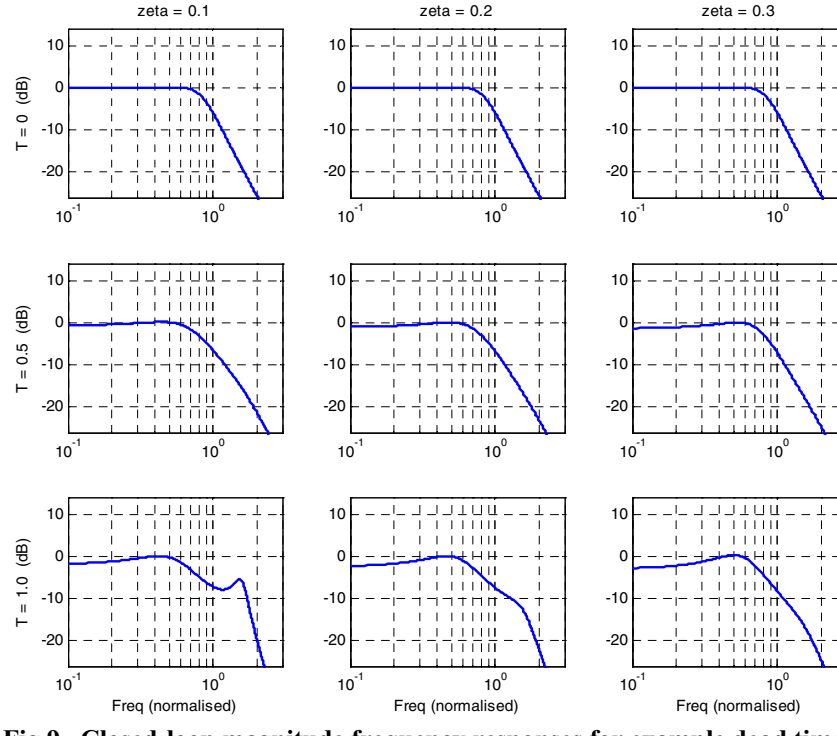

Fig 9. Closed-loop magnitude frequency responses for example dead time and damping values, assuming T=0 for controller design

5 SENSITIVITY TO MASS VARIATION

In earthquake simulation, the mass can vary significantly, from just the bare table mass to the table plus a payload of several times this mass. In the example given previously, the 11 tonne nominal mass can in reality be as low as 5 tonnes or as high as 25 tonnes. The variation in expected closed-loop frequency response for these mass variations, assuming no re-tuning of the controller, is shown in Figure 10. The three curves are for 5 tonnes, 11 tonnes and 25 tonnes; the proportional and acceleration gains are correct, according to the procedure outlined previously, for the 11 tonne mass. By inspection of the plots of the characteristic functions (Figure 11), the closed-loop responses can be explained. In particular, the closed-loop characteristic function for the largest mass passes very close to the origin, thus resulting in the very significant resonance.

From Figure 11 it would appear that a higher acceleration feedback gain is required when the mass is large, and a lower gain is required when the mass is low. This implies that differential pressure (or load) feedback may be preferable, as in this case the effective acceleration feedback gain does change in proportion to mass. Figure 12 shows the closed-loop frequency responses for differential pressure feedback, where the gains have been calculated for the intermediate (11 tonne) mass. The characteristic functions are plotted in Figure 13. There is a clear reduction in the sensitivity to mass variation.

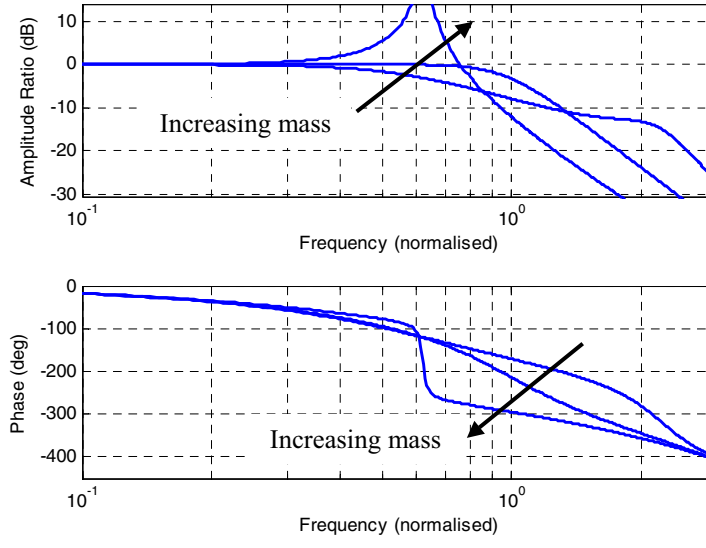

Fig 10. Closed-loop frequency responses for varying mass

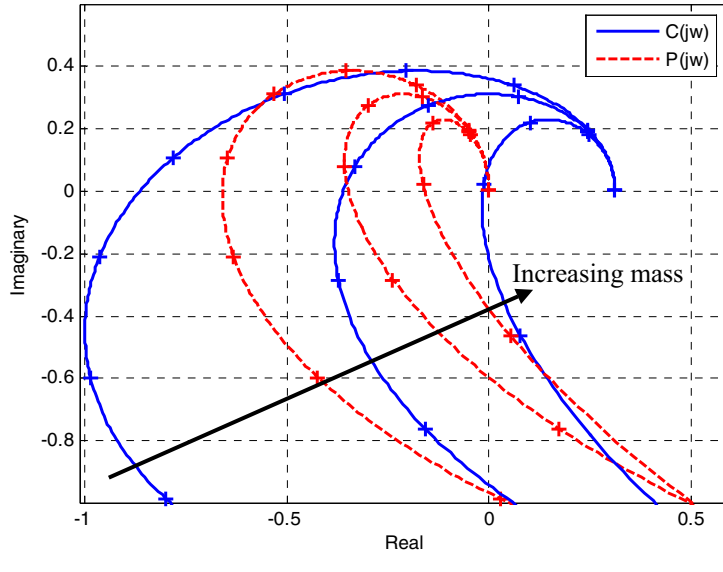

Fig 11. Polar plots of characteristic functions for varying mass (crosses indicate intervals of ω = 0.2)

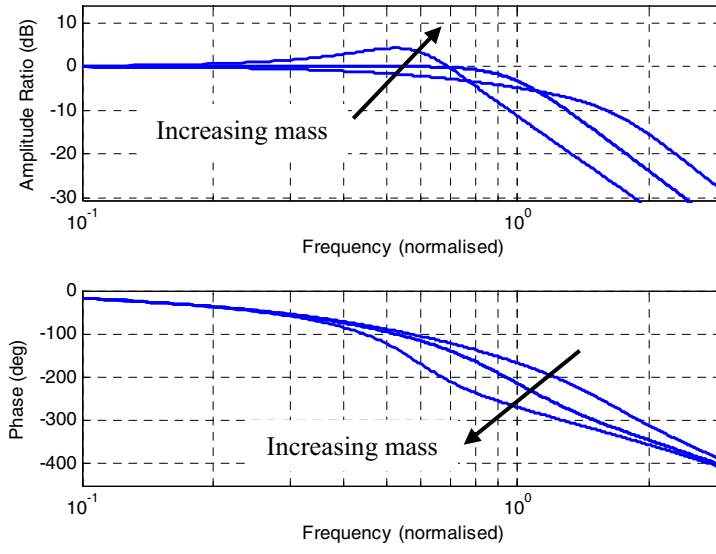

Fig 12. Closed-loop frequency responses for varying mass – differential pressure feedback

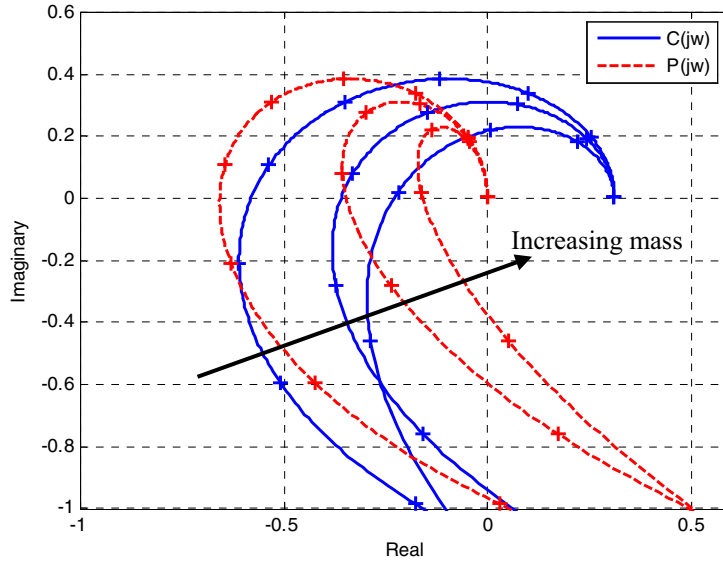

Fig 13. Polar plots of characteristic functions for varying mass – differential pressure feedback (crosses indicate intervals of $\omega = 0.2$)

6. VALIDATION USING NON-LINEAR SIMULATION

The results have been validated using a non-linear simulation of one actuator in an earthquake simulation table. This is the actuator for which measured data is presented in Section 2. This simulation includes the following features:

- the valve spool dynamic characteristics (as identified in Section 2)
- a spool slew rate limit (maximum velocity)
- a small valve overlap (the valve is nominally zero-lapped, but manufacturing tolerances are biased towards overlap), in which the flow gain is reduced by 50%
- the conventional orifice equation, i.e. each valve orifice flow rate is proportional to the square root of pressure drop
- valve body saturation – i.e. pressure drop in the valve body
- manifold pressure drop
- oil volume variation, i.e. the two oil volumes between piston and valve, which include oil trapped in the manifold, change as the piston moves, varying actuator stiffness
- mechanical stiffness and damping between the piston and the table.

Table 1 contains the key model parameters. Figure 14 compares the plant frequency response with the measured response from the real system, showing a close match. In both cases the frequency response is estimated from time signals acquired during excitation of the system with a swept sine signal whilst in proportional position control. Figures 15 and 16 show the closed-loop frequency responses obtained from the simulation for acceleration and differential pressure feedback respectively; these plots should be compared with Figures 10 and 12. Although the trend is similar, i.e. the differential pressure feedback appears less sensitive to mass variation than the accleration feedback, the advantage is less distinct. The much reduced resonant peak with acceleration feedback when the mass is larger (25 tonnes) can be explained by the non-linear damping effect in hydraulic systems – i.e. when the valve spool displacement is greater (which may be expected at resonance) the effective damping is larger.

Table 1. Parameters for non-linear simulation model

Valve	Rated flow (for 70 bar pressure drop)	200 l/min
	Natural frequency	120 Hz
	Dead time	3.5 ms
	Slew rate (time for ramp to fully open)	5 ms
	Overlap	1 %
Cylinder	Rated stall force	340 kN
	Piston area	127 cm^2
	Stroke	80 mm
	Total oil volume	1270 cm^3
	Piston mass	56 kg
Manifold	Rated flow (for 70 bar pressure drop)	1000 l/min
	Volume (total between valve and cylinder)	480 cm^3
Load	Table and specimen mass (nominal)	11 tonnes
	Mechanical stiffness	950 kN/mm
	Mechanical damping	920 kNs/m

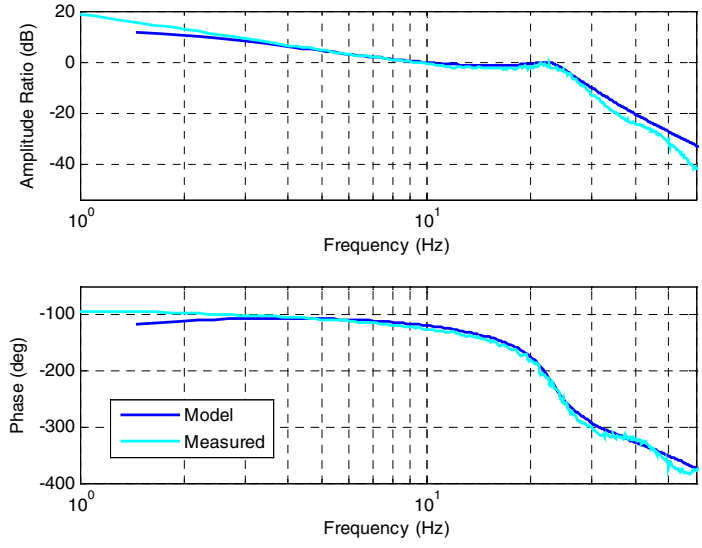

Fig. 14 Comparison of simulation model with measured data

7. CONCLUSIONS

A new controller design method for electrohydraulic servosystems with inertial loads has been proposed, in which proportional and acceleration feedback gains are designed taking proper account of valve-related phase lag. By inspection of measured data, it is demonstrated that a dead time can be a better simple valve model than a first order lag.

A detailed, validated, non-linear simulation model is used to verify the controller design method. The simulation is for one actuator of an seismic table, which is a prime example of a servosystem with a large inertial load encountered in the testing industry. Payload mass can vary widely in such systems, and the analysis indicates than in fact differential pressure feedback is less sensitive to this mass variation than acceleration feedback. Simulation results verify this, although the advantage is less distinct.

Where position and acceleration are measured, it is also possible to estimate velocity. A 'Three Variable Controller' which includes velocity could be designed using an extension of the concepts presented here, and will be the subject of future investigation.

REFERENCES

1. Plummer, A.R., (2004) "Modal control for a class of multi-axis vibration table" Control 2004, Bath, UK, Sept 04.
2. Jelali, M, Kroll, A (2003) "Hydraulic servo-systems" Springer-Verlag, London.
3. Bell, R, de Pennington, A (1969) "Active compensation of lightly damped electro-hydraulic cylinder drives using derivative signals" Proc IMechE, 184,Pt 1,No 4, 83-98.
4. Ogawa, N., Ohtani, K, Katayama, T, Shibata, H. (2001) "Construction of a three dimensional large scale shaking table and development of core technology" Phil Trans R Soc Lond, A 359, 1721-51.

5. McCloy, D, Martin H R, Control of Fluid Power: Analysis and Design. Ellis Horwood, Chichester, 1980.
6. Plummer, A R (2003) "A servohydraulic control system for implementing virtual components in mechanical systems" PTMC 2003, Bath, September 2003, 131-146.
7. Plummer, A R (2001) "Iterative velocity control for a high speed hydraulic actuator" PTMC 2001, Bath, September 2001, 339-354.
8. Plummer, A.R., (2005) "Closed-loop velocity control for an electrohydraulic impact test system" PTMC 2005 Bath, September 2005, 75-90.

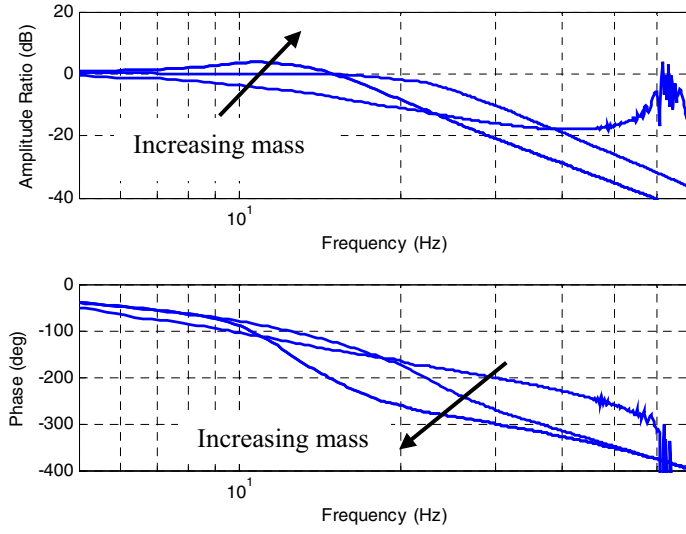

Fig 15. Non-linear simulation: closed-loop frequency responses for varying mass – acceleration feedback

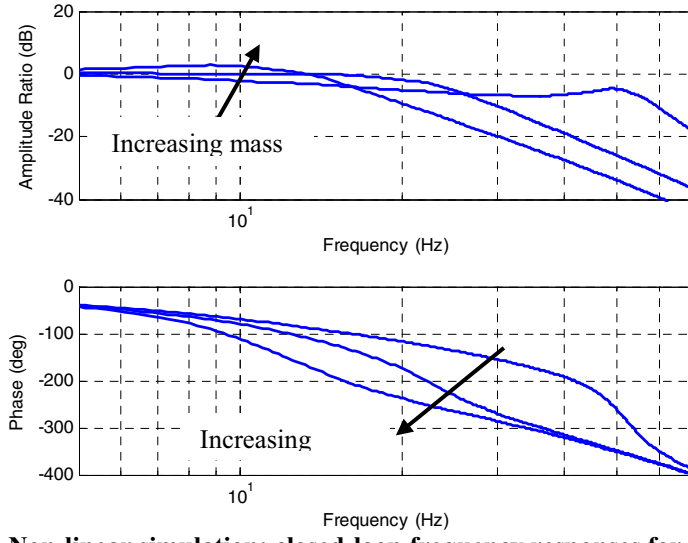

Fig 16. Non-linear simulation: closed-loop frequency responses for varying mass – differential pressure feedback

Return to Contents

Force-Based Impedance Control of Hydraulic Manipulators and its Relationship with Position-Based Impedance Control

Ali Muhammad*, Jouni Mattila*, Mikko Siuko* and Matti Vilenius*
* Institute of Hydraulics and Automation, Tampere University of Technology

ABSTRACT

The force control of hydraulic manipulators is more challenging than that of electrical manipulators, as electrical actuators are torque sources whereas hydraulic actuators are essentially position/velocity sources. Also, hydraulic actuators behave far more nonlinearly. Hence, Force-Based Impedance Control (FBIC) is far less investigated in comparison to Position-Based Impedance Control (PBIC) for hydraulic manipulators. This paper shows the implementation of FBIC for hydraulic manipulators. Furthermore, a relationship has been established between FBIC and PBIC. It has been shown that equivalent force and position controllers can be obtained for the inner loops of FBIC and PBIC respectively using the established relationship.

Power Transmission and Motion Control 2006 Edited by Dr D N Johnston and Professor K A Edge

NOMENCLATURE

Table 1: Nomenclature

b_d	Desired viscous friction
b_e	Viscous friction of environment
b_r	Viscous friction of robot/manipulator
FBIC	Force-Based Impedance Controller
FC	Force Controller
F_d	Desired force
F_e	Force from environment
F_g	Force due to gravity
F_n	Nominal force
F_r	Force on the robot/manipulator
H	Transfer function of hydraulics
K_d	Differential gain
k_d	Desired stiffness
k_e	Stiffness of environment
K_p	Proportional gain
k_r	Stiffness of robot/manipulator
m_d	Desired inertia
m_e	Inertia of the environment
m_r	Inertia of the robot/manipulator
PBIC	Position-Based Impedance Controller
PC	Position Controller
u	Control signal
X_n	Nominal displacement
X_e	Displacement of Environment
Z_d	Desired impedance
Z_e	Impedance of environment
Z_r	Impedance of robot/manipulator
ξ	Damping ratio
τ	Torque
ω_n	Natural frequency

1. INTRODUCTION

The primary purpose of a robot is to perform certain specified manipulation tasks in its environment. These manipulation tasks can be categorized into two major classes: non-contact tasks and contact tasks. In the case of a non-contact task, a manipulator performs motions in unconstrained environment and follows position trajectories in free space. Spray painting, welding and simple pick-and-place operations (when geometry of environment is known accurately enough) are examples of non-contact tasks where position control can provide satisfactory performance.

However, a wide variety of robot applications require the end-effecter of the manipulator to come into contact with its environment and perform complex manipulation tasks. This category of manipulation tasks is classified as contact tasks. Assembling, drilling and machining are few examples of contact tasks where motions through unstructured and insufficiently known environment are required. In such cases, task-space force control of manipulators becomes essential. Two major approaches have been widely adopted for the force control of manipulators: hybrid force/position control and impedance control. In hybrid force/position control, the task-space is divided into degrees of freedom in which either position or force is controlled. In impedance control, the relationship between position and force at the end-effecter of manipulator is controlled rather than only position or force. Hybrid force/position control and impedance control can be combined into hybrid impedance control (1, 2), which allows the simultaneous regulation of impedance and either force or motion.

The objective of an impedance controller is to establish a desired dynamic relationship between the endpoint position and the environment contact forces. The feedback loops at the manipulator joints are closed in a way that the manipulator appears as specified impedance to its environment, which, in turn, behaves as admittance to the manipulator. Two types of impedance control have been researched and implemented since its introduction by Hogan (3) in 1985: Position-Based Impedance Control (PBIC) and Force-Based Impedance Control (FBIC.) The PBIC consists of an inner position feedback loop with an outer force feedback loop. In this approach the contact force information is used to modify the desired position of the end-effecter, which is applied to the inner position feedback loop. In effect, PBIC softens a stiff position source. The FBIC consists of an inner force feedback loop with an outer position feedback loop. In this approach, position is measured and force commands are issued to meet the target impedance. In effect, FBIC stiffens a soft force source.

Most research with impedance control has been done for manipulators with electrical actuators where the actuator torque is proportional to the input current. However, implementation of impedance control for manipulators with hydraulic actuators is not so straightforward. Hydraulic actuators are essentially position/velocity sources, where actuator velocity is proportional to input valve voltages. Although impedance control has been applied on hydraulic manipulators (4, 5, 6), only PBIC has been reported. Implementation of FBIC for hydraulic manipulators is more challenging as it requires the tuning of highly non-linear inner force loop. It is a well known fact that force control of hydraulic manipulators is a challenging problem (7). In addition, the implementation of FBIC requires the acceleration feedback in the outer loop. Lawrence (8) not only specifies

rules for the selection of impedance parameters but also suggests the guidelines for deciding when to use PBIC or FBIC. He argued that FBIC is better suited to provide small stiffness. It is suited where manipulator gravity loads are small and motions are slow.

In teleoperation systems, accuracy and safety are major issues. FBIC is a possible solution for the slave manipulators where large velocities are not required. However, this technique has not yet been tested for hydraulic manipulators and it needs investigation. This paper discusses the implementation of FBIC for hydraulic manipulators. Furthermore, a relationship has been established between FBIC and PBIC by the authors here. It has been shown that equivalent controllers can be obtained using the established relationship. The goal is to investigate and generalize the force control techniques for hydraulic manipulators and to widen the scope of application. In our future work the research will continue to extend the number of degrees of freedom to obtain a practical hydraulic manipulator particularly suitable for teleoperation systems such as the one needed in International Thermonuclear Experimental Reactor (ITER.)

In the following section we mention the hardware setup used for the experimentation. Theoretical description and practical implementation of FBIC is discussed in Section 3. In Section 4 a relationship has been established between FBIC and PBIC with supporting experimental results. In the last section conclusions are drawn on the basis of these results.

2. EXPERIMENTAL SETUP

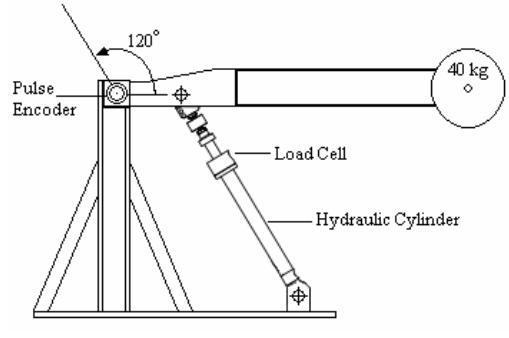

Figure 1: Hydraulic test bench

Experiments were performed using the hydraulic test bench sketched in Figure 1. Cylinder dimensions are 35/25-300 mm and it can drive the manipulator arm up to 120°. A load of 40 kg is attached at the end of the arm to give it a realistic behaviour of a manipulator link. The cylinder is driven by a flow control servo valve with a flow rate of 4 l/min at a nominal pressure of 3.5 MPa. The cylinder is equipped with a load cell with a load capacity of 50 kN. The position of the arm is measured using a pulse encoder. The control and measurements were performed at a sample frequency of 1 KHz. A supply pressure of 12 MPa is used. The schematic in Figure 2 represents the hydraulic circuit diagram of the setup.

A hard metal surface is used as the environment. The position of this metal surface is approximately known. Throughout the experimentation a nominal force is first selected and then a position command is issued such that the tip of the arm comes in contact with the metal surface. Position and force responses are recorded and have been presented as results.

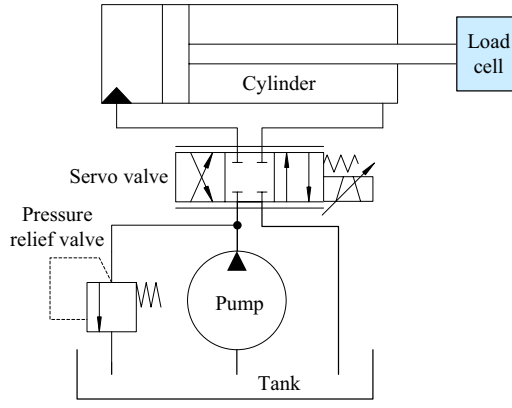

Figure 2: Schematic of hydraulic circuit

3. FORCE-BASED IMPEDANCE CONTROL

The FBIC consists of an inner force feedback loop with an outer position feedback loop. In this approach, position is sensed and the corresponding force is obtained according to the desired impedance. This force is issued to the inner loop together with the commanded force. In this way the force command is modified to comply with the desired impedance. Indeed, FBIC can be regarded as a scheme which stiffens a soft force source.

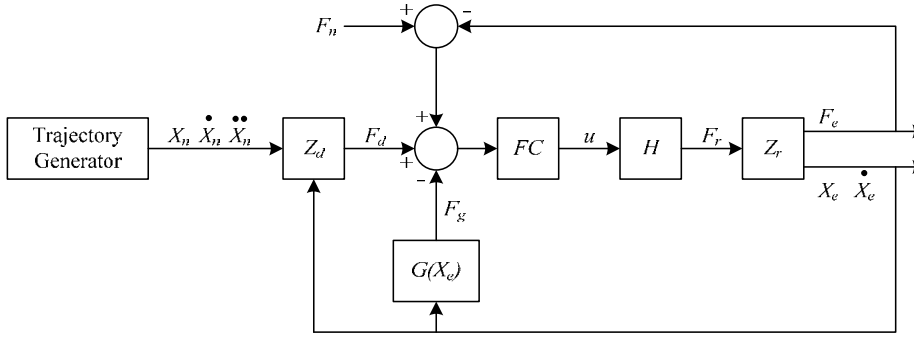

Figure 3: Block diagram of FBIC

Figure 3 shows a general block diagram of a FBIC scheme. Here 'H' is the transfer function of flow control servo-valve and of hydraulic cylinder, 'Z_d' is the desired impedance of the manipulator and 'FC' stands for Force Controller. The above scheme also realizes the

gravity compensation force 'F_g', thus the static forces due to the manipulator's own mass are compensated. The function '$G(X_e)$' is obtained by the least square approximation using the experimental data. The movement of the hydraulic cylinder is kept within the linear region of motion. Control signal 'u' to the servo-valve can be derived from block diagram of Figure 3 as in Equation 1.

$$u = FC \cdot (F_n - F_e - F_g) + FC \cdot Z_d (X_n - X_e) \tag{1}$$

Here 'X_n' and 'X_e' are the nominal and actual motion of the manipulator.

With Z_d=0 in Figure 3, the block diagram will reduce to a simple force controller. The gain of this controller can be tuned to find out the optimum response. In this case a simple proportional controller is used. The gain of the controller is modified over a range where force response remains desirable. Figure 4 shows the two cases of force tracking.

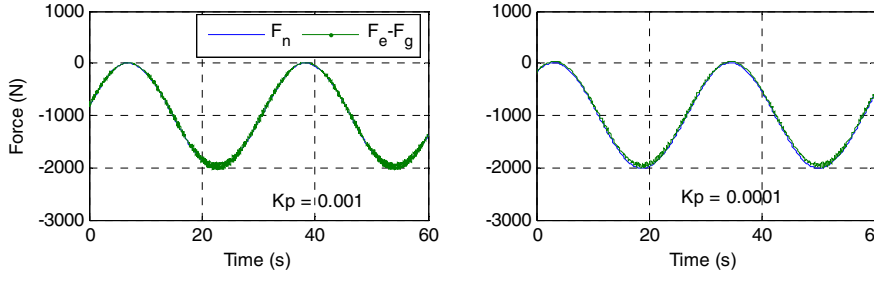

Figure 4: Force response of inner loop

From the plots of Figure 4, following result can be obtained:

$$F_n - F_e - F_g \approx 0 \qquad \text{if} \qquad \{0.0001 \le K_p \le 0.001\} \tag{2}$$

Here 'K_p' is the gain of proportional controller.

Impedance model of a manipulator and the environment is widely discussed by many researchers (9). A general model with the inclusion of desired impedance is given in Figure 5.

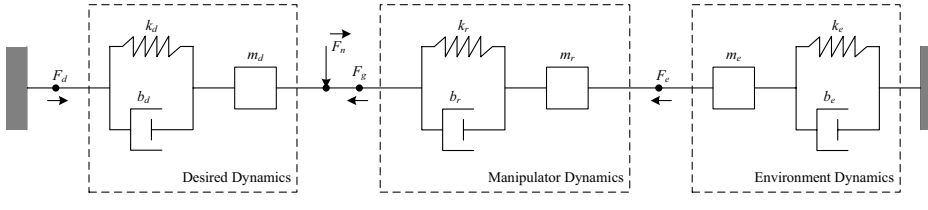

Figure 5: Impedance model of manipulator and environment

Here '*k*', '*b*' and '*m*' are stiffness, viscous and inertial parameters of impedance respectively, while subscripts '*d*', '*r*' and '*e*' refer to the desired, the robot/manipulator and the environment respectively. The Identification and the involvement of manipulator's and environmental impedance will be considered in our future work. From the model in Figure 5 the relationship between the manipulator and the environment forces can be described by Equation 3.

$$F_d + F_n - F_e - F_g = Z_d(X_n - X_e) \tag{3}$$

Using the approximation obtained in Equation 2 and the substitution of desired impedance will result in Equation 4 below.

$$F_d = m_d(\ddot{X}_d - \ddot{X}_e) + b_d(\dot{X}_d - \dot{X}_e) + k_d(X_d - X_e) \tag{4}$$

This implementation requires the acceleration feedback in the outer loop. Acceleration measurements can be obtained by numerical differentiation of position and velocity signals from the encoder, but this will result in the amplification of measurement noise and the obtained signal will not be useful for the control anymore. A suggested solution (3) is to calculate the required acceleration of the manipulator according to desired impedance, measured forces, velocity and position signals. A dynamic model of the manipulator is used to compute required forces to achieve a required acceleration. In our case, the velocity measurements are obtained by the numerical differentiation of position signal from the encoder. Acceleration feedback is ignored and only the desired acceleration from trajectory generator is fed forward. Indeed in many applications where high velocities of manipulator joints are not required and accuracy of task performance is a major issue (such as teleoperation) the higher order derivatives of displacement can be ignored. Equation 4 can be reduced to a stiffness controller.

$$F_d = k_d(X_d - X_e) \tag{5}$$

Saldudean (6) chose the desired impedance parameters in a way that the closed loop system has a desirable dynamics in the contact regime. Assuming no forces are acting on manipulator, desired values of inertia and damping can be obtained by:

$$m_d = \frac{k_d}{\omega_n^2} \tag{6}$$

$$b_d = 2\xi\omega_n \cdot m_d \tag{7}$$

Hence, we can select the impedance parameters of Equation 4 so that manipulator depicts the required dynamics of a stable system. The natural frequency of the system is determined as 147 rad/s and damping ratio is selected as 1. Using Equations 6 and 7, the desired values of viscosity and inertia are determined for the chosen value of the desired stiffness. The proportional force controller of the inner loop is tuned to obtain the optimum response. Table 2 below gives a set of desired impedance parameters.

Table 2: Impedance parameters

k_d (kN/m)	b_d (N/(m/s))	m_d (kg)	K_p
1	13.7	0.05	0.001
10	137	0.5	0.0002
50	685	2.35	0.0001

Figure 6 shows the plots of the force and the position response for each of the cases mentioned in Table 2. A smaller nominal force has been selected for the first experiment (Figure 6a); otherwise with a desired stiffness as low as 1 kN/m the manipulator will fall under the nominal force. This will make the position tracking impossible. Selection of nominal force has been done randomly for the last three cases (Figures 6b, 6c and 6d.)

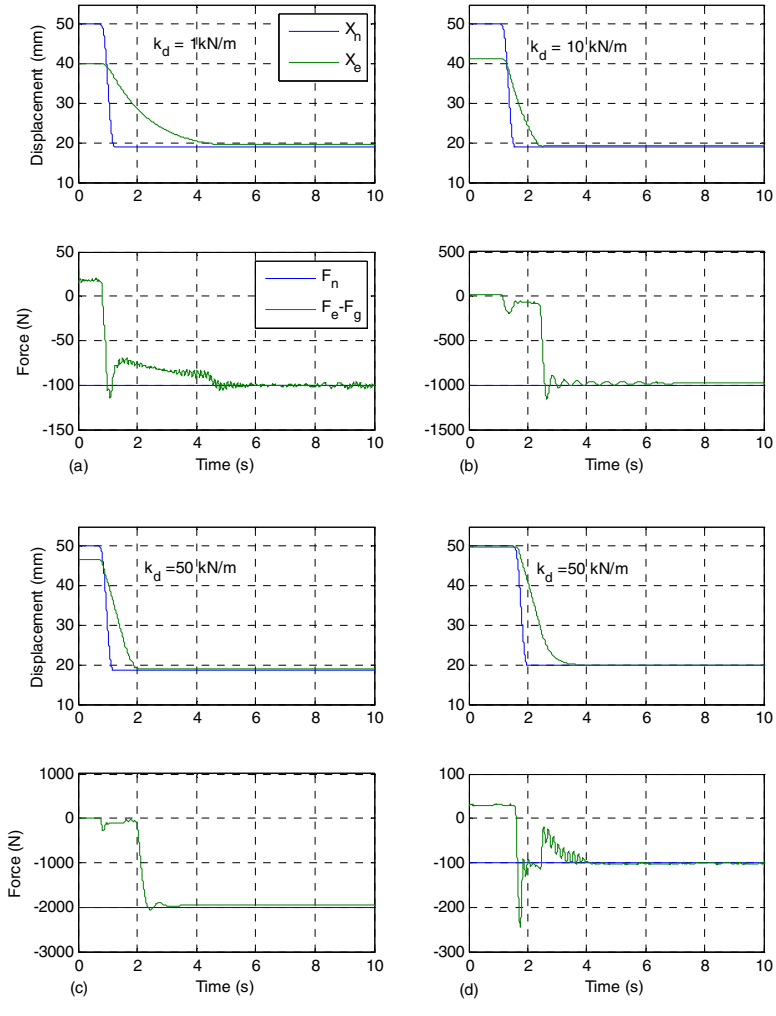

Figure 6: Position and force response of FBIC

4. RELATIONSHIP BETWEEN FBIC AND PBIC

It is widely understood that equivalence exists between explicit force control and impedance control. Both types of controllers can be converted to each other and when optimized, should have similar bandwidths (10). Expressions to obtain equivalent PBIC and explicit force controllers have been derived, implemented and verified by several researchers (11, 12).

In the following discussion we develop a relationship between FBIC and PBIC. Very general implementations of both impedance controllers are used here. Equation 1 for the control signal of a FBIC can be restated below as in the following way:

$$u_{FBIC} = FC \cdot (F_n - F_e - F_g) + FC \cdot Z_d (X_n - X_e) \tag{8}$$

Figure 7 is a simplified block diagram of a PBIC (10).

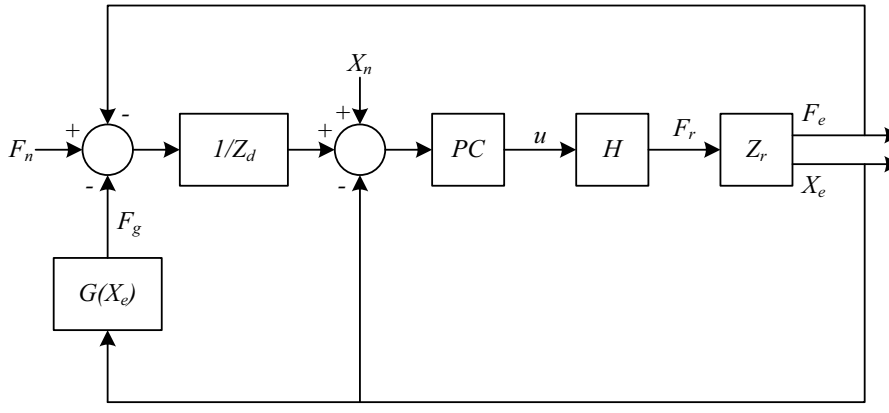

Figure 7: Block diagram of PBIC

Here '*PC*' stands for the position controller. The control signal obtained from the block diagram above can be described by Equation 9.

$$u_{PBIC} = \frac{PC}{Z_d} \cdot (F_n - F_e - F_g) + PC(X_n - X_e) \tag{9}$$

Equations describing the control signals for both controllers have a similar structure. The relationship can be obtained by equating the coefficients of Equations 8 and 9.

$$PC = Z_d . FC \tag{10}$$

Equation 10 is an important result which can lead to many conclusions, one of which, for a desired impedance, an equivalent inner loop position controller for PBIC exist of an inner

loop force controller for FBIC and vice versa. Equation 10 can be used to find out these equivalent controllers.

A first order impedance model mentioned in the Equation 11 below is chosen for the experimental verification of the Equation 10. The inertial term has been left out from this model for the sake of simplicity and to avoid the use of acceleration feedback.

$$Z_d = b_d s + k_d \tag{11}$$

A proportional controller is used to tune the inner loop of FBIC with a proportional gain of 'K_p'. Table 3 below summarizes the calculated parameters and controller gains. It is obvious that an equivalent proportional-derivative position controller needs to be implemented for a proportional force controller. Same stiffness and viscous parameter are used as in Table 2 of Section 3 and respective values of gains are calculated for the position controller.

Table 3: Impedance parameters and controller gains

Z_d		Force controller	Position controller	
k_d (kN/m)	b_d (N/(m/s))	K_p	K_p	K_d
1	13.7	0.001	1	0.0137
10	137	0.0002	2	0.0274
50	685	0.0001	5	0.0685

Figures 8 and 9 show the force and position response plots for each of the cases in Table 3. The plots show a great deal of correlation between FBIC and its equivalent PBIC. Both position and force responses of two implementations match very closely.

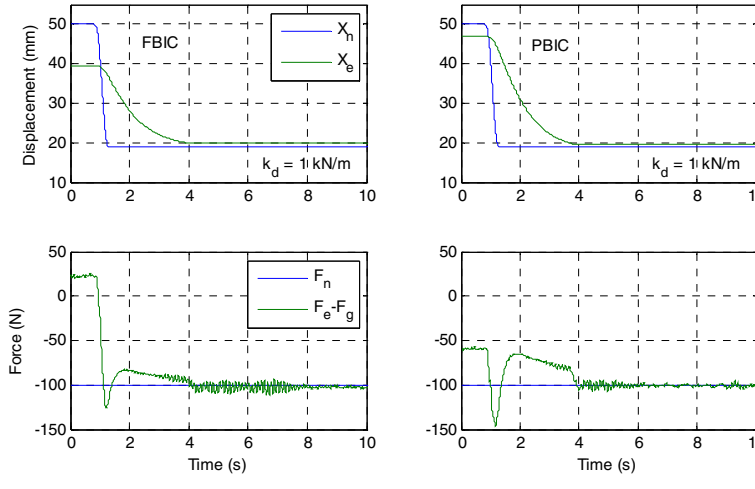

Figure 8: Position and force response of equivalent FBIC and PBIC

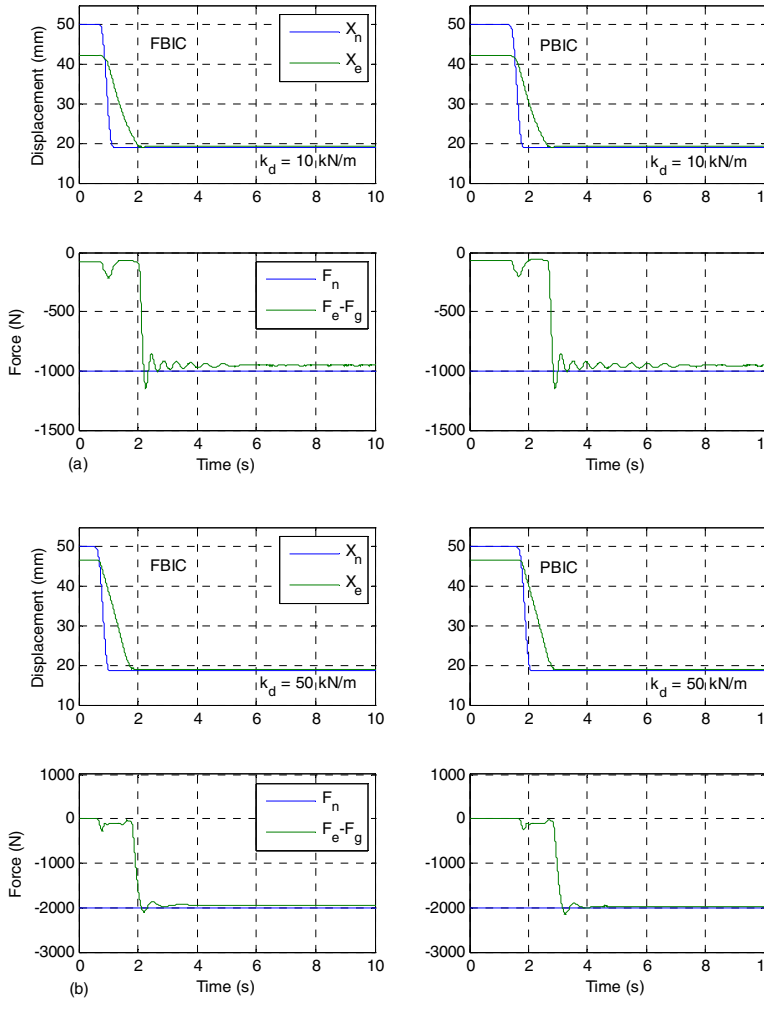

Figure 9: Position and force response of equivalent FBIC and PBIC

5. CONCLUSION

Force-based impedance control is implemented for a single degree-of-freedom hydraulic manipulator. Despite the fact that the force control of hydraulic actuators is a challenging task, it was shown that a desired dynamics of the manipulator can be achieved with a stable position and force response. A relationship is established to find a position controller for inner loop of PBIC equivalent to the force controller for inner loop of FBIC. The relationship is experimentally verified and from results it can be concluded that similar response can be obtained from either of the two implementations of impedance control.

The work presented in this paper is an effort to find similarities and limitations of the two implementations of the impedance control for hydraulic manipulators. Further research will be carried out, such as, identification and inclusion of manipulators and environmental dynamics. Testing of FBIC with 'stiffer' values of desired impedance and at the same time PBIC with 'softer' values. In our future work the research will continue to extend the number of degrees of freedom to obtain a practical hydraulic manipulator particularly suitable for teleoperation systems such as the one needed in International Thermonuclear Experimental Reactor (ITER.)

ACKNOWLEDGEMENTS

This work, supported by the European Communities under the contract of Association between EURATOM/TEKES, was carried out within the framework of the European Fusion Development Agreement. The views and opinions expressed herein do not necessarily reflect those of the European Commission.

REFERENCES

(1) Anderson R.J., Spong M.W, "Hybrid impedance control of robotic manipulators", Robotics and Automation, IEEE Journal of Robotics and Automation Volume 4, Issue 5, Oct. 1988 Page(s): 549 – 556

(2) Liu G.J., Goldenberg A.A., "Robust hybrid impedance control of robot manipulators", Robotics and Automation, 1991. Proceedings., 1991 IEEE International Conference on 9-11 April 1991 Page(s): 287 – 292 vol.1

(3) Hogan N., "Impedance control: an approach to manipulation: Parts I, II, III", Journal of Dynamic Systems, Measurement and Control, Vol. 107, pp. 1–24 , 1985.

(4) Bilodeau G., Papadopoulos E., "A model-based impedance control scheme for high-performance hydraulic joints", Proc. of the International conference on Intelligent Robots and Systems, 1998, Victoria, Canada.

(5) Heinrichs B., Sepehri N., Thornton-Trump A.B., "Position-based impedance control of an industrial hydraulic manipulator**",** Control Systems Magazine, IEEE Volume 17, Issue 1, Feb. 1997 Page(s):46 – 52

(6) Salcudean S. E., Tafazoli S., Lawrence P. D., Chau I., "Impedance control of a teleoperated mini excavator**",** Advanced Robotics, 1997. ICAR '97. Proceedings., 8th International Conference on 7-9 July 1997 Page(s):19 – 25

(7) Tafazoli S. , W. de Silva, Lawrence P. D., "Tracking control of an electrohydraulic manipulator in presence of friction", IEEE Transactions, Control System Technology, vol. 6, pp. 401 – 411, May 1998

(8) Lawrence D. A., "Impedance control stability properties in common implementations", Robotics and Automation, 1988. Proceedings., 1988 IEEE International Conference on 24-29 April 1988 Page(s):1185 – 1190 vol.2

(9) Eppinger S.D., Seering W.P., "Three dynamic problems in robot force control", IEEE Transactions on Robotics and Automation, Volume 8, Issue 6, Dec. 1992 Page(s):751 – 758

(10) De Schutter J., Bruyninckx H., Spong M., "Force control: a bird's eye view", Proc. Of IEEE CSS/RAS International Workshop on Control Problems in Robotics and Automation: Future Directions, 1997, San Diego, USA.

(11) B. Heinrichs, N. Sepehri, "Relationship of position-based impedance control to explicit force control: theory and experiments", Proceedings of the American Control Conference, San Diego, California, June 1999. Page(s): 2072 – 2076

(12) Volpe R., P. Khosla, "The equivalence of second order impedance control and proportional gain explicit force control", International Journal of Robotics Research, Volume 14, 1995, Page(s): 574 – 589

DETECTION AND INFLUENCE OF CYLINDER MOUNTING BACKLASH IN A HYDRAULIC POSITION SERVO

Esa Mäkinen and Tapio Virvalo
Institute of Hydraulics and Automation
Tampere University of Technology
33101 Tampere, Finland
fax +358 3 3652240
e.mail: esa.makinen@tut.fi, tapio.virvalo@tut.fi

ABSTRACT

Studies with a pneumatic position servo have shown that it is difficult to detect mounting backlash by only monitoring the position error. Is the situation different or the same in hydraulics? In this paper, the detection and influence of cylinder mounting backlash in a hydraulic position servo is studied. A high performance position control system is realized by using a State Controller. The methods to detect the backlash and the influence of the backlash on the system performance are presented. The influence and the detection of the backlash are discussed and the results are enlarged based on the simulations.

KEYWORDS: Position servo, backlash, detection, condition monitoring

1. INTRODUCTION AND MOTIVATION

It is well known that the backlash causes some uncertainty and inaccuracy especially in closed loop servo systems (1). There are many publications concerning with the backlash in general, especially in different gearing systems typically in connection with electric drives. However, a comprehensive literature study did not find any published studies dealing with the backlash in hydraulic or pneumatic position servo applications (2).

A backlash may occur in different places in closed loop fluid power servo systems. A backlash is typically in mechanical assemblies such as between the body of a machine and an actuator (cylinder) or between an actuator and a load. From the closed loop control point of view, there are two different cases. The backlash could be either inside the control loop or outside as shown in Figure 1. The inside case, using the position feedback y_a depicted in the figure, is used in this study.

Earlier similar investigation with a pneumatic drive showed somewhat surprising results (2). Even a very large backlash seems to have very little influence on the position accuracy.

Power Transmission and Motion Control 2006 Edited by Dr D N Johnston and Professor K A Edge

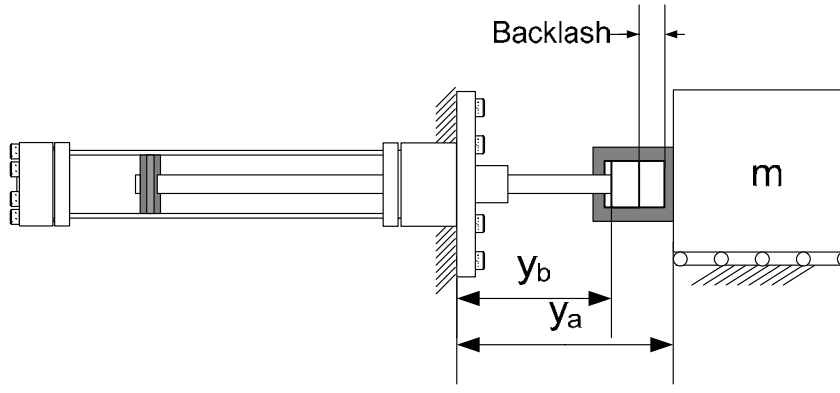

Figure 1. Backlash inside control loop (y_a), backlash outside control loop (y_b).

From the application, condition monitoring and maintenance points of views at least the following questions should be considered. How big the backlash might be without influencing too much the performance of the system? How to detect the backlash from other disturbances? How to detect the backlash due to wear? The basic idea is to study how to detect the backlash without any extra sensors. The available information from the system is included in the following issues: position measurements with high-resolution incremental encoder, estimated velocity, estimated acceleration, and controller output. In practice, important features of position servo systems from application point of view are stability, steady state accuracy, overshoot and settling time. These features are also quite easy to monitor in practical applications. In the pneumatic study (2) the best method to detect the backlash was achieved by analyzing the acceleration signal.

The main motivations for this study were:

- Condition control is increasingly important
- Earlier investigation with the pneumatic drive (2) showed that, in some cases, the backlash has a very insignificant influence on the steady state and dynamics performance and it is difficult to detect
- There is a lack of published research reports on the influence and detecting principles of different nonlinearities like the backlash

2. EXPERIMENTAL SET UP

The specifications of the system are as follows:

- Cylinder 63/36-500 (piston diameter/rod diameter-stroke, mm)
- Load mass 2850kg
- Supply pressure 120bar
- Servo valve:
  - Nominal flow= 50l/min (pressure drop/notch 35bar)
  - Hysteresis =0.3%
  - Bandwidth =500rad/s (-90° phase shift and -3dB amplitude damping rates)
- Incremental encoder resolution 0.002mm, analog-to-digital converter 12 bit

- The performance requirements of the system without the backlash are as follows:
  - Positioning accuracy 0.02mm
  - Allowed overshoot 0.02mm
  - Settling time 1s with 100mm stroke
- Studied backlash levels 0mm, 0.1mm and 0.5mm

3. EXPERIMENTAL RESULTS

Experimental tests were carried out with a P-controller and State Controller. The P-controller is simple, robust and the most often used in position servo applications. The State Controller is another commonly used controller type especially in demanding position servo applications. With the State Controller better steady state and dynamic performances are achieved utilizing the velocity and acceleration feedbacks to increase the damping of the system. The drawback of the State Controller is that it is not so robust than the P-controller. On the other hand, with the State Controller, the influence of the backlash should be bigger and more easily detectable.

In the following experimental tests the velocity and acceleration signals were generated as typically; i.e. differentiated directly from the position signal measured with a high-resolution encoder.

With both controllers, long and short strokes in both directions were tested. The end point (280 mm) in all the test strokes was chosen so that the natural frequency is at the minimum. The lengths of the strokes were chosen so that, in the case of the long strokes, the maximum velocities are reached and the outputs of the controllers are saturated. With the short strokes, the maximum velocities are not reached and the controller outputs are not saturated, but the controller outputs are anyway at a sufficiently high level; i.e. more than 50 % of the maximum.

The test responses were as follows, where the plus sign means the outward and minus the inward direction:

- Long ± 200mm stroke with the P-controller
- Short ± 80mm stroke with the P-controller
- Long ± 100mm stroke with the State Controller
- Short ± 10mm stroke with the State Controller

The influence of the backlash was studied with the three backlash cases; i.e. 0mm, 0.1mm and 0.5mm. In every case the controller was first manually tuned with the 0mm backlash to have an optimum behaviour; i.e. the best possible accuracy and good dynamic behaviour without overshoot. In every case the same controller parameters were used and the controllers were not retuned when the backlash was added to the system.

Typical long and short stroke position responses with the P-controller are shown in the Figure 2 and with the State Controller in the Figure 3. With the long strokes, the position error, relative controller output, velocity and acceleration signals are shown but with the short strokes, only velocity and acceleration signals are shown in these figures.

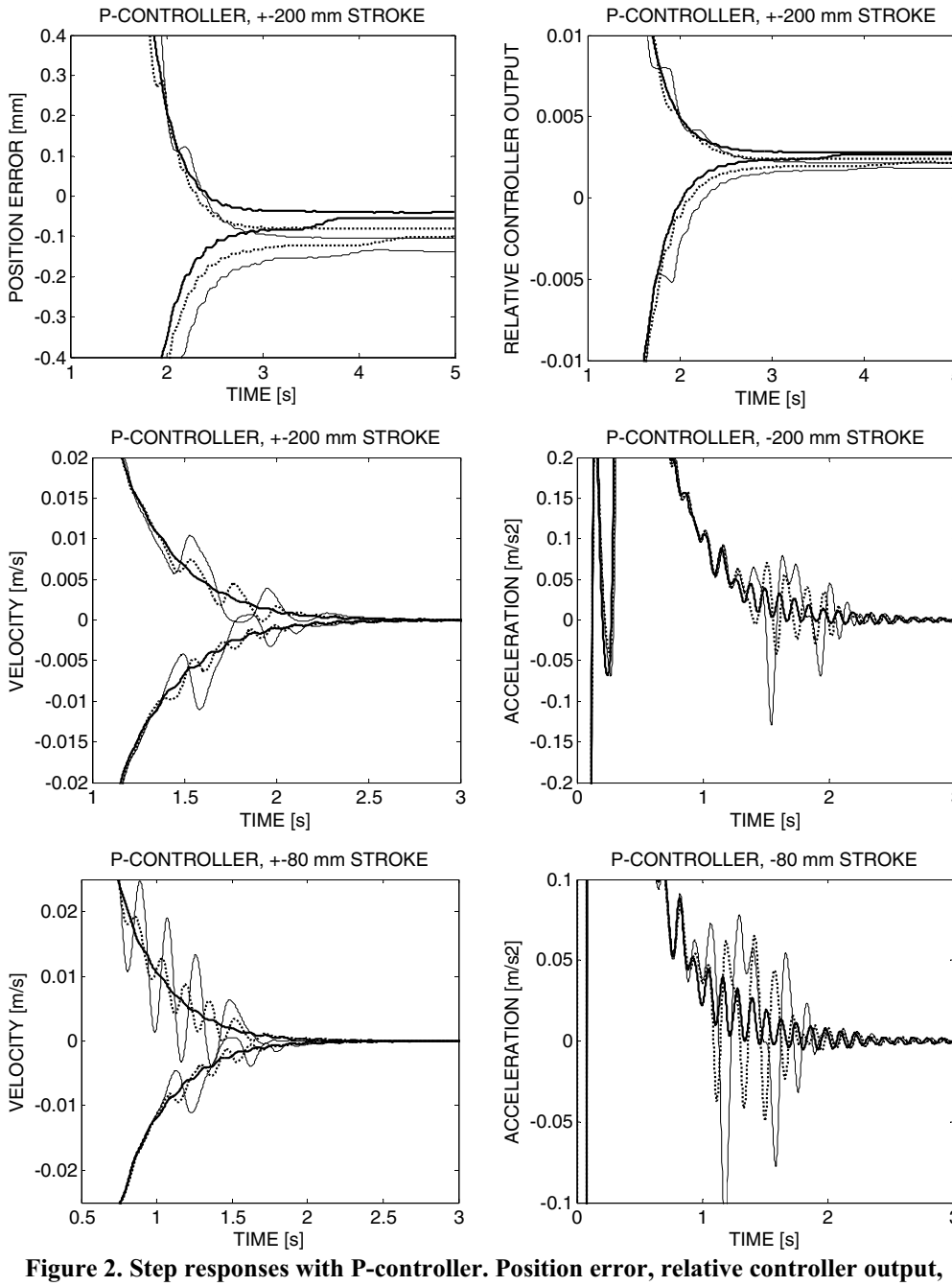

Figure 2. Step responses with P-controller. Position error, relative controller output, velocity and acceleration responses with backlash 0mm (thick solid), 0.1mm (dash) and 0.5mm (thin solid).

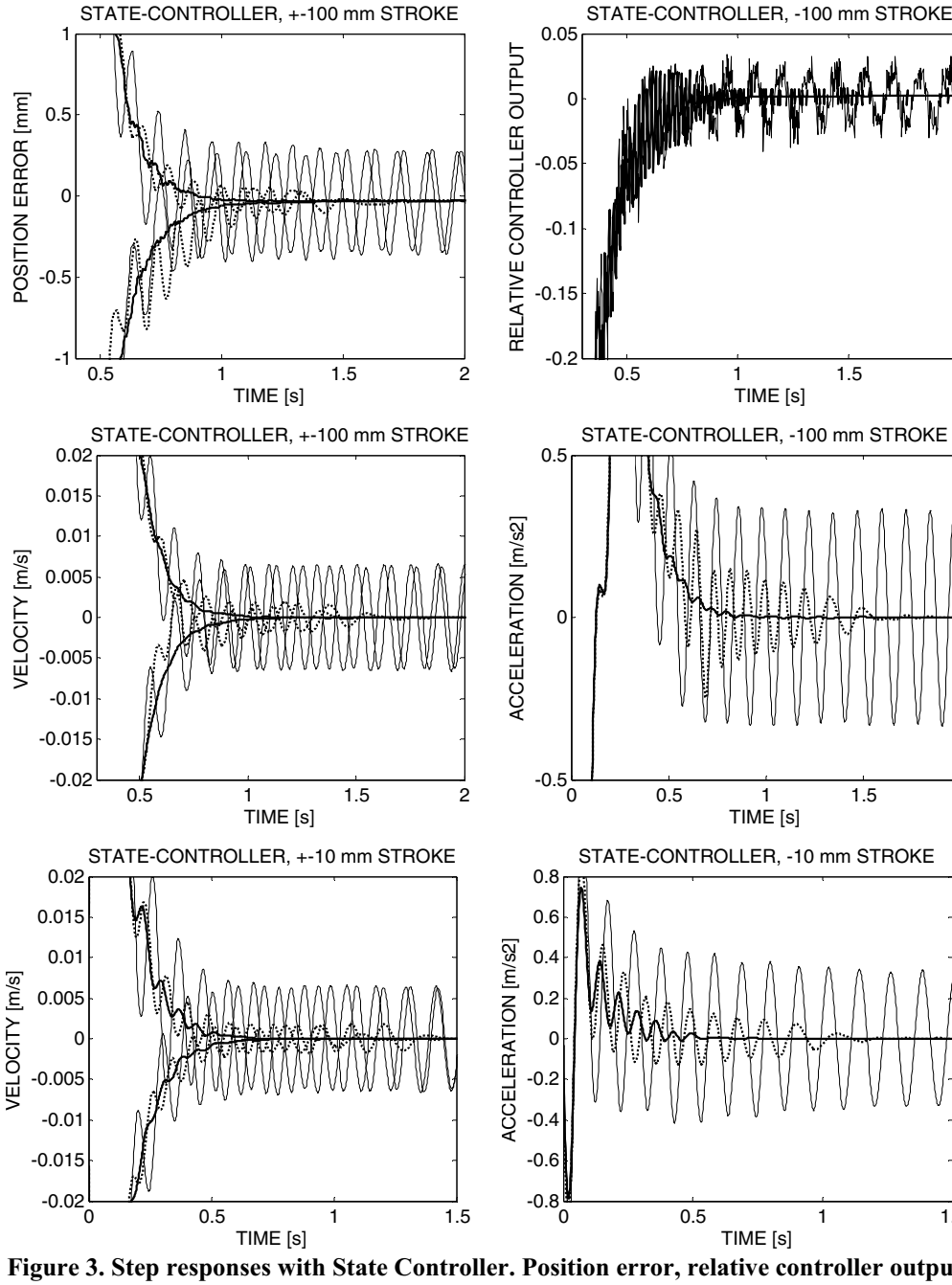

Figure 3. Step responses with State Controller. Position error, relative controller output, velocity and acceleration responses with backlash 0mm (thick solid), 0.1mm (dash) and 0.5mm (thin solid).

With both controllers the influence of the backlash on the position error is minor. A small zero point shift of the position error curves with the different backlashes could be result of some other reasons as well. Also from the relative controller output curves the influence of the backlash is not easily detected. With the P-controller the control signal is behaving a very similar way in every case. With the State Controller there is a small oscillation (2-5 %) visible in the relative controller output signal curves. For clarity, with the State Controller, these curves are presented only in one direction and only with the 0mm and 0.5mm backlash cases. The backlash increases the oscillation but there is a small oscillation also when the backlash is zero.

The influence of the backlash is clearly visible in the velocity and acceleration curves at the end of the steps. For clarity, with both controllers, acceleration curves are presented only in one direction and only with the 0mm and 0.5mm backlash cases. With the P-controller the amplitude of the velocity and acceleration oscillation is about 2-3 %. With the State controller the oscillation amplitude is also about 2-3 % but the acceleration amplitude is clearly higher, about 5-10%.

4. NON-LINEAR MODEL OF STUDIED SYSTEM

Simulation is a powerful tool, whereby the influence of different system parameters on the behaviour of systems is studied. In most cases an experimental set-up is costly and in order to generalize results many modifications should be done. This means very hard and time consuming work. Simulation can be based on a linear or non-linear model. The benefits of a linear model are its simplicity and cost-effective calculus as well as generalization of results. The main drawbacks are that real systems are not linear, especially hydro-mechanical systems, and understanding of results requires good knowledge of the application. With non-linear models better results can be achieved. Non-linear models are based on physical facts or more abstract thinking. Quite often researchers have reasonably good understanding about the studied phenomena, but all details are not known. Abstract models are common in the simulations of hydraulic systems.

A good practice is to verify and validate non-linear models with suitable experimental tests. In this case the study is carried out in the following way. The servo valve, cylinder and basic load including friction forces are modeled in the normal way (3). The backlash is modeled based on the abstract model depicted in Figure 4.

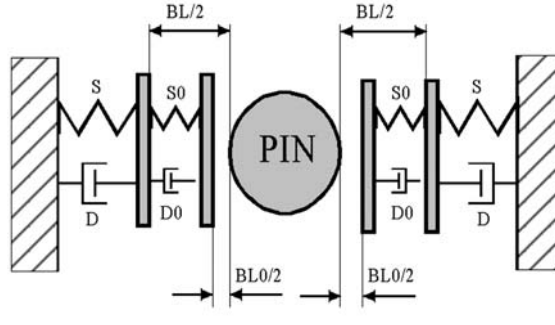

Figure 4. Abstract model for backlash modelling.

5. VERIFICATION OF NON-LINEAR BASIC MODEL

The non-linear model is verified for the following conditions

- Open loop velocity and piston force step responses with full load without the backlash.
- State controlled closed loop position control with the 0.5mm backlash.

The validation of the basic model is better with the open loop system, because the controller overcomes the influence of non-linearities quite powerfully. Basic calculations give rather good results in the steady state and non-linear cases, but the dynamic behaviour is more difficult. Quite a good picture about the dynamic behaviour of the basic system is got by comparing the measured and simulated open loop velocity and force step responses. As an example, some open loop responses without the backlash are shown in Figure 5.

The oscillation frequencies and amplitudes of the measured and simulated velocity responses match well. The simulated piston force response shows also good matching in the oscillation frequency, but the first peaks of the simulated response are much higher than measured. Anyway, it can be stated that the measured and simulated results match reasonably well and validate that the non-linear model is applicable.

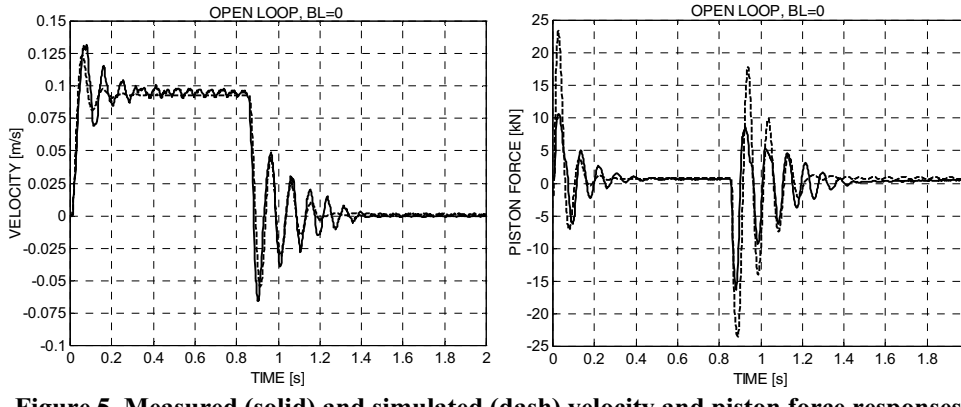

Figure 5. Measured (solid) and simulated (dash) velocity and piston force responses, open loop, without backlash.

The good dynamic and steady state performance of hydraulic cylinder drives in position control applications can be achieved with the State Controller. On the other hand state controlled hydraulic position servos are not robust. As an example, some measured and simulated responses of the state controlled position servo system are presented in Figure 6.

According to these results, the basic model can be considered good enough in these kinds of cases.

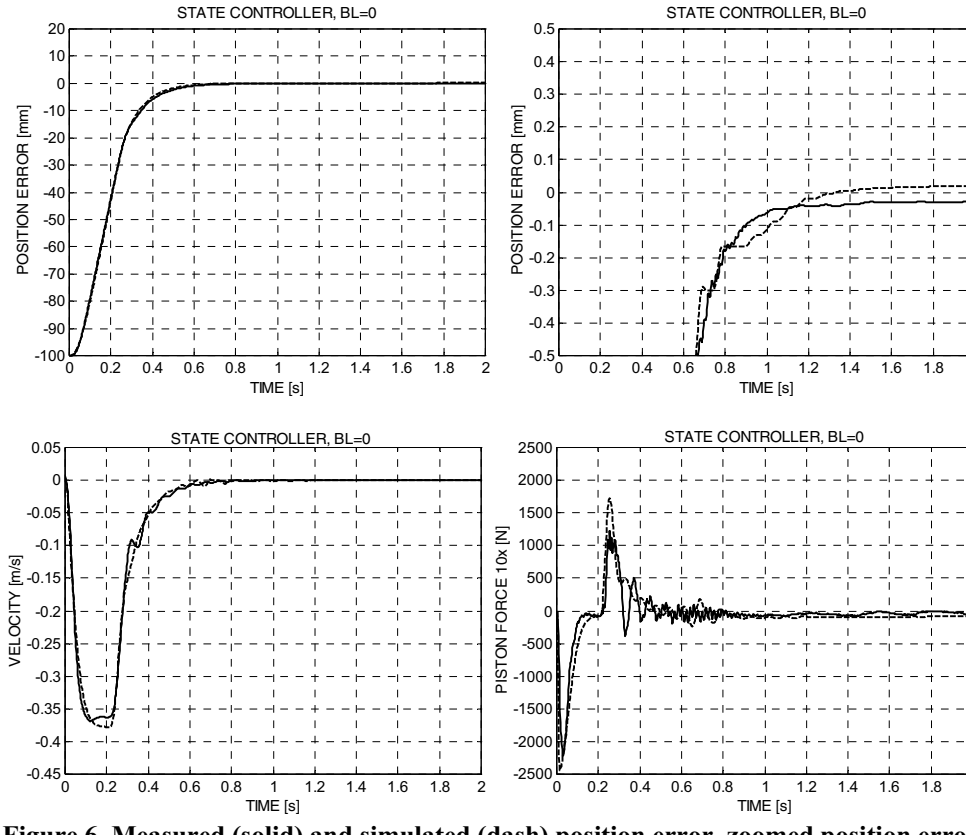

Figure 6. Measured (solid) and simulated (dash) position error, zoomed position error, velocity and piston force of state controlled position servo with 100mm stroke without backlash.

6. VERIFICATION OF NON-LINEAR MODEL OF SYSTEM WITH BACKALSH

In order to test the validation of the abstract backlash model some additional comparisons are done. As an example of the further validation of the non-linear model the measured and simulated responses of the state controlled system are studied.

The velocity and position error step responses of the state controlled system are shown in Figure 7. The matching of both responses is fairly good. Both measured and simulated responses show that the backlash clearly influences the behaviour of the system due to the finely tuned controller. These examples of the validation show that the non-linear model can be used to study the influence of the backlash on the behaviour of hydraulic cylinder drives. However, it should be noticed that the model is highly non-linear and so the generalization should be done very carefully.

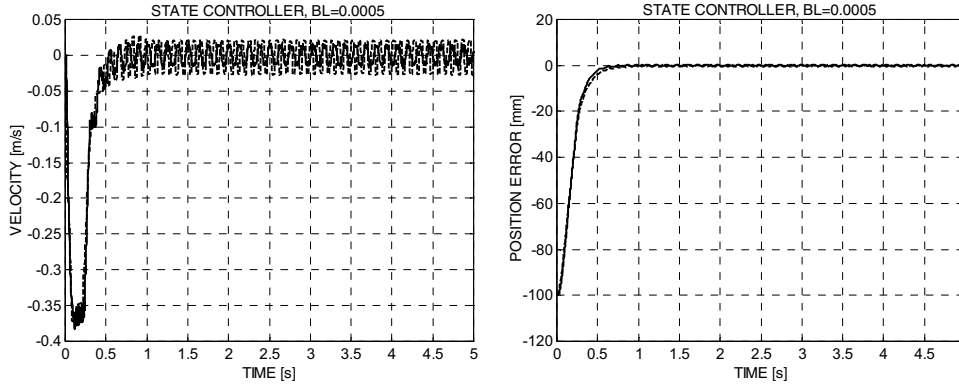

Figure 7. Measured (solid) and simulated (dash) velocity and position error responses, State Controller, backlash 0.5mm.

7. POSSIBILITIES TO DETECT BACKLASH

Simulations show that the backlash has a surprisingly small effect on the steady state position error. In practice the position sensor is the only sensor used in hydraulic cylinder driven position servos. The detection of the backlash has to be based on the position measurement and perhaps also on the output of the controller. An incipient backlash is fairly difficult to detect from the position or position error signal.

It is quite easy to compute the velocity and acceleration of the load from the position signal. Normally, acceleration is presented as a function of the time, but it can be presented also as a function of the position error. The estimation of the acceleration of the basic system is presented in Figure 8 with these both methods. When the load approaches the steady state position (position error less than 1mm) there are still slight oscillations in the motion and small acceleration peaks, less than 1ms^{-2}, can be detected during this phase.

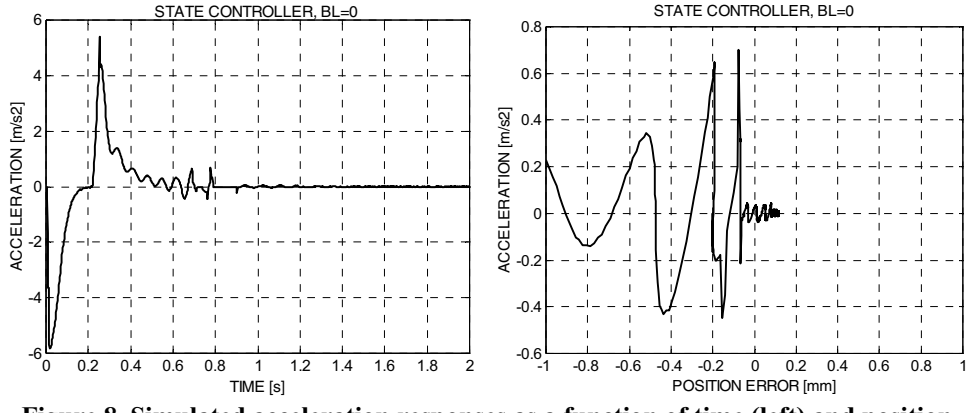

Figure 8. Simulated acceleration responses as a function of time (left) and position error (right), without backlash. Position error axis limited to ±1mm.

The accelerations at the end of the movements are shown as a function of the position error in Figure 9 when the backlash is 0.01mm and 0.05mm. In both cases, acceleration peaks are clearly higher than in the 0mm backlash case (Figure 8). The backlash of 0.01mm causes even a higher effect than the backlash of 0.05mm; i.e. the actual size of the backlash is not proportional to the size of the acceleration peaks. However, the existence of even quite a small backlash can be detected, which gives good possibilities to detect an incipient backlash.

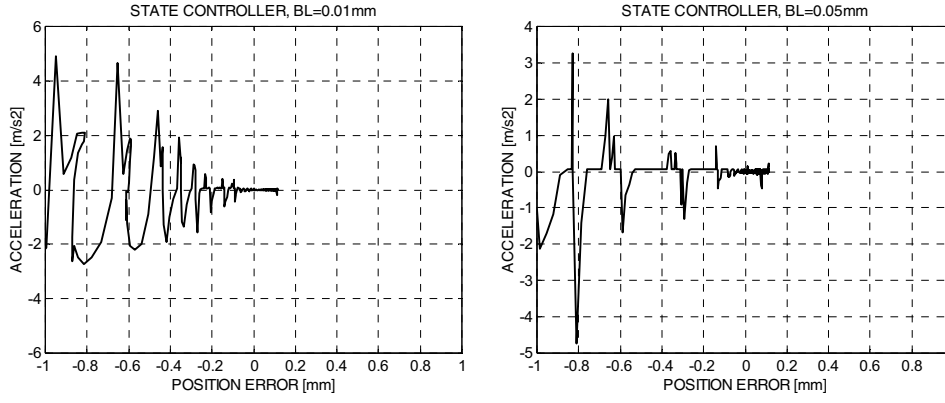

Figure 9. Zoomed acceleration as a function of position error, with 0.01mm backlash (left) and with 0.05mm backlash (right). Position error axis limited to ±1mm.

8. DETECTING PRINCIPLE OF BACKLASH

This study concentrates detecting the backlash in a quite finely tuned position servo. In this case it means that the state controlled position servo is studied. The simulation is used in testing a simple detection method. The following goals are set to detect the backlash:

- Only a position sensor is used.
- Detection method should be simple.
- Detection method should work in real time.

The following detecting algorithm is designed, Figure 10, based on simulation results. The principle of the algorithm is as follows. When the position error *er* is smaller than a certain limit ("*er<eplim and er>0*" or "*er>enlim and er<0*") the flag *erflag* is set, When the flag is set the acceleration is compared to certain limits ("*a>aplim*" or "*a<anlim*"). If the actual acceleration overcomes either of these limits, the corresponding counter is incremented ("*p=p+1*" or "*n=n+1*"). The position error *er* is calculated in the normal way and the acceleration *a* is obtained by differentiation from the position signal. The tuning parameters are the positive and negative limits *eplim*, *enlim*, *aplim*, and *anlim* of the position error and acceleration. The algorithm is run inside the control cycle. After every movement the results of the counters *p* and *n* are studied. The sum of the contents of the counters indicates how often the acceleration has overcome the set limits. When this sum overcomes a certain limits during several movements a warning about an incipient backlash is given.

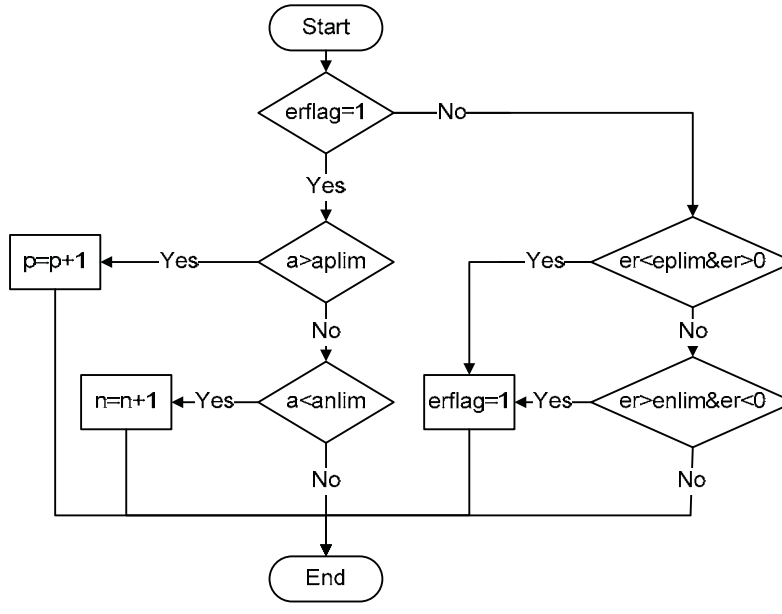

Figure 10. Principle of backlash detecting algorithm.

The examples of the detecting window are shown in Figure 11, when the limits of the position error signal are ±1mm and the limits of the estimated acceleration are ±1ms^{-2}. According to these examples the selected limits seem to be reasonable.

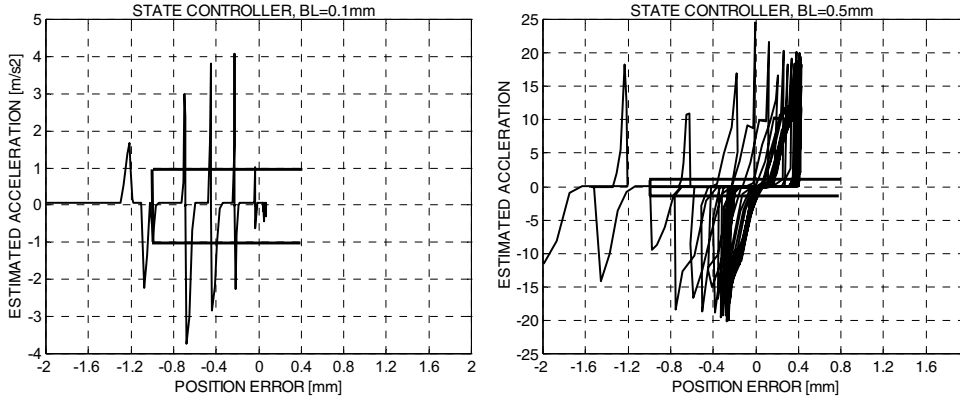

Figure 11. Estimated acceleration as a function of position error and detecting window. 0.1mm backlash (left) and 0.5mm backlash (right). Position error axis limited to ±2mm.

In order to test the detection method some additional simulations are done. The *erflag* is set when one of the error limits is reached as can be seen in Figure 12. When the backlash is zero the estimated acceleration does not reach the limits of the acceleration. With the 0.05mm backlash both error and acceleration limits are reached and the sum of the detecting counters is 10, which might cause warning about an incipient backlash.

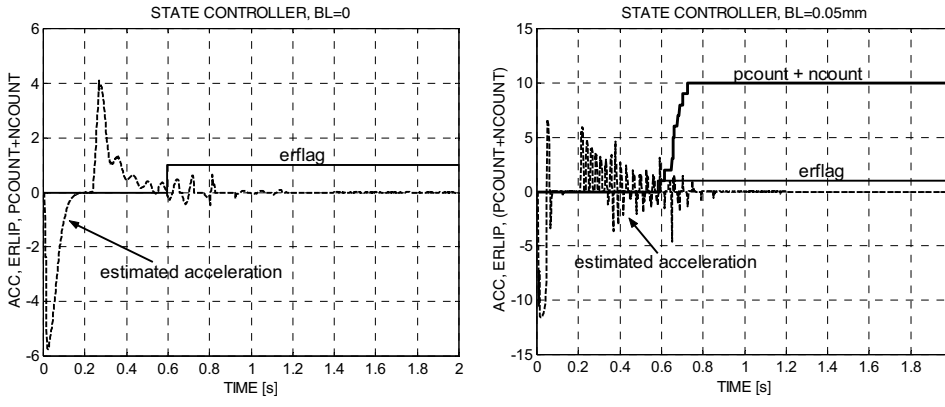

Figure 12. Estimated acceleration error flag when backlash is 0mm (left). Estimated acceleration, error flag and sum of pcount and ncount when backlash is 0.05mm (right).

9. DISCUSSION

Some backlash is necessary for assembly work. In addition, to backlash there are many other non-linearities affecting the performance of hydraulic position servo systems causing some difficulties to detect the influence of the backlash.

An adjustable backlash was implemented to the test set-up. However, an ideal pure backlash was not achieved, because of an existing test rig was utilized, which had some mechanical problems; i.e. a small misalignment of the cylinder and the load motions and rough non machined surfaces for new assemblies.

The cylinder was mounted with a rigid front end flange, but the rod end mounting in the backlash assembly allowed somewhat free radial motion. However, there ware unexpected strong oscillations in outward motions those are supposed to be due to some kinds of sticking problems.

The sticking could be one potential non-linearity in practical applications as well an interesting phenomenon for future studies.

10. CONCLUSIONS

Based on the experimental and simulation studies carried out in this study the following conclusion can be made:

- An incipient backlash is difficult to detect in loosely tuned (P-controlled) position servos
- A small backlash (0.01mm) can be detected and it causes harmful phenomena in finely tuned position servos (state controlled)
- The estimation of the load acceleration seems to be a good method to detect an incipient backlash

- It is a little uncertain to deduce the size of an incipient backlash, because the larger backlash might generate a smaller effect on the performance of servo system than the smaller backlash. For instance, the 0.01mm backlash caused a higher effect than the 0.05mm backlash. However, the existence of even quite a small backlash can be detected.
- A backlash between the piston rod and the load causes quite small disturbance to the steady state position accuracy of a position servo.
- A small backlash causes oscillations inside the backlash in finely tuned position servos, which might increase wear.

11. FURTHER WORK

In hydraulic position servos there are many non-linearities which might cause system oscillations. An individual phenomenon, or most likely some combination of non-linearities, can cause system oscillations. Changes in system parameters can also cause instability in finely tuned position servo systems. A big challenge is to find out how to detect a real reason for poor behaviour of position servo systems.

12. REFERENCES

1. Merrit H. E. Hydraulic Control Systems, Wiley & Sons Inc., 1967.358 p.
2. Mäkinen, E. & Virvalo, T. Detecting and influence of cylinder mounting backlash in pneumatic position servo. Proceedings of 4th. International Fluid Power Conference, (4.IFK), March 25-26, 2004, Dresden
3. Virvalo, T. Modelling hydraulic position servo realized with commercial components. 3rd International Conference on Fluid Power Transmission and Control, Zhejiang University, Hangzhou China, 13-16 September 1993. 6 p.

Return to Contents

Hydraulic Fluids, Sensors and Testing II

DESIGN OF INTEGRATED PRESSURE, FLOW, AND TEMPERATURE SENSOR FOR HYDRAULIC SYSTEMS

Charles W. Groepper
University of Minnesota
1100 Mechanical Engineering
111 Church St SE
Minneapolis MN 55455
groep004@umn.edu
(612) 845-8690

Dr. Tianhong Cui
University of Minnesota
1100 Mechanical Engineering
111 Church St SE
Minneapolis MN 55455
tcui@me.umn.edu
(612) 626-1636

Dr. Perry Y. Li
University of Minnesota
1100 Mechanical Engineering
111 Church St SE
Minneapolis MN 55455
pli@me.umn.edu
(612) 626-7815

Dr. Kim A. Stelson
University of Minnesota
1100 Mechanical Engineering
111 Church St SE
Minneapolis MN 55455
kstelson@me.umn.edu
(612) 625-6528

ABSTRACT:

The pressure difference between the inner and outer radii of an elbow is evaluated for suitability for flow measurement in fluid power systems. This pressure difference will be measured with a MEMS sensor, which also can measure the system pressure and temperature. Design tools used in the analysis include computational fluid dynamics (CFD) simulation and experimental measurement. Two alternative calibration methods are presented. When the first method is used for calibration, the elbow flow meter exhibits a linearity of 1.7%, an average accuracy of 1.5%, and a repeatability of 1.1% over a turndown range of 12:1. Slightly less accuracy

and less sensitivity to viscosity variation was noted when the second calibration method was used.

NOMENCLATURE:

Symbol	Description	Units
ρ	Fluid Density	kg/m^3
V	Average Fluid Velocity	m/s
D	Pipe Diameter	m/s
R	Radius of Elbow Curvature	m
r	Pipe Inner Radius	m
μ	Fluid Viscosity	Pa-s
ΔP	Pressure Difference	Pa
π	Dimensionless Variable	-
Re	Reynolds Number	-
Eu	Euler Number	-

INTRODUCTION:

Many machines rely on fluid power technology as a means of energy transmission. Some examples include assembly line robots, construction equipment, and cranes. These examples all

Power Transmission and Motion Control 2006 Edited by Dr D N Johnston and Professor K A Edge

share one similarity; they rely on the measurement of pressure, flow, and temperature for process control and monitoring. Traditionally, the measurement of these process variables is accomplished through the addition of stand alone sensing components to the fluid power system. In a previous paper, an alternative sensing method for fluid power systems has been proposed [1]. This method is to integrate small, multifunction MEMS sensors into existing fluid power components. The flow rate is measured indirectly with the method, in that small pressure drops that exist due to existing geometry are correlated to the flow rate. As an example, the suitability of a typical ¼" (6.35mm) elbow geometry with curvature to diameter ratio of unity is evaluated in this paper.

MEMS pressure and temperature sensing is a mature technology [2-6]. Therefore, the primary challenge with the proposed sensing method is the establishment of the pressure flow correlations. Specifically, the challenge is to account for effects of density and viscosity variation with temperature on the measured pressure difference between the inner and outer radii of an elbow at various flow rates.

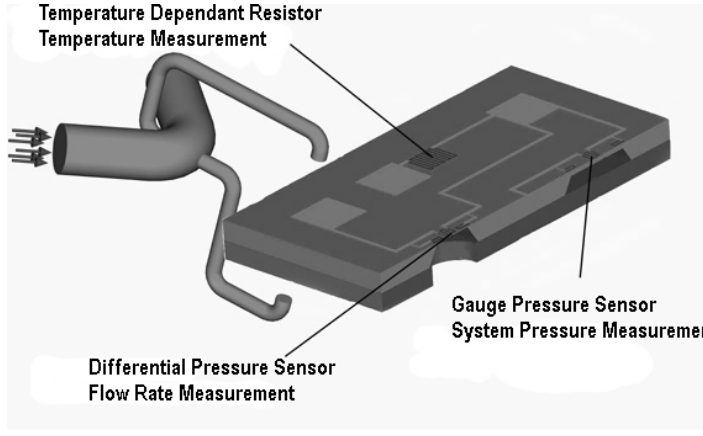

Figure 1: *Overview of the Integrated PQT Sensing Principle*

The integrated pressure, flow, and temperature (PQT) sensing method is shown in Figure 1. Development of the sensor follows a logical sequence consisting of five steps, which can be seen in Figure 2. First, the validity of the flow rate measurement principle is established through the use of CFD methods and experimental measurement. The data collected with these methods can then be used to develop a calibration procedure which takes into account the variation of the fluid viscosity and density with temperature. When an effective calibration method is developed, a single die multifunction MEMS based sensor can be designed and fabricated based on the pressure signals experienced during the calibration procedure. Finally, the MEMS sensor is integrated into an elbow, and the resulting PQT sensor characterized.

The focus of this paper is on the pressure flow calibration procedure for typical elbows. A more in depth description of the MEMS sensor design and fabrication can be found in a complimentary paper [7].

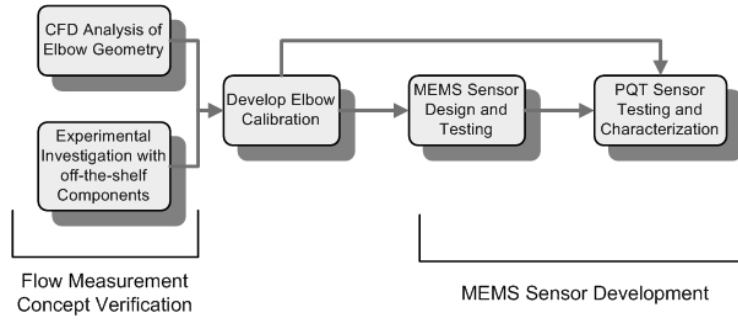

Figure 2: *PQT Sensor Development Steps*

The use of elbows to measure flow is a historical concept and considerable literature exists on the subject [8-20]. A majority of the literature focuses on the use of large elbows for water flow measurement in irrigation, a turbulent flow condition. When the elbow is used for the typical size, viscosities, and flow rates encountered in a fluid power system, the flow is laminar. Therefore, further research is needed to evaluate the use of an elbow for flow measurement in laminar flow.

CFD DESIGN:

The use of CFD software allows the parameters of the flow through elbows to be quickly evaluated. In this investigation, parameters included the effect of flow development on the observed pressure differential, the effect of density and viscosity on the flow field, and the optimum locations for pressure taps.

For any CFD analysis, the design of the mesh is an important consideration if valid solutions are to be obtained. The majority of the elements are placed in the areas of the highest gradients in pressure and velocity. Care should be taken such that the mesh is not too coarse in other areas, propagating errors into the regions of interest. Similarly, care also needs to be taken in the assignment of boundary conditions, so the imposition of an unrealistic boundary condition does not influence the flow phenomena in the regions of interest.

In our previous documentation, all computational results were obtained using meshes of tetrahedral elements[1]. In this work, the computational results have been greatly refined using mapped brick meshes. Mapped brick meshes offer several advantages compared to tetrahedral elements including faster solution times and greater control over element placement. For these reasons, brick element meshes were used in all of the CFD investigations to follow.

The entrance regions selected for study are representative of the inlet lengths expected while integrating the PQT sensor into fluid power components. Often, the inlet will be on the order of ten pipe diameters, or less. The study was performed at various Reynolds numbers, however, only the results obtained with a middle range Reynolds number of 650 will be presented. In classical pipe flow, this Reynolds number would require an entrance length of thirty-nine pipe diameters before the elbow to ensure fully developed flow. For all cases examined in the study, the velocity profile at the inlet was assumed to be constant, a worse-case-scenario. The results can be seen in Figure 3. Note the differential pressure has been normalized as the Euler number.

For all of the inlet lengths investigated, the study was performed with both the number of elements separating the entrance from elbow and the spacing of the elements held constant. Performing the study in this way allowed some numerical effects to be separated from the physical phenomena. For the case of constant element spacing, very short entrance lengths resulted in very few elements separating the boundary condition from the region of interest. It is expected the results obtained using this method to be error prone. From Figure 3 it is evident the number of

elements in the entrance region has little effect on the solution. Therefore, comparison of the results obtained with constant element spacing to the results obtained with a constant number of elements validates the accuracy of the constant number of elements solution. There is a reduction in the differential pressure signal as the entrance length is reduced. Although the signal is attenuated, the simulations predict the elbow can be used successfully to infer a flow rate with entrance lengths as small as two pipe diameters.

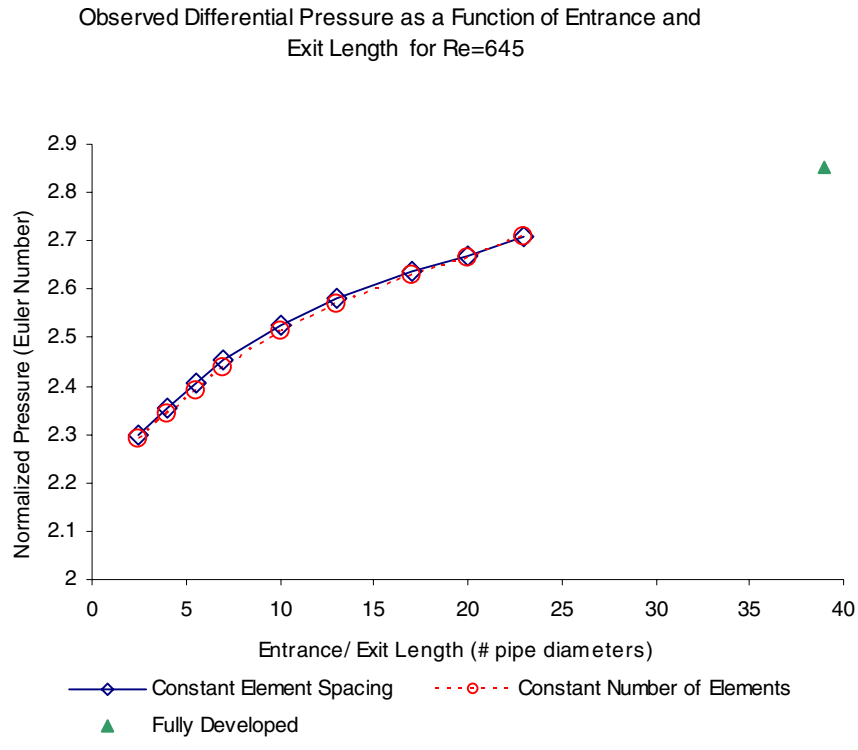

Figure 3: *Entrance Length Study Results for Reynolds number of 645*

CFD methods were also used to evaluate the effects of viscosity on the flow using non-dimensional variables. The differential pressure can be normalized as the Euler number, and the flow can be normalized as the Reynolds number. Using these dimensionless quantities, the effect of altering the fluid viscosity will only change the Reynolds number, while a change in the velocity or density will change both the Reynolds number and the Euler number. To demonstrate the effectiveness of the non-dimensional approach, the results of two elbows with different dimensions are shown. Both elbows have a curvature to diameter ratios of unity, and both reduce to a single governing relationship shown in Figure 4.

Historically, elbow meters have been created with pressure taps located on a 45^{o} plane. This location does not provide the maximum differential pressure signal, but does allow the elbow to be used as a bi-directional meter. If bi-directional service is not needed, more suitable pressure tap locations offering a higher differential output signal can be found. To perform the investigation, CFX was used to examine the pressure distributions along the walls of the elbow. From Figure 5 is it evident the location of the outer pressure tap provides the greatest influence on the differential pressure output signal. The optimum location for the outer tap is 55^{o}-60^{o} with respect to the inlet. A stronger pressure signal is noted with the inner tap located approximately

80° from the inlet. This is not a suitable location, as the flow separates from the wall at an angle of 45°-50° from the flow inlet. A more suitable location for the inner pressure tap is at the local minimum which occurs at an angle of approximately 25°-30° from the flow inlet.

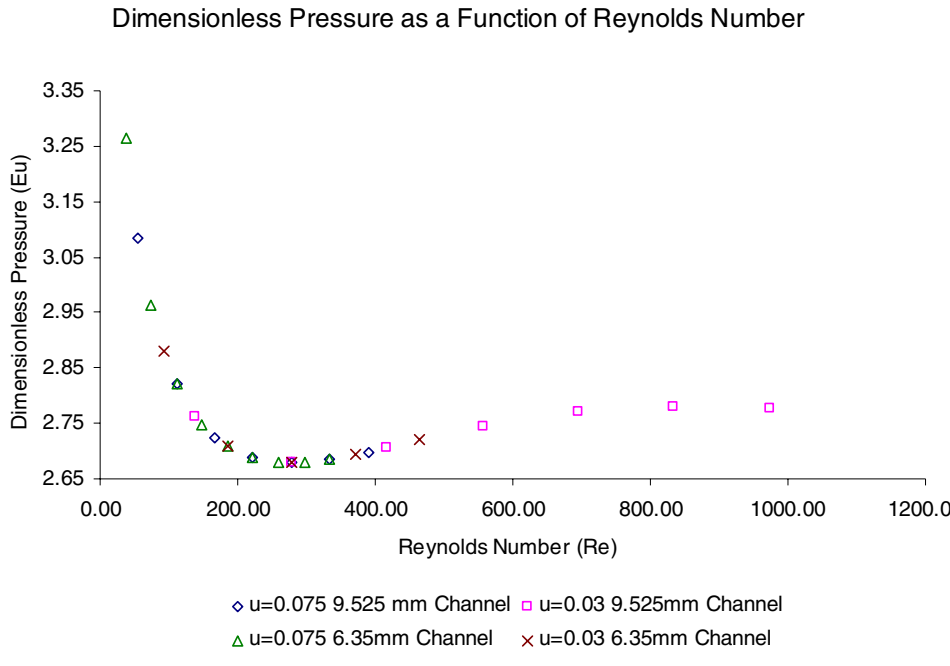

Figure 4: *Elbow pressure-flow characteristics shown in a non-dimensional basis*

The finite diameter of the pressure tap introduces an error. Shaw [21] states the error is proportional to the diameter and length of the tap and to the wall shear at the pressure tap location. For this reason, the wall shear must be evaluated while searching for optimum pressure tap locations. The typical locations of the maximum wall shear are show in Figure 6. In this figure, the fluid flow is from the top of the page to the left. The standard 45° plane pressure taps are located in areas of low wall shear, as is the improved signal 25°/55° location. The most unsuitable locations for pressure taps from a wall shear standpoint would be on the outer radius immediately following the elbow, and on the inner radius immediately preceding the elbow.

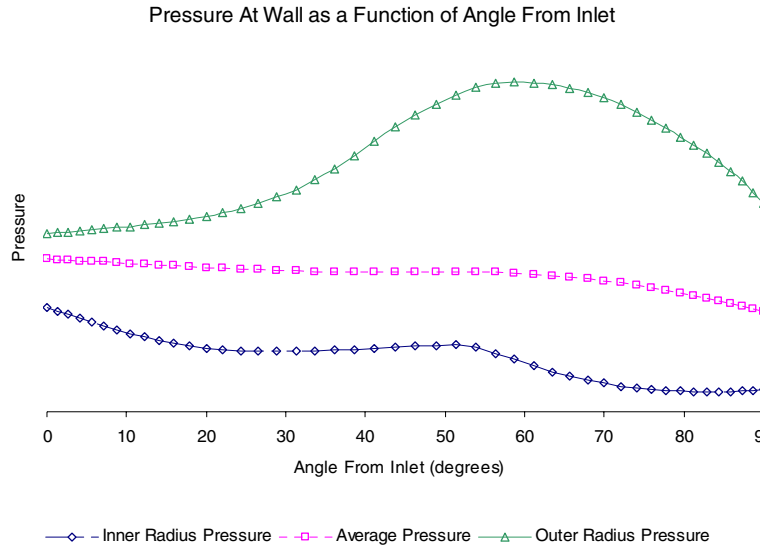

Figure 5: *Pressure Distribution at Wall for Typical Elbow Geometry*

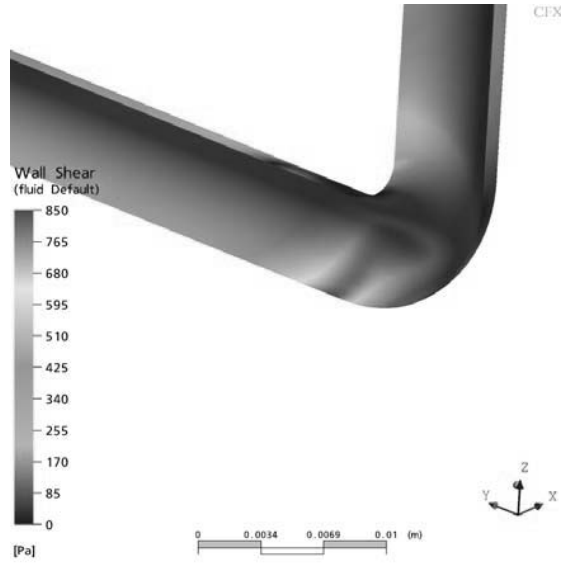

Figure 6: *Contour Map Showing Wall Shear Magnitude*

EXPERIMENTAL DESIGN:

Laboratory experiments were performed to satisfy two primary objectives. The first objective was to verify the use of an elbow as a flow meter for fluid power systems. The second

objective was to compare the numerical and CFD predictions. The apparatus used for experimental investigation is shown as Figure 7. The flow is controlled by a simple needle valve ahead of the experimental elbow apparatus. To maintain a constant back pressure across the experimental elbow apparatus, a relief valve is in-line between the elbow apparatus and the return to tank.

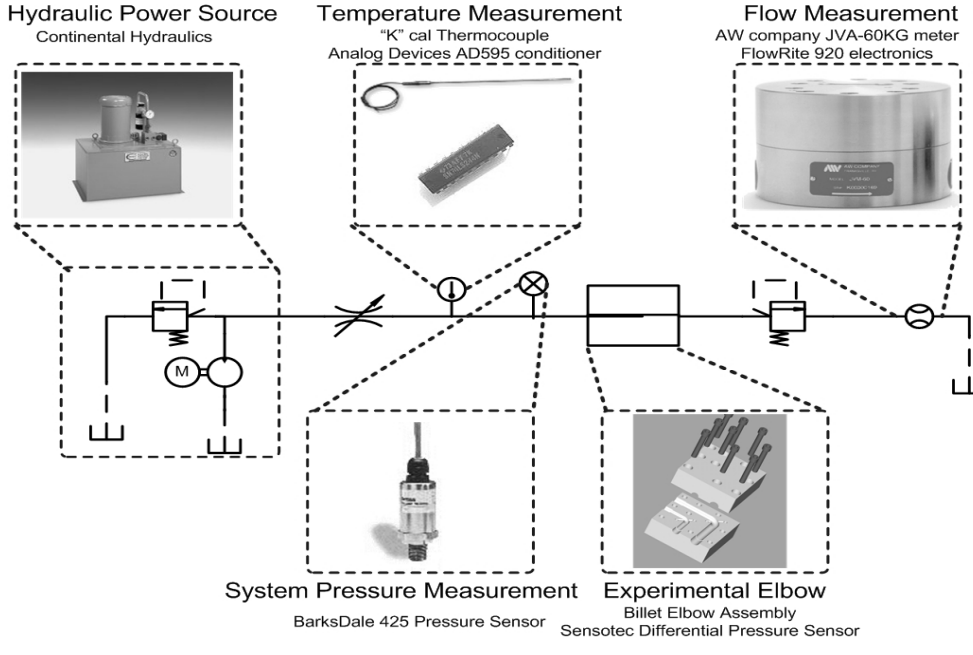

Figure 7: *Experimental Apparatus for Elbow Flow Meter Evaluation*

For a direct comparison to be made to CFD results, the experimental test geometry needs to be precise. High-precision elbow geometry was CNC machined from 1020 steel to accomplish this purpose, and can be seen in Figure 7. To obtain high precision pressure measurement, care was taken in the design of the pressure taps according to the work of Shaw [21]. Using differing transient response models, Holman and Benedict both show the transient response of the pressure taps to be a sole function of the geometry for a given fluid [22, 23]. Therefore, the design of the pressure taps is a trade-off between accuracy in the pressure reading and the transient response time of the tap. Figure 8 shows the tradeoff in graphical form. Based on the design, pressure taps with a hydraulic diameter of ~1.0mm were used, which provide measurement errors less than 1.0% and have a transient response time of less than 200 ms.

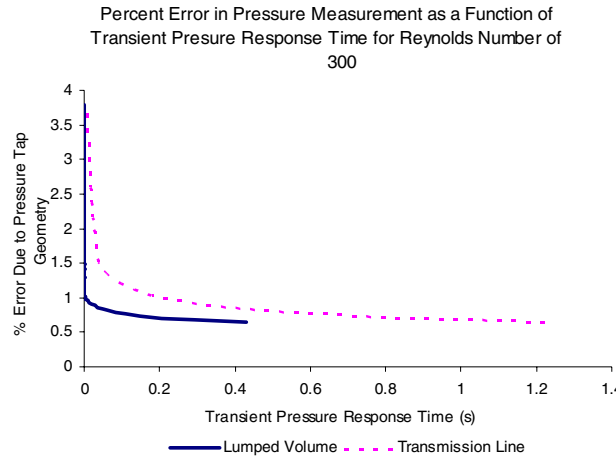

Figure 8: *Pressure Tap Measurement Error as a Function of Transient Response Time*

Pressure-flow data gathered experimentally at various operating temperatures is shown in Figure 9. Note the flow measurement have been done with a positive displacement meter, which provides virtually viscosity (temperature) independent flow measurement. In a previous work, the pressure-flow relations had been established with a turbine type meter, and the viscosity dependence of this meter resulted in data showing much greater viscosity dependence than the current corrected result. The data now compares exceptionally well to CFD predictions.

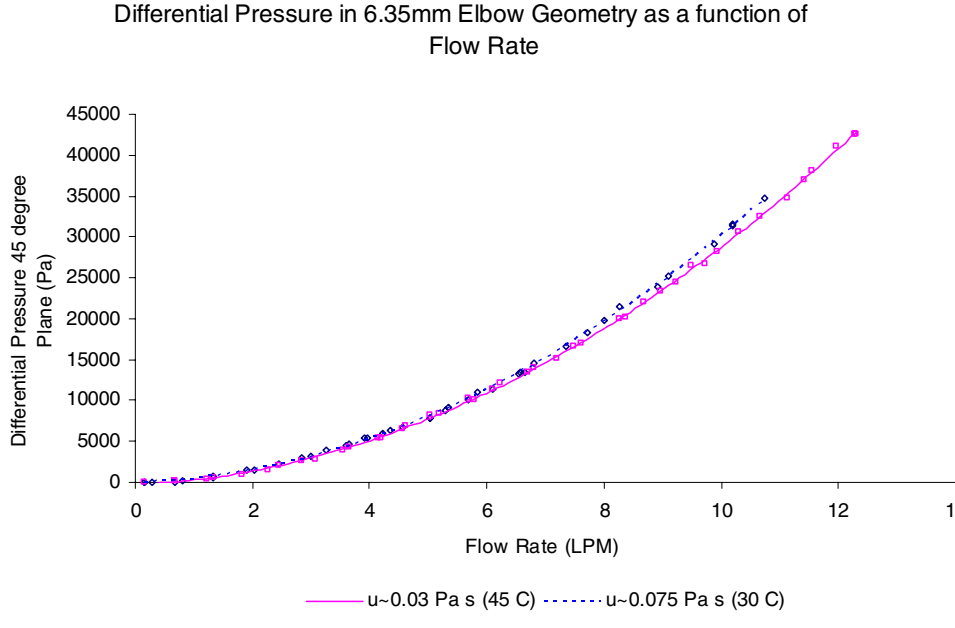

Figure 9: *Pressure-Flow Relationship for various temperatures with a ¼" (6.35mm) diameter flow channel*

To better understand the temperature dependence noted by the fluid in Figure 9 both the temperature-viscosity relationship, and the temperature-density relationship of the fluid were experimentally measured. In this way, a solid knowledge of the flow phenomena could be known to provide a direct comparison to CFD results, and to provide solid data for a calibration procedure.

Radhakrishnan states the viscosity of hydraulic fluids can increase by as much as 25% as the fluid ages [24]. To ensure the viscosity used in the calibration procedure was correct, the viscosity of the fluid in the test bench was measured by using a Brookfield rotational viscometer. The data point marked "room temp" is an average reading taken using all rotational speeds.

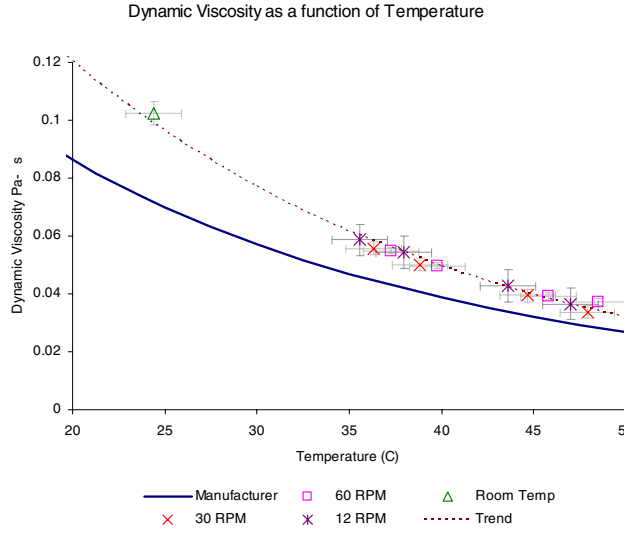

Figure 10: *Measured Viscosity of Mobile 1 DTE 25 Hydraulic Oil*

The density of the hydraulic fluid was also measured to verify compliance with the manufacturer's specification and to establish a density-temperature relationship, since petroleum manufacturers seldom state density at more than one temperature. The result of the density evaluation can be seen in Figure 11.

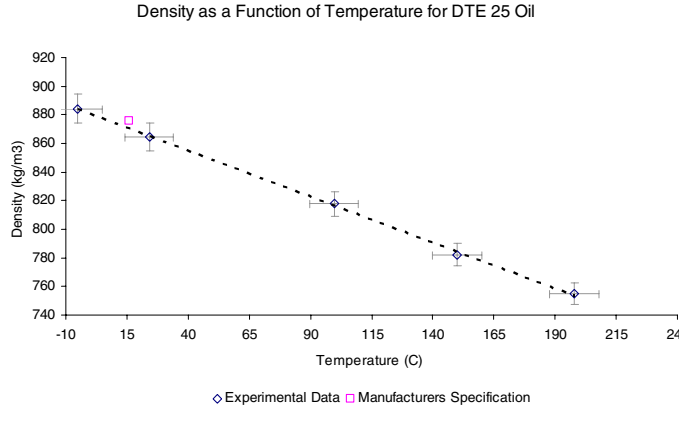

Figure 11: *Measured Temperature-Density Relationship for Mobile 1 DTE 25 Hydraulic Oil*

CALIBRATION METHOD:

The primary purpose of the experimental investigation was to gather differential pressure, temperature and flow information from standard elbow geometry in order to develop a suitable calibration scheme. Although the calibration procedure in this section is applied to elbow geometry, the procedure could be successfully applied to any geometry providing repeatable pressure-flow characteristics. The temperature dependency of the pressure-flow correlations for the elbow is quite evident from Figure 9. Since the density-temperature, and viscosity-temperature relations were directly measured for the DTE 25 working fluid, all variables governing the flow phenomena are known.

The calibration schemes use a dimensional analysis. This approach allows for compensation of all pertinent variables, which is necessary to account for temperature effects. An analysis which is highly viscosity dependant is presented first, followed by a less viscosity dependant approach.

The basic theory of dimensional analysis states the following "If an equation involving k variables is dimensionally homogeneous, it can be reduced to a relationship among k-r independent dimensionless products, where r is the minimum number of reference dimensions required to describe the variables" [25]. For the case of laminar flow in an elbow, there are 3 reference dimensions and 5 variables, resulting in two dimensionless terms. One possible set of dimensionless variables is shown as Equation 1 and Equation 2 respectively. π_1 is twice the Reynolds number squared multiplied by the Euler Number. The second dimensionless term, π_2 is the Reynolds number.

$$\pi_1 = \frac{\Delta P \rho D^2}{\mu^2} = 2 R_e{}^2 Eu \tag{1}$$

$$\pi_2 = \frac{V \rho D}{\mu} = R_e \tag{2}$$

In a previous work, another dimensionless pressure term was presented, an Euler number modified with a geometry constant. In the current work, a comparison between the use of this term, and the dimensionless pressure term shown as Equation 1will be drawn. The alternative pressure term is shown as Equation 3.

$$\pi_3 = \frac{\Delta P}{\rho V^2 \ln\left[\frac{R+r}{R-r}\right]} = Eu_{\text{mod}} \tag{3}$$

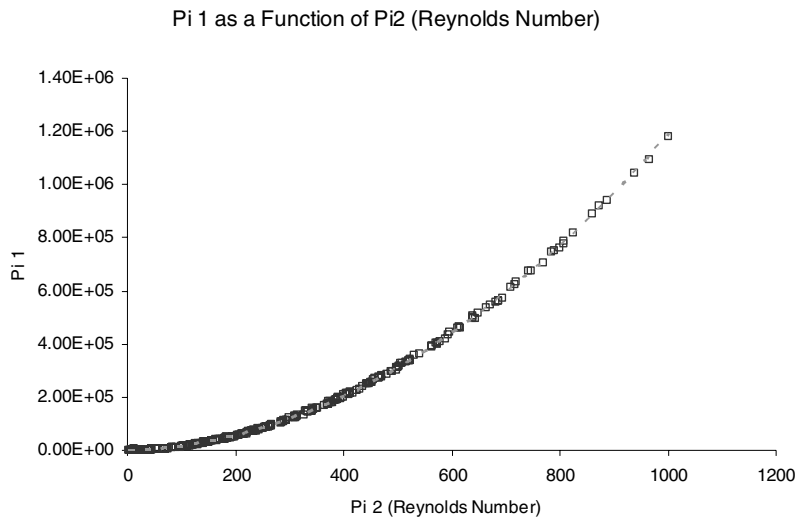

Figure 12: *Calibration Curve for First Calibration Method*

Application of the dimensionless calibration method requires that relationships between the two dimensionless terms be drawn. These relationships can be seen graphically as Figure 12 for the first method, and Figure 13 for the second method. The relationship between π_1 and the Reynolds number is quadratic as shown in Figure 12. When the second method is used, significant scatter in the data is noted, however, an linear relationship between the modified Euler number and the reciprocal of the Reynolds number can be seen.

The data shown in Figure 12 can easily be characterized by a second order least squares polynomial curve fit. The basic form of this curve can be seen as Equation 4.

$$\pi_1 = C_1 R_e^{\ 2} + C_2 R_e \tag{4}$$

The definition of π_1 and R_e can be substituted into Equation 4 as shown in Equation 5.

$$\frac{\Delta p \rho D^2}{\mu^2} = C_1 \left[\frac{\rho V D}{\mu} \right]^2 + C_2 \left[\frac{\rho V D}{\mu} \right] \tag{5}$$

Rearrangement and collection of terms results in a quadratic equation in the average velocity, shown as Equation 6.

$$\frac{C_1 \rho D}{\mu} V^2 + C_2 V - \frac{\Delta p D}{\mu} = 0 \tag{6}$$

The average velocity, and hence the flow rate can easily be determined from Equation 6 through the use of the quadratic equation. A similar quadratic in the velocity results when the second calibration method is used.

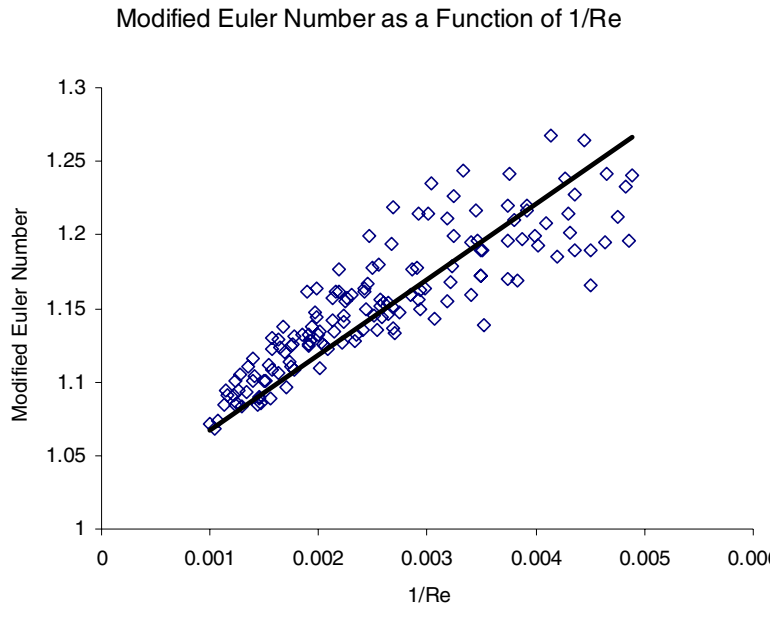

Figure 13: *Calibration Curve for Second Calibration Method*

The data shown as Figure 13 can be fit using linear least squares. The basic form of this curve is shown in Equation 7.

$$Eu_{\mathrm{mod}} = S\left(\frac{1}{R_e}\right) + I \tag{7}$$

The definition of the modified Euler number and R_e can be substituted into Equation 7 to obtain Equation 8.

$$\frac{\Delta p}{\rho V^2 \ln\left[\dfrac{R+r}{R-r}\right]} = S\left[\frac{\mu}{\rho V D}\right] + I \tag{8}$$

Rearrangement and collection of terms results in a quadratic equation in the average velocity, shown as Equation 9.

$$-\Delta P + V\left[S\left(\frac{\mu}{D}\right)\ln\left[\frac{R+r}{R-r}\right]\right] + V^2\left[I\rho\ln\left[\frac{R+r}{R-r}\right]\right] = 0 \tag{9}$$

The average velocity, and hence the flow rate can easily be determined from Equation 9 through the use of the quadratic equation.

Elbow Meter Performance:

Figure 14 shows the performance curve of the elbow meter when the second calibration procedure is used. A graphically similar result is obtained when the first method is used, with improved performance noted in the two to four LPM flow range. When the second calibration procedure is used, the elbow meter exhibits a linearity of 3%, an average accuracy of 2.0%, and a repeatability of 1.42% over a turndown of 12:1. Restricting the turndown of the meter to 8.0:1 with the second calibration method improves the linearity to 2.3% and the average accuracy to 1.9%. When the first calibration method is applied, the elbow meter exhibits a linearity of 1.7%, an average accuracy of 1.5%, and a repeatability of 1.1% over a turndown ratio of 12:1.

Although the performance of the elbow meter was diminished with the second calibration method was used, the method relies less on the fluid viscosity. Therefore, the method is expected to exhibit superior performance results when a greater amount of uncertainty is present in the viscosity.

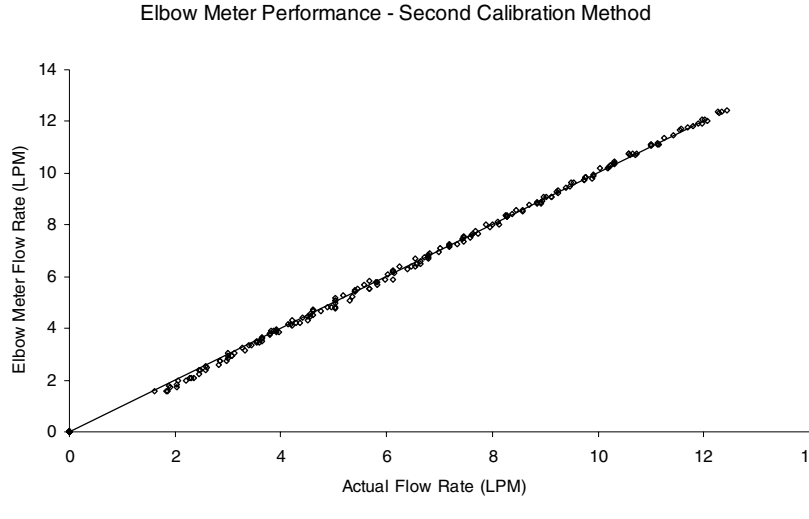

Figure 14: *Elbow Meter Performance Curve from Second Calibration Method*

Conclusion:

The pressure difference arising between the inner and outer radii of an elbow has been evaluated for suitability for use as an inferred flow measurement method. The viscosity and density dependence of the pressure-flow relationships has been studied using both CFD simulation and experimental measurements. These design tools predict the elbow can be used to infer flow rate in the presence of significant variation of viscosity and density. The data gathered experimentally was used to develop two calibration methods. When the first method is used for calibration, the elbow flow meter exhibits a linearity of 1.7%, an average accuracy of 1.5%, and a repeatability of 1.1% over a turndown range of 12:1. The second calibration approach proved to be less accurate; however, the method is more suitable for use in conditions where the viscosity is uncertain.

Acknowledgement:

The authors are grateful for the assistance of Professor Ephraim Sparrow and his student, Jimmy Tong. Their assistance and expertise with CFX computational software is second to none.
This project has been sponsored by the Cooperative Network for Research (CNR) in motion control through fluid power group of the National Fluid Power Association.

References:

1. Groepper, C. W., et al. *Integrated Pressure, Flow, and Temperature Sensing for Hydraulic Systems*. in *ASME-IMECE2005-82002*. 2005. Orlando Florida: ASME.
2. Bistue, G., et al., *A Micromachined Pressure Sensor For Biomedical Applications.* Journal of Micromechanics and Microengineering, 1997. 7: p. 244-246.
3. Boillat, M., VanDerSchoot, B., and Droz, B., *A High-Precision Piezoresistive Flow Sensor for Microdosing Applications.* Sensors, 2000. September.
4. Chevroulet, *A Pressure Sensor for a Smart Barameter.* Sensors, 2000. May.
5. Eaton, W. and Smith, J., *Micromachined Pressure Sensors: Review and Recent Developments.* Smart Materials and Structures, 1997. 6: p. 530-539.
6. Fung, C., Harris, R., and Zhu, T., *Multifunction Polysilicon Pressure Sensors for Process Control.* Sensors, 1999. October.
7. Groepper, C. W., et al. *Fabrication of Integrated Pressure, Flow, and Temperature Sensor for Hydraulic Systems*. in *ASME-IMECE2006-13211*. 2006. Chicago Illinois: ASME.
8. Addison, H., *The use of Pipe Bends as Flow Meters.* Engineering, 1938: p. 227-229.
9. Dean, W., *Note on Motion in a Curved Pipe.* Philosophical Magazine Letters, 1927. 4(20): p. 208-223.
10. Dean, W., *The Streamline Motion of Fluid in a Curved Pipe.* Philosophical Magazine Letters, 1928. 5(30): p. 673-695.
11. Dean, W., *Fluid Motion in a Curved Channel.* Proceedings: Royal Society London 1928. A121: p. 402-420.
12. Einhellig, R., Schmitt, C., and Fitzwater, J. *Flow Measurement Opportunities Using Irrigation Pipe Elbows*. in *American Society of Civil Engineers:Hydraulic Measurements and Experimental Methods, 2002 Proceedings of the Specialty Conference*. 2002. Estes Park Colorado: ASCE.
13. Eustice, J., *Flow of Water in Curved Pipes.* Proceedings of the Royal Society of London, 1910. 84(568): p. 107-118.
14. Lansford, W., *Use of an Elbow in a Pipe Line as a Means of Measuring the Flow of Water.* Bulletin of Associated State Engineering Societies, 1934. IX(2).
15. Lansford, W., *The Use of an Elbow in a Pipe Line for Determining the Rate of Flow in the Pipe.* Univ. of Illinois Engrg. Experiment Sta. Urbana Ill. , 1936. Bulletin No 289: p. 5-33.
16. Levin, A., *A Flow Metering Apparatus.* In Spring Meeting of ASME, 1914. Paper Number 1436: p. 239-254.
17. Nishiyama, S., et al., *Hydraulic Design of Bypass Flow Meter Using the Bend Pipe.* Proceedings of the International Conference on Agriculteral Engineering, 1999: p. II247-II254.
18. Taylor, D. and McPherson, M., *Elbow Meter Performance.* Journal American Water Works Association, 1954: p. 1087-1095.
19. Taylor, G., *The Criterion for Turbulence in Curved Pipes.* Proceedings of the Royal Society of London, 1929. 124(794): p. 243-249.
20. Yarnell, D. and Nagler, F., *Flow of Water Around Bends in Pipes.* Transactions of the ASCE, 1935. 100: p. 1018-1043.
21. Shaw, R., *The Influence of Hole Dimensions on Pressure Measurements.* Journal of Fluid Mechanics, 1960. 7(4): p. 550-564.
22. Benedict, R. P., *Fundamentals of Temperature, Pressure and Flow Measurements*. Vol. 3. 1984, New York, New York: John Wiley. 425-491.
23. Holman, J., *Experimental Methods for Engineers*. 1966, New York, New York: McGraw Hill 155-157.
24. Radhakrishnan, M., *Hydraulic Fluids: A Guide to Selection, Test Methods and Use.* 2003.
25. Buckingham, E., *On Physically Similar Systems: Illustrations of the use of Dimensional Equations.* Physical Review, 1914. 4: p. 345-376.

Return to Contents

A test-rig for the characterisation of fast check valves

By A. Plöckinger*, B. Manhartsgruber, and R. Scheidl****

* Linz Center of Mechatronics GmbH
** Johannes Kepler University Linz; Institute of Machine Design and Hydraulic Drives

ABSTRACT

While the measurement of the dynamic properties of a standard spool valve for directional flow control is a well defined task in the fluid power community, the characterisation of check valves is much less clear.

In the first case, the response of the spool position to various inputs like steps or sinusoids is measured. The comparison between the desired spool position (input) and the measured output is shown as a step response plot and/or as a bode diagram in the data sheet. The influence of a flow rate across the metering edges of the valve is often not shown in these figures, yet it is always present due to flow forces acting on the spool. However, the flow forces tend to influence mainly the magnitude of the transfer function between the desired and the actual spool position. The phase lag responsible for stability problems is only marginally affected. Therefore, the interaction between the controlled flow and the spool actuation is often neglected.

In the case of a check valve the situation is completely different. The only forces acting on the flow restricting element are the spring load and the forces exerted by the fluid. While it is in principle possible to measure the movement of the flow restricting element there is no demand signal to compare with.

In the literature the dynamics of check valves is often characterised by the eigenfrequency of the spring-loaded restricting element not taking into account the interaction with the flow. This paper shows that there is a significant influence of the surrounding hydraulic fluid. Furthermore, details on a test rig and a measurement procedure for the dynamic characterisation of check valves are given.

Power Transmission and Motion Control 2006 Edited by Dr D N Johnston and Professor K A Edge

1 NOMENCLATURE

Symbol	Description	Value	Optimized value	Unit
x	position of the plate	-	-	mm
Q_N	nominal flow at a pressure drop Δp_N	30	-	l/min
Δp_N	nominal pressure drop	5	-	bar
F	eigenfrequency of the check valve	417	-	Hz
E	modulus of elasticity	2.1e5	-	N/mm^2
E_{Oil}	modulus of elasticity of fluid	16000	-	bar
ρ	density of the fluid	860	-	kg/m^3
ν	kinematic viscosity of fluid	46	69	mm^2/s
d_{Z1}	diameter of volume Z1	40	-	mm
L_{Z1}	length of volume Z1	100	-	mm
V_{Z1}	volume Z1 (capacity)	130	142	cm^3
d_1	diameter of pipe (inductivity)	12.1	-	mm
$L1$	length of pipe (inductivity)	500	0.6	mm
d_{Z2}	diameter of big volume Z2	125	105	mm
L_{Z2}	length of big volume Z2	0.8	0.75	m
V_{Z2}	volume Z2	9800	6500	cm^3

2 INTRODUCTION

Check valves are relatively simple and cheap devices with numerous applications in fluid power. For most standard applications the dynamic performance of such valves is not significant. Various attempts to find compact and fast check valves at the market for a hydraulic variable valve train (VVT) application, developed at the Linz Center of Competence in Mechatronics (in short LCM), failed. Similar statements have been given by other research groups active in this field. Obviously, the development and the systematic study of fast check valves seemingly has not been an important subject of published research so far. A simple, easy to manufacture, and relatively fast check valve has been developed at LCM for the above mentioned VVT application (see (1)). Such fast check valves are of high relevance also for the realisation of switching techniques ((2), (3)). In such fast switching applications the dynamic response, i.e. the time needed for opening and closing the valve is very important. Due to the usual design concept of check valves it can be expected that the fast opening of the valve is not a difficult issue, because the difference

pressure acts directly on the closing element, a ball, poppet, or a plate. But for valve closing the flow and pressure situation and the resulting closing forces and the resistances by the fluid hindering a fast motion create a much more difficult to analyse situation. If very rapid changes of pressure and flow rate occur at such valves, these simple models fail. The usual models for the behaviour of a check valve are oriented on quasi static processes, i.e., pressure and flow rate changes which are slow compared to some characteristic opening and closing time of the valve.

For active, e.g. switching valves a clear conception exists how to measure an opening and closing time. There is a command signal which can be used to trigger a time-meter and a clear moment of reaching the commanded position. The response can be clearly related to an ideal (the commanded) curve. Different measures of the dynamic performance can be derived from this simple and applicable model.

In case of a check valve the external command signal is missing, it reacts only to its internal hydraulic state, in terms of pressure and flow rate. In the quasi static case, the "internal command" is either the pressure difference at its ports or the flow rate, both being to some extent equivalent. But in case of very fast state changes, for instance if waves are propagating over a valve or high frequent pressure and flow oscillations occur, this equivalence of pressure and flow rate is no more true and no clear "internal command signal" can be defined.

Whenever such universally applicable definitions of a performance characteristics of a technical system or device are missing an experimental test has to be defined. Such tests should be oriented on some preferably simple model of the behaviour of the system.

This paper is reporting about the attempts to find such a model and its experimental realisation.

3 DESIGN AND CHARACTERISTICS OF A SIMPLE CHECK VALVE

The device of interest is a simple check valve (1), conceptually quite similar to the so called `reed valves` used for smaller compressors (see, e.g. (4)). As Figure 1 and Figure 2 show, it consists of a circular plate and an integrated helical spring and its counter piece is a supporting element with one or several bores and a very smooth (e.g., grinded) surface. To avoid a spring overload, also on the opposite side of the supporting element a displacement limiter can be applied. The spring holds the plate in contact with the surface to form a sealing pair in case of a negative pressure but permits a flow if the pressure difference p_A-p_B is positive.

Table 1: Functional requirements and design data of check valve acc. to Figure 1 and Figure 2

Pressure to hold	800 bar	Nominal flow rate at Δp=5 bar	30 l/min
Intended closing time T_C	0.5 ms	Material	spring steel
Disk diameter	10 mm	Plate thickness	0.8 mm
Diameters of 4 feeding bores	3.5 mm	Spring rate of helical spring	3.9 N/mm

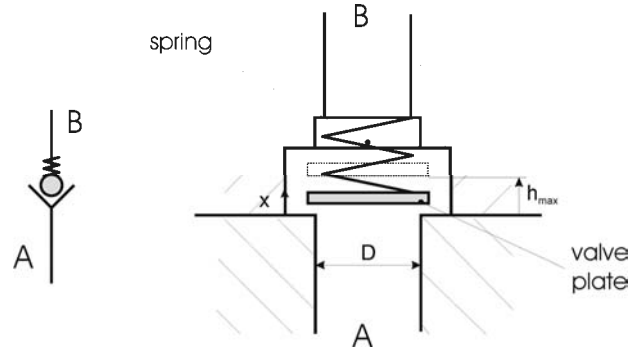

Figure 1: A simple check valve

The valve shown in Figure 2 was conceived for an application with the functional requirements and design data according to Table 1.

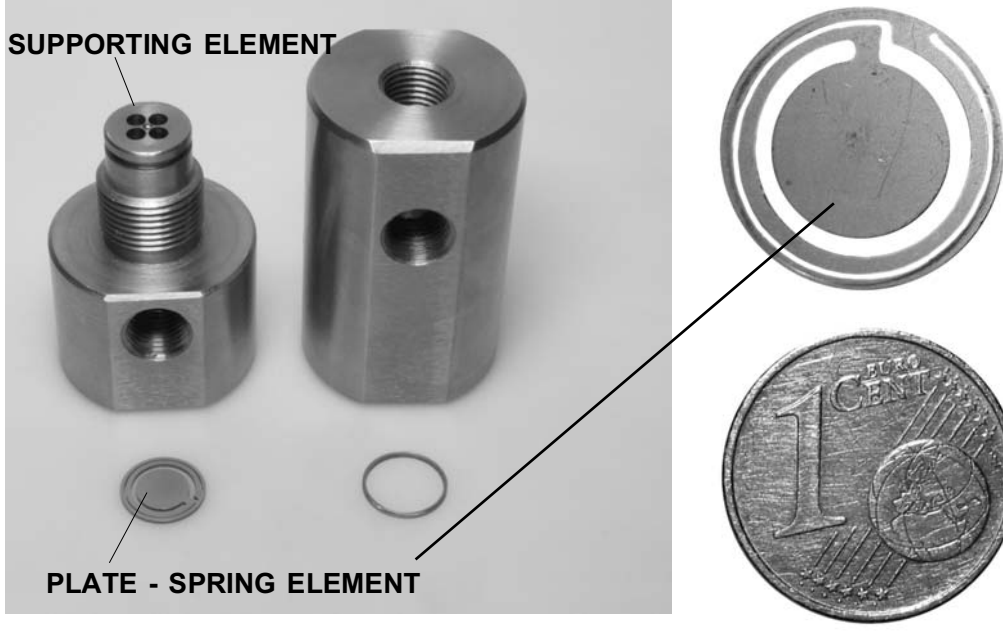

Figure 2: A test device for the check valve

The spring rate was determined such that the natural frequency of oscillation of the plate corresponds to the intended closing time T_S.

The design shown in Figure 2 permits a very cheap manufacturing of the plate spring, it can be laser cut or etched from a metal sheet. Furthermore, its drag characteristics let expect that a fast closing occurs in case of a fast flow reversal.

4 MODEL AND TEST RIG TO CHARCATERISE THE CHECK VALVE'S DYNAMICS

Any measurement of a process must be related to some model understanding of this. The model of the dynamic behaviour of the valve is oriented towards an ideal check valve which opens and particularly closes immediately when the flow reverses or comes to a standstill. In order to get rid of the ambiguity of flow and pressure reversal, the test process should keep these signals in phase. Furthermore, since strongly fluctuating flow rates in hydraulics cannot be measured reasonably today, the test arrangement should also provide an easy way to derive the flow rate from some pressure signals.

There are other approaches which are oriented towards the characterisation of servo valves. The small signal response of servo-valves can be characterised adequately by frequency response curves, because the nonlinearity of those valves is related to the amplitude of the spool's motion. For a check valve such measurements can be made as well. But they can't be significant if a check valve is entering its intrinsic function range, namely to stop a flow in one direction, since this is related to mechanical contact, a hard nonlinearity which destroys the validity of frequency domain based methods. But of course, it is a way to get information on the valve's dynamics off the closed position.

4.1 An ideal test rig to determine a check valve's dynamic response

The circuitry proposed as an ideal test system and the signals of several states in the intended test procedure are sketched in Figure 3. Basically, it is a one degree of freedom hydraulic oscillator formed by an inductivity *(V5)* and a capacity *(Z1)*. To provoke oscillations the system is connected to an (ideal) pressure source p_S and a fast switching valve *V2*. The valve *V2* is kept open until a constant (steady state) flow rate according to the hydraulic resistances has formed and is then closed very rapidly. The inductivity will make the flow to continue for a short while and the pressure in *Z1* will increase in this phase. Also, the check valve – the specimen to be measured – will stay open, at least partially.

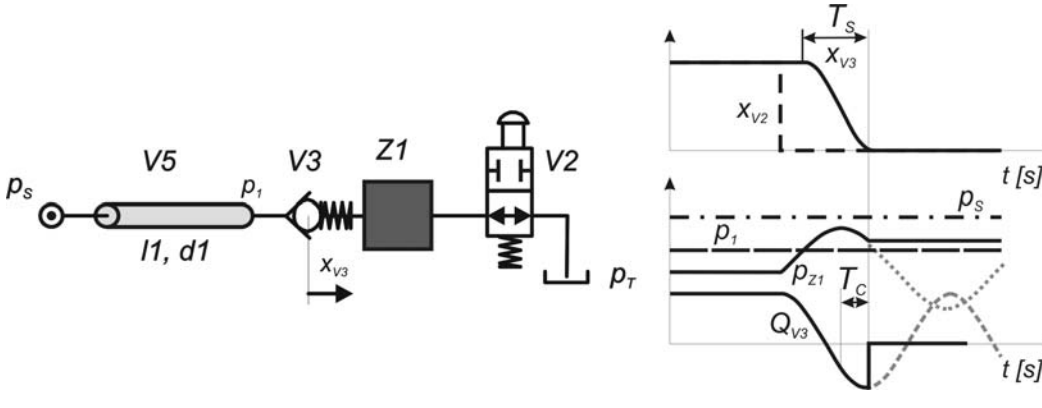

Figure 3: Ideal test rig to measure a check valve's dynamic behaviour

The flow in *V5* comes to a standstill when the pressure in *Z1* reaches it maximum value. Immediately after, the flow reverses. An ideal check valve would prevent that. Any real valve will need some time T_C to close. This time would be a measure of its closing dynamics. Off course, due to the nonlinearity this time will depend on the amount of the steady state flow rate and, may be, also on the frequency of this provoked oscillation. The frequency can be altered by modifying the inductivity of *V5* and/or the capacity of *Z1*. If a certain application with a known characteristic frequency of the flow reversal is on hand, this frequency can be realised in the test rig and the response of the valve could be measured under conditions very close to practice.

4.2 The real test rig and its imperfections

The component hydraulic inductivity was an ordinary pipe of length L_I=800 mm and inner diameter d_I=12 mm. The proper check valve components plate – spring element, supporting element, distance ring, and closing element are shown in Figure 2, its arrangement in Figure 5. The capacity is a tube of diameter d_{ZI}=40 mm and length L_{ZI}=100 mm with a G ¼" adapter for a pressure sensor. The fast switch-off valve was a specially designed and manufactured valve (see Figure 6), comprising the sleeve and spool of a nominal size 10 servo valve, a spring to hold the spool in the open position, a falling mass which is guided in an acrylic glass tube to actuate the valve closing and an inductive position sensor of type POSIC PM0100 to measure the spool position.

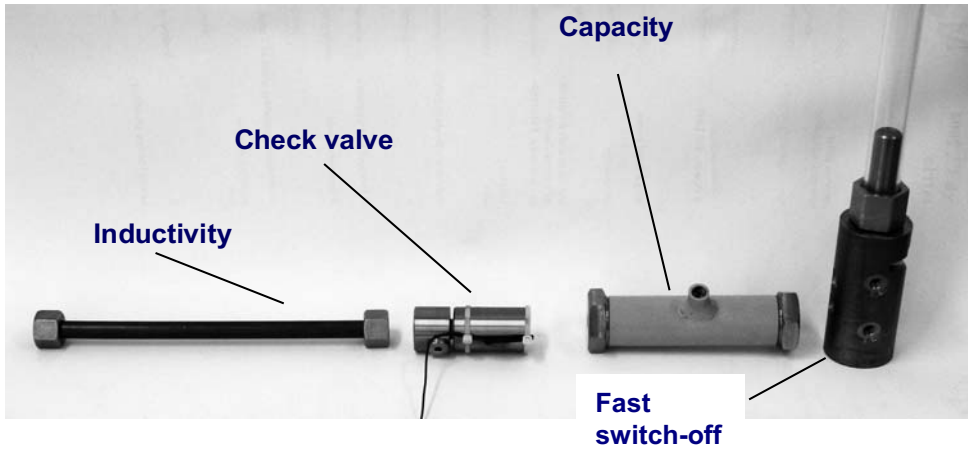

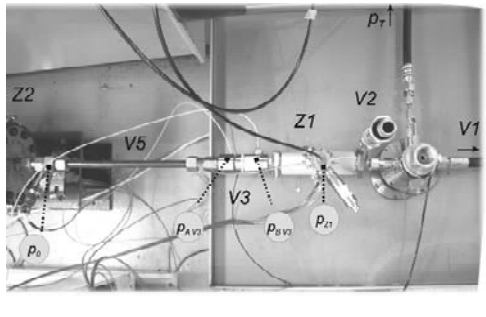

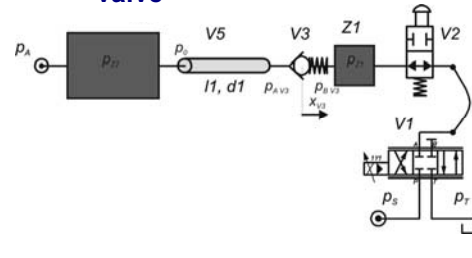

Figure 4: Main components of the test rig (upper picture) and whole arrangement (lower figure and picture)

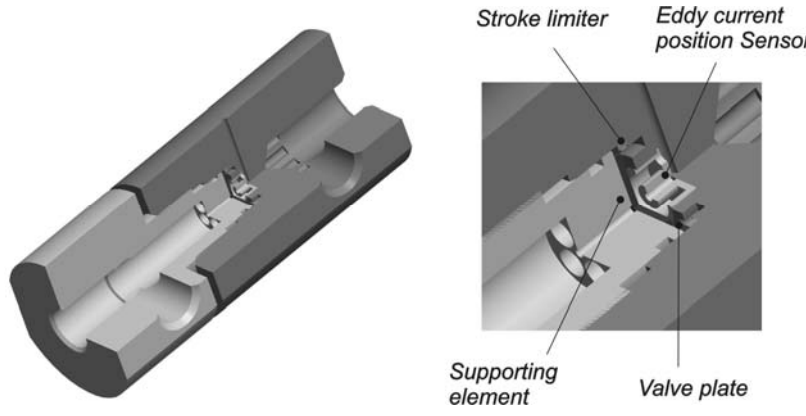

Figure 5: The check valve device

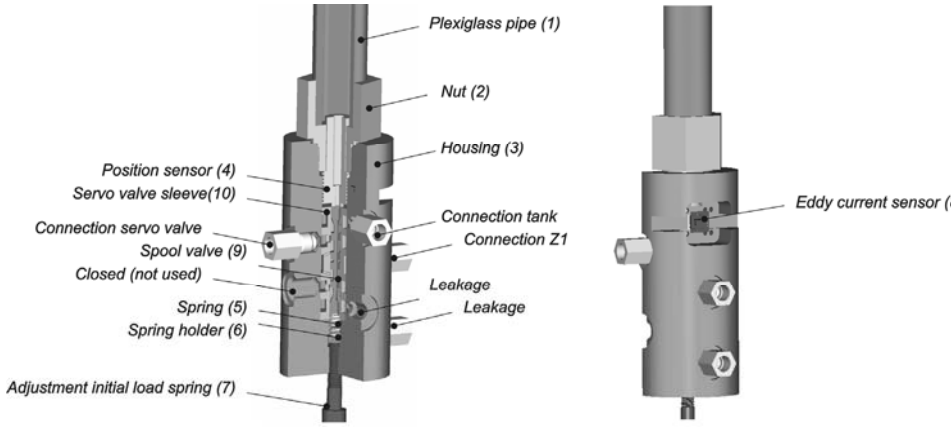

Figure 6: The fast switch-off valve

With this valve a shut-off time of 0.3 ms could be achieved. A servo valve between switch-off valve and tank to enhance the adjustment of the steady state flow rate and a large cavity, realised as a large tube (length L_{Z2}=800 mm, diameter d_{Z2}=125 mm) to mimic a constant pressure source, have been added.

First measurement results as given by Figure 7 show that the test rig does not have this idealised and wanted properties of a simple hydraulic oscillator, but that quite complex wave propagation phenomena are disturbing the expected simple picture. Neither does the pressure p_{Z1} in the capacity show up the truncated sinusoidal curve nor do the difference pressure $\Delta p_{AB} = p_{AV3} - p_{BV3}$ over the check valve and the entrance pressure p_A correlate with the expectations. The test rig's imperfections are resulting mainly from several parasitic inductivities that are due to the diverse connections and – regarding the big tube – its finite (and not zero) length.

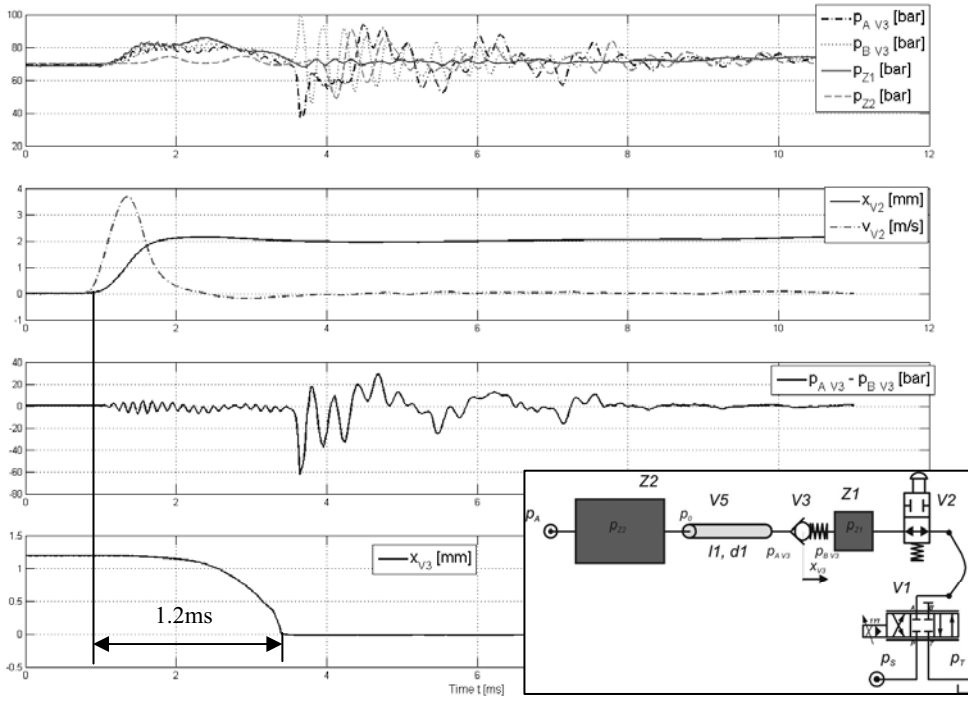

Figure 7: First measurement results indicating complex wave propagation phenomena occurring in the system

Basically, there are two different ways out of the dilemma: (i) to improve the test rig, which in this case only would be feasible with much higher expenses, because all the components needed to be re-designed and re-manufactured to get rid of these inductivities, or (ii) to adapt the model to the test rig as built.

The authors decided to adapt the model, since a test rig improvement which comes very close to the ideal situation would have been too costly and, furthermore, the success not reliably predictable.

5 A REFINED MODEL OF THE WAVE PROCESSES

To obtain a good model of the system, a series of measurements and an identification procedure have been carried out. Components with a certain extension in length (the components *Z2* and *V5* in Figure 8) have been modelled by pipe elements. It was a result of the identification procedure that, in contrast to the original intentions, also the large tube (component *Z2*) had to be modelled as such. Furthermore, some parasitic inductivities and throttles had to be added. The final model structure is depicted in Figure 9.

For the identification frequency domain methods have been applied. For wave propagation modelling in the identification procedure the well known frequency transfer function of a circular tube with a parallel flow, as developed in (5), has been applied.

The correspondence between simulation and experiment in terms of frequency response curves for the original parameter values and for those after the parameter identification process are shown in Figure 10 and Figure 11.The parameter values prior to and after identification are listed in the nomenclature table at the beginning of the paper.

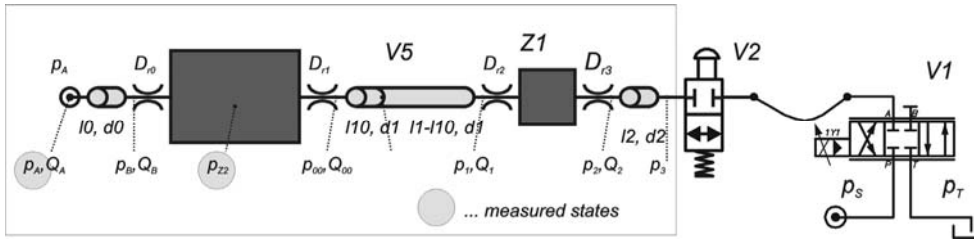

Figure 8: Starting model structure of the test rig

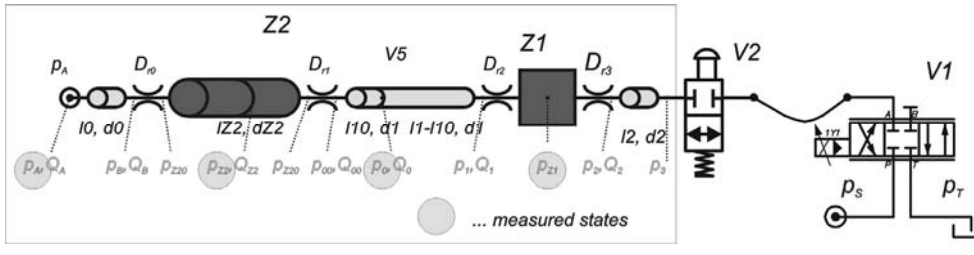

Figure 9: Final model structure of the test rig

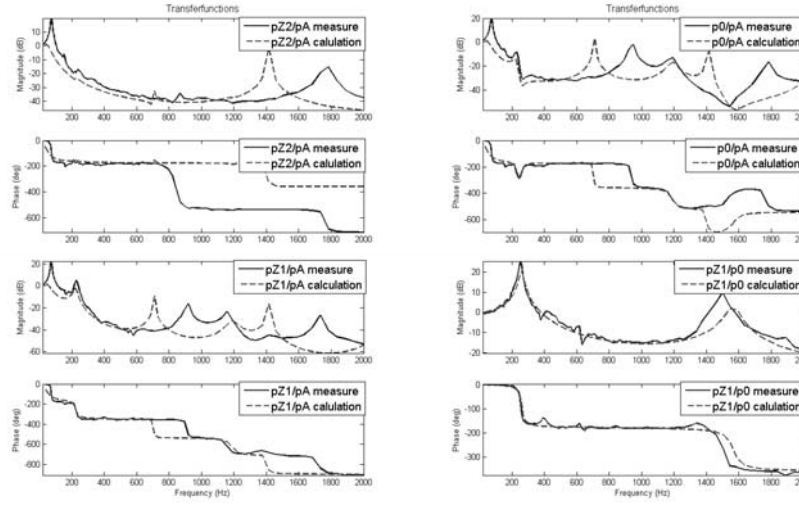

Figure 10: Measured and computed frequency response curves for the test rig prior to parameter identification

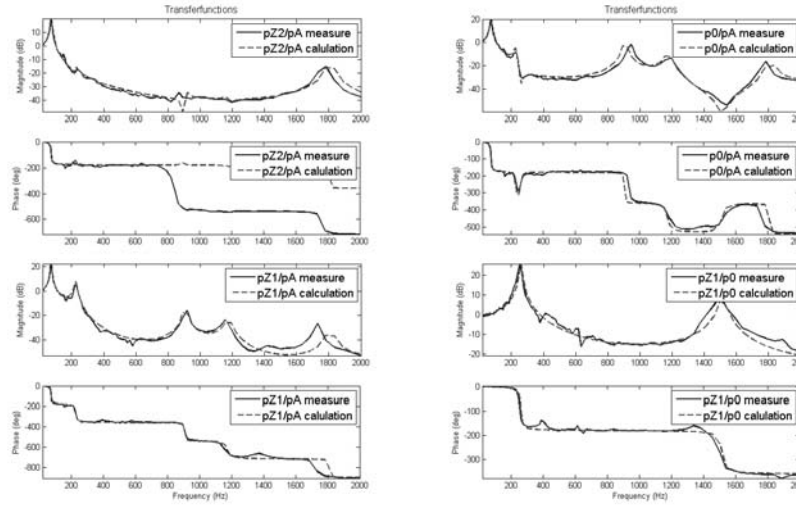

Figure 11: Measured and computed frequency response curves for the test rig after parameter identification

6 RESULTS

Since a check valve is a nonlinear element, time domain modelling and simulation is required. Wave propagation in the two elements Z2 and V5 was modelled by the methods of characteristics, applying a Zielke-Suzuki model ((6), (7)). A model in Matlab/Simulink with a charateristic time step of T=1.4e-005 s was used.

The identified model allows to compute also the flow rates at different nodes of the hydraulic system. With this computed flow rate at the end of the pipe V5 the flow rate passing the check valve and with it the dynamical behaviour of the check valve can be identified.

The series of measurements shown in Figure12 correspond to different steady state flow rates. The time span between the sign reversal of the flow rate at the check valve and the sudden stop of this flow is the characteristic closing time T_C. The fact that the sudden breakdown of the flow over the check valve and the opening distance of the plate-spring element coincide confirms the validity of the evaluation procedure and the simulation, respectively.

The closing time T_C does not depend strongly on the steady state flow rate and was found to be approximately 0.6 ms. This value is in good agreement with a quarter of the computed oscillation period of the first oscillation mode of the free plate spring element (not affected by the hydraulic fluid or contacting element), computed with a Finite Element model, which was found to be 0.603 ms ($Tc=1/(4\,f)$).

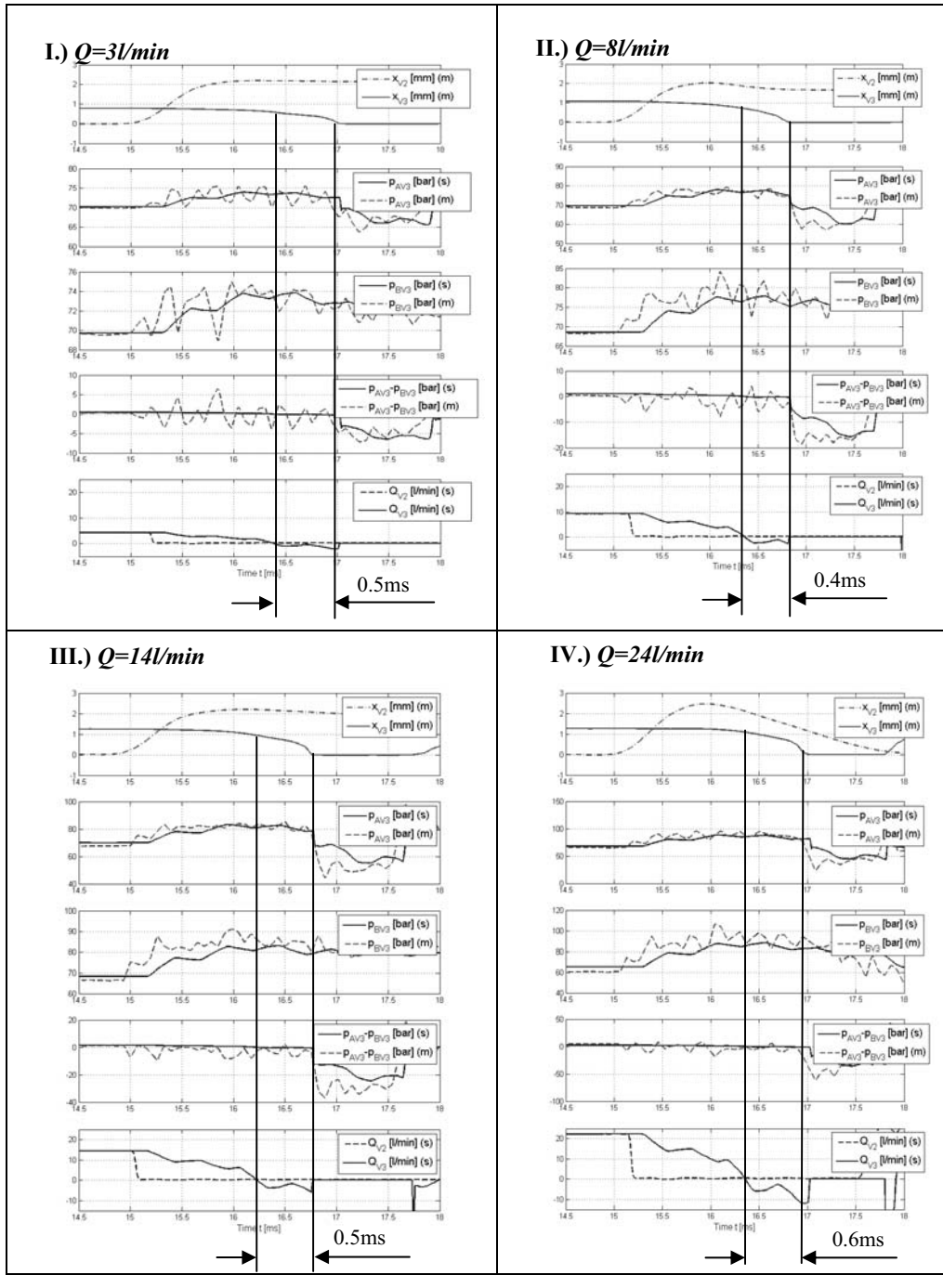

Figure 12: Measured (m) and computed (s) pressure signals and computed flow rates of a series of experiments to identify the dynamical behaviour of a check valve

7 SUMMARY AND OUTLOOK

The measurement of a check valve's dynamical behaviour under fast changes of flow rate and pressures is a difficult task. The intention to get the information without knowing the flow over the check valve failed. By using a rather complex simulation model and a sound work in parameter identification a good agreement between the predicted and measured dynamics of the check valve could be achieved.

The check valve is already successfully used for the VVT application and will be one of our key elements in the realisation of switching techniques ((2), (3)).

ACKNOWLEDGEMENT

The authors gratefully acknowledge the sponsoring of this work by the 'Linz Center of Competence in Mechatronics' in the framework of the K*plus* program of the Austrian government. This program is funded by the Austrian government, the province of Upper Austria and the Johannes Kepler University Linz.

REFERENCES

(1) Plöckinger, A., Development and Laboratory Tests of a Cheap, Robust, and Fast Check Valve for Industrial Applications, Proc. Ninth Scandinavian International Conference on Fluid Power (SICFP'05) - Extended Abstract, June 1-3, 2005, Linköping, Sweden.

(2) Scheidl, R. , Manhartsgruber, B., Kogler, H., Hydraulic Switching Control with a Nonlinear Converter, Proc. Mathmod 2006, February 8-10, 2006, Vienna; publisehd in I. Troch, F. Breitenecker (Eds.:); Series ARGESIM Reports, ISBN 3-901608-30-3; ARGESIM Report no. 30.

(3) Scheidl, R., Manhartsgruber, B. Mikota, G., Winkler, B., State of the Art in Hydraulic Switching Control – Components, Systems, Applications, Proc. Ninth Scandinavian International Conference on Fluid Power (SICFP'05) - Extended Abstract, June 1-3, 2005, Linköping, Sweden.

(4) Hoerbiger Kompressortechnik Internet product information: http://www.hoerbigerkompressortechnik.de/index_e.html (March, 8th, 2006).

(5) D'Souza, A., Oldenburger, R., Dynamic Response of Fluid Lines, Trans. ASME, Journal Basic Engng, 86 (1964), pp. 589-598.

(6) Zielke W., Frequency-Dependent Friction in Transient Pipe Flow, Trans. ASME, Journal Basic Engng., 90 (1968), pp. 109-115.

(7) Suzuki, K., Toketomi, T., Sato, S., Improving Zilke's Method of Simulating Frequency Dependent Friction in Laminar Liquid Pipe Flow, Trans ASME, Journal of Fluids Engineering 113(4), pp. 567-573, 1991.

TEST METHODS FOR FLOW SHARING DIRECTIONAL VALVES

P. Marani1, G. Ansaloni[1], R. Paoluzzi[1], A. Fornaciari[2]
[1]Imamoter C.N.R., Via Canal Bianco, 28 – 44044 Cassana-Ferrara - Italy
[2]Walvoil S.p.A., Via Adige 13/d, 42100 Reggio Emilia - Italy

ABSTRACT

This paper presents the results of a study regarding procedures to qualify Load Sensing Flow Sharing (LSFS) distributors especially under dynamic conditions. In spite of their popularity, as they enhance control of loads solving problems of interference even in saturated pump condition, no normative reference exists addressing the performance of LSFS systems.

For this reason, a set of test methods aimed at evaluating and comparing the different solutions available have been developed. These methods can be classified according to the type of load, imposed by valves or by actuators. In the first case the loads are predominantly dissipative, in the second case the inertial component is predominant. The test method proposed allows the evaluation of the system dynamic behaviour according to response time, undershoot and overshoot of physical variables.

The first test with valves is a sudden pressure variation on one out of two active sections. The objective is to evaluate the behaviour of the device when the generation of the LS signal switches from one section to another.

The second test with valves is the rapid actuation of a section. It evaluates the behaviour of the system with sudden variations of flow rate. This test it is intended to induce a transition between saturation and non-saturation.

The tests with inertial loads consist in the actuation of spools in order to study the control of purely inertial loads as they can induce dynamic instability of LSFS systems and affect their performance.

The paper presents the proposed testing procedure together with a set of experimental data on their application.

Power Transmission and Motion Control 2006 Edited by Dr D N Johnston and Professor K A Edge

1. NOMENCLATURE

P_u	load pressure	[bar]
p_{LS}	load sensing pilot pressure	[bar]
p_p	pump delivery pressure	[bar]
Δ	differential pressure	[bar]
Q	volume flow rate	[l/min]
A	orifice area	[mm^2]

2. INTRODUCTION

One of the major drawbacks of traditional load sensing (LS) circuits, both in their pressure compensated or simple version, is their inability to cope efficiently with an overall flow demand exceeding the maximum flow capability of the pumping unit. This condition is usually referred to as flow saturation.

Flow Sharing Load Sensing distributors have been introduced in order to limit the problems due to uncontrolled movements in flow saturation, when multiple sections are actuated at the same time. According to a generally accepted principle, all the flow rates in active sections are kept constant at the value occurring when the saturation condition is reached. This condition is usually recognized by the drop in ability to keep the LS pilot pressure at its required value.

Two main strategies can be identified in the implementation of the flow sharing (FS) principle, and they can be classified according to the position of the local compensator with respect to the main valve[1]:

- Upstream compensation
- Downstream compensation

Circuits belonging to the former class may be considered as adaptations of the general principle depicted in Figure 1, based on normally open compensators with two pilot pressure ports. Circuits belonging to the latter class are adaptations of the schematic of Figure 2, based on normally closed compensators with four pilot ports.

1. Actually, other classifications may be proposed, for example according to the handling strategy for the load sensing pressure signal, but they can be relevant only for the analysis of special arrangements which may be found in several patents on the topic.

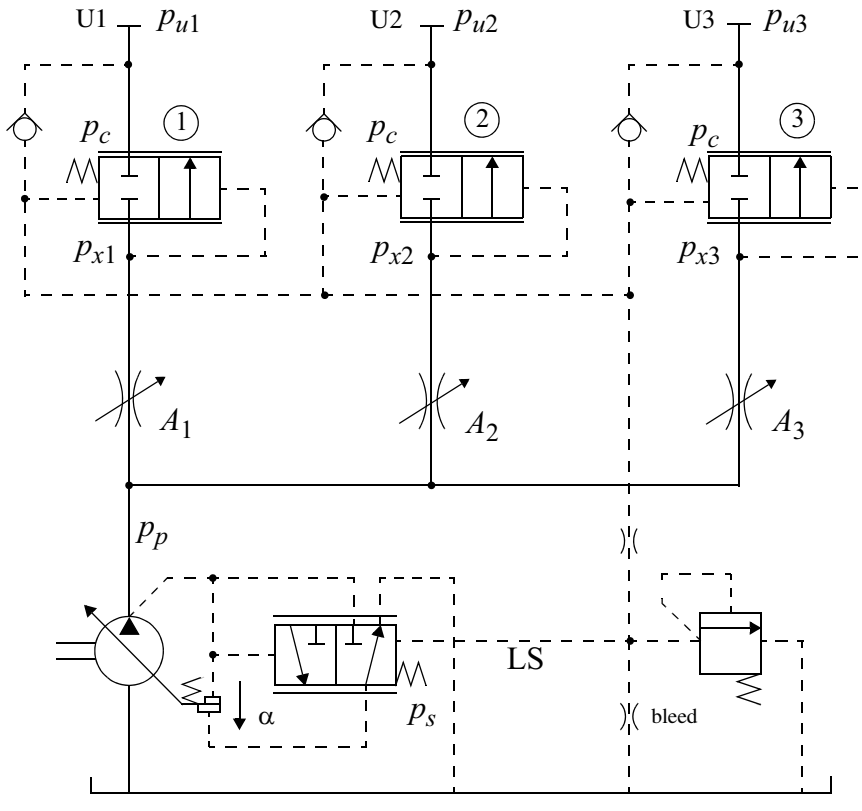

Figure 1: General schematics of downstream FSLS system

Referring to the circuit of Figure 2[1], the LS operation is simply understood supposing that two sections are actuated at the same time, with different load pressures. Assuming that U1 pressure is lower than U2, the local equilibrium of the compensator is given by:

$$p_p - p_{LS} = p_x - p_u$$

Where p_p is the pump delivery pressure, p_{LS} the load sensing pilot pressure, p_x the pressure in the connection line between valve and local compensator, and p_u the local load pressure.

The pressure drop across the distributor (main valve plus compensator) is therefore given by:

$$\Delta = p_p - p_{LS}$$

1. The procedure does not change taking into consideration the upstream architecture instead.

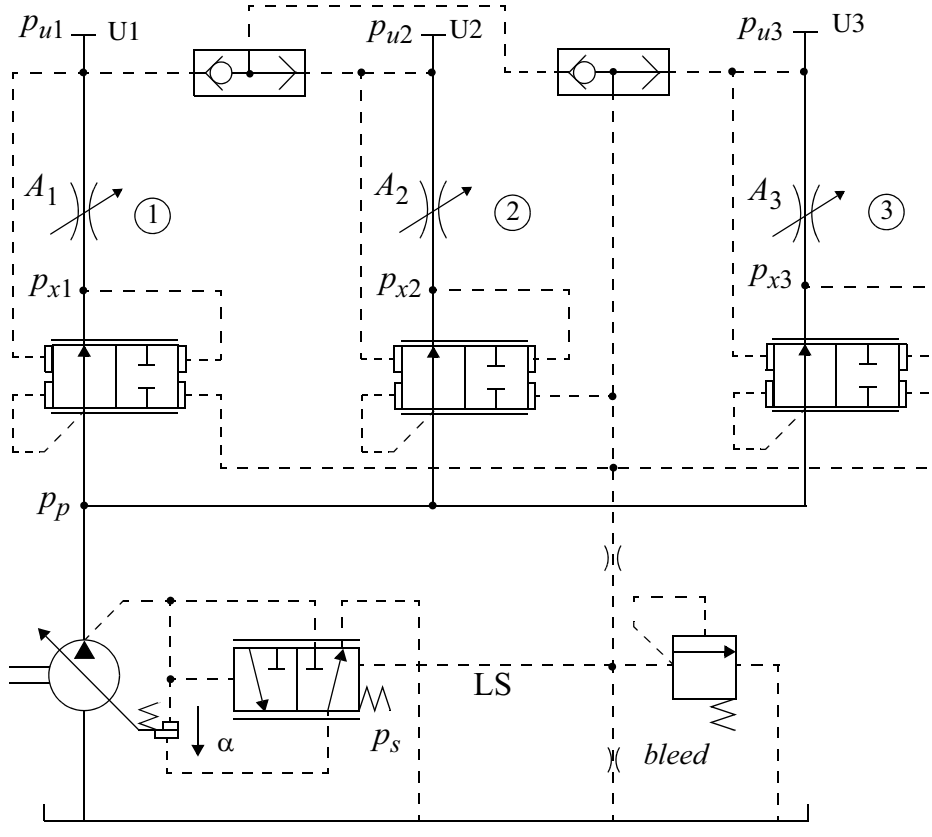

Figure 2: General schematics of upstream FSLS systems

This means that the pressure drop, and therefore local flow rate, is a function of the main spool position, according to the general LS principle. This situation does not change if the actuated sections are more than two and, much more important, is such that if the LS pressure signal drops due to the occurrence of the flow saturation conditions, all the compensators tend to close at the same time, thus reducing the flow rate across each section, overriding the external demand, in order to keep the ratio of the flow rate across different sections constant. This last feature is usually referred to as "flow sharing" to highlight the sharing of the available flow rate that occurs when saturation is reached.

Although many commercial products exist on the market which apply this principle [1,2,3,4], no common procedure exist in order to assess their performance and compare their ability to compensate for the occurrence of saturation conditions.

The main purpose of this contribution is to propose an experimental procedure as a potential candidate to the comparative evaluation of performance, showing a first set of experimental and simulation results on its practical application.

3. FLOW-SHARING ARCHITECTURES

Many different architectures exist implementing the general principle of flow-sharing, but the majority of them can be classified observing the position of the local compensators with respect to the main directional valve spool. According to this classification, the downstream architecture can be identified with the general schematics of Figure 1, where the main spool is simply identified by a variable orifice. As it can be easily seen, downstream compensation simply relies on the comparison of two pilot pressures.

Upstream compensation features a more complex pilot signal comparison, and can be referred to the schematic of Figure 2. Four pilot pressures are handled by the local compensators in order to implement the requested action.

It can be easily shown that both circuits apply the general load sensing compensation when a single section is actuated, perform local compensation on the section having the lower load in case of multiple actuation, and apply a proportional reduction of the flow on all sections when flow saturation occur.

A more detailed classification may be attempted through a search among the wealth of patents produced during recent years. For instance in [5] more than 120 different patents have been reviewed and classified according to a principle identifying three more categories, according to the generation and handling of the LS signal.

4. STEADY-STATE CHARACTERISTIC

A FSLS system must be able to react to flow saturation, but must also be able to act as a conventional LS system when multiple actuations, but no saturation, exist. A first test must therefore check the precision of the implementation of the LS principle in non-saturated conditions.

The LS principle basically means that the flow rate supplied by one section depends only on the position of the spool in the main valve, being insensitive to both local load pressure and load pressure on other sections (interference).

The experimental evaluation of this feature implies at least the use of two sections, according to the simplified circuit of Figure 3. The LS compensator of pump 2 is not detailed for the sake of simplicity. The pump is driven at constant speed by an electric motor 1, and safe pressure limits are imposed by a relief valve 3. Two pilot relief valve (4 and 5) impose the load pressure independently on the two sections. Pressures and flow rate values are measured where relevant.

A first trivial set of tests (not reported here) is the ability of the system to keep the flow rate constant on a single section when the load is varied, this was done in the experimental characterization at five distinct valve positions (flow rate values) imposing a ramp increase

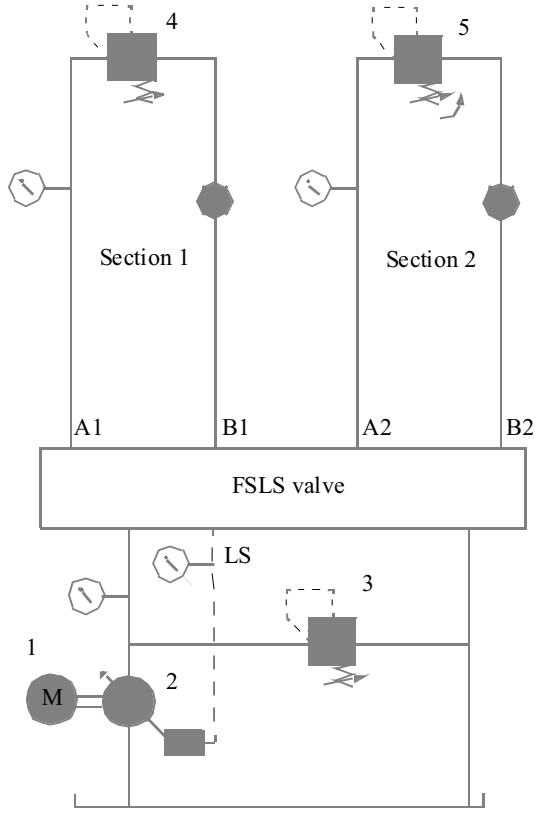

Figure 3: Simplified circuit for interference test

of the load pressure starting from the stand-by value up to the nominal pressure (safely below the setting of valve 3).

A more interesting test involves the ability of the system to perform local compensation, therefore implementing the ideal characteristic depicted in Figure 4.

With a constant load pressure on section 2, the load pressure of section one is ramped from stand-by pressure value to its maximum, forcing the dominant section 2 to become a dependant section when the section generating the LS signal switches from 2 to 1. The flow rate across the two sections should not be affected by this pressure switching. This test was performed at two different constant pressure levels (30 and 100 bar) and two positions for each active section.

A complete characterization of a multiple section distributor would imply the testing, in groups of two, of all possible combinations of sections having different area functions, in order to assess the performance of the local compensator.

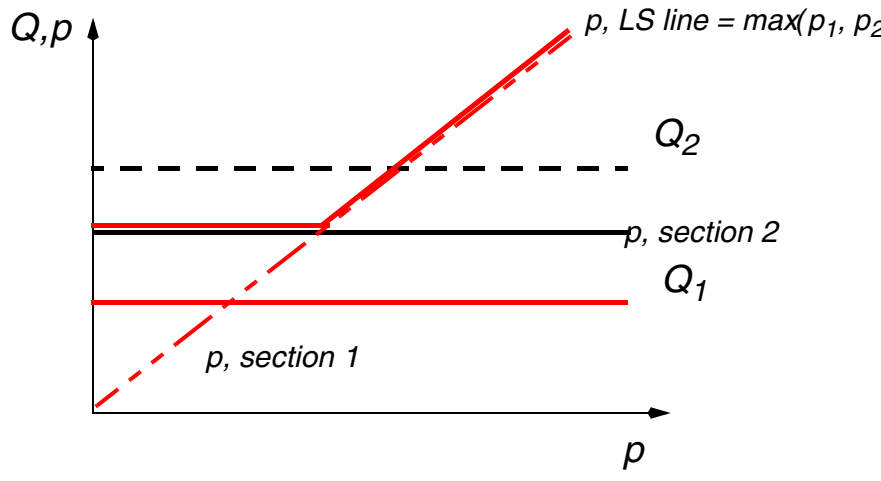

Figure 4: Ideal response to ramp increase of load pressure

A typical example of the experimental curves obtained with this test is shown in Figure 5, where the similitude with the ideal response is clearly evident.

The main figures of merit in this characterization are the step in flow values when the switching between LS signal generation occurs (value A in Figure 5) and the maximum flow rate variation during the test (value B in Figure 5).

The flow saturation may be induced by two distinct cases:

1. a user action on the distributor requesting a flow whose summation is higher than the maximum flow supplied by the pump;

2. a reduction of the flow delivered by the pump at constant flow demand (spool position) by the user.

The former is more frequent in practice, the latter is more suitable for laboratory testing, where the test may be carried out at a fixed spool position and load pressure, progressively reducing the flow supplied by the pump to induce flow saturation ideally until the zero flow conditions. The ideal characteristic to be expected during this test is presented in Figure 6.

The practical results of this test are shown in Figure 7. Two aspects must be noticed in the comment to these results:

1. they have been recorded without bleed flow (the relevant port in the tested distributor was capped);

2. the characteristic was insensitive to the switch between dominant section.

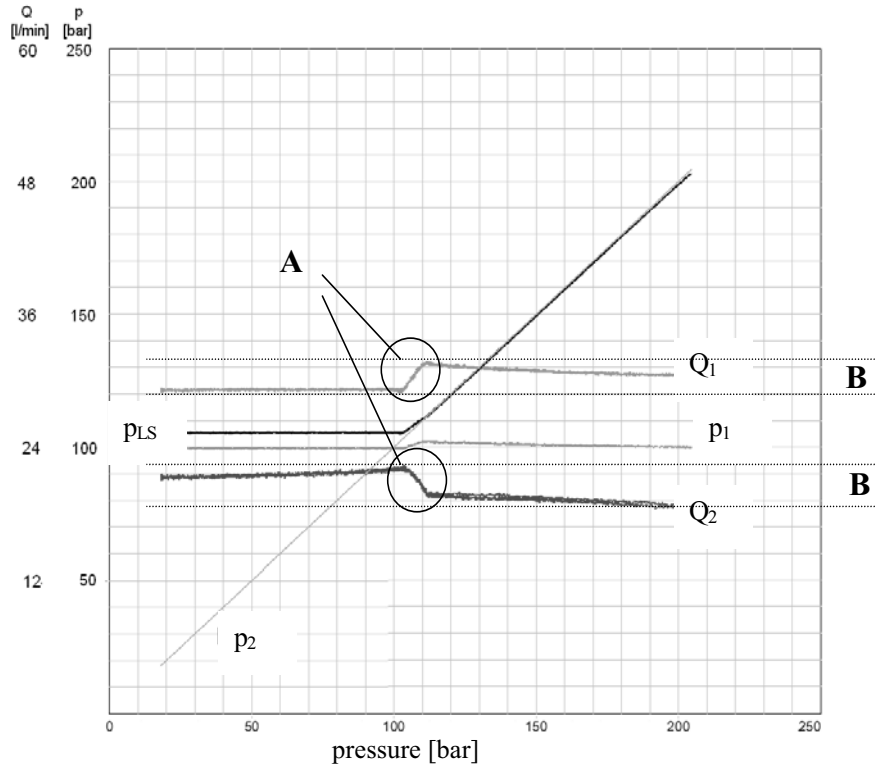

Figure 5: Example of experimental results of a ramp load in section 2

The increase in the value of the LS line pressure was due to the load characteristic of the relief valve used to simulate the load pressure (blue lines). As it can be seen the experimental characteristics shows all the relevant features of the ideal behaviour, i.e. a proportional decrease of flow across sections as the saturation condition evolves (red and green line), and the progressive drop of the pressure differential generated in the LS line (orange line).

It is worth noting that the introduction of the bleed in the LS pilot line has the effect of introducing an error in the characteristics, and the flow curves do not pass through the origin of the diagram (Figure 8).

The effect is extremely significant at very low values of the available flow rate, where the simultaneous actuation may be unacceptably compromised.

As to the practical effects of this feature, it must be noted that they have little chances to occur in practice, especially in the case of coupling with a fixed displacement pump, because the rotational speed of the internal combustion engine providing the driving torque in this

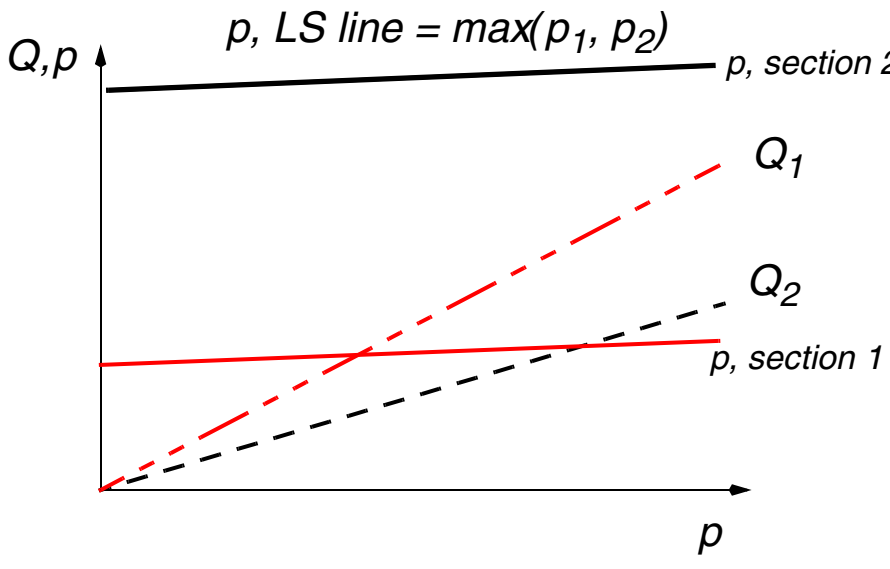

Figure 6: Ideal characteristic of the induced saturation test

case would be below the lower limit setting. The figure has therefore much more the meaning of a limit behaviour against the ideal case than an actual performance indicator.

5. DYNAMIC CHARACTERISTIC

Apart from the traditional characterization of the dynamic response of a single section to external actuation, such as a step change in load pressure or a ramp in main spool position, the main feature of a FSLS valve is its ability to cope with the conditions where the section generating the LS pressure signal switches due to the variation in external loads. This condition frequently happens for instance in the combined work cycle of an earthmoving machine. During this transient, called "switching upon actuators", the compensators exchange their role in the generation of the LS pressure signal, and during the transient uncontrolled movements and unexpected transients may occur. The qualification of the system may be based upon the time needed to reach the new stable configuration when a step change in load forces the switching between the role played by two different sections.

The test circuit needed for this purpose may be derived from the circuit explained in Figure 3, and is represented in Figure 9.

The role of driving the load change is played by valves 4a and 4b, according to the position of valve 5, which was positioned downstream of the relief valves in order to reduce the influence of its overlap on the transient response. All the measurement points used in the test rig are evidenced by the transducer symbols on the diagram. In the test the two valves 4a and

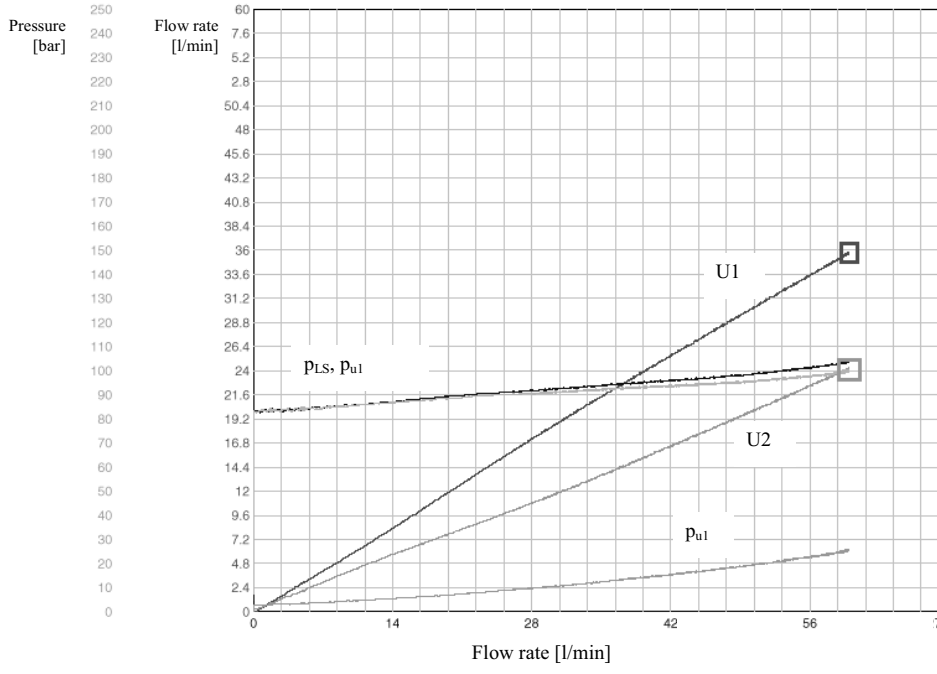

Figure 7: Induced saturation test, bleed orifice capped.

4b were set at pressure values respectively of 180 and 50 bar, with valve 6 set at 100 bar. The action on valve 5 forces the first section to switch from dominant to dependant and vice-versa. The test may be carried out in both normal and saturated flow conditions at different (fixed) spool positions in the actuated sections.

Figure 10 shows a typical result of the test in non-saturated conditions (saturated condition behaviour is similar) with two sections actuated with an increase in the load (section 1 switches from dependant to dominant).

The sequence is clearly identified by the time values from t_0 to t_3. At time t_0 the starting point is with section 1 at a lower pressure and the LS pilot pressure is generated by section 2. When valve 5 of Figure 9 switches, the flow rate across section 1 starts decreasing according to its need to increase its pressure to the new value (180 bar). At time t_1 the pressure on section 1 becomes higher than section 2, and the system must switch; the load pressure on section 1 equals the pump delivery pressure, therefore the flow to section 1 drops to zero (stall of the actuator). This phase lasts slightly less than 0.05 s.

At time t_2 the load pressure on section 1 and pump delivery pressure decouples, and the flow to the first actuator returns increasingly positive until to time t_3 where the nominal pressure

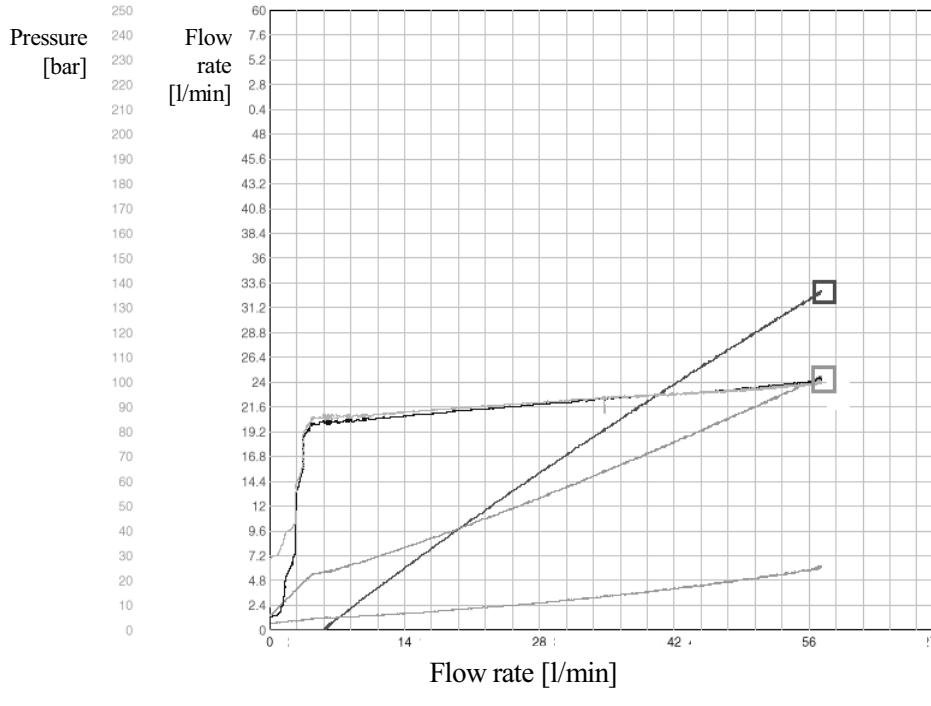

Figure 8: Induced saturation test, bleed orifice effect.

drop across the section is restored. It is worth noting that section 2 during the transient experiences some variations in its value, due to the effect of the pressure changes on the local compensator equilibrium.

The switch back to the initial condition generates a simpler transient, which is reported in Figure 11.

Its characterization requires the use of just two time values and there is no drop to zero of available flow rate to the actuators, although the cross effect on section 2 is amplified.

A further dynamic characterization can be identified in the reaction of the system to a fast actuation on one section when two other sections are in steady state operation (typical situation occurring in the swing-and-dump operation of a hydraulic excavator). The boxcar input to the spool position of the third section may additionally induce the system to enter the flow saturation condition. The result of a test reproducing these conditions is reported in Figure 12.

When the third section (numbered 3 in figure) is actuated (at higher load) it causes the LS line to pressurize, and the system enters saturated conditions. The local compensators of the

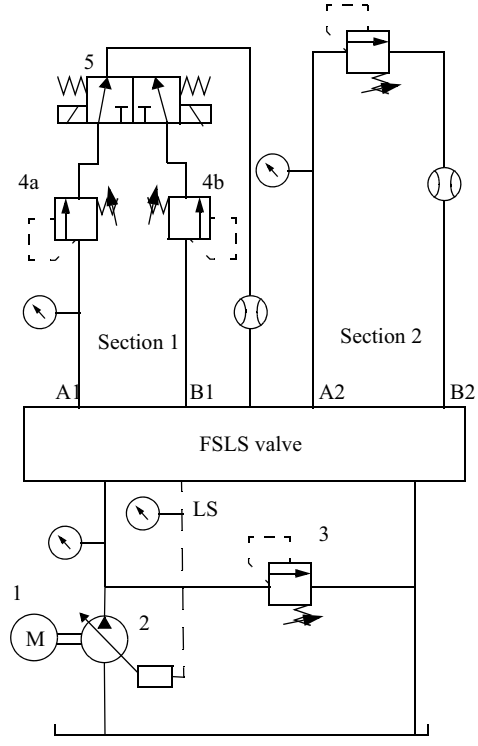

Figure 9: circuit layout in the switching test

two active sections need to adapt to the new load conditions, with a strong interaction with the third section, whose net flow drops to zero. When the LS line is fully pressurized, the local compensators find their equilibrium position, which, according to the general features of the flow sharing device, maintain the relative value of the flow in the two unactuated sections unchanged, but with lower absolute values. The full transient lasts 0.15 s, but it is worth noting that this figure is significantly affected by the intrinsic response of the flow supply circuit, whose characteristics are impossible to decouple from the local distributor characteristics, confirming the need for a close tuning of the FSLS distributor against the supply circuit in order to improve the system overall performance. The transient when the third actuation is removed is definitely simpler. The system now leaves the saturated condition and turns back to traditional behaviour in 0.1 s with the only remarkable feature of a transient peak in LS pressure when the third section spool closes.

6. DYNAMIC SIMULATION

In order to check the possibility of the use of the proposed qualification process within the main stream of product development, it was also decided to carry out a parallel program of dynamic simulation with three major objectives:

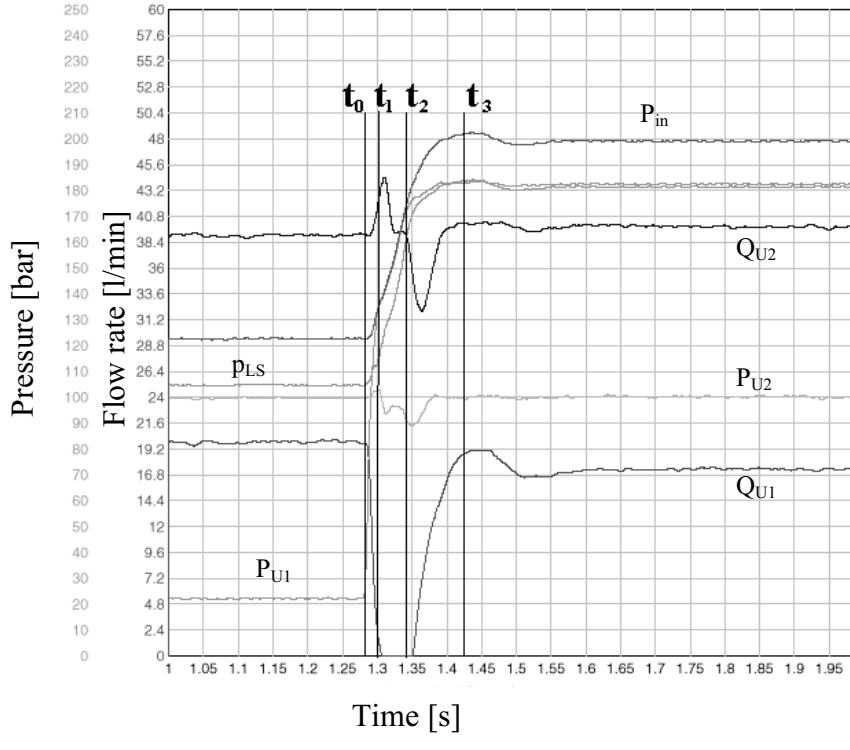

Figure 10: Experimental results in the switching test

1. to compare the test bench results with the simulation in order to tune the mathematical model and to validate its results;

2. to provide a virtual testing environment where the set of boundary conditions and design parameters can be easily changed;

3. to develop a design environment able to assist the designer in assessing the mutual compatibility of the distributor architecture with different practical applications.

The simulation environment chosen was AMEsim v 4.1.3, as it was the simulation environment already used inside Walvoil. All the components used to simulate the system belong to the standard program libraries [8], but an extensive use of a combination of elementary components was necessary to construct the needed system architecture.

A partial view of the simulation model, together with the equivalent hydraulic circuit of the tested FSLS valve is shown in Figure 13. the use of basic library elements is evident. The compensator was modelled taking into account its dynamics; conversely the main valve was

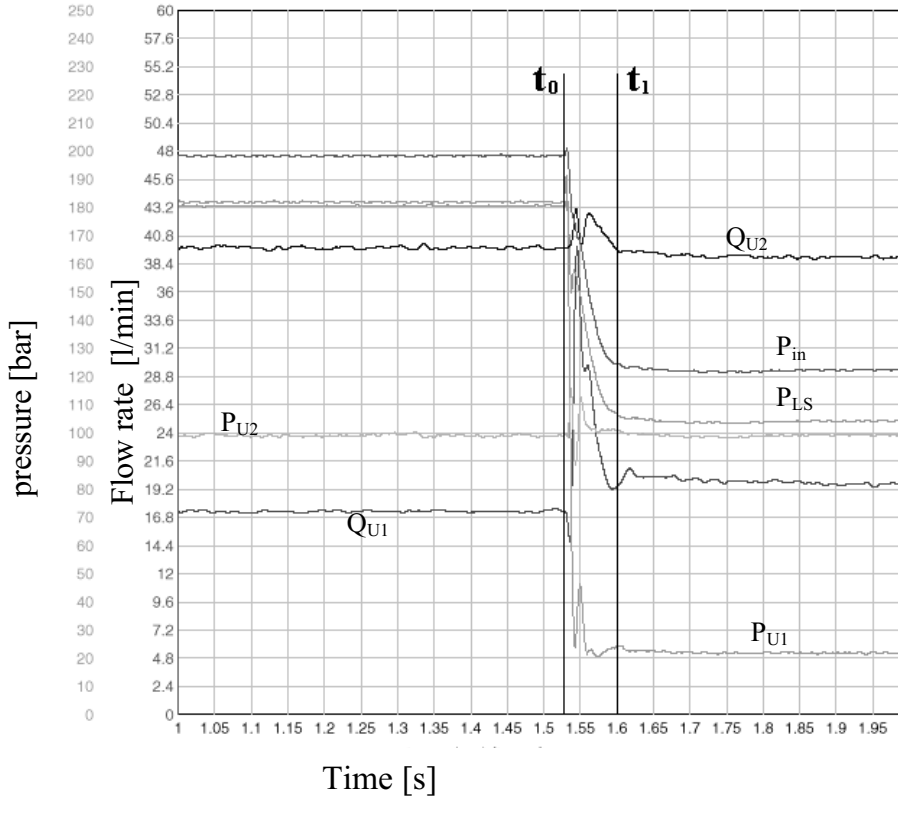

Figure 11: Experimental results in the switch back test

modelled simply as a network of variable orifices, whose area is described by interpolating actual metering area data.

Among the extremely large set of data collected, Figure 14 shows the results of a simulation resembling the “switching upon actuators” test already presented in Figures 9 and 10.

The similitude between the responses shown in Figures 12 and 14 are evident, and especially the definition and comparison of the time sequence already described is fully applicable to this numerical characterization and gives results which support the full qualification of the simulation model.

7. EFFECT OF INERTIA LOAD

As generally recognized, inertia loads are the most challenging environment to test the performance of hydraulic control valves. This is due to the strong interaction with the circuit

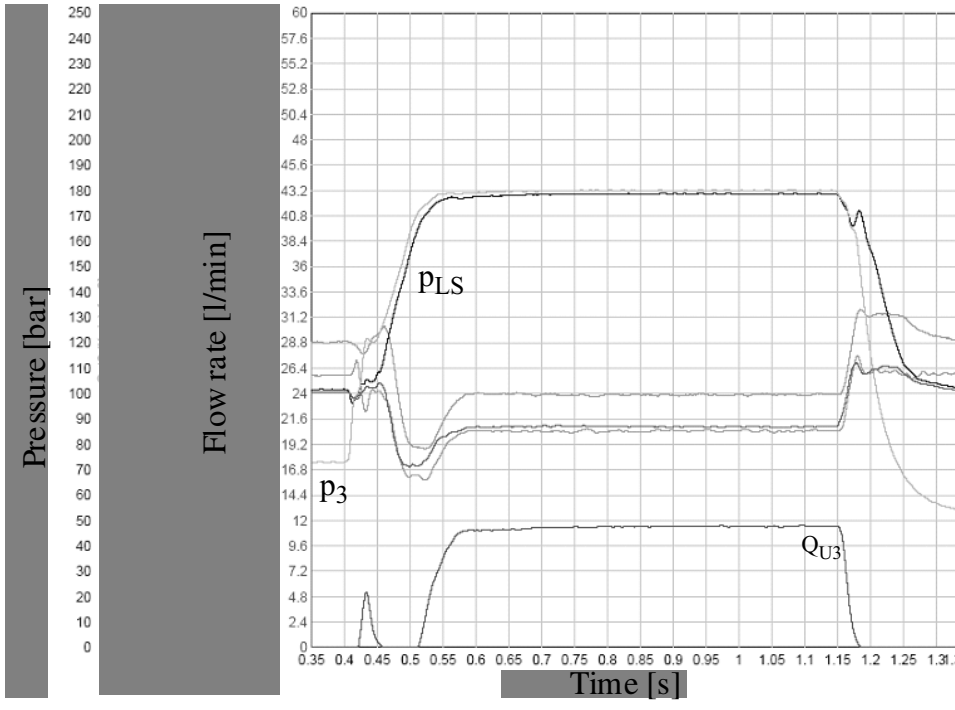

Figure 12: Experimental result of three sections test

dynamics and to the sign change of the load characteristic during transients. Inertia loads are especially relevant to the main target application of FSLS valves in mobile earthmoving, agricultural and construction equipment.

The effect of inertia loads can be tackled either with physical tests on a real machine, with tests on a test rig able to introduce inertia effects or by simulation. The third option can be easily accomplished once a simulation model is available, and the first one is made difficult by the need to tailor the devices to individual machine needs. General trends can be derived by physical experiments only using the second option.

To this purpose a test rig was designed and built in order to induce and evaluate inertia effects on FSLS valves.

The test rig is composed of (Figure 15):

- a supply circuit with a power of 30 kW, driven by one electrical motor connected to a LS variable displacement pump;
- a service circuit driven by a 12 kW electric motor to supply remote commands and cooling circuit;

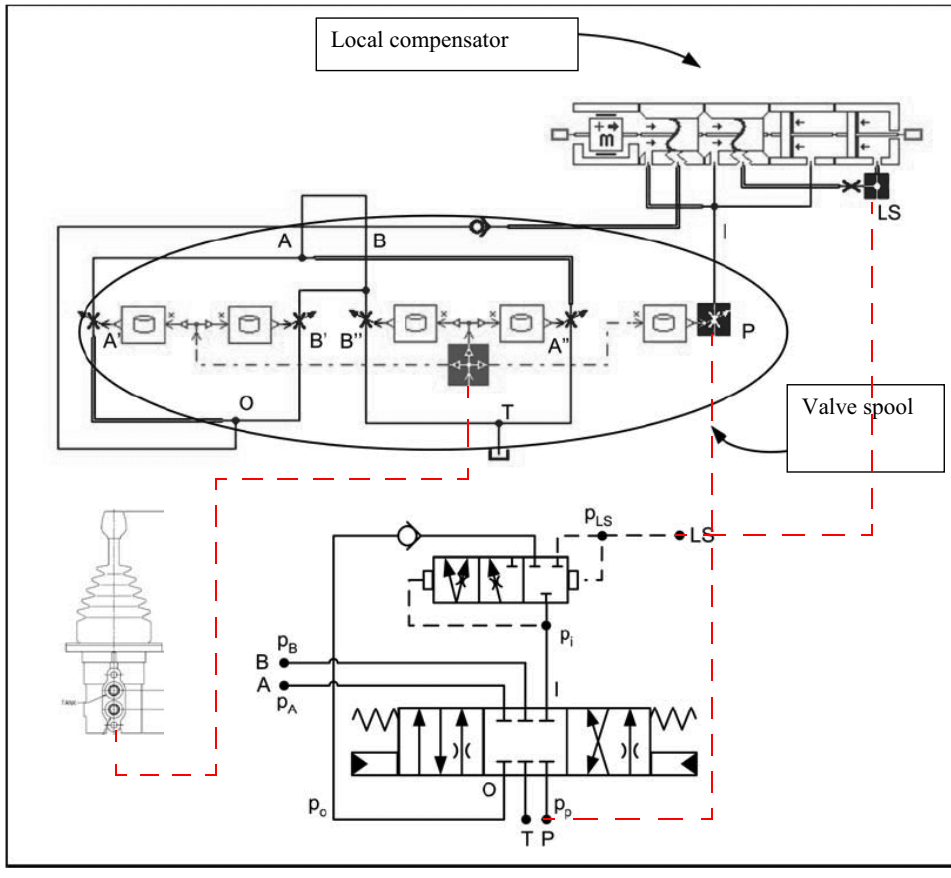

Figure 13: Circuit layout in the simulation model

- a series of connectors to accommodate the FSLS valve together with the necessary transducers and related data acquisition chain (not detailed here)
- a load section composed by three hydraulic motors coupled with variable inertia flywheels with integral rotational speed transducers.

A picture of the physical layout of the test rig is presented in Figure 16.

- a supply circuit with a power of 30 kW, driven by one electrical motor connected to a LS variable displacement pump;
- a service circuit driven by a 12 kW electric motor to supply remote commands and cooling circuit;
- a series of connectors to accommodate the FSLS valve together with the necessary transducers and related data acquisition chain (not detailed here)
- a load section composed by three hydraulic motors coupled with variable inertia flywheels with integral rotational speed transducers.

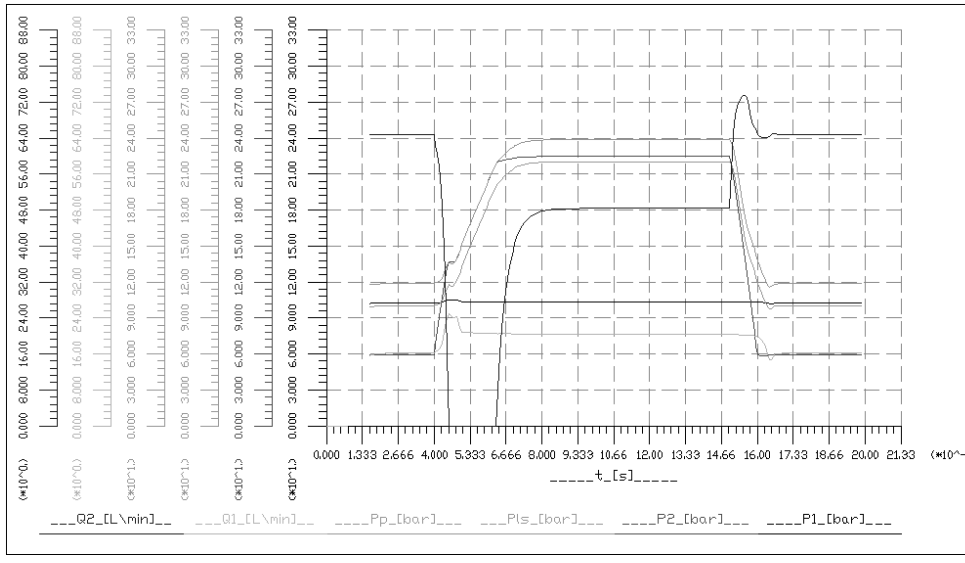

Figure 14: Typical result of the simulation. Switching upon actuators test.

A picture of the physical layout of the test rig is presented in Figure 16.

The main type of experimental test carried out was referred to the actuation *on* and *off* of a section with the two other sections at fixed position with increasing values of inertia load. Three actuation ramps were used, lasting 0.46, 2.3 and 4.6 seconds respectively. The results were also classified according to the degree of saturation induced, computed as the ratio between the difference of the total flow rate ideally requested by the sections and the nominal pump flow rate and the pump flow rate itself:

$$S = \frac{(\sum Q_i - Q_p)}{Q_p} 100 \text{ in \%} \tag{1}$$

In all cases the effect of inertia was also evaluated against a pure resistive load induced by a loading valve downstream the motor inducing a 100 bar counterpressure. No mechanical loads were imposed on the shafts in addition to inertia. All the tests were executed in both unsaturated and saturated flow conditions.

The loading sequence and data collection was fully automated using a customised program implemented in LabView® and specifically tailored to handle all outputs (three analogue signals) and inputs (eight analogue signals and five digital counters) needed for the test execution.

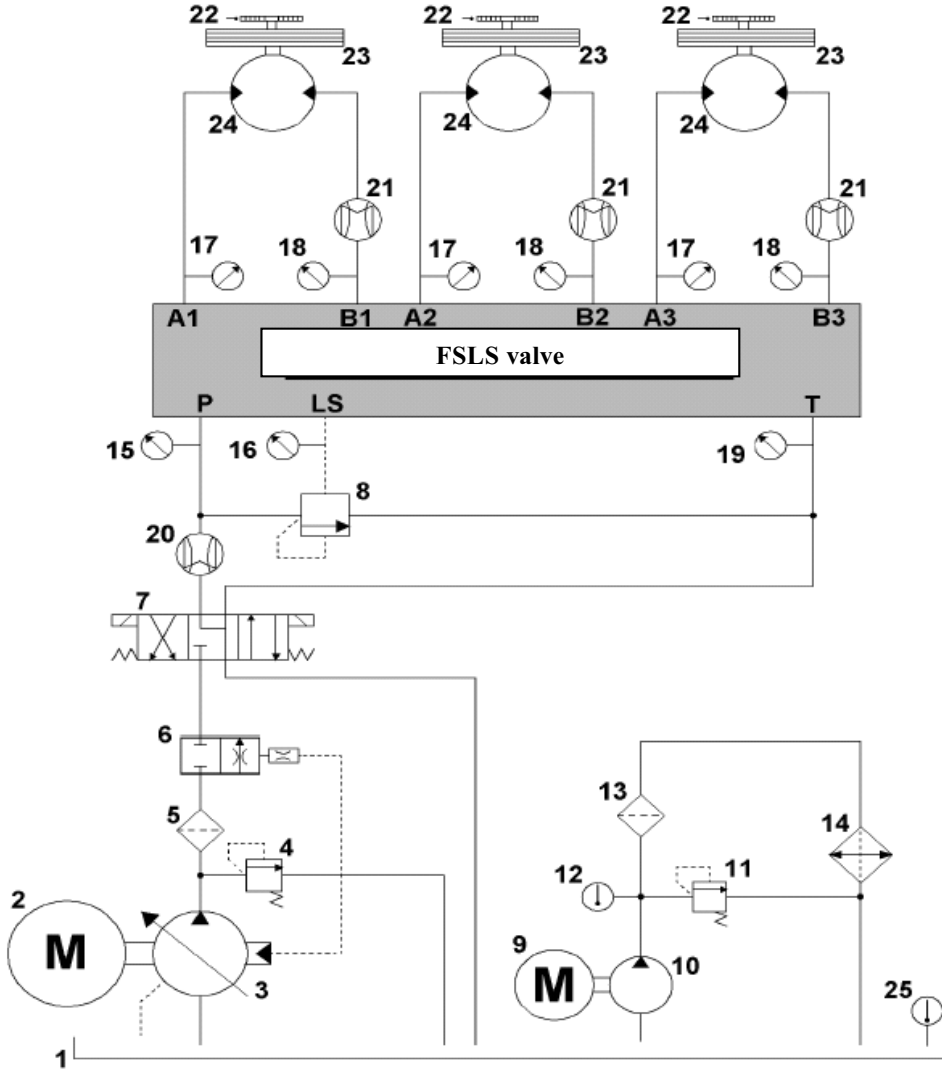

Figure 15: Circuit layout of the test rig for evaluation of inertia effects.

Four different characteristic times were considered to analyse the transient in terms of time response:

- t_1 as the load switching time, i.e. the total time when a section switches from dependant too dominant in terms of generation of the LS signal;
- t_2 as the time difference between the first overshoot and the undershoot of the response to the positive gradient actuation ramp;

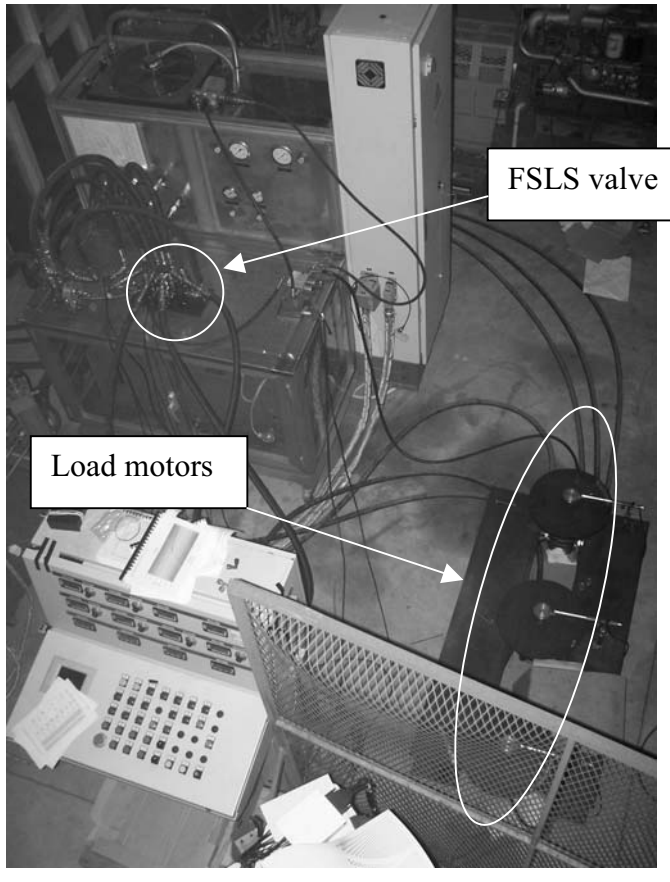

Figure 16: Picture of the experimental test rig (aerial view)

- t_3 as the time where the pressure drops below the 4 bar used as actuation threshold for anti-cavitation valve;
- t_4 as the time difference between the first undershoot and overshoot in the negative gradient actuation ramp.

Figure 17 shows an example of the definition of the above mentioned parameters in when the anti-cavitation valve acts and when it does not take an active part to the transient.

An example of the results is shown in Figure 18 in the case of actuation according to a boxcar input signal to the electro-hydraulic actuator of the section having the higher inertia load.

The transient response of the different pressures in the circuit show a complex transient, lasting close to 7 seconds. The distributor under test was composed of six different sections, but only three out of the six available were actuated. The three actuated sections are numbered 3, 5 and 6, and the input is given to section 5. Section 6 is kept at low inertia and

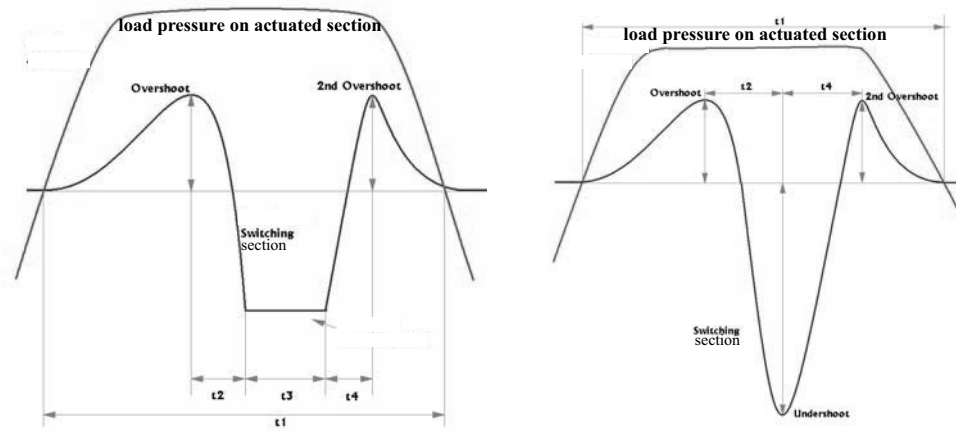

Figure 17: Definition of the characteristic time used to analyse the transient response.

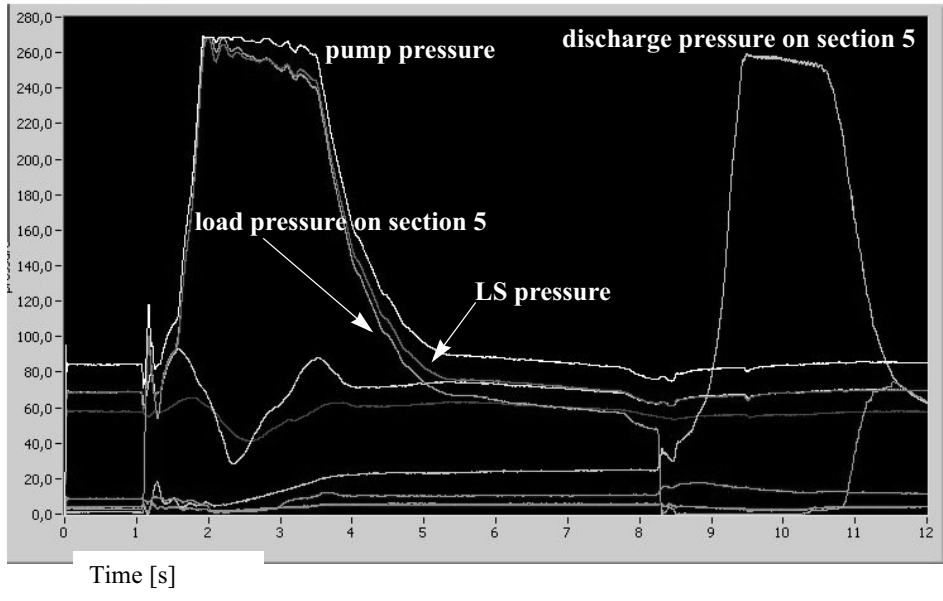

Figure 18: Screen dump of pressure time histories during an experiment

section 3 and 6 have been kept to a nominal flow request of 15 and 20 l/min respectively. The nominal pump flow rate is 80 l/min.

Similar data were collected and analysed in terms of rotational speed and flow rate delivered, with their analysis based on the degree of variation of requested flow rate for unactuated sections and time needed to reach steady state values for the actuated one.

The total number of tests executed and the data acquired was very large, and a standardised analysis comparison procedure is still being developed in order to allow for a more comprehensive understanding of the performance. An example of possible data aggregation is shown inFigure 19, based on the comparison of pressure over- and undershoots expressed in %, with actuation of section 3.

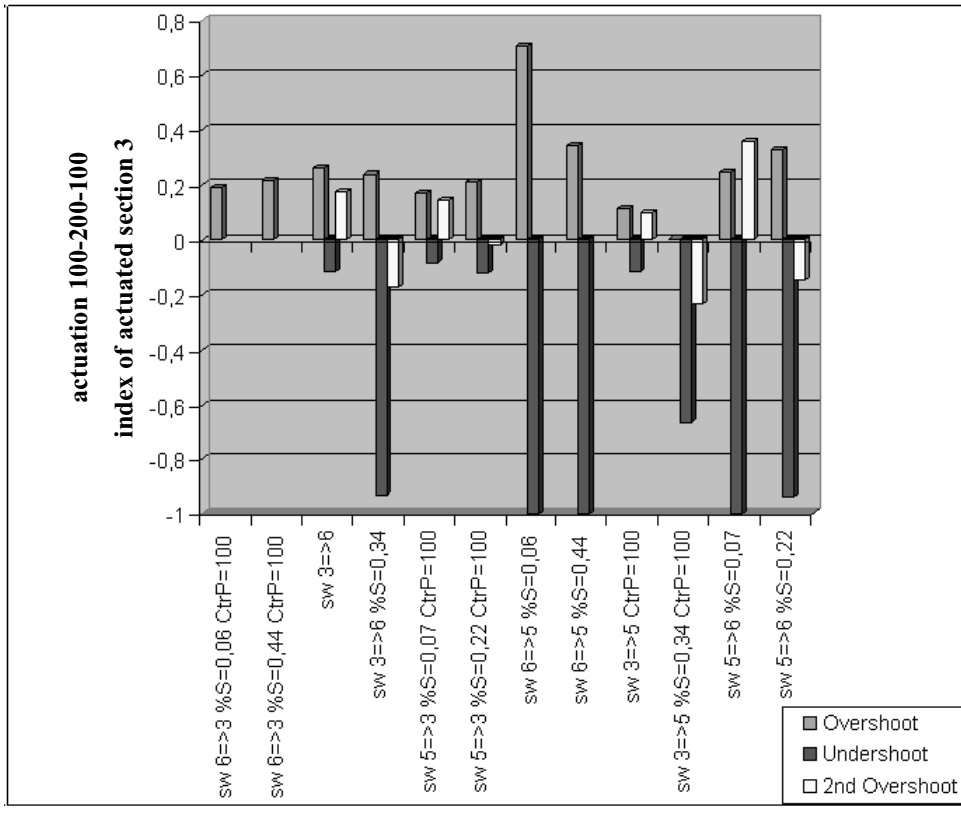

Figure 19: Example of comparison of aggregated data from experimental analysis

The data are classified according to the general coding

sw#=>#%S=***y.yy*** CtrP=***zzz***

Where # indicates the switching of the section generating the LS pressure signal, ***y.yy*** indicated in unit fraction the saturation level and ***zzz*** is the counterpressure, if relevant,

expressed in bar and imposed to the actuated section by a loading valve on the motor discharge line.

9. CONCLUSIONS

A comprehensive method of experimental tests for flow sharing directional valves has been presented, together with some samples of the types of data collected and proposed analysis procedures.

Basically the method includes three hierarchical test sequences:

1. Steady state characteristic of anti-saturation features

2. Resistive load dynamic response

3. Inertia load dynamic response

Three distinct test methods were developed and presented and an example of tuning of numerical models based on experimental test results was shown. All the presented data support the conclusion that the proposed procedure is able to adequately describe the main features of FSLS valves in order to make a relative comparison of performance possible in a defined environment, representative of actual operating conditions.

Some work is still needed to assess the classification method and the synthetic representation of data from the inertia load tests, but preliminary activity shows that it is possible to highlight defined trends directly linked to design features.

10. REFERENCES

1. Sugiyama et ali, Patent US 5.146.747,15/09/92
2. Wilke et ali, Patent US6.098.403, 08/08/00
3. Hamamoto, Patent US5.937.645, 17/08/99
4. Leidinger et ali, Patent US5.609.089, 11/03/97
5. Marani P., Caratterizzazione sperimentale di un distributore Load Sensing Antisaturazione, MSc Thesis, University of Modena and Reggio Emilia, 2004 (in Italian)
6. Ognibene E.,Sistemi Oleodinamici Load Sensing di Seconda Generazione, MSc Thesis, University of Modena and Reggio Emilia, 1998 (in Italian).
7. Derosa D., Caratterizzazione dinamica e stazionaria di un distributore Load Sensing Antisaturazione, MSc Thesis, University of Modena and Reggio Emilia, 2004 (in Italian)
8. AMEsim User's Manual, v. 4.1.3, Imagine S.A., Roanne, France
9. Ansaloni G., Analisi numerica delle prestazioni di distributori Load Sensing Antisaturazione, MSc Thesis, University of Modena and Reggio Emilia, 2005 (in Italian)

10. ISO 6403- Hydraulic Fluid Power Valves Controlling Flow and Pressure - Test Methods, 1988
11. ISO 10770-1 - Hydraulic Fluid – Electrically Modulated Hydraulic Control Valves, 1998
12. P.R. Ukrainetz, D.V. Bitner, P.N. Nikiforuk, Load Interaction in a Multi-Load, Load sensing Pump Hydraulic Driven System, Proceeding of the 41st national conference on fluid power. Detroit, April, 29, 1986, pp 83-9
13. Gu Linyi, Wang Qingfeng, Research on Noninterference Control of Multiple Actuators Load Sensing System with High Inertia in Construction Machinery, proceedings of the fifth International Conference On Fluid Power Transmission And Control (ICFP 2001), Hangzhou, China.
14. Henrik Petterson, Petter Krus, Arne Jansson, Jan-Ove Palmberg, The Design of Pressure Compensators for Load Sensing Hydraulic Systems, UKACC International Conference on Control. Control '96, (CP427), p. 1456 -1461, Exeter, UK, 2-5 Sept. 1996 , ISBN: 0 85296 666 0.
15. Yasuo Aoki, Kazuo Uehara, Kazuyuky Hirose, Tadao Karakama, Kouichi Morita, Teruo Akiyama, Yosuke Oda, Load Sensing Fluid Power Systems, SAE Paper 941714, International Off-Highway & Powerplant Congress and Exposition, Milwakee, Wisconsin, September, 12-14, 1994

Return to Contents

High Performance Valves

A hydraulic control valve for PWM actuation at 400 Hz

Bernhard Manhartsgruber
Institute of Machine Design and Hydraulic Drives
Johannes Kepler University, Linz, Austria

ABSTRACT

The concept of switching converters known from the control of electrical drives can also be applied to hydraulic control systems. A number of such concepts relies upon the pulse width modulation (PWM) of an actuator pressure by a periodically switching valve. In order to keep the good dynamic properties of valve controlled drives, the PWM frequency has to be much higher than the typical eigenfrequency of the driven mechanical system. Therefore, two major problems arise.

Firstly, the pressure variations induced by the periodic switching of the consumer ports between the high and the low system pressure port have to be decoupled both at the supply side and at the consumer side to prevent excessive noise propagation and high frequency actuation of the driven mechanical system.

And secondly, the switching valve has to be very fast compared to commercially available products. Furthermore, the power available for the actuation of this valve is limited in order to keep the energetic benefits provided by the switching control.

In this paper, a novel valve design is presented. A prototype with a flow rating of 100 l/min at 5 bar pressure drop has been built and successfully tested. The basic design is that of a 3/3 directional control valve, with a constant high pressure supply port and a constant low pressure supply port both equipped with hydraulic accumulators. The third port is pulse width modulated between the low and the high pressure port at a frequency of approximately 400 Hz. The so called duty-cycle, i. e. the relative connection time to high pressure within one PWM period is controllable between 0 and 100 % during the PWM operation allowing for the control of a connected consumer. Besides some details on the design of this valve, the paper shows simulation results regarding the use of the prototype in a hydraulic switching converter.

1 INTRODUCTION

Hydraulic motion control systems compete with electrical drives in a large number of applications. Only where the special features of hydraulic systems like the high power density or the simple achievement of translatory motion control can compensate for the known drawbacks like noise and leakage this competition will be won by hydraulic systems.

Power Transmission and Motion Control 2006 Edited by Dr D N Johnston and Professor K A Edge

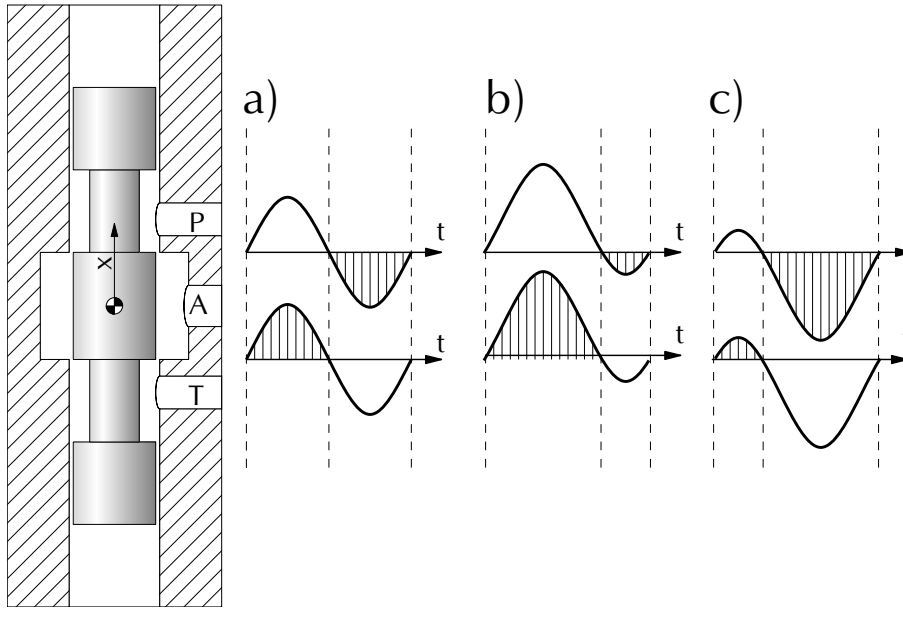

Figure 1: Working principle – (a) 50 %, (b) 30 %, (c) 70 % PWM duty cycle.

Before comparing fluid power with electrical solutions for a certain motion control application, one has to bear in mind that on both sides a number of different solutions will exist for the same problem. For controlled hydraulic systems the first choice is with respect to the nature of the control input. This may either be resistance control or displacement control. The hydraulic servo drive with resistance control is doubtless the solution offering the highest bandwidth for heavy duty closed-loop motion control. However, this advantage is bought at the expense of a very poor energetic efficiency. Therefore, the fluid power motion control system with a constant high pressure supply buffered by accumulators and a high-end servo-valve for resistance control is only of interest if no other technology can achieve the specifications.

Displacement control – either on the primary (pump) or secondary (motor) side – on the other hand offers a solution with good energetic efficiency. However, compared to electrical drives the control input is typically more expensive simply because of the low cost of power electronics for induction motor control. The reason can be found in the complex design and high cost of hydraulic control valves compared to the control devices used in electrical drives like transistors and thyristors. A look back in the history of electrical drives reveals that the hydraulic servo drive with resistance control corresponds to the d.c. motor with a constant supply voltage controlled by a big, tunable series resistor.

While it is difficult to find an electrical counterpart for a displacement-controlled hydraulic system like a swash plate axial piston pump, it is easy to see that no commercially available fluid power technology corresponds to the concept of switching converters for d.c. motor control in power electronics. This lack of fluid power technology is not due to a basic impossibility of using the same ideas as applied in switching electrical power converters. The basic elements of a switching valve, a capacity and an inductivity are available also on the

fluid power side. The concept is not even new to the fluid power world as we can learn from John Whitehursts 1772 invention of a manually controlled so-called pulsation engine [4]. The idea became famous as the self acting hydraulic ram pump invented by Joseph-Michel Montgolfier in 1779. It relies upon the use of the kinetic energy of a column of water in an inclined pipe for the generation of a pressure level that exceeds the value of the hydrostatic pressure at the lower end of the same pipe with the fluid at rest. The conversion of kinetic energy of the moving fluid into high pressure is achieved by rapidly closing a valve.

If the concept is to be used for the control of hydraulic drives with a bandwidth comparable to that of existing solutions, the typical frequencies of the switching process should be approximately one order of magnitude above the eigendynamics of the controlled process. Very much alike to the limit frequencies of servo-valves this gives a range of approximately 50 to 1000 Hz for the frequency of the switching process. However, while the limit frequency of a servo valve is defined for sinusoidal spool motion, the task of the valve is to provide a rapid transition from one switching state to the other. To give again a rule of thumb, the switching time should not exceed 10 % of the period time of the switching process. This results in allowable switching times from 2 ms down to 100 microseconds for the mentioned switching frequency range.

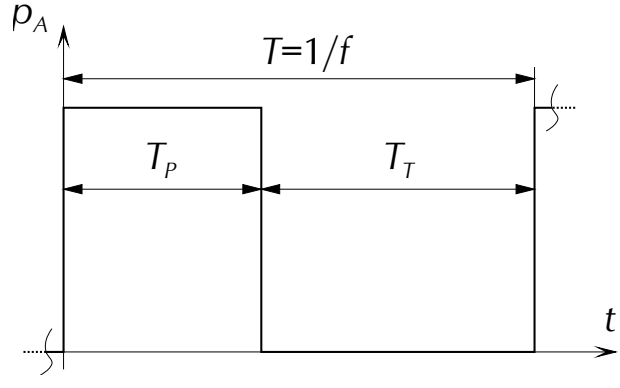

Figure 2: Pulse width modulation.

2 A PWM SPOOL VALVE

The basic idea for the PWM spool valve is very simple and can be traced back at least to the flow regulator patents [1, 3]. A standard valve concept with a spool in a sleeve is used to form a 3/3 way control valve. In order to achieve a PWM modulation, the spool performs a periodic motion resulting in the consumer port being switched between the pump pressure p_P and the tank line pressure p_T. Let the hydraulic consumer be a simple capacity. This is the case if the consumer port is blocked and the only load for the metering edges of the valve comes from the compression and decompression of the fluid within the consumer port duct of the valve. The distances within this duct are assumed to be negligible compared to the length of waves propagating through the fluid in the interesting frequency range. Therefore, the consumer port pressure p_A can be computed from a first order, ordinary differential equation

Table 1: Example parameter set.

E'	$1.4 \cdot 10^9$	Pa	effective bulk modulus of compressibility
ρ	850	$\frac{\text{kg}}{\text{m}^3}$	mass density of the fluid
α	0.6	-	discharge coefficient
d	30	mm	spool diameter
r	0.75	-	active circumferential length ratio
a	0.5	mm	spool oscillation amplitude
ω	$2\pi \cdot 400$	rad/s	spool oscillation frequency
p_P	320	bar	high supply pressure
p_T	20	bar	low supply pressure

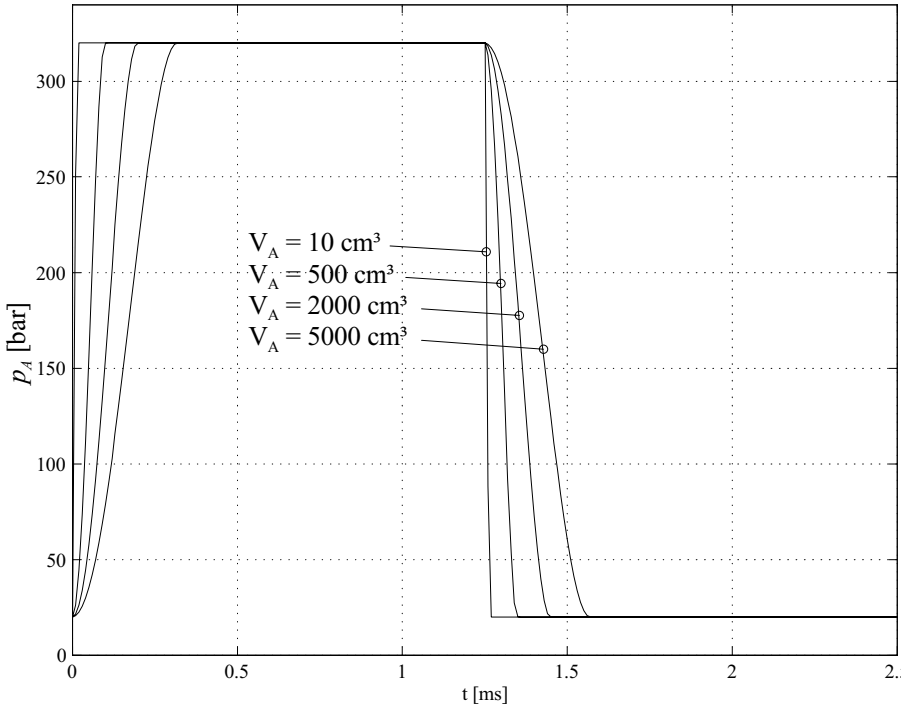

Figure 3: Pulse width modulation of p_A for various values of V_A.

$$\frac{V_A}{E'}\frac{dp_A}{dt} = Q_{PA} - Q_{AT}. \tag{1}$$

The right hand side describes the flow balance into and out of the consumer duct volume V_A. A constant effective bulk modulus of compressiblity E' is assumed to simplify the calculations. This assumption may not be admissible if the bulk modulus varies significantly due to dissolved air or simply because of a large pressure range. The supply pressures p_P and p_T are assumed to be constant. This is only justified if special attention is paid to the decoupling of

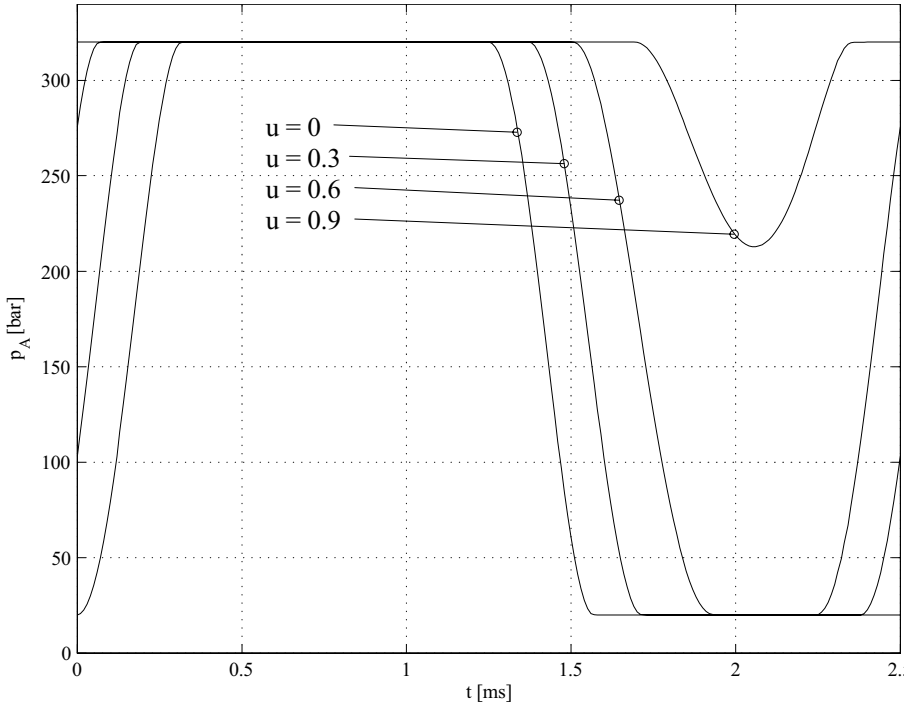

Figure 4: Pulse width modulation of p_A for various values of u.

the PWM process from the supply system, for instance by the use of hydraulic accumulators.

As only a part of the circumferential edge on the control spool is released by windows in the sleeve, the effective circumferential length is given by $d\,\pi\,r$ where $0 < r < 1$ is the ratio of the open window length compared to the full circumference on the spool diameter d. Leakage flow effects arising from the small radial clearance between spool and sleeve are neglected and the flow across the two metering edges is computed by the standard sharp-edged orifice formula $Q = \alpha\, A\, \sqrt{2\,\Delta p\,/\rho}$ where the discharge coefficent α is around 0.6 and the orifice area A is assumed to be simply the product of the effective circumferential length $d\,\pi\,r$ times the axial spool displacement. Assuming a critical center geometry of spool and sleeve, the volumetric flow rate from the high pressure supply into the consumer duct is

$$Q_{PA} = \alpha\, d\pi r\, \mathrm{sg}\,(x)\ \sqrt[\wedge]{\frac{2\,(p_P - p_A)}{\rho}}, \tag{2}$$

whereas the flow exiting the consumer duct towards the low pressure supply reads

$$Q_{AT} = \alpha\, d\pi r\, \mathrm{sg}\,(-x)\ \sqrt[\wedge]{\frac{2\,(p_A - p_T)}{\rho}}. \tag{3}$$

The opening and closing of the two metering edges is modelled by a function sg defined as

$$\mathrm{sg}\,(x) = \begin{cases} x & x > 0 \\ 0 & \text{else} \end{cases}. \tag{4}$$

and a modified square root function

$$\hat{\sqrt{x}} = \mathrm{sign}\,(x)\,\sqrt{|x|}$$

enables the modelling of flow in both directions. Assuming a sinusoidal spool motion

$$x = x_0 + a\,\sin(\omega t) \tag{5}$$

the goal is now to find the periodic solution for the pressure p_A. A substitution of the equations (2-5) into the differential equation (1) gives

$$\frac{dp_A}{dt} = \frac{E'}{V_A}\sqrt{\frac{2}{\rho}}\alpha\, d\pi r\, a \left(\underbrace{\frac{x_0}{a}}_{u} + \sin(\omega t) \right) \begin{cases} \hat{\sqrt{p_P - p_A}} & \text{for } x_0 + a\,\sin(\omega t) > 0 \\ \hat{\sqrt{p_A - p_T}} & \text{else} \end{cases} \tag{6}$$

An ideal pulse width modulation would result in a pressure signal as shown in Figure 2. The duty cycle is defined as the ratio of the relative connection time to the pump pressure port P, i. e.

$$u_{PWM} = \frac{T_P}{T}.$$

The duty cycle u_{PWM} is controlled by the ratio $u = x_0/a$. For given supply pressures p_P and p_T and a given PWM frequency ω, there is only one parameter $\frac{E'}{V_A}\sqrt{\frac{2}{\rho}}\alpha\, d\pi r\, a$ remaining in eq. (6). Therefore, the system behaviour depends only on the ratio of the valve size vs. the size of the consumer port volume V_A. For the parameter set given in Table 1 the results for $u = 0$ are given in Fig. 3. The case $V_A = 500$ cm^3 with varying u is shown in Fig. 4.

3 THE VALVE PROTOTYPE

In section 2, a concept for hydraulic PWM actuation using a sinusoidal motion of a valve spool was proposed without addressing the issue of spool motion generation. While the dither motion of the spool in servo-valves is similar with respect to the superimposition of a sinusoidal motion, the motion control system for the spool cannot simply be copied from a servo valve. The power needed by a flapper-nozzle system for a sinusoidal spool motion at 400 Hz with full spool travel would be much too large. Direct-drive valves operating the spool by a solenoid or a voice-coil drive face the same problem as long as the kinetic energy of the moving spool is dissipated and not recuperated. One way to overcome this problem is to use a spring attached to the spool in order to create a spring mass system that can be excited at its eigenfrequency resulting in a sinusoidal spool motion [3]. The spring could be a mechanical spring – for instance a coil spring as used in many direct-drive valves – or it could be formed by the compressibility of the hydraulic fluid in the chambers faced by the frontal areas of the spool. If a mechanical spring is used there is still the problem of the

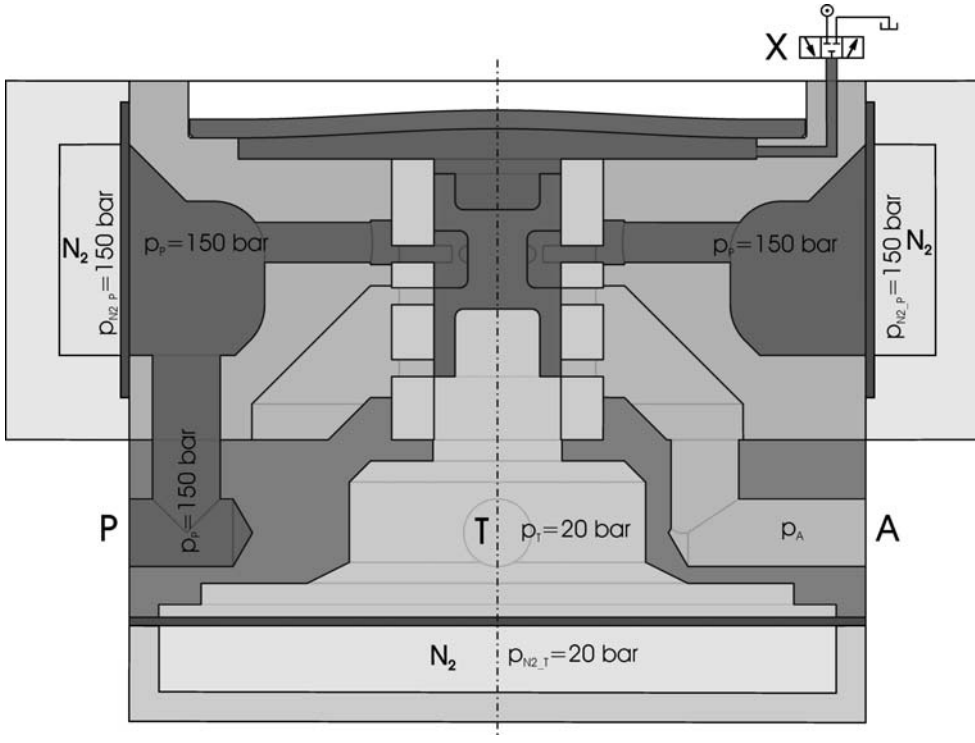

Figure 5: Design of the prototype.

displacement flow at the frontal areas of the spool. Usually these areas face a chamber filled with the hydraulic fluid. In a prototype these areas could be exposed to air at environmental pressure but the external leakage generated by this approach is not acceptable for a practical solution.

The effect of fluid compressibility in the aforementioned chambers is not new to the fluid power community. In a proper servo-valve design, the eigenfrequency of the spring-mass system formed by the two chambers at the frontal areas of the spool and the mass of the spool is kept high enough to prevent a deterioration of the closed loop bandwidth of the spool motion control. Typical eigenfrequencies for servo-valves are at a few kHz. The idea presented in this paper is to use an eigenfrequency as low as 400 Hz and excite the spring mass oscillator at this frequency.

The comparison with the hydraulically stiff arrangement of the spools in servo valves shows that the problem is not to add an additional spring to the system but to lower the stiffness. Therefore, the use of mechanical springs in parallel to the 'oil-springs' formed by the confined compressible fluid is not an option. A solution using only the fluid compressibility on the other hand results in quite large volumes.

Figure 5 shows the design of the PWM valve prototype. The bottom frontal area of the spool faces the low pressure supply port which is buffered by a custom-built hydraulic accumulator integrated into the valve body. Therefore, the force acting upwards onto the bottom area of the spool is nearly constant.

The restoring force is generated by a circular plate on top of the valve. If the spool moves upwards the displaced fluid deforms this plate and a pressure is built up in the room between the spool and the plate. The large diameter of the plate results in a relatively small plate deflection compared to the spool travel. The spool oscillation bias x_0 is controlled hydraulically by a pilot valve attached to the control port X. The resonant excitation is performed either electromagnetically by using the deflecting plate as an armature for a solenoid or by a piezo actuator pushing the plate center. Another possibility is to use a fast servo valve both for bias control and excitation.

Without the resonant excitation the valve can be operated as a standard 3/3 servo valve for directional control. The flow rating of 100 l/min at 5 bar pressure drop is reached with a spool displacement of 1.15 mm. The design of the spool and sleeve pair allows for a spool displacement of $\pm$ 4 mm around the hydraulic zero point. Therefore, a pulse width moduluation with 50 % duty cycle would be possible with an oscillation amplitude of 4 mm while the general case with an arbitrary duty cycle between 0 and 100 % restricts the admissible oscillation amplitude to 2 mm. First experiments with electromagnetic excitation were designed with a rough estimation of the viscous damping between spool and sleeve and with the assumption that the static characteristics of the solenoid could be used for predicting the excitation at 400 Hz. The goal was to reach an oscillation amplitude of at least 1.5 mm. However, due to excessive eddy-current damping the measured amplitude was restricted to 0.5 mm. The excitation system will be changed in order to enlarge the attainable spool oscillation amplitude.

4 SIMULATION OF AN APPLICATION

In order to achieve a good pulse width modulation of the port pressure p_A the oscillation amplitude a must be large. For simple load cases like the one discussed in section 1, design formulas can be derived analytically. For a more realistic application of a PWM valve the dimensioning of the valve is much more complicated. A simulation model in SIMULINK is set up for the benchmark system according to Fig. 6. In this system a PWM valve is used to control a hydraulic winch motor. A so-called wave converter is used for the proper connection between the PWM valve and the load. This converter consists of a pipework with a pipe ring of lengh L and a branch pipe of length $L/4$. The distance between the PWM valve and the branch point in the pipe ring is $L/4$. The load – a hydraulic motor – is attached at the center of the branch pipe and drives a winch. The wave converter is described in the patent [5] . Further background information can be found in [7]. For the operation of the converter, the length L must correspond to one wave length a the PWM frequency ω

$$L = \frac{c_0 2\pi}{\omega}$$

where $c_0 = \sqrt{\frac{E'}{\rho}}$ is the speed of wave propagation depending on the effective bulk modulus E' and the fluid density ρ. The simulation model uses a method of characteristics [8] with a time step of 10^{-6} s and a laminar friction model due to Kagawa [2] for the mathematical modelling of the wave propagation in the pipework.

An important issue in switching hydraulic systems is the avoidance of cavitation. In the case of the wave converter, the consumer port of the valve is the critical point where cavitation is likely to occur. A recently proposed countermeasure [6] is the application of a very small

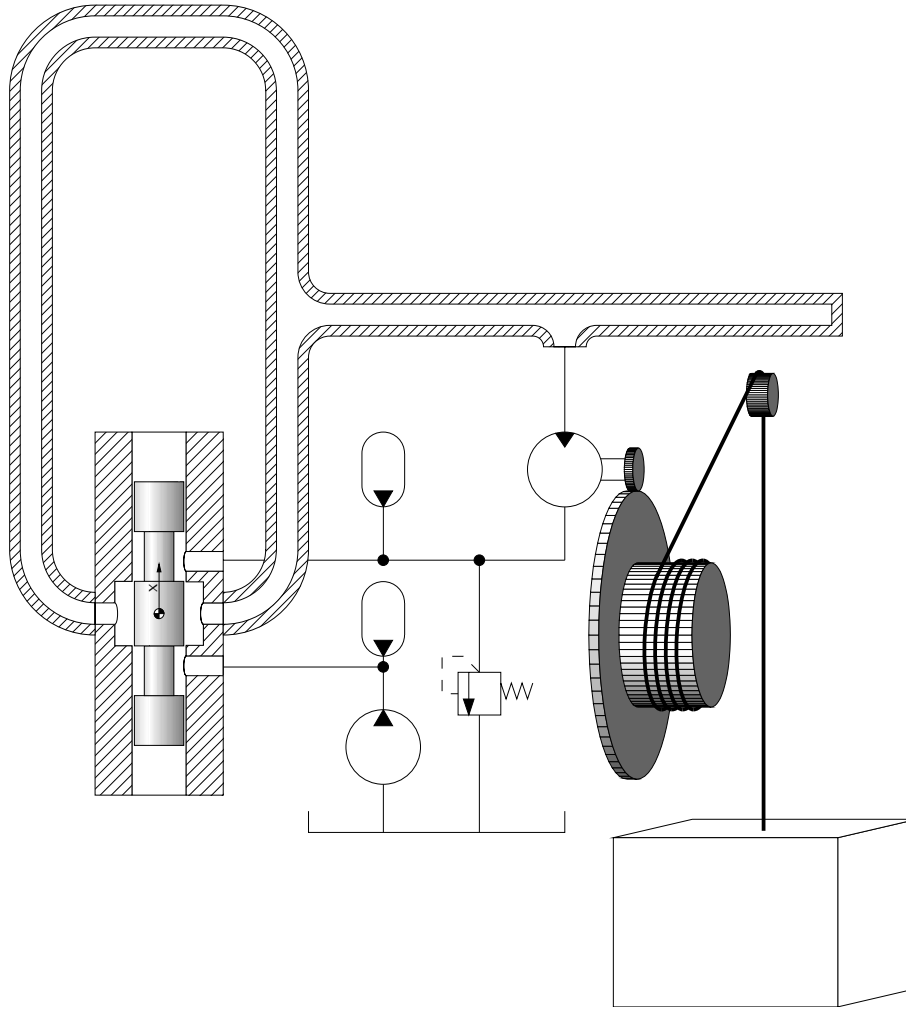

Figure 6: Benchmark: Hydraulic winch drive.

hydraulic accumulator at the consumer port of the valve. A tiny nitrogen volume of 0.2 cm^3 is assumed to be installed at the consumer port. The pre-pressurization of this volume is 20 % of the low supply pressure. Therefore, this accumulator becomes very stiff during the high pressure phase of the PWM cycle and acts as a buffer against cavitation durcing the low pressure phase. The simulation model assumes adiabatic behaviour of the nitrogen volume and negligible hydraulic resistance at the fluid side of the sealing element between fluid and nitrogen. While the energetic efficiency of the hydraulic converter is lowered by the anti-cavitation accumulator, the device makes a cavitation-free operation possible without a huge valve size.

Another important parameter is the diameter of the pipes used for the wave-converter. In this paper, a constant inner diameter of 20 mm is assumed for the whole converter pipework. The viscosity of the hydraulic fluid is assumed to be constant at 30 mm^2/s.

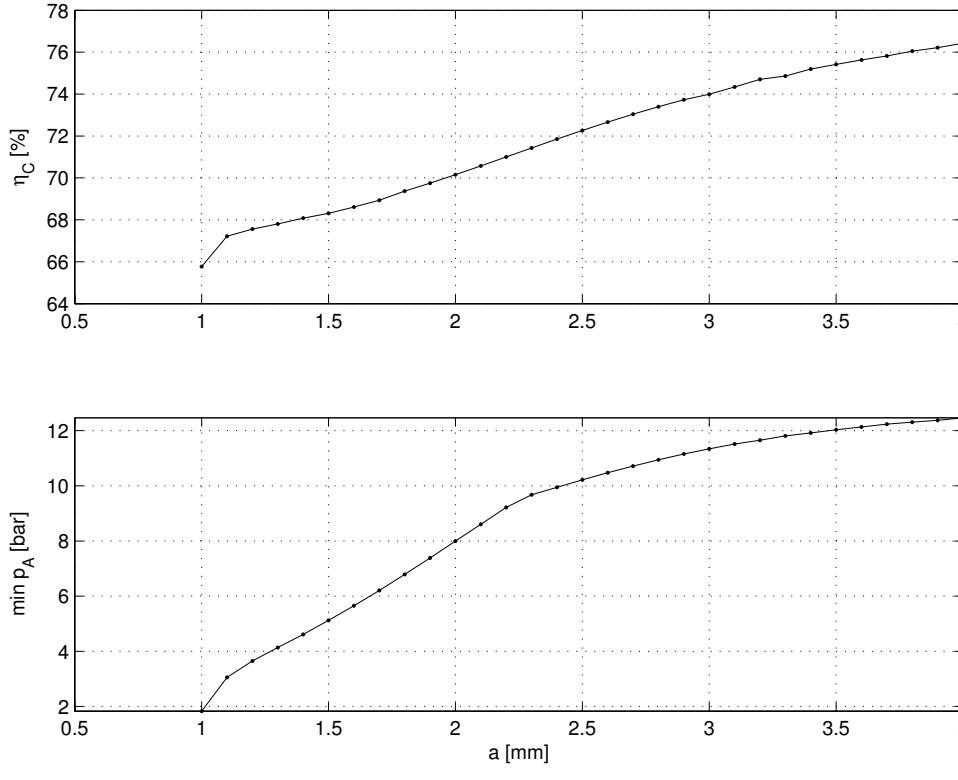

Figure 7: Converter efficiency and minimum of the pressure p_A.

The load, i.e. the hydraulic motor driving the winch, is represented in the model by an additional concentrated volume of 250 cm^3 and a simple constant flow rate consumption of 63 l/min at the converter output. This corresponds to the case of constant motor speed with the neglection of the flow ripple of the hydraulic motor. The pressure at the converter output is controllable via the duty cycle of the pulse width modulation. A simple PI control scheme is built into the model adjusting the duty cycle in order to reach a converter output pressure equal to the mean value of the high pressure p_P and the low pressure p_T. This is a load case where the pressure differential at the motor and thus the motor torque is 50 % of the available maximum value. The simulation is carried out long enough to reach steady-state conditions and the values computed during the last PWM period in the simulation are used for computing the efficiency of the hydraulic converter. Fig. 8 shows the valve opening x, the flow rate $Q_{PA} - Q_{AT}$ and the consumer port pressure p_A at the valve and the load pressure $p_L$which is the difference between the pressure at the converter output and the low supply pressure p_T. The efficiency can now be computed from

$$\eta_C = \frac{\int_0^{\frac{2\pi}{\omega}} Q_L p_L\,(t)\,dt}{\int_0^{\frac{2\pi}{\omega}} Q_{PA}\,(t)\,p_P dt - \int_0^{\frac{2\pi}{\omega}} Q_{AT} p_T dt - \frac{2\pi}{\omega} Q_L p_T}.$$

This converter efficiency η_C heavily depends on the oscillation amplitude a of the valve.

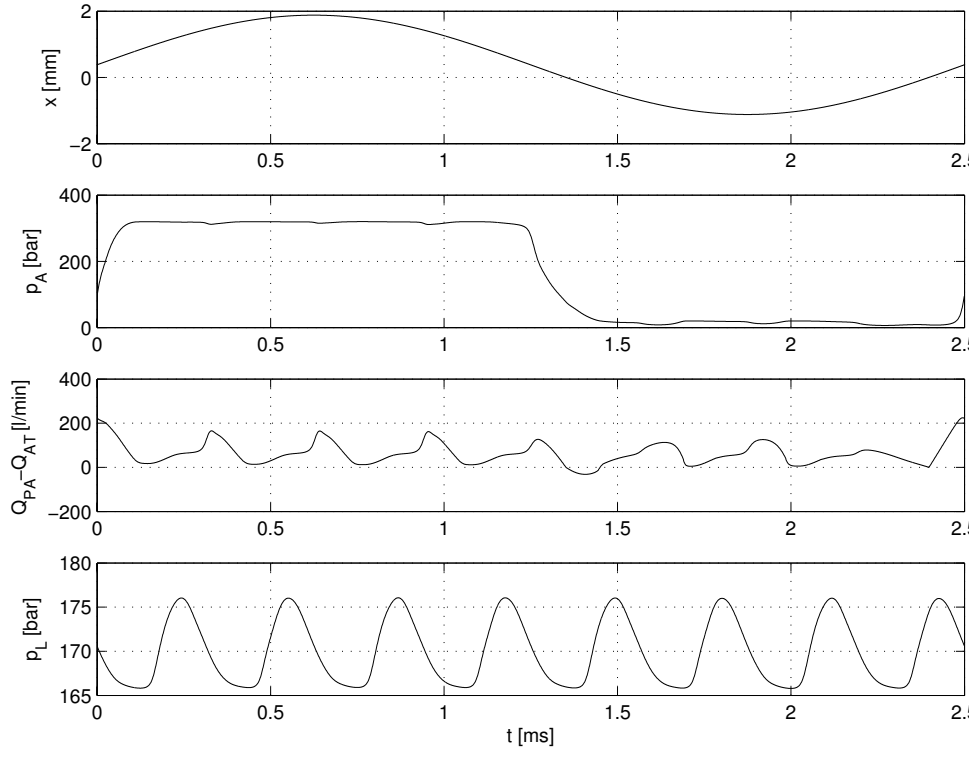

Figure 8: One steady state period for $a = 1.5$ mm.

Results from a series of simulations with different values of a are given in Fig. 7. The pressure at the converter inlet – i.e. at the consumer port of the PWM valve – must not drop to zero in order to avoid cavitation. The minimum of this pressure signal during one PWM period is also depicted in Fig. 7.

For large hydraulic winches, the use of a constant pressure supply system together with a control valve is not a good idea because of the huge amount of dissipation. Therefore, a standard solution is a pump controlled system using variable displacement pumps to control the motor flow rate. In some applications even the motor is a variable displacement unit in order to enlarge the range of controllable speeds, especially to get a smooth start and stop behaviour. The system with a switching converter proposed in this paper must be compared against existing solutions with respect to engergetic efficiency, control performance, noise emission, and component cost. In this paper, only the engergetic efficiency problem is adressed.

The switching converter is only a control element and does not replace a pump transforming mechanical into fluid power. Therefore, the overall degree of efficiency will be deteriorated by the switching converter in applications where the load only consumes energy. However, in applications where the load acts both as a consumer and as a generator there is the chance of recuperating energy that can be stored in the hydraulic accumulators on the P and T port of the PWM valve. Examples for such applications can be found in the winch drives of mobile cranes, in the swing drives of earth moving equipment, or even in the traction drive of cargo-

handling vehicles operating frequently in a back and forth motion. For a simple calculation, the example of a crane winch shown in Fig. 6 is analysed under the assumption that the winch is repeatedly lifting and lowering a load. Clearly this operation does not make sense without operating other drives of the crane like swing or boom movement because the load should be moved from the pick-up point to a different location. This combination of several hydraulic loads on one diesel engine may sometimes result in the benefitial situation that an overrunning load is powering other hydraulic consumers. However, there is also a good chance that during the cargo handling motion in a first phase both the winch drive and for instance the swing drive are consuming power while in a second phase the winch is lowering the load and the swing drive is also acting as an overrunning load due to the deceleration of the rotary inertia of the crane.

Table 2: Converter efficiency η_C according to eq. (7).

% η_P / η_M	80	85	90	95
80	73	71	69	67
85	72	70	68	66
90	71	69	67	65
95	70	68	66	64

In a first step, the conventional solution is analysed. The power for the winch drive is typically deliverd by a diesel engine driving an axial piston pump. The power output at the shaft of the diesel engine is converted into fluid power by the pump with a degree of efficiency η_P. If minor losses in the pipework of the hydrostatic transmission can be neglected, the fluid power output of the pump is converted back to mechanical power by the hydraulic winch motor with a degree of efficiency η_M. Friction losses a the bearings of the winch and the deflexion pulley are included in the motor efficiency η_M for simplicity. When the load is lowered the hydrostatic transmission will overrun the diesel engine resulting in an almost zero fuel consumption in this phase. Assuming equal duration and absolute vertical velocity for the lifting and lowering phase, a lifting power P_L can be computed as the product of weight times vertical velocity. The mean power output of the diesel engine will then be $\frac{1}{2}\frac{P_L}{\eta_M \eta_P}$ where the factor $\frac{1}{2}$ is due to the approximately zero fuel consumption during the lowering phase.

The proposed system using a switching converter results in a third degree of efficiency introduced in the chain between the diesel engine and the lifted load. The converter takes fluid power from the pump and delivers it to the hydraulic motor with a degree of efficiency η_C. During the lifting phase the diesel power consumption will be $\frac{P_L}{\eta_P \eta_C \eta_M}$ while in the lowering phase energy is recuperated into the hydraulic accumulators at a rate of $P_L \eta_M \eta_C$. The mean power consumption of the hydraulic pump is therefore $\frac{1}{2}\left(\frac{P_L}{\eta_P \eta_C \eta_M} - P_L \eta_M \eta_C\right)$. The proposed solution using a switching converter results in a lower mean power output of the diesel engine if

$$\frac{1}{2}\left(\frac{P_L}{\eta_P \eta_C \eta_M} - P_L \eta_M \eta_C\right) < \frac{1}{2}\frac{P_L}{\eta_M \eta_P}$$

which means

$$\eta_C > \frac{\sqrt{1 + 4\eta_M^2 \eta_P}}{2\eta_M^2 \eta_P} \tag{7}$$

for the converter efficiency. The efficiencies of the hydraulic pump and motor can be expected between 80 and 95 %. The resulting minimum converter efficiency is given in Table 2. A converter efficiency of around 70 % is obviously sufficient in order to reach the same overall energy consumption as the conventional solution.

5 CONCLUSIONS AND OUTLOOK

A PWM valve based on a standard spool and sleeve concept has been designed. The pulse width modulation is achieved by shifting the zero point of a sinusoidal spool motion. A crucial point is the oscillation amplitude needed to guarantee energy efficient operation of the PWM valve in a hydraulic switching converter. For an example system the sizing problem for the valve has been answered by a simulation model.

Much more work is needed to improve the valve prototype and to gain better understanding in the dynamic behaviour of PWM controlled hydraulic drives.

References

[1] R.V. Burton. US Patent 2,996,045: Time modulated hydraulic servo valve.

[2] T. Kagawa, I.-Y. Lee, A. Kitagawa, and T. Takenaka. High speed and accurate computing method of frequency-dependent friction in laminar pipe flow for characteristics method. *Trans Jap Soc Mech Engrs B*, 49:2638–2644, 1993.

[3] Hans-Christof Klein. US Patent 3,490,337: Flow regulator, 1970.

[4] J.A. Krol. *A critical survey of the existing information relating to the automatic hydraulic ram. Part I.* PhD thesis, University of London, 1947.

[5] R. Scheidl, W. Leitner, Riha G., and D. Schindler. US Patent 5,974,800: Device for actuation of a hydrostatic drive, 1999.

[6] R. Scheidl, B. Manhartsgruber, and H. Kogler. Hydraulic switching control with nonlinear converters. In F. Breitenecker and I. Troch, editors, *5th MATHMOD Vienna*, 2006.

[7] R. Scheidl, D. Schindler, G. Riha, and W. Leitner. Basics for the energy efficient control of hydraulic drives by switching techniques. In J. Lückel, editor, *Proceedings of the Third Conference on Mechatronics and Robotics*, pages 118–131, Stuttgart, October 1995. Teubner.

[8] Benjamin E. Wylie and Victor L. Streeter. *Fluid Transients in Systems*. Prentice Hall, 1993.

Optimization of a Fast Switching Valve for Big Flow Rates

Bernd Winkler
Linz Center of Mechatronics GmbH; Altenbergerstrasse 69; A-4040 Linz, AUSTRIA
Rudolf Scheidl
Institute of Machine Design and Hydraulic Drives; Altenbergerstrasse 69; A-4040 Linz, AUSTRIA

ABSTRACT

In this paper the optimization of a fast switching valve regarding the critiria rubustness to flow forces and low cost under the constraints of a nominal flow rate of at least 40 l/min and a switching time of about 1ms is presented. The basis for the optimization process is a concept of a switching valve which was derived from three previous designs, all of which had been prototyped. The main difficulties that have to be overcome are: (i) Spool sticking problems, if tiny land structures are applied, (ii) flow forces which are substantially disturbing the spool motion, (iii) flow oscillations generated by fast switching which create unpleasant noise and pressure pulsation. Problem (i) can be avoided by a specific spool and land design which stabilizes the centered spool position. Flow force reduction can be achieved by shape modification of the spool and the grooves in the sleeve but may conflict with problem (i). The faster the valve the smaller the parasitic hydraulic inductivities of the interior flow channels of the valve have to be. Avoiding such problems gives decisive design constraints in which the optimization problem has to be embedded. Optimization parameters have been spool diameter, spool stroke, and inertia. Flow forces could be reduced considerably by a CFD analysis of different designs of land structures. The resulting design was realized as a new prototype which fulfills the demands on switching time and flow rate. Furthermore, the design is simple, which promises a cheap production.

1 NOMENCLATURE

x	[m]	spool position	n_{St}	[1]	number of stages
m	[kg]	mass	α	[1]	flow coefficient
d	[Ns/m]	damping coefficient	d_S	[m]	spool diameter

Power Transmission and Motion Control 2006 Edited by Dr D N Johnston and Professor K A Edge

F_M	[N]	magnetic force	Δp	[bar]	pressure drop
F_{Sp}	[N]	spring force	ε	[rad]	jet angle
F_F	[N]	fluid force	A_{flow}	[m²]	flow passage area
F_0	[N]	spring preload	ρ	[kg/m³]	oil density
k	[N/mm]	spring rate			

2 INTRODUCTION

This work aims at the development of a switching valve which fulfills the following requirements:

- flow rate of at least 40 l/min
- a switching time of about 1ms
- low costs (about 50 € manufacturing costs)
- 2/2-way configuration
- reliable functionality for pressures up to 315 bar
- possibility to place de-coupling accumulators close to the metering edge

Three previous prototypes, of which part of the development and research work has been published in [1, 3], fulfilled the demands on switching time, flow rate and decoupling of pressure pulsations caused by the switching process. However, they failed to switch reliably, when very high pressure differences persistently were present at the valve ports. This is a well known problem related to flow forces even for industrial switching valves. Thus, one of the main difficulties to be overcome in the opimization process is to guaranty reliable switching of the valve for pressure drops on the metering edge of up to high values (in our case 315 bar) under the constraint of a cheap design.

To succeed in this optimization problem one has to focus mainly on the three following items.

- Avoidance of spool sticking problems due to the tiny land structures. This problem and its solution are already described in [1, 2, 3].
- An optimized shape of the land structures shall reduce flow forces. To find such a design extensive use is made of CFD analysis.
- Reduction of noise and pressure pulsation. The main contribution by the valve design is the reduction of inductivities between metering edges and decoupling accumulators.

In a first step a mathematical model of the valve's dynamics is set-up, comprising the equation of motion of the spool and the magnetic and the flow force, to evaluate the influence of the diverse design parameters on the functional requirements switching time and robustness against the disturbing flow force.

3 MATHEMATICAL MODELS

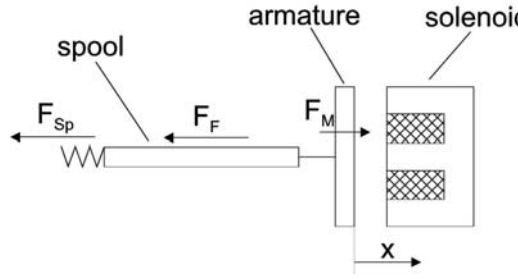

Figure 1: Mechanical model of the spool motion

3.1 Equation of motion for the spool

The mathematical model of the valve is based on the simple mechanical model depicted in Figure 1. The spool is directly connected to the armature of the electro-magnetic valve actuator. Its magnetic force is opposed by a spring for valve closure. The equation of motion reads

$$m\ddot{x} + d\dot{x} = F_M - F_{Sp} - F_F \tag{1}$$

The damping coefficient d is assumed to be constant over the spool stroke x. The nonlinear damping effect due to oil squeezing in the narrow gap between armature and solenoid is neglected. This effect becomes only significant when the spool approaches its open position, which has only marginal influence on the switching time.

The mass m of all moved parts is the sum of the masses of the spool, the armature, and one third of the spring. The spool mass depends directly on some of the optimization parameters like spool stroke, spool diameter, and some characteristics of the valve sleeve. As far as possible, these influences were taken into account.

The spring force F_{Sp} is given by $F_{Sp} = F_0 + k\,x$. F_0 is the preload of the spring in the open position of the valve (for x = 0) and k is the spring rate. The spring characteristics F_0 and k decisively influence the switching time for valve opening and closing.

2.1 The magnetic force

The force F_M of the solenoid depends mainly on the position of the armature x and the current through the coil. The solenoid applied for this valve is a commercially available, high force, and low inductivity magnet of type Heinzmann SM05-S1. A model of its force has been derived in [5] using a network model of the magnetic flux taking also leakage flux and saturation effects but no eddy currents into account. The result of this model of the magnet SM05-S1 are shown in Figure 2 which clearly indicates the magnetic saturation for higher ampere turns and a small air gap.

To keep energy consumption and coil heat-up as low as possible, the current feed follows a certain characteristic. A high current at the start – for the indicated solenoid it exceeds 100 amps - shall provide a fast switching, a low current of about 6 amps is sufficient to hold the valve in its open position against the spring force.

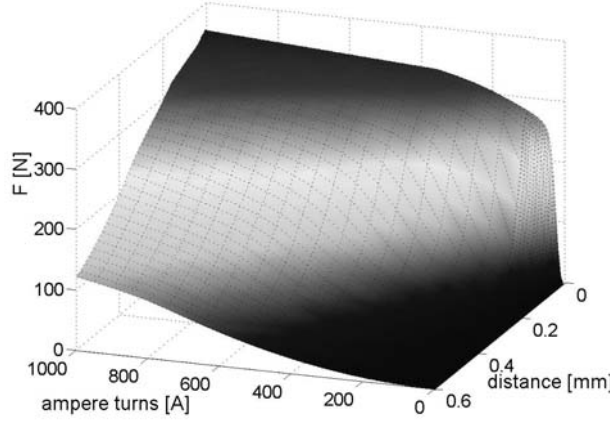

Figure 2: Solenoid characteristics

2.2 The flow force

The flow force F_F can basically be derived from the equation (2) (see also [5]):

$$F_F = n_{st} 2\alpha d_S \pi \Delta p \, x \cos(\varepsilon) \tag{2}$$

n_{St} is the number of stages in the valve, α is the flow coefficient, d_S is the spool diameter. Equation (2) describes the flow force at one metering edge. The flow path of the fluid for the fully opened valve is shown in Figure 3. The oil has to pass two metering edges on its way through one stage. The pressure drop at each metering edge depends on the spool position. The trapezoidal shape of the sealing land is necessary to avoid spool sticking problems [2].

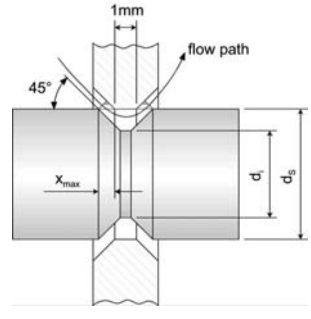

Figure 3: Flow path geometry

The specific flow path geometry results in the following flow force formula

$$F_F = F_{F1} - F_{F2} \tag{3}$$

$$F_{F1} = 2\alpha d_S \pi \Delta p_1 x_1 \cos(\varepsilon_1) \tag{4}$$

$$F_{F2} = 2\alpha d_S \pi \Delta p_2 x_2 \cos(\varepsilon_2) \tag{5}$$

The pressure drops Δp_1 and Δp_2 are derived from equation (6) and (7).

$$\Delta p = \Delta p_1 + \Delta p_2 \tag{6}$$

$$\alpha A_{flow1(x)} \sqrt{\frac{2}{\rho}} \sqrt{\Delta p_1} = \alpha A_{flow2(x)} \sqrt{\frac{2}{\rho}} \sqrt{\Delta p_2} \tag{7}$$

For verification of this simple model a comparison with experimental results obtained from a prototype of a previous design stage was made. A parameter identification was carried out to determine the values of the jet angles $\varepsilon_1, \varepsilon_2$, of (4) and (5) which have been assumed to be identical and found to be 62.5°. Figure 4 shows this comparison which justifies this model.

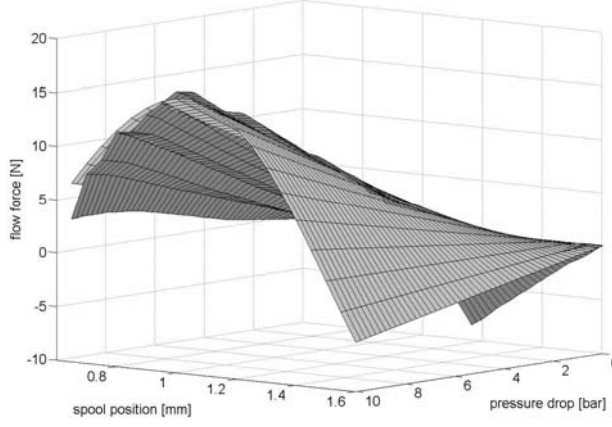

Figure 4: Comparison of theoretical (light gray) and experimental (gray) flow force

4 SIMULATION RESULTS

With the mathematical models of Section 3 extensive parameter studies have been made using Matlab/Simulink as a simulation platform. The parameters and the range of their variation for the optimization studies are

- spool diameter (4mm – 15mm),
- spool stroke without overlap (0.2mm – 0.5mm), and
- number of stages (5 - 11).

The two design parameters spring rate k and spring forces F_0 are not included in the parameter studies because their optimal choices can be derived directly from the following consideration. A high spring rate and a low spring preload is the optimal combination for fast switching. The spring rate is limited by geometrical and strength limitations and this limit turned out to be approximately 40 N/mm. This value was taken for the optimization procedure.

Further parameters for the optimization study of the valve are:

- steel density: 7850kg/m³
- oil density: 860kg/m³
- flow coefficient: 0.6
- jet angle: 62.5°
- spring preload: 2N
- maximum pressure drop: 300bar

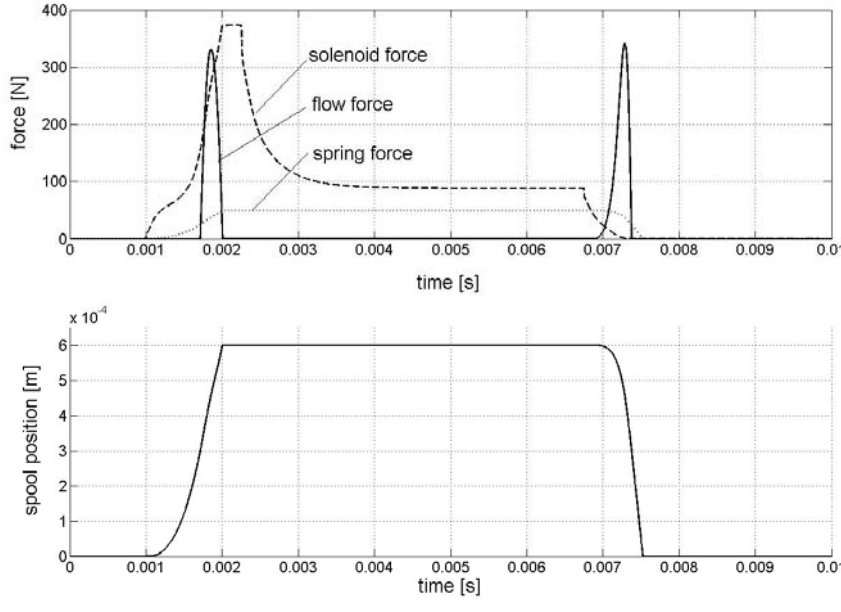

Figure 5: Representative simulation result

Figure 5 shows one typical simulation run of the parameter study. The signal to open the valve is set at 1ms. The corresponding forces (solenoid force, flow force and spring force) are shown in the upper diagram of Figure 5. The solenoid force results from a coil voltage of 20V applied for 1.25ms to quickly open the valve and a coil voltage of 3V for holding the spool in its open position for the rest of the opening period (4.5ms). The flow force begins to rise just when the spool gets out of the overlap and reaches its maximum at half

open position. For the fully opened valve the flow forces are completely compensated due to the design of spool and sleeve (see Section 5). The spool position signal in Figure 5 shows a decelerating course when the flow and the spring force overcome the solenoid force.

To get a good understanding of the global influence of the three optimization parameters on the functional requirements and constraints respectively, simulation runs for a grid of parameter values spanning the feasible parameter space have been performed. In order to see the influence of the functional requirements and constraints, all these simulation runs have been repeated for different levels of these requirements/constraints. A special visualization method was used to show three different result attributes for different points in a 3D parameter space.

Figure 6 depicts the result for switching time and nominal flow rate for a pressure difference of 300bar persisting at the valve's two ports. For each parameter combination which accomplishes a full stroke - despite the high flow forces – within the given switching time and which reaches or exceeds the nominal flow rate of 40 l/min, a ring and a star in its center is set. The darkness of the star indicates the nominal flow rate (from white for 40l/min and below to black for 60l/min and above). The darkness of the ring indicates the switching time (from black for 0.8ms to white for 1.5ms). The darker the ring-star marker the better the parameter combination.

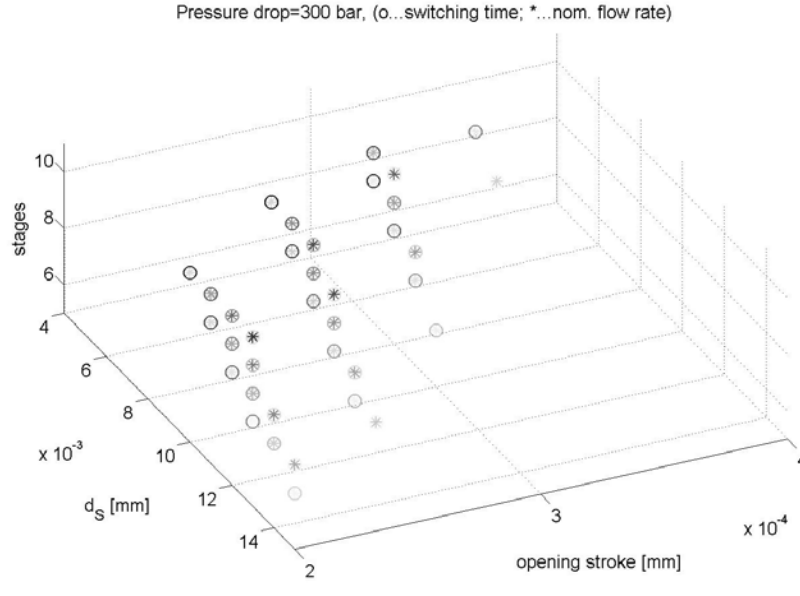

Figure 6: Parameter combinations fulfilling the functional requirements

Taking into account additional constraints like to use a standardized diameter (10mm, 12mm, …), low leakage, the optimal parameter combination has been found to be:

- spool diameter: 10 mm
- opening stroke: 0.3 mm
- number of stages: 7

5 OPTIMIZATION OF THE METERING EDGE

Due to the high significance of flow forces an optimized shape of the metering edge is essential to achieve the design goals.

The simplest method to reduce the flow forces is to bring the jet angle close to 90°. For a rectangular and sharp-edged metering edges a jet angle of 69° is reported in literature [5].

Due to the special shape of our original design (45° trapezoidal shape) a lower jet angle can be expected (see Figure 7). An axisymmetric CFD simulation [6] of this design, the velocity field of which is shown in Figure 7, yielded a jet angle of about 45°.

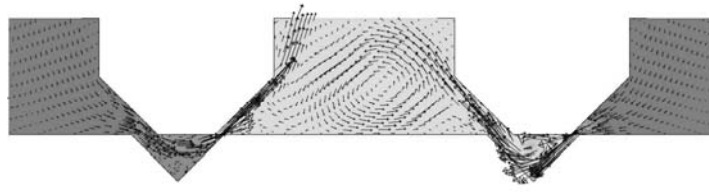

Figure 7: Flow for the origin trapezoidal sealing land shape (half opened valve)

Any modification to obtain a jet angle higher than this 45° must not destroy the specific elastic deformation properties of the trapezoidal sealing lands which have been found to guarantee a stable centered spool position and prevent spool sticking (for detailed information see [2]). The best design found under these constraints are shoulders as shown in Figure 8. This design results in a jet angle ε close to 69°. Moreover, the nominal flow of this design is increased. Values for the pressure drop at each metering edge are given in Table 1.

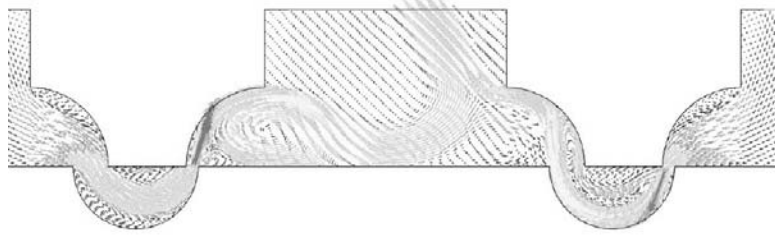

Figure 8: Flow for the optimized round shape design

The flow forces of the round shape design are reduced almost to one third of those of the trapezoidal design.

	right metering edge	left metering edge
trapezoidal geometry	Δp=2.11x10^7 Pa	Δp=1.92x10^7 Pa
round geometry	Δp=1.69x10^7 Pa	Δp=0.78x10^7 Pa

Table 1: Comparison of pressure losses for round and trapezoidal geometry

6 VALVE DESIGN

With this optimal parameter combination and spool and sleeve shapes respectively a simple, easy to manufacture, low manufacturing costs promising embodiment design had to be found. Moreover, the design must allow to place accumulators for pressure pulsation attenuation closely to the metering edges, in order to reduce the parasitic inductivities which are the main sources of unpleasant noise in switching [7].

The main design requirements are listed below:

- simple and cheap design
- save connection between spool and armature
- easy maintenance
- low inductivities
- NG10 mounting plate

Figure 9 shows the realized final prototype. It is charactarized by only one valve housing containing the mounting plate and fittings for the decoupling accumulators.

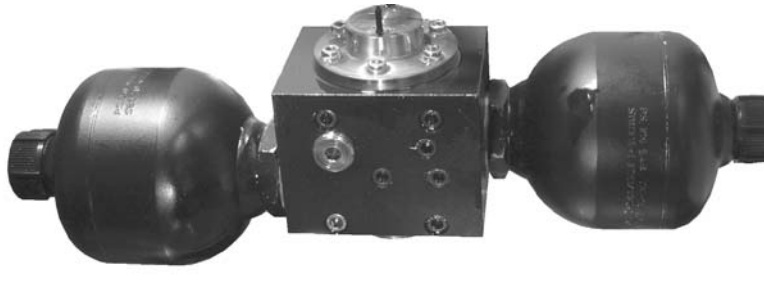

Figure 9: The new valve prototype

7 EXPERIMENTAL RESULTS

For the new prototype the steady state flow characteristics, leakage, switching time, and dependency of switching time on pressure levels have been measured.

6.1 The steady state flow characteristics

Figure 10 depicts the volumetric flow of the new valve for different spool positions. The valve is open from 0.3mm to 0.6mm. The used flow meter is not able to detect a flow below 8 l/min. Thus, in this area a zero flow is depicted.

A nominal flow rate of 45l/min for a 5 bar pressure difference is achieved. This exceeds the expected flow rate of 40 l/min by about 12%.

The leakage of the valve is 0.05 l/min at 250bar pressure difference. This value is within the tolerance for a valve of such a size.

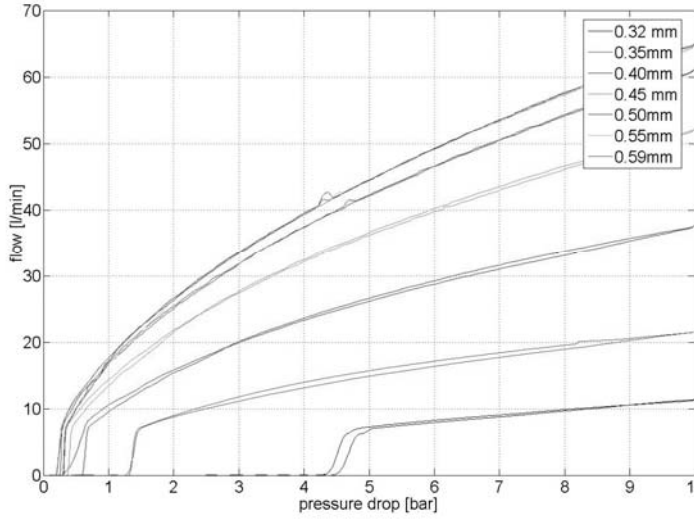

Figure 10: Flow rate of the new prototype for different spool position

6.2 Switching time

Both the time for opening and for closing the valve are of interest. Via the spring preload the closing time can be adjusted.

Figure 11 shows the spool movement and the coil current with different spring preloads for opening the valve. As expected, the valve switches fastest with a low preload.

Remarkably, the switching time for a larger pre-load does not increase substantially, only the delay time is rising. The dashed line shows the configuration with the highest spring preload and additional measures against oil adherence (grooves in the stop discs and bores in the armature). The gain in performance regarding the switch-off time can be seen in Figure 12.

The current signals have a peak value of about 120 amps which is necessary to reach such fast switching. The pronounced steeper rise of current after about 0.7 ms of its onset stems from the saturation of the solenoid which lowers the magnet's inductivity. However, there is a strong need for optimization by improved solenoid concepts. They have to reduce current consumption decisively.

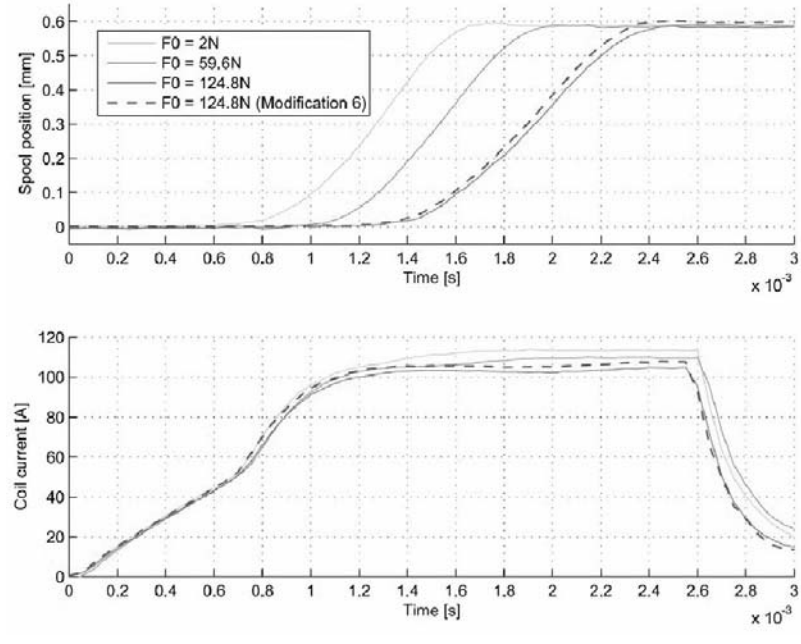

Figure 11: Valve opening

Figure 11 confirms that the demand on switching time (1ms) can be fulfilled. High spring pre-loads are necessary to achieve the intended short switch-off times (see Figure 12).

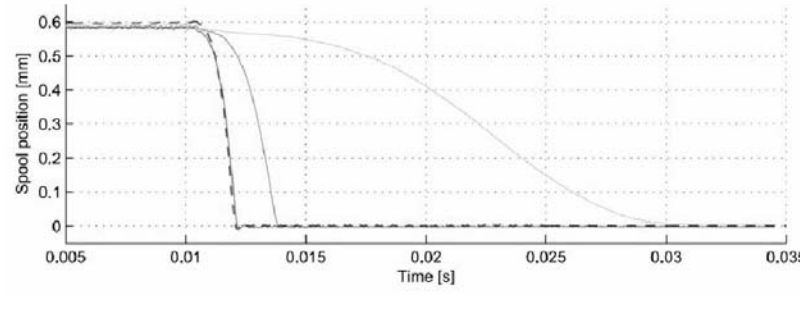

Figure 12: Valve closing

Previous designs of the switching valve have failed to open safely for high pressure differences, which cause extremely high flow rates to pass the valve and, consequently, create very high flow forces.

The measurement results for various pressured differences from 14 to 140 bars are shown in Figure 13. These results show that the influence of the pressure difference on the switching time is marginal. Thus the robustness of the valve to flow forces is sufficiently high.

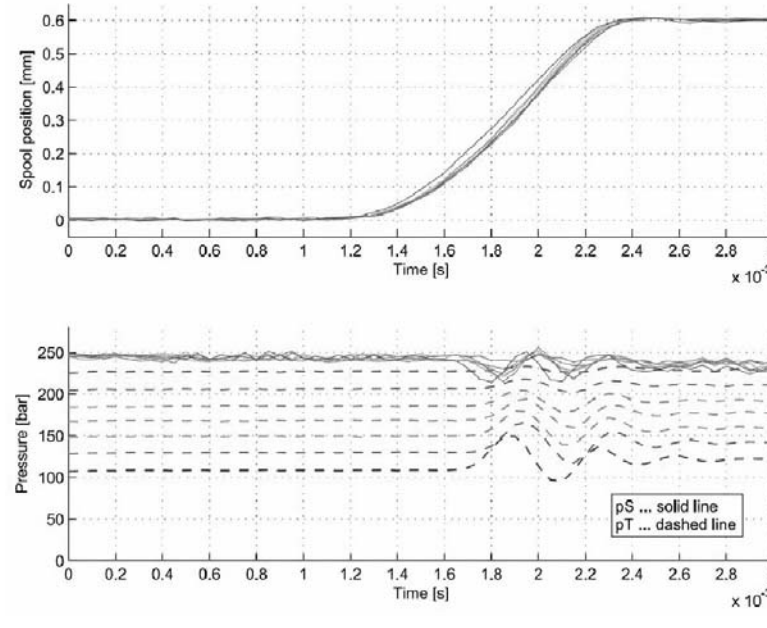

Figure 13: Influence of the pressure difference on the switching time

8 CONCLUSIONS

The aim of the described optimization process was the improvement of a switching valve with respect to robustness to flow forces and costs. The optimization led to an optimal parameter set of spool diameter, spool opening stroke, and number of stages. Additionally, the shape of the sealing lands with respect to flow forces and nominal flow rate was optimized and a proper embodiment design of the valve for simple components which permits a low cost manufacturing has been developed.

ACKNOWLEDGMENTS

The authors gratefully acknowledge the sponsoring of this work by the 'Linz Center of Competence in Mechatronics' in the framework of the Kplus program of the Austrian government. This program is funded by the Austrian government, the province of Upper Austria and the Johannes Kepler University Linz.

REFERENCES

1. **Winkler, B.;** Development of a Fast Low-cost Switching Valve for Big Flow Rates, In the Proceeding of the 3rd FPNI-PhD Symposium on Fluid Power, Terrassa, Spain, 2004

2. **Winkler, B., Mikota, G., Scheidl, R., Manhartsgruber, B.;** Modeling and Simulation of the Elasto-Hydrodynamic Behavior of Sealing Gaps, In the Proceeding of the 1st International Conference on Computational Method in Fluid Power Technology, Melbourne, Australia, 2003.

3. **Scheidl, R., Steiner, B., Winkler, B., Mikota, G.;** Basic problems in fast hydraulic switching valve technology; Proc. Sixth Internat. Conference on Fluid Power Transmission and Control (ICFP05), April 5-8, Hangzhou, 2005.

4. **Krimbacher, N.;** Entwicklung eines Magnetkraftmodells, Internal report Linz Center of Competence in Mechatronics, 2001.

5. **Merrit, H. E.;** Hydraulic Control Systems, John Wiley & Sons, ISBN 0471596175, 1967

6. **Krainz, W.;** Strömungstechnische Untersuchung eines schnell schaltenden Hydraulikventils; Internal report Linz Center of Competence in Mechatronics, July 2005.

7. **Scheidl, R., Manhartsgruber, B. Mikota, G., Winkler, B.;** State of the Art in Hydraulic Switching Control – Components, Systems, Applications, Proc. Ninth Scnadinavian International Conference on Fluid Power (SICFP'05) - Extended Abstract, June 1-3, 2005, Linköping, Sweden

New Concepts and Design of High Response Hydraulic Valves Using Piezo-Technology

Dipl.-Ing. M. Reichert
Univ.-Prof. Dr.-Ing. H. Murrenhoff
Institute for Fluid Power Drives and Controls, RWTH Aachen University, Germany

ABSTRACT

A hydraulic valve is a key component which limits reference response and disturbance reaction of a linear drive. The valve should provide the drive with a sufficient volume flow in order to compensate the compressibility of oil and to achieve a feasible cylinder stroke at high operation frequency. The performance of valve depends primarily on the dynamics of electromechanical actuators which drive the valve spool directly or indirectly. The use of fast and stiff piezoelectric actuators as valve drives offers advantages for high dynamic response of the valve and consequently of the whole hydraulic system.

1. INTRODUCTION

This paper presents two new concepts and design of high response hydraulic valves with use of piezo-technology. These valves will offer advantages for systems in which the dynamics are limited by the valve response. Examples of such systems are material testing machines, hexapod drives in flight and car simulators, punch presses, dynamic regulation of variable displacement pumps, injection moulding machine drives and active vibration damping systems in industrial machinery.

2. VALVE WITH A PIEZO-DRIVEN PILOT STAGE

Due to the small stroke of a piezo-actuator (approx. 0.1% of its length) it can drive a valve of a low volume flow only. This flow would be insufficient to drive a cylinder directly. Nevertheless, the flow is sufficient to build up a pressure in the small chambers of a valve pilot stage. The first concept deals with a use of piezo-driven pilot stage as a hydraulic amplifier for the main stage with a higher nominal flow rate.

2.1 Concept

The pilot stage comprises of four variable hydraulic flow resistors. Each flow resistor is implemented as a piezo-actuated 2/2-way poppet valve. The pilot stage is mounted on a

Power Transmission and Motion Control 2006 Edited by Dr D N Johnston and Professor K A Edge

main stage of a conventional servovalve. The pilot stage pressures P_{AV} and P_{BV} are varied by a continuous displacement of the pilot valves. The spool of the main stage is driven by these pressures in a position control loop.

Figure 1 clarifies the difference between the well known nozzle flapper pilot stage with two variable flow resistors A2 and B2 and two constant flow resistors A1 and B1 (on the left) and the piezo-driven pilot stage with four variable flow resistors (on the right).

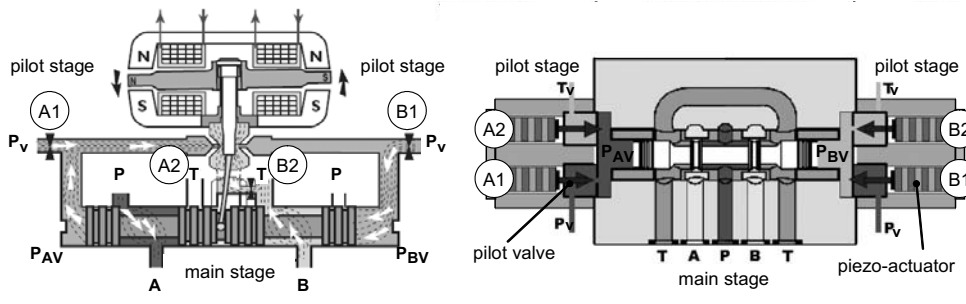

Figure 1 Conventional nozzle flapper pilot stage and piezo-driven pilot stage

One of the operation modes of the pilot stage is driving the pilot valves pairwise in opposite directions. While valves A2 and B1 are closing, valves B2 and A1 are opening and vice versa. By changing the stroke of each pilot valve and the phase lag between them, different operation modes of the pilot stage can be achieved.

The use of the highest hydraulic power amplification of four variable resistors on the one hand and fast piezo-actuators on the other hand will provide the valve with the expected high dynamics.

2.2 Component design

In the following the design of the components and of the whole valve system will be outlined.

2.2.1 Valve dimensioning

A mathematical model of the valve has been set and analyzed in respect of a maximal stroke of the main stage spool as a function of spool diameter, pilot chamber volume and pilot flow (1). Due to a small usable piezo stroke of approx. 30 µm the pilot flow is restricted to 5 l/min at a pilot valve pressure drop of 150 bar. A conventional main stage of the servovalve D765 MOOG with a spool diameter of 6.6 mm has been chosen so that the hydraulic eigenfrequency of the pilot operated valve is more than 2 times as much as the desired maximal operation frequency.

2.2.2 Pilot valve design

Each pilot valve has been designed as a poppet valve. A multilayer piezo-actuator from a diesel injector with a nominal full stroke of 0-40 µm and a driving voltage range of 0-160 V pushes the pilot valve spool and opens the valve. A stiff membrane closes the valve when the actuator contracts.

The valve seat has been designed with respect to minimal flow forces (2). The static pressure forces acting on the spool have been compensated. The reduction of external forces acting on the spool allows the piezo-actuator to expand to a maximal stroke.

Figure 2 presents calculated (ANSYS CFX) and measured volume flow and stationary flow forces.

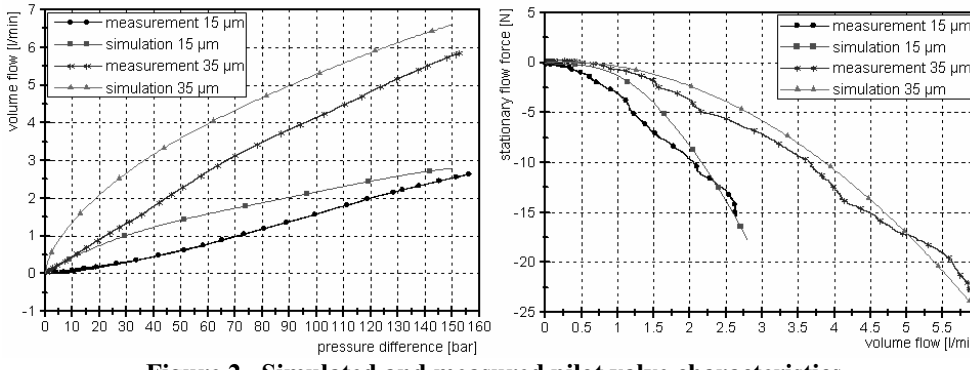

Figure 2 Simulated and measured pilot valve characteristics

2.2.3 Complete valve design

The main challenge of the complete valve design is to keep a pilot chamber volume as small as possible. Consequently, the pilot valves should be arranged close to each other. This is the reason why the piezo-actuators are mounted at the different sides of the pilot stage blocks (Figure 3). The upper pilot valves connect the supply to the pilot chambers. The lower pilot valves connect the pilot chambers to the tank.

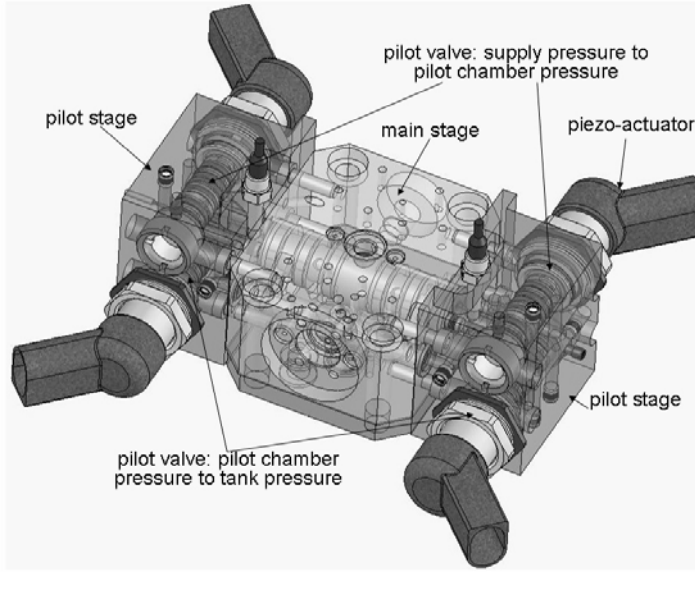

Figure 3 Complete valve design

The position of the main stage spool is measured by an LVDT and is used for a feedback control. Figure 4 shows the valve prototype manufactured at IFAS. The pilot chamber volume is ca. 1.4 cm^3.

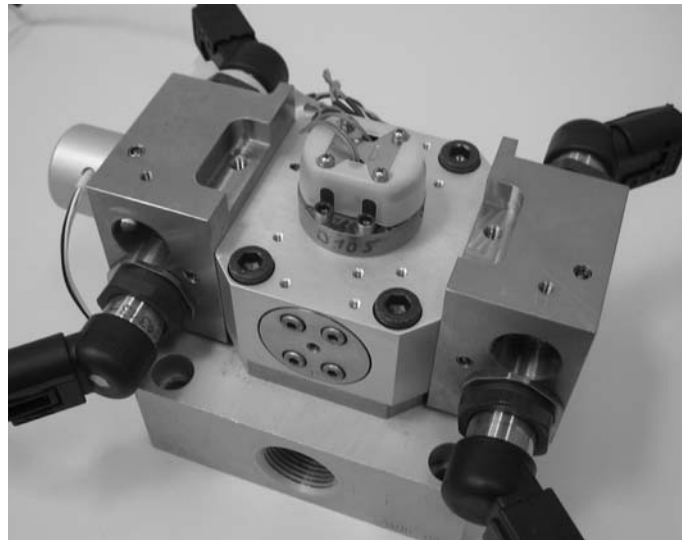

Figure 4 Valve prototype

2.3 System performance

A simulation model has been set for the whole valve (Figure 5). The electrical amplifiers for the piezo-actuators are modelled as PT1-elements. The amplifiers drive the actuators with a current i_P. The current accumulates in the actuator to an electrical charge q_P. This is represented by the integrators in the model. The piezo stroke h is proportional to the charge. A PDT1-controller closes the feedback position control loop.

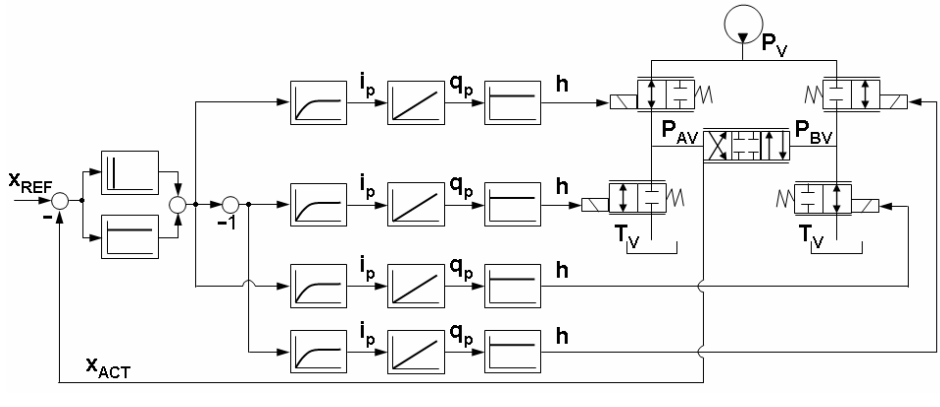

Figure 5 Simulation model of the valve

Figure 6 shows the frequency response of the piezovalve and that of the conventional pilot operated valve (dashed line) of the same size. -3dB-frequency response of the piezovalve is at 330 Hz for 95%-signal. -3dB corresponds here to the main stage spool stroke of ± 0.6 mm and the main flow rate of 38 l/min. The -90°-frequency is beyond 1 kHz. For the simulation a conservative pilot flow of 3.5 l/min has been assumed. The eigenfrequency of the valve at 2125 Hz can be recognized in the figure. It corresponds to an analytically calculated value of 2400 Hz.

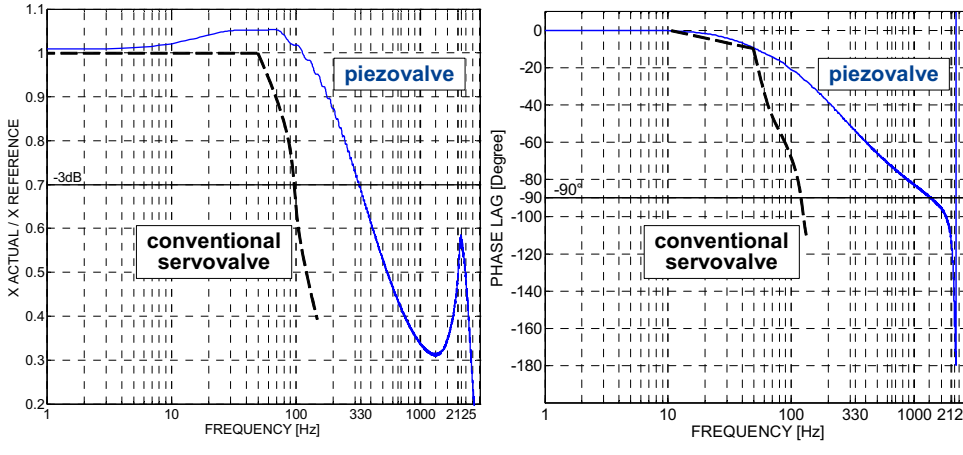

Figure 6 Simulated frequency response

3. HYBRID VALVE

Another new concept of a high response valve implies a modification of a direct driven servovalve (3). In contrast to the conventional actuation of a spool in an immovable sleeve this concept includes the actuation of both the spool and the sleeve. This design allows reacting faster to sudden load variations of a hydraulic cylinder by driving the sleeve in the opposite direction to the spool and thereby enlarging the valve control orifice.

3.1 Concept

Figure 7 shows a linear drive controlled by a hybrid valve and an example of the valve design. Here the spool is driven by a conventional actuator (i.e. proportional magnet, voice coil or permanent magnet linear force motor) and the sleeve is actuated by a piezo-stack.

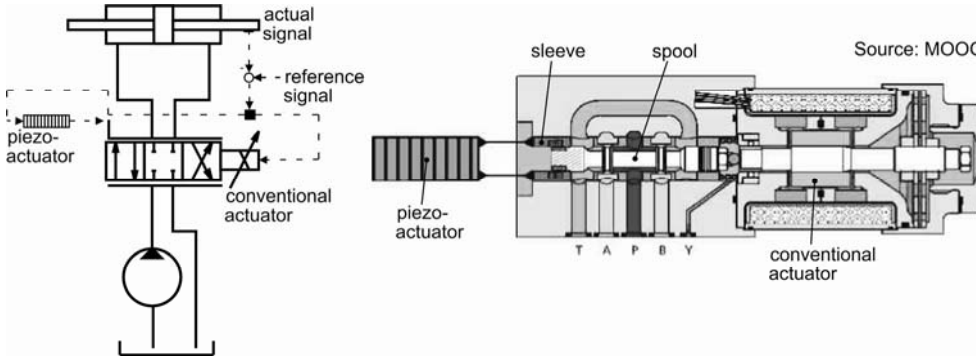

Figure 7 Hybrid valve concept

The cylinder is driven in a position control loop. The position deviation signal is amplified by a controller and transmitted to the actuators. The actuators drive the spool and the sleeve in the opposite directions. This results in a faster opening of the control orifice within a small signal operation till the piezo-actuator achieves the full stroke. Both the spool and the sleeve are driven in a position closed loop in order to avoid a drift of a conventional actuator, to compensate a hysteresis of a piezo-actuator and to hold a required position at changing external forces (i.e. flow forces, friction forces).

Due to the lower mass of the spool it can be advantageous to drive the spool with a piezo-actuator and to actuate a sleeve with a conventional valve drive. Generally, the force of the piezo-actuator reduces with an increasing stroke. External forces acting on a piezo-actuator should be considered as they cause an offset of the stroke or reduce it.

3.2 System performance

In the following a linear drive controlled by the hybrid valve will be considered in respect of reference response and disturbance reaction. Firstly, a curve family of hydraulic amplification of the valve will be derived and will be compared to that of a conventional valve design. Secondly, a simulation model will be introduced. Finally, the results of a simulation will be discussed.

3.2.1 Valve hydraulic amplification

A conventional system of two control edges with a moveable spool and a stable sleeve is considered (4). The system has a symmetrical underlap y_0, supply pressure p_0, tank pressure $p_T=0$, working pressure p_A and working volume flow $Q_A=Q_1-Q_2$. It is assumed that the spool travel is smaller than the underlap size $y \leq |y_0|$ (Figure 8).

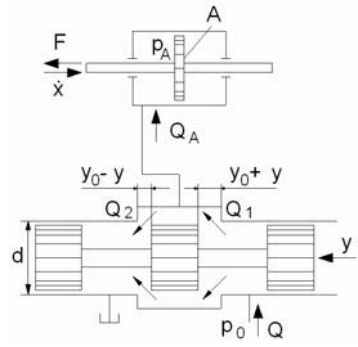

Figure 8 Two control edge hydraulic system (spool is moveable, sleeve is stable)

Hydraulic amplification of this system is:

$$\frac{Q_A}{Q_0} = \frac{y}{y_0} + \left|\frac{y}{y_0}\right| \sqrt{2\left(1 - \frac{p_A}{p_0}\right)} - \frac{y}{y_0} \sqrt{2\frac{p_A}{p_0}}$$

with a volume flow Q_0 at the middle position of the spool:

$$Q_0 = B y_0 \sqrt{\frac{p_0}{2}}$$

Figure 9 shows specific working flow and specific working pressure as a function of specific spool position.

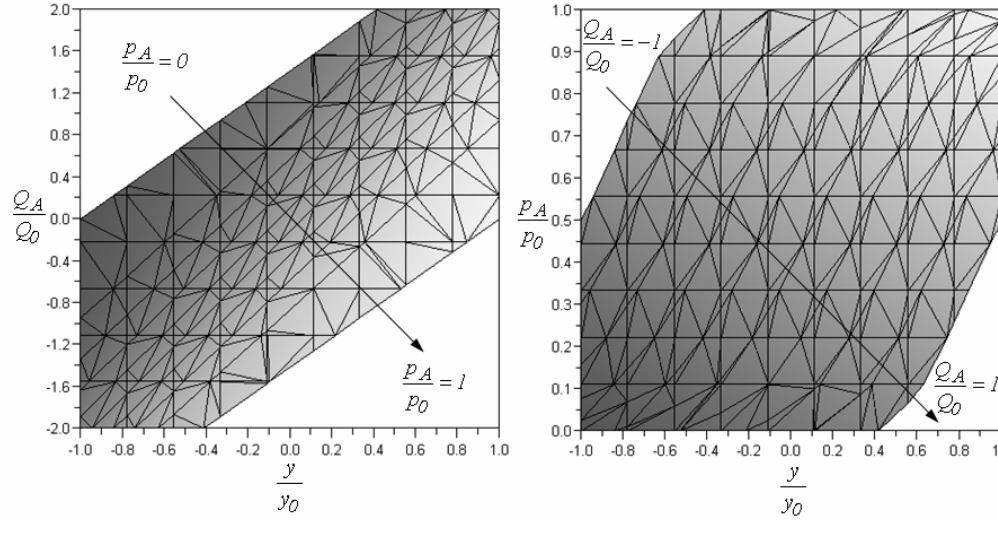

Figure 9 Amplification curve family of a two control edge system (spool is moveable, sleeve is stable)

In case of a moveable sleeve the superposition of the deflections should be considered (Figure 10).

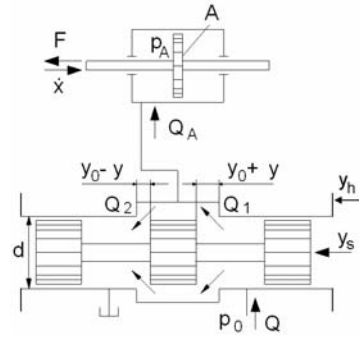

Figure 10 Two control edge hydraulic system (spool and sleeve are moveable)

Assuming the position of the spool, driven by a piezo-actuator, according to: $y_S = \hat{y}_S \sin(\omega t)$ and the position of the sleeve, driven by a conventional actuator, according to $y_h = -\hat{y}_h \sin(\omega t)$ the hydraulic amplification can be derived as:

$$\frac{Q_A}{Q_0} = \frac{C_d}{C_{dTM}} + (k+1)\frac{y_h}{y_0}\left|\sqrt{2\frac{C_d}{C_{dTM}} - \frac{p_A}{p_0}}\right| - \frac{C_d}{C_{dTM}} - (k+1)\frac{y_h}{y_0}\left|\sqrt{2\frac{p_A}{p_0}}\right|$$

with

$$k = \frac{\hat{y}_s}{\hat{y}_h}$$

As the spool stroke (approx. ± 20 µm) is much less than the sleeve stroke (approx. ± 1 mm), the variable k has its maximum when both of the amplitudes are equal. Figure 11 shows specific working flow and specific working pressure as a function of specific sleeve position for the case k=1.

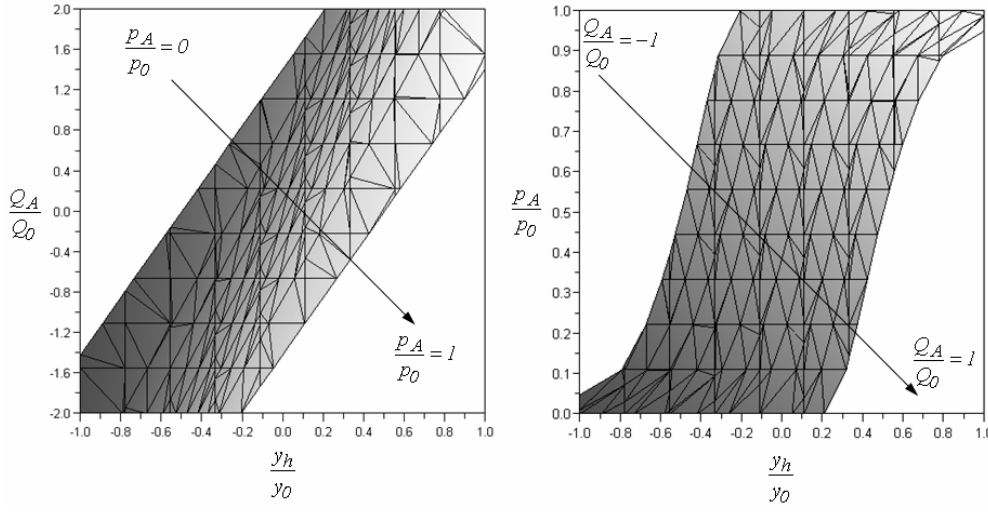

Figure 11 Amplification curve family of a two control edge system (spool and sleeve are movable)

Comparing figures 9 and 11, it can be seen that the volume flow amplification and the pressure amplification (i.e. slope of the curves) are higher for the hybrid valve as far as the stroke of the sleeve and the stroke of the spool are equal. This clarifies the fact that the hybrid valve is efficient in the small signal operation when the stroke of a conventional actuator is of the same size as that of the piezo-actuator.

A calculation shows that the maximal curve slope for a hybrid valve is twice as much as for a conventional valve. The same relationship can be obtained considering a four control edge system. It can thus be concluded that the flow-stroke amplification V_{Qy} and the pressure-stroke amplification V_{py} of the hybrid valve are twice as much as those for a conventional valve within a small signal operation.

3.2.2 Reference response of the cylinder

A simulation model has been made with a simulation tool for hydraulic and pneumatic systems DSHplus (5). The model consists of an equal area cylinder, hybrid valve, pressure supply and controller. The hybrid valve has been modelled on the basis of direct driven control valve D633 by MOOG. Both the sleeve and the spool follow the command signal of the linear force motor and the piezo-actuator respectively as PT2-elements. The maximum velocities of the actuators are restricted to feasible values. Table 1 gives a review of the parameters of the modeled components.

Table 1 Simulation model components

Hydraulic cylinder		on the basis of CGS 280, Bosch Rexroth AG	
piston rod diameter	50 mm	maximal cylinder load due to acceleration, friction	4.3 kN
piston diameter	55 mm	additional sudden load step	1.5 kN
maximal stroke	± 200 mm	load resonant frequency	12 Hz
nominal force	25 kN	cylinder damping	0.28
cylinder weight load	1000 kg		
Hybrid valve		on the basis of D633, MOOG, 4/3-direct driven control valve	
nominal flow	40 l/min at valve pressure drop 70 bar	spool drive	preloaded piezo-actuator, 0…160 V
sleeve drive	permanent magnet linear force motor, ± 10 V	spool stroke	± 20 µm
sleeve stroke	± 1 mm	spool dynamics	approx. 10 kHz
sleeve dynamics	60 Hz at -90°-frequency for 90%-signal		
Supply pressure		135 bar	

The system has been designed for an optimal efficiency when a maximal load pressure drop of the cylinder is 2/3 of the supply pressure. Figure 12 shows a simulated response of the cylinder controlled by a conventional valve (on the left) and by the hybrid valve (on the right) to a rectangular reference signal with an amplitude of 100 mm. A simple P-controller is used in both cases.

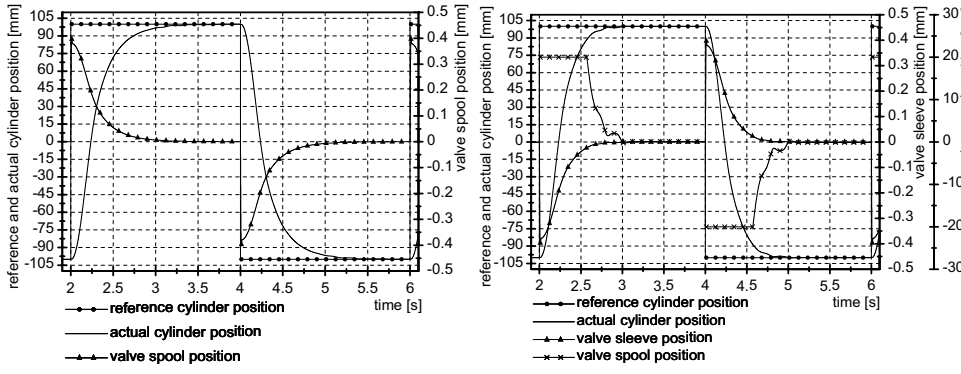

Figure 12 Reference response of the cylinder controlled by a conventional valve (on the left) and the hybrid valve (on the right)

The comparison of the systems shows that the cylinder controlled by the hybrid valve reaches 90% of reference signal step (200 mm) at approx. 15% faster than the one controlled by a conventional valve (Figure 13).

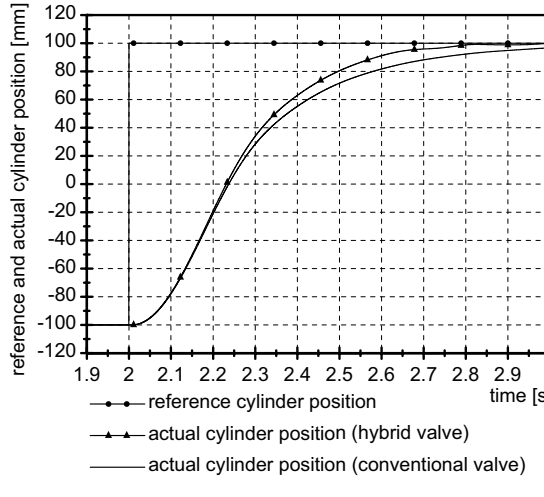

Figure 13 Comparison of reference responses

3.2.3 Disturbance reaction of the cylinder

A disturbance reaction of a hydraulic cylinder is essential when a sudden external load acts on it. The compressibility of the oil in the cylinder chambers leads to a position deviation under load. A valve should provide the drive with a compensating flow as quickly as possible.

Figure 14 shows a simplified model of a cylinder with a position control loop (4). Here the valve is represented as a PT2-element.

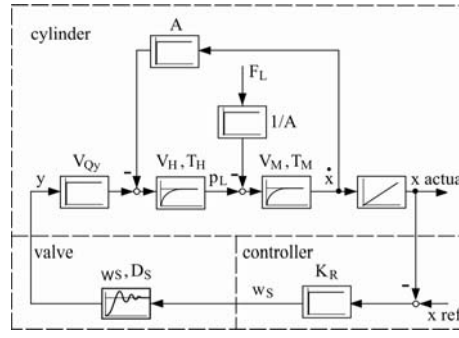

Figure 14 Cylinder model

If an internal leakage of the cylinder is neglected the cylinder stiffness under load is given as:

$$L = -\frac{dF_L}{dx} = A \cdot K_R \cdot V_{py}$$

with V_{py} as a pressure-stroke amplification of the valve. It has been shown before that the hybrid valve has a higher V_{py} than a conventional valve. Figure 15 shows a simulated response of the cylinder controlled by a conventional valve (on the left) and by the hybrid valve (on the right) to a load step of 1.5 kN. A simple P-controller is used in both cases.

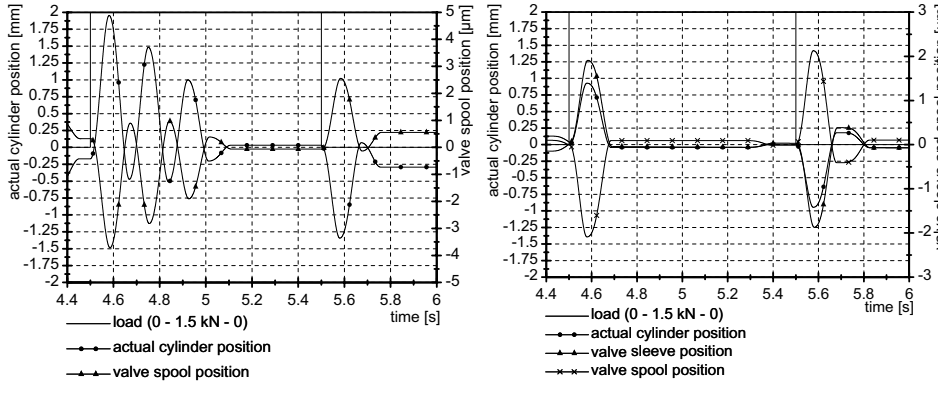

Figure 15 Disturbance response of the cylinder controlled by a conventional valve (on the left) and the hybrid valve (on the right)

It can be seen that a higher pressure-stroke amplification of the hybrid valve results in an increased cylinder stiffness under load. The deflection of the cylinder due to the load step can be reduced at 50%. There is no cylinder oscillation after the load step in case of an appropriate adjustment of the P-controller.

3.3 Design challenges

In the following some challenges of the hardware and control design for a proper performance of the hybrid valve will be outlined.

3.3.1 Challenges in hardware design

The hybrid valve concept implies two moving parts – the sleeve and the spool. The sleeve should be fitted with a spool at the inner diameter and with a valve body at the outer diameter. In order to limit friction forces an exact guidance of the both parts is essential. Furthermore, a mechanical adjustment should be integrated in order to position the piezo-actuated spool in a hydraulic zero point of the valve. The valve should posses a minimal underlap between the sleeve and spool control edges. An overlap would reduce the usable piezo-actuator stroke. In addition, both the sleeve and the spool should be optimized with respect to flow forces and static pressure forces.

3.3.2 Challenges in control design

The main challenge in control design is a generation of two input signals for a conventional actuator and a piezo-actuator of the valve from a single control deviation signal of the cylinder position. The use of two independent P-controllers for driving the sleeve and the spool in the opposite directions showed that the control loops can bring each other to oscillation. The reason for this is unequal eigenfrequencies of the both actuators. Besides, the piezo-actuator should be driven in zero position after each valve response. It is necessary in order to use the full piezo stroke for the next control deviation. During the transfer of the piezo-actuator (i.e. of the spool) in its zero position the sleeve should follow the spool in order to preserve the currently required valve opening.

4. CONCLUSION

In the light of growing requirements in the dynamics of hydraulic linear drives the response of a control valve should be improved. The use of modern and relatively low-priced piezo-actuators from the automotive industry makes the development of these valves possible. Two different concepts for new high response valves have been presented, analyzed and simulated. Although the stroke of the piezo-actuator is very small it is possible to control the volume flow, which is sufficient to drive a main stage of a valve with a higher nominal flow rate or to increase a stiffness of a cylinder when it is subject to a sudden load step.

REFERENCE LIST

(1) Reichert, M.: Entwicklung einer piezobetriebener Vorsteuerstufe zum Aufbau hochdynamischer hydraulischer Ventile, 1. Rexroth Doktoranden Kolloquium, March 2005

(2) Bauer, F., Reichert, M.: The use of piezo-actuators for high dynamic servovalves, O+P Zeitschrift für Fluidtechnik, June 2005

(3) Deutsches Patent 102 41 977.9-14, Hochdynamische Servo-Ventilsteuervorrichtung

(4) Murrenhoff, H.: Servohydraulik, RWTH Aachen, Shaker Verlag, 2002

(5) http://www.fluidon.com/

Return to Contents

A Novel Seat Valve with Reduced Axial Forces

Timo Lauttamus*, Matti Linjama*, Matti Nurmia† and Matti Vilenius*

*Institute of Hydraulics and Automation
Tampere University of Technology

†Department of Physics
University of Jyväskylä

ABSTRACT

Seat type valves have many benefits but because of unbalanced poppet a big force is required to keep the valve open. Also, they tend to close spontaneously when the pressure difference over the valve increases. Some research has been made to compensate the forces in seat valves, but they have required internal seals which increase friction and make valves less durable. A different approach to compensate static forces is studied in this paper. In this simple valve full pressure forces are present in closed position, but vanish when valve starts to open. Experimental results show that the novel structure has great potential.

Keywords: seat valve, force compensation

1. INTRODUCTION

In category of ON/OFF-valves the benefits of direct operated seat type structure are obvious. They are simple, reliable and insensitive to contamination and they have very small leak compared to spool structure valves. Also their function does not depend from pressure as in pilot operated valves. The major drawback of the concept is the unbalanced poppet that leads to the need of continuous control current to keep the valve open and great work required for opening. Because of continuous current, solenoid actuator has to be big in order to dissipate the generated heat, which increases the size and volume of the whole valve. Heat from continuous use also restricts the maximum solenoid current, which decreases the available maximum force. These features together cause the typical flaws of

Power Transmission and Motion Control 2006 Edited by Dr D N Johnston and Professor K A Edge

seat type valves: opening requires a lot of work and they tend to close spontaneously when the pressure differential over the valve increases.

The principle of a typical normally closed seat type solenoid valve is described in Fig. 1a. The construction usually includes a return spring that closes the valve with force F_k. A solenoid actuator is used to open the valve by pulling the poppet against the spring with a force F_s. A typical force curve and opening work are shown in Fig. 1b. When the valve is closed, a force created by pressure differential ($\Delta p = p_{in} - p_{out}$) and area of sealing A presses the poppet tightly to the seat (Fig. 1b, *1*). When the valve is opened, pressure drops in between the shutting parts due to change of speed and flow direction of fluid. This causes a pressure differential which affects to the corresponding area creating a closing force F_p. Now it can be seen that the valve stays open if $F_s > F_p + F_k$ (the effect of flow forces caused by momentum of flow are neglected). As the distance between the poppet and the seat increases, the force F_p slowly goes down until the poppet is so far from the seat that there is no pressure differential over it. The increase of pressure differential however increases the force F_p and eventually the sum of the closing forces becomes greater than the sum of the opening forces and the valve is closed despite of the energy driven into the coil. Typically maximum distance x_{max} between the poppet and the seat is also short and the force F_p can never reach zero, as shown in Fig 1b, which leads to constant need of external energy to keep the valve open (Fig. 1b, *2*).

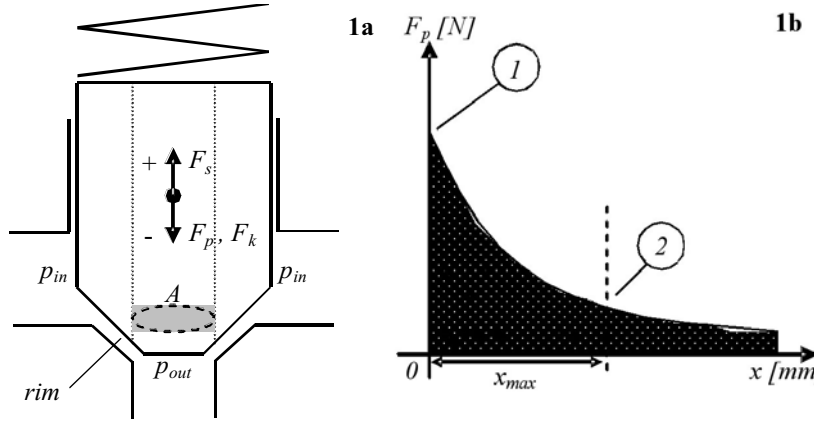

Figure 1 Principle and force curve of typical seat type valve

If the described phenomenon can be overcome, it is possible to develop a valve that maintains its state despite of the pressure differential and requires less energy to open. This leads to faster response and lower energy consumption. Some research has already been done to solve the primary problem of a seat valve. A popular approach has been use of combined spool-seat-structure with mushroom shaped poppet illustrated in Fig. 2 [1], [2], [3], [4], [5], [6]. The function principle of the structure is as follows. Pressure balance over the poppet is achieved by conducting the internal pressure p_1 to both sides of poppet and directing the inflow via midsection of poppet. This leads to full pressure compensation when the valve is closed. As the valve opens, pressure on both ends of the poppet is the same, but in restriction area *a* pressure drops as speed and direction of flow changes which

causes a pressure differential that tends to close the valve. This force is compensated with a brim-like structure *b* which is affected by an impulse force of the flow hitting brims surface. The only drawback of the idea is that a sealing is required to separate the pressure volumes. The sealing creates friction which slows the valve down. However, the structure is simple and it has been used in some commercially available valves such as Hydac WS08W-01 [7] and FMW 3NC [6].

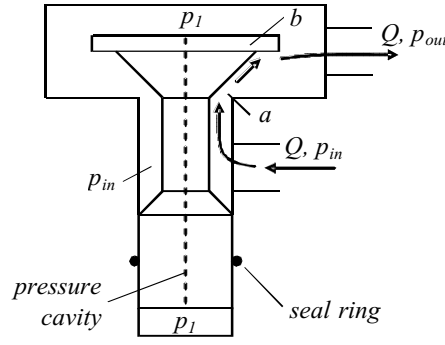

Figure 2 Principle of mushroom shaped poppet

It is not certain who was the first one to use the idea, but one of the first reports in which the idea is implemented is an article by Engelsdorf and Dunken in 1980 [1]. Also Yousong *et al.* have studied the mushroom shaped poppet and they achieved in compensating 80 % of axial force [2]. The structure makes it possible to manufacture fast valves as FMW 3NC, which has stationary poppet and moving sleeve. Wennmacher studied the valve in his dissertation and measured response times of 1,5 ms [6].

This approach of compensating axial forces in seat valves has been studied widely and it has even been commercially adopted. However the structure requires dynamic seal which causes friction and may be unreliable. Next an idea of force compensation based on series of restriction chokes is discussed. By our knowledge a series of restrictions has not been used before in order to compensate axial forces affecting to spool or poppet of a hydraulic valve.

2. OPERATION PRINCIPLE OF FORCE COMPENSATION

Compensation of axial forces in this novel valve is based on series of three restrictions between valve poppet and seat equipped with steps. The original idea for minimization of opening work is by emeritus professor Matti Nurmia from the University of Jyväskylä and focuses in decreasing response time. The schematic of the valve is shown in Fig. 3 and the idea is as follows. When the valve is closed, it is sealed by the poppet and the rim of the inmost step of the seat. The pressure p_{in} is conducted past the other steps, so in this point the force keeping the valve closed is the same as in normal valve discussed earlier. When the valve is opened, the restrictions lower the pressure so that pressure above the poppet p_2 minimizes the closing force F_p. Now with suitable geometry it is possible to implement

such a valve that after it has been opened a bit, the resultant of the forces affecting to the poppet is very small. This leads to low energy consumption as work required for opening, which equals the area below the force curve (Fig. 2b), is small and the valve may stay in open state without external energy. Low energy consumption leads to small heat generation, which allows the valve to be small. Small opening work also suggests that the novel valve may be very fast.

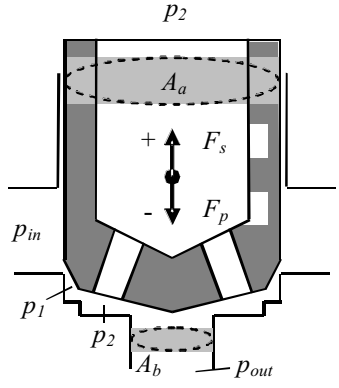

Figure 2 a Cross section of the poppet

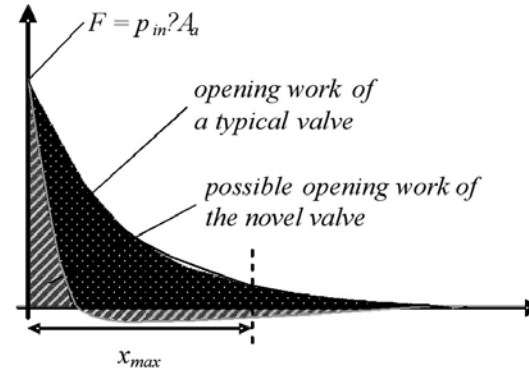

Figure 2 b Force graph

3. DEVELOPMENT OF THE VALVE

Development of the valve begins by defining the objectives and continues with theoretical study of restriction chokes and inside geometry of the valve. The last touches will be put to the geometry by CFD calculations. The primary objective of the process is to develop a semi-micro valve with a minimal required opening force by using a series of restrictor chokes. The secondary objective is to do this without losing the flow capacity.

3.1 Theoretical Study

Triple restriction between the valve poppet and the seat can be modeled by equation of turbulent flow (Eq. 1). From equation of turbulent flow the flow coefficient _, the area A, the square root of 2 and _ can be combined as single coefficient K (Eq. 2). Then it can be assumed, that the flow through all restrictions is the same, as in Eq. 3.

$$Q = \mu \cdot A \cdot \sqrt{\frac{2 \cdot (p_a - p_b)}{\rho}} \tag{1}$$

$$K_i = \mu_i \cdot A_i \cdot \sqrt{\frac{2}{\rho}} \tag{2}$$

$$Q = K_1 \cdot \sqrt{p_{in} - p_1} = K_2 \cdot \sqrt{p_1 - p_2} = K_3 \cdot \sqrt{p_2 - p_{out}} \tag{3}$$

Now the volume flow and pressures p_1 and p_2 can be solved from Eq. 3 as function of inflow and outflow pressure, if the flow areas A_i are known. This leads to describing the physics of the valve with equations 4, 5 and 6.

$$Q(p_{in}, p_{out}) = K_1 \cdot \sqrt{p_{in} - \frac{p_{in} \cdot K_1^2 + \frac{p_{in} \cdot K_1^2 \cdot K_2^2 + p_{out} \cdot K_2^2 \cdot K_3^2 + p_{out} \cdot K_1^2 \cdot K_3^2}{K_1^2 \cdot K_2^2 + K_2^2 \cdot K_3^2 + K_1^2 \cdot K_3^2} \cdot K_2^2}{K_1^2 + K_2^2}} \tag{4}$$

$$p_2 = \frac{p_{in} \cdot K_1^2 \cdot K_2^2 + p_{out} \cdot K_2^2 \cdot K_3^2 + p_{out} \cdot K_1^2 \cdot K_3^2}{K_1^2 \cdot K_2^2 + K_2^2 \cdot K_3^2 + K_1^2 \cdot K_3^2} \tag{5}$$

$$p_1 = \frac{p_{in} \cdot K_1^2 + p_2 \cdot K_2^2}{K_1^2 + K_2^2} \tag{6}$$

Geometry and areas required in previous functions can be solved with trigonometry. Because the poppet is dual-cone-shaped and restrictions are formed between it and the steps of the seat, flow cross-sections of each restriction are shaped like a truncated cone. Therefore flow cross-section areas can be calculated with Eq. 7.

$$A_i = \pi \cdot (2 \cdot r_i - \frac{x}{2} \cdot \sin(2\alpha_i)) \cdot x \cdot \sin\alpha_i \tag{7}$$

The areas under pressure can be solved from the geometry of valve. The following assumptions are made: the supply pressure p_{in} does not interact with the structure, pressure p_1 affects axially to the circular area of the poppet between the outmost and the middle step of the seat, pressure p_2 affects axially to the area between the inmost and the middle step and to the whole upside area of the poppet, tank pressure p_{out} affects axially to the area of the flow cavity of the valve. The preliminary dimensioning is based on this theoretical study.

3.2 CFD calculations

The next step in developing process was finalizing the geometry using modern finite element method based CFD-software. The software used was COMSOL Multiphysics 3.2 and it was used in incompressible Navier-Stokes-mode. Also adaptive mesh refinement was used with original settings of the software. Simulations were conducted in series of operation points which led to several models and representing the results as curves consisting of points. The simulated flow was not fully laminar or turbulent, but something in between, so additional damping was utilized by using streamlined diffusion, which increased damping in the direction of the flow. The models were generated with CAD and then imported to Multiphysics in which they were turned into 2D axial symmetry geometry. In each simulation case the distance between the poppet and the seat was varied with step of 0,025 mm, when the distance was less than 0,40 mm and else with 0,05 mm step. Density and kinematical viscosity of the fluid were set to 870 kg/m^3 and 0,04 Pa_s, which corresponded with the typical VG 46 oil used in laboratory in temperature of 40 ºC.

The schematic of the geometry and refined mesh are shown in Fig. 3a, in which the pressure cavities are also seen (arrow). As a result of simulation are field diagrams of flow speed and pressure (Fig. 3b) from which the force affecting the poppet and volume flow can be calculated. The curves are shown together with the experimental results in chapter 4.4.

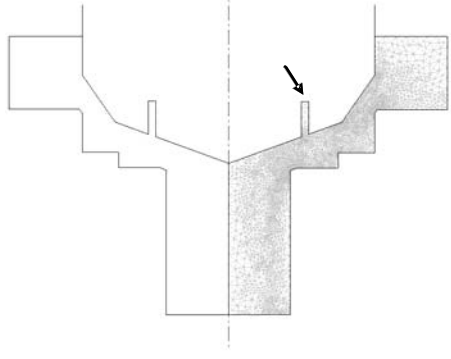

Figure 3 a Schematic of the geometry and the mesh

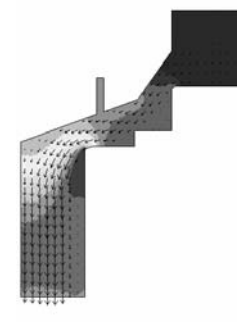

Figure 3b Typical pressure field

To compare the characteristics of the novel valve and a typical valve some additional simulations were also conducted. The typical geometry included a poppet with a diameter of 2,2 mm, a cone angle of 70º and a seat with a similar flow cavity as in the novel valve, but without the stepping restrictions. Also these results are represented in chapter 4.4 with the experimental results.

3.3 Prototype

After dimensioning, a prototype and a test platform were built. Dimensions of the poppet and the seat are illustrated in Fig. 4. Because the position of the poppet and the force affecting it were to be measured, a rod was attached to the poppet. The rod altered the structure so, that total force could not be measured directly. However, opening force affecting to the poppet (F_{op}) could be measured as well as the pressure upon the poppet (p_2). With this data it was possible to calculate the total force.

To make sure that force measurement could be done, clearances and concentricity of the rod and the rod cavity of the test platform were studied closely. It was noted that the clearance between the rod and the cavity had to be small enough to keep the pressure inside the platform, but also wide enough to make sure that the rod did not stick to the wall. As diameter of the pressure cavities of the poppet was 0,4 mm, it was calculated that clearance between the rod and its cavity should be less than 30 _m. This led to production tolerance h7/H7, which means maximum clearance of 24 _m for a hole with diameter of 4,0 mm. To ensure low friction, the poppet was made of silver steel (DIN 115CrV3) and the seat and the sliding part of the test platform were made of brass.

The preliminary study and early CFD-simulations had suggested a poppet movement range of 0,4 mm, however during the laboratory measurements it was discovered that movement range should be increased and later a range of 0,6 mm was adopted.

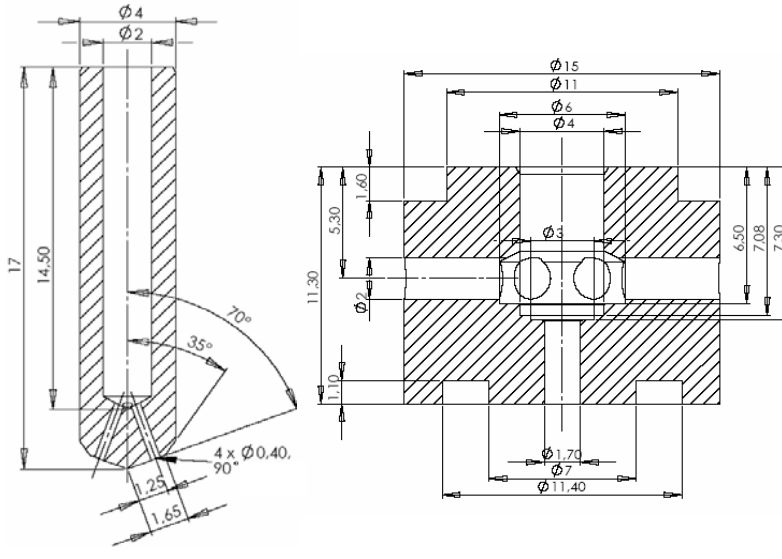

Figure 4 Dimensions of the poppet and seat

4. STATIC PERFORMANCE OF THE DEVELOPED VALVE

After the test platform had been manufactured, the static characteristics of the valve were studied by laboratory measurements. Results include force and flow as function of poppet distance with different supply pressures and pressure differentials. Also a graph with volume flow as function of pressure differential with static poppet distance and supply pressure is presented.

4.1 Measurement System

The hydraulic circuit diagram of the measurement system is shown in Fig. 5a. Its power unit included a variable displacement pump, a return filter, a cooling circuit and a tank. The primary measurement circuit consisted of a pressure filter, an accumulator (which dampened the vibrations in supply pressure), pressure relief valve, test platform and adjustable restriction valve. Hydraulic oil used in the system was Shell Tellus T 46. Pressures were measured by three transducers, the opening force affecting to the poppet was measured via the rod by a force transducer and the volume flow was measured by a gear type flow meter. The poppet's position was measured by a dial gauge, whose head was in contact with a planar surface of a metal sheet attached to the rod. The test platform is illustrated in Fig. 5b.

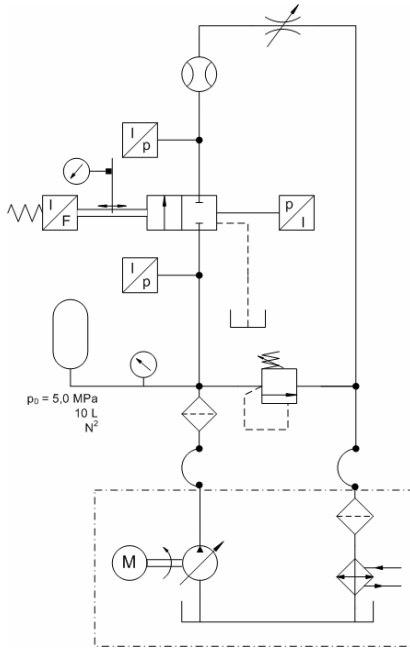

Figure 5a Hydraulic circuit diagram of the measurement system

Figure 5b Test platform

Measured signals were captured by PC and a dSPACE DS1102 controller board which was programmed with Matlab and Simulink software.

Experiments were conducted with three supply pressures (10,0 MPa, 14,0 MPa, 21,0 MPa) and three or two pressure differentials (1,0 MPa, 5,0 MPa, 10,0 MPa / 9,5 MPa). Each measurement was repeated three times to eliminate random errors.

4.2 Measurement Methods

Before the measurements, transducers were calibrated and a Simulink chart was created to scale and name the signals for dSPACE. Measurement conditions were also standardized. The supply pressure was set by the pressure regulator of the pump and the pressure relief valve in measurement circuit. The pressure differential over the test platform was set by the restrictor valve. Pressure range was defined as 3% from the nominal value. Before starting the measurements, hydraulic oil was preheated by pumping it through the pressure relief valve until the tank temperature display showed 40 ºC.

The measurements were conducted as operational points from which data files were captured by dSPACE controller. Each file contained one second of data with sampling period of 1 ms. Captured signals were supply pressure p_{in}, outflow pressure p_{out}, internal pressure of the test platform p_2, opening force F_{op}, volume flow Q and position of the poppet x. The position x was varied similarly to CFD simulations.

Capturing operational points included a certain protocol. First the position of the poppet was set by an adjustment nut and the dial gauge. Then the supply pressure was checked and

the pressure differential was set by the restrictor valve. Then, to eliminate sticking, the rod was rotated 45º back and forth several times. After that the system was left to stabilize for at least 15 seconds and the pressures and position were checked again and. If their values had not changed, the operational point was captured by dSPACE.

In experiments the poppet was always moved from its extreme position to the closed position, because defining of the poppet position was difficult when the valve was nearly closed.

4.3 Analytical Methods

Operational points were processed point by point. First captured signals were filtered with a function that dampened single peaks from them. It processed the signal in groups of five samples proceeding one sample at time and creating a new enhanced signal. From each original sample groups the highest and the lowest value were neglected and a mean of the remaining three samples was calculated. This mean was then relocated to the new signal array with the same index as the third sample of the processed sample group. The method included no interaction between the enhanced and the original signal. After filtering, the operation point was presented as mean of signals.

The total force affecting to the poppet could not be measured directly, but it had to be calculated as in Eq. 8. Also a closing force affecting to the poppet of the valve in closed state was calculated as in Eq. 9 and marked as F_*.

$$F_{tot} = F_{op} + F_{dg} + F_r - F_{cl} \tag{8}$$

$$F_* = A_a \cdot p_{in} \tag{9}$$

Because measurements were conducted from open state to the closed state there was a random offset in the position of the poppet. This was compensated by observing the volume flow and pinpointing the position in which the flow ceased and then adding to each position signal a corresponding offset so, that when the flow was zero, also the position was zero.

Because each measurement was conducted at three times, finally a mean of three graphs was calculated to represent the results as a single graph.

4.4 Experimental Results

The experimental results are shown as pairs in following figures. Each pair consists of a graph representing the total force and a graph representing the volume flow as a function of x. The first experiments were conducted with poppet movement range of 0,4 mm as described in chapter 4.2, but the results showed that adequate range should be 0,6 mm. That is why the movement range in 10,0 MPa measurements is shorter than in the others.

In graphs, force affecting to the poppet in closed state is marked as F_*. Theoretical curves of the typical seat valve are printed with dash line and noted as “Typ.” Simulated curves of the novel valve are printed with solid line and noted as “Sim.” Measured curves are printed with dot, x or + with dotted line and noted as “Mea.” It is important to note that the first points of each measured force curve are not reliable, because the point in which the contact

between the poppet and the seat happened is not completely determined. However, the later points are reliable.

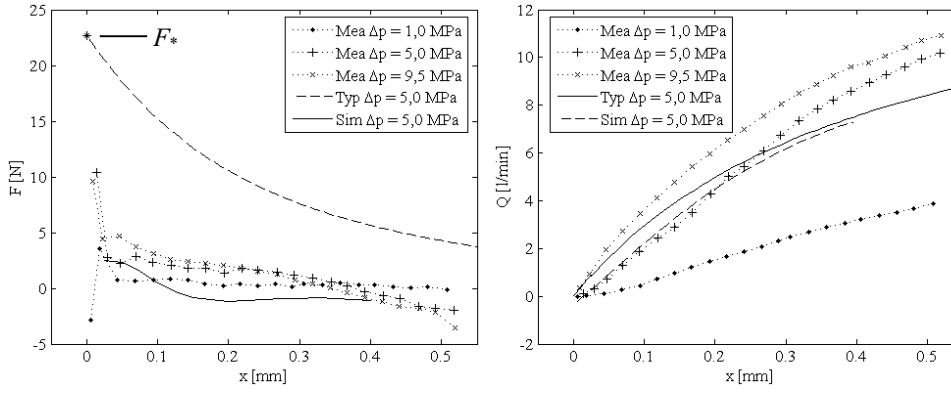

Figure 6 p_{in} = 10,0 MPa

Figure 6 presents the results for supply pressure of 10,0 MPa. It can be seen that the measured total force is minimized right after the valve is opened. Despite of the short movement range of the poppet, force reaches zero level as the distance between the shutting parts increases. The first points of measured force curves are not fully reliable, because due to measurement arrangements the closing point of the valve was not totally predictable, but it had to be determined while analyzing the data.

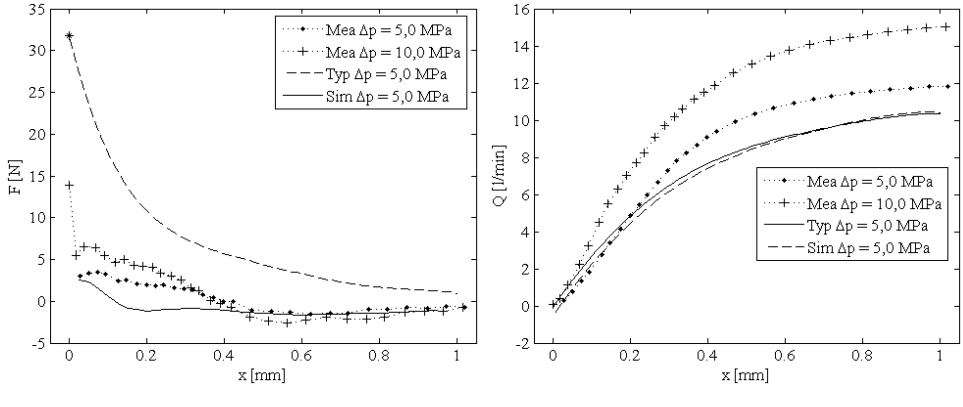

Figure 7 p_{in} = 14,0 MPa

Figure 7 represents the results with supply pressure of 14,0 MPa. Trend of the total force is the same as in previous figure, but because of longer movement the behavior of the force can be better studied. It can be seen that measured total force correlates moderately with the simulated force (solid line) and before all the difference between the simulated axial force of a typical valve is greater than the measured force. Flow graph shows that increasing movement range from 0,4 mm to 0,6 mm is justified.

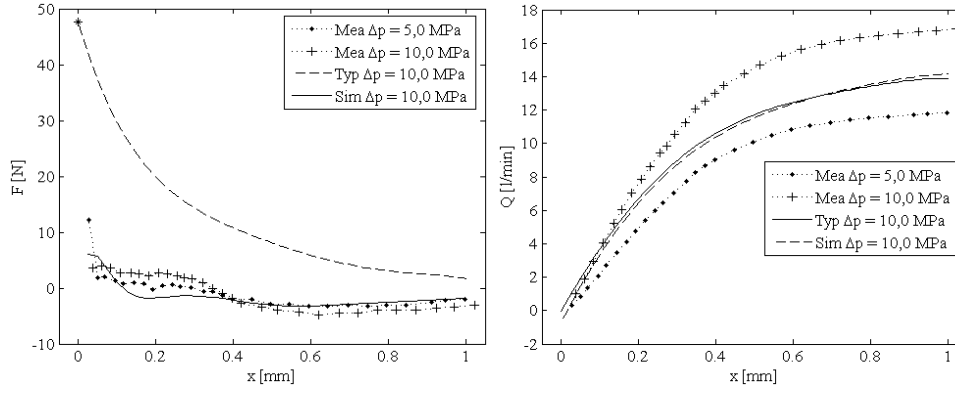

Figure 8 p_{in} = 21,0 MPa

Results with supply pressure of 21,0 MPa (Fig. 8) supports the assumption that developed valve works as planned.

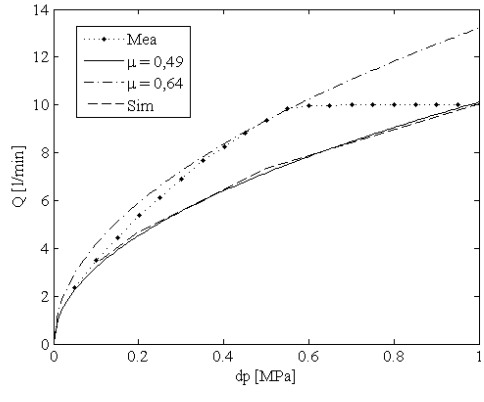

Figure 9 Q(_p), p_{in} = 10,0 MPa, x = 0,4 mm

Volume flow as function of pressure differential (Fig. 9) was measured only with supply pressure of 10,0 MPa and with poppet distance of 0,4 mm. The graph is augmented by two curves of turbulent flow with different flow coefficient _ and simulated volume flow to show the difference between simulated and measured results. Graph also shows the saturation of the flow as cavitation occurs, when the pressure differential is 5,5 MPa.

4.5 Inaccuracy of the Results

The maximum inaccuracy of the results can be calculated by partial differentiating the Eq. 10 and multiplying each differential with corresponding inaccuracy as shown in Eq. 11 in which F_i represents measured quantity whose inaccuracy is Y_e.

$$dF_{tot} = \sum_{i=1}^{n} \left(\frac{\partial F_{tot}}{\partial F_i}\right) \cdot Y_e \qquad (10)$$

By placing the variables, maximum inaccuracy of the total force can be represented in following way. The inaccuracy of the mass m_e appears twice, because masses were measured in two parts.

$$dF_{tot} = \left|\frac{\partial F_{tot}}{\partial F_{mea}} \cdot f_e\right| + \left|\frac{\partial F_{tot}}{\partial m_{dg}} \cdot m_e\right| + \left|\frac{\partial F_{tot}}{\partial m_r} \cdot m_e\right| + \left|\frac{\partial F_{tot}}{\partial A_a} \cdot a_{a\_e}\right| + \left|\frac{\partial F_{tot}}{\partial p_2} \cdot p_{2\_e}\right| \qquad (11)$$

The calculated maximum inaccuracy of force F_{tot} depends upon pressure p_2, but dependence is negligible. Therefore maximum inaccuracy of the total force dF_{tot} equals ± 1,9 N. The maximum inaccuracy of volume flow can be calculated in similar way and therefore: dQ = ± 0,24 l/min. Due to the way of calculation, the maximum inaccuracy is quite pessimistic. The inaccuracy of position x is determined by the accuracy of the dial gauge which is ± 0,011 mm.

5. DISCUSSIONS AND CONCLUSIONS

In spite of inaccuracy of the results, the outcome is encouraging. Comparison of force graphs with different supply pressure and pressure differential shows that the triple restriction structure reduces the axial force so that the total force is always smaller than the theoretical axial force of a typical valve. When the valves are closed, the total force is the same, but when the poppet is lifted a bit, the total force in triple restriction valve drops drastically. After opening, the total force reaches zero level as the distance between the shutting parts reaches approximately value of 0,4 mm and then goes to negative. When the valve has reached its open state and the distance between the shutting parts is 0,6 mm, the total force is approximately -5 N with supply pressure of 21,0 MPa and pressure differential of 10,0 MPa (Fig. 8). The theoretical total force in typical seat valve under same conditions is 7 N. The corresponding results with supply pressure of 14,0 MPa and pressure differential of 5,0 MPa are -1,5 N and 3,5 N (Fig. 7). This shows that the force compensation is over 100 %. The results also show that the effect takes place despite the supply pressure or pressure differential.

The second objective was to maintain the flow capacity despite extra restrictions. The flow graphs in figures 7 and 8 show that the simulated flow curve of the developed valve is almost overlapping with the simulated curve of a typical valve. The similarity of simulated flow curves with and without restrictions suggests that CFD-software calculated volume flow as turbulent flow. This is also supported by flow graph in Fig. 9 which suggests that in reality the flow is in transition region. Because the CFD-computed volume flow only correlates with measured results within a magnitude and the difference between simulated and measured curves is 18 % - 20 % for the triple restriction valve, it can not be said reliably that the flow capacity of the developed valve is better than in typical valve. However, it seems that it is not worse.

The static characteristics of the developed valve are as follows. Nominal pressure 21 MPa, flow capacity 10 l/min with pressure differential of 5,0 MPa. Force compensated poppet with movement range of 0,6 mm and diameter of 4,0 mm.

The experimental results represented in this paper indicate that the theory is correct and the axial force can be fully compensated with a special geometry of the seat and the poppet, which makes it possible to construct a valve that has a simple bistable hydraulic part. Theory also suggests that this structure is scalable, so same idea can be used to produce a variety of valves with different size. But as these results only tell the static characteristics, more work is to be done to make the most of this idea.

ACKNOWLEDGEMENT

The research was supported by the Academy of Finland (Grant No. 80411).

REFERENCES

[1] Englesdorf, K., Dunken, P. Entwicklung und erprobung eines zweiwege-miniatursitzventils. O + P: Ölhydraulik und Pneumatik 1980. Vol. 24, No. 4, pp. 293 - 298.

[2] Yousong, S., Yongwu, L., Shanshan, P., Mian, L. & Dinghua, L. A new type of fast-acting on-off valve. Proceedings of the 1st International Symposium on Fluid Power Transmission and Control, Beijing, China. October 13. - 15., 1991. pp. 34 - 37.

[3] Cui, P., Burton, R.T., & Ukrainetz, P.R. Development of a high speed ON/OFF valve. International Off-Highway and Power Plant Congress and Exposition, Milwaukee, Wisconsin, USA. September 9. - 12., 1991. pp. 21 - 25.

[4] Yifei, H., Shuxing, Y., Yu, W. & Fan, C**.** A method of removing the flow force on high speed electric-hydraulic on-off valves. Fluid Power Transmission and Control Proceedings of the 2nd International Conference, Hangzhou, China. 1989. pp. 305 - 307.

[5] Wang, H., Cui, W. Study and improvement of the differential single-stage relief valve's characteristics. Fluid power transmission and control proceedings of the 2nd international conference, Hangzhou, China. 1989. pp. 308 - 310.

[6] Wennmacher, G. Untersuchung und Anwendung schnellschaltender elektrohydraulischer ventile für den einsatz in kraftfahrzeugen. Aachen 1996, Verlag der Augustinus Buchhandlung. 183 p.

[7] Hydac International. Solenoid directional valve SAE8-cartridge – 205 bar: 2/2-normally closed WS08W-01 poppet type - direct operated. http://212.88.134.40/pdf/e5924-1-03-02_ws08w01.pdf 2002. (visited 16.2.2006)

Piloting the Valve Spool by Using a Through Axial Shaft

Dr. Mohamed A. Elgamil

Assistant Professor, Dept. of Mechanical Design & Production
Faculty of Engineering, Cairo University, Giza, EGYPT
hamedeen@yahoo.com

ABSTRACT

In this paper, a method to use a through axial shaft passing through the spool in piloting its position is described. The shaft has helical like grooves, while the spool has through holes in front of these grooves. Turning the shaft about its axis establishes the variation in the control orifice areas between the holes and the grooves, and then connects the pilot pressures at the two spool ends with the supply pressure and/or the tank pressure. Due to the helical like groove shape, the spool movement results in regaining the original control orifice areas values. This response provides a feedback action that makes the spool position follows the shaft turning angle value.

KEYWORDS

Pilot valve, flapper nozzle, jet pipe, static performance, control orifice, downstream orifice, through axial shaft

1. INTRODUCTION

Huge flow forces, inertia forces and other forces compared with the electromagnetic driver capabilities in electrohydraulic valves make the usage of pilot stage valve necessary to control large flow rates. The common pilot valve types used for that purpose are flapper nozzle and jet pipe. These valves are installed away from the driven main spool, therefore the main spool mass, the oil volume trapped between it and the main stage and the performance of the pilot valve itself are important for the valve dynamic response [1 to 8]. Two land spools are simple and small in inertia, but they are unstable and tend to lodge inside large openings [1, 2 and 3]. It was shown how to remedy these problems in [10, 11 and 14]. These references as well as [13] showed that instability forces may be useful in increasing valve speed of response. In this paper, a method to use a through axial shaft passing through the spool in piloting its position is described. The shaft has helical like grooves, while the spool has through holes in front of these grooves. Turning the shaft about its axis establishes the variation in the control orifice areas between the holes and the grooves, and then connects the pilot pressures at the two spool ends with the supply pressure and/or the tank pressure. Due to the helical like groove shape, the spool movement results in regaining the original control orifice areas values. This response provides a feedback action that makes the spool position follow the shaft turning angle value.

Power Transmission and Motion Control 2006 Edited by Dr D N Johnston and Professor K A Edge

One (or two) torque motors could be used to drive the shaft to turn about its axis. This axis has the shaft's lowest second moment of inertia. No extra components to feed the spool position back are needed.

2. TWO LAND SPOOL WITH OPEN CENTER PILOT TYPE

Best design for two land spools is open center type, with continuous pilot flow similar to that in flapper nozzle and jet pipe types. Zero lap designs are also suitable for two land spools; however they make spool shape much more complicated. Zero lap designs are more suitable for three land spools as described later.

Figure (1) shows a cross section in the valve including the spool and the through pilot shaft, while Fig.(2) shows top view of the spool and the through pilot shaft only. All orifices and formed grooves are divided and symmetrically distributed to keep balance. Then the mentioned parameters and variables are the total ones for calculations. The explanation for one group is applicable for the other symmetrical group.

The spool has two symmetrical holes connecting the supply pressure to the pilot shaft. The pilot shaft has two grooves; each connects the control orifice formed by the overlap between the spool hole and the shaft groove helical edge to one spool end side. Turning the pilot shaft about its axis leads to an increase in the control orifice area in the right side and decrease the control orifice area in the left as shown in Fig.(1) and Fig.(2). This establishes a pressure difference between the two sides and hence pushes the spool to the left. The spool movement decreases the control orifice area in the right side and increase the control orifice area in the left till both almost regain their original values and become near to be equal. The deviation will be the sufficient value required to generate the pressure difference that balance the flow forces on the spool. Assume that the flow rates through the control orifices are q_1 & q_3, and the flow rates through the downstream orifices are q_2 & q_4 as shown in Fig.(1), then:

$$q_1 = C_d\, k_1\, a \sqrt{\frac{2(p_s - p_1)}{\rho}} \tag{1}$$

$$q_2 = C_d\, a \sqrt{\frac{2(p_1 - p_T)}{\rho}} \tag{2}$$

$$q_2 = k_{q2/1}\, q_1 \tag{3}$$

$$q_3 = C_d\, k_2\, a \sqrt{\frac{2(p_s - p_2)}{\rho}} \tag{4}$$

$$q_4 = C_d\, a \sqrt{\frac{2(p_2 - p_T)}{\rho}} \tag{5}$$

$$q_4 = k_{q4/3}\, q_3 \tag{6}$$

Where C_d is the discharge coefficient (constant), a is the downstream area (constant), k_1 & k_2 are the ratios between the control orifice areas and the downstream orifice area, k_{q2l1} & k_{q4l3} are the ratios between the flow rates though the downstream orifices and the flow rates through the corresponding control orifices, p_s is the supply pressure, p_T is the tank pressure, and p_1 & p_2 are the pilot pressures.

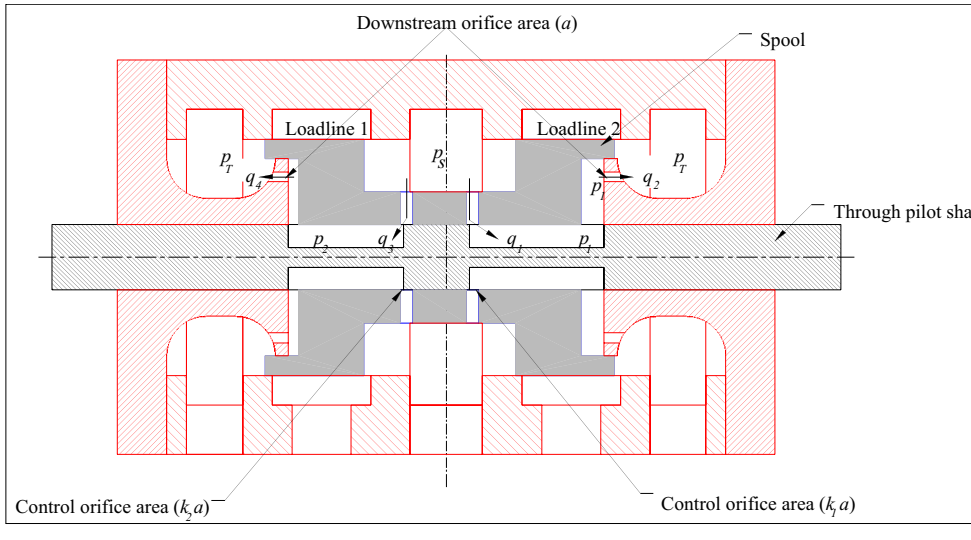

Figure 1: Cross section in two land spool valve with through axial pilot shaft

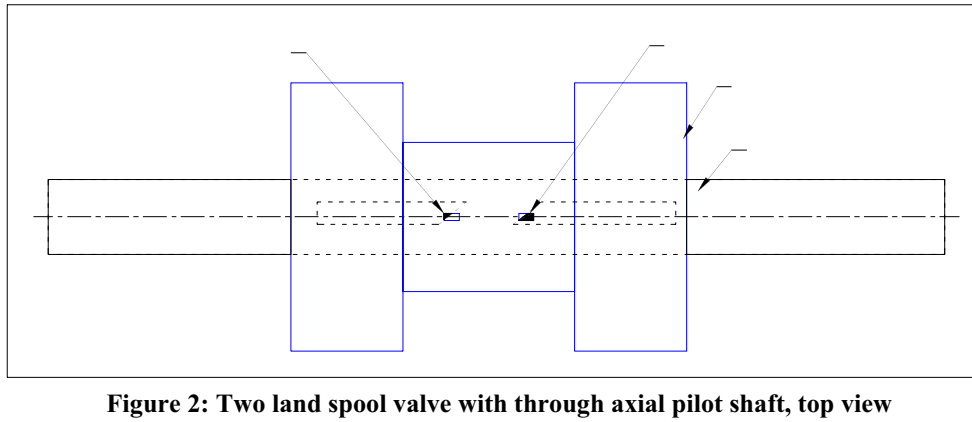

Figure 2: Two land spool valve with through axial pilot shaft, top view

Assuming $(p_T = 0)$, and solving eqns. (1 to 3), it can be shown that:

$$p_1 = \frac{(k_1 k_{q2/1})^2}{1 + (k_1 k_{q2/1})^2} p_s \tag{7}$$

A ratio k_{p1ls} between p_1 and p_s can be defined as:

$$k_{p1/s} = \frac{(k_1 k_{q2/1})^2}{1 + (k_1 k_{q2/1})^2} \tag{8}$$

Similarly, solving eqns. (4 to 6), it can be shown that:

$$p_2 = \frac{(k_2 k_{q3/4})^2}{1 + (k_2 k_{q3/4})^2} p_s \tag{9}$$

and

$$k_{p2/s} = \frac{(k_2 k_{q3/4})^2}{1 + (k_2 k_{q3/4})^2} \tag{10}$$

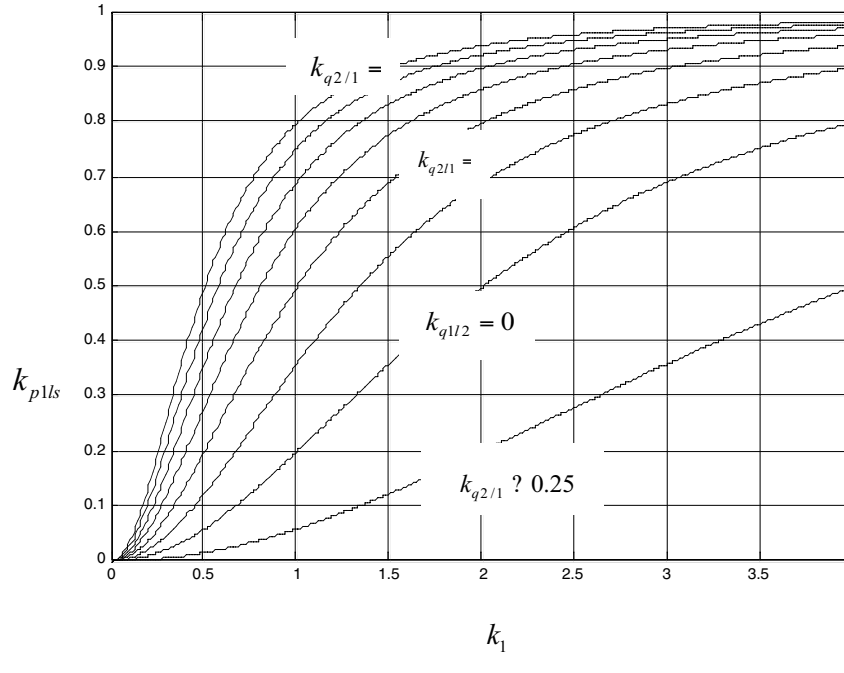

Figure 3: Variation of $k_{p1/s}$ w.r.t. k_1 at various $k_{q2/1}$ values

Figure 3 shows the variation of $k_{p1/s}$ w.r.t. k_1 at various $k_{q2/1}$ values, this relation is also applicable for $k_{p2/s}$ w.r.t. k_2 . For the expansion side (where $k_{q2/1} < 1$) the control orifice area gradient with respect to the input shaft angle should be large enough to provide sufficient flow to displace the spool plus sufficient flow to pass through the downstream orifice while building sufficient pressure at this side. On the other hand, for the contraction side (where $k_{q2/1} > 1$) the control orifice area gradient with respect to the input shaft angle should be designed to permit sufficient reduction in pressure at this side. It may be reasonable to fully close this control orifice when the error between the input and the spool position is large. Thus, it may be concluded that the control orifice area gradient should not necessarily be linear or symmetrical at both sides.

The stand still steady state conditions $(k_{q2/1} = k_{q4/3} = 1)$ is considered to get the largest valve resistance to displacing the spool from its stand still position by any disturbance rather than the input, and to get highest sensitivity to the input, then Eqns.(8 to 10) can be rewritten as:

$$p_1 = \frac{k_1^2}{1 + k_1^2} p_s \tag{11}$$

$$k_{p1/s} = \frac{k_1^2}{1 + k_1^2} \tag{12}$$

$$p_2 = \frac{k_2^2}{1 + k_2^2} p_s \tag{13}$$

$$k_{p2/s} = \frac{k_2^2}{1 + k_2^2} \tag{14}$$

At the largest resistance and sensitivity, $\frac{dk_{p1/s}}{dk_1}$ should be maximum; i.e. $\frac{d^2 k_{p1/s}}{dk_1^2} = 0$.

Then the value of k_1 at idle position should be selected at this value (i.e. k_1= 0.577) or nearby because the value of $dk_{p1/s} / dk_1$ does not vary too much at this value and its vicinity. The maximum value of $dk_{p1/s} / dk_1$ is 0.65. It could be noted that at $k_1 = 3$ the pilot pressure p_1 equals 90% of the supply pressure p_s . The results are shown in Fig.(4).

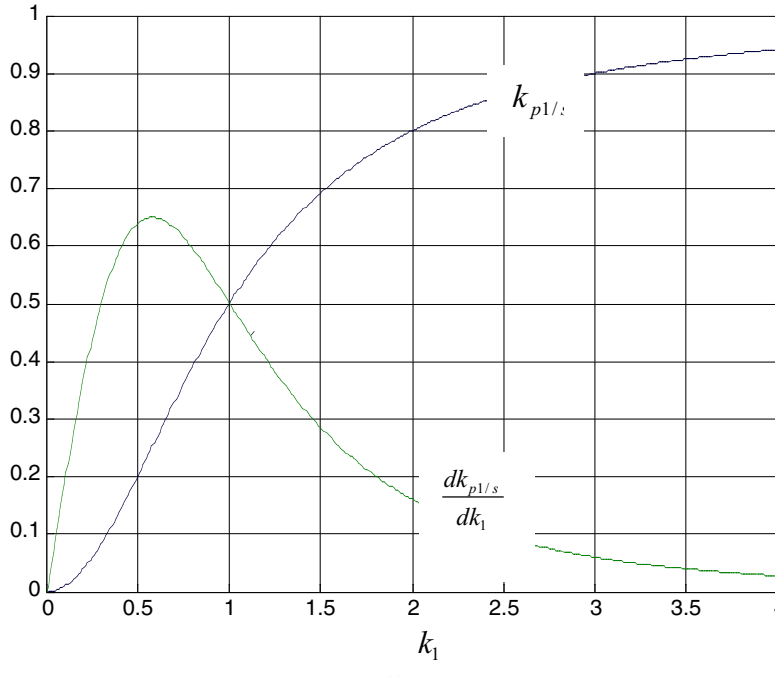

Figure 4: Variation of $k_{p1/s}$ and $\frac{dk_{p1/s}}{dk_1}$ w.r.t. k_1 at stand still steady state conditions

3. THREE LAND SPOOL WITH CLOSED CENTER PILOT TYPE

Closed center design (with proper lapping conditions) may be preferable for the pilot application because of fast pressure and flow response to control orifice area input change. This fast response is due to the absence of downstream orifice. Fast pressure and flow response will be reflected positively on the valve speed of response.

A three land spool is more suited to use closed center design than two land spool because contrary to two land spool, it is subjected to both supply and tank ports along its length. Two land spool is subjected to one of them only along its length, and to accommodate a control orifice with the other, some extensions should be added. This modification is possible, but it will make the design more complicated. Figure (5) shows a cross section of a three land spool valve with through axial pilot shaft. Turning the shaft about its axis will connect one side (right side in this case) with the supply pressure, and simultaneously connect the other side with the tank. In Fig.(5), the flow q_1 enters the right side to increase the oil pressure and volume at the right side, while flow q_2 exits to tank to reduce the oil volume at the left side. This tends to displace the spool to left till the control orifices are closed again. The governing equations are those of closed center valves.

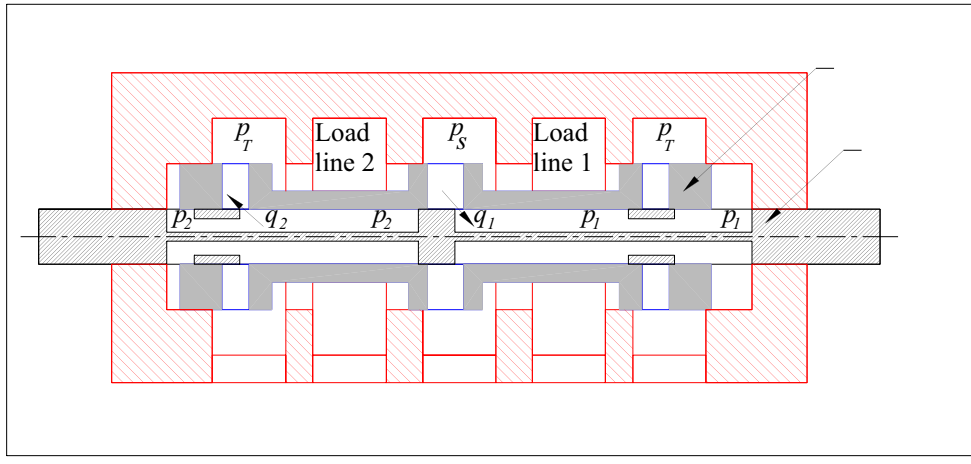

Figure 5: Cross section in three land spool valve with through axial pilot shaft

It should be noted that the spool should not rotate in any case; otherwise it couldn't keep the relative locations between the different openings. To prevent this rotation, the pilot shaft axis could be shifted away from the spool axis.
Four land spools are also suited to use both open center and closed center pilot valve designs; however it is better to use closed center pilot valves design for the reasons mentioned before. Two and three land spools means shorter spools, and hence less spool inertia. Consequently shorter pilot shaft leads to less shaft second moment of inertia and better dynamic performance.

4. CONCLUSION

A method to use a through axial shaft passing through the spool in piloting its position was described. Both open center pilot valves design and closed center pilot valves design are suitable to be used with two land spools and three land spools, however open center designs are more suited to use with two land spools and closed center designs are more suited to use with three or more land spools. Governing equations for open center design were derived and analyzed. It was shown that the ratio between the control orifice area and the downstream orifice area at idle position should be around 0.577. It was shown that the control orifice area gradient should not necessarily be linear or symmetrical at both positive and negative directions.

REFERENCES

[1] Lee, S-Y., and Blackburn, J. F.,1952, "Contributions to hydraulic control 2-transient flow forces and valve instability," ASME Machine Design Division, Vol. 74, pp. 1013-1016.

[2] J. F. Blackburn, G. Reethof, and L. L. Shearer 1960 “Fluid Power Control”, MIT Press, Cambridge, MA.

[3] Hebert E. Merritt, 1967, Hydraulic Control System, Wiley, NY.

[4] D.McCloy and H. R. Martin, 1973, “The Control of Fluid Power Control”, Wiley, NY.

[5] Anthony Esposito, “Fluid Power with Application”. Prentice-Hall International, Inc., 1997.

[6] Frank Yeaple. “Fluid Power Design Handbook”, Marcel Dekker Inc. 1996

[7] M.Borghu, M. Milani, and R. Paoluzzi,"Transient flow force estimation on the pilot stage of a hydraulic valve,"Proceedings of the ASME-IMECE FPST-Fluid Power Systems , Tech., Vol. 5, pp. 157-162, 1998.

[8] D.Wang, R. Dolid, M. Donath, and J. Albright, 1995 "Development and verification of a two-stage flow control servovalve model," Proceedingsof the ASME-IMECE FPST-Fluid Power Systems , Tech., Vol. 2, pp. 121-129.

[9] Funk, J. E., Wood, D.J., and Chao, S. P., 1972, "The transient response of orifices and very short lines," ASME J. Basic Eng.,94, No. 2, pp. 483-491.

[10] Elgamil, M. A. “Investigation of New Hydraulic Control Valves", Ph.D Thesis, Kobe University. Japan 1999.

[11] Elgamil, M. A., & Kanki, H. “New Methods for Flow Force Reduction and Spool Drives in Proportional and Servo Valves”. The 4th International Research/Expert Conference, Zenica’98 October 2-3, 1998. (pp. 26 - 33). University of Sarajevo, Faculty of Mechanical Engineering in Zenica

[12] Martin, D.J., and Burrows, C. R., 1976, "The dynamic characteristics of an electrohydraulic servovalve," ASME J. Dyn.Syst.., Meas., Control, 98, No. 4, pp.395-406.

[13] Kailash Krishnaswamy, Perry Y. Li "On Using Unstable Electrohydraulic Valves for Control" Journal of Dynamic Systems, Measurment, and Control MARCH 2002 Vol. 124

[14] Elgamil, M. A., & Kanki, H. “Sliding fluid valve with low sensitivity to flow forces”, Egyptian Research Academy – Patent app. no. 1198/97 on 12/11/1997, Patent no. 21968 on 8/5/2002.

[15] Elgamil, M. A.“ Hydraulic pool valve with rectified jet angle, and hybrid valves and their drives”, Egyptian Research Academy – Patent app. no. 190/98 on 17/2/1998, Patent no. 21969 on 8/5/2002.

Authors' Index

Power Transmission and Motion Control 2006 Edited by Dr D N Johnston and Professor K A Edge

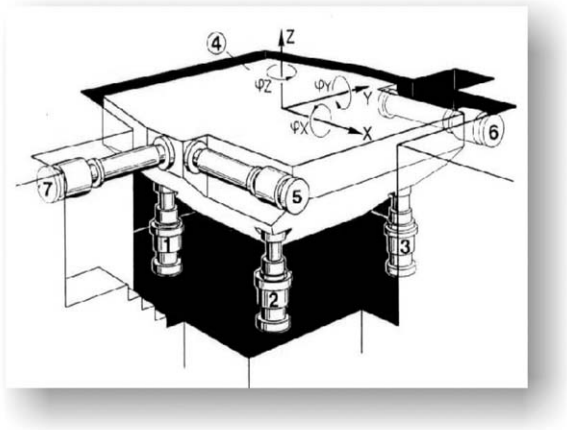

Power Transmission and Motion Control (PTMC) 2006 comprises 29 papers presented at PTMC 2006 – one of a series of annual International Symposia held at the University of Bath. This collection of papers reports on the latest research in the fields of hydraulic and pneumatic moion control worldwide.

Topics include:

- Control
- Energy efficiency and the environment
- Fluid dynamics and noise
- Hydraulic fluids, including water and ‘smart’ fluids
- Sensors and testing
- Drives, transmissions and actuators
- Hydraulic and pneumatic components and systems
- Modelling and simulation
- Fault analysis and diagnosis
- Off-road, marine and industrial applications

This volume will be of particular interest to researchers and practitioners working in the fields of power transmission, motion control, hydraulics and pneumatics.

ISBN 08-6197-135-3
9 780861 971350